AD-738 841

THE TRAPPED RADIATION HANDBOOK

JOHN B. CLADIS, ET AL

LOCKHEED PALO ALTO RESEARCH LABORATORY
PALO ALTO, CALIFORNIA

DECEMBER 1971

BEST SELLERS

FROM
NATIONAL
TECHNICAL
INFORMATION
SERVICE

Comparison of Energy Consumption Between West Germany and the United States
PB-245 652/ PAT 112 p. PC$5.50/MF$3.00

A Comprehensive Policy to Ameliorate Adverse Impacts of Transportation Facilities
PB-247 823/ PAT 138 p. PC$6.00/MF$3.00

A Comprehensive Policy to Ameliorate Adverse Impacts of Transporation Facilities, Appendix
PB-247 824/ PAT 310 p. PC$9.75/MF$3.00

Demand for Coal for Electricity Generation 1975–1984
PB-245 216/ PAT • 40 p. PC$4.00/MF$3.00

A National Study of Adolescent Drinking Behavior, Attitudes and Correlates
PB-246 002/ PAT 405 p. PC$11.00/MF$3.00

Energy from Coal: Guidelines for the Preparation of Environmental Impact Statements
PB-242 960/ PAT 258 p. PC$9.00/MF$3.00

Energy Versus the Environment: The Issues
PB-246 382/ PAT 35 p. PC$4.00/MF$3.00

Improving the Dissemination of Scientific and Technical Information: A Practitioner's Guide to Innovation
PB-247 057/ PAT 203 p. PC$7.75/MF$3.00

Investigation and Evaluation of Cracking in Austenitic Stainless Steel Piping of Boiling Water Reactor Plants
PB-246 645/ PAT 123 p. PC$5.50/MF$3.00

Pipeline Industry's Practices Using Plastic Pipe in Gas Pipeline Facilities and the Resulting Safety Factors
PB-247 301/ PAT 436 p. PC$11.75/MF$3.00

NOx Combustion Control Methods and Costs for Stationary Sources. Summary Study.
PB-246 750/ PAT 117 p. PC$5.50/MF$3.00

Reactor Safety Study: An Assessment of Accident Risks in U.S. Commercial Nuclear Power Plants
PB-248 200/SET/ PAT 2,504 p. 8 Volumes PC$61.00

Report on Sulfur Oxide Control Technology
PB-246 667/ PAT 89 p. PC$5.00/MF$3.00

Research Evaluation of a System of Natural Air Conditioning
PB-243 496/ PAT 364 p. PC$10.50/MF$3.00

Retrofitting a Residence for Solar Heating and Cooling: The Design and Construction of the System
PB-247 482/ PAT 101 p. PC$5.50/MF$3.00

Saudi Arabia Five-Year Plan, 1975–1980
PB-246 572/ PAT 683 p. PC$16.25/MF$3.00

Shotcrete Practice in Underground Construction
PB-248 765/ PAT 501 p. PC$12.75/MF$3.00

Short-Term Coal Forecast, 1975–1980
PB-247 073/ PAT 120 p. PC$5.50/MF$3.00

State Energy Information Systems: A Survey
PB-247 457/ PAT 64 p. PC$4.50/MF$3.00

A Study of Fixed Capital Requirements of the U.S. Business Economy
PB-248 690/ PAT 84 p. PC$5.00/MF$3.00

Sulfates and the Environment—A Review
PB-248 122/ PAT 155 p. PC$8.75/MF$3.00

HOW TO ORDER

When you indicate the method of payment, please note if a purchase order is not accompanied by payment, you will be billed an addition $5.00 *ship and bill* charge. And please include the card expiration date when using American Express.

Normal delivery time takes three to five weeks. It is vital that you order by number or your order will be manually filled, insuring a delay. You can opt for *airmail delivery* for a $2.00 charge per item. Just check the *Airmail Service* box. If you're really pressed for time, call the NTIS Rush Order Service. (703) 557-4700. For a $10.00 charge per item, your order will be airmailed within 48 hours. Or, you can pick up your order in the Washington Information Center & Bookstore or at our Springfield Operations Center within 24 hours for a $6.00 per item charge.

You may also place your order by telephone or TELEX. The order desk number is (703) 557-4650 and the TELEX number is 89-9405.

Whenever a foreign sales price is NOT specified in the listings, all foreign buyers must add the following charges to each order: $2.50 for each paper copy; $1.50 for each microfiche; and $10.00 for each Published Search.

Thank you for your interest in NTIS. We appreciate your order.

METHOD OF PAYMENT

☐ Charge my NTIS deposit account no._____

☐ Purchase order no._____

☐ Check enclosed for $_____

☐ Charge to my American Express Card account number

Card expiration date_____

Signature_____

☐ Airmail Services requested

NAME_____

ADDRESS_____

CITY. STATE. ZIP_____

Item Number	Quantity		Unit Price*	Total Price*
	Paper Copy (PC)	Microfiche (MF)		
			Sub Total	
			Additional Charge	
			Enter Grand Total	

*All Prices Subject to Change
8/76

Clip and mail to:

NTIS

National Technical Information Service
U.S. DEPARTMENT OF COMMERCE
Springfield, Va. 22161
(703) 557-4650 TELEX 89-9405

AD-738841

DNA 2524H

THE TRAPPED RADIATION HANDBOOK

Compilers and Editors-in-Chief:

John B. Cladis
Gerald T. Davidson
Lester L. Newkirk

December 1971

Project Officer: Dr. Charles A. Blank

Published by:

General Electric Company, TEMPO
DNA Information and Analysis Center
816 State Street
Santa Barbara, California 92103

For Defense Nuclear Agency
Under Contract DA-49-146-XZ-570

This publication was sponsored under NWER Subtask HC047,
Work Unit No. 02

Includes Changes 1 and 2

ACKNOWLEDGMENTS

The Defense Nuclear Agency sincerely appreciates the contributions of these people to the publication and contents of this handbook:

Mr. A.D. Anderson	Lockheed Palo Alto Research Laboratory
Dr. C.A. Blank	HQ, Defense Nuclear Agency
Dr. J.B. Cladis	Lockheed Palo Alto Research Laboratory
Mr. D.L. Crowther	Lockheed Palo Alto Research Laboratory
Dr. G.T. Davidson	Lockheed Palo Alto Research Laboratory
Dr. J.F. Fennell	St. Louis University
Mr. W.E. Francis	Lockheed Palo Alto Research Laboratory
Dr. J.A. George	St. Louis University
Mr. W.H. Harless, Jr.	Lockheed Palo Alto Research Laboratory
Dr. R.W. Hendrick, Jr.	General Electric Company—TEMPO
Dr. J.L. Hickerson	St. Louis University
Dr. R.T. Hoverter	St. Louis University
Dr. C.H. Humphrey	Lockheed Palo Alto Research Laboratory
Dr. G.V. Maldonado	St. Louis University
Dr. D.J. Manson	St. Louis University
Dr. B.M. McCormac	Lockheed Palo Alto Research Laboratory
Dr. G.H. Nakano	Lockheed Palo Alto Research Laboratory
Dr. L.L. Newkirk	Lockheed Palo Alto Research Laboratory
Dr. S.L. Ossakow	Lockheed Palo Alto Research Laboratory
Dr. A.M. Peterson	Stanford Research Institute
Mr. F.H. Sage, III	General Electric Company—TEMPO
Dr. J.F. Vesecky	Stanford Research Institute
Dr. J.I. Vette	NASA—Goddard Space Flight Center
Dr. M. Walt	Lockheed Palo Alto Research Laboratory
Dr. A.H. Weber	St. Louis University

Unclassified

Security Classification

DOCUMENT CONTROL DATA - R&D

(Security classification of title, body of abstract and indexing annotation must be entered when the overall report is classified)

1. ORIGINATING ACTIVITY (Corporate author) Lockheed Palo Alto Research Laboratory Lockheed Missiles & Space Company Palo Alto, California 94304	2a. REPORT SECURITY CLASSIFICATION Unclassified 2b. GROUP

3. REPORT TITLE

The Trapped Radiation Handbook

4. DESCRIPTIVE NOTES (Type of report and inclusive dates)

Handbook of Trapped Radiation, January 1968—June 1970

5. AUTHOR(S) (Last name, first name, initial)

Editors: John B. Cladis, Gerald T. Davidson, and Lester L. Newkirk

6. REPORT DATE	7a. TOTAL NO. OF PAGES	7b. NO. OF REFS
December 1971	732	599

8a. CONTRACT OR GRANT NO.	9a. ORIGINATOR'S REPORT NUMBER(S)
DA-49-146-XZ-570 b. PROJECT NO. NWER XAXH c. Task and Subtask CO47 d. Work Unit 02	LMSC/695953 9b. OTHER REPORT NO(S) (Any other numbers that may be assigned this report) DNA 2524H

10. AVAILABILITY/LIMITATION NOTICES

Each transmittal of this document outside the agencies of the U.S. Government must have prior approval of Director, Defense Atomic Support Agency, Washington, D. C.

11. SUPPLEMENTARY NOTES	12. SPONSORING MILITARY ACTIVITY
PRICES SUBJECT TO CHANGE	Director Defense Nuclear Agency Washington, D. C. 20305

13. ABSTRACT

The Trapped Radiation Handbook provides useful information and design data for scientists and engineers engaged in the design of spacecraft systems that must operate in the trapped radiation environment. It contains not only a compilation of useful charts and graphs but also abbreviated derivations of equations and developments of concepts in a wide range of subject matter pertinent to the radiation belts. It is intended to be helpful to scientists who are beginning studies or research in this field as well as to scientists who are actively engaged in magnetospheric research. These subjects are discussed: The Magnetosphere; Features and Mathematical Models of the Earth's Magnetic Field; The Motion of Charged Particles in the Field; The Properties of the Particles in the Natural Radiation Belts; Source and Loss Mechanisms; The Artificial Radiation Belts that have resulted from tests of nuclear devices conducted at high altitudes; The Phenomenology of Nuclear Detonations and Beta Injection Processes; The Effects of Trapped Particles—Both Natural and Fission Betas—on Materials and Devices: The Irradiation of Circular Orbit Satellites by Trapped Particles of (1) the natural environment, (2) environments produced by weapon tests at various L-values, and (3) an estimated wartime environment; The Synchrotron Radiation Emitted by the Trapped Electrons; and the Vulnerability of Operational Systems in the Environments (1), (2), and (3) mentioned previously.

DD FORM 1 JAN 64 1473

Unclassified

Security Classification

Unclassified

Security Classification

14. KEY WORDS	LINK A		LINK B		LINK C	
	ROLE	WT	ROLE	WT	ROLE	WT
Trapped Radiation Handbook						
Description of Trapped Particles						
Artificial Radiation Belts						
Trapped Radiation Effects						
Synchrotron Radiation						
Trapped Radiation Doses						
Vulnerability of Systems to Trapped Particles						
Trapped Particles injected by Nuclear Devices						

INSTRUCTIONS

1. **ORIGINATING ACTIVITY:** Enter the name and address of the contractor, subcontractor, grantee, Department of Defense activity or other organization *(corporate author)* issuing the report.

2a. **REPORT SECURITY CLASSIFICATION:** Enter the overall security classification of the report. Indicate whether "Restricted Data" is included. Marking is to be in accordance with appropriate security regulations.

2b. **GROUP:** Automatic downgrading is specified in DoD Directive 5200.10 and Armed Forces Industrial Manual. Enter the group number. Also, when applicable, show that optional markings have been used for Group 3 and Group 4 as authorized.

3. **REPORT TITLE:** Enter the complete report title in all capital letters. Titles in all cases should be unclassified. If a meaningful title cannot be selected without classification, show title classification in all capitals in parenthesis immediately following the title.

4. **DESCRIPTIVE NOTES:** If appropriate, enter the type of report, e.g., interim, progress, summary, annual, or final. Give the inclusive dates when a specific reporting period is covered.

5. **AUTHOR(S):** Enter the name(s) of author(s) as shown on or in the report. Enter last name, first name, middle initial. If military, show rank and branch of service. The name of the principal author is an absolute minimum requirement.

6. **REPORT DATE:** Enter the date of the report as day, month, year; or month, year. If more than one date appears on the report, use date of publication.

7a. **TOTAL NUMBER OF PAGES:** The total page count should follow normal pagination procedures, i.e., enter the number of pages containing information.

7b. **NUMBER OF REFERENCES:** Enter the total number of references cited in the report.

8a. **CONTRACT OR GRANT NUMBER:** If appropriate, enter the applicable number of the contract or grant under which the report was written.

8b, 8c, & 8d. **PROJECT NUMBER:** Enter the appropriate military department identification, such as project number, subproject number, system numbers, task number, etc.

9a. **ORIGINATOR'S REPORT NUMBER(S):** Enter the official report number by which the document will be identified and controlled by the originating activity. This number must be unique to this report.

9b. **OTHER REPORT NUMBER(S):** If the report has been assigned any other report numbers *(either by the originator or by the sponsor)*, also enter this number(s).

10. **AVAILABILITY/LIMITATION NOTICES:** Enter any limitations on further dissemination of the report, other than those imposed by security classification, using standard statements such as:

(1) "Qualified requesters may obtain copies of this report from DDC."

(2) "Foreign announcement and dissemination of this report by DDC is not authorized."

(3) "U. S. Government agencies may obtain copies of this report directly from DDC. Other qualified DDC users shall request through _____."

(4) "U. S. military agencies may obtain copies of this report directly from DDC. Other qualified users shall request through _____."

(5) "All distribution of this report is controlled. Qualified DDC users shall request through _____."

If the report has been furnished to the Office of Technical Services, Department of Commerce, for sale to the public, indicate this fact and enter the price, if known.

11. **SUPPLEMENTARY NOTES:** Use for additional explanatory notes.

12. **SPONSORING MILITARY ACTIVITY:** Enter the name of the departmental project office or laboratory sponsoring *(paying for)* the research and development. Include address.

13. **ABSTRACT:** Enter an abstract giving a brief and factual summary of the document indicative of the report, even though it may also appear elsewhere in the body of the technical report. If additional space is required, a continuation sheet shall be attached.

It is highly desirable that the abstract of classified reports be unclassified. Each paragraph of the abstract shall end with an indication of the military security classification of the information in the paragraph, represented as *(TS), (S), (C), or (U)*.

There is no limitation on the length of the abstract. However, the suggested length is from 150 to 225 words.

14. **KEY WORDS:** Key words are technically meaningful terms or short phrases that characterize a report and may be used as index entries for cataloging the report. Key words must be selected so that no security classification is required. Identifiers, such as equipment model designation, trade name, military project code name, geographic location, may be used as key words but will be followed by an indication of technical context. The assignment of links, rules, and weights is optional.

1a

Unclassified

Security Classification

DNA 2524H
Change 1

THE TRAPPED RADIATION HANDBOOK

Compilers and Editors-in-Chief:

John B. Cladis
Gerald T. Davidson
Lester L. Newkirk

Revised
2 January 1973

Project Officer: Dr. Charles A. Blank

Published by:

General Electric Company, TEMPO
DNA Information and Analysis Center
816 State Street
Santa Barbara, California 92103

For Defense Nuclear Agency
Under Contract DA-49-146-XZ-570

This publication was sponsored under NWER Subtask HE017,
Work Unit No. 08

2 January 1973

LIST OF EFFECTIVE PAGES

Title Page	Last Change
Title Page	2 January 1973
ii	2 January 1973
iii thru iv	Original
v thru viii	2 January 1973
ix thru xxxvi	Original
1-1 thru 1-22	Original
2-1 thru 2-6	Original
2-7 thru 2-8	2 January 1973
2-9 thru 2-10	Original
2-11 thru 2-12	2 January 1973
2-13 thru 2-32	Original
2-33 thru 2-34	2 January 1973
2-35 thru 2-66	Original
3-1 thru 3-6	Original
3-7 thru 3-8	2 January 1973
3-9 thru 3-98	Original
4-1 thru 4-88	Original
5-1 thru 5-8	Original
5-9 thru 5-12	2 January 1973
5-13 thru 5-44	Original
5-45 thru 5-46	2 January 1973
5-47 thru 5-100	Original
6-1 thru 6-60	Original
7-1 thru 7-30	Original
8-1 thru 8-2	2 January 1973
8-3 thru 8-80	Original
8-81 thru 8-82	2 January 1973
8-83 thru 8-90	Original
9-1 thru 9-36	Original
10-1 thru 10-9	Original
11-1 thru 11-34	Original
11-35 thru 11-36	2 January 1973
11-37 thru 11-60	Original
12-1 thru 12-6	Original
13-1 thru 13-20	Original
14-1 thru 14-2	Original
14-3 thru 14-4	2 January 1973
15-1 thru 15-16	Original

DNA 2524H
Change 2

THE TRAPPED RADIATION HANDBOOK

Compilers and Editors-in-Chief:

John B. Cladis
Gerald T. Davidson
Lester L. Newkirk

Revised
1 November 1973

Project Officer: Dr. Charles A. Blank

Prepared for:
Defense Nuclear Agency
Washington, D.C. 20305
by Lockheed Palo Alto Research Laboratory
Under Contract DNA 001-73-C-0065
NWER Subtask HC047-08

Published by:
DASIAC
General Electric Company—TEMPO
Santa Barbara, California 93102
Under Contract DNA 001-74-C-0014
NWED Subtask DC001-08

1b

1 November 1973

RECORD OF REVISIONS

Revision No.	Date of Issue	Date of Receipt	Entered By

LIST OF EFFECTIVE PAGES

Page	Last Change
Title Page	1 November 1973
ii	1 November 1973
iii thru xxxviii	1 November 1973
1-1 thru 1-22	Original
2-1 thru 2-6	Original
2-7 thru 2-8	2 January 1973
2-9 thru 2-10	Original
2-11 thru 2-12	2 January 1973
2-13 thru 2-32	Original
2-33 thru 2-34	2 January 1973
2-35 thru 2-66	Original
3-1 thru 3-6	Original
3-7 thru 3-8	2 January 1973
3-9 thru 3-98	Original
4-1 thru 4-88	Original
5-1 thru 5-8	Original
5-9 thru 5-12	2 January 1973
5-13 thru 5-44	Original
5-45 thru 5-46	2 January 1973
5-47 thru 5-100	Original
6-1 thru 6-60	Original
7-1 thru 7-30	Original
8-1 thru 8-2	1 November 1973
8-3 thru 8-4	Original
8-5 thru 8-6	1 November 1973
8-7 thru 8-12	Original
8-13 thru 8-35	1 November 1973
8-35A thru 8-35D	1 November 1973
8-36	1 November 1973
8-37 thru 8-80	Original
8-81 thru 8-82	2 January 1973
8-83 thru 8-84	Original
8-85 thru 8-86	1 November 1973
8-87 thru 8-88	Original
8-89 thru 8-90	1 November 1973
9-1 thru 9-36	Original
10-1 thru 10-9	Original
11-1 thru 11-34	Original
11-35 thru 11-36	2 January 1973
11-37 thru 11-60	Original
12-1 thru 12-6	Original
13-1 thru 13-20	Original
14-1 thru 14-2	Original
14-3 thru 14-4	2 January 1973
15-1 thru 15-16	Original
D1 thru D8	1 November 1973

ACKNOWLEDGMENTS

The Defense Nuclear Agency sincerely appreciates the contributions of these people to the publication and contents of this Handbook:

Mr. A.D. Anderson	Lockheed Palo Alto Research Laboratory
Dr. C.A. Blank	HQ, Defense Nuclear Agency
Dr. J.B. Cladis	Lockheed Palo Alto Research Laboratory
Mr. D.L. Crowther	Lockheed Palo Alto Research Laboratory
Dr. G.T. Davidson	Lockheed Palo Alto Research Laboratory
Dr. J.F. Fennell	St. Louis University
Mr. W.E. Francis	Lockheed Palo Alto Research Laboratory
Dr. J.A. George	St. Louis University
Mr. W.H. Harless, Jr.	Lockheed Palo Alto Research Laboratory
Dr. R.W. Hendrick, Jr.	General Electric Company—TEMPO
Dr. J.L. Hickerson	St. Louis University
Dr. R.T. Hoverter	St. Louis University
Dr. C.H. Humphrey	Lockheed Palo Alto Research Laboratory
Maj. S. Kennedy	HQ, Defense Nuclear Agency
Dr. G.V. Maldonado	St. Louis University
Dr. D.J. Manson	St. Louis University
Dr. B.M. McCormac	Lockheed Palo Alto Research Laboratory
Dr. G.H. Nakano	Lockheed Palo Alto Research Laboratory
Dr. L.L. Newkirk	Lockheed Palo Alto Research Laboratory
Dr. S.L. Ossakow	Lockheed Palo Alto Research Laboratory
Dr. A.M. Peterson	Stanford Research Institute
Mr. F.H. Sage, III	General Electric Company—TEMPO
Mr. J.W. Schallau	Lockheed Palo Alto Research Laboratory
Dr. J.F. Vesecky	Stanford Research Institute
Dr. J.I. Vette	NASA—Goddard Space Flight Center
Dr. M. Walt	Lockheed Palo Alto Research Laboratory
Dr. A.H. Weber	St. Louis University

PREFACE

The Trapped Radiation Handbook was compiled at the request of DNA to provide useful information and design data for scientists and engineers engaged in the design of spacecraft systems that must operate in the trapped radiation environment. The Handbook originally was conceived as a concise volume of easily located and assimilated facts. It was soon realized, however, that much of the fundamental material is not readily accessible to users of this book. Therefore, the final product consists of more than a compilation of useful facts; it contains abbreviated, but essentially complete, derivations of equations and developments of concepts in a wide range of subject matter pertinent to the radiation belts.

In its present form, the Handbook also should serve as a valuable initial reference for scientists who are beginning studies or research in this field. Moreover, space scientists who are engaged actively in magnetospheric research will find numerous charts and graphs that will be useful in their everyday work. For these scientists, the derivational material will not delay access to the needed information because mot of the useful data are contained in figures that are grouped in specified locations, accompanied by sufficient explanatory information that reference to the text is unnecessary. Note, however, that research on the radiation belts and related subjects is progressing so rapidly that some of the data presented here will be soon out of date.

The first four sections are introductory: Sections 1 through 3 provide the fundamental physics and Section 4 is a description of the observational aspects of the natural trapped radiation belts. A brief description of the magnetosphere and phenomena affecting trapped particles is given in Section 1. Section 2 gives a description of the pertinent features of the geomagnetic field. Mathematical models of the field are discussed and many graphs and useful quantities are assembled in an appendix of that section. The motion of charged particles in the geomagnetic field and the development of the

adiabatic invariants of the motion are described in Section 3. A compilation of charts and graphs related to various parameters of the particle motion is provided in the appendix of that section. Section 4 describes the temporal, spatial, and energy distributions of the trapped particles in the natural radiation belts.

Sections 5, 6, and 7 are concerned with the process of formation of the natural and artificial radiation belts. Section 5 treats the basic physical mechanisms: source and loss processes, plasma instabilities, particle diffusion, wave particle interactions, acceleration processes, and magnetospheric convection. Section 6 is a description of the artificial radiation belts that have resulted from U.S. and Russian high-altitude weapon tests. Included in that section are the electron inventories for the Argus tests, the Teak and Orange detonations, Starfish, and the three Russian tests of 1962. Section 7 describes the way in which electrons are injected by a nuclear detonation. It discusses the phenomenology of nuclear detonations, injection processes, the flux in the beta tube, and the diminution of the flux due to atmospheric absorption and eastward-drift motion of the trapped electrons.

The next three sections are concerned principally with the effects of the trapped radiation environment on spacecraft systems. Section 8 considers the radiation effects of the particles—both natural and fission betas—on materials and devices. The fluxes are integrated along circular satellite orbits and are converted to daily doses or equivalent 1-MeV electron fluences that are received through various shielding thicknesses. The results are presented as a function of the altitude of the orbit for various orbit inclinations and for environments due to (1) the natural protons and electrons, (2) the betas injected by single nuclear detonations at certain L-values, and (3) the maximum beta flux expected from multiple bursts. Section 9 treats the synchrotron radiation that is emitted by the trapped electrons due to their spiraling motions around the geomagnetic field lines. Section 10 discusses the vulnerability of operational systems to the natural radiation and to the weapon-test and wartime environments of trapped and untrapped betas. A reader who is seeking information on the effects of these environments on a spacecraft system would be advised to turn to that section first. References are given to pertinent information provided in the preceding sections.

Section 11 contains useful information on these auxiliary topics: (1) techniques of trapped radiation measurements, (2) fission physics,

(3) the earth's atmosphere and ionosphere, (4) a compilation of available computer programs related to trapped radiation, and (5) some statistical data and information on satellites that have been launched into earth orbits. Section 12 presents a brief summary of progress that has been made in the investigation of the radiation belts and discusses some remaining problems. Section 13 is a glossary of symbols. Section 14 gives useful constants and conversion factors. A subject index follows.

An extensive work of this magnitude would not have been possible without the aid of many people whose contribution we wish to acknowledge. In addition to the authors cited directly, we wish to thank Dr. Gerhardt Haerendel and Dr. Carl-Gunne Fälthammar who reviewed Sections 3 and 5 and offered many helpful comments that improved those sections. Mr. William E. Francis and Dr. Sidney L. Ossakow prepared several graphs and tables and also checked and proofread the numerous equations appearing in the Handbook. We are grateful to Mr. Edward A. Wegner and his group of artists and draftsmen for the quality and workmanship of the finished drawings and graphs. Finally, special thanks are due Mrs. Caroline Toyota who was responsible for typing most of the manuscript and who displayed considerable patience in typing the numerous revisions to the text that were required while the manuscript was being prepared. The effort was conducted under the general direction of Dr. Martin Walt.

Despite the great care taken to prevent errors, the authors realized that they will occur in an effort of this magnitude. We would therefore appreciate that the DNA Project Officer, Dr. C. A. Blank (Mail Code RAAE), be notified of errors that are found so that corrections may be made in future revisions of the Handbook. Suggestions for alterations and additions that would improve the helpfulness of the Handbook also would be appreciated.

John B. Cladis
Gerald T. Davidson
Lester L. Newkirk

Lockheed Palo Alto Research Laboratory

June 1970

CONTENTS

SECTION 5

SECTION 6

SECTION 7

SECTION 8

SECTION 9

SECTION 10

SECTION 11

SECTION 12

SECTION 13

SECTION 14

SECTION 15

ILLUSTRATIONS

TABLES

Preceding page blank

AUTHORS

Section 1. John B. Cladis, Lockheed Palo Alto Research Laboratory.

Section 2. Lester L. Newkirk, Lockheed Palo Alto Research Laboratory.

Section 3. Gerald T. Davidson, Lockheed Palo Alto Research Laboratory.

Section 4. James L. Vette, NASA—Goddard Space Flight Center.

Section 5. Gerald T. Davidson, Lockheed Palo Alto Research Laboratory

Section 6. Martin Walt, Lockheed Palo Alto Research Laboratory.

Section 7. Gerald T. Davidson, Lockheed Palo Alto Research Laboratory, and Roy W. Hendrick, Jr., General Electric—TEMPO.

Section 8. David L. Crowther, William H. Harless, Jr., and J.W. Schallau, Lockheed Palo Alto Research Laboratory.

Section 9. A.M. Peterson and J.F. Vesecky, Stanford Research Institute.

Section 10. John B. Cladis and Billy M. McCormac, Lockheed Palo Alto Research Laboratory.

Section 11. "Supplementary Topics:"

Section 11.1. George H. Nakano, Lockheed Palo Alto Research Laboratory.

Section 11.2. Charles H. Humphrey, Lockheed Palo Alto Research Laboratory.

Section 11.3. Albert D. Anderson, Lockheed Palo Alto Research Laboratory.

Section 11.4. Fred H. Sage, III, General Electric—TEMPO.

Section 11.5. Lester L. Newkirk, Lockheed Palo Alto Research Laboratory.

Section 12. John B. Cladis, Lockheed Palo Alto Research Laboratory.

SECTION 1

THE MAGNETOSPHERE

J.B. Cladis, Lockheed Palo Alto Research Laboratory

1.1 INTRODUCTION

The magnetosphere is that region above the earth where the geomagnetic field has an important role in physical processes. The lower boundary is the ionosphere, and the outer boundary is the magnetopause—the interface between the geomagnetic field and the solar plasma. A short description is given in this section of the magnetosphere and of some physical processes that affect trapped particles. This section, therefore, provides a "setting" for the radiation belts and defines terms and features that are used repeatedly in succeeding sections. The discussion begins with the environment in interplanetary space and generally proceeds inward toward the earth's surface.

1.2 CONDITIONS IN INTERPLANETARY SPACE

1.2.1 The Solar Wind

The solar wind is the plasma that continuously streams radially outward from the sun. It consists of protons, electrons, and a small fraction (about 4 percent) of alpha particles in proportions that preserve the electrical neutrality. The number density varies from about 3 to 30 protons per cubic centimeter, the proton temperature varies from about 10^4 to 10^6 °K, and the streaming velocity varies from about 250 to 800 kilometers per second (References 1 and 2). Since the streaming velocity is much greater than the thermal velocity, the flow is supersonic. The flow often is referred to as being super-Alfvénic since the streaming velocity is greater than the Alfvén velocity (the velocity of hydromagnetic waves).

1.2.2 The Interplanetary Magnetic Field

The solar magnetic field is imbedded in the interplanetary plasma. In the vicinity of the earth, the field intensity varies from about 2 to 7 gammas (1 gamma = 10^{-5} gauss). The direction of the field

varies considerably, but, on the average, the magnetic field lines are in the configuration of an Archimedes spiral (Figure 1-1). This pattern of the field was predicted by Parker (Reference 3) and is due to the combination of the rotation of the sun and the "stretching out" of the field lines by the radial flow of the plasma. Therefore, the spiral angle is dependent on the streaming velocity of the plasma. In the vicinity of the earth, the spiral usually makes an angle of about 45 degrees with the sun-earth line. The direction of the interplanetary field along the spiral is away from the sun in certain sectors and toward the sun in other sectors. This sector structure rotates with the sun and has been found to remain essentially constant over several rotations of the sun (Reference 4). In Figure 1-1, the plus signs (away from the sun) and minus signs (toward the sun) at the circumference of the figure indicate the direction of the measured interplanetary magnetic field during successive 3-hour intervals. Parentheses around a plus or a minus sign indicate a time during which the field direction has moved beyond the "allowed regions" (Figure 2 of Reference 4) for a few hours in a smooth and continuous manner. The inner portion of the figure is a schematic representation of a sector structure of the interplanetary magnetic field that is suggested by these observations.

1.2.3 Conditions in Interplanetary Sectors

The solar wind parameters are shown to vary in a fairly regular manner as a sector width moves across the vicinity of the earth (Reference 5). Generally the streaming velocity of the plasma and the magnetic field intensity have moderate values near the beginning of a sector, rise to their maximum values within a few days, and decrease to low values near the end of the sector. The number density behaves somewhat differently by increasing more sharply to a maximum value (within a day after the beginning of a sector), decreasing to a broad minimum near the center of the sector, and increasing again toward the end of the sector.

1.3 INTERACTION OF SOLAR WIND WITH GEOMAGNETIC FIELD

1.3.1 The Magnetopause

The earth's magnetic field presents an obstacle to the solar wind. The interplanetary field does not impede appreciably the solar plasma because the frontal pressure of the solar stream, $1/2\ nmV^2$, is much greater than the pressure of the magnetic field, $B^2/8\pi$ (n is the number density in protons per cubic centimeter, m is the proton mass in grams, V is the streaming velocity in centimeters per second, and B is the magnetic field intensity in gauss (Section 5.4.1). Therefore, the solar plasma carries the interplanetary field along in its

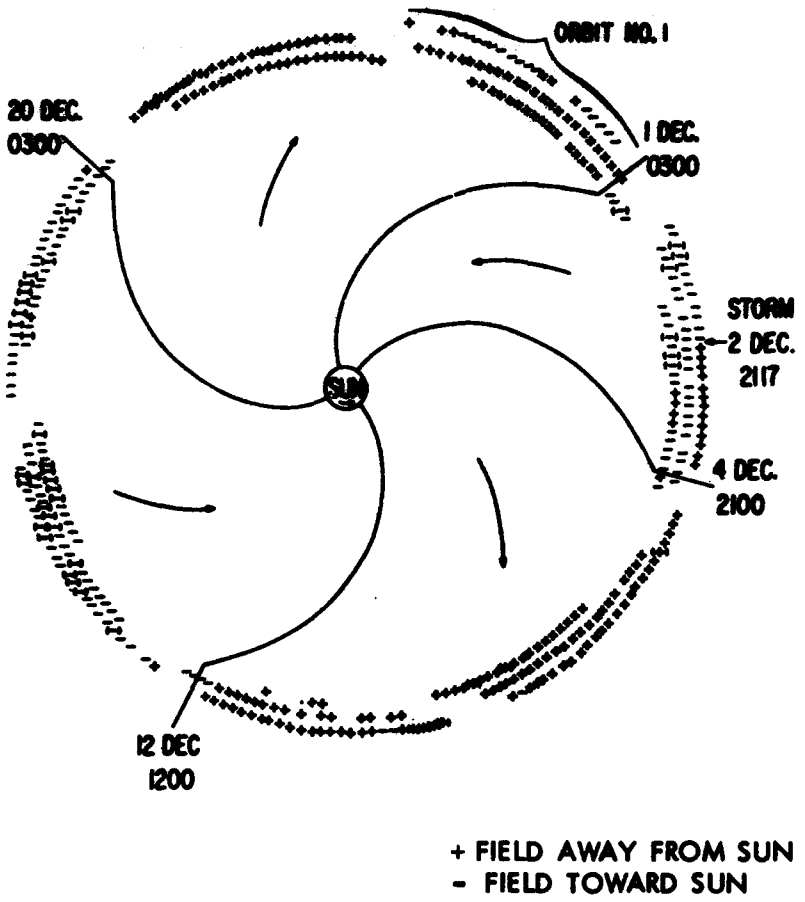

Figure 1-1. Pattern of the solar magnetic field (Reference 4).

motion. Similarly, in regions where the pressure of the solar plasma is greater than the pressure of the earth's magnetic field, the plasma continues to advance against the field. The plasma advance is stopped at the points where the particle and field pressures are balanced. The interface between the solar plasma and the geomagnetic field is called the magnetopause. Figure 1-2 depicts the characteristics of the magnetosphere in the plane of the noon-midnight magnetic meridians. Dipole field lines are dashed for comparison. The neutral surface lies in the antisolar direction and appears to be rooted to the dipole lines at about 10 R_E (References 41 and 42). Along the sun-earth line, the magnetopause usually is located about 10 earth radii (R_E) from the center of the earth. On one occasion it was observed to move to less than 6 R_E from the center of the earth (Reference 6).

1.3.2 The Bow Shock Wave

A collision-free bow shock is produced upstream from the magnetopause. The location and shape of this shock wave are similar to those expected for an ordinary aerodynamic shock wave produced by an obstacle having the shape of the magnetopause in a supersonic flow. The solar wind appears to behave as a continuous fluid over the entire magnetosphere (References 7 and 8).

1.3.3 The Magnetosheath

The region between the magnetopause and the bow shock is generally referred to as the magnetosheath or the transition region. This region contains the flow of the solar plasma as it is disturbed by the presence of the earth. As the "magnetized" solar plasma crosses the bow shock, the streaming velocity becomes subsonic, the proton number density increases about a factor of 4, the angular spread of the proton velocity vectors increases considerably (becoming approximately isotropic near the subpolar point), the proton velocity distribution becomes quasi-thermal (thermal with a high-energy tail to several KeV), and the interplanetary field "frozen" in the plasma becomes compressed (References 9, 10, and 11). As the plasma moves around the earth toward the tail region, the bulk velocity in the antisolar direction again increases due to the adiabatic expansion of the plasma.

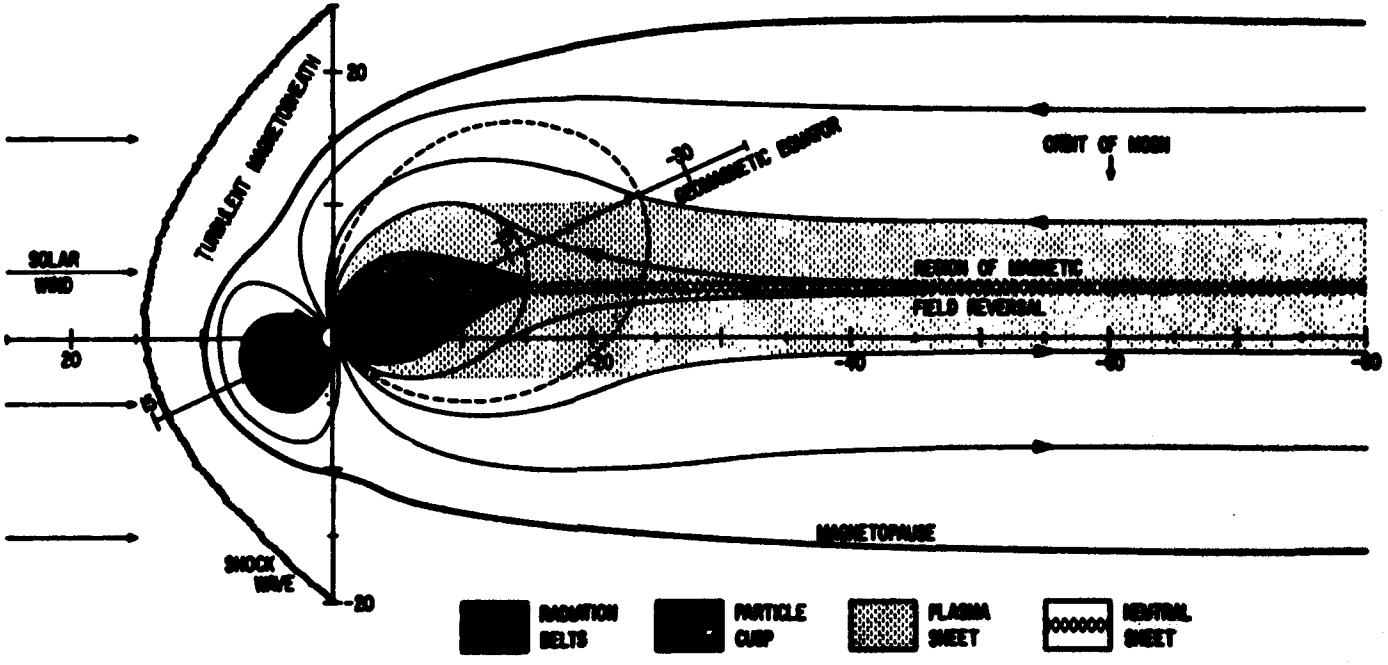

Figure 1-2. Geomagnetic tail configuration of the magnetosphere for large tilt of dipole axis to solar wind.

1.3.4 The Magnetospheric Tail

The magnetospheric tail is that region shown in Figure 1-2 where the field lines emanating from the polar caps of the earth are drawn back in the antisolar direction by the motion of the solar plasma. It is sometimes called the geomagnetic tail or the magnetotail. Evidence exists that the tail extends to at least 1,000 R_E (References 12 and 13). The magnetic field intensity diminishes very slowly in the antisolar direction. At about 30 R_E, the intensity varies from about 10 to 20 gammas (Reference 14). Note that the field lines in the northern and southern halves of the tail are directed oppositely. Such a configuration can persist only if a highly conductive plasma—the neutral sheet—exists in the region of the field reversal. It consists of electrons and protons of number densities 0.1 to 3 per cubic centimeter. The electron spectra are quasi-thermal, and average energies range from about 200 eV to more than 12 KeV. The proton energies range from about 1 to 20 KeV (Reference 15). The neutral sheet appears to begin near the plane of the geomagnetic equator at the geocentric distance of 10 ± 3 R_E and to extend along the tail parallel to the antisolar direction (Reference 17). The neutral sheet exhibits diurnal and seasonal variations because the geomagnetic equator wobbles (1) from the 11.5-degree displacement of the magnetic axis from the rotational axis of the earth and (2) from the 23.5-degree displacement of the rotational axis from the normal to the ecliptic plane.

The plasma sheet consists of a high-energy plasma (number density ~0.3 to 1 per cubic centimeter, mean electron energy ~0.5 to 2 KeV, and mean proton energy ~2 to 10 KeV) located around the earth on field lines that intersect the earth's surface in a narrow latitude band just above the auroral zone. In the midnight meridian, it is located as indicated in Figure 1-2. In every meridian around the earth, it appears to have a sharp inner boundary at magnetic field lines that cross the equatorial plane at distances greater than about 10 R_E. However, during times of geomagnetic disturbances called magnetic bays or polar substorms (Section 2), the inner boundary of the plasma sheet on the evening side of the magnetosphere moves inward to 5 or 6 R_E at the equator (Reference 18).

1.3.5 The Auroral Zone

The auroral zone is located near the high-latitude field lines shown in Figure 1-2 that define the outer limit of the stably trapped particles (Section 4) in the radiation belts. On the average, the zone forms an

oval in local magnetic time coordinates (Section 2). The zone is at higher magnetic latitudes (70 to 80 degrees) at local noon than it is at local midnight (65 to 75 degrees). During unusual magnetic disturbances, aurorae move to much lower latitudes.

The magnetic field lines that pass through the auroral zone contain energetic electrons and protons that are streaming almost continuously into the atmosphere. Usually fluxes are in the order of 10^8 per square centimeter per second but they increase to as high as 10^{12} per square centimeter per second during magnetic storms. Their energies are in the order of 10 KeV (Section 4). Aurorae are produced when these energetic particles excite the nitrogen and oxygen of the upper atmosphere. The light emission occurs at altitudes as low as about 100 kilometers, which is approximately the altitude that can be reached by a 10-KeV electron.

Magnetic disturbances that enhance the particle flux in the auroral zones often also increase the total number of trapped particles in the radiation belts. Therefore, the source of the auroral particles also appears to be the principal source of the radiation belts. Whether these particles originate from the magnetosphere or from the solar wind is still unknown. But the energization and transport of the particles must certainly be caused by the interaction of the solar wind with the earth's field. The observed inward motion of the plasma sheet during magnetic storms may be an important clue to this process.

1.4 THE RADIATION BELTS

The charged particles that constitute the earth's radiation belt are generally more energetic than the particles in the auroral zone. They are trapped by the geomagnetic field in the region shown in Figure 1-2. In succeeding sections of the handbook, the motion and distribution of the particles in the geomagnetic field as well as source and loss mechanisms are discussed in detail. In this section, a qualitative description is given of some of the salient features of the trapped particles.

1.4.1 Particle Motion

MOTION ALONG FIELD LINES. A charged particle in motion in a time-invariant magnetic field is acted upon by a magnetic force perpendicular to both the direction of motion of the particle and the direction of the magnetic field. Hence, the

energy of the particle remains constant, but the direction of the particle continuously changes. As a result, the particle moves in a spiral; a magnetic field line passes through its center of curvature. The pitch angle of the particle is defined as the angle between the direction of the field line and the direction of the particle velocity. The motion of an electron in the geomagnetic field and the pitch angle (α_o) of the electron at the equator are depicted in Figure 1-3. The pitch angle has a minimum angle value at the equator and is 90 degrees at the mirror point. In addition to spiraling along the field line, the electron drifts with the velocity V_g toward the east. Particles having a positive charge rotate about the field line in the opposite direction.

As it spirals down a field line, the particle approaches a region where the magnetic field intensity is increasing—that is, where magnetic lines of force are converging. In that region, the magnetic force acting on the particle develops a component that opposes the forward motion of the particle along the field line. Therefore, the forward velocity of the particle decreases and, since energy is conserved, the velocity perpendicular to the field line increases. Hence, the pitch angle increases. The particle penetrates to a point, the

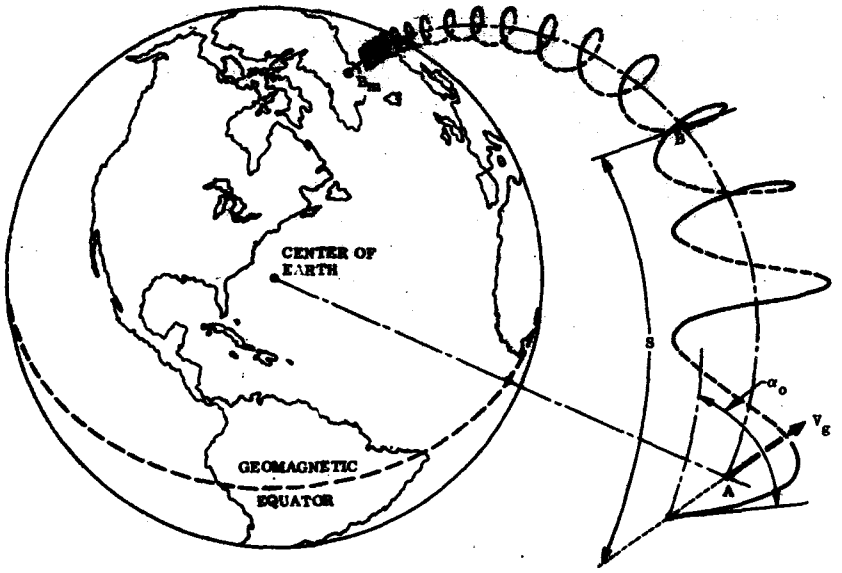

Figure 1-3. Motion of an electron trapped in the geomagnetic field.

so-called mirror point, where the pitch angle is 90 degrees. From that point, it moves in the opposite direction. Since the field also converges at the other end of the field line, the particle becomes repeatedly reflected at the two mirror points. In this manner, particles are confined or trapped in the geomagnetic field. The time required for a particle to go from one mirror point to the other and back again is called the bounce period. If it does not encounter other particles or electromagnetic disturbances along its path, the particle will always mirror at the same value of the magnetic field intensity (Section 3).

AZIMUTHAL DRIFT OF PARTICLES. Because of the gradient and curvature of the earth's field, the gyroradius of a particle varies within a gyration period so that the motion projected onto a plane perpendicular to a field line does not generate a circle but a cycloidal-like figure. The effect causes positively charged particles to drift toward the west and electrons to drift toward the east—thus forming a shell that surrounds the earth. The shape of the shell is roughly the surface constructed by rotating a field line about the dipole axis.

The shells are designated by L-values. In a distorted dipole field, the L-values of the shells are fairly difficult to compute (Section 3). However, in a dipole field, the L-value merely is equal to the distance in earth radii from the center of the dipole to the equatorial crossing point of the field line.

1.4.2 Adiabatic Invariants

Determination of the motion of an energetic charged particle in an arbitrary magnetic field is facilitated greatly by the existence of three adiabatic invariants of the motion (Section 3). The first is the magnetic moment of the particle gyrating about a field line:

$$M = \frac{p^2 \sin^2 \alpha}{2mB} \qquad (1\text{-}1)$$

where p is the momentum of the particle, m is the particle mass, and α is the pitch angle of the particle at the point where the magnetic field intensity is B. M is a constant of the motion if the magnetic field is fairly uniform over the dimensions of the particle orbit and if the time variation of the magnetic field is small during a gyroperiod. In a static magnetic field, p is constant. Hence Equation 1-1 gives the

relationship between α and B along the field line. The particle mirrors at the point $B = B_m$ where $\alpha = \pi/2$. Equation 1-1 also shows that p^2 varies as B_m when B_m varies slowly with time.

The second adiabatic invariant is

$$J = \oint p \cos \alpha \, dS \qquad (1\text{-}2)$$

where $p \cos \alpha$ is the momentum of the particle along the field line and dS is an element of length along the field line. The line integral is from one mirror point of the particle to the mirror point at the opposite end of the field line and back again. This invariant is also called the integral invariant or the longitudinal invariant. J is constant when the time variation of the magnetic field is small during a bounce period of the particle—that is, during the time required for the particle to travel from one mirror point to the other and back again. In a static magnetic field, the invariants M and J describe completely the surface or shell in which the particle remains constrained during its drift motion around the earth.

The third adiabatic invariant is the flux invariant:

$$\Phi = \int B dA \qquad (1\text{-}3)$$

where Φ is the total magnetic flux enclosed by the drift shell of the particle. The integral is over an area enclosed by the shell. Φ is constant when the time variation of B is small in the time required for the particle to drift around the earth. When B changes in this manner, Equation 1-3 shows that the drift shell of the particle contracts or expands in a manner so that the enclosed magnetic flux remains the same.

1.4.3 Loss of Particles

The particle motions discussed previously become disturbed by electromagnetic fluctuations and by collisions with neutral and ionized constituents of the earth's atmosphere. Collisions and electromagnetic variations that violate the first adiabatic invariant of a particle cause changes in its energy and/or its pitch angle. These parameters of the particle are governed by a diffusion process (Section 5). Particles whose pitch angles decrease will have mirror points deeper in the atmosphere where absorption is more likely to occur. Hence, pitch angle diffusion causes particles continually to be precipitated

or dumped in the atmosphere. Trapped particles, especially protons, also may lose so much energy by particle interactions at high altitudes that they may become indistinguishable from the thermal plasma. Protons of energy less than about 100 KeV may even leave the trapping region by losing their charges in charge-exchange collisions (Section 5).

Electromagnetic variations of periods greater than the gyroperiod but less than the azimuthal drift period may cause changes in the L-shells of the particle. This process is called radial or L-shell diffusion. It is an important means by which particles are distributed in the radiation belts. By radial diffusion, particles are removed from the radiation belts by transport across the inner or outer boundaries of the trapping region.

1.4.4 Source of Particles

Two mechanisms appear to be responsible principally for the population of the radiation belts. One is by an inward transport of particles across L-shells from the outermost closed field lines of the earth. This process also was mentioned previously as contributing to the loss of trapped particles. The transport is by radial diffusion (References 19 and 20). Section 5 contains evidence supporting the concept of particle transport into the radiation belts from the outer boundary.

The other prominent source —possibly responsible for the high-energy protons that appear at $L < 2$ (Section 4) — is the decay of cosmic ray albedo neutrons. Neutrons of broad energy and angular distributions are produced by collisions between cosmic rays and nuclei of the earth's atmosphere. Some of these neutrons either diffuse or move directly out of the dense atmosphere toward high altitudes. Since they have a radioactive half life of about 11 minutes, some neutrons will decay in flight producing protons (which have nearly the same energies and initial directions as the neutrons) and electrons. The protons and electrons will be trapped in the field if they have initial directions sufficiently inclined to the magnetic field lines that they will have mirror points above the dense atmosphere. This process, together with mathematical formulations of other source and loss mechanisms, are discussed in detail in Section 5.

1.5 MAGNETOSPHERIC ELECTRIC FIELDS

Quasi-stationary electric field components along magnetic field lines cannot persist for times greater than about 100 seconds because charged particles of the thermal plasma, which have high mobilities along field lines, neutralize the electric field. However, electric fields across magnetic field lines are not restrained as easily. Charges cannot cross magnetic field lines to neutralize the electric field except in the region of the ionosphere where the collision rate becomes appreciable. Nevertheless, the effective resistance of the ionosphere is fairly high and quasi-stationary electric field strengths up to tens of millivolts per meter have been observed (References 22 and 23).

The presence of these electric fields cause charged particles to drift in the direction of $\bar{E} \times \bar{B}$, where $\bar{E}$ and $\bar{B}$ are the electric and magnetic field intensities, respectively (Section 3). The drift motion is perpendicular to $\bar{E}$ and $\bar{B}$, and is the same for every charged particle, regardless of its velocity, mass or charge.

Since particles of a thermal plasma do not drift rapidly because of influences such as a gradient or curvature of the magnetic field (Section 3), the plasma along a magnetic field line behaves in an $\bar{E} \times \bar{B}$ field as an element of a fluid in a velocity field. In fact, whenever the electric field component along the magnetic field is negligible, the motion of the plasma is described by means of the hydromagnetic equations (Section 3), which are similar to the equations governing the motion of a fluid. In the magnetosphere, the thermal plasma often undergoes a circulative motion referred to as magnetospheric convection (Section 1.6) because of its resemblance to convection in a fluid.

Sometimes it is conceptually helpful to regard the magnetic field lines as moving with the $\bar{E} \times \bar{B}$ drift velocity and the thermal plasma to be "tied" to the field lines rather than to regard the plasma as drifting across magnetic field lines (Reference 24). This concept is valid in the magnetosphere where the electric field component along magnetic field lines is small.

Some of the more prominent electric field systems in the magnetosphere are discussed in the following paragraphs.

1.5.1 Corotation Electric Field

Collisions between the charged particles of the ionosphere and the neutral constituents of the atmosphere cause the ionospheric plasma to corotate with the earth. In a stationary frame of reference (nonrotating) in which the magnetic field is considered to be at rest, the motion of the plasma across magnetic field lines induces an electric field. Since the magnetic field lines are very nearly equipotentials, as discussed above, the electric field is propagated into the magnetosphere along magnetic lines of force. It is easy to show that, for a dipole magnetic field, the electric field configuration also causes the magnetospheric plasma to corotate with the earth.

The electric field lies in magnetic meridian planes and is directed toward the local centers of curvature of the field lines. The electrical potential between a pole and the equator is about 100 KV, and the horizontal component of the electric field intensity at a latitude of 45 degrees is about 15 millivolts per meter (Reference 24). At low L-values, the dipole field lines remain undistorted during rotation. At altitudes greater than a few earth radii, the field lines become distorted by the distant current sources (Section 2). At latitudes above the auroral zone, the field lines are drawn back into the magnetospheric tail. But still, at low altitudes, the field lines rotate with the ionosphere.

This electric field, of course, is not present in a frame of reference that rotates with the earth. Hence, the thermal plasma engaged in the corotation is not influenced by the field. However, more energetic particles, which do not remain on a field line, are influenced by the corotation electric field. This field principally affects the motions of particles that have energies less than about 10 KeV (References 25 and 26).

1.5.2 Electric Fields Inferred from Ionospheric Currents

Other electric fields that affect low-energy trapped particles are inferred from ionospheric current systems (Section 2). The currents are due to the differential response of ions and electrons to electric and magnetic fields in the altitude range of 90 to 140 kilometers. The ions encounter many collisions with neutral particles during an ion gyration period; hence, they tend to move with the winds. Conversely, the electrons undergo many gyrations in the magnetic field between collisions; hence, their motions are principally controlled by the magnetic and electric fields. Two driving mechanisms for these

currents are therefore possible—high-altitude winds, which put ions in motion, and electric fields, which preferentially move the electrons. The former mechanism is more important at low latitudes and the latter appears to be more important at high latitudes.

THE IONOSPHERIC DYNAMO. The Sq current system discussed in Section 2 results from a dynamo effect. The expansion of the atmosphere, due to the tidal and heating action of the sun, causes the ionospheric plasma to move across magnetic field lines. This motion generates an electric field that drives the ionospheric currents. As in the case of the corotation electric field, the magnetic field lines, approximately equipotentials, cause the electric field to be applied in the magnetosphere. This electric field has been verified by measurements in Reference 27, and the effect of the electric field on trapped particles has been studied in References 25, 26, and 28.

THE MAGNETOSPHERIC DYNAMO. The S_d ionospheric current system, which is usually prominent at high latitudes, is believed to be driven by an electric field generated in the outer magnetosphere by the interaction of the solar wind with the earth's field. Some theories that have been proposed to explain the source of this field are presented in the following subsection. Taylor and Hones (Reference 29) computed the magnetospheric electric field inferred by the current system and showed that this electric field—by accelerating solar wind particles that were initially in the magnetopause—could account for the energetic particles observed in the auroral zones.

1.6 MAGNETOSPHERIC CONVECTION

During times of magnetic storms, the magnetosphere exhibits dynamical properties that include the formation of the S_d ionospheric currents mentioned previously, the inward motion of the plasma sheet, enhanced auroral-particle precipitation, magnetic bays and associated micropulsations (Section 2), rapid transport of energetic particles in the radiation belts, the asymmetric ring current, and inward motion of the plasmapause. These properties can be explained qualitatively by assuming that during times of increased solar wind pressure, especially when the interplanetary magnetic field has a southward component, an electric field appears that is generally directed from the dawn to the dusk sides of the magnetosphere.

1.6.1 Flow of Plasma

The electric field causes plasma to flow in the magnetosphere. The flow is directed generally through the magnetosphere from the tail toward the sun. Near the earth, the combination of the convection field and the corotation field results in the flow pattern shown in Figure 1-4. The dashed lines depict the motion in the equatorial plane of field lines which are principally influenced by the convection field. The dotted lines closer to the earth depict the motion of field lines that are affected principally by the corotation field. Only the field lines within the closed solid line corotate with the earth.

1.6.2 Motion of Accelerated Particles

Charged particles in the tail region become accelerated to moderate energies due to the inward motion of the magnetic field lines (References 30 and 31). When they reach distances within about 10 earth radii from the center of the earth, the particles' energies are generally so high that their azimuthal drift velocities, due to the magnetic field configuration, become comparable to the inward $\overline{E} \times \overline{B}$ drift velocity. Hence, an appreciable charge separation occurs with electrons drifting toward the east and protons drifting toward the west. Together these motions of the charges establish a westward flowing electrical current. The charge separation does not preclude the continued azimuthal drift of the particles because the charges tend to be neutralized by currents in the thermal plasma that travel along magnetic field lines at high altitudes and across field lines in the lower ionosphere where the collision frequency is high. However, the onset of the charge separation may trigger micropulsations (Reference 32).

The minimum L-values reached by the electrons and protons depends principally on the strength of the convection field. The computations in Reference 33 show that, in a field of 0.3 millivolts per meter, the electrons reach a minimum L-value of about 3 on the dawn side of the earth and the protons reach minimum L-value of about 5 on the dusk side.

1.6.3 The Plasmasphere

The density of the thermal plasma generally diminishes steadily toward higher L-values. But near the limiting L-values of the convective flow (Figure 1-4), the density diminished precipitously,

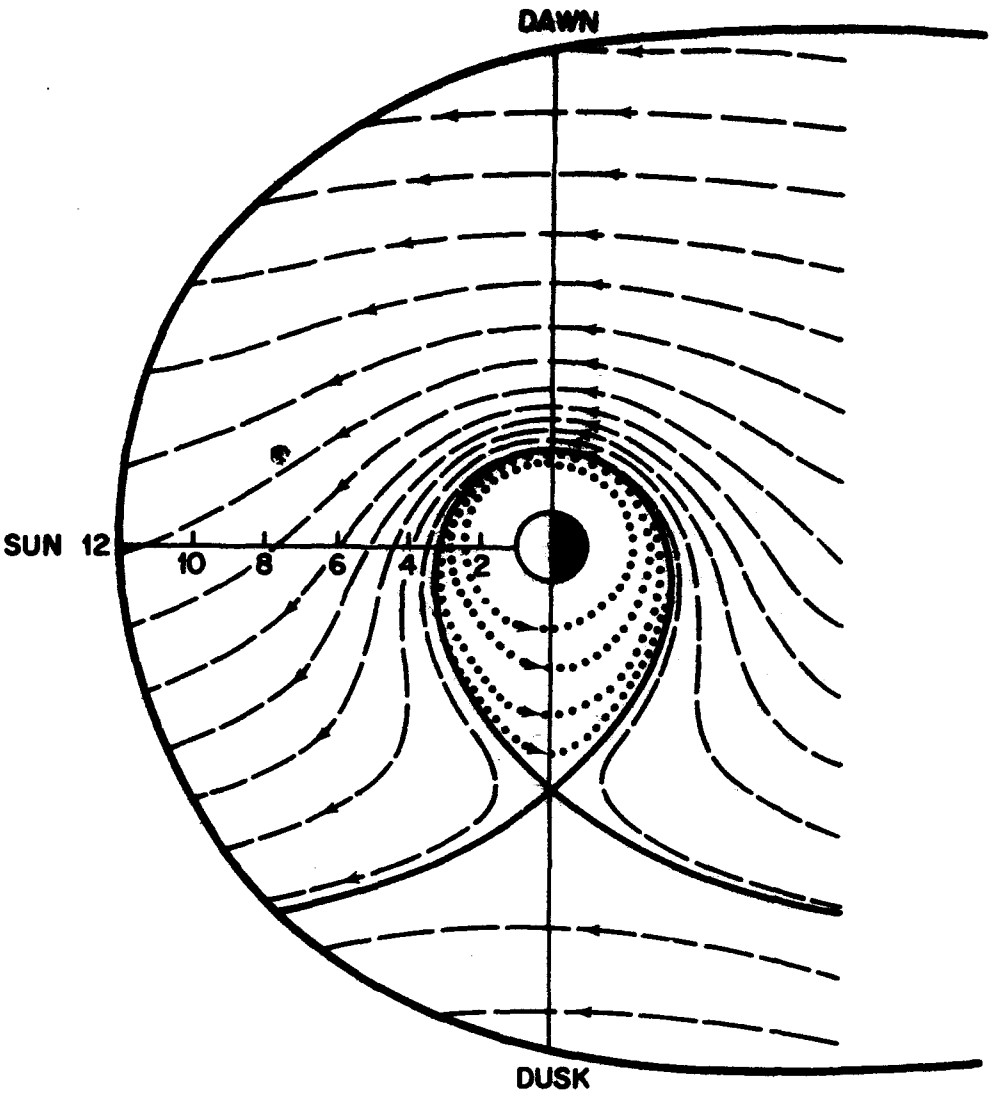

Figure 1-4. Flow of magnetic field lines in the equatorial plane resulting from a uniform dawn-to-dusk electric field across the magnetosphere and the corotation field (Reference 43).

often by several orders of magnitude within a fraction of an earth radius. The break in the density contour is referred to as the plasmapause or as Carpenter's knee, in honor of Carpenter's discovery of this feature by means of his whistler measurements (Reference 34). The plasmapause is now confirmed by direct satellite measurements (References 18, 35, 36, 37, and 38). The dense plasma region within the plasmapause is called the plasmasphere. The configuration and dynamical motion of the plasmasphere appear to result from the convection process. The convection field causes the thermal plasma, which diffuses upwards from the ionosphere along magnetic field lines, to drift out of the magnetosphere along the flow lines shown in Figure 1-4.

1.6.4 Theory of Magnetospheric Convection

Theories of magnetospheric convection are discussed in a recent review article (Reference 21). Two of the more prominent theories are the closed magnetospheric model in Reference 30 and the open magnetospheric model in Reference 39.

In the closed model, the magnetic field lines of the earth are closed and confined in a cavity by the solar plasma, and the convection is caused by a viscous interaction between the motion of the solar wind and the magnetospheric plasma. The mechanism of the interaction is not specified. Only a momentum transfer from the solar wind to the plasma on the closed geomagnetic field lines near the magnetopause is assumed. This momentum causes these outer magnetospheric field lines to move toward the antisolar direction. Two convection cells are established (Section 5.6) that cause field lines at lower latitudes to convect forward, toward the sun. The forward motion of the plasma results generally in the flow pattern discussed previously.

In the open model, high-latitude magnetic field lines are not all closed--some become connected with the interplanetary magnetic field. Connection is favored when the interplanetary field has a component opposite to the direction of the geomagnetic field line. The connection occurs principally on the sunward side of the magnetosphere where the solar wind compresses the interplanetary field lines against the magnetopause. Those geomagnetic field lines that become connected to the interplanetary field lines then are moved by the solar wind to the magnetospheric tail. Magnetic flux is conserved by the reconnection of the oppositely directed geomagnetic field lines in the neutral sheet and subsequent convection of the field lines forward in the magnetosphere, toward the sun. Again the forward convection is similar to the discussed flow.

Data are being obtained on large-scale electric fields and on magnetospheric plasma motions (Reference 40), but definitive information of whether the magnetosphere is closed or open is not yet available.

REFERENCES

1. J.H. Wolfe and D.S. Intriligator. "The Solar Wind Interaction with the Geomagnetic Field," Space Science Rev., 10, 511, 1970.

2. A.J. Hundhausen, J.R. Asbridge, S.J. Barne, H.E. Gilbert, and I.B. Strong. "Vela 3 Satellite Observations of Solar Wind Ions: A Preliminary Report," J. Geophys. Res., 72, 87, 1967.

3. E.N. Parker, "Dynamics of the Interplanetary Gas and Magnetic Fields," Astrophys. J., 128, 664, 1958.

4. J.M. Wilcox and N.F. Ness, "Quasi-Stationary Corotating Structure in the Interplanetary Medium," J. Geophys. Res., 70, 5793, 1965.

5. J.M. Wilcox. "The Interplanetary Magnetic Field. Solar Origin and Terrestrial Effects," Space Sciences Rev., 8, 258, 1968.

6. W.D. Cummings and P.J. Coleman, Jr. "Magnetic Fields in the Magnetopause and Vicinity at Synchronous Altitude," J. Geophys. Res., 73, 5699, 1968.

7. W.I. Axford, "The Interaction Between the Solar Wind and the Earth's Magnetosphere," J. Geophys. Res., 67, 3791, 1962.

8. P.J. Kellogg, "Flow of Plasma Around the Earth," J. Geophys. Res., 67, 3805, 1962.

9. N.F. Ness, C.S. Scearce, and J.B. Seek, "Initial Results of the IMP 1 Magnetic Field Experiment," J. Geophys. Res., 69, 3531, 1964.

10. J.H. Wolfe, R.W. Silva, and M.A. Myers. "Observations of the Solar Wind During the Flight of IMP 1," J. Geophys. Res., 71, 1319, 1966.

11. H. V. Argo, J. R. Asbridge, S. J. Bame, A. J. Hundhausen, and I. B. Strong. "Observations of Solar Wind Plasma Changes Across the Bow Shock," J. Geophys. Res., 72, 1989, 1967.

12. J. H. Wolfe, R. W. Silva, D. D. McKibbin, and R. H. Mason. "Preliminary Observations of a Geomagnetic Wake at 1000 Earth Radii," J. Geophys. Res., 72, 4577, 1967.

13. N. F. Ness, C. S. Scearce, and S. C. Canterano. "Probable Observation of the Geomagnetic Tail at 10^3 Earth Radii by Pioneer 7," J. Geophys. Res., 72, 3769, 1967.

14. N. F. Ness. "The Earth's Magnetic Tail," J. Geophys. Res., 70, 2989, 1965.

15. S. J. Bame, J. R. Asbridge, H. E. Felthauser, E. W. Hones, and I. B. Strong, "Characteristics of the Plasma Sheet in the Earth's Magnetotail," J. Geophys. Res., 72, 113, 1967.

16. K. A. Anderson. "Energetic Electron Fluxes in the Tail of the Geomagnetic Field," J. Geophys. Res., 70, 4741, 1965.

17. T. W. Speiser and N. F. Ness. "The Neutral Sheet in the Geomagnetic Tail: Its Motion, Equivalent Currents, and Field Line Connection Through It," J. Geophys. Res., 72, 131, 1967.

18. V. M. Vasyliunas. "A Survey of Low-Energy Electrons in the Evening Sector of the Magnetosphere with OGO 1 and OGO 3," J. Geophys. Res., 73, 2839, 1968.

19. M. P. Nakada, J. W. Dungey, and W. N. Hess. "Theoretical Studies of Protons in the Outer Radiation Belts," Space Science, 5, North Holland Publishing Co., 1964, and J. Geophys. Res., 70, 3529, 1965.

20. L. L. Newkirk and M. Walt. "Radial Diffusion Coefficient for Electrons at $1.76 < L < 5$," J. Geophys. Res., 73, 7231, 1968.

21. W. I. Axford. "Magnetospheric Convection," Reviews of Geophys., 7, 421, 1969.

22. g. Häerendel, R. Lüst, E. Rieger, and H. Völk. "Highly Irregular Artificial Plasma Clouds in the Auroral Zone," p. 293, Atmospheric Emissions, ed. by B.M. McCormac and A. Omholt, Van Nostrand Reinhold Company, 1969.

23. E.M. Wescott, J.D. Stolarid, and J.P. Heppner. Electric Fields in the Vicinity of Auroral Forms from Motions of Barium Vapor Releases, Report X-612-69-62, Goddard Space Flight Center.

24. H. Alfven and Carl-Gunne Fälthammar. Cosmical Electrodynamics, Oxford University Press, 1963.

25. J.B. Cladis, G.T. Davidson, W.E. Francis, L.L. Newkirk, L.R. Tepley, M. Walt, and R.C. Wentworth. Search for Possible Loss Processes for Geomagnetically Trapped Particles (N/A), Lockheed Report No. M-57-65-1 and DASA Report No. 1713, 1965.

26. E.W. Hones, Jr. "Motions of Charged Particles Trapped in the Earth's Magnetosphere," J. Geophys. Res., 68, 1209, 1963.

27. G. Haerendel, R. Lüst, and E. Rieger. "Motions of Artificial Ion Clouds in the Upper Atmosphere," Planet. Space Sci., 15 1, 1967.

28. H. Maeda. "Electric Fields in the Magnetosphere Associated with Daily Geomagnetic Variations and Their Effects on Trapped Particles," J. Atmospheric and Terrestrial Phys., 26, 1133, 1964.

29. H.E. Taylor and E.W. Hones, Jr. "Adiabatic Motion of Auroral Particles in a Model of the Electric and Magnetic Fields Surrounding the Earth," J. Geophys. Res., 70, 3605, 1965.

30. W.I. Axford and C.O. Hines. "A Unifying Theory of High-Latitude Geophysical Phenomena and Geomagnetic Storms," Can. J. Phys., 39, 1433, 1961.

31. W.I. Axford. "Interaction Between the Solar Wind and the Magnetosphere," Physics of Geomagnetic Phenomena, ed. by S. Matsushita and W.H. Campbell, p. 1243, Academic Press, New York, 1968.

32. J.B. Cladis. "Dynamical Motion of Geomagnetic Flux Tube Resulting from Injection of High-Energy Particles," Earth's Particles and Fields, ed. by B.M. McCormac, p. 307, Reinhold Book Corporation, 1968.

33. L.D. Kavanagh, Jr., J.W. Freeman, Jr., and A.J. Chen. "Plasma Flow in the Magnetosphere," J. Geophys. Res., 73, 5511, 1968.

34. D.L. Carpenter. "Whistler Studies of the Plasmapause in the Magnetosphere, 1, Temporal Variations in the Position of the Knee and Some Evidence on Plasma Motions Near the Knee," J. Geophys. Res., 71, 693, 1966.

35. K.I. Gringauz. "The Structure of the Ionized Gas Envelope of Earth from Direct Measurements in the U.S.S.R. of Local Charged Particle Concentrations," Planetary Space Sci., 11, 281, 1963.

36. J.H. Binsack, "Plasmapause Observations with the M.I.T. Experiment on IMP 2," J. Geophys. Res., 72, 5231, 1967.

37. H.A. Taylor, Jr., H.C. Brinton, and M.W. Pharo, III, "Contraction of the Plasmasphere During Geomagnetically Disturbed Periods," J. Geophys. Res., 73, 961, 1968.

38. C.R. Chappell, K.K. Harris, and G.W. Sharp. "A Study of the Influence of Magnetic Activity on the Location of the Plasmapause as Measured by OGO-5," J. Geophys. Res., 75, 50, 1970.

39. J.W. Dungey. "The Interplanetary Magnetic Field and the Auroral Zones," Phys. Rev. Letters, 6, 47, 1961.

40. J.W. Freeman, Jr. "Observation of Flow of Low-Energy Ions at Synchronous Altitude and Implications for Magnetospheric Convection," J. Geophys. Res., 73, 4151, 1968.

41. W.N. Hess. The Radiation Belt and Magnetosphere, Blaisdell Publishing Co., 1968.

42. N.F. Ness. "Observations of the Interaction of the Solar Wind with the Geomagnetic Field During Quiet Conditions," Solar-Terrestrial Physics, ed. by J.W. King and W.S. Newman, p. 57, Academic Press, New York, 1967.

43. C.R. Chappell, K.K. Harris, and G.W. Sharp. "The Morphology of the Bulge Region of the Plasmasphere," J. Geophys. Res., 75, 3848, 1970.

SECTION 2

THE GEOMAGNETIC FIELD

L.L. Newkirk, Lockheed Palo Alto Research Laboratory

2.1 INTRODUCTION

The geomagnetic field is generated by various primary sources of magnetism located within the earth and in the surrounding magnetosphere. Near earth, the internal magnetization of the earth (believed to be produced by electric currents flowing in the earth's core) is the major source and is known as the main or permanent field. It is the dominant field in the trapping region of space and exerts the controlling magnetic force that leads to particle trapping.

The main field can be represented to an accuracy of about 90 percent by the magnetic field that would result from a tilted dipole positioned at the earth's center. The remaining 10 percent of the field consists of large, regional anomalies covering thousands of square miles and of small surface field anomalies caused by local magnetic ore deposits. The main field shows a secular variation that is characteristically a fraction of a percent change in the field per year. In some cases involving trapped radiation, the simple dipole approximation to the field is adequate. In most studies, however, a more accurate field representation is required, given by a many termed spherical harmonic expansion fitted to measured values of the field. This field representation is applicable out to 5 to 6 R_E. Beyond this distance, a system of currents flowing on the boundary and in the tail region of the magnetosphere (due to the solar wind geomagnetic field interaction) creates fields that distort the geomagnetic field from the main field configuration.

Field models that incorporate the effect of these currents have been developed and provide a description of the geomagnetic field at large distances. Also, perturbing effects at low altitudes due to ionospheric currents and at several earth radii due to ring currents sometimes must be included in field representations.

The geomagnetic field, like other large-scale phenomena found in nature, is never absolutely quiescent or undisturbed. Field amplitude measurements versus time show a variety of disturbances having time durations lasting from only a fraction of a second to as long as several days. The patterns are irregular in some cases and smooth in others and may have a partially periodic or oscillatory structure. The amplitude variations range from a small fraction of one gamma (10^{-5} gauss) to several hundred gammas. Many of the disturbances are localized events, but others encompass a significant portion of the magnetosphere. Some of the disturbances undoubtedly play a strong role in the particle supply and loss processes that determine the intensities of radiation belts.

The numerous types of magnetic disturbances, along with their causes, will be discussed in subsequent portions of this section. Appendix 2A describes some of the magnetic indices used in trapped radiation studies to characterize the relative intensities of magnetic disturbances.

2.2 MAGNETIC FIELD ELEMENTS

The geomagnetic field at a point customarily is denoted either by the vector $\bar{F}$ of traditional usage or, more recently, by the conventional vector $\bar{B}$. Figure 2-1 illustrates seven magnetic elements that are commonly used to describe $\bar{B}$ on the earth's surface. The scalar B represents the total field intensity. The elements X, Y, and Z are the north, east, and vertical components (or $-B_\theta$, B_ϕ, and $-B_r$ in a spherical coordinate system) and have positive senses in the directions indicated. The magnetic declination D is the angle between X and the horizontal intensity H and is given by the deviation of a compass from true north. A positive declination results from an eastward deflection. The inclination or dip angle I is the angle between H and B and is given by the dipping of a magnetic needle below the horizontal plane. I has a positive sense when directed downward.

Routine measurements of surface geomagnetic field elements and their time variations are recorded continuously at permanent magnetic observatories and temporary stations. To supplement these measurements, magnetic surveys are made every few years to cover land and sea areas away from the fixed observatories and stations. In addition, satellite measurements of the geomagnetic field in space are made now and have become an important part of the effort to map the earth's magnetic field, thus providing comprehensive coverage in a relatively short time.

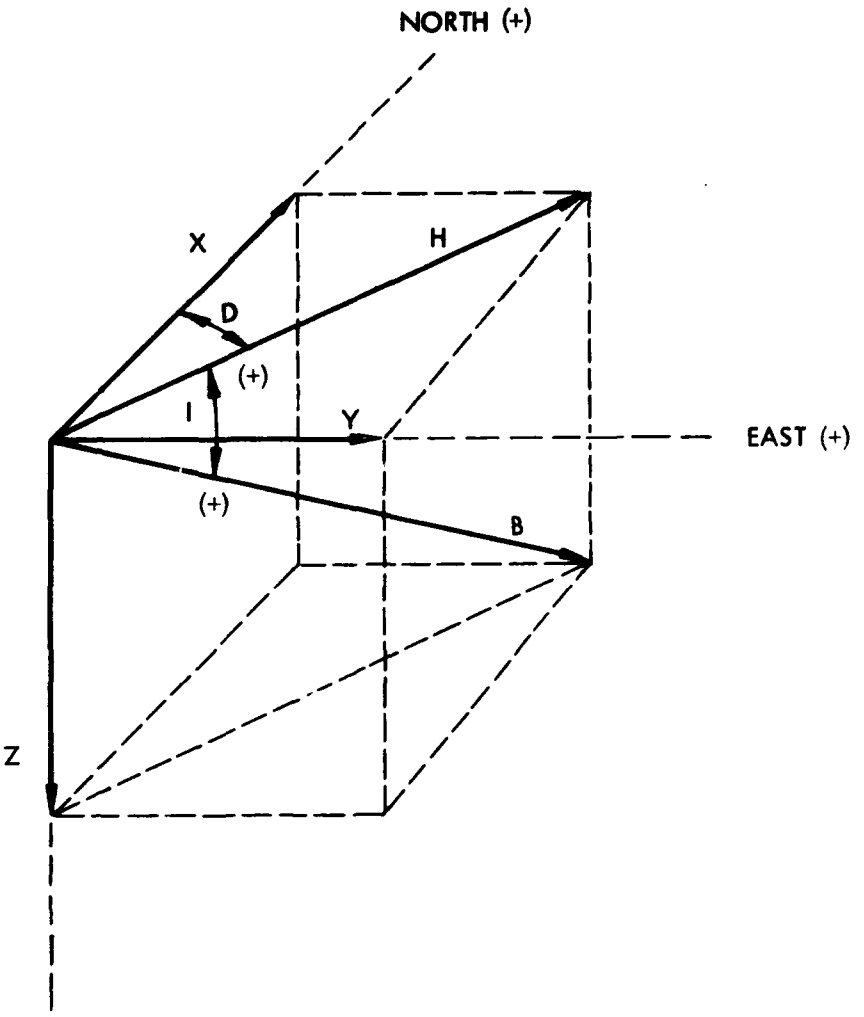

D = DECLINATION

H = HORIZONTAL INTENSITY

B = TOTAL INTENSITY

I = INCLINATION

Z = VERTICAL COMPONENT

X = NORTH COMPONENT

Y = EAST COMPONENT

Figure 2-1. Elements of the geomagnetic field.

To completely specify the vector $\overline{B}$ requires the measurement of three independent elements of the field. Any of the remaining field elements can be determined since each is a known function of the measured set. The elements B, D, and I usually are measured aboard aircraft and survey ships at sea. In land surveys, H (or Z, occasionally) is substituted for B. In space measurements, satellites generally measure the total field intensity and sometimes obtain field components relative to the satellite trajectory or to the sun. Figures 2-2 and 2-3 show the surface magnetic field elements B and I for epoch 1965 (Reference 1). The charts show isomagnetic lines along which the respective geomagnetic field elements are constant. Variations in the data due to the long-term, or secular, variations in the field during the period of observation are taken into account in preparing charts like these. Because the secular changes are only partially predictable, magnetic charts are revised periodically. The secular variation in the total field intensity B at epoch 1960 is shown in Figure 2-4.

2.3 THE DIPOLAR FIELD OF THE EARTH

The simplest approximation to the geomagnetic field is the field that would result from an earth-centered dipole directed southward and inclined at 11.5 degrees to the earth's rotational axis (north and south poles at 78.5°N, 291°E and at 78.5°S, 111°E, respectively). An improved approximation is the field that would originate from a dipole displaced 0.0685 earth radii from the earth's center toward a direction defined by geographic latitude 15.6°N and longitude 150.9°E. The intersections of the displaced dipole axis with the earth's surface are at 81.0°N, 84.7°W and at 75.0°S, 120.4°E (Reference 2). Because the north pole of the magnetic dipole field is located in the southern geographic hemisphere, the sense of the field direction is from south toward north. The field intensity at the equator on the surface is about $B_E \approx 0.312$ gauss (Reference 3).

A simple dipole field has these components (Reference 4) in a spherical coordinate system:

$$B_r = \frac{2M}{r^3}\cos\theta = 2B_o\left(\frac{R_o}{r}\right)^3\cos\theta \qquad (2\text{-}1a)$$

$$B_\theta = \frac{M}{r^3}\sin\theta = B_o\left(\frac{R_o}{r}\right)^3\sin\theta\,, \qquad (2\text{-}1b)$$

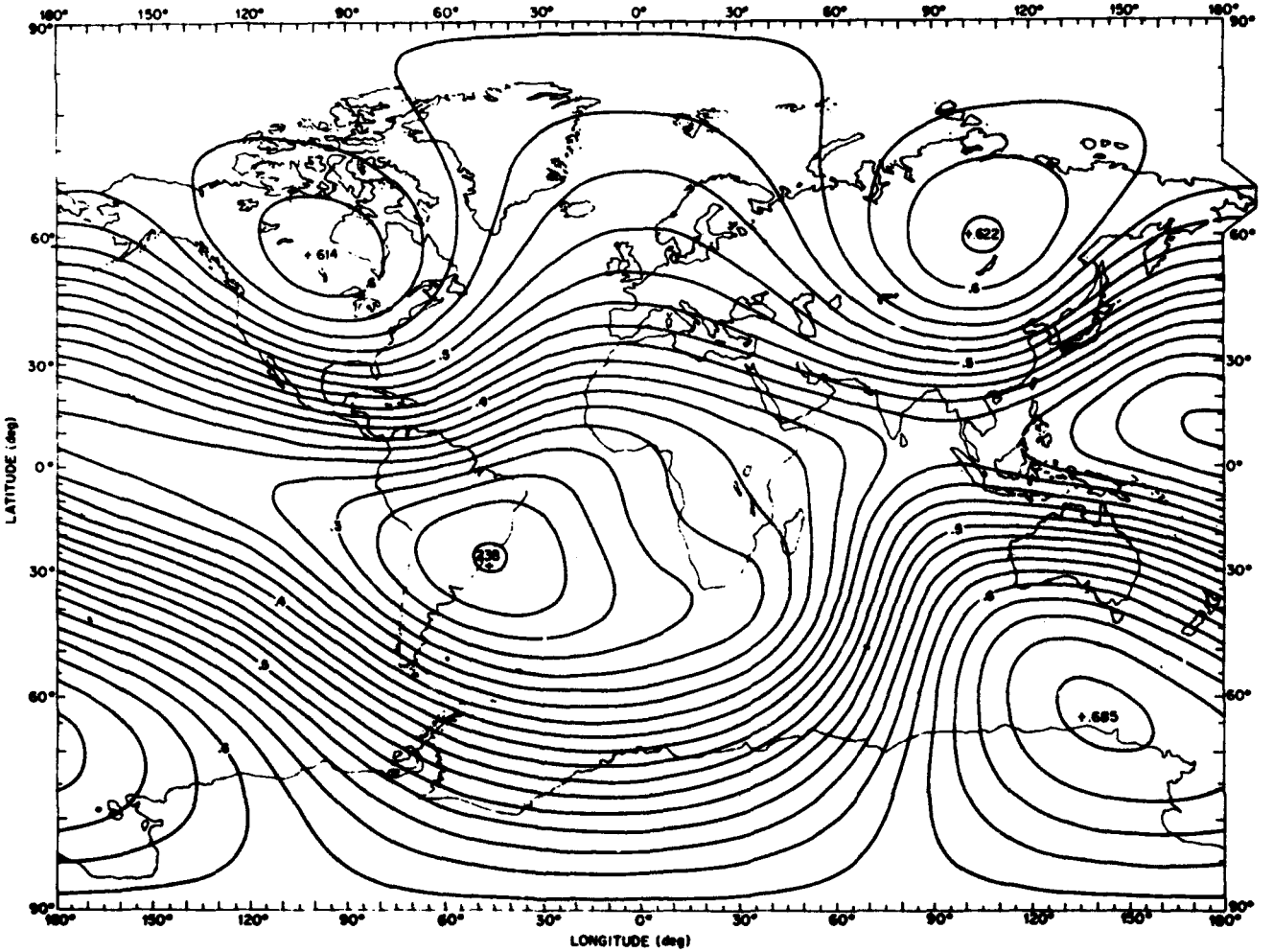

Figure 2-2. Isocontours of surface geomagnetic field intensity B (in gauss) for epoch 1965 (Reference 1).

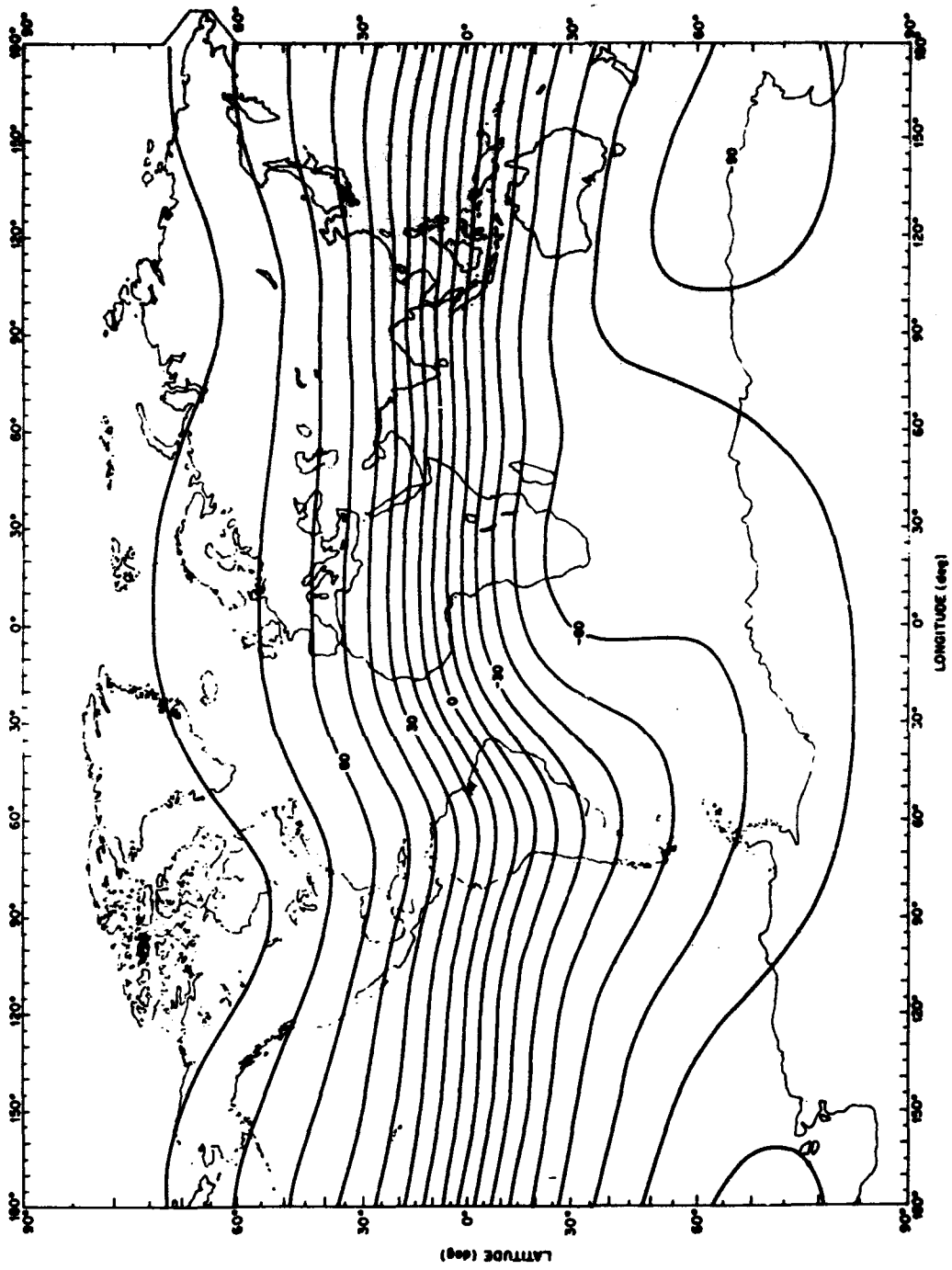

Figure 2-3. Isocontours of magnetic inclination I (in degrees) at the earth's surface for epoch 1965 (Reference 1).

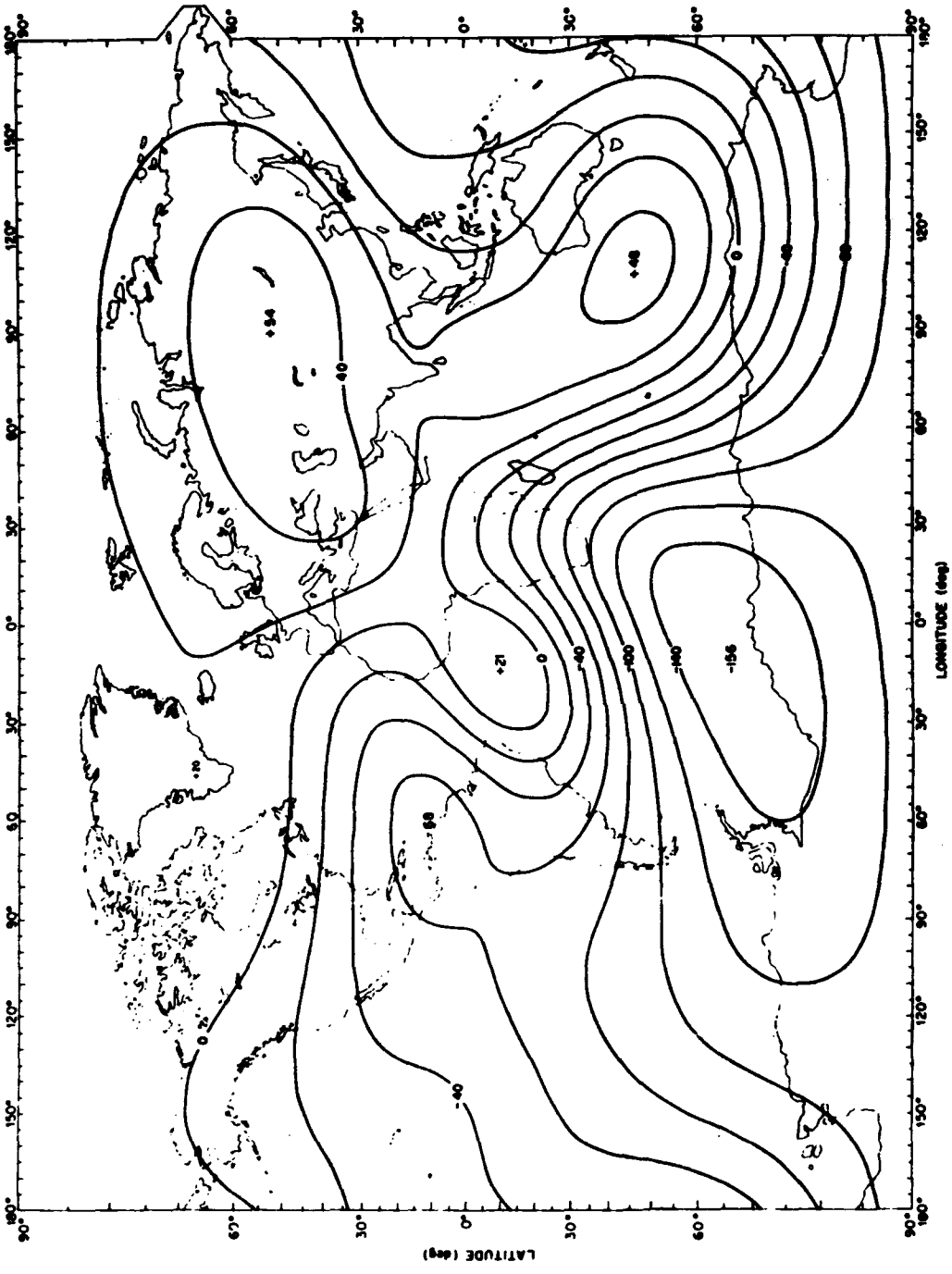

Figure 2-4. Isocontours of the secular change in the surface field intensity B (in gammas, 10^{-5} gauss) per year for epoch 1960 (Reference 1).

whereas the dipole field in a cylindrical coordinate system has the following coordinates:

$$B_R = -\frac{3MRz}{\left(R^2 + z^2\right)^{5/2}} \qquad (2\text{-}2a)$$

$$B_z = +\frac{M\left(R^2 - 2z^2\right)}{\left(R^2 + z^2\right)^{5/2}} . \qquad (2\text{-}2b)$$

The magnetic moment (M) of the earth's field is approximately $M_E \approx -8.07 \times 10^{25}$ gauss $cm^3 \approx 0.312$ gauss (earth radii)^3. The magnetic field at the equator, where $R = r = R_o$, is denoted by B_o. The components of the earth's field are sketched in Figures 2-5 and 2-6 (south is in the -z direction).

The intensity of a magnetic field is the vector sum of its components; in spherical coordinates

$$B = \sqrt{B_r^2 + B_\theta^2} = \frac{M}{r^3}\sqrt{1 + 3\cos^2\theta} , \qquad (2\text{-}3)$$

and in cylindrical coordinates

$$B = \sqrt{B_R^2 + B_z^2} = M\sqrt{\frac{R^2 + 4z^2}{\left(R^2 + z^2\right)^4}} . \qquad (2\text{-}4)$$

The field lines, which have everywhere the direction of the vector $\bar{B}$, are defined by the following equations. In spherical coordinates

$$r = R_o \sin^2\theta \qquad (2\text{-}5)$$

and in cylindrical coordinates

$$R^2 R_o = \left(R^2 + z^2\right)^{3/2} . \qquad (2\text{-}6)$$

One half of a field line has been sketched in Figures 2-5 and 2-6. Several representative field lines are shown in Figure 2-7 along with contours of equal field intensity. Each field line is labeled according to its equatorial intersection $R_o = LR_E$. The constant-B curves are equivalent to:

$$B \approx \frac{0.312}{L^3}\sqrt{\frac{1 + 3\sin^2\lambda}{\cos^6\lambda}} .$$

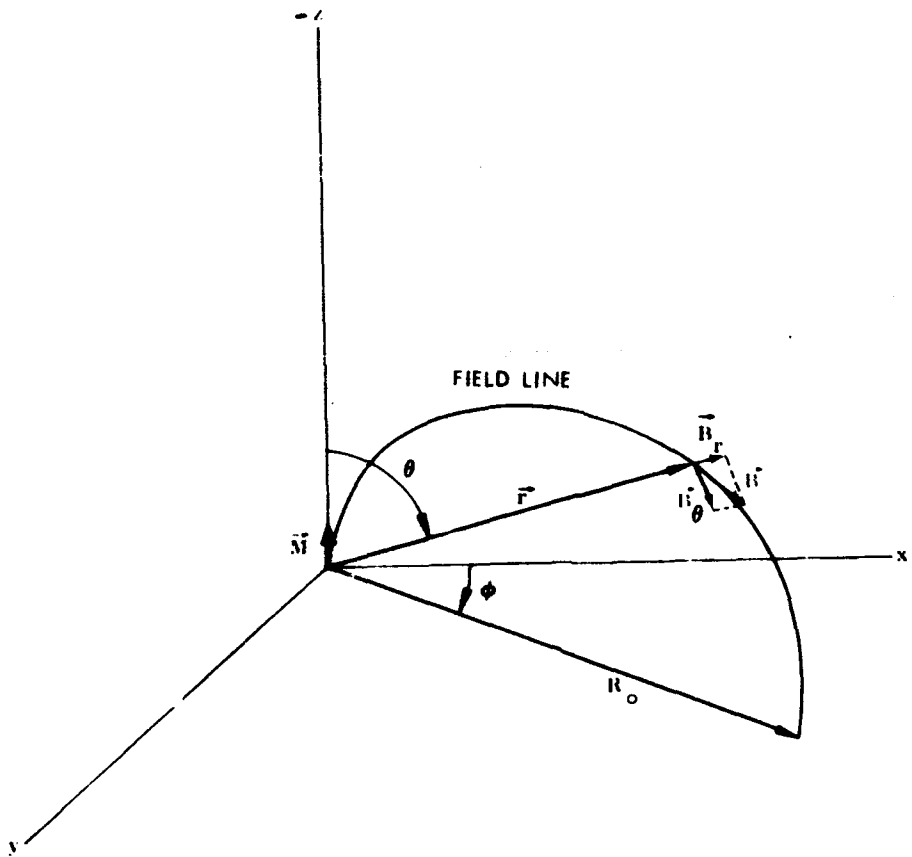

Figure 2-5. A magnetic dipole field in spherical coordinates.

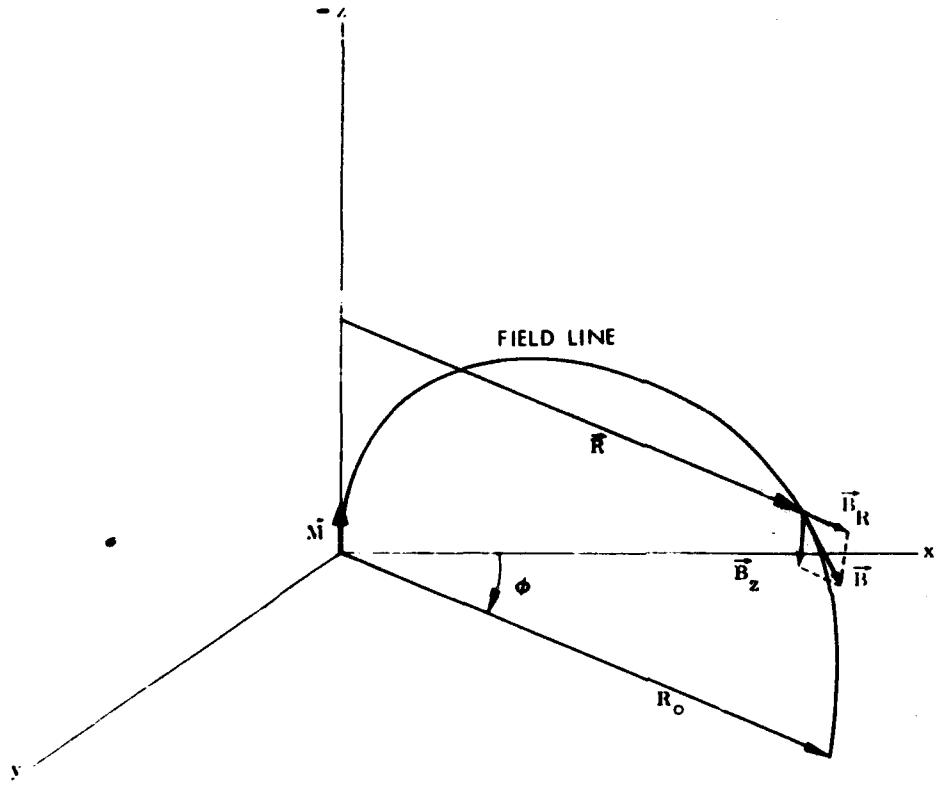

Figure 2-6. A magnetic dipole field in cylindrical coordinates.

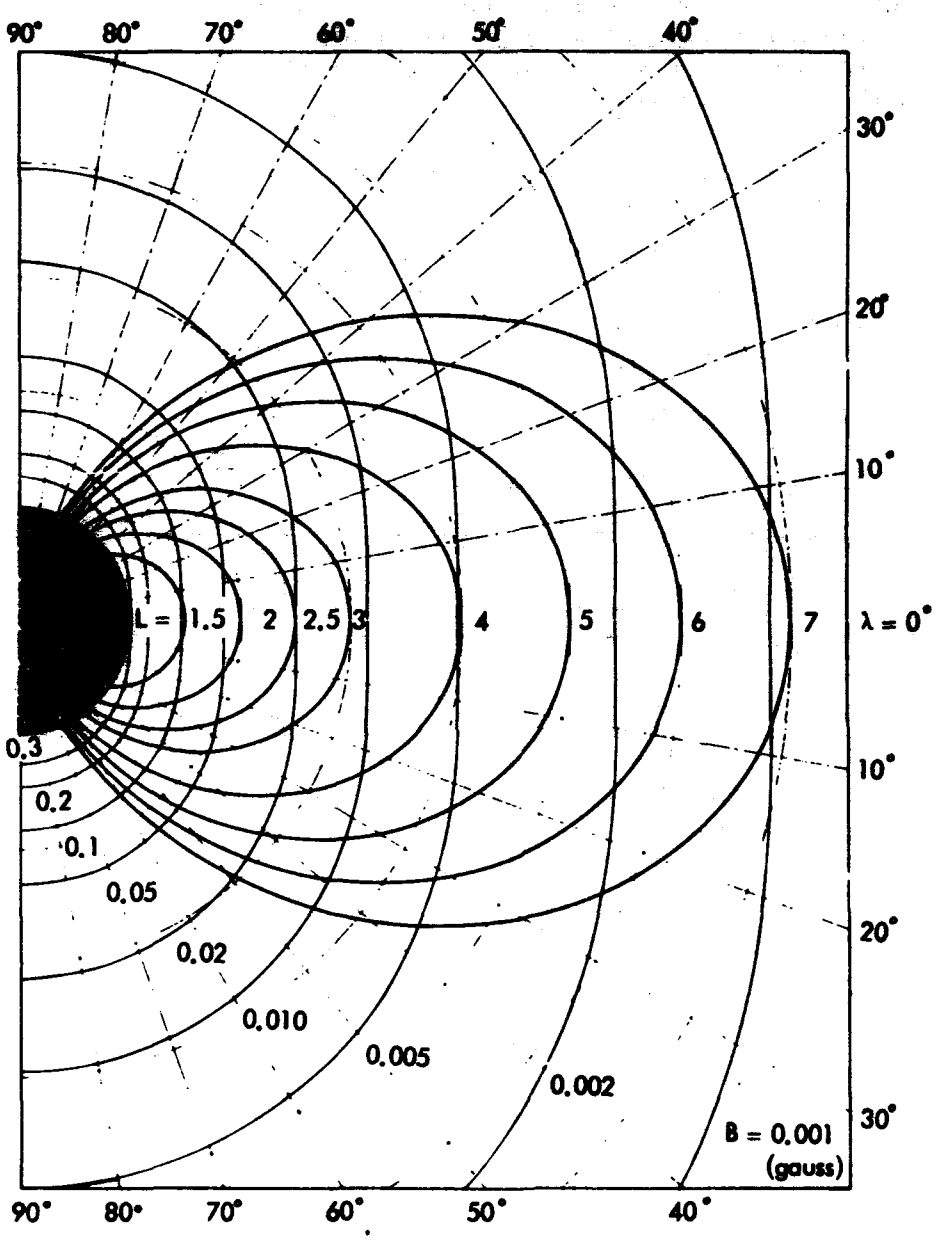

Figure 2-7. Constant-B surfaces in a dipole field.

Numerical magnitudes correspond to the earth's field. When the constant-B curves are rotated about the polar axis, the result is a closed, egg-shaped constant-B surface (see Figure 3-11). R_E is the radius of the earth, λ is latitude, and L corresponds to the magnetic shell parameter in Reference 5.

2.3.1 Distance Along Field Line and Volume Between Shells of Field Lines

The distance (S) measured along a field line from the equator is a useful parameter and is sometimes used to identify a point on a field line. As a function of $\xi = \sin\lambda = \cos\theta$, the differential distance element for a dipole field is

$$dS = R_o\sqrt{1 + 3\xi^2}\, d\xi \ . \qquad (2\text{-}7)$$

The integrated distance along a dipole field line from equator to $\xi = \sin\lambda$ is:

$$S = \frac{R_o}{2}\left[\xi\sqrt{1 + 3\xi^2} + \frac{1}{\sqrt{3}} \ln\left(\sqrt{3}\xi + \sqrt{1 + 3\xi^2}\right)\right] . \qquad (2\text{-}8)$$

S is plotted in Figure 2-8 (in units $R_o = LR_E$) (see Table 3B-1). The scale at the bottom of the figure is the equatorial pitch angle of a particle that mirrors at the corresponding latitude. Up to 50-degree latitude, S may be determined with fair accuracy by means of the empirical formula:

$$S \approx 0.019\,\lambda\, R_o$$

where λ is expressed in degrees. At 90-degree latitude, $S = 1.3802\, R_o$.

The derivative of magnetic field intensity along the field line is

$$\frac{dB}{dS} = \frac{B_o}{R_o} \frac{3\xi\left(3 + 5\xi^2\right)}{\left(1 - \xi^2\right)^4\left(1 + 3\xi^2\right)} \ . \qquad (2\text{-}9)$$

From Equation 2-7, the volume between two cylindrically symmetric shells bounded by dipole field lines is fairly simple to obtain. If the shells are located at an equatorial distance $R_o = R_E L$ and separated by a small distance $\delta R_o = R_E \delta L$, the volume included between the two L-shells is:

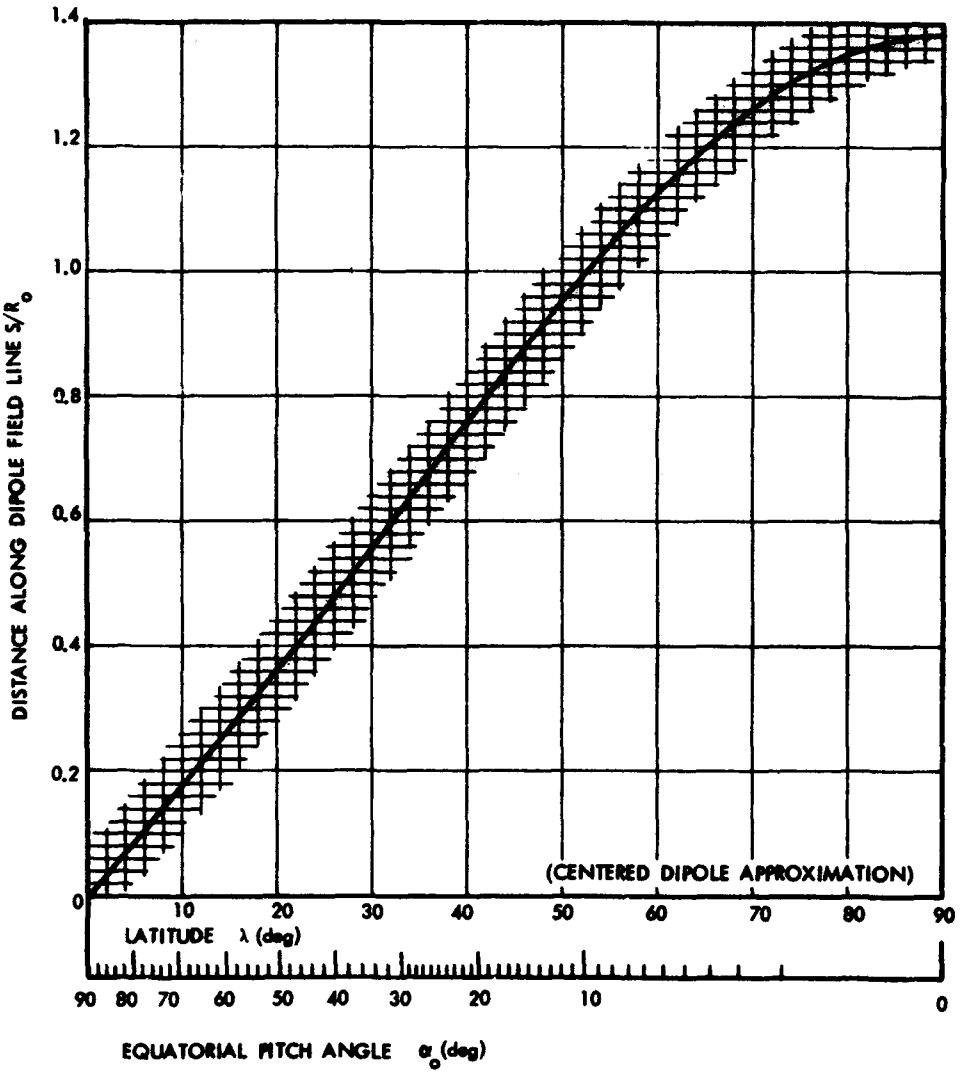

Figure 2-8. Distance along a dipole field line measured from the equator.

$$\delta V = 4\pi R_E^3 \sqrt{1 - \frac{1}{L}}\left[\frac{16}{35} L^3 + \frac{8}{35} L^2 + \frac{6}{35} L + \frac{1}{7}\right] \delta L \quad . \quad (2\text{-}10)$$

The total volume contained between the earth's surface and a shell of field lines with an equatorial intersection at R_o is plotted in Figure 2-9 as a function of $L = R_o/R_E$. In these equations, R_E is the radius of the earth and L corresponds to the magnetic shell parameter of McIlwain (Section 3).

2.3.2 Geomagnetic Coordinate Systems

Various coordinate systems based on the geomagnetic field are used in place of geographic coordinates to simplify the study of trapped radiation and other phenomena in space that are controlled or influenced by the field. The most elemental geomagnetic coordinate system is one aligned with the centered dipole. It is shown in Figure 2-10, superimposed on geographic coordinates. The points where the dipole axis intersects the earth's surface serve to locate the geomagnetic (or dipole) north and south poles (78.5°N, 291°E and 78.5°S, 111°E, respectively). The geomagnetic equator lies in a plane passing through the center of the earth and perpendicular to the dipole axis.

Angular positions in this system are expressed as geomagnetic (or dipole) latitude and geomagnetic longitude. The prime geomagnetic meridian contains the geographic south pole and lies approximately along the geographic meridian 290°E (70°W) over most of its length. In analogy with the definition of local geographic time, local geomagnetic time is defined in terms of the angular position (in hours) of the sun relative to the geomagnetic meridian of the observer. Geomagnetic noon occurs when the sun is in the geomagnetic meridian plane of the observer.

An accurate coordinate system of geomagnetic latitude and geomagnetic longitude [based on the field-line configuration given by the international geomagnetic reference field 80-term expansion (References 7 and 8) for epoch 1969.75] has been prepared in Reference 9. In this system, the latitudes are invariant latitudes (see Equation 2-15), and the meridian surfaces are defined by families of field lines intersecting radial lines in a predetermined equatorial plane. North and south polar plots and world maps of this system of geomagnetic latitude and longitude are provided in Appendix 2B for the surface of the earth and at a 3,000-kilometer altitude.

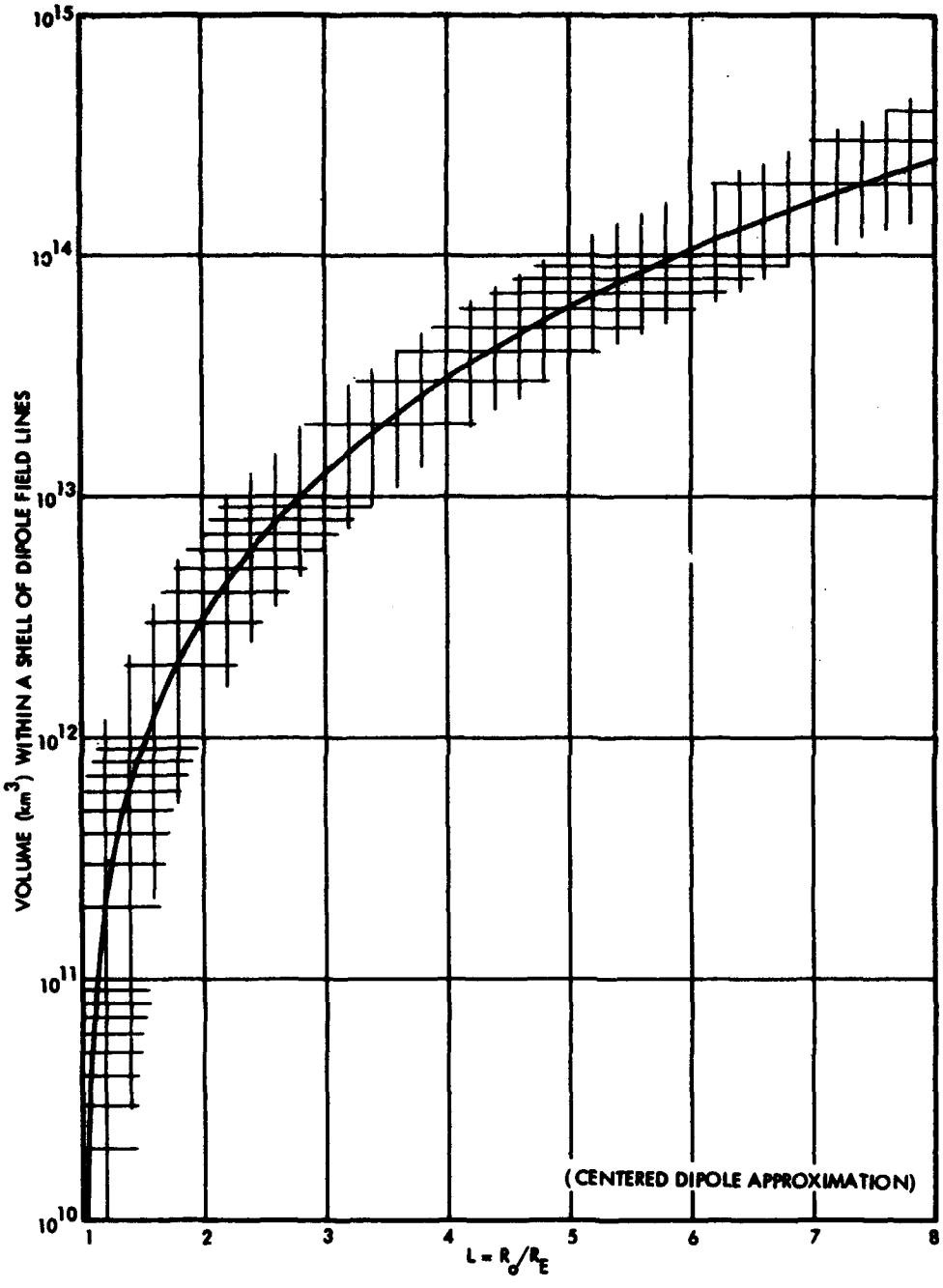

Figure 2-9. Volume contained within a shell of dipole field lines.

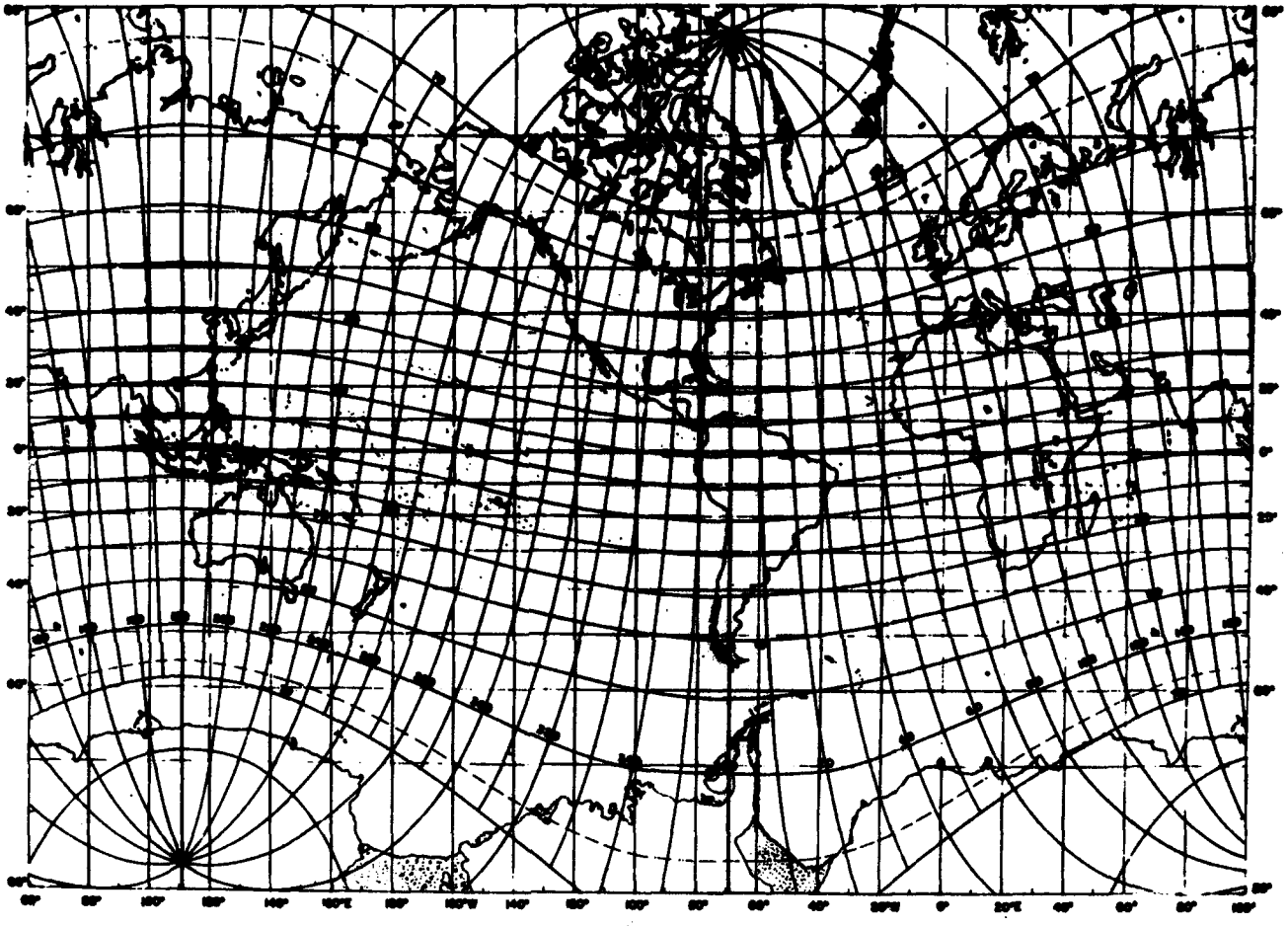

Figure 2-10. The geomagnetic coordinate system given by a centered dipole, superimposed on geographic coordinates (Reference 6).

A coordinate system of considerable utility is one in which each dipole field line is labeled by the magnetic shell parameter $L = R_o/R_E$ (Reference 5) and a point on the field line is identified by the field intensity B at the point. Sometimes the geomagnetic latitude, the distance S along the field line, or a set of curves defined by:

$$r = \left[\text{constant}\right]\sqrt{\cos\theta} \qquad (2\text{-}11)$$

which are orthogonal to the field lines are employed instead of B to specify points on the field line.

The analysis of trapped particles is complicated because the geomagnetic field actually has a high degree of azimuthal asymmetry. Symmetric coordinate systems based on the terrestrial dipole are found to have only limited applicability. Various coordinate systems, based on parameters analogous to some of those described previously for a dipole field, have been proposed with the intent of restoring some of the aspects of azimuthal symmetry (Reference 5). Trapped particle populations thereby can be described in terms of an idealized dipole field with strict azimuthal symmetry. The discussion of coordinate systems of this kind, which involve equations of motion, are deferred until Section 3.4.3.

2.4 THE SPHERICAL HARMONIC EXPANSION OF THE FIELD

Although the simple dipole approximation is useful in some cases, a higher order approximation generally is required to describe the field in most trapped radiation studies.

With the assumption that electric currents are negligible in the region above the earth, the magnetic field $\bar{B}$ is due only to the internal sources of the main field and can be expressed as the negative gradient of a magnetic potential Ψ_m that satisfies Laplace's equation:

$$\bar{B} = -\nabla\Psi_m \quad . \qquad (2\text{-}12)$$

The general solution for Ψ_m can be expressed as a sum of spherical harmonics (Reference 10):

$$\Psi_m \cong R_E \sum_{n=1}^{n'} \left(\frac{R_E}{r}\right)^{n+1} \sum_{m=0}^{n} P_n^m(\theta) \cdot \left[g_n^m \cos m\phi + h_n^m \sin m\phi\right] ; \; r \geq R_E \qquad (2\text{-}13)$$

where r is the radial distance from the earth's center, R_E is the earth's radius, and θ and ϕ are geographic colatitude and east longitude, respectively. The Schmidt functions (Reference 10):

$$P_n^m(\theta) = \left[\frac{(n-m)!\left(2-\delta_{o,m}\right)}{(n+m)!}\right]^{1/2} P_{n,m}(\theta) \qquad (2\text{-}14)$$

are multiples of the associated Legendre functions $P_{n,m}(\theta)$ of degree n and order m; the Kronecker delta $(\delta_{o,m})$ equals one if m = 0 and equals zero if $m \neq 0$. The g_n^m and h_n^m are constants referred to as Gaussian coefficients whose values (to some maximum $\acute{n}$) are obtained from a best fit to measured values of the surface magnetic field components (Equation 2-12). Once the g_n^m and the h_n^m are known, Ψ_m is completely determined and defines the field for $r \geq R_E$. Analytic techniques have been developed recently that allow Gaussian coefficients to be derived from measured values of the total field intensity rather than from measured field components (Reference 11), thus making possible the utilization of numerous satellite measurements.

Ψ_m is sometimes expanded in Gauss-normalized, associated-Legendre functions (Reference 10) rather than in Schmidt-normalized functions. Either representation is valid, of course, but some practicable value exists in using Schmidt functions since the magnitudes of the corresponding g_n^m and h_n^m then will indicate the relative contribution of the various terms in the series.

2.4.1 Field Models

Tables of Gaussian coefficients have been determined by a number of investigators. The field models that have been applied to trapped radiation studies are:

1. The Jensen and Whitaker (JW) 569-coefficient model (Reference 12)
2. The Jensen and Cain (JC) 48-coefficient model (Reference 13)
3. The Goddard Space Flight Center [GSFC (9/65)] 99-coefficient model (Reference 14)
4. The Goddard Space Flight Center [GSFC (12/66)] 120-coefficient model (Reference 15).

The JW and JC models are static models and represent the field in 1955 and 1960 respectively. The JW model was used to reduce Explorer 4 data. The JC model has been used for several years and has become the model used most widely for interpreting trapped radiation data. The GSFC (9/65) model takes secular variation of the field into account by including first derivatives with respect to time of the initial 48 coefficients. The GSFC (12/66) model contains second-time derivatives as well as first-time derivatives in all its coefficients. It is a recent field model (epoch 1965) and is thought to be more accurate than the other three models noted above (References 15, 16, and 17). Comparisons with experimental values suggest that this model gives results in error by no more than a few tens of gammas [1 gamma (γ) = 10^{-5} gauss], although this conclusion awaits further investigation. Coefficients for the JC model are given in Table 2-1. The charts in Appendix 2C show contours of the total field intensity at various altitudes, as determined from the Jensen and Cain field model. Tables of coordinate points defining geomagnetic field lines are given in Reference 18 for a representative group of field lines distributed around the earth.

2.4.2 B, L Coordinates

The charts in Appendix 2C also show contours of constant-L, where L is the parameter associated with a magnetic shell (Reference 5) in the geomagnetic field and is analogous to the $L = R_0/R_E$ defined for a dipole field in Section 2.3.2. L is discussed in detail in Section 3.

A coordinate system employing B and the parameter L is used extensively to describe the distribution of trapped particles in radiation belts. Because of the azimuthal asymmetry of the geomagnetic field, the altitude of a constant-B, L contour around the earth will vary with longitude. Figure 2-11 shows the variation for several values of B on the magnetic shell L = 1.20. B is in gauss. The curves are based on the field model in Reference 13. Similar graphs are also given in Appendix 2D for L = 1.12, 1.60, 2.20, and 3.50. These graphs are useful because trapped particles experience similar changes in their mirror point altitudes as they drift around the earth. (Trapped particle motion is discussed in Section 3.)

For the cases shown, the variations in altitude are appreciable; maximum variations of 1,200 to 1,500 kilometers occur in the southern hemisphere. The minimum altitude for a given value of B is observed to occur in the southern hemisphere near 315°E longitude.

Table 2-1. Spherical harmonic coefficients (gammas) of the geomagnetic field for epoch 1960 (Reference 13).

n	m	g_n^m	h_n^m	n	m	g_n^m	h_n^m
1	0	30411.2		5	0	1625.6	
1	1	2147.4	-5798.9	5	1	-3440.7	- 79.6
2	0	2403.5		5	2	-1944.7	-200.0
2	1	- 5125.3	3312.4	5	3	- 60.8	459.7
2	2	- 1338.1	- 157.9	5	4	277.5	242.1
3	0	- 3151.8		5	5	69.7	-121.8
3	1	6213.0	1487.0	6	0	-1952.3	
3	2	- 2489.8	- 407.5	6	1	- 485.3	-575.8
3	3	- 649.6	21.0	6	2	321.2	-873.5
4	0	- 4179.4		6	3	2141.3	-340.6
4	1	- 4529.8	-1182.5	6	4	105.1	- 11.8
4	2	- 2179.5	1000.6	6	5	22.7	-111.6
4	3	700.8	43.0	6	6	111.5	- 32.5
4	4	- 204.4	138.5				

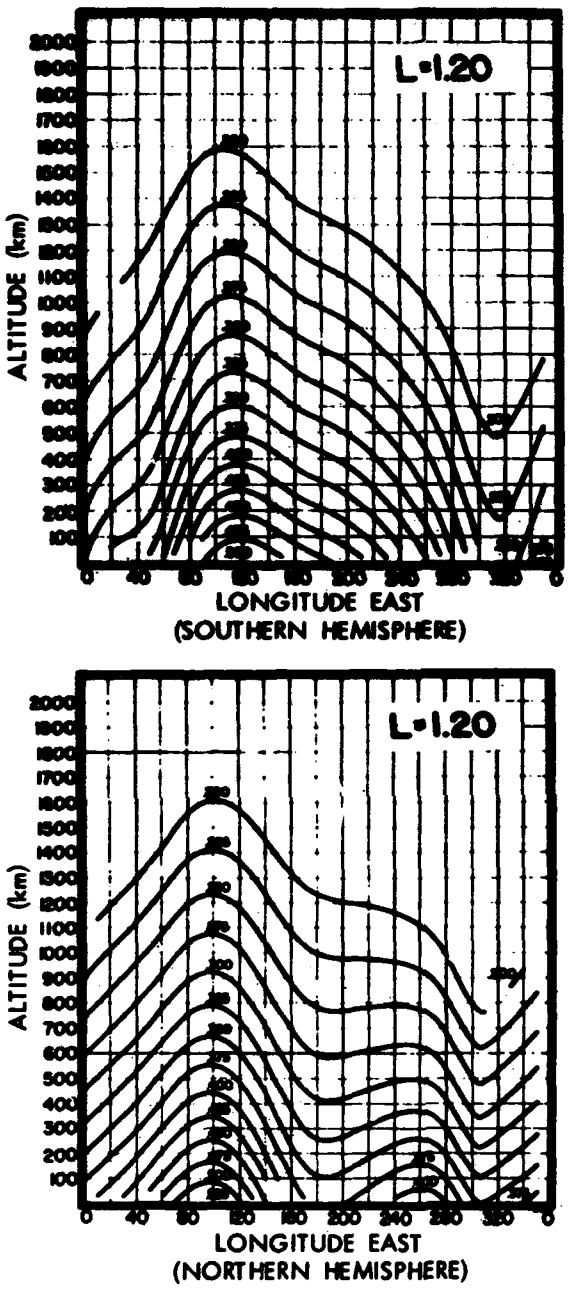

Figure 2-11. Altitude versus longitude for constant-B traces on the magnetic shell L = 1.20 (Reference 19).

More precisely, the minimum altitudes occur in the southern Atlantic near Brazil in a region of low field values (Figure 2-2) known variously as the South American, South Atlantic, or Brazilian anomaly. However, this feature of the geomagnetic field is not really anomalous, but is just the result of the field lines dipping closer to the earth in the anomaly region because of the eccentricity of the geomagnetic field with respect to the earth's center.

The South American anomaly is important in trapped radiation studies because it is a region where particle losses due to atmospheric scattering (Section 4.7) are enhanced as a consequence of the denser atmosphere encountered by the particles as they move through their minimum altitudes. A comprehensive graph of minimum altitudes in the anomaly as a function of B and L is presented in Figure 2-12. Particle measurements in the B, L regions below 1,000 kilometers should show solar cycle effects because of changes in atmospheric density and composition. Also see Section 4.7.

For easy visualization, fluxes in B, L space are sometimes transformed to polar coordinate space r, λ defined by the dipole relations (Reference 5). Figure 2-13 shows a mapping of polar coordinates onto the B, L plane by means of the dipole relations:

$$B = \frac{0.312}{r^3}\left(4 - \frac{3r}{L}\right)^{1/2}, \quad r = L\cos^2\lambda$$

In these relations, r is expressed in units of earth radii. At low values of λ, determining numerical values from Figure 2-7 may be preferable. Some caution should be exercised in using the figure because of the asymmetry of the geomagnetic field.

The invariant latitude (Λ) defined by the expression:

$$\cos^2\Lambda = 1/L \qquad (2\text{-}15)$$

is sometimes used to organize auroral or particle precipitation data near earth. It is interpreted as the latitude where the magnetic shell whose value is L intersects the earth. Table 2-2 gives values of Λ versus L for 0.5-degree intervals in Λ from 0 to 89.5 degrees.

2.5 DISTANT MAGNETIC FIELD

The geomagnetic field at distances beyond about six earth radii is considerably distorted by the presence of plasma currents flowing in

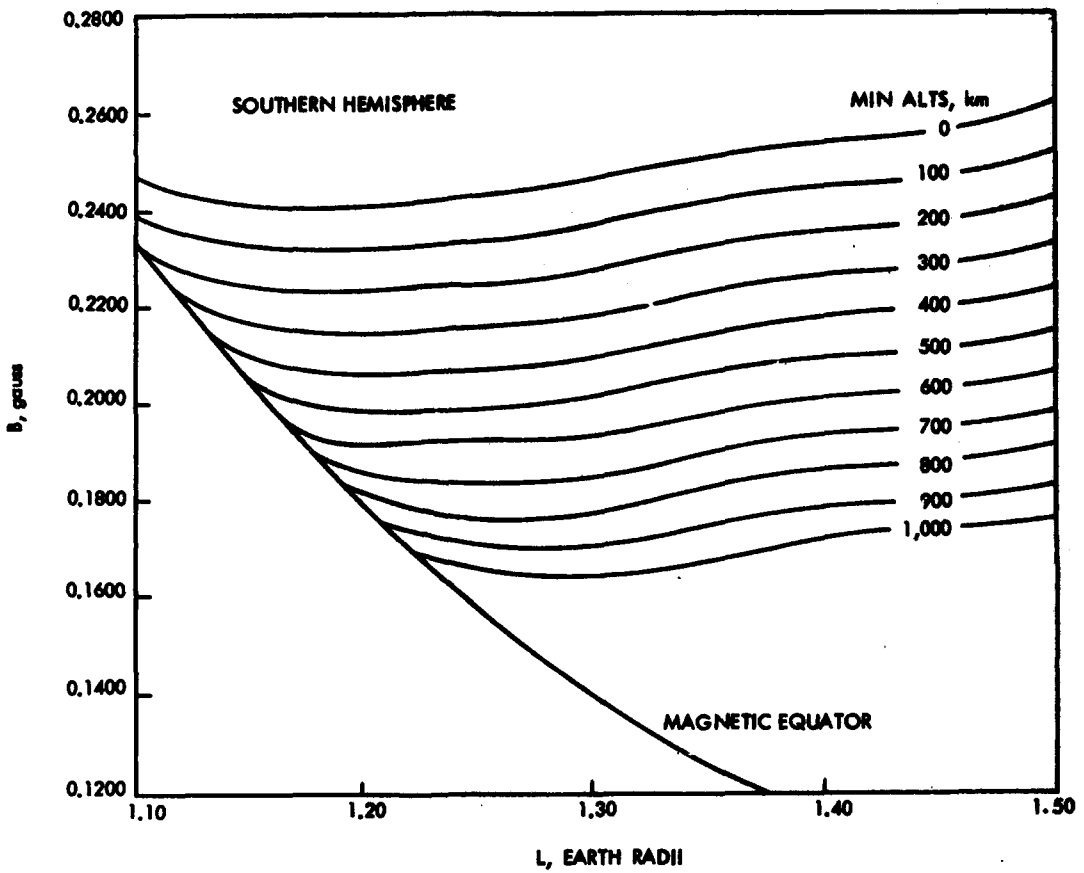

Figure 2-12. Values of minimum altitudes in the southern hemisphere as a function of B, L.

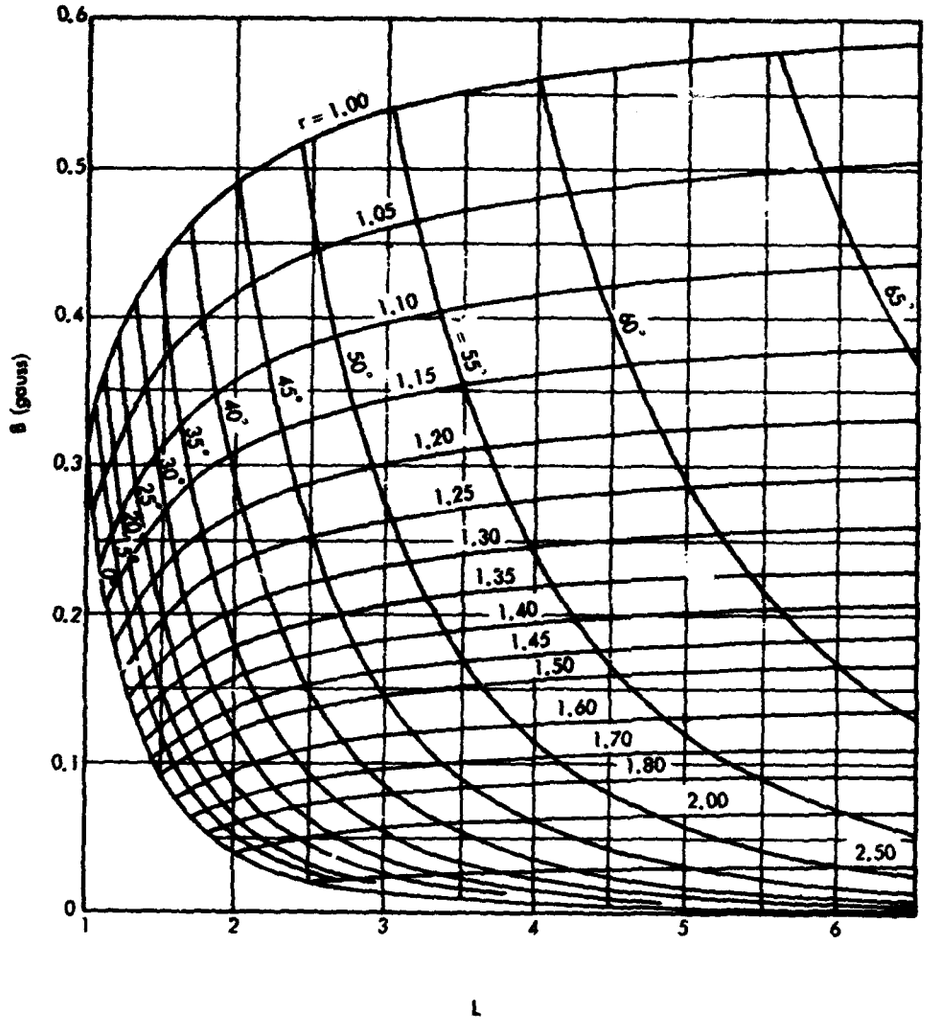

Figure 2-13. Mapping of the r, λ coordinates on to the B,L plane by means of the dipole relations.

Table 2-2. Tabular values of invariant latitude Λ (degrees) versus L.

Λ	L	Λ	L	Λ	L	Λ	L
.0	1.0000	22.5	1.1716	45.0	2.0000	67.5	6.8284
.5	1.0001	23.0	1.1802	45.5	2.0355	68.0	7.1261
1.0	1.0003	23.5	1.1891	46.0	2.0723	68.5	7.4447
1.5	1.0007	24.0	1.1982	46.5	2.1105	69.0	7.7865
2.0	1.0012	24.5	1.2077	47.0	2.1500	69.5	8.1536
2.5	1.0019	25.0	1.2174	47.5	2.1910	70.0	8.5486
3.0	1.0027	25.5	1.2275	48.0	2.2335	70.5	8.9745
3.5	1.0037	26.0	1.2379	48.5	2.2776	71.0	9.4344
4.0	1.0049	26.5	1.2486	49.0	2.3233	71.5	9.9322
4.5	1.0062	27.0	1.2596	49.5	2.3709	72.0	10.4721
5.0	1.0077	27.5	1.2710	50.0	2.4203	72.5	11.0590
5.5	1.0093	28.0	1.2827	50.5	2.4716	73.0	11.6985
6.0	1.0110	28.5	1.2948	51.0	2.5250	73.5	12.3970
6.5	1.0130	29.0	1.3073	51.5	2.5805	74.0	13.1621
7.0	1.0151	29.5	1.3201	52.0	2.6383	74.5	14.0024
7.5	1.0173	30.0	1.3333	52.5	2.6984	75.0	14.9282
8.0	1.0198	30.5	1.3470	53.0	2.7610	75.5	15.9515
8.5	1.0223	31.0	1.3610	53.5	2.8263	76.0	17.0864
9.0	1.0251	31.5	1.3755	54.0	2.8944	76.5	18.3497
9.5	1.0280	32.0	1.3905	54.5	2.9655	77.0	19.7617
10.0	1.0311	32.5	1.4059	55.0	3.0396	77.5	21.3465
10.5	1.0344	33.0	1.4217	55.5	3.1171	78.0	23.1335
11.0	1.0378	33.5	1.4381	56.0	3.1980	78.5	25.1588
11.5	1.0414	34.0	1.4550	56.5	3.2826	79.0	27.4664
12.0	1.0452	34.5	1.4724	57.0	3.3712	79.5	30.1116
12.5	1.0491	35.0	1.4903	57.5	3.4639	80.0	33.1634
13.0	1.0533	35.5	1.5088	58.0	3.5611	80.5	36.7098
13.5	1.0576	36.0	1.5279	58.5	3.6629	81.0	40.8634
14.0	1.0622	36.5	1.5475	59.0	3.7698	81.5	45.7716
14.5	1.0669	37.0	1.5678	59.5	3.8821	82.0	51.6285
15.0	1.0718	37.5	1.5888	60.0	4.0000	82.5	58.6955
15.5	1.0769	38.0	1.6104	60.5	4.1240	83.0	67.3304
16.0	1.0822	38.5	1.6327	61.0	4.2546	83.5	78.0337
16.5	1.0877	39.0	1.6558	61.5	4.3921	84.0	91.5231
17.0	1.0935	39.5	1.6795	62.0	4.5371	84.5	108.8564
17.5	1.0994	40.0	1.7041	62.5	4.6902	85.0	131.6461
18.0	1.1056	40.5	1.7295	63.0	4.8518	85.5	162.4476
18.5	1.1120	41.0	1.7557	63.5	5.0228	86.0	205.5089
19.0	1.1186	41.5	1.7827	64.0	5.2037	86.5	268.3177
19.5	1.1254	42.0	1.8107	64.5	5.3955	87.0	365.0896
20.0	1.1325	42.5	1.8397	65.0	5.5989	87.5	525.5820
20.5	1.1398	43.0	1.8696	65.5	5.8150	88.0	821.0345
21.0	1.1474	43.5	1.9005	66.0	6.0447	88.5	1459.3566
21.5	1.1552	44.0	1.9326	66.5	6.2893	89.0	3283.1318
22.0	1.1632	44.5	1.9657	67.0	6.5500	89.5	13131.4805

the tail of the magnetosphere and currents in the magnetopause arising from the interaction of the solar wind with the geomagnetic field.

A spherical harmonic expansion of the boundary current field is derived by Mead (Reference 20), based on the boundary surface and boundary currents determined by Mead and Beard (Reference 21). The model contains the assumption that the impinging solar wind is field free and is reflected specularly from a plasma-free dipole field oriented perpendicular to the sun-earth line. Mead found that the boundary current field, except near the boundary, could be approximated to within about 3 percent by a simple expansion involving only two coefficients. For this case, the components of the total field (dipole + boundary current) at a given point are:

$$- B_\theta(\text{gauss}) = \frac{0.31 \sin\theta}{r^3} + \frac{0.25 \sin\theta}{R_b^3} +$$

$$\frac{0.21\, r}{R_b^4}(2\cos^2\theta - 1)\cos\phi \qquad (2\text{-}16a)$$

$$B_\phi(\text{gauss}) = \frac{0.21\, r}{R_b^4}\cos\theta \sin\phi \qquad (2\text{-}16b)$$

$$- B_r(\text{gauss}) = \frac{0.62\cos\theta}{r^3} - \frac{0.25\cos\theta}{R_b^3} +$$

$$\frac{0.42\, r}{R_b^4}\sin\theta\cos\theta\cos\phi \qquad (2\text{-}16c)$$

where r is the geocentric distance in earth radii, θ is the colatitude, ϕ is the local time measured from the midnight meridian, and R_b is the geocentric distance in earth radii to the magnetosphere boundary along the sun-earth line. The boundary distance is related to solar wind parameters by the formula:

$$R_b = 1.068\left(M_E^2/4\pi\, mnu^2\right)^{1/6} \qquad (2\text{-}17)$$

where n is the ion density, m the ion mass, and u the stream velocity of the solar wind. M_E is the dipole moment of the earth.

Using a description of the distorted field, basically the same as given by the Equations 2-16a, 2-16b, and 2-16c but including the higher order terms, Mead has calculated the field-line configuration in the magnetosphere and presents the results in several useful graphs and diagrams in his article. Figure 2-14 shows field lines in the noon-midnight meridian plane, as compared with a pure dipole field. The latitudes where the field lines intersect the earth's surface are noted in the figure. Field lines emerging at less than 60-degree latitude ($L \lesssim 4R$) are not distorted appreciably from a dipole configuration. This model is believed to provide a good fit to the distorted field during quiet times on the day side of the magnetosphere and out to about 5 R_E on the night side (at times of the equinoxes when the geomagnetic axis is nearly perpendicular to the sun-earth line).

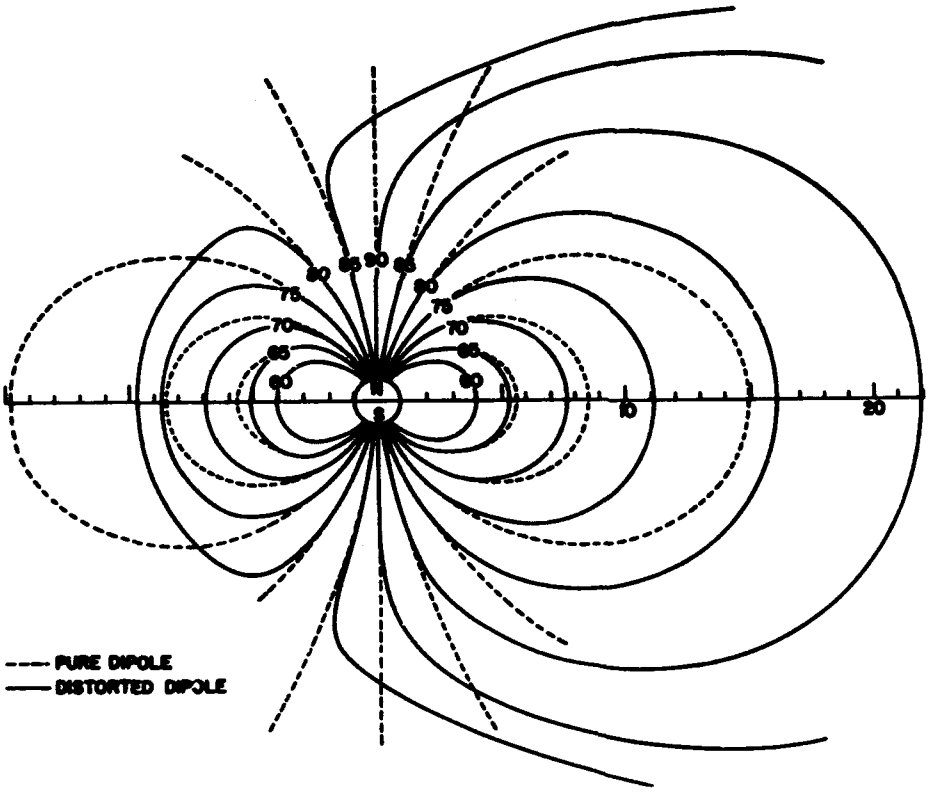

Figure 2-14. Field-line configuration in the noon-midnight meridian plane, with $R_b = 10\ R_E$ (Reference 20).

Williams and Mead (Reference 22) modified the Mead and Beard model simply by adding vectorially to Mead's distorted field model (Reference 20) an additional field to represent the effects of the plasma currents associated with the neutral sheet that separates oppositely directed field lines in the tail of the magnetosphere. The added field is two-dimensional and is pertinent only near the noon-midnight meridian plane of symmetry.

The geometry chosen to represent the additional field is shown in Figure 2-15. The x-axis points away from the sun and the y-axis points south. The components of the field produced by a semi-infinite current sheet in the geomagnetic equatorial plane and extending from R_1 to R_2 in the x direction are:

$$B_x = -2J(\theta_2 - \theta_1) \qquad (2\text{-}18a)$$

$$B_y = 2J \log (\rho_2/\rho_1) . \qquad (2\text{-}18b)$$

Current flow is out of the plane of the paper; J is the current density (per unit length) in electromagnetic current units. Figure 2-16 shows the resulting magnetic field configuration in the noon-midnight meridian plane for $R_1 = 10\ R_E$, for $R_2 = 40\ R_E$, and for a value of J that produces a field of 40 gammas immediately adjacent to the sheet. Latitudes where the field lines intersect the earth's surface are given. The general effect of a neutral sheet field is to stretch out the lines of force in the tail region.

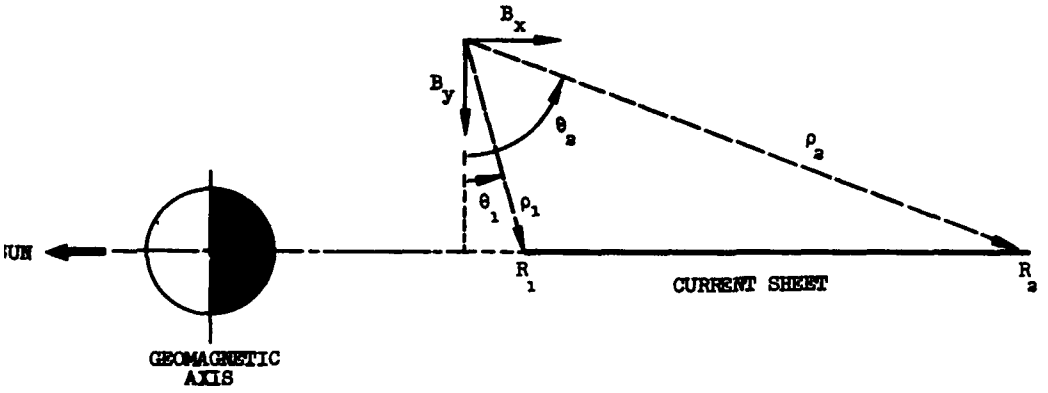

Figure 2-15. Coordinate system used to define the field due to a semi-infinite current sheet (Reference 22).

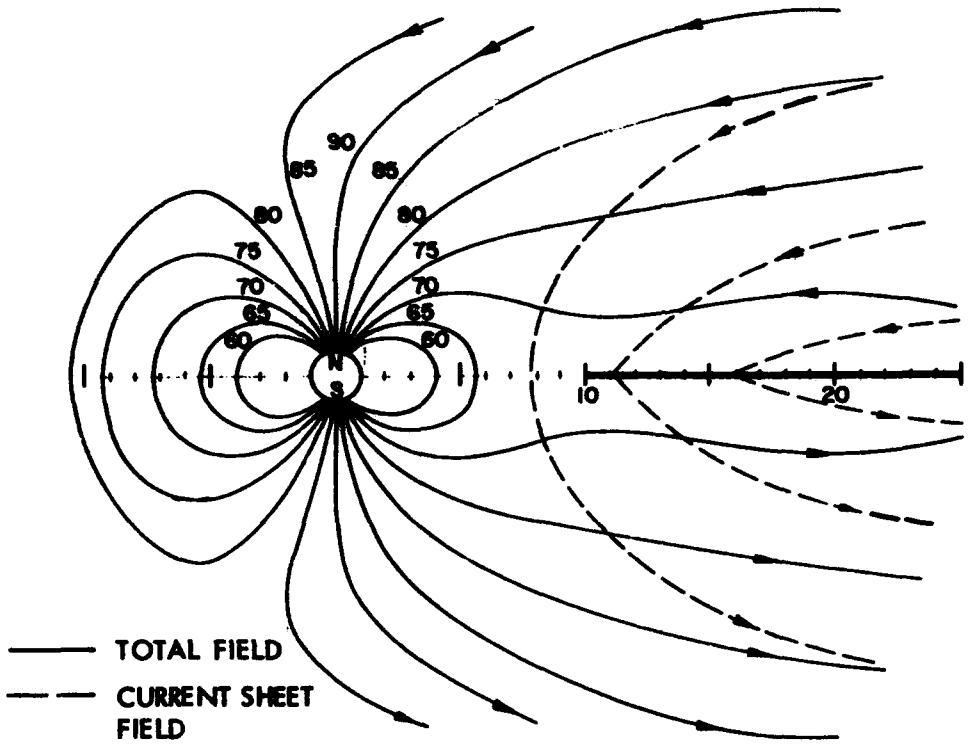

Figure 2-16. Field-line configuration in the noon-midnight meridian plane, including the field due to a current sheet (Reference 22).

2.6 GEOMAGNETIC TRANSIENT VARIATIONS

2.6.1 Solar Quiet and Lunar Daily Variations

The continuous traces of the three magnetic elements recorded at any station consistently show a daily time variation that is correlated with local time. The maximum variation occurs near local noon and is on the order of 0.1 percent of the total field. On some days, the variations are smooth and regular; on other days, the changes are irregular because of magnetic disturbances superimposed on the smooth variation. The days in which irregular variations are recorded are said to be magnetically active or disturbed days; those with smooth traces are called magnetically quiet days.

The average variation patterns, derived for the field components from suitably chosen quiet-day records at a station, collectively define a variation field denoted by Sq, the solar quiet daily variation. For each component, the variation is reckoned using the daily mean value of the component at the station as a base line. The global distribution of Sq varies systematically with latitude. In the magnetic equatorial zone, the maximum variation in the horizontal intensity H near local noon is characteristically about 100 gammas, and at higher latitudes is -25 to -50 gammas.

Sq is also dependent on the season of the year and the phase of the solar cycle. At the June solstice, Sq is enchanced in the northern hemisphere and diminished in the southern hemisphere. At the December solstice, the situation is reversed. At sunspot maximum, Sq increases.

The daily variation of the field also includes a component having a period of 0.5 lunar day ($\approx$ 12.42 hours) and a pattern that varies systematically with the phase of the moon. This variation is less than 0.1 that of Sq. The average of this component of the magnetic variation over many lunar days at a station is called the lunar daily variation, L, (not to be confused with the L-shell parameter). L is somewhat enhanced during sunlight hours and displays seasonal changes indicating that the sun, as well as the moon, plays a controlling role.

Spherical harmonic analysis of Sq or L data from a world network of stations is used to determine the equivalent electric current systems responsible for the observed magnetic variations. About two thirds of the variations in Sq or in L is found to be due to current sources external to the earth and the remaining one third to internal currents induced within the earth's surface layers by variable external currents. The external currents responsible for Sq and L are found to flow at approximately the same altitude ($\sim$100 kilometers). The ratio of average external Sq and L current intensities is about 30 to 1.

The Sq and L electric current systems are produced by convective movement of the conducting upper atmosphere across the earth's magnetic field lines. The motion of the upper atmosphere occurs as a result of pressure and temperature differentials in the atmosphere brought about by solar heating and tidal forces. By analogy with an electric dynamo, this mechanism is referred to as the atmospheric dynamo (Reference 23).

For a detailed discussion of solar quiet and lunar daily variations, including plots of Sq and L and their associated current systems, see Reference 24.

From rocket measurements, X rays are known to be emitted by solar flares. On arrival at earth, these X rays cause an increase in ionization in the sunlit hemisphere, particularly at lower levels. The overhead current system is enhanced, often producing an observable magnetic field variation called a solar flare effect (sfe) or a crochet (Reference 25). The variation lasts 10 to 60 minutes and is manifested as an augmentation of Sq. Ionospheric currents due to solar flares occur lower in the ionosphere than Sq currents and sometimes seem to flow in the night hemisphere but with reduced intensity.

2.6.2 Geomagnetic Storms

A severe and long-lasting magnetic disturbance that occurs worldwide is called a magnetic storm (References 25 and 26) and often is accompanied by auroral displays and polar ionospheric disturbances. The rate of occurrence of magnetic storms varies with the solar sunspot cycle.

Magnetograms obtained at low- and middle-latitude stations indicate that many storms undergo a similar pattern of development as the storms progress. The start of a typical storm is characterized by an abrupt increase in H and is known as the sudden commencement (S.C.) of the storm. The increase is typically 20 to 30 gammas with a rise time of 2 to 6 minutes; it is largest at stations near the magnetic equator. The 2- to 8-hour interval during which the value of H remains above its undisturbed value is known as the initial phase of the storm.

The main phase of the storm follows and lasts 12 to 24 hours during which H decreases to values that are typically 50 to 100 gammas below the prestorm value. The final stage of the storm, known as the recovery phase, commences and H gradually recovers to its normal level in 1 to 3 days, although recovery time as long as 20 to 30 days is not uncommon. Individual storm records show irregularities. The initial and main phases tend to be noisy. Often during the main phase, large amplitude fluctuations occur with periods of about 0.5 hours. Some storms do not conform to this classic pattern and have features that are missing or not easily identified.

The simultaneous storm records obtained at auroral zone and polar cap stations are markedly different from this regular storm pattern and are characterized by extremely large and sometimes very rapid changes. Careful analysis is required to detect the regular storm variations in the high-latitude records.

The analysis of storms has shown that the typical storm variation over the earth can be described conveniently by two components: (1) Dst (or DST), which is symmetric about the geomagnetic axis, and (2) DS (or Ds), which is a function of longitude relative to the sun (Reference 25). Both components are also dependent on magnetic latitude and storm time (time measured from the start of the storm).

Changes in the dynamic pressure of the solar wind blowing against the geomagnetic field are believed to be a cause of magnetic storms (Reference 27). The solar wind suddenly increases, compressing the magnetic field (S.C.) and maintains the compression for a time (initial phase). An outward distention then occurs (main phase) and is followed by a relaxation of the field to its prestorm value (recovery phase). Some uncertainty exists whether the main phase is produced by an outward distention of the field because of hot plasma generated by attendant processes or whether, instead, the main phase is produced by a westward ring current (circling the earth at several earth radii) consisting of electrons and positive ions that are trapped or injected in the magnetosphere (Reference 25).

Recent experiments suggest that an increase in solar wind pressure may not be a necessary condition for the generation of all magnetic storms (References 28 and 29). Instead, the southward component of the interplanetary field appears to play the major role, an enhancement in this component being strongly correlated with the initiation of some magnetic storms.

2.6.3 Sudden Impulses and Bays

An impulsive change (generally an increase) of several gammas in the magnetic field followed by a gradual return to the normal field value and without subsequent large field changes is called a sudden impulse (S.I. or si) (Reference 25). The changes occur simultaneously at stations all over the world and are similar in characteristics to S.C.'s, but have smaller amplitudes and less abrupt changes in field intensity.

Another type of simple magnetic disturbance is characterized by a gradual increase or decrease in the field followed by a return, perhaps with small oscillations, to the undisturbed field value. These disturbances last 1 to 2 hours and generally are preceded and followed by undisturbed conditions. The horizontal component of the field is affected most strongly and departs from undisturbed field values by 5 to 20 gammas at midlatitude stations and is perhaps a factor of 10 greater at higher latitudes. These disturbances are known as magnetic bays because the resulting curves of field intensity (principally H) recorded at a station resemble a bay as it appears drawn on a map (Reference 30). Magnetic bays are most pronounced at high latitudes and occur principally at night near local midnight. Positive bays occur several times more frequently than do negative bays. The generation of magnetic bays and sudden impulses is related to changes in the solar wind pressure and to changes in the southward component of the interplanetary field (References 28 and 29).

2.7 GEOMAGNETIC PULSATIONS

2.7.1 Micropulsations

Micropulsations are geomagnetic field fluctuations that occur in the ultra low frequency (ULF) region below about 3 hertz (Reference 31). They have periods ranging from about 0.2 seconds to 10 minutes and amplitudes varying from a fraction of one gamma to several tens of gammas. Figure 2-17 is an approximate representation of the power spectrum of magnetic fluctuations at the earth's surface (References 32, 33, and 34). The figure is a composite of data recorded in various frequency ranges (References 32, 35, 36, 37, 38, and 39). Though the general trend of the data presented in the figure may be accepted as a fair representation of actual average conditions, substantial uncertainties still exist in the interrelationship between various types of disturbances. The ranges of proton and electron gyrofrequencies, ν_i and ν_e, respectively, are indicated. The range of periods τ and characteristic amplitudes δH are indicated for several classes of fluctuations. The micropulsation spectrum is bordered at low frequencies by storm time and Sq phenomena and at high frequencies by extra low frequency (ELF) phenomena.

Certain types of micropulsations have been classified according to the assignments shown in the figure. Micropulsations are divided into two general types: continuous pc and irregular pi. A pc micropulsation displays amplitude variations that are quasi-sinusoidal.

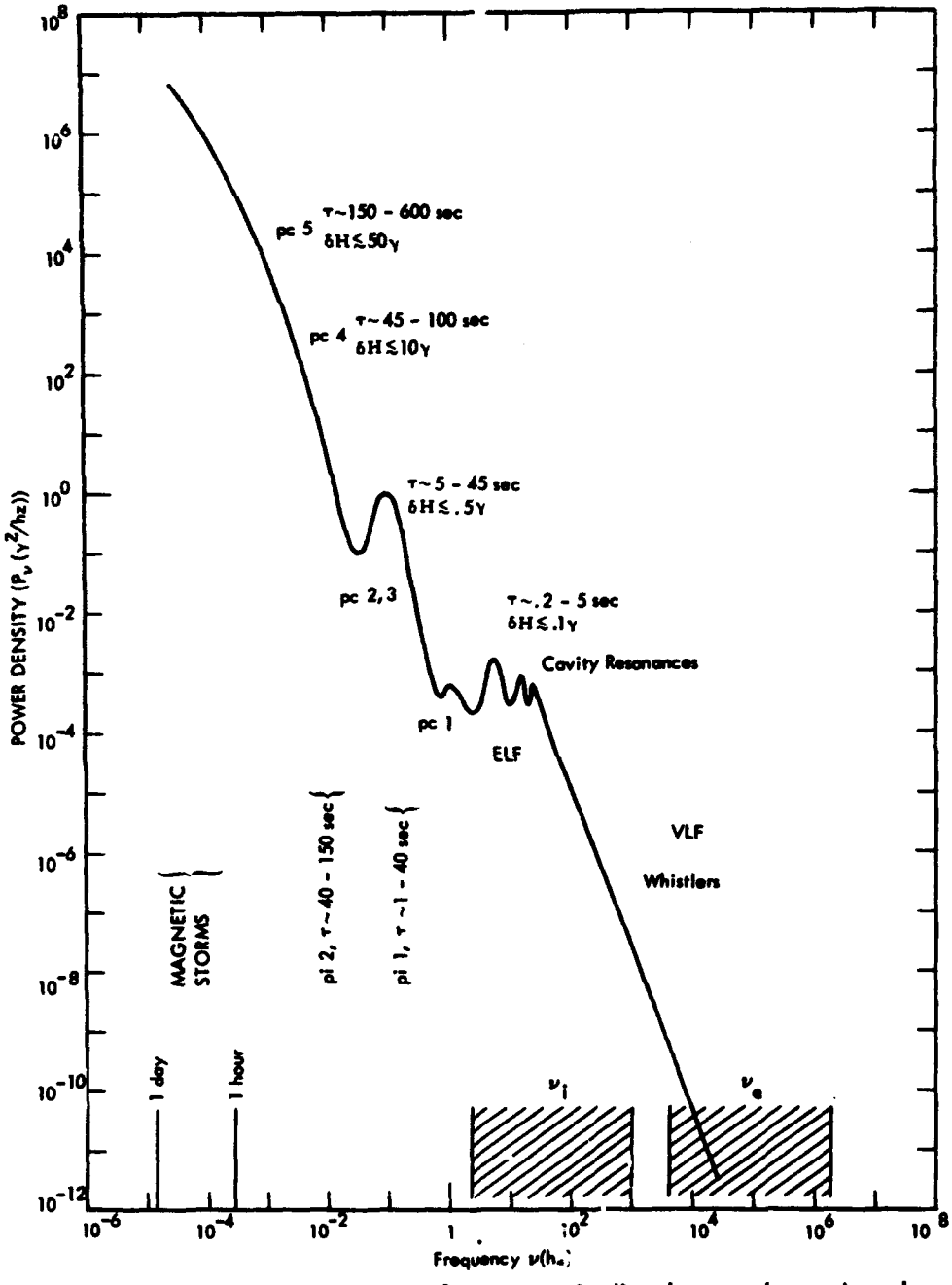

Figure 2-17. Power spectrum of geomagnetic disturbances observed on the earth's surface.

A pi micropulsation has irregularities in both frequency and amplitude. The pc 1 pulsations have amplitude traces that resemble beads on a string and are sometimes referred to as pearls (also hydromagnetic, hm, emissions, and pp). In older literature, pc 5s were known as giant pulsations (Pg) because of large amplitudes.

2.7.2 ELF Pulsations

Pulsation frequencies ranging from about 3 to 3,000 hertz make up the ELF region. The principal pulsations occurring in this frequency range are ELF sferics slow-tails, earth-ionosphere cavity resonances, and ELF emissions (Reference 31).

Sferics (an abbreviation for atmospherics) are electromagnetic signals from atmospheric electrical discharges that propagate in the wave guide formed by the ground and the lower edge of the ionospheric E-region (Reference 40). The waveform of a sferic recorded at a large distance from the source consists of a main high frequency (mostly VLF) oscillatory head, frequently followed by a lower frequency (ELF) tail-like oscillation that is sometimes referred to as a slow-tail (Reference 41). Slow-tails commonly last about 20 milliseconds and have frequency components mainly in the range 30 to several hundred hertz.

Cavity resonance signals are disturbances that are resonantly excited by lightning transients in the concentric spherical cavity formed by the earth's surface and the lower region of the ionosphere (Reference 42). The power spectra of the signals often show maxima near 7.8, 14.1, 20.3, 26.4, and 32.5 hertz.

Occasionally, whistlers and other phenomena that normally occur at higher frequencies in the VLF (very low frequency) range sometimes produce lower frequency components in the ELF region. Also, proton whistlers (Reference 43) and emissions (Reference 44), attributed to radiation at the gyrofrequency of auroral protons, have been observed in the ELF range.

2.7.3 Whistlers and VLF Emissions

Whistlers are field pulsations observed in the frequency range from 300 to 30,000 hertz (Reference 45). They are produced by the electromagnetic disturbance from lightning. A part of the energy from the disturbance penetrates the ionosphere and propagates along

geomagnetic field lines to the opposite hemisphere. The higher frequency components of the disturbance signal arrive first as a result of wave dispersion by the ionosphere. Much of the power is in the audio range (50 to 20,000 hertz). After conversion to audible sound, the signal is perceived as a variable pitch "whistle" lasting a fraction of a second to 2 or 3 seconds. Whistler echoes often are produced when the signal is reflected several times from the end points of its path. Whistlers are more apt to occur at nighttime, probably because of reduced absorption in the ionosphere. The peak in whistler activity occurs near 50-degree geomagnetic latitude; few whistlers are heard near the geomagnetic equator or poles. Nuclear detonations also produce whistlers with characteristics essentially the same as those of natural whistlers.

VLF emissions are other phenomena having frequencies in the whistler range (Reference 45) and are believed to originate from the excitation of whistler mode waves by charged particles streaming along field lines. The most common VLF emission is known as chorus (or dawn chorus) and consists of a series of oscillations producing sounds that resemble birds chirping at dawn. Another kind of emission is a noise known as hiss, produced by continuous broadband emission in the 1- to 20,000-hertz range. Periodic VLF emissions are a type consisting of short bursts repeated at regular intervals, typically of several seconds. They are believed to be caused by a whistler and its echoes triggering other emissions in the ionosphere, perhaps through the agency of streaming instabilities (Section 5). A complete discussion of these and other types of VLF emissions is contained in Reference 45.

APPENDIX 2A
GEOMAGNETIC INDICES

The K-index is designed to measure the degree of magnetic disturbance produced at a station by the solar wind, geomagnetic field interaction. It is intended to serve as an indicator of solar wind activity and is determined at a station for every 3-hour interval during the day, commencing at 0000 Universal Time.

K is based on the amplitude range R of the most disturbed magnetic component observed within a 3-hour interval at the station after Sq and L variations, solar flare effects, and long-term recovery effects have been eliminated from the observations. The ranges of R (in gammas) that define K on a quasi-logarithmic scale for the standard (midlatitude) magnetic observatory are shown in Table 2A-1.

Table 2A-1. Ranges of R (in gammas) that define K on a quasi-logarithmic scale.

K	R (γ)	K	R (γ)
0	0 - 5	5	70 - 120
1	5 - 10	6	120 - 200
2	10 - 20	7	200 - 330
3	20 - 40	8	330 - 500
4	40 - 70	9	≥ 500

To take the latitude dependence of magnetic variations into account, different R scales are adopted at other stations to yield frequency distributions in K that agree with the distribution at the standard observatory. Thus, a K of 9 represents 300 gammas or more at low latitudes and 2,500 gammas or more at auroral zone stations.

The Kp (planetary) 3-hour index is designed to measure the worldwide, or planetary, geomagnetic activity and is based on K-values from

12 stations located at magnetic latitudes varying from 48 to 63 degrees. These K-indices are processed to eliminate local effects and then translated into standardized indices Ks on a finer scale of 28 grades from 0o, 0+, 1-, 1o, 1+, 2-, 2o, 2+, 3-, ... to 7+, 8-, 8o, 8+, 9-, 9o. Kp is the average of the 12 Ks values and also is expressed on the same scale as Ks. A Kp value of 0o indicates an exceptionally quiet period and the value 9o denotes the most severe storm conditions.

A measure of magnetic activity that is approximately linear is sometimes preferred for certain investigations. The 3-hour equivalent planetary amplitude, called ap, was constructed for this purpose by converting Kp to the scale shown in Table 2A-2.

Table 2A-2. Equivalent amplitude ap versus Kp.

Kp	ap	Kp	ap
0o	0	5-	39
0+	2	5o	48
1-	3	5+	56
1o	4	6-	67
1+	5	6o	80
2-	6	6+	94
2o	7	7-	111
2+	9	7o	132
3-	12	7+	154
3o	15	8-	179
3+	18	8o	207
4-	22	8+	236
4o	27	9-	300
4+	32	9o	400

The numerical value of ap is said to be in units of 2 gammas (e.g., for Kp = 4+, ap = 64 gammas) because at the standard observatory the average range in gammas of the most disturbed field element for a given Kp is twice ap. When the eight ap values for one day are

averaged, a new index Ap is obtained known as the daily equivalent planetary amplitude.

Similar scales also have been derived for individual stations and are termed ak and Ak. The index ak, known as the equivalent 3-hour range, is a reconversion of K into a linear scale, and the index Ak, called the equivalent daily amplitude at a station, is the average of the eight ak values for a day. A detailed discussion of magnetic indices is given in Reference 46.

APPENDIX 2B

MAPS OF THE GEOMAGNETIC LATITUDE AND LONGITUDE

This appendix contains north polar, south polar, and world maps of geomagnetic latitude and geomagnetic longitude at the earth's surface and at 3,000-kilometers altitude (Reference 9). The plots are based on the IGRF field model (References 7 and 8) for epoch 1969.75. λ and ϕ are geographic latitude and longitude, and Λ and Φ are geomagnetic latitude and longitude.

Polar azimuthal equidistant projection

NORTH, 0 KM ALT

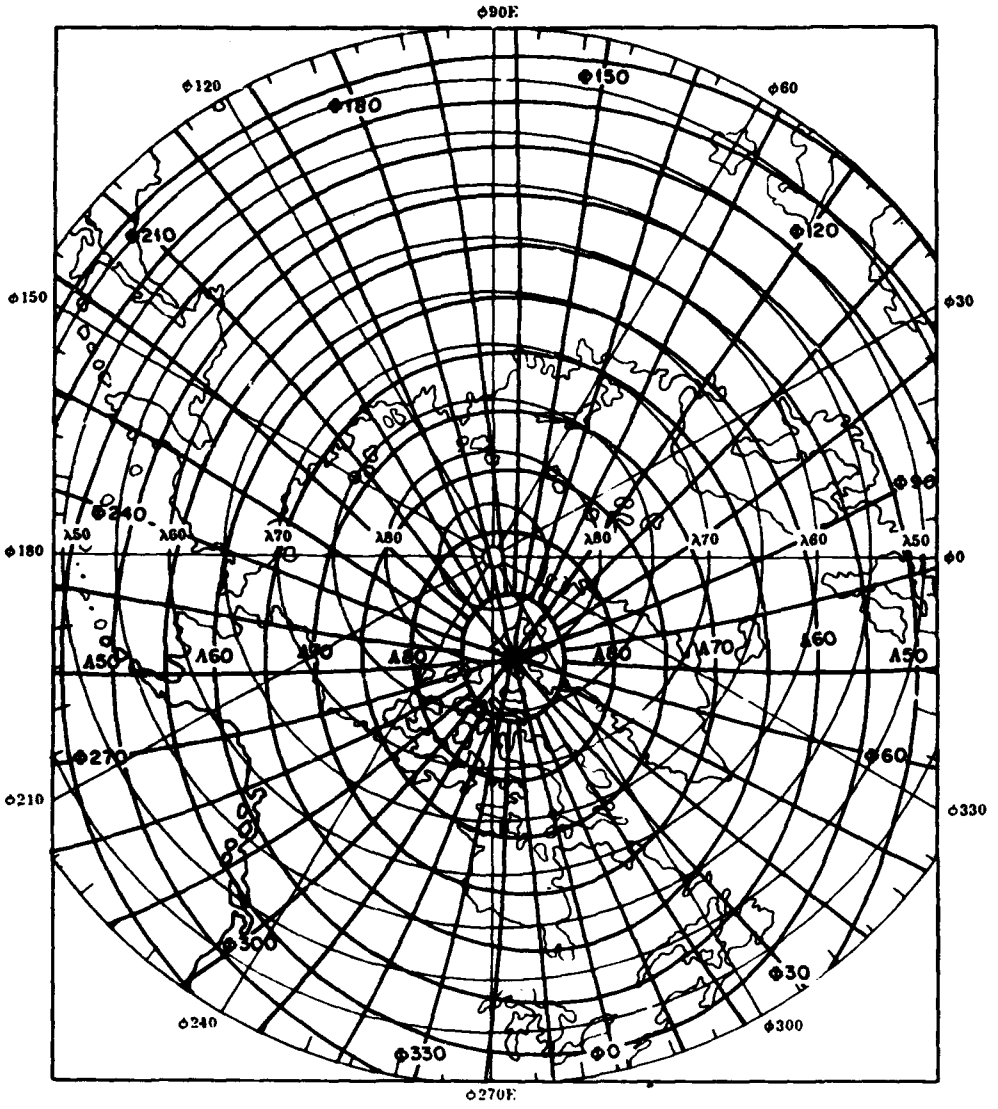

Figure 2B-1. North polar plot of geomagnetic coordinates at 0-kilometer altitude.

Polar azimuthal equidistant projection

SOUTH, 0 KM ALT

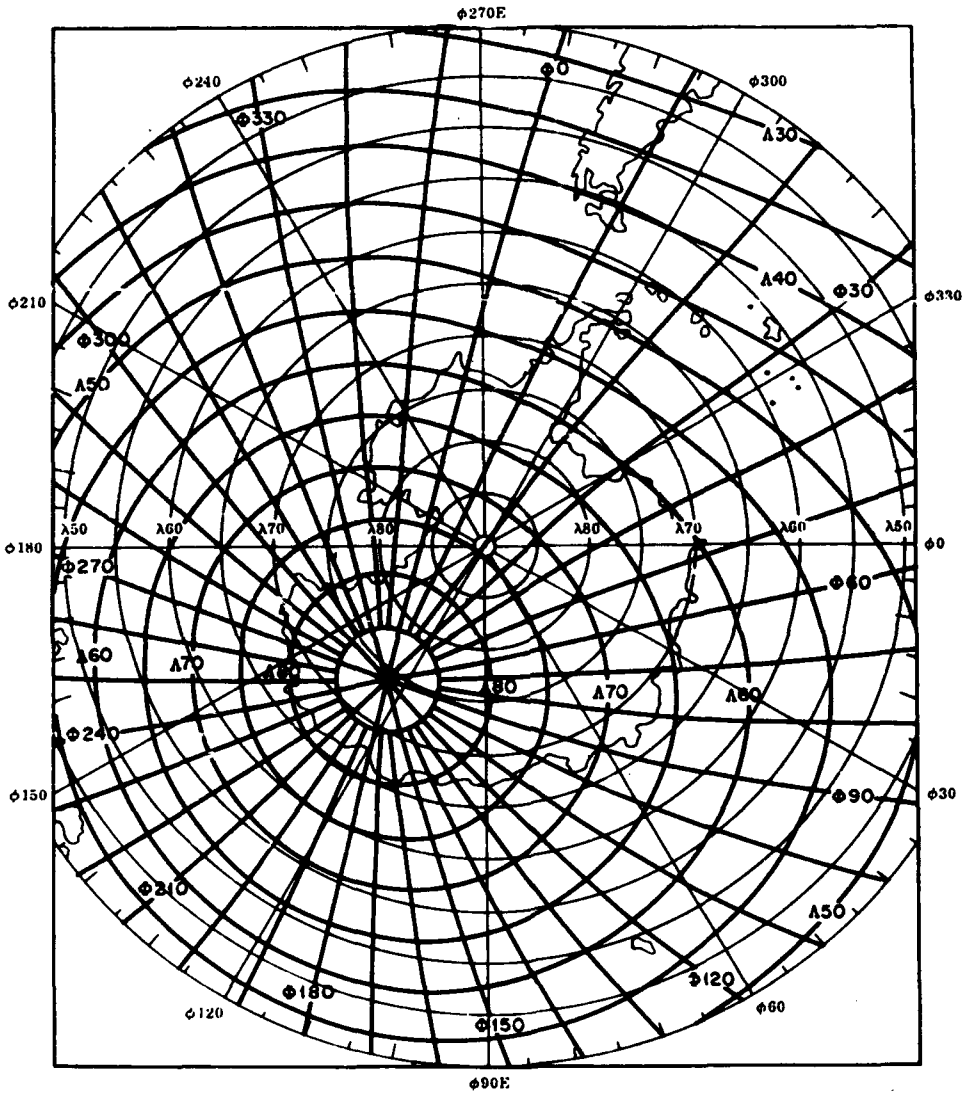

Figure 2B-2. South polar plot of geomagnetic coordinates at 0-kilometer altitude.

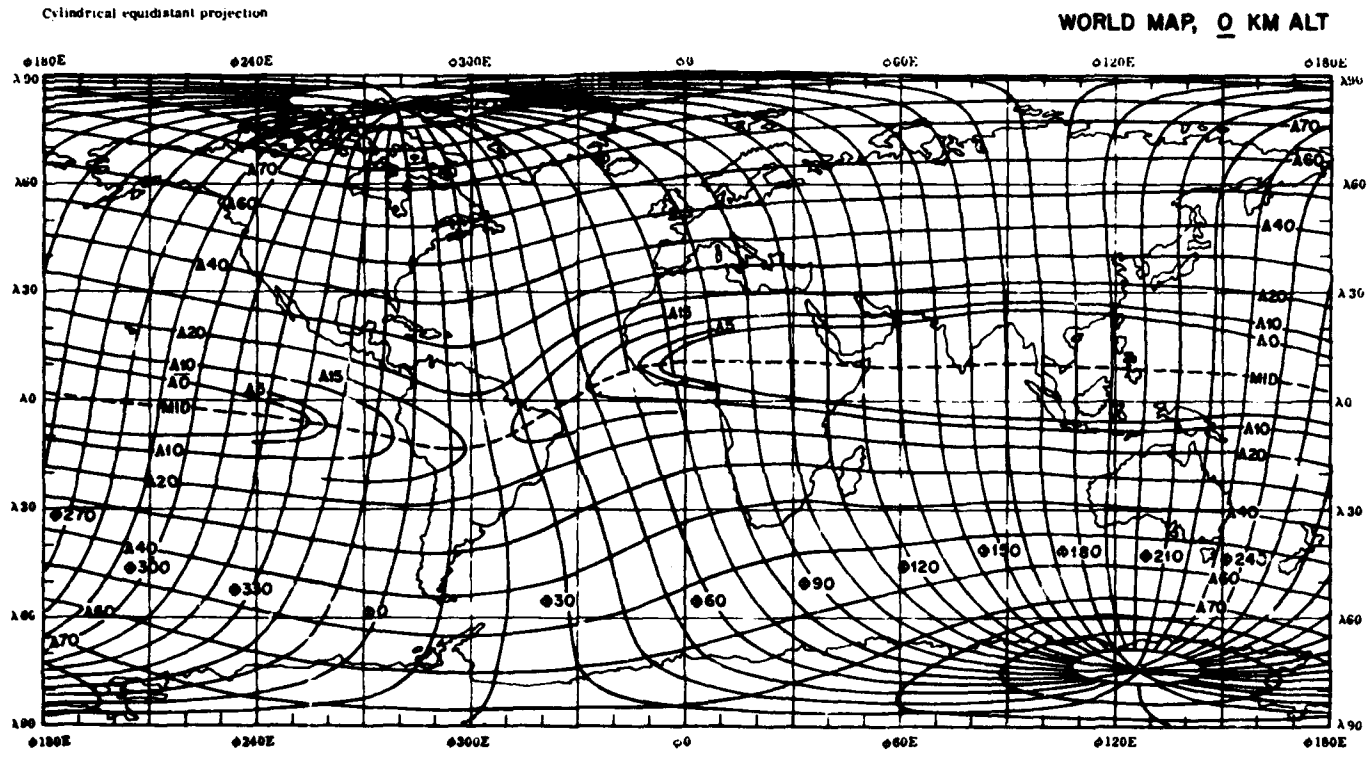

Figure 28-3. World map of geomagnetic coordinates at 0-kilometer altitude.

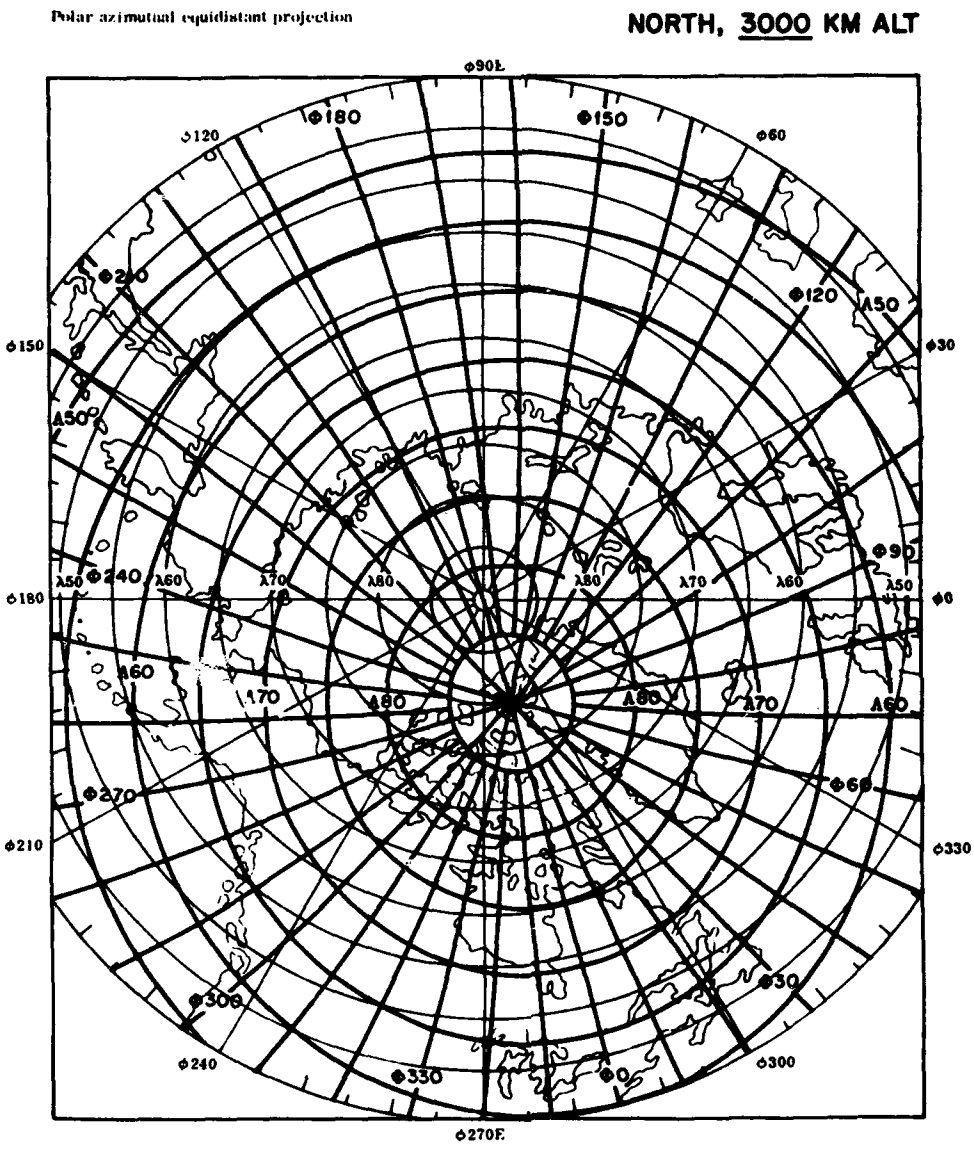

Figure 2B-4. North polar plot of geomagnetic coordinates at 3,000-kilometer altitude.

Polar azimuthal equidistant projection

SOUTH, 3000 KM ALT

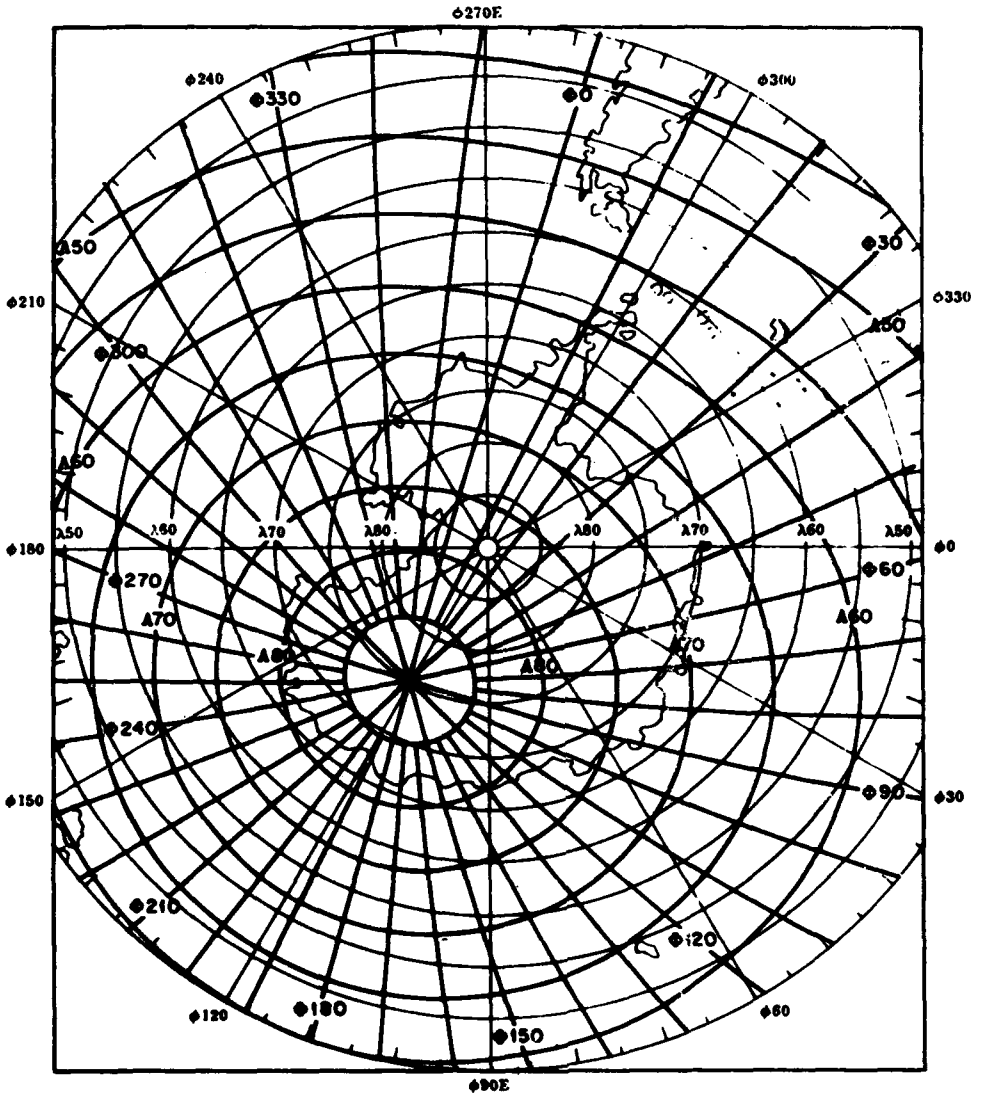

Figure 2B-5. South polar plot of geomagnetic coordinates at 3,000-kilometer altitude.

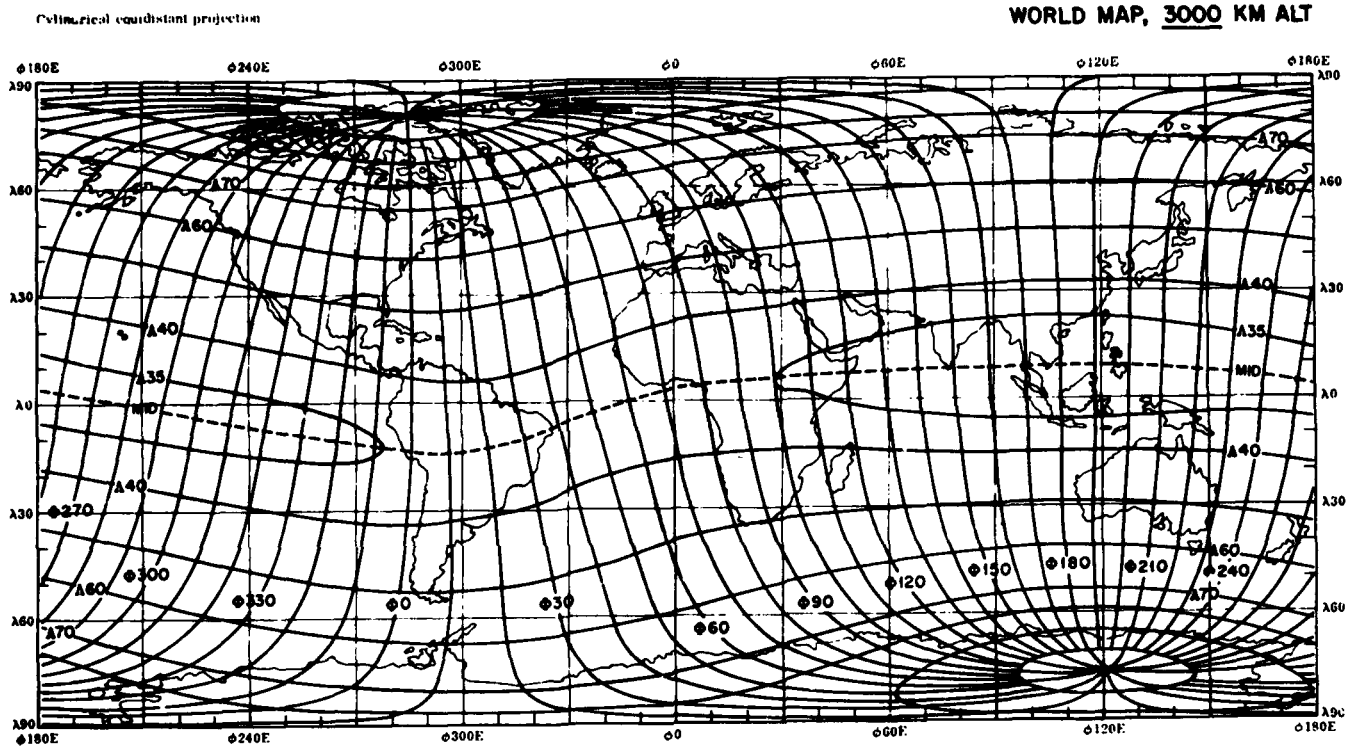

Figure 2B-6. World map of geomagnetic coordinates at 3,000-kilometer altitude.

APPENDIX 2C

CONTOURS B, L FOR VARYING ALTITUDES

This appendix contains contours of constant-B in gauss and contours of constant-L in earth radii at 100-, 400-, 800-, 1,600-, and 2,000-kilometers altitude (References 13 and 47).

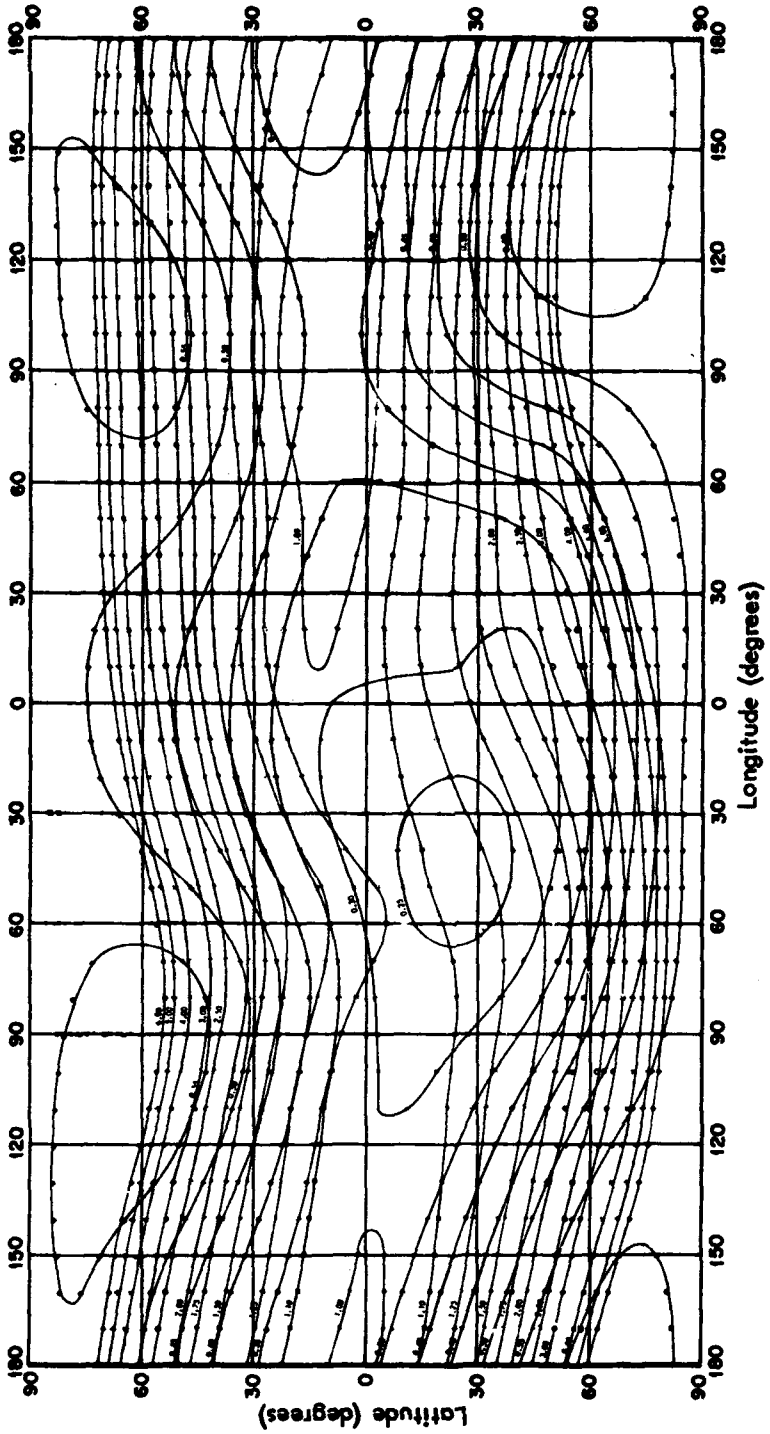

Figure 2C-1. Contours of constant-B and constant-L at 100-kilometer altitude.

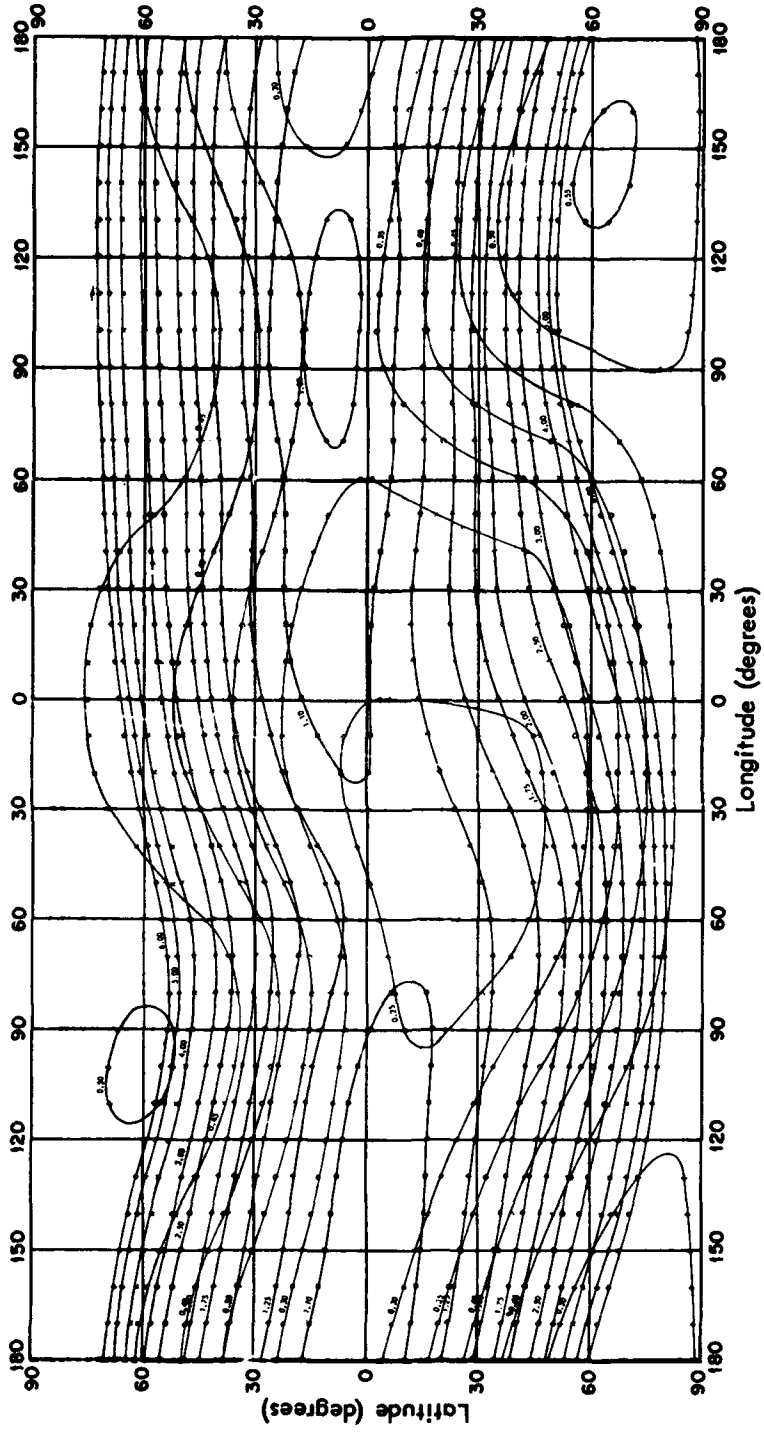

Figure 2C-2. Contours of constant-B and constant-L at 400-kilometer altitude.

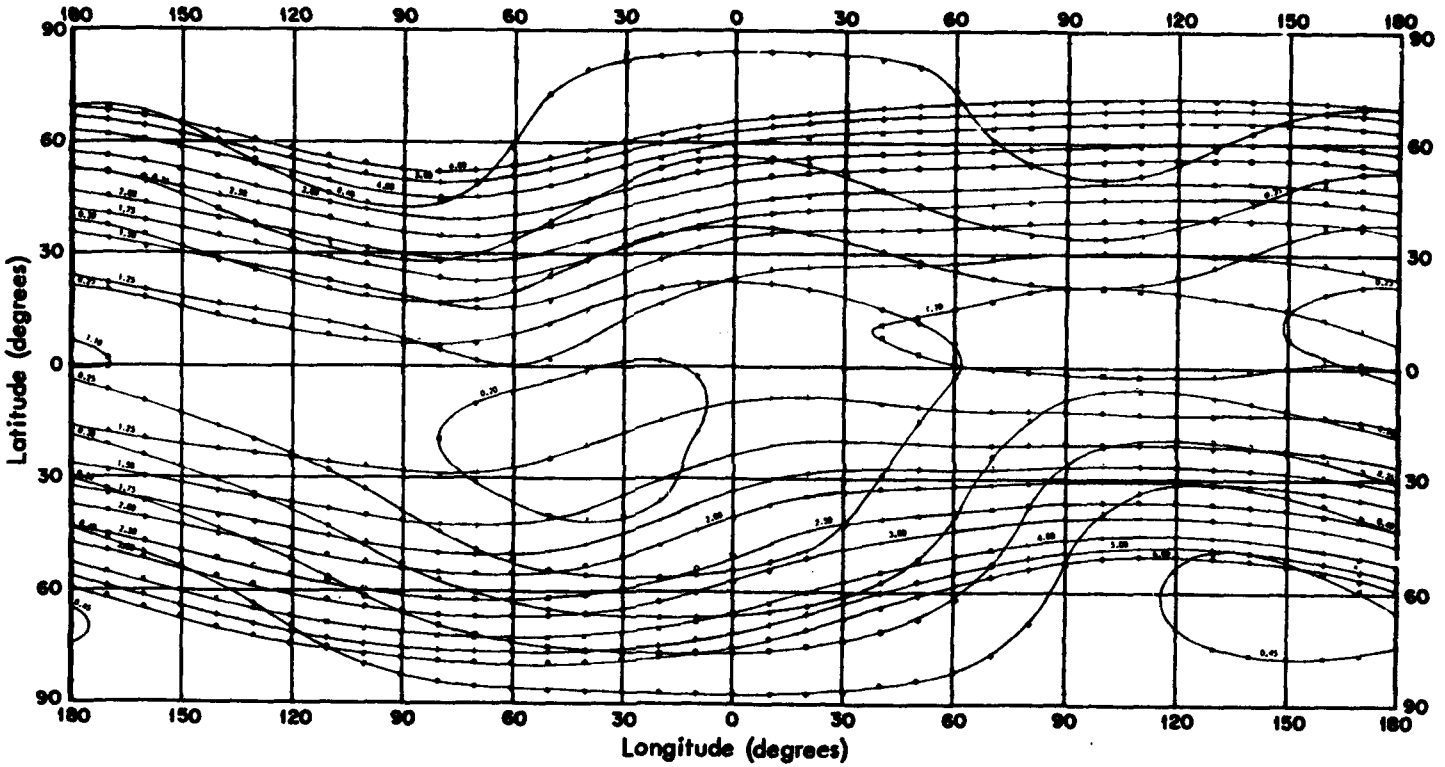

Figure 2C-3. Contours of constant-B and constant-L at 800-kilometer altitude.

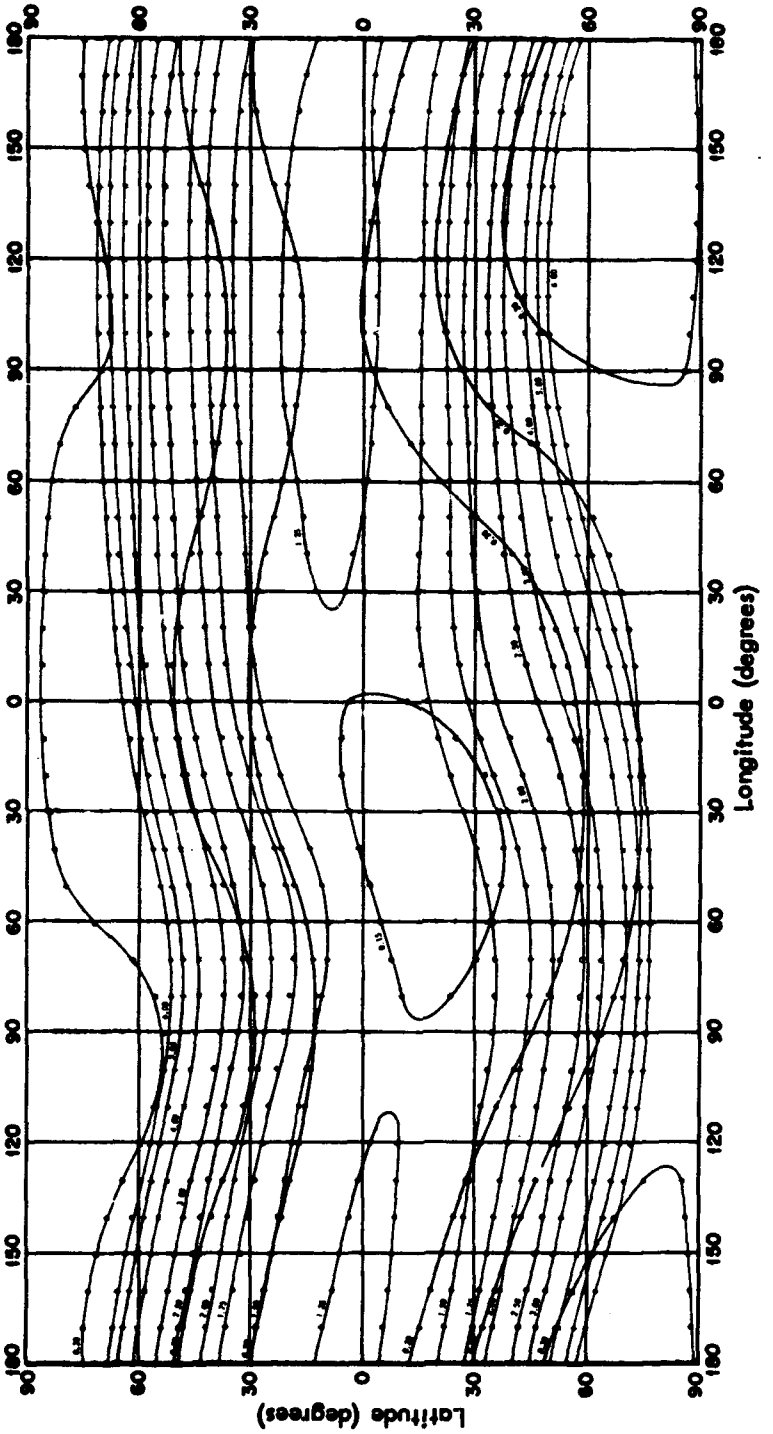

Figure 2C-4. Contours of constant-B and constant-L at 1,600-kilometer altitude.

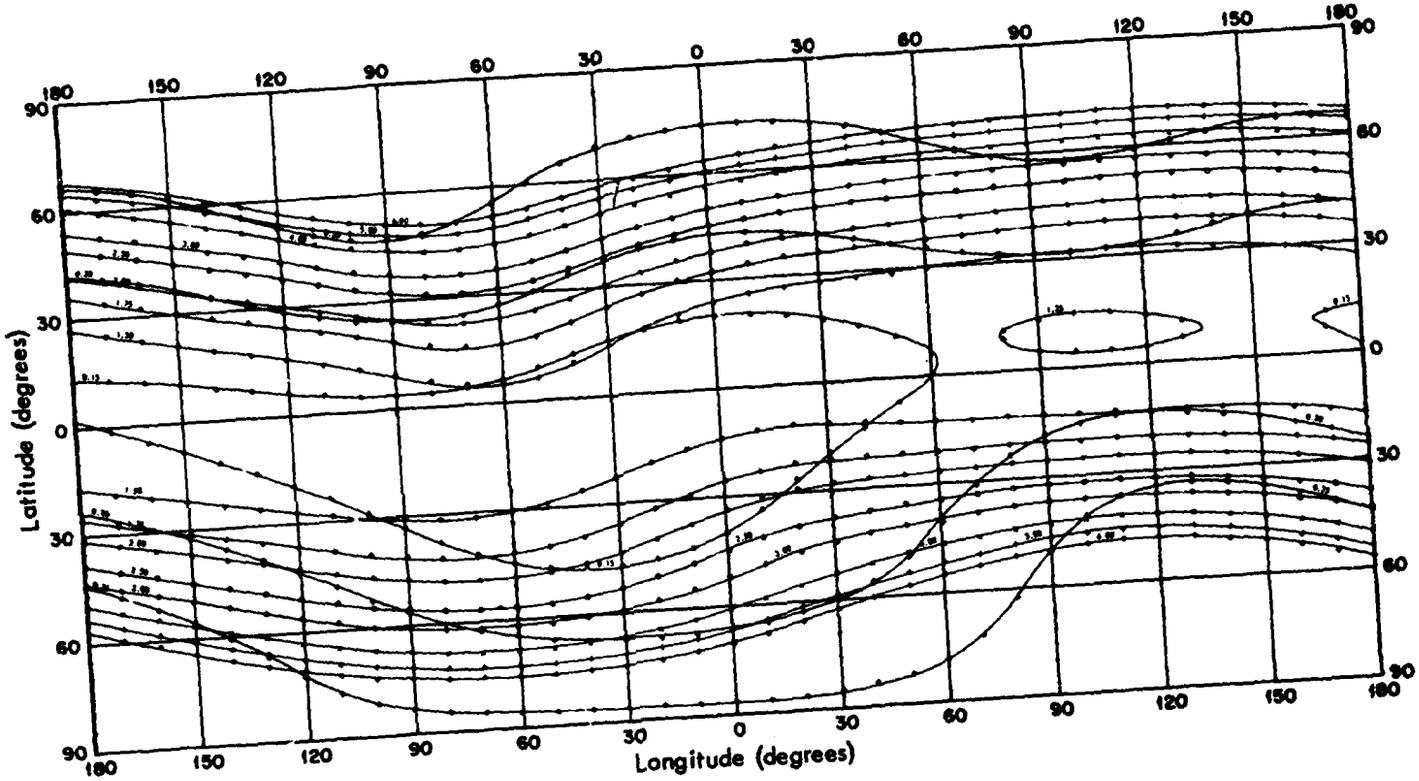

Figure 2C-5. Contours of constant-B and constant-L at 2,000-kilometer altitude.

APPENDIX 2D

CONSTANT-B VERSUS ALTITUDE, LONGITUDE, AND MAGNETIC SHELL NUMBER

This appendix contains plots of altitudes of constant-B in gauss versus longitude on the magnetic shells L = 1.12, 1.20, 1.60, 2.20, and 3.50 (References 13 and 19).

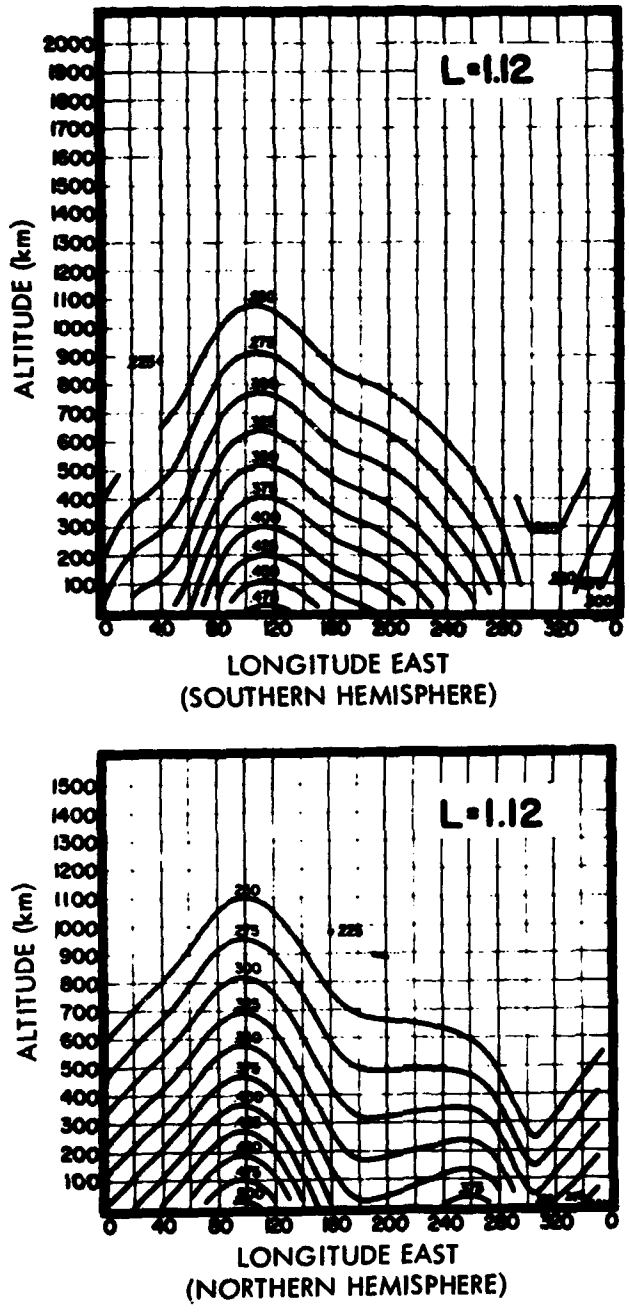

Figure 2D-1. Altitudes of constant-B for L = 1.12.

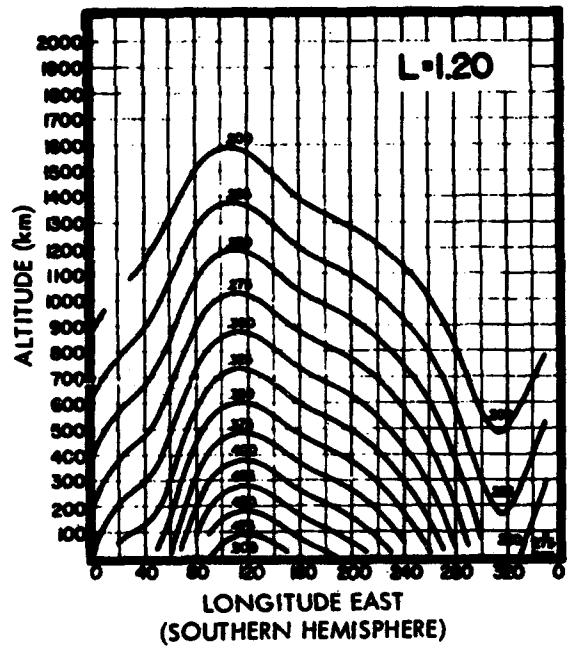

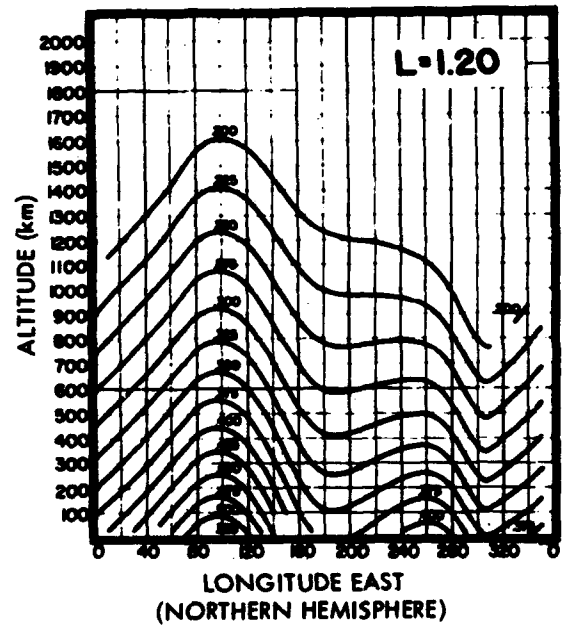

Figure 2D-2. Altitudes of constant-B for L = 1.20.

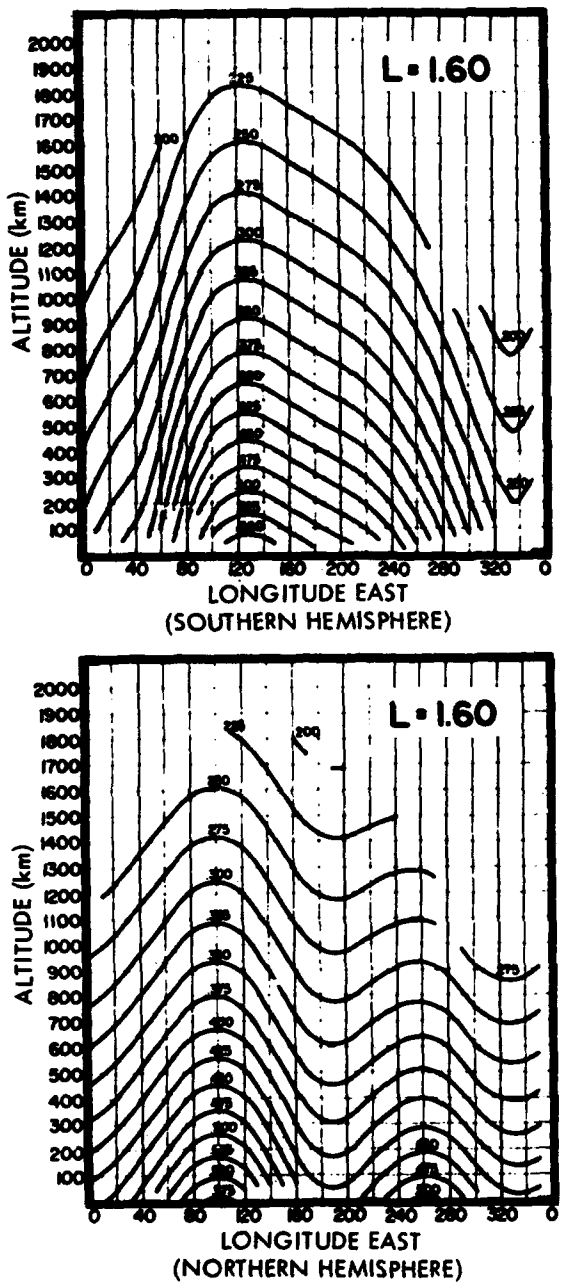

Figure 2D-3. Altitudes of constant-B for L = 1.60.

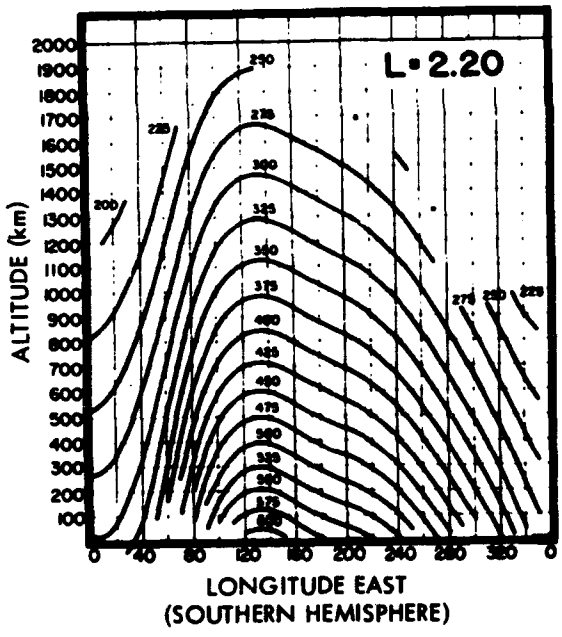

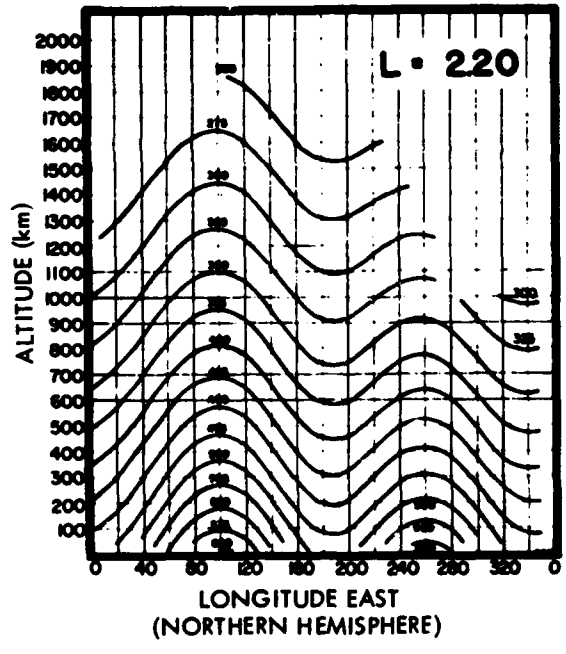

Figure 2D-4. Altitudes of constant-B for L = 2.20.

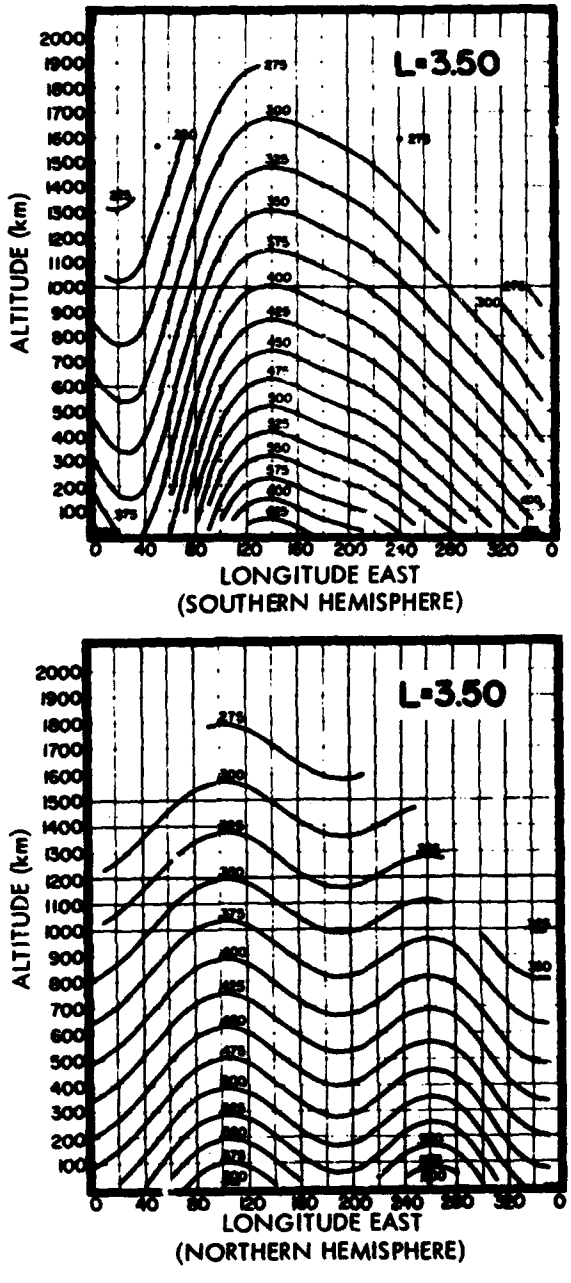

Figure 2D-5. Altitudes of constant-B for L = 3.50.

REFERENCES

1. J.C. Cain, W.E. Daniels, S.J. Hendricks, and D.C. Jensen. "An Evaluation of the Main Geomagnetic Field, 1940-1962," J. Geophys. Res., 70, 3647-3674, 1965.

2. W.D. Parkinson and J. Cleary. "The Eccentric Geomagnetic Dipole," J. Geophys. Res., 1, 346, 1958.

3. H.T. Finch and B.R. Leaton. "The Main Magnetic Field—Epoch 1955," Geophys. Supp. RAS, 7, 314, 1957.

4. M. Abraham and R. Becker. The Classical Theory of Electricity and Magnetism, Hafner, New York, translation, 283 pp.

5. C.E. McIllwain. "Coordinates for Mapping the Distribution of Magnetically Trapped Particles," J. Geophys. Res., 66, 3681-3691, 1961.

6. Handbook of Geophysics, Revised Edition, United States Air Force The Macmillan Co., New York, 1960.

7. J.C. Cain and S.J. Cain. "Derivation of the International Geomagnetic Reference Field," International geomagnetic reference field 10/68, NASA Preprint, X-612-68-501, December, 1968.

8. IAGA Commission 2, Working group 4, Analysis of the Geomagnetic Field, "International geomagnetic reference field 1965.0," J. Geophys. Res., 74, 4407-4408, 1969.

9. J.E. Evans, L.L. Newkirk, and B.M. McCormac. North Polar, South Polar, World Maps and Tables of Invariant Magnetic Coordinates for Six Altitudes: 0, 100, 300, 600, 1000, and 3000 km, DASA 2347, Lockheed Palo Alto Research Laboratory, Palo Alto, Calif., October, 1969.

10. S. Chapman and J. Bartels. Geomagnetism, II, 609-669, Oxford Univ. Press, London, 1940.

11. A.J. Zmuda. "A Method for Analyzing Values of the Scalar Magnetic Intensity," J. Geophys. Res., 63, 477-490, 1958.

12. D.C. Jensen and W.A. Whitaker. "A Spherical Harmonic Analysis of the Geomagnetic Field," J. Geophys. Res., 65, 2500, 1960.

13. D.C. Jensen and J.C. Cain. "An Interim Magnetic Field," J. Geophys. Res., 67, 3568-3569, 1962.

14. S.J. Hendricks and J.C. Cain. "Magnetic Field Data for Trapped Particle Evaluations," J. Geophys. Res., 71, 346-347, 1966.

15. J.C. Cain, S.J. Hendricks, R.A. Langel, and W.V. Hudson. "A Proposed Model for the International Geomagnetic Reference Field, 1965," preprint, Goddard Spaceflight Center, Greenbelt, Md., 1967.

16. J.C. Cain, R.A. Langel, and S.J. Hendricks. "Magnetic Chart of the Brazilian Anomaly—a Verification," preprint, Goddard Spaceflight Center, Greenbelt, Md., 1967.

17. P.J. Lindstrom and H.H. Heckman. "B-L Space and Geomagnetic Field Models," J. Geophys. Res., 73, 3441-3447, 1968.

18. E.H. Vestine and W.L. Sibley. Geomagnetic Field Lines in Space, Rand Corp. Rept. R-368, Santa Monica, Calif., December, 1960, 110 pp.

19. B. Venkatesan. "Isocontours of Magnetic Shell Parameters B and L," J. Geophys. Res., 70, 3771-3780, 1965.

20. G.D. Mead. "Deformation of the Geomagnetic Field by the Solar Wind," J. Geophys. Res., 69, 1181-1195, 1964.

21. G.D. Mead and D.B. Beard. "Shape of the Geomagnetic Field Solar Wind Boundary," J. Geophys. Res., 69, 1169-1179, 1964.

22. D.J. Williams and G.D. Mead. "Nightside Magnetosphere Configuration as Obtained from Trapped Electrons at 1100 Kilometers," J. Geophys. Res., 70, 3017-3029, 1965.

23. H. Maeda. "Variations in Geomagnetic Field," Space Science Rev., 8, 555-590, 1968.

24. S. Matsushita. "Solar Quiet and Lunar Daily Variation Fields," Physics of Geomagnetic Phenomena, I, 301-424, ed. by S. Matsushita and W.H. Campbell, Academic Press, New York, 1967.

25. S. Matsushita. "Geomagnetic Disturbances and Storms," Physics of Geomagnetic Phenomena, II, 793-819, ed. by S. Matsushita and W.H. Campbell, Academic Press, New York, 1967.

26. S. Chapman and J. Bartels. "The Morphology of Magnetic Disturbances," Geomagnetism, I, 272-338, Oxford University Press, London, 1940.

27. E.N. Parker. "Disturbance of the Geomagnetic Field by the Solar Wind," Physics of Geomagnetic Phenomena, II, 1153-1202, ed. by S. Matsushita and W.H. Campbell, Academic Press, New York, 1967.

28. C. Rostoker and C.-G. Fälthammar. "Relationship Between Changes in the Interplanetary Magnetic Field at the Earth's Surface," J. Geophys. Res., 72, 5853-5863, 1967.

29. D.H. Fairfield and L.J. Cahill, Jr. "Transition Region Magnetic Field and Polar Magnetic Disturbances," J. Geophys. Res., 71, 155-169, 1966.

30. S. Chapman and J. Bartels. "Bays, Pulsations, and Minor Disturbances," Geomagnetism, I, 338-355, Oxford University Press, London, 1940.

31. W.H. Campbell. "Geomagnetic Pulsations," Physics of Geomagnetic Phenomena, II, 821-909, ed. by S. Matsushita and W.H. Campbell, Academic Press, New York, 1967.

32. C.W. Horton and A.A.J. Hoffman. "Magnetotelluric Fields in the Frequency Range .03 to 7 Cycles per Kilosecond, 1. Power spectra," J. Res. Natl. Bur. Stand. USA, 66D, 487-494, 1962.

33. W.H. Campbell. "Geomagnetic Pulsation," Physics of Geomagnetic Phenomena, II, 821-909, ed. by S. Matsushita and W.H. Campbell, Academic Press, New York, 1967.

34. W.H. Campbell. "Rapid Geomagnetic Field Variations Observed at Conjugate Locations," Radio Sci., 3, 726-739, 1968.

35. W.H. Campbell. "Studies of Magnetic Field Micropulsations With Periods of 5 to 30 seconds," J. Geophys. Res., 64, 1819-1826, 1959.

36. J.B. Wilcox and E. Maple. Navord Report 4004, U.S. Naval Ord. Lab., White Oak, Md., 1957.

37. L.R. Tepley and R.C. Wentworth. Structure and Attenuation of Hydromagnetic Emissions, II, 73, Lockheed Physical Sciences Lab., Report No. 1, AFCRL-62-32(II), Palo Alto, Calif., 1962.

38. M. Balser and C.A. Wagner. "Observations of Earth-Ionosphere Cavity Resonances," Nature, 188, 638-643, 1960.

39. A.D. Watt and E.L. Maxwell. "Characteristics of Atmosphere Noise from 1 to 100 kc," Proc. I. R. E., 45, 787-794, 1957.

40. A. Kimpara. "Lightning Flashes and Atmospherics," Progress in Radio Science, IV, 5-12, ed. by F. Horner, Elsevier Publishing Co., New York, 1965.

41. A.L. Hales. "A Possible Mode of Propagation of the 'Slow' or 'Tail' Component in Atmospherics," Proc. Roy. Soc. London, A, 193, 60-71, 1948.

42. T. Madden and W. Thompson. "Low-Frequency Electromagnetic Oscillations of the Earth-Ionosphere Cavity," Rev. Geophys., 3, 211-254, 1965.

43. D.A. Gurnett, S.D. Shawhan, N.M. Brice, and R.L. Smith. "Ion Cyclotron Whistlers," J. Geophys. Res., 70, 1665-1688, 1965.

44. A. Egeland, G. Gustaffson, S. Olsen, J. Aarons, and W. Barron. "Auroral Zone Omissions Centered at 700 cycles per second," J. Geophys. Res., 70, 1079-1082, 1965.

45. R.A. Helliwell. Whistlers and Related Ionospheric Phenomena, Stanford University Press, Stanford, Calif., 1965, 349 pp.

46. J. V. Lincoln, "Geomagnetic Indices," Physics of Geomagnetic Phenomena, I, 67-100, ed. by S. Matsushita and W. H. Campbell, Academic Press, New York, 1967.

47. W. F. Dudziak, D. D. Kleinecke, and T. J. Kostigen. Graphic Displays of Geomagnetic Geometry, RM 63TMP-2, DASA 1372, General Electric Co., Santa Barbara, Calif., 1963, 60 pp.

SECTION 3

THE MOTION OF CHARGED PARTICLES IN THE EARTH'S MAGNETIC FIELD

G.T. Davidson, Lockheed Palo Alto Research Laboratory

3.1 INTRODUCTION

The primary factor determining the motion of a charged particle near the earth, but outside most of the tangible atmosphere, is the Lorentz force (References 1, 2, and 3):

$$\overline{F} = \frac{q}{c} \bar{v} \times \overline{B} \qquad (3\text{-}1)$$

where q is the charge on an individual particle, $\bar{v}$ is the (vector) velocity of the particle, and $\overline{B}$ is the geomagnetic field intensity at the location of the particle. Here, cgs gaussian units are employed (Appendix 3A has a discussion of unit systems), hence the occurrence of the speed of light (c) in the denominator of Equation 3-1.

The Lorentz force is directly responsible for restraining a trapped particle and keeping it within a well-defined region around the earth. Other forces may influence trapped particles, but their effects generally amount only to small perturbations. In particular, electric fields can occur within the magnetosphere (References 4 and 5), especially in association with magnetic fluctuations where Maxwell's induction equation:

$$\nabla \times \overline{E} = - \frac{1}{c} \frac{\partial \overline{B}}{\partial t} \qquad (3\text{-}2)$$

must be satisfied. Although electric fields along the magnetic field direction may be necessary to explain auroral phenomena and related high-latitude events (References 6 through 10), they are not expected to occur as steady long-lived features of the trapped radiation regions.

Gravitational forces on trapped particles are weak and generally may be ignored (Section 3.3.1). However, mechanical forces must be accounted for in the collisions between particles, especially in collisions of fast charged particles with electrons and atoms having

merely thermal velocities. Radiation belt particles with kinetic energies amounting to thousands or millions of eV are not affected grossly by collisions with other particles. But subtle cumulative effects will tend to gradually alter the particle motions over extended time periods.

To simplify the presentation, this section has been restricted principally to the motion of charged particles in a steady state dipolar magnetic field of the earth and outside the atmosphere. The discussion of weak transient phenomena, such as interparticle collisions or brief fluctuations in the magnetic field, is deferred to Section 5.

The subsection that immediately follows this introduction contains the complete equation of motion of a charged particle. The direct integration of the equation of motion also is discussed. Direct integration generally is found to be cumbersome and impractical. However, some general principles facilitate the description of particle motion without detailed integration of trajectories. These principles make up the remainder of Section 3. The simplest general principle is that the particle motion may be described as a circular motion about a point that moves relatively slowly with respect to the fixed field lines. This is the basis of the guiding center approximation of Section 3.3.

A more sophisticated approach, discussed in Section 3.4, is through some set of constants of the motion. A trapped charged particle has 3 degrees of freedom. According to the concepts of classical mechanics, the motion is completely described if a constant of the motion is found for each degree of freedom. Three constants of motion, the adiabatic invariants, correspond to the azimuthal motion with respect to a magnetic field line, to the motion parallel to the field line, and to the azimuthal motion with respect to the axis of symmetry of the field.

Strictly speaking, the adiabatic invariants are only constants of motion in a steady state field, but they may be regarded as true constants of motion in many circumstances. When the constants of motion are known, treating the trapped particles via the statistical properties of the system becomes possible, as discussed briefly in Section 3.5.

Further elaborations on the statistical approach are outlined in Section 3.6 where the radiation belts are regarded explicitly as a

plasma. The term plasma customarily refers to an electrically neutral, highly ionized gas that under certain conditions behaves as a fluid obeying laws of motion similar to those that are invoked in classical hydrodynamics.

3.2 THE MOTION OF AN ELECTRICALLY CHARGED PARTICLE IN A MAGNETIC DIPOLE FIELD

3.2.1 The Equation of Motion of a Charged Particle

The forces influencing a particle of momentum $\bar{p}$, rest mass m, velocity $\bar{v}$, and electric charge q may be combined in a generalized (vector) equation of motion (Reference 3):

$$\frac{d\bar{p}}{dt} = q\bar{E} + \frac{q}{c}\bar{v}\times\bar{B} + m\bar{G} + \bar{F}_c \quad . \tag{3-3}$$

The various terms on the right of the equal sign in Equation 3-3 are due to electric field $\bar{E}$, magnetic field $\bar{B}$, gravitational field $\bar{G}$, and mechanical forces $\bar{F}_c$ experienced in collisions with other particles or solid objects. The electric and gravitational forces are velocity independent. The magnetic force must be proportional to the velocity and directed perpendicular to the velocity and to the magnetic field. The collisional forces have a complicated relation to particle velocities. The treatment of the effects of collisions is discussed briefly in Sections 3.6 and 5.2.

RELATIVISTIC CORRECTIONS TO THE RELATIONS BETWEEN MASS, VELOCITY, MOMENTUM, AND ENERGY. When the velocity of a particle is low, the momentum in Equation 3-3 may be replaced by the product of (constant) rest mass and velocity. The left side of that equation is then equivalent to

$$\frac{d\bar{p}}{dt} = m\frac{d\bar{v}}{dt} \quad . \tag{3-4}$$

Many particles in the radiation belts have velocities near the speed of light, so it is advisable when considering those particles to use strictly relativistic relations between mass, velocity, and momentum (Reference 3). The relativistic momentum is

$$\bar{p} = \frac{m\bar{v}}{\sqrt{1 - v^2/c^2}} \equiv \gamma m\bar{v} \quad . \tag{3-5}$$

The apparent relativistic mass of a fast particle is the product of the rest mass m and the dilation factor:

$$\gamma \equiv \frac{1}{\sqrt{1 - v^2/c^2}} = \sqrt{1 + p^2/m^2c^2} \quad . \tag{3-6}$$

The total energy of a relativistic particle is

$$\mathcal{E} = \gamma mc^2 \tag{3-7}$$

The kinetic energy T is of more utility and is equal to the total energy minus the rest mass energy mc^2:

$$T = (\gamma - 1)\, mc^2 = \left(\sqrt{1 + p^2/m^2c^2} - 1\right) mc^2 \quad . \tag{3-8}$$

At low velocities, the familiar relation:

$$T \approx \frac{1}{2} mv^2 \tag{3-9}$$

is adequate. This is just the first term in the expansion of Equation 3-8 in a power series with respect to v^2/c^2.

The inverse relations that may be used to obtain momentum and velocity from the kinetic energy are

$$p = \frac{1}{c}\sqrt{T(T + 2mc^2)} \tag{3-10}$$

$$v = \frac{c\sqrt{T\,(T + 2mc^2)}}{T + mc^2} \quad . \tag{3-11}$$

A convenient unit in which kinetic energies usually are designated is the electron volt (eV) $\approx 1.602 \times 10^{-12}$ erg. The standard abbreviations for million electron volts (10^6 eV) and billion electron volts (10^9 eV) are MeV and GeV, respectively. The most frequently used rest mass energies are the electron rest mass energy $m_e c^2 \approx 0.5110$ MeV and the proton rest mass energy $m_p c^2 \approx 938.2$ MeV. The customary unit of momentum is eV/c (or MeV/c). In the previous equations, pc may be replaced by the numerical magnitude of momentum

in eV/c units. The energy momentum relation in electron volt units for electrons is

$$p\left(\frac{MeV}{c}\right) \approx \sqrt{T(MeV)\left[T(MeV) + 1.0220\right]} \quad , \tag{3-12a}$$

and for protons is

$$p\left(\frac{MeV}{c}\right) \approx \sqrt{T(MeV)\left[T(MeV) + 1876.4\right]} \quad . \tag{3-12b}$$

These latter two equations, together with Equation 3-11, are presented in Figures 3B-5 and 3B-6. At low energies, the energy-velocity relations become for electrons:

$$v(cm \cdot sec^{-1}) \sim 5.93 \times 10^{10}\sqrt{T(MeV)} \tag{3-13a}$$

and for protons:

$$v(cm \cdot sec^{-1}) \sim 1.384 \times 10^{9}\sqrt{T(MeV)} \quad . \tag{3-13b}$$

3.2.2 The Gyro-Motion of a Charged Particle in a Magnetic Field

Because the magnetic force has no component in the direction of particle motion, the sole effect of a static magnetic field is to alter the direction of the momentum vector $\bar{p}$. The rate of change of kinetic energy is the product of Equation 3-3 by velocity (Reference 3) or

$$\frac{dT}{dt} = \bar{v} \cdot \frac{d\bar{p}}{dt} = q\bar{v} \cdot \bar{E} + m\bar{v} \cdot \bar{G} + \bar{v} \cdot \bar{F}_c \quad . \tag{3-14}$$

There is no exchange of energy between a constant magnetic field and charged particles. The equation of motion of a particle solely under the influence of a magnetic field can be written in a form nearly identical with the nonrelativistic formula except that the relativistic mass, γm, appears in place of the rest mass:

$$\gamma m \frac{d\bar{v}}{dt} = \frac{q}{c}\bar{v} \times \bar{B} \tag{3-15}$$

A force acting always perpendicular to the direction of motion can be understood as a centripetal force which causes the particle to move in a circular orbit (References 1 and 4). Figure 3-1 illustrates the

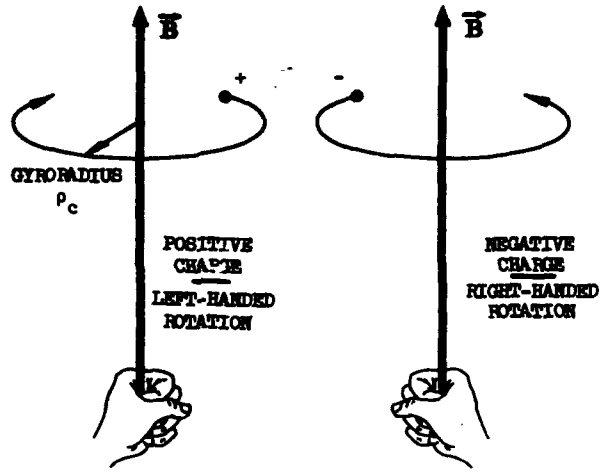

Figure 3-1. The gyro-motion of charged particles in a uniform magnetic field.

the motion of positively and negatively charged particles in a uniform magnetic field. Positively charged particles gyrate in the direction indicated by the fingers of a left hand that grasps the field lines in such a fashion that the thumb points along the field direction. Conversely, negatively charged particles gyrate in a right-handed sense. A charged particle in a uniform magnetic field rotates with an angular frequency, the gyro-frequency or cyclotron frequency:

$$\omega_c = \frac{qB}{\gamma mc} \tag{3-16a}$$

for electrons:

$$\omega_e(\text{radian sec}^{-1}) \approx 1.759 \times 10^7 \frac{B}{\gamma} \tag{3-16b}$$

$$\nu_e(\text{Hz}) = \frac{\omega_e}{2\pi} \approx 2.799 \times 10^6 \frac{B}{\gamma} \tag{3-16c}$$

and for protons:

$$\omega_i(\text{radian sec}^{-1}) \approx 9.580 \times 10^3 \frac{B}{\gamma} \tag{3-16d}$$

$$\nu_i(\text{Hz}) = \frac{\omega_i}{2\pi} \approx 1.525 \times 10^3 \frac{B}{\gamma} \tag{3-16e}$$

where B is measured in gauss, and both the angular frequencies ω_c and the linear frequencies ν_c are given. To avoid confusion elsewhere, the subscript i is used to denote any quantities pertaining to ions, even when the type of ion has been specified. Gyro-periods, $t_c = 1/\nu_c$, are given in Figure 3B-9, Appendix 3B, for the geomagnetic field.

The radius of the circular orbit, the gyro-radius ρ_c, is the velocity of the particle divided by the gyro-frequency; or

$$\rho_c = \frac{v_\perp}{\omega_c} = \frac{p_\perp c}{qB} \qquad (3\text{-}17a)$$

$$\rho_c(\text{cm}) = 3.336 \times 10^3 \frac{p_\perp(\text{MeV/c})}{B} \qquad (3\text{-}17b)$$

Equation 3-17b is valid for electrons or any singly charged ions. The subscript $_\perp$ means that the transverse component, perpendicular to the field lines, is to be used.

These results are true if an electric field (or gravitational field) is aligned in the same direction as the magnetic field. In that case, a charged particle describes a helical trajectory with a varying pitch and gyro-radius. The consequences of more complicated field configurations are discussed in Sections 3.3 and 3.4.

2.3.3 Direct Integration of the Equations of Motion—Störmer Orbits

When Equation 2-4, describing a dipole field, is inserted in Equation 3-33, some general classes of solutions can be obtained for the motion of a charged particle in a dipolar field. A dimensionless equation of motion can be constructed by replacing the time variable t by the distance along the trajectory:

$$s = \int_{t_0}^{t} v\,dt \quad . \qquad (3\text{-}18)$$

Conservation of energy requires that, in cylindrical coordinates,

$$\left(\frac{\partial R}{\partial s}\right)^2 + R^2\left(\frac{\partial \phi}{\partial s}\right)^2 + \left(\frac{\partial z}{\partial s}\right)^2 = 1 \quad . \qquad (3\text{-}19)$$

The ϕ component of the motion equation can be reduced immediately (after multiplication by R) to an equation that is readily integrable. The result is an angular momentum relation (Reference 11):

$$R^2 \frac{\partial \phi}{\partial s} = \pm C_s^2 \frac{R^2}{\left(R^2 + z^2\right)^{3/2}} + 2C_s\Gamma \quad . \tag{3-20}$$

The negative sign on the first right-hand term is necessary for negative particles. The Störmer unit

$$C_s = \sqrt{\frac{|q| M_E}{pc}} \tag{3-21}$$

is a constant dimensionally equivalent to a length; and Γ is a constant of integration, the Störmer angular momentum parameter. M_E is the magnetic dipole moment of the earth (as defined in Section 2-2). Numerically, the Störmer unit is (for the earth's magnetic field)

$$C_s(\text{km}) \approx \frac{1.565 \times 10^6}{\sqrt{p(\text{MeV/c})}} \approx \frac{1.14 \times 10^{-2}}{\sqrt{p(\text{cgs})}} \tag{3-22a}$$

$$C_s(R_E) \approx \frac{244.0}{\sqrt{p(\text{MeV/c})}} \quad . \tag{3-22b}$$

Two variables of integration might be eliminated with the aid of Equations 3-19 and 3-20. A complete solution, however, usually must be arrived at through numerical integration over the remaining variable (however, see Reference 12). Many such computations were performed by Störmer (Reference 11), though they pertain mostly to nontrapped orbits.

FORBIDDEN REGIONS IN A DIPOLE FIELD. The spatial regions wherein Equation 3-20 has real solutions are restricted. The boundaries of the forbidden regions (Reference 11), which a charged particle cannot enter, may be located with the aid of a new variable:

$$\Xi \equiv 1 - R^2\left(\frac{\partial \phi}{\partial s}\right)^2 = \left(\frac{\partial z}{\partial s}\right)^2 + \left(\frac{\partial R}{\partial s}\right)^2 \quad . \tag{3-23}$$

The angular momentum relation (Equation 3-20) is equivalent to a radial distance condition:

$$R = \frac{\Gamma \pm \sqrt{\Gamma^2 \pm \sqrt{1 - \Xi}\sin^3\theta}}{\sqrt{1 - \Xi}} \quad . \tag{3-24}$$

Because Ξ (being the sum of two squared quantities) is never less than zero, limits exist on the permitted values of R. The forbidden regions, for which Equation 3-24 has no solutions, are symmetric about the z-axis. Figure 3-2 depicts the projections of forbidden regions (shaded) on an azimuthal R,z plane for several values of Γ.

When $\Gamma < -1$, permanent trapping can occur. Two separate permitted regions exist. The inner one is closed completely. A particle cannot enter or leave the trapping region unless Γ becomes equal to -1 while R is simultaneously less than C_s. Before the discovery of trapped particles in the geomagnetic field, the trapping region was not expected to be filled because a drastic alteration of momentum is necessary to trap a particle arriving from a great distance (References 11 and 13).

Special solutions exist to the equations of motion if a charged particle is restricted to the equatorial plane. Some sample equatorial orbits are shown in Figure 3-3. The trapped orbits ($\Gamma = 1$) consist of a roughly circular (gyro) motion on which is imposed a steady azimuthal drift. The boundaries of the forbidden regions in the equatorial plane are just the intersections of the limiting surfaces of Figure 3-2 with the equatorial (z = 0) plane. The limits on radial distance at the equator are

$$-R^2 < 1 + 2\Gamma R < R^2 \quad . \tag{3-25}$$

Equation 3-25 is plotted in Figure 3-4.

MOTION IN THE MERIDIAN PLANES OF A DIPOLE FIELD. The meridian plane components of charged particle motion in an azimuthally symmetric field can be derived with the aid of the variable Ξ, which plays the role of a potential (the Störmer potential) in an R, z plane. The expression:

$$\frac{\partial^2 \overline{R}_2}{\partial s^2} = \frac{1}{2} \nabla \Xi \tag{3-26}$$

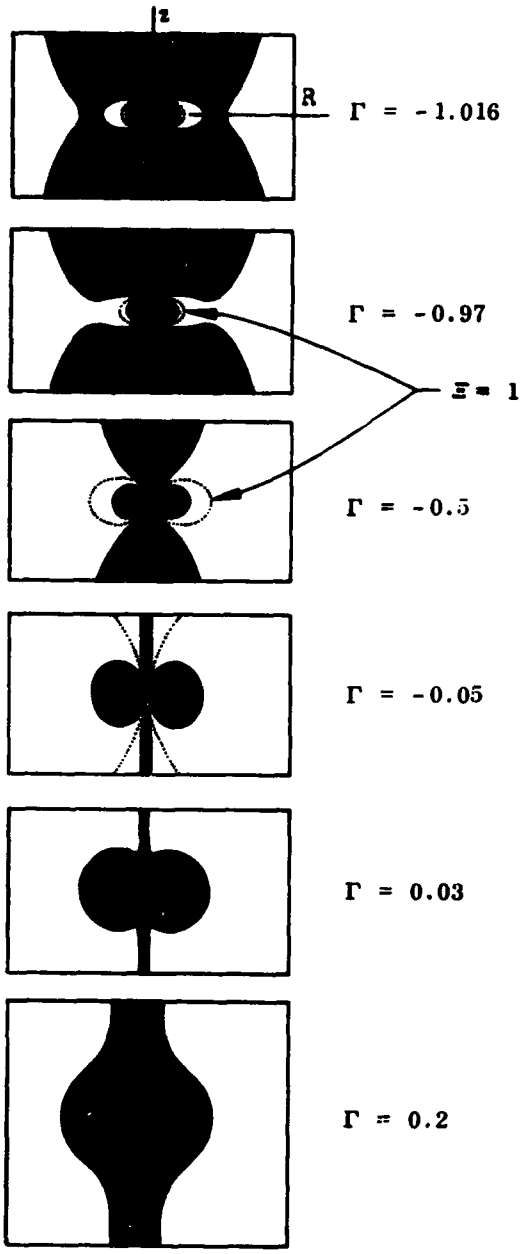

Figure 3-2. Forbidden regions in a dipolar magnetic field.

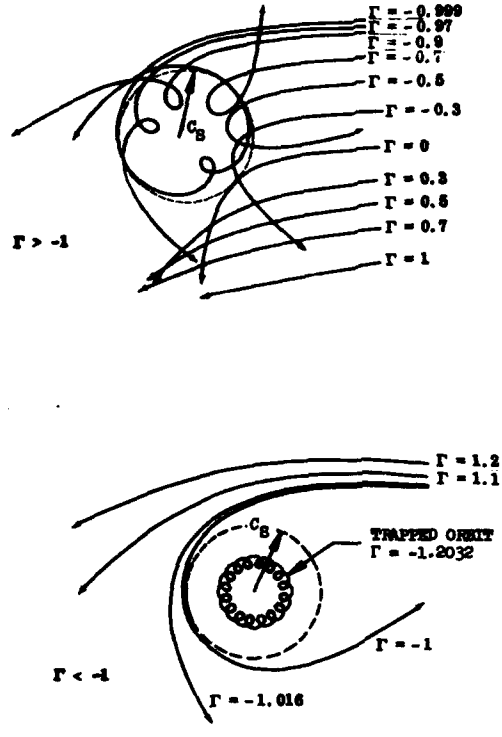

Figure 3-3. Sample charged particle orbiting in the equatorial plane of a magnetic dipole field (Reference 11).

results from the equation of motion, where $\bar{R}_2$ must be understood as a two-component vector lying in the meridian plane. Figure 3-5 shows several field lines superimposed on the Ξ = constant curves near the origin of coordinates. Figure 3-6 shows several computed particle trajectories. The curve $\Xi = 1$ is identical with a field line having an equatorial crossing at $R_o = -C_s/2\Gamma$. The remainder of the Ξ = constant curves diverge away from the field lines as R increases. The effective force $[-\nabla\Xi/2]$ therefore has a component directed outward from the origin along the field lines. The force and its resolution into components are shown at points P and Q of Figure 3-5.

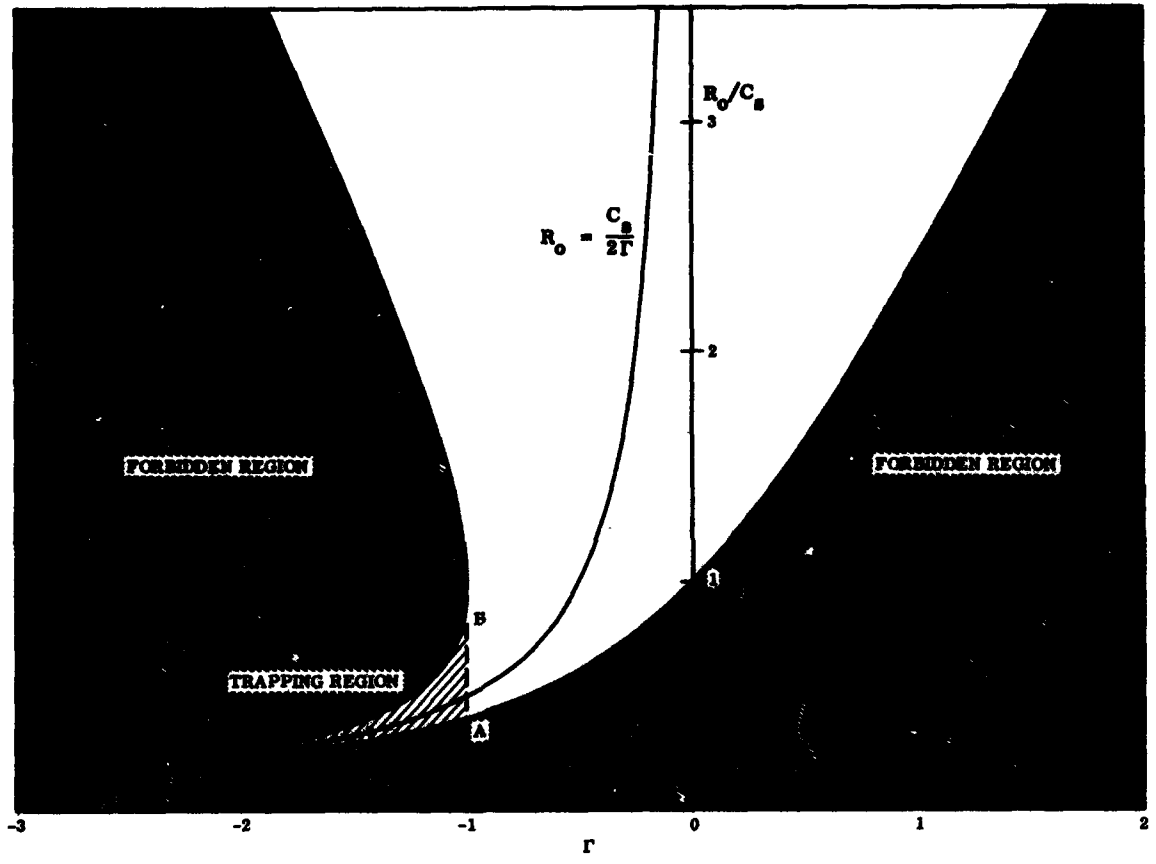

Figure 3-4. Limits of stable trapping in a dipole field as derived from the Störmer orbit theory.

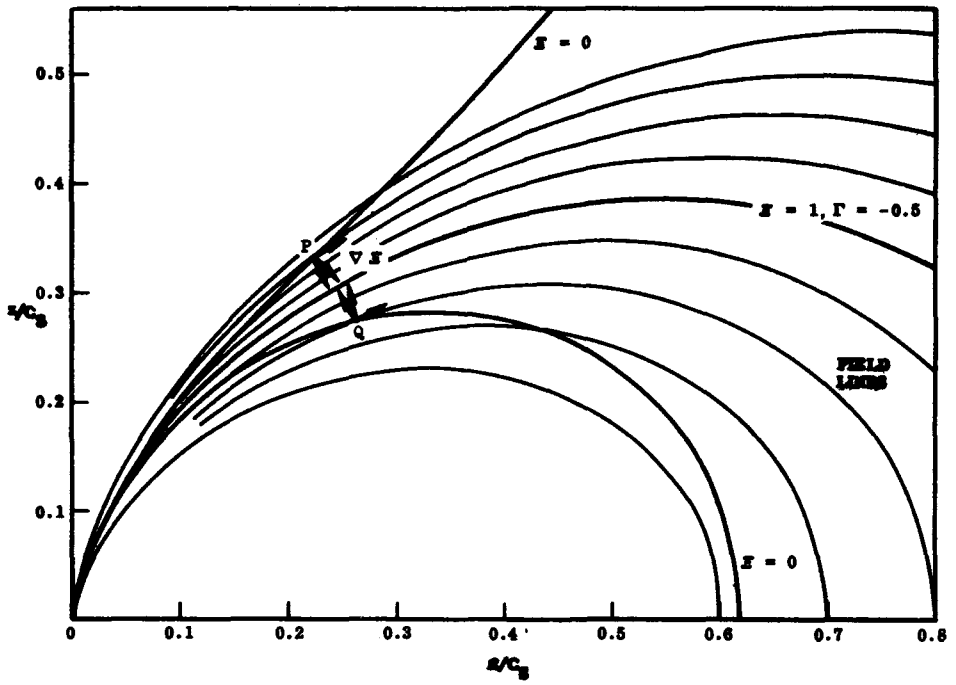

Figure 3-5. Curves of constant Ξ (the Störmer potential) superimposed on dipole field lines.

A charged particle approaching the polar regions of a dipole field is subject to a retarding force that tends to turn it back. When the particle's trajectory eventually reaches one of the limiting curved surfaces, all the particle's motion is in the ϕ direction (Equation 3-23). At that point, the turning point, the velocity component along the field lines is reversed and the particle begins to leave the polar region (References 14 and 15). This is the phenomenon of magnetic reflection, which enables trapped particles to bounce back and forth many times between two points at comparable altitudes in opposite hemispheres.

Figure 3-6 illustrates the behavior of particles near the polar regions of a dipole field. Magnetic reflection occurs for all particles except the singular case (the solid curve near $\Xi = 1$) where the trajectory passes through the origin of coordinates. Though the orbits in this diagram are not closed, similar behavior is expected for trapped particles, except that the separation of the $\Xi = 0$ curves would be much less. The center of gyration (the guiding center, Section 3.3) of a trapped particle moves on a closed surface (the invariant surface, Section 3.4.3), which is nearly coincident with the surface $\Xi = 1$.

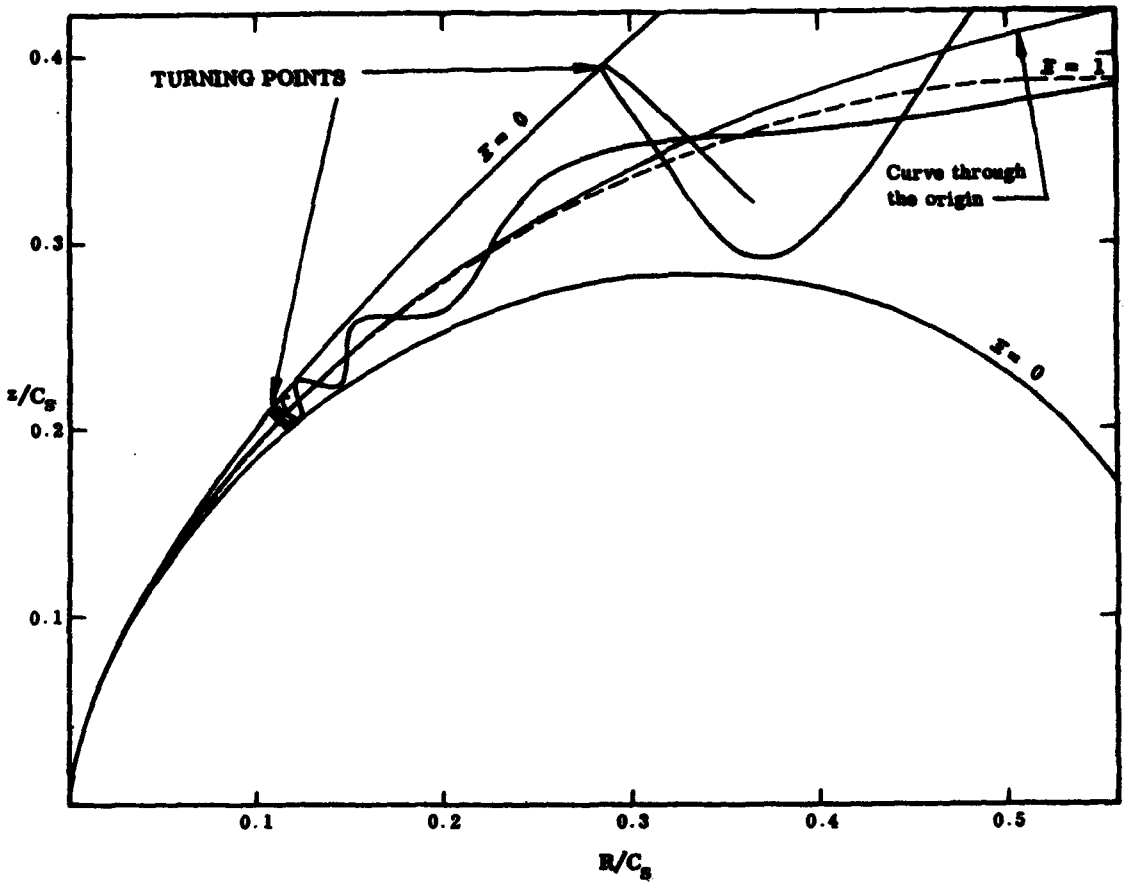

Figure 3-6. Sample charged particle orbits in a dipolar magnetic field, projected onto a meridian plane (Reference 11).

TRAPPING LIMITS IN THE GEOMAGNETIC FIELD. If particles are to be permanently trapped, the parameter Γ must be less than -1. If the mean equatorial crossing of trapped particles is equated to the equatorial intersection of the curve $\Xi = 0$, the necessary criterion for trapping (Reference 16) is

$$\frac{C_s}{2R_o} = -\Gamma > 1 \quad . \tag{3-27}$$

When numerical magnitudes are inserted (from Equation 3-22) the Störmer trapping criterion is

$$L\sqrt{p(\text{MeV/c}} < 122 \quad . \tag{3-28}$$

Throughout this section, L usually denotes R_o/R_E in a strictly dipolar field. A particle trapped below L = 6 cannot have a momentum greater than about 4.4 MeV/c. In the case of electrons, the corresponding maximum kinetic energy is about 400 MeV (Figure 3B-6). The maximum allowed kinetic energy of trapped protons in the same region is about 90 MeV. When the true distorted geomagnetic field is considered, the trapping criteria differ slightly from those preceding (References 17, 18, and 19). For rough calculations, the criteria given here generally should suffice.

3.3 THE GUIDING CENTER APPROXIMATION

3.3.1 Drift Motion—the $\bar{E} \times \bar{B}$ Drift

Whenever the forces affecting a charged particle do not vary greatly over a distance comparable with the particle's gyro-radius, the trajectory can be described approximately as a circular motion about a moving point, the guiding center (References 1, 2, and 4). Viewed from the guiding center, a particle appears to move in a circular orbit, but the guiding center may follow a complex path. The guiding centers of permanently trapped particles (Sections 3.2.3 and 3.4.3) are constrained to remain on a closed surface.

In some cases the motion is exactly cycloidal so that the guiding center moves with uniform velocity, the drift velocity. This occurs when a uniform electric field is aligned perpendicular to a homogenous magnetic field. All particle orbits in the planes perpendicular to $\bar{B}$ appear to be exactly circular when viewed in a coordinate system moving with the $\bar{E} \times \bar{B}$ drift velocity (Reference 4). The $\bar{E} \times \bar{B}$ drift velocity:

$$\bar{V}_D = c \frac{\bar{E} \times \bar{B}}{B^2} \qquad (3\text{-}29)$$

is independent of mass or charge—positive and negative particles drift together with the same velocity.

Figure 3-7 illustrates the way in which charged particles move in crossed electric and magnetic fields. A positive particle starting at point P with a finite kinetic energy will be accelerated until it reaches point Q where its kinetic energy and, consequently, its orbital radius are maximum. As the particle progresses from point Q, it is retarded until at point R its kinetic energy attains a minimum value. The trajectory is cyclic—no net progress is made in the direction of the electric field and, hence, no increase is made in the average kinetic energy. The motion of a negative particle in the same circumstances is similar except that the gyro-motion and the electric force are in the opposite sense.

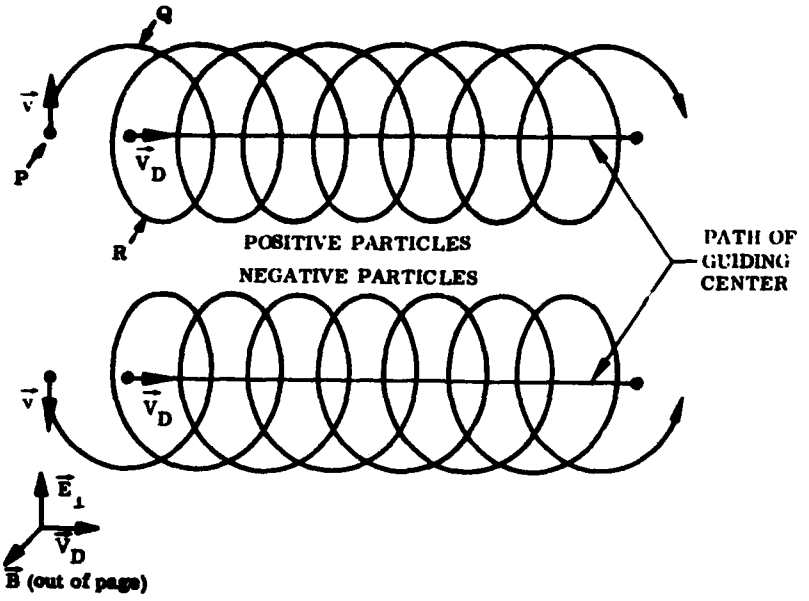

Figure 3-7. Motion of a charged particle in crossed electric and magnetic fields.

DRIFT MOTION RESULTING FROM GENERALIZED FORCES. A generalized force $\bar{F}_\perp$ acting perpendicularly to the magnetic field causes a drift motion with a drift velocity

$$\bar{V}_D = \frac{c}{q} \frac{\bar{F}_\perp \times \bar{B}}{B^2} \quad . \tag{3-30}$$

Figure 3-8 illustrates this type of drift motion for comparison with Figure 3-7. The direction of drift motion now depends on the sign of the electrical charge. Therefore, particles with different charges drift at different rates and a current is set up across the magnetic field. If the force $F_\perp$ acts most strongly on the heavier, positively charged particles, the resulting current density is

$$J \cong n_+ \frac{\bar{F}_\perp \times \bar{B}}{B^2} \tag{3-31}$$

where n_+ is the number density of positive particles (the current has been expressed in electromagnetic units (emu), which eliminates an expected factor of c; see Appendix 3A).

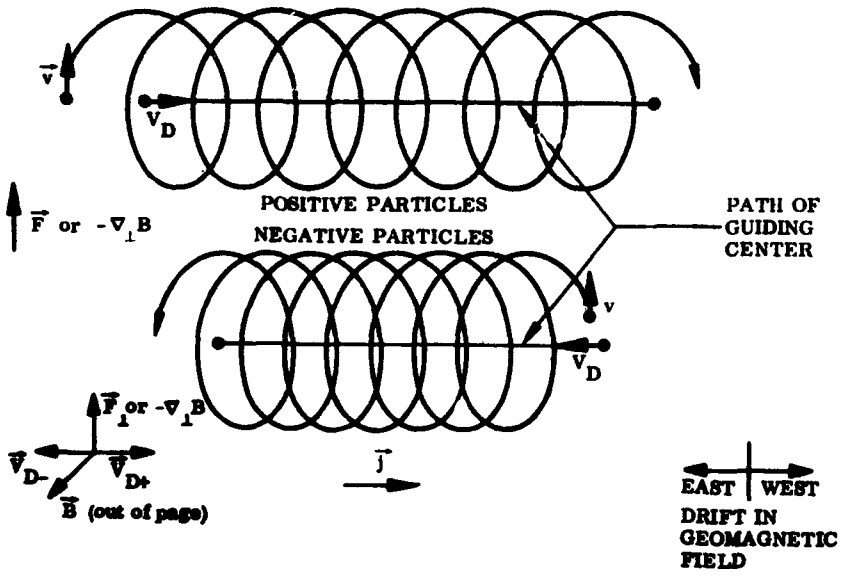

Figure 3-8. Motion of a charged particle in a nonhomogenous magnetic field or in a magnetic field with a superimposed charge-independent transverse force field.

THE GRAVITATIONAL DRIFT. Gravitational forces on trapped particles are weak and usually insignificant except for effects such as the gravitational drift current. The gravitational force on a trapped proton, for example, is only about 2×10^{-22} cgs—much less than the magnetic force on a thermal velocity proton, about 10^{-15} cgs. The discrepancy is even greater for electrons, yet the gravitational drift causes a separation of protons and electrons. The gravitational (eastward) drift velocity of protons is

$$V_G(\text{km/sec}) = 1.0 \times 10^{-6} \left(\frac{R_E}{r}\right)^2 \frac{\cos I}{B} \qquad (3\text{-}32)$$

where I is the inclination of the field line from the horizontal. The maximum gravitational drift velocity at the equator is

$$V_G(\text{km/sec}) \approx 3.3 \times 10^{-6} L \quad . \qquad (3\text{-}33)$$

THE FIELD LINE CURVATURE DRIFT. If field lines bend with a radius of curvature greater than the gyro-radii, the trajectories of charged particles also are bent so that their guiding centers closely follow the field lines (References 4, 20, and 21, also Section 3.2.3). The force in Equation 3-30 could be replaced by the virtual centrifugal force acting on a particle moving along a curved field line. The radius of curvature of a field line is related to the spatial gradient of the field intensity through Maxwell's equation:

$$\nabla \times \bar{H} = 0 \quad . \qquad (3\text{-}34)$$

The curvature drift velocity (References 4 and 40) is

$$\bar{V}_c = - \frac{p_{\parallel}^2}{\gamma m^2} \cdot \frac{\nabla_{\perp} B \times \bar{B}}{\omega_c B^2} \quad . \qquad (3\text{-}35)$$

The component of momentum along the field lines is denoted by $p_{\parallel}$, likewise $\nabla_{\perp} B$ represents that component of the gradient of field intensity that lies perpendicular to the field lines.

THE GRADIENT-B DRIFT. In a nonhomogeneous magnetic field, the radius of curvature of a particle orbit is variable. Figure 3-8 may be interpreted as depicting the trajectory of a particle in a magnetic field which varies in a direction perpendicular to the field lines.

The particle does not return to the point from which it started but experiences a drift in the direction perpendicular to the gradient of the field, $\nabla_\perp B$. The motion is quite similar to the $\bar{F} \times \bar{B}$ drift except that the trajectory in this case is not truly cycloidal—the guiding center "wobbles" about a straight line perpendicular to $\nabla_\perp B$ (Reference 4). The calculated drift velocities are only approximate. Their accuracy becomes poorer as the scale of the field variation approaches the gyro-radius. The gradient-B drift velocity to first order in $\nabla_\perp B$ (References 4 and 22) is

$$\bar{V}_g = - \frac{p_\perp^2}{2\gamma m^2} \frac{\nabla_\perp B \times \bar{B}}{\omega_c B^2} \quad . \tag{3-36}$$

The gradient-B drift and curvature drift velocities may be combined in one expression:

$$\bar{V}_g = - \left(\frac{p_\perp^2}{2} + p_{||}^2 \right) \frac{\nabla_\perp B \times B}{\gamma m^2 \omega_c B^2}$$

$$= - \left(\frac{v_\perp^2}{2} + v_{||}^2 \right) \gamma \frac{\nabla_\perp B \times \bar{B}}{\omega_c B^2} \quad . \tag{3-37}$$

The total drift velocity of Equation 3-37 often is called the gradient-B drift velocity. For simplicity, it will be thus designated throughout the remainder of this volume.

In the geomagnetic field that decreases with $1/r^3$, the drift velocity is proportional approximately to L^2 . The drift velocity in the azimuthal direction at any latitude, λ , is

$$\bar{V}_g = - \left(\frac{p_\perp^2}{2} + p_{||}^2 \right) \frac{3cL^2}{\gamma mqR_E B_E} \frac{(1 + \sin^2\lambda) \cos^5\lambda}{(1 + 3 \sin^2\lambda)^2} \quad . \tag{3-38a}$$

At the equator where $\sin \lambda = 0$, the latitude-dependent part of Equation 3-38 equals 1, and the drift velocity (eastward) for electrons becomes

$$V_g(\text{km/sec}) = 14.76\left(p_\perp^2 + 2p_\parallel^2\right)\frac{L^2}{\gamma} = 3.86\left(\frac{v_\perp^2}{c^2} + 2\frac{v_\parallel^2}{c^2}\right)\gamma L^2 \quad . \tag{3-38b}$$

The corresponding drift velocity (westward) for protons is

$$V_g(\text{km/sec}) = -8.04 \times 10^{-3}\left(p_\perp^2 + 2p_\parallel^2\right)\frac{L^2}{\gamma} \; -7080\left(\frac{v_\perp^2}{c^2} + 2\frac{v_\parallel^2}{c^2}\right)\gamma L^2 \tag{3-39a}$$

which in the nonrelativistic limit is

$$V_g(\text{km/sec}) \sim -15.1(T_\perp + 2T_\parallel)\frac{L^2}{\gamma} \quad . \tag{3-39b}$$

Momentum here is in MeV/c units and energy in MeV. For relativistic electrons, the magnitudes of the energy "components" may be used in place of the momentum. In Equations 3-39a and 3-39b, a positive velocity results when the drift motion is toward the east. Electrons generally drift toward the east and positively charged particles drift toward the west.

The gradient-B drift current induces a magnetic field that, inside a region enclosed by the path of the guiding center, opposes the main field of the earth. The drift current may be thought of as a diamagnetic current (Section 3.3.2; References 1 and 20).

The gradient-B drift is much faster than the gravitational drift for electrons and fast protons. The mean of $(v_\perp^2/2 + v_\parallel^2)$ for isotropically distributed thermal particles is 3 kT/m . k is Boltzmann's constant 1.38×10^{-16} cgs, and T is the temperature (Reference 2). The mean drift velocity of thermal particles at the equator due to the nonhomogeneity of the field is

$$V_g\,(\text{km/sec}) \cong 4 \times 10^{-9}\, TL^2 \quad . \tag{3-40}$$

A mean temperature of about 2,000°K appears to be a fair assumption for both electrons and ions in the trapped radiation belts (References 23 through 27). The drift velocity of thermal particles then is

$$V_g\,(\text{km/sec}) \cong 8 \times 10^{-6}\, L^2 \quad , \tag{3-41a}$$

which is comparable with the gravitational drift velocity of protons (Equation 3-32).

3.3.2 Magnetic Reflection

Generally, a nonhomogeneous magnetic field has regions where the field lines converge. In those regions, the magnetic force $(q/c)\bar{v} \times \bar{B}$ has a small component directed along the field lines. This component tends to deflect a charged particle away from a region of increasing field strength.

The magnetic force components are depicted in Figure 3-9. The relative magnitudes of the force components are variable. Usually the centripetal force is the major part of the magnetic force. When the retarding force along the field lines is relatively weak, the equation of motion yields an acceleration (or deceleration) in the field direction $\bar{B}$ (References 4 and 21):

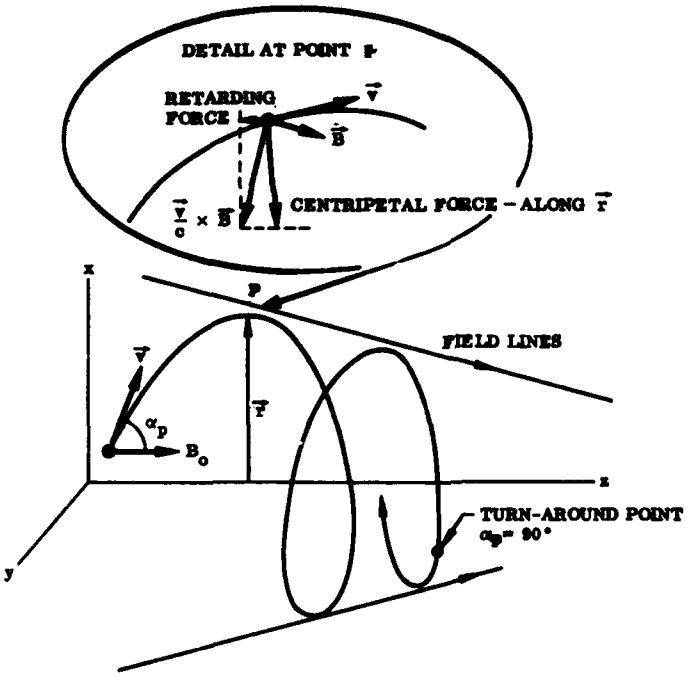

Figure 3-9. Components of the force acting on a positively charged particle in a converging magnetic field.

$$\frac{dv_{\parallel}}{dt} \cong - \frac{1}{2} \frac{v_{\perp}^2}{\gamma B} \frac{d\bar{B}}{dS} \qquad (3\text{-}41b)$$

to first order in the variation of B with distance S along the field line. The similarity to the drift velocity Equation 3-37 especially should be noted. Here, too, gravitational effects are comparable with the field inhomogeneity effects for thermal velocity protons.

The radial component of the equation of motion reduces to:

$$\frac{dv_{\perp}}{dt} \cong \frac{1}{2} \frac{v_{\parallel} v_{\perp}}{\gamma B} \frac{dB}{dS} \quad . \qquad (3\text{-}42)$$

But $v_{\parallel}\, dB/dS$ is just the time rate of change of magnetic field intensity as experienced by a spiraling particle. Equation 3-42 therefore yields the simple relation:

$$v_{\perp}^2 \propto B \quad . \qquad (3\text{-}43)$$

Charged particles in a converging magnetic field travel toward the "ends" of the field only as far as the turnaround or mirror points (Reference 1) where $p_{\perp}^2$ is equal to p^2, the total momentum squared. This definition of the turnaround points is not in exact accord with Section 3.2.3. For all practical purposes, the turnaround point is regarded simply as the location where there is no component of momentum along the general direction of the field. To avoid confusion, the term mirror point will be used here except when the specific meaning of Section 3.2.3 is intended.

If the magnetic field is closed at two ends, charged particles will continue to "bounce" back and forth until they either lose energy or are deflected by some external process. Figure 1-3 shows how charged particles move in the earth's field (ignoring drift motion).

It is convenient to define the pitch angle α_p as the angle between the particle's momentum and the magnetic field (some of the early literature on magnetic trapping refers to the pitch angle as the complement of the angle defined here). The pitch angle is indicated in Figures 1-3 and 3-9. Equation 3-43 is equivalent to a simple relation which gives, at any point, the pitch angle variation in a magnetic field:

$$\sin \alpha_p = \sqrt{B/B_m} \qquad 3\text{-}44$$

Equation 3-44 is presented numerically in Figure 3B-1. B_m is the field strength at the mirror point. The pitch angle attains its minimum, α_o, at the equator. A smallest allowed α_o, the cutoff pitch angle, exists for any field line. Particles with smaller pitch angles would be lost rapidly because they penetrate deeply into the atmosphere (References 28, 29, and 30). The cutoff pitch angle:

$$\alpha_c = \arcsin\left(\sqrt{B_o/B_{[\text{atmosphere}]}}\right) \tag{3-45}$$

is plotted in Figures 3B-3 and 3B-4.

THE MAGNETIC MOMENT OF A CHARGED PARTICLE. The proportionality of $p_\perp^2$ and B ensures that the magnetic flux $\pi\rho_c^2 B$ within an orbit remains constant. This result can be shown to be true generally, even in a magnetic field that varies with time (Reference 21). Charged particles behave as a diamagnetic medium—their motion induces a magnetic field in opposition to the externally applied field (References 1, 20, 31, and 32). The product of the area enclosed by the orbit multiplied by the current around the perimeter is the magnetic moment of a single gyrating particle. The magnetic moment of a charged particle in a magnetic field:

$$M = \frac{p_\perp^2}{2mB} = \frac{p^2}{2m\,B_m} \tag{3-46}$$

is a constant if Equation 3-43 is valid. The energy-dependent factor in the latter equation is plotted in Figure 3B-7.

THE BOUNCE AND DRIFT PERIODS. The total time elapsed between successive reflections, the bounce period is

$$t_b = \frac{4}{v}\int_o^{S_m} \frac{dS}{\cos\alpha_p} \equiv \frac{R_o}{v}\, g(\alpha_o) \quad . \tag{3-47}$$

A rather good empirical approximation for particles trapped in the earth's magnetic field (Reference 33) is

$$t_b(\text{sec}) \approx 0.11\,\frac{L}{v/c}\,(1 - 0.43\sin\alpha_o) \quad . \tag{3-48}$$

Bounce periods are generally several orders of magnitude greater than gyro-periods ($\approx 10^{-1}$ second compared with $\approx 10^{-6}$ to 10^{-5} second for trapped electrons). Bounce periods are shown in Figures 3B-9 and 3B-10 and Table 3B-1.

Because it varies along a field line, the azimuthal drift velocity must be averaged over a complete bounce period. The average drift velocity on the equator (Equations 3-38 and 3-39) is given quite well by the empirical approximation (References 33, 34, 35, and 36):

$$V_g \approx \frac{3c}{2eB_E R_E} L^2 E \frac{v^2}{c^2}\left(\frac{1 + 0.43 \sin \alpha_o}{1.43}\right) \quad (3\text{-}49a)$$

$$V_g \text{ (km/sec)} \approx 5.3 L^2 E \frac{v^2}{c^2} (1 + 0.43 \sin \alpha_o) \quad (3\text{-}49b)$$

The drift period is the circumferential distance on the equator divided by the average drift velocity. A useful empirical approximation for the drift period in the geomagnetic field is

$$t_d \approx \frac{4\pi eB_E R_E^2}{3mc^3} \frac{1.43}{L\gamma(v/c)^2 (1 + 0.43 \sin \alpha_o)} \quad (3\text{-}50a)$$

for electrons:

$$\frac{4\pi eB_E R_E^2}{3mc^3} \approx 1.038 \times 10^4 \text{ second} \quad (3\text{-}50b)$$

and for protons:

$$\approx 5.655 \text{ second}. \quad (3\text{-}50c)$$

Drift periods are generally several orders of magnitude greater than bounce periods. Numerical values of drift periods can be found in Figures 3B-12 through 3B-14.

3.3.3 The Motion of Field Lines

If charged particles gyrating in a magnetic field are to maintain a constant magnetic moment during changes in the field strength, their kinetic energies also must change. Energy normally is not exchanged between a static magnetic field and charged particles. However, a variable magnetic field induces an electric field that can accelerate charged particles. The induced electric field $\bar{E}_i$ is given by Faraday's law, which states that the integral $\oint \bar{E}_i \cdot d\bar{s}$ taken

along the perimeter of a closed surface is proportional to the rate of change of magnetic flux,

$$\Phi = \int_{\text{surface}} \bar{B} \cdot d\bar{A}, \tag{3-51}$$

across the surface (Reference 13), or:

$$\oint \bar{E}_i \cdot d\bar{s} = -\frac{1}{c} \frac{\partial \Phi}{\partial t} = -\frac{1}{c} \int_{\text{surface}} \frac{\partial \bar{B}}{\partial t} \cdot d\bar{A} \quad . \tag{3-52}$$

If the magnetic field is homogeneous, it is easily demonstrated that the induced field accelerates a charged particle just enough that the magnetic moment is maintained constant (Reference 20). The situation in a nonhomogeneous field is more complicated, mainly because magnetic field lines (the number of which is proportional to magnetic flux) must move to accommodate the addition of more field lines. It can be demonstrated that, when the time scale for field variations is much greater than the gyro-period, the gyrating charged particles must move with the field lines in such a manner that the magnetic moment is preserved (Reference 21).

A simple case is the axially symmetric field subjected to an axially symmetric increase in field strength. A cross section of the field is shown in Figure 3-10. This sketch may be taken to represent

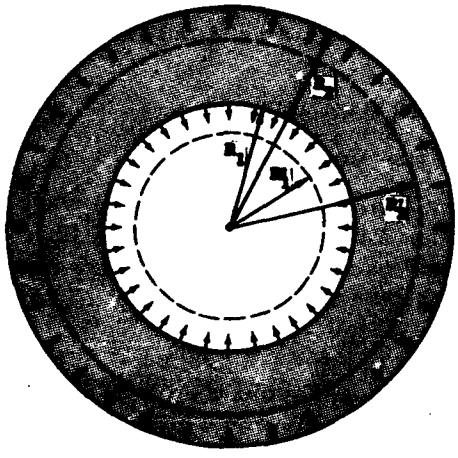

Figure 3-10. Equatorial cross section of a uniformly varying, axially symmetric field.

an equatorial section of the geomagnetic field. As the field changes, an arbitrarily selected annular region between R_1 and R_2 must move inward or outward to a new position $R_1' - R_2'$, if the magnetic flux is to be preserved. When the field is changing at a rate proportional to $R^{-n} (n < 2)$, the radial velocity of the field lines (on the equator) is

$$V_R = \frac{\partial R_o}{\partial t} = \frac{R_o}{n-2} \frac{\partial B}{\partial t} \frac{1}{B_o} . \qquad (3\text{-}53)$$

An increase in the field strength results in compression of the field. This is essentially what happens during the sudden commencement phase (Reference 37) of a magnetic storm (Section 2.2.5). The induced azimuthal electric field (Equation 3-52) is

$$E_\phi = - \frac{R_o}{2c} \frac{\partial B}{\partial t} . \qquad (3\text{-}54)$$

The $\bar{E} \times \bar{B}$ drift velocity computed from this electric field is just sufficient that particles move inward with the velocity given by Equation 3-53.

The field lines are commonly regarded as being "frozen" in the plasma of charged particles (References 1, 4, 31, and 38 through 42). The plasma and field lines behave as a continuous fluid subject to the same sort of dynamical laws as a classical, highly conducting fluid. The fluid model of a plasma is discussed in more detail in Section 3.6.

3.4 THE ADIABATIC APPROXIMATION

3.4.1 Hamilton's Equations: Constants of Motion

The guiding center approximation is useful when approximate trajectories are desired. An alternative method is to find the constants of the motion or to find quantities that are very nearly constants of the motion, such as the magnetic moment of a charged particle (Sections 3.3.2 and 3.3.3).

In the classical Hamilton-Jacobi theory of mechanics, a constant generalized momentum, p_i, is one whose canonical conjugate coordinate, q_i, does not appear in the Hamiltonian, $H(p_i q_i)$ (Reference 3). This assertion follows directly from Hamilton's equations:

$$\frac{\partial q_i}{\partial t} = \frac{\partial H(q_i, p_i)}{\partial p_i} \qquad (3\text{-}55)$$

$$\frac{\partial p_i}{\partial t} = - \frac{\partial H(q_i, p_i)}{\partial q_i} \qquad (3\text{-}56)$$

When certain of the coordinates, for example q_k, p_k, are cyclic, a prescription for constructing constants of the motion is to form the action integrals

$$j_k = \oint p_k \, dq_k \quad . \qquad (3\text{-}57)$$

The customary notation for a line integral is employed—the integration is to be carried over a closed path in phase space (q,p space). By means of the canonical transformation from p, q to w, j coordinates, a Hamiltonian is constructed that does not explicitly contain the coordinates w_k conjugate to j_k. Therefore, the action integrals are the desired constants of the motion.

The motion of a charged particle in a magnetic field has some obvious cyclic properties. The gyro-motion about the field lines has a corresponding action integral, for example j_1. If the field is closed or constricted at the ends another j_2 corresponds to the repeated reflection of particles at the constrictions. In addition, if the field has some sort of azimuthal symmetry, a (generally slow) cyclic drift motion exists about the axis of symmetry, for which a third invariant j_3 can be constructed. Since 3 degrees of freedom exist, three j's should be adequate to fully describe the motion.

CURVILINEAR COORDINATES—EULER POTENTIALS. An especially useful representation of a magnetic field is one in which two coordinate axes are aligned perpendicular to the field lines. The transverse coordinates are designated by α and β. The α and β axes are surely orthogonal to $\bar{B}$ if the condition:

$$\bar{B} = \nabla\alpha \times \nabla\beta \qquad (3\text{-}58)$$

is satisfied (References 21, 43, and 44). The third coordinate is related to the distance along the field line through the simple formula:

$$\chi = \int_0^S \bar{B} \cdot d\bar{S} \qquad (3\text{-}59)$$

The usual designation γ is avoided here because of the possibility of confusion with the relativistic dilation factor.

Because the vector potential:

$$\bar{A} = \alpha \nabla \beta \qquad (3\text{-}60)$$

so intimately involves α and β, the coordinates α, β, and χ often are referred to as Euler Potentials (References 45 and 46).

A suitable representation for α and β in a dipole field for spherical coordinates is

$$\alpha = -\frac{M_E}{r} \sin^2 \theta \qquad (3\text{-}61a)$$

$$\beta = \phi \qquad (3\text{-}61b)$$

and for cylindrical coordinates is

$$\alpha = -\frac{M_E}{(R^2 + z^2)^{3/2}} \qquad (3\text{-}62a)$$

$$\beta = \phi \qquad (3\text{-}62b)$$

where M_E is the dipole moment. The curves defined by the simultaneous conditions α = constant and β = constant are recognized immediately as the field lines (Equations 2-1 and 2-2). Detailed computations of Euler Potentials in the geomagnetic field have been performed by Stern (References 19, 45, 46, 47, and 48).

HAMILTONIAN OF A CHARGED PARTICLE. The Hamiltonian of a charged particle is just equal to the total energy (References 21 and 44):

$$H = \sqrt{B^2 p_\chi^2 c^2 + 2mc^2 MB + m^2 c^4} + q\Psi \cdot \qquad (3\text{-}63a)$$

In the nonrelativistic limit

$$H \sim \frac{B^2}{2m} p_\chi^2 + MB + q\Psi + mc^2 \quad . \qquad (3\text{-}63b)$$

The last term on the right of Equation 3-63a is the contribution of the electric potential, Ψ; the second term within the square root has been written for convenience in terms of the particle's magnetic moment M.

The momenta conjugate to α, β, and χ (References 44 and 49) are

$$p_\alpha = 0 \tag{3-64}$$

$$p_\beta = \frac{q\alpha}{c} \tag{3-65}$$

$$p_\chi = \frac{\gamma m}{B^2} \frac{\partial \chi}{\partial t} \, . \tag{3-66}$$

A special advantage of using α, β coordinates is that α and β are canonical conjugates of each other, provided a new Hamiltonian $H' = (c/q)H$ is defined so that

$$\frac{\partial \beta}{\partial t} = \frac{c}{q} \frac{\partial H}{\partial \alpha} = \frac{\partial H'}{\partial \alpha} \tag{3-67}$$

$$\frac{\partial \alpha}{\partial t} = - \frac{c}{q} \frac{\partial H}{\partial \beta} = - \frac{\partial H'}{\partial \beta} \, . \tag{3-68}$$

Equations 3-67 and 3-68 might be employed to determine the drift velocities ($\partial\beta/\partial t$ is $\partial\phi/\partial t = \omega_d$). In practice, this procedure is apt to be awkward and to have no great advantage over the guiding center approximation.

3.4.2 Adiabatic Invariants

When the motion of a particle is not strictly periodic (the orbits are not closed), the action integrals, j_i, are adiabatic invariants which only approximate constants when the magnetic and electric fields are sufficiently uniform along the trajectories (References 21, 50, and 51). The adiabatic invariants might be expanded in small parameters, ϵ_1, ϵ_2, and ϵ_3, so that:

$$j_1 \sim \text{(constant)} \times (M_0 + \epsilon_1 M_1 + \epsilon_1^2 M_2 + \dots) \quad (3\text{-}69)$$

$$j_2 \sim \text{(constant)} \times (J_0 + \epsilon_2 J_1 + \epsilon_2^2 J_2 + \dots) \quad (3\text{-}70)$$

$$j_3 \sim \text{(constant)} \times (\Phi_0 + \epsilon_3 \Phi_1 + \epsilon_3^2 \Phi_2 + \dots) \quad . \quad (3\text{-}71)$$

ϵ_i is generally the characteristic period divided by a time scale corresponding to the field fluctuations (References 21, 52 through 55, and 65).

FIRST ADIABATIC INVARIANT. The first adiabatic invariant can be identified with the magnetic moment. When the motion is truly cyclic, the first action integral can be written with the aid of Green's theorem as a surface integral (References 44 and 49):

$$j_1 = \frac{q}{c} \iint_{[\text{orbit}]} d\alpha\, d\beta \quad . \quad (3\text{-}72)$$

But α and β were defined in such a fashion that the magnetic flux across a χ = constant surface is proportional to the area of the surface or:

$$\Phi = \iint_{[\text{surface}]} d\alpha\, d\beta \quad . \quad (3\text{-}73)$$

The magnetic moment is proportional to the flux across the orbit (Section 3.3.2), which is, in turn, proportional to the first action integral. The magnetic moment can be formaliy identified with the first term on the left in Equation 3-69. Considering any but the first terms in the expansions of Equations 3-69, 3-70, and 3-71 is often not practical. M therefore is referred usually to as the first adiabatic invariant.

SECOND ADIABATIC INVARIANT. The second action integral is simply

$$j_2 = \oint p_\chi d\chi \propto \oint p_{\parallel} dS \quad . \quad (3\text{-}74)$$

The J integral,

$$J = 4\int_0^{S_m} p_{\parallel} dS = 4\int_0^{S_m} p \cos \alpha_p dS , \qquad (3\text{-}75)$$

accordingly, should be a constant in a strictly periodic system. It may be referred to as the second adiabatic invariant or integral invariant. The somewhat confusing designation longitudinal adiabatic invariant also is used occasionally (References 21, 44, and 56).

THIRD ADIABATIC INVARIANT. In a two-dimensional system, M and J would suffice to determine the dynamical behavior. The supplementary third adiabatic invariant or flux invariant, Φ, is analogous to the magnetic moment. The magnetic moment is proportional to the flux across a surface bounded by the particle orbit, and Φ is the flux across a constant X surface bounded by the guiding center trajectory. The third adiabatic invariant is defined in the geomagnetic field so that it is equal to the total flux exterior to the guiding center trajectory in the equatorial plane.

In the earth's dipole field, the magnetic flux across the equatorial plane, the third adiabatic invariant, is

$$\Phi = 2\pi B_E R_E R_o \qquad (3\text{-}76a)$$

$$\Phi \text{ (gauss } R_E^2) \approx 1.960\ L \quad . \qquad (3\text{-}76b)$$

The constancy of Φ in a static field is obvious. Its usefulness is that it is also an adiabatic invariant in a time-varying field (References 21 and 44). An immediate consequence of Φ invariance is that trapped particles move inward with the field lines when the field is compressed (Section 3.3.3).

3.4.3 Invariant Surfaces

The loci of the guiding center motion lie on a surface—the invariant surface (Reference 56). Figure 3-11 is a sketch of an invariant surface (a constant-B surface is sketched to show the lines of intersection B_{m1} and B_{m2}—the traces of the particles' mirror points). An invariant surface is constructed of field lines and is open at the ends where it intersects the surface $B = B_m$ = constant. If Φ is to remain constant, the

invariant surface must be single valued—the intersection with a constant-K surface must be a closed curve. A set of three adiabatic invariants defines a unique invariant surface. However, the details of particle motions relative to the surface are left unspecified.

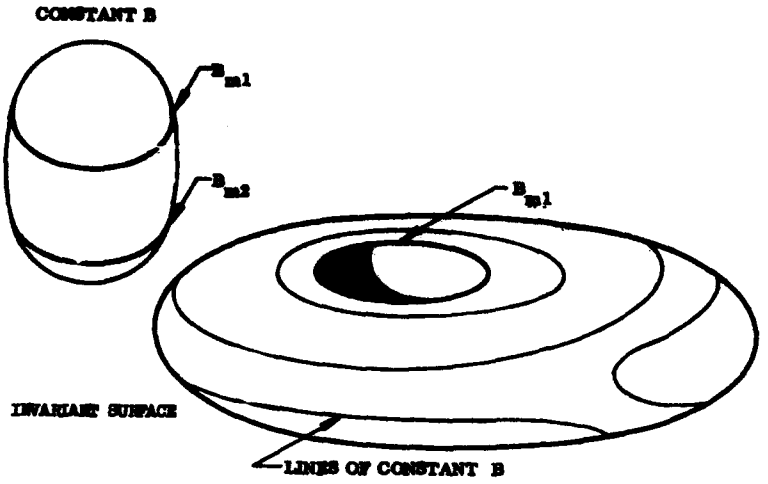

Figure 3-11. An adiabatic invariant surface in the geomagnetic field.

In the absence of electric fields, the total momentum is constant so the parallel component, $p_{\parallel}$, is a function of B alone. Therefore, the J integral may be replaced by a degenerate integral invariant (References 21, 44, 57, and 58):

$$I = \frac{J}{p} = 4R_o \int_0^{S'_m} \sqrt{(B_m - B)/B_m}\, dS' \qquad (3\text{-}77)$$

which depends only on two parameters B_o (or R_o) and B_m (or S_m). S' is the dimensionless variable S/R_o. Computations of I are presented in Table 3B-1; also see Figures 3B-11 and 3B-15. A constant-I surface can be constructed through the set of mirror points of all particles having the same I = J/p. Figure 3B-15 shows some of the constant-I surfaces in a dipole field. The boundaries of an invariant surface are the intersections of a constant-I surface and a constant-B surface. The invariant surface is made up of all the field lines that pass through the boundary curves thus defined.

McILWAIN L-PARAMETER. The invariant surface in a symmetric field can be located with the aid of only two parameters, say R_o and B_m or $L = R_o/R_E$ and B_m. In an unsymmetric field, a parameter remains which specifies the equatorial intersection of an invariant surface and may be identified with L. In the symmetric field, a simple functional relation exists between L and I:

$$\frac{L^3 B_m}{B_E} = f\left(\frac{I^3 B_m}{B_E}\right) . \qquad (3\text{-}78)$$

The McIlwain L-parameter has been defined for the geomagnetic field according to the numerical values of f computed for the idealized dipole field (References 48 and 59). This definition may yield an L-parameter that is quite different from R_o/R_E, especially at large L-values (Reference 60). Computed values of L are shown in Appendixes 2C and 2D.

L-SHELLS. The actual shape of an invariant surface can be deduced only from the equations of motion. It is certainly not symmetric when the field is not symmetric. Also, the guiding centers do not exactly follow the field lines, though this effect usually can be ignored (Section 3.2.3). The most important complicating factor is that drift motions may not be exactly in the azimuthal direction nor even necessarily in the same direction for different particles. Two particles differing in one or more of the adiabatic invariants may start on the same field line and subsequently drift toward different field lines. Because any particle must return after one complete circuit to the field line from which it started, the maximum splitting of two invariant surfaces should be near 180-degree longitude from the region where they intersect.

In the inner part of the radiation belts, below about $L \approx 3$, the splitting of invariant surfaces is insignificant—less than 1 percent of R_o (References 60 and 67). The average location of all the intersecting invariant surfaces usually is referred to as an L-shell. The low L-shells are degenerate. One value of L locates a set of invariant surfaces with different mirror point traces. For convenience, think of L-shells as being closed or intersecting the earth's surface.

The splitting of invariant surfaces beyond $L \approx 3$ is great enough that it may have observable consequences. Figure 3-12 shows how

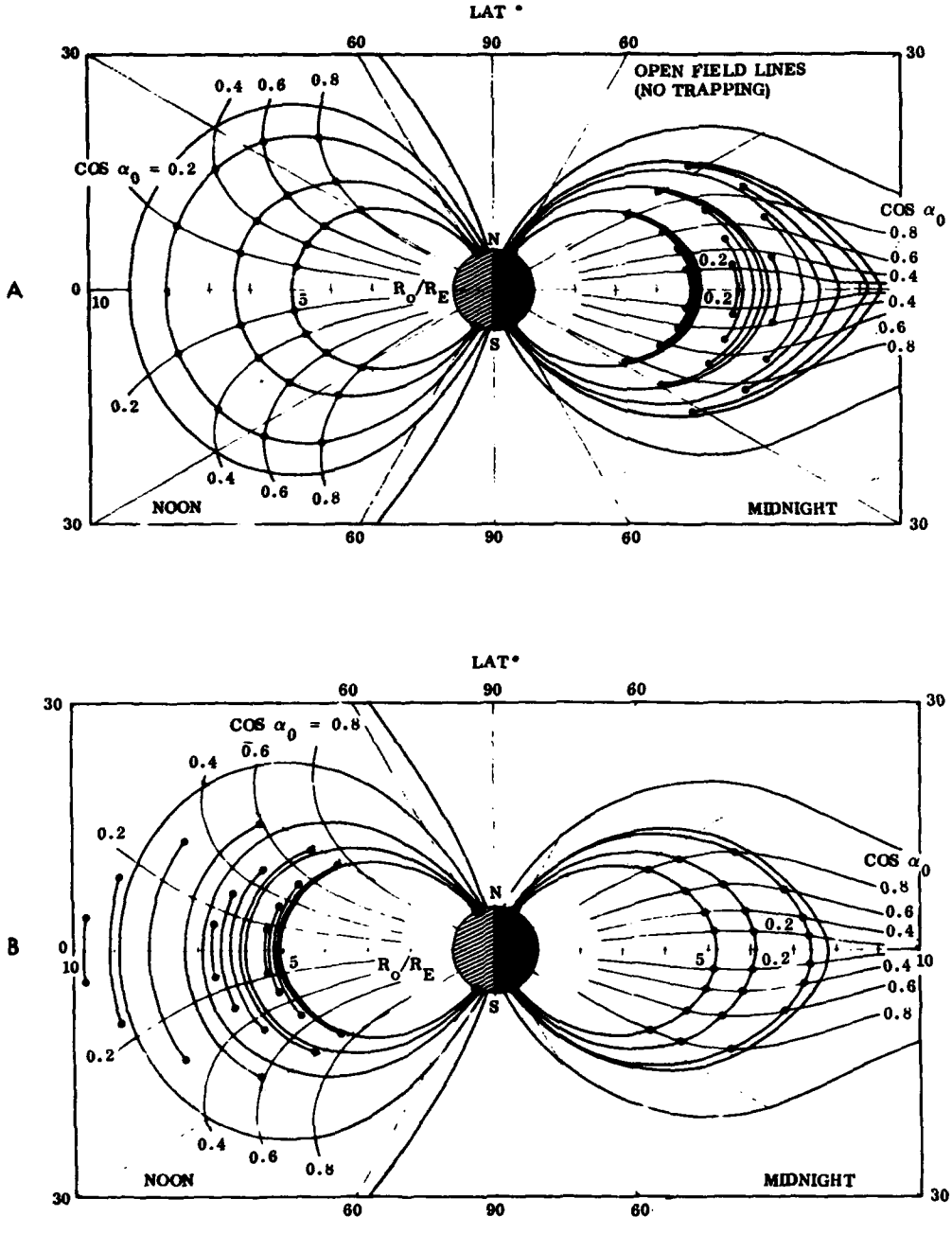

Figure 3-12. Splitting of invariant surfaces in the geomagnetic field (Reference 58).

invariant surfaces differ on the sunlit and dark sides of the earth (Reference 58). Figure 3-12a shows a section of the invariant surfaces for particles starting on the sunlit side of the earth; Figure 3-12b is for particles starting on the dark side. The dots correspond to mirror points, labeled with $\mu_o = \cos \alpha_o$. The boundaries of the trapping region are shown approximately; they are not necessarily coincident with invariant surfaces. Particles mirroring at low altitudes on the dark side of the earth are displaced radially outward so that on the sunlit side their orbits are outside the trapping region (Section 1.3). Similarly, particles mirroring at high latitudes on the sunlit side will not remain within the trapping region on the dark side.

3.5 LIOUVILLE'S THEOREM

3.5.1 Generalized Liouville's Theorem

When the energies of individual particles are conserved, their distribution functions should be conserved according to Liouville's theorem. A distribution function $f(\bar{x}, \bar{p})$, in a phase space comprising position x and momentum p coordinates, is defined so that the number of particles in the phase space volume element $d^3x d^3p$ is $f(\bar{x}, \bar{p})\, d^3x d^3p$. The distribution function need not involve explicitly the momentum and position coordinates; a particularly useful representation is $f(\alpha, \beta, J, M)$ in adiabatic invariant space.

The equation that guarantees conservation of particles is

$$\frac{df(\alpha, \beta, J, M)}{dt} = \frac{\partial f}{\partial t} + \frac{\partial}{\partial \alpha}\left(f \frac{\partial \alpha}{\partial t}\right) + \frac{\partial}{\partial \beta}\left(f \frac{\partial \beta}{\partial t}\right) = 0 \quad . \tag{3-79}$$

Elimination of $(\partial/\partial\alpha)(\partial\alpha/\partial t)$ and $(\partial/\partial\beta)(\partial\beta/\partial t)$ with the aid of Equations 3-55 and 3-56 gives Liouville's equation:

$$\frac{\partial f}{\partial t} + \frac{\partial \alpha}{\partial t}\frac{\partial f}{\partial \alpha} + \frac{\partial \beta}{\partial t}\frac{\partial f}{\partial \beta} = 0 \quad . \tag{3-80}$$

Therefore, f is constant along a dynamical trajectory (Reference 44).

3.5.2 Liouville's Theorem in B, L Coordinates

A simple and useful formulation of Liouville's theorem can be derived for a distribution function $f(\mu)$, which is an explicit function of the cosine of the pitch angle, μ. A group of particles with the

same adiabatic invariants are confined (ignoring azimuthal drift motion) to a flux tube, the volume enclosed by a set of field lines. The rate at which particles leave one end of a segment of a flux tube is

$$\frac{dN(\mu)}{dt} \cdot d\mu = f(\mu, B)\, v\mu\, d\mu\ \delta A \qquad (3\text{-}81)$$

where δA is the cross-sectional area $d\alpha\, d\beta$. The number of particles leaving the flux tube segment must be the same as the number entering at the opposite end. The pitch angle and δA are both simple functions of magnetic field strength. It follows that, if two points connected by a dynamical trajectory are labeled 1 and 2, Liouville's equation for particle distributions on a field line is

$$f[\mu_1(B_1),\ B_1] = f[\mu_2(B_2),\ B_2] \quad . \qquad (3\text{-}82)$$

μ_1 and μ_2 are pitch angle cosines of a single group of particles at the points where the magnetic intensities are B_1 and B_2, respectively.

A consequence of Equations 3-80 and 3-82 is that f on any invariant surface is a function of B alone (Reference 44). The coordinates B, L are adequate to specify trapped particle densities at any point in the geomagnetic field.

OMNIDIRECTIONAL FLUX. Trapped particle number densities customarily are presented in terms of the intensity (or directional flux or specific intensity):

$$j(\mu) = f(\mu)\ v \quad . \qquad (3\text{-}83)$$

The intensity j(0) [or j_m or j(90°)] at the mirror points is particularly useful. The distribution function $f(\mu, B_o)$ at the equator is just equal (according to Liouville's theorem) to the distribution function $f(0, B_m)$ at the mirror points where:

$$B_m = B_o/(1 - \mu_o^2) \quad . \qquad (3\text{-}84)$$

The quantity that usually is plotted in B, L coordinates is the omnidirectional flux:

$$J = 2\pi \int_{-1}^{1} j(\mu)\, d\mu \quad , \qquad (3\text{-}85)$$

(often written with a subscript, i.e., J_o or $J_{[omni]}$). The omnidirectional flux is just 4π times the intensity averaged over all angles. The omnidirectional flux should not be confused with the net flux:

$$F = \int_{[\text{all angles}]} j \cos \zeta \, d\Omega \tag{3-86}$$

which is the rate per unit area at which particles cross a plane surface, ζ is the angle between the velocity vector and the normal to the surface, $d\Omega$ is the increment of solid angle. The flux, F, can be negative or positive, depending on whether more particles cross the surface from one side or the other. With regard to the trapped particles, F has a meaning only when referred to a solid detector surface, otherwise:

$$F = 2\pi \cos \zeta' \int_{-1}^{1} j(\mu) \, \mu d\mu \sim 0 \tag{3-87}$$

where ζ' is the angle between the field line and the normal to the surface.

Since J is a function of B, it also may be regarded as a function of $\mu_o' = \sqrt{1 - B_o/B}$. With the aid of Liouville's equation (Equation 3-82), the omnidirectional flux can be written as an integral involving the equatorial intensity $j(\mu_o, \mu_o') = j(\mu_o, B_o)$:

$$J(B) = J(\mu_o') = 4\pi \int_{\mu_o'}^{1} j(\mu_o, B_o) \frac{B\mu_o \, d\mu_o}{B_o \sqrt{1 - B(1 - \mu_o^2)/B_o}} \tag{3-88a}$$

$$= 4\pi \int_{\mu_o'}^{1} j(\mu_o, \mu_o') \frac{\mu_o \, d\mu_o}{(1 - \mu_o'^2)\sqrt{1 - (1 - \mu_o^2)/(1 - \mu_o'^2)}} \, . \tag{3-88b}$$

The inverse relation that yields j as a function of J is complicated. Detailed solutions are available elsewhere (References 61 and 62).

3.6 HYDROMAGNETIC MODEL OF A PLASMA

3.6.1 Collisions Between Charged Particles— Collective Behavior

In any ensemble of particles, collisions occur between particles. These result in transfer of momentum. The electrostatic forces between charged particles decrease slowly as the mutual separation increases. Therefore, where a plasma is relatively tenuous, the most important interactions are between charged particles. The interaction forces between charged particles become negligible only beyond the Debye length or Debye shielding radius:

$$\lambda_D = \sqrt{\frac{kT_e}{4\pi n_e e^2}} \qquad (3\text{-}89a)$$

$$\lambda_D(\text{cm}) = 6.9\sqrt{\frac{T_e(k)}{n_e(\text{cm}^{-3})}} \qquad (3\text{-}89b)$$

where T_e and n_e are, respectively, the effective temperature and number density of "thermal" electrons. The shielding of electrostatic forces is due to thermal fluctuations in the free electron gas (References 1 and 2). The effective temperature of the free electrons, the electron temperature T_e, therefore should be expected to appear in the Debye length formula. The electron temperature above the atmosphere is about 1,500 to 2,000 K (References 23 through 27), which results in a Debye length of

$$\lambda_D(\text{cm}) \approx \frac{300}{\sqrt{n_e(\text{cm}^{-3})}} \quad . \qquad (3\text{-}90)$$

The Debye length in the lower trapped radiation belts is about 2 to 10 centimeters.

The number of particles within a sphere of radius λ_D, the Debye sphere, is a measure of the importance of collective behavior. When few particles occur within a Debye sphere, each particle interacts only with its nearest neighbors. But when each particle interacts simultaneously with thousands of other particles, any perturbation in the particle distribution will result in transient electric and magnetic fields that are felt by many particles. These fields tend to restore

the original particle distribution. Oscillations can occur as in any mechanical system where restoring forces restrain the excursions from equilibrium. The trapped particle belts are subject to a wide variety of oscillation phenomena. Oscillations and waves in the magnetosphere are discussed briefly in Section 4. A systematic treatment of oscillations in ionized gases demands more space than is available here. For further reading, see especially References 63 and 64.

3.6.2 Boltzmann's Equation

It is advantageous to treat the behavior of a plasma statistically through the evolution of a distribution function f. Liouville's equation must be modified to take account of interparticle collisions and nonconservation of f. The generalization of Liouville's equation is Boltzmann's equation (References 20, 65, 66, and 75):

$$\frac{\partial f}{\partial t} + \frac{1}{\gamma m}\,\bar{p}\cdot\nabla f + \bar{F}\cdot\nabla_p f = \left(\frac{\delta f}{\delta t}\right)_{[\text{collisions}]} . \qquad (3\text{-}91)$$

The notation ∇_p has been used to denote the gradient $(\partial/\partial p_1\,,\ \partial/\partial p_2\,,\ \partial/\partial p_3)$ in momentum space. Considering the strictly relativistic Boltzmann equation usually is not necessary. Most of the particles in the radiation belts have velocities not significantly greater than the thermal speed. Throughout the remainder of this section, the momentum is replaced by $m\bar{v}$.

Boltzmann's equation in the absence of collisions is entirely equivalent to the orbit equations of Sections 3.2 and 3.3 (References 20, 40, and 41).

MOMENTS OF BOLTZMANN'S EQUATION. Boltzmann's equation can be approximately solved if fluid-like equations are constructed by means of an averaging procedure (References 1, 20, and 40). Two important quantities are the number density:

$$n_k = \iiint f_k\,(\bar{x}, \bar{v}, t)\, d^3v \qquad (3\text{-}92)$$

and the streaming velocity:

$$\bar{u}_k = \frac{1}{n_k} \iiint f_k\,(\bar{x},\ \bar{v},\ t)\,\bar{v}\, d^3v \equiv \langle\bar{v}\rangle \qquad (3\text{-}93)$$

of particles of species k. These may be regarded as moments of the distribution function weighted by powers of v. Another useful moment is the stress tensor or pressure tensor:

$$\bar{\bar{P}}_k = m_k \iiint f_k(\bar{x}, \bar{v}, t)\, \bar{v}\bar{v}\, d^3\bar{v} - n_k m_k \bar{u}_k \bar{u}_k \quad . \tag{3-94}$$

Dyadic notation has been employed for the tensor $\bar{\bar{P}}$ (Reference 67). Another way of writing $\bar{\bar{P}}$ is in terms of the components:

$$P_{ij} = nm \langle v_i v_j \rangle - nm \langle v_i \rangle \langle v_j \rangle \quad . \tag{3-95}$$

The first moment of Boltzmann's equation (averaged over $\iiint d^3v$) is the equation of continuity:

$$\frac{\partial n_k}{\partial t} + \nabla \cdot n_k \bar{u}_k = 0 \quad , \tag{3-96}$$

which guarantees that particles are conserved.

The second moment of Boltzmann's equation (averaged over $\iiint \bar{v} d^3v$) is the momentum conservation equation:

$$n_k m_k \left(\frac{\partial \bar{u}_k}{\partial t} + \bar{u}_k \cdot \nabla \bar{u}_k \right) - n_k q_k \left(\bar{E} + \frac{1}{c}\, \bar{u}_k \times \bar{B} \right) + \nabla \cdot \bar{\bar{P}}_k = \bar{F}_c \quad . \tag{3-97}$$

The effects of collisions between different types of particles are combined in the term $\bar{F}_c$.

The third moment is of less immediate interest. It describes the transfer of energy and is somewhat analogous to a heat-transfer equation (Reference 20).

3.6.3 Hydromagnetic Equations

The similarity of Equations 3-96 and 3-97 to the equations of hydrodynamics is obvious. A plasma often can be considered as a continuous fluid in which the total mass velocity (or average streaming velocity) is

$$\bar{V} = \frac{\sum_k n_k m_k \bar{u}_k}{\sum_k n_k m_k} = \frac{1}{\rho} \sum_k n_k m_k \bar{u}_k \qquad (3\text{-}98)$$

The density ρ is the sum of all $n_k m_k$'s. The electrical current density (in emu) is

$$\bar{J} = \frac{1}{c} \sum_k n_k q_k \bar{u}_k = \frac{e}{c} \left[\sum_{\text{ions}} (n_i Z_i) \bar{u}_i - \sum_{\text{electrons}} n_e \bar{u}_e \right] . \qquad (3\text{-}99)$$

$+Z_i e$ is the total charge on an ion. When the Boltzmann equations for electrons and ions are combined, the result is the hydromagnetic equations (References 1, 20, 38, 40, 41, and 42) or magnetohydrodynamic equations. The mechanical force equation is

$$\rho \frac{\partial \bar{v}}{\partial t} = \bar{J} \times \bar{B} - \nabla \cdot \bar{\bar{P}} , \qquad (3\text{-}100)$$

and Ohm's law is

$$\frac{m_e c}{n_e c^2} \frac{\partial \bar{J}}{\partial t} = \bar{E} + \frac{1}{c} \bar{V} \times \bar{B} + \frac{1}{n_e e} \nabla \cdot \bar{\bar{P}}_e - \frac{1}{n_e e} \bar{J} \times \bar{B} - \frac{\bar{J}}{\sigma} . \qquad (3\text{-}101)$$

Spatial derivatives and terms of order m_e/m_i have been ignored.

Equation 3-100 is still recognizable as the basic equation of motion of a fluid. Equation 3-101 has been called Ohm's law because of its similarity to the conventional Ohm's law for a conductor. The last term on the right in Equation 3-101 contains all the effects of collisions between positive and negative particles. The proportionality of this term to $\bar{J}$ does not follow directly from Boltzmann's equation, but rather from the assumption that the momentum exchange between unlike particles should be proportional to their relative velocities (Reference 1). The constant of proportionality $1/\sigma$ is called the electrical resistivity because, in a uniform, steady state plasma with no magnetic fields, Equation 2-121 reduces to the familiar form of Ohm's law. The inverse of electrical resistivity is the electrical conductivity. The conductivity is approximately

$$\sigma \approx \frac{n_e e^2}{m_e c^2 \nu_c} \qquad (3\text{-}102)$$

where ν_c represents the frequency of collisions between electrons and ions (References 1, 68, and 69).

FIELD EQUATIONS. A continuity equation for electrical charge follows immediately from Boltzmann's equation. It is (Reference 1) the charge conservation equation:

$$\frac{\partial Q}{\partial t} + c\, \nabla \cdot \bar{J} = 0 \quad . \qquad (3\text{-}103)$$

The localized excess charge density is

$$Q = \sum_k n_k q_k \quad . \qquad (3\text{-}104)$$

The diamagnetism of a plasma, mentioned in Section 3.3.3, is a general result which makes possible including the gyro-motion part of the current in the total magnetic field. Maxwell's equations, which describe the electric and magnetic fields of a plasma, are then (References 1 and 70)

$$\nabla \cdot \bar{E} = 4\pi Q \qquad (3\text{-}105)$$

$$\nabla \cdot \bar{B} = 0 \qquad (3\text{-}106)$$

$$\nabla \times \bar{E} = -\frac{1}{c}\frac{\partial \bar{B}}{\partial t} \qquad (3\text{-}107)$$

$$\nabla \times \bar{B} = \frac{1}{c}\frac{\partial \bar{E}}{\partial t} + 4\pi \bar{J} \quad . \qquad (3\text{-}108)$$

The units of these equations are discussed in Appendix 3A. $\bar{J}$ is only that part of the current due to the relative motion of different components of the plasma. The appropriate measure of the magnetic field is $\bar{B}$, which here is called the magnetic field intensity. (B conventionally is referred to as the flux density or magnetic induction. The designation magnetic intensity or field strength conventionally is reserved for $H = B/(\text{permitivity})$.) The magnetic moments of individual particles are included in B, which is the field that would be measured at any point.

SOLUTIONS OF THE HYDROMAGNETIC EQUATIONS. A complete description of a plasma requires one more equation—an equation of state relating n_e and P. Employing a simplified equation of state usually is sufficient and desirable; in the trapped radiation belt, n_e can be assumed nearly independent of P.

The dynamics of a plasma, including flow and wave motions, can be treated by methods similar to those developed for the solution of problems in classical hydrodynamics (References 38 and 71). A special complication of hydromagnetics is that the pressure is a tensor (References 40, 41, and 42). This means that motion along the magnetic field direction is not simply related to the transverse motion, nor does the motion along the field correspond very well with the motion of a massive fluid. Only for waves and flow transverse to the magnetic field is the hydrodynamic analogy entirely valid.

TRANSVERSE DRIFT CURRENTS. A rather confusing aspect of Equation 3-101 is that it does not predict a steady current due to a gradient in the magnetic field strength (as in Equation 3-37). This drift current actually is contained implicitly in the pressure gradient term. If $\nabla P = 0$, the density of guiding centers of particles drifting in some arbitrary direction is balanced exactly by the density of guiding centers of particles drifting in the opposite direction. However, if the plasma is of finite extent or has a region in which ∇P is finite, it is possible for a current to flow (Reference 1).

3.6.4 Electrical Conductivity Tensor

When pressure gradients can be ignored, the Ohm's law equation (Equation 3-101) resembles the conventional Ohm's law in that J and E appear only linearly, although they may be in different directions. If the fields and current have parts that vary sinusoidally proportional to real part $(e^{i\omega t})$, the time derivatives can be replaced by

$$\frac{\partial}{\partial t}\left(e^{i\omega t}\right) \rightarrow i\omega\left(e^{i\omega t}\right) \quad .$$

Equation 3-101 reduces to (Reference 2)

$$\frac{m_e c}{n_e e^2} i\omega \bar{J} = \bar{E} - \frac{1}{n_e e} \bar{J} \times \bar{B} - \frac{\bar{J}}{\sigma} \quad . \qquad (3\text{-}109)$$

The current and electric field may be decomposed into vectors parallel and perpendicular to $\bar{B} = \bar{B}_o + \bar{B}\ (e^{i\omega t})$:

$$\bar{E} = \bar{E}_{\parallel} + \bar{E}_{\perp} \tag{3-110}$$

$$\bar{J} = c\sigma_o \bar{E}_{\parallel} + c\sigma_1 \bar{E}_{\perp} + c\sigma_2 \frac{\bar{B}}{B_o} \times \bar{E}_{\perp} \quad . \tag{3-111}$$

The tensor equations:

$$\bar{J} = c\bar{\bar{\sigma}} \cdot \bar{E} \tag{3-112}$$

$$\bar{\bar{\sigma}} = \begin{bmatrix} \sigma_1 & -\sigma_2 & 0 \\ \sigma_2 & \sigma_1 & 0 \\ 0 & 0 & \sigma_o \end{bmatrix} \tag{3-113}$$

are identical with the preceding equations and usually are preferred. Note that no universal agreement exists on the choice of signs in the off-diagonal (σ_2) components of $\bar{\bar{\sigma}}$. The notation here is perhaps the more frequently used.

CONDUCTIVITY TENSOR IN AN IONIZED GAS. Equations 3-109, 3-110, and 3-111 can be solved readily for the specific electrical conductivity σ_o, the Pederson conductivity σ_1, and the Hall conductivity σ_2. The total current is the sum of contributions from all types of particles. The total conductivity is the sum of ion and electron contributions:

$$\bar{\bar{\sigma}} = \bar{\bar{\sigma}}_i + \bar{\bar{\sigma}}_e \quad . \tag{3-114}$$

The components of the conductivity tensor (in emu) (References 72, 73, and 74) are

$$\sigma_o = -i \frac{n_e e^2}{c^2} \left[\frac{1}{m_i(\omega - i\nu_i)} + \frac{1}{m_e(\omega - i\nu_e)} \right] \quad (3\text{-}115)$$

$$\sigma_1 = -i \frac{n_e e^2}{c^2} \left\{ \frac{(\omega - i\nu_i)}{m_i[(\omega - i\nu_i)\omega_i^2]} + \frac{(\omega - i\nu_e)}{m_e[(\omega - i\nu_e)^2 - \omega_e^2]} \right\} \quad (3\text{-}116)$$

$$\sigma_2 = \frac{n_e e^2}{c^2} \left\{ \frac{\omega_i}{m_i[(\omega - i\nu_i)^2 - \omega_i^2]} - \frac{\omega_e}{m_e[(\omega - i\nu_e)^2 - \omega_e^2]} \right\} . \quad (3\text{-}117)$$

The frequencies ν_i and ν_e are, respectively, the rate of collisions of ions with neutral particles and the rate of collisions of electrons with all heavy particles.

The conductivities in the zero-frequency limit are

$$\sigma_o \sim \frac{n_e e^2}{c^2} \left(\frac{1}{m_i \nu_i} + \frac{1}{m_e \nu_e} \right) \sim \sigma \quad (3\text{-}118)$$

$$\sigma_1 \sim \frac{n_e e^2}{c^2} \left[\frac{\nu_i}{m_i(\nu_i^2 + \omega_i^2)} + \frac{\nu_e}{m_e(\nu_e^2 + \omega_e^2)} \right] \quad (3\text{-}119)$$

$$\sigma_2 \sim \frac{n_e e^2}{c^2} \left[\frac{\omega_i}{m_i(\nu_i^2 + \omega_i^2)} + \frac{\omega_e}{m_e(\nu_e^2 + \omega_e^2)} \right] \quad (3\text{-}120)$$

As the collision frequency become negligible, σ_o becomes very large whereas σ_1 and σ_2 approach zero. The contribution of each component,

$$\left(\frac{\pm n_e e^2}{m_e c^2 \omega_c}\right),$$

to the Hall conductivity is exactly the same as would be given by the $\bar{E} \times \bar{B}$ drift. The total Hall current is zero. The current transverse to the magnetic field must be equivalent to the $\bar{E} \times \bar{B}$ drift current. However, in a steady state ($\omega \sim 0$), electrons and ions drift together so that no transverse current is expected.

The actual direction of Hall current flow depends on the relative importance of two terms. With the sign selected here, σ_2 is generally positive in the ionosphere between 70 and several hundred kilometers altitude (References 27, 73, and 74). The Hall conductivity in the ionosphere is quite large; it is responsible for the polar electrojets—strong currents which flow across the geomagnetic field lines (Reference 73).

APPENDIX 3A

ELECTRIC AND MAGNETIC UNITS

Since the confusion among about six basic electric and magnetic unit systems extends to the literature of plasma and space physics, a dictionary for translating from one system to another has been included.

Rationalized meter-kilogram-second (mks) units are very practical for engineering problems and textbook expositions. Much of that practicality is lost in plasma physics because the relations between $\overline{E}$, $\overline{D}$, $\overline{H}$, and $\overline{B}$ employ the free-space values of permeability and permittivity. In that case, retaining $\overline{D}$ and $\overline{H}$ as quantities distinct from $\overline{E}$ and $\overline{B}$ is no longer necessary. The advantages of a rationalized unit system vanish when Maxwell's equations are written in terms of $\overline{E}$ and $\overline{B}$ exclusively. Maxwell's equations, together with the Lorentz force equation, the continuity equation, and the hydromagnetic equations, are presented in Table 3A-1 for comparison among the more important unit systems. Electric and magnetic unit conversion factors of major parameters found in Table 3A-1 can be found in Table 3A-2.

A rationalized system of centimeter-gram-second (cgs) units exists—the Heaviside-Lorentz units. This system is seldom used. The purely electrostatic (esu) unit system appears frequently in textbooks but it leaves much to be desired as a practical unit system because the permeability of free space is $\mu_o = 1/c^2$. The electromagnetic unit (emu) system is more practical because B and H have the same dimensions. However, the permittivity of free space ϵ_o must be $1/c^2$. The equations of the field and the equations of motion are identical in esu and in emu units.

Maxwell's equations have a particularly satisfying symmetry in a mixed unit system in which electrical quantities are in emu. This system, customarily called the gaussian unit system, has the same dimensions for $\overline{E}$, $\overline{D}$, $\overline{H}$, and $\overline{B}$; ϵ_o and μ_o are both equal to 1.

Table 3A-1. Fundamental electrical and magnetic equations.

Equation	mks	emu	esu	gaussian
	Maxwell's Equations			
3A-1	$\bar{D} = \epsilon \bar{E}$ $\epsilon_o = 10^7/4\pi c^2$	$\epsilon_o = 1/c^2$	$\epsilon_o = 1$	$\epsilon_o = 1$
3A-2	$\bar{B} = \mu \bar{H}$ $\mu_o = 4\pi \times 10^{-7}$	$\mu_o = 1$	$\mu_o = 1/c^2$	$\mu_o = 1$
3A-3	$\nabla \cdot \bar{D} = Q$	$\nabla \cdot \bar{D} = 4\pi Q$	...	...
3A-4	$\nabla \cdot \bar{B} = 0$	...	...	...
3A-5	$\nabla \times \bar{E} = -\frac{\partial \bar{B}}{\partial t}$	$\nabla \times \bar{E} = -\frac{\partial \bar{B}}{\partial t}$	...	$\nabla \times \bar{E} = -\frac{1}{c}\frac{\partial \bar{B}}{\partial t}$
3A-6	$\nabla \times \bar{H} = \frac{\partial \bar{D}}{\partial t} + \bar{J}$	$\nabla \times \bar{H} = \frac{\partial D}{\partial t} + \bar{J}$	...	$\nabla \times \bar{H} = \frac{1}{c}\frac{\partial \bar{D}}{\partial t} + \frac{4\pi}{c}\bar{J}$ (modified: $\nabla \times \bar{H} = \frac{1}{c}\frac{\partial \bar{D}}{\partial t} + 4\pi\bar{J}$)
3A-7	$\bar{F} = Ze(\bar{E} + \bar{v} \times \bar{B})$ $e = 1.6021 \times 10^{-19}$	$\bar{F} = Ze(\bar{E} + \bar{v} \times \bar{B})$ $e = 1.6021 \times 10^{-20}$	... $e = 4.8029 \times 10^{-10}$	$\bar{F} = Ze(\bar{E} + \frac{1}{c}\bar{v} \times \bar{B})$ $e = 4.8029 \times 10^{-10}$
3A-8	$\frac{\partial Q}{\partial t} + \nabla \cdot \bar{J} = 0$	$\frac{\partial Q}{\partial t} + \nabla \cdot \bar{J} = 0$	...	$\frac{\partial Q}{\partial t} + \nabla \cdot \bar{J} = 0$ (modified: $\frac{\partial Q}{\partial t} + c\nabla \cdot \bar{J} = 0$)
	Hydromagnetic Equations			
3A-9	$\nabla \cdot \bar{E} = 4\pi c^2 \times 10^{-7} Q$	$\nabla \cdot \bar{E} = 4\pi c^2 Q$		$\nabla \cdot \bar{E} = 4\pi Q$
3A-10	$\nabla \times \bar{B} = \frac{1}{c^2}\frac{\partial E}{\partial t} + 4\pi \times 10^{-7}\bar{J}$	$\nabla \times \bar{B} = \frac{1}{c^2}\frac{\partial \bar{E}}{\partial t}$		$\nabla \times \bar{B} = \frac{1}{c}\frac{\partial \bar{E}}{\partial t} + \frac{4\pi}{c}\bar{J}$ (modified: $\nabla \times \bar{B} = \frac{1}{c}\frac{\partial \bar{E}}{\partial t} + 4\pi\bar{J}$)
3A-11	$\rho\frac{\partial \bar{V}}{\partial t} = \bar{J} \times \bar{B} - \nabla \cdot \bar{\bar{P}}$	...		$\rho\frac{\partial \bar{V}}{\partial t} = \frac{1}{c}\bar{J} \times \bar{B} - \nabla \cdot \bar{\bar{P}}$ (modified: $\rho\frac{\partial \bar{V}}{\partial t} = \bar{J} \times \bar{B} - \nabla \cdot \bar{\bar{P}}$)
3A-12	$\frac{m}{ne^2}\frac{\partial \bar{J}}{\partial t} = \bar{E} + \bar{V} \times \bar{B} - \frac{1}{ne}\bar{J} \times \bar{B} + \frac{1}{ne}\nabla \cdot \bar{\bar{P}}_e - \bar{J}/\sigma$			$\frac{m}{ne^2}\frac{\partial \bar{J}}{\partial t} = \bar{E} + \frac{1}{c}\bar{V} \times \bar{B} + \frac{1}{nec}\bar{J} \times \bar{B} - \frac{\bar{J}}{\sigma}$ (modified: $\frac{mc}{ne^2}\frac{\partial \bar{J}}{\partial t} = \bar{E} + \frac{1}{c}\bar{V} \times \bar{B} + \frac{1}{ne}\bar{J} \times \bar{B} - \frac{\bar{J}}{c\sigma}$)

Note:
[a]Same as preceding column

Table 3A-2. Electric and magnetic unit conversion factors.

Symbol	mks → emu	mks → esu	mks → gauss	emu → gauss	esu → gauss	esu → emu
E electric field	1×10^{6}	$1 \times 10^{-4}/3$	$1 \times 10^{-4}/3$	$1 \times 1/c$	1×1	$1 \times c$
D electric displacement	$1 \times 4\pi \times 10^{-5}$	$1 \times 12\pi \times 10^{5}$	$1 \times 12\pi \times 10^{5}$	$1 \times c$	1×1	$1 \times 1/c$
H magnetic field	$1 \times 4\pi \times 10^{-3}$	$1 \times 12\pi \times 10^{-7}$	$1 \times 4\pi \times 10^{-3}$	1×1	$1 \times 1/c$	$1 \times 1/c$
B flux density	1×10^{4}	$1 \times 10^{-6}/3$	1×10^{4}	1×1	$1 \times c$	$1 \times c$
Q charge density	1×10^{-7}	$1 \times 3 \times 10^{3}$	$1 \times 3 \times 10^{3}$	$1 \times c$	1×1	$1 \times 1/c$
J current density (modified)	1×10^{-5}	$1 \times 3 \times 10^{5}$	$1 \times 3 \times 10^{5}$ (1×10^{-5})	$1 \times c$ (1×1)	1×1 ($1 \times 1/c$)	$1 \times 1/c$
σ conductivity (modified)	1×10^{-11}	$1 \times 9 \times 10^{9}$	$1 \times 9 \times 10^{9}$ (1×10^{-11})	$1 \times c^{2}$ (1×1)	1×1 ($1 \times 1/c^{2}$)	$1 \times 1/c^{2}$

It is a matter of choice whether $\overline{J}$ should be regarded as a magnetic quantity or as an electrical quantity. Usually $\overline{J}$ is an electrical quantity, hence the factor of $1/c$ multiplying $\overline{J}$ in Equation 3A-6. It may be easier to relate J to the practical units (amp/m^2 or even amp/cm^2), when only $\overline{E}$ and $\overline{D}$ are regarded as electrical quantities. The resulting unit system is more akin to the emu system than to the esu system. These "modified" gaussian units have been used in the preceding section with the emu conductivity. Ohm's law then has an unexpected factor of c.

APPENDIX 3B

SUPPLEMENTARY TABLES AND GRAPHS

Many of the more useful equations of Section 3 have been converted to numerical relations that are presented here as an aid in rapid calculations. Some figures, especially Figures 3B-15 through 3B-19, are relevant to cross L-shell diffusion as discussed in Section 5.

Table 3B-1 contains important charged particle parameters in a dipole field. Pitch angles, bounce period integrals, second adiabatic invariant integrals, and other related parameters are given in the table. Column 6 is the distance along the field line, S/R_o. The bounce period integral (column 7),

$$\frac{1}{R_o} \int_0^{S_m} dS/\mu \quad ,$$

and the adiabatic invariant integral (column 8),

$$\frac{1}{R_o} \int_0^{S_m} \mu dS \quad ,$$

are just one fourth of the integrals $\mathcal{J}$ and $\mathcal{J}$ plotted in Figure 3B-11. For any specified set of adiabatic invariants, $L = R_o/R_E$ is a function only of $\mathcal{J}/\sin \alpha_o$, which is tabulated in column 9 (except for a missing factor of 16). Column 10 gives $L/A \equiv L\ (Mm/J^2)$. The last column is the mirror point field B_m divided by A^3; A is in cgs units (a factor 10^{50} has been extracted). The information in this table is also presented in the figures that follow. Powers of 10 are listed after each entry, thus "1.000 + 2" is $1 \times 10^2 = 100$.

Table 3B-1. Important charged particle parameters in a dipole field.

MIRROR LATITUDE (DEG)	SINE LATITUDE	B(MIRROR)/B(EQ.)	PITCH ANGLE (DEG)	COSINE (P,A)	DISTANCE TO EQ. /(L-ONE)	MIRROR INTEGRAL	AD, INV. INTEGRAL	AD, INV. INTEGRAL /B(ME(P,A))	LOG 10CONST.	B(MIRROR) / A CUBED * 1.0E+50
.0	.000000	1.0000	90.0000	.000000	.00000	.74048	.00000	0.000	0.000	UNDEFINED
.2	.003491	1.0001	89.9797	.007405	.00349	.74054	.00002	2.338- 9	1.671+09	4.492+21
.4	.006981	1.0002	89.9593	.014809	.00698	.74059	.00009	9.121- 9	2.673+10	1.634+18
.6	.010472	1.0005	89.9390	.022211	.01047	.74069	.00016	1.827- 8	1.354+11	1.259+16
.8	.013962	1.0009	89.9187	.029611	.01396	.74074	.00032	3.269- 8	4.279+11	3.988+14
1.0	.017452	1.0014	89.8984	.037009	.01745	.74088	.00051	5.077- 8	1.049+12	2.738+13
1.2	.020942	1.0020	89.8781	.044402	.02093	.74102	.00073	7.313- 8	2.169+12	3.069+12
1.4	.024432	1.0027	89.8578	.051791	.02442	.74117	.00099	9.936- 8	4.017+12	4.829+11
1.6	.027922	1.0035	89.8375	.059175	.02791	.74136	.00130	1.301- 7	6.857+12	9.711+10
1.8	.031411	1.0044	89.8172	.066553	.03140	.74160	.00164	1.647- 7	1.098+13	2.361+10
2.0	.034899	1.0055	89.7968	.073924	.03492	.74185	.00203	2.033- 7	1.676+13	6.865+ 9
2.2	.038388	1.0067	89.7765	.081288	.03842	.74211	.00249	2.481- 7	2.454+13	2.121+ 9
2.4	.041876	1.0079	89.7562	.088644	.04191	.74241	.00292	2.930- 7	3.480+13	7.439+ 8
2.6	.045363	1.0093	89.7359	.095991	.04541	.74277	.00342	3.440- 7	4.798+13	2.891+ 8
2.8	.048850	1.0106	89.7156	.103328	.04891	.74307	.00397	3.992- 7	6.459+13	1.179+ 8
3.0	.052336	1.0124	89.6953	.110654	.05241	.74349	.00456	4.589- 7	8.529+13	5.107+ 7
3.2	.055822	1.0141	89.6749	.117972	.05591	.74379	.00519	5.219- 7	1.104+14	2.351+ 7
3.4	.059306	1.0159	89.6546	.125278	.05941	.74428	.00585	5.886- 7	1.409+14	1.134+ 7
3.6	.062791	1.0179	89.6343	.132568	.06291	.74479	.00655	6.612- 7	1.779+14	5.704+ 6
3.8	.066274	1.0199	89.6140	.139847	.06642	.74534	.00730	7.372- 7	2.203+14	2.976+ 6
4.0	.069756	1.0221	89.5937	.147113	.06993	.74577	.00808	8.174- 7	2.704+14	1.606+ 6
4.2	.073238	1.0244	89.5734	.154363	.07343	.74633	.00891	9.018- 7	3.294+14	8.924+ 5
4.4	.076719	1.0268	89.5531	.161599	.07696	.74677	.00977	9.904- 7	3.976+14	5.097+ 5
4.6	.080199	1.0293	89.5328	.168819	.08048	.74737	.01068	1.083- 6	4.757+14	2.981+ 5
4.8	.083678	1.0320	89.5125	.176023	.08397	.74802	.01162	1.180- 6	5.644+14	1.787+ 5
5.0	.087156	1.0347	89.4923	.183209	.08749	.74854	.01260	1.282- 6	6.661+14	1.092+ 5
6.0	.104528	1.0514	89.3579	.218861	.10510	.75179	.01839	1.854- 6	1.394+15	1.210+ 4
7.0	.121869	1.0690	89.2267	.253997	.12277	.75599	.02494	2.537- 6	2.610+15	1.876+ 3
8.0	.139173	1.0904	89.0952	.288526	.14051	.76094	.03193	3.338- 6	4.308+15	3.716+ 2
9.0	.156434	1.1147	88.9638	.322420	.15833	.76610	.03923	4.250- 6	7.327+15	8.869+ 1
10.0	.173648	1.1447	88.8323	.355593	.17622	.77187	.04693	5.288- 6	1.134+16	2.491+ 1
11.0	.190809	1.1771	88.7006	.388027	.19422	.77843	.05498	6.455- 6	1.689+16	7.823
12.0	.207912	1.2135	88.5688	.419674	.21234	.78598	.06340	7.755- 6	2.438+16	2.612
13.0	.224951	1.2561	88.4369	.450454	.23058	.79434	.07218	9.197- 6	3.429+16	9.788- 1
14.0	.241922	1.2993	88.3047	.480238	.24893	.80307	.08133	1.078- 5	4.717+16	3.865- 1
15.0	.258819	1.3483	88.1719	.508787	.26738	.81224	.09079	1.253- 5	6.368+16	1.630- 1
16.0	.275637	1.4045	87.9440	.536867	.28576	.82186	.10070	1.449- 5	8.461+16	7.239- 2
17.0	.292372	1.4695	87.8065	.564264	.30443	.83197	.11101	1.664- 5	1.109+17	3.296- 2
18.0	.309017	1.5327	87.6732	.589548	.32317	.84262	.12178	1.902- 5	1.439+17	1.618- 2
19.0	.325568	1.6047	87.5396	.614497	.34208	.85384	.13300	2.162- 5	1.858+17	8.079- 3
20.0	.342020	1.6891	87.4054	.638454	.36108	.86568	.14484	2.399- 5	2.333+17	4.169- 3

Table 3B-1—continued.

21.0	.388366	1.7777	48.3918	.661420	.38020	.86461	.20146	2.691- 1	2.936+17	2.191- 3
22.0	.374607	1.8763	46.4902	.643399	.36944	.87498	.21964	3.009- 1	3.669+17	1.185- 3
23.0	.360731	1.9848	49.2169	.734490	.41678	.88561	.23796	3.352- 1	4.554+17	6.549- 4
24.0	.346737	2.1044	43.5791	.724435	.43624	.89639	.25678	3.725- 1	5.625+17	3.690- 4
25.0	.332618	2.2362	41.9691	.743517	.45779	.90732	.27608	4.128- 1	6.909+17	2.119- 4
26.0	.438371	2.3817	40.3489	.761664	.47744	.91837	.29583	4.565- 1	8.449+17	1.232- 4
27.0	.453995	2.5424	38.6407	.778893	.49718	.92957	.31601	5.039- 1	1.029+18	7.277- 5
28.0	.469472	2.7202	37.3238	.795224	.51700	.94089	.33636	5.551- 1	1.249+18	4.394- 5
29.0	.484610	2.9172	35.8178	.810688	.53690	.95226	.35703	6.107- 1	1.517+18	2.634- 5
30.0	.500000	3.1357	34.3428	.825283	.55687	.96366	.37883	6.708- 1	1.824+18	1.612- 5
31.0	.515038	3.3784	32.9572	.839094	.57694	.97521	.40045	7.361- 1	2.196+18	9.991- 6
32.0	.529919	3.6490	31.5670	.852029	.59698	.98670	.42237	8.068- 1	2.639+18	6.198- 6
33.0	.544639	3.9507	30.2981	.864221	.61707	.99817	.44457	8.834- 1	3.165+18	3.888- 6
34.0	.559193	4.2879	28.8788	.875662	.63720	1.00964	.46701	9.670- 1	3.791+18	2.434- 6
35.0	.573576	4.6656	27.5704	.886378	.65735	1.02108	.48967	1.058	4.535+18	1.561- 6
36.0	.587785	5.0897	26.3117	.896394	.67750	1.03245	.51253	1.156	5.420+18	9.976- 7
37.0	.601815	5.5673	25.0705	.905743	.69763	1.04374	.53556	1.264	6.472+18	6.406- 7
38.0	.615661	6.1059	23.8727	.914447	.71771	1.05498	.55874	1.381	7.726+18	4.130- 7
39.0	.629320	6.7146	22.7004	.922535	.73769	1.06614	.58204	1.508	9.221+18	2.672- 7
40.0	.642788	7.4059	21.5957	.930035	.75756	1.07721	.60543	1.648	1.100+19	1.734- 7
41.0	.656059	8.1914	20.4506	.936974	.77727	1.08813	.62890	1.800	1.313+19	1.128- 7
42.0	.669131	9.0879	19.3730	.943379	.79776	1.09885	.65241	1.967	1.568+19	7.355- 8
43.0	.681998	1.0114+ 1	18.3271	.949277	.81797	1.10947	.67594	2.150	1.873+19	4.801- 8
44.0	.694658	1.1292+ 1	17.3128	.954684	.83727	1.12023	.69947	2.350	2.239+19	3.137- 8
45.0	.707107	1.2649+ 1	16.3341	.959605	.85685	1.13063	.72297	2.571	2.680+19	2.050- 8
46.0	.719340	1.4218+ 1	15.3870	.964193	.87629	1.14090	.74641	2.814	3.211+19	1.340- 8
47.0	.731354	1.6039+ 1	14.4576	.968324	.89558	1.15103	.76977	3.083	3.852+19	8.793- 9
48.0	.743145	1.8160+ 1	13.5717	.972077	.91471	1.16094	.79302	3.379	4.629+19	5.711- 9
49.0	.754710	2.0641+ 1	12.7134	.975479	.93363	1.17069	.81614	3.708	5.575+19	3.721- 9
50.0	.766044	2.3559+ 1	11.8905	.978543	.95239	1.18029	.83910	4.072	6.723+19	2.419- 9
51.0	.777145	2.6994+ 1	11.0971	.981303	.97092	1.18968	.86189	4.478	8.128+19	1.568- 9
52.0	.788011	3.1071+ 1	10.3359	.983776	.98924	1.19890	.88446	4.930	9.852+19	1.014- 9
53.0	.798635	3.5927+ 1	9.6038	.985985	1.00728	1.20792	.90680	5.435	1.194+20	6.527-10
54.0	.809017	4.1744+ 1	8.9028	.987950	1.02500	1.21674	.92889	6.001	1.448+20	4.185-10
55.0	.819152	4.8746+ 1	8.2346	.989699	1.04240	1.22534	.95068	6.636	1.764+20	2.678-10
56.0	.829038	5.7230+ 1	7.5990	.991225	1.05946	1.23378	.97219	7.355	2.193+20	1.694-10
57.0	.838671	6.7547+ 1	6.9877	.992572	1.07619	1.24199	.99336	8.165	2.703+20	1.068-10
58.0	.848048	8.0245+ 1	6.4074	.993734	1.09259	1.24998	1.01417	9.085	3.346+20	6.686-11
59.0	.857167	9.5901+ 1	5.8610	.994773	1.10861	1.25775	1.03461	1.0136 1	4.141+20	4.133-11
60.0	.866025	1.1534+ 2	5.3418	.995657	1.12395	1.26532	1.05469	1.133+ 1	5.202+20	2.557-11
61.0	.874620	1.3948+ 2	4.8517	.996417	1.14107	1.27264	1.07427	1.270+ 1	6.540+20	1.599-11
62.0	.882948	1.7044+ 2	4.3901	.997066	1.15629	1.27978	1.09345	1.428+ 1	8.271+20	9.918-12
63.0	.891007	2.1003+ 2	3.9596	.997617	1.17101	1.28666	1.11217	1.612+ 1	1.053+21	6.611-12
64.0	.898794	2.6273+ 2	3.5617	.998080	1.18531	1.29333	1.13039	1.825+ 1	1.356+21	4.303-12
65.0	.906308	3.2847+ 2	3.1717	.998464	1.19932	1.29976	1.14811	2.075+ 1	1.745+21	2.917-12
66.0	.913545	4.1341+ 2	2.8191	.998790	1.21283	1.30595	1.16531	2.364+ 1	2.276+21	1.895-12
67.0	.920505	5.2848+ 2	2.4942	.999054	1.22584	1.31191	1.18196	2.718+ 1	2.959+21	1.142-13
68.0	.927184	6.8459+ 2	2.1904	.999269	1.23844	1.31765	1.19809	3.139+ 1	3.903+21	3.380-13
69.0	.933580	8.9756+ 2	1.9148	.999443	1.25046	1.32312	1.21358	3.634+ 1	5.368+21	1.888-13
70.0	.939693	1.1934+ 3	1.6648	.999581	1.26227	1.32836	1.22846	4.244+ 1	7.388+21	9.578-14
71.0	.945519	1.6114+ 3	1.4275	.999690	1.27343	1.33337	1.24275	4.980+ 1	1.009+22	4.897-14
72.0	.951057	2.2131+ 3	1.2150	.999774	1.28408	1.33812	1.25640	5.914+ 1	1.418+22	2.432-14
73.0	.956305	3.0976+ 3	1.0295	.999839	1.29421	1.34262	1.26941	7.065+ 1	2.023+22	1.167-14
74.0	.961262	4.4269+ 3	.8610	.999887	1.30382	1.34688	1.28179	8.530+ 1	2.849+22	5.384-15
75.0	.965926	6.4442+ 3	.7115	.999923	1.31289	1.35089	1.29342	1.042+ 2	4.007+22	2.388-15
76.0	.970296	9.7551+ 3	.5801	.999949	1.32144	1.35466	1.30440	1.286+ 2	5.720+22	9.993-16
77.0	.974370	1.5139+ 4	.4657	.999967	1.32946	1.35819	1.31468	1.618+ 2	8.061+23	3.999-16
78.0	.978148	2.4356+ 4	.3671	.999979	1.33693	1.36148	1.32424	2.047+ 2	1.731+23	1.484-16
79.0	.981627	4.0872+ 4	.2834	.999987	1.34386	1.36453	1.33308	2.595+ 2	2.944+23	4.996-17
80.0	.984808	7.2117+ 4	.2134	.999993	1.34998	1.36713	1.34118	3.302+ 2	5.258+23	1.548-17
81.0	.987688	1.3521+ 5	.1578	.999996	1.35566	1.36961	1.34854	4.196+ 2	9.967+23	4.260-18
82.0	.990268	2.7322+ 5	.1076	.999998	1.36078	1.37183	1.35515	7.083+ 2	2.034+24	1.813-18
83.0	.992546	4.0776+ 5	.0735	.999999	1.36531	1.37379	1.36100	1.080+ 3	4.588+24	2.880-19
84.0	.994522	1.5270+ 6	.0484	1.000000	1.36924	1.37549	1.36608	1.688+ 3	1.155+25	3.091-20
85.0	.996195	4.5580+ 6	.0269	1.000000	1.37257	1.37694	1.37039	2.923+ 3	3.464+25	3.410-21
86.0	.997564	1.7327+ 7	.0136	1.000000	1.37531	1.37812	1.37392	9.710+ 3	1.326+26	2.320-22
87.0	.998630	9.7270+ 7	.0038	1.000000	1.37743	1.37903	1.37667	1.357+ 4	7.469+26	7.280-24
88.0	.999391	1.1864+ 9	.0017	1.000000	1.37889	1.37984	1.37862	4.584+ 4	8.524+27	9.574-26
89.0	.999848	7.0754+10	.0002	1.000000	1.37987	1.38005	1.37963	3.670+ 5	5.458+28	1.387-27
90.0	1.000000	UNDEFINED	.0000	1.000000	1.38017	1.38017	1.38017	UNDEFINED	UNDEFINED	0.000

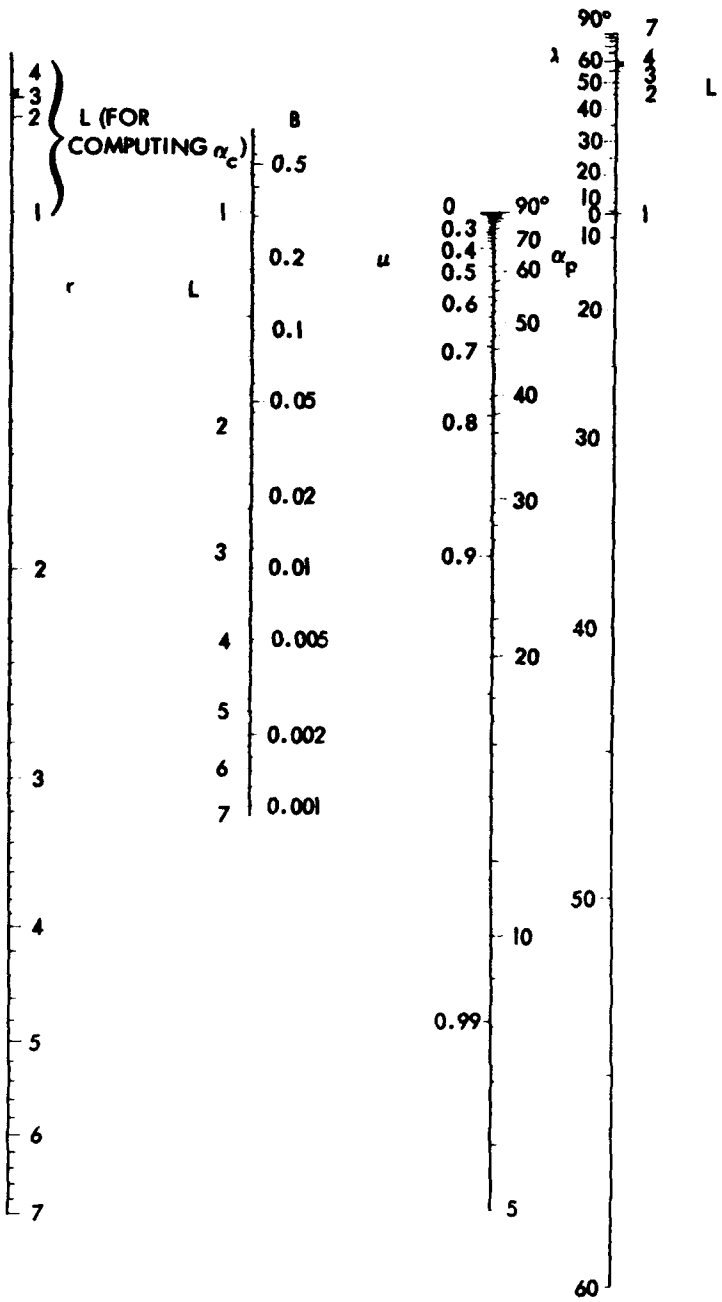

Figure 3B-1a. Nomograph for computing magnetic fields and pitch angles.

Figure 3B-1b illustrates, step by step, how to use the nomograph. To find magnetic field intensity from L and latitude λ, locate L (1) in the second strip, locate λ in the fourth strip (2), r/R_E (3) is given by the intersection with the first strip, locate λ (4) in the upper part of the fourth strip; the intersection with the second strip gives B (5).

To find pitch angle at any magnetic intensity B, locate L (1) in second strip and α_o (2) in third strip. A straightedge through these points determines a point on the first strip (3). Rotating the straightedge about the point on the first strip gives B (4) and α_p (5) everywhere in second and third strips. A simplified method of finding cutoff pitch angles is to connect a straightedge through L in the upper part of the first strip and the same L in the second strip. The intersection with the third strip gives α_c.

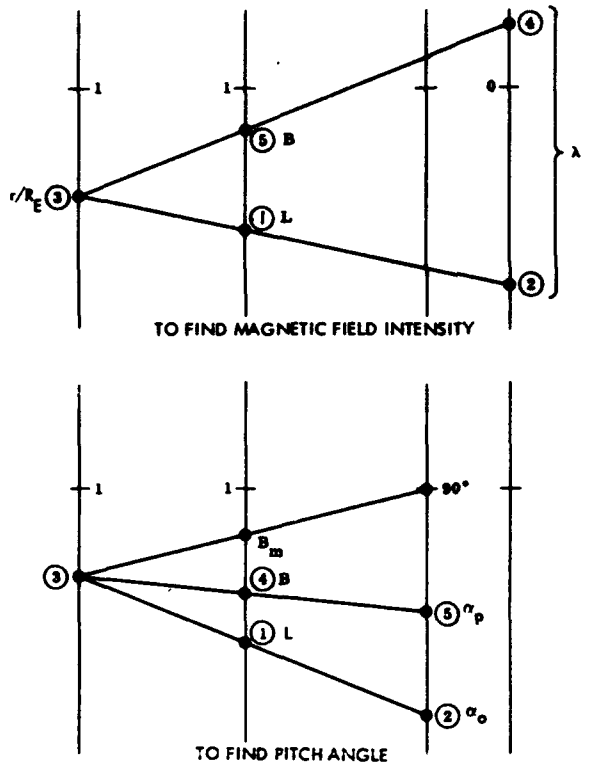

Figure 3B-1b. Step-by-step use of the nomograph.

Figure 3B-2 gives a pitch angle as a function of field intensity. The pitch angle at any point in a mirror field is a function only of the field intensity B at that point and the mirror point field B_m. Numerical values are plotted here according to Equation 3-44. These results should be independent of the configuration of the field. The intersection with the ordinate at the left gives the ratio of mirror field to equatorial field, B_o. The intersection with the abscissa at the bottom is the equatorial pitch angle, α_o.

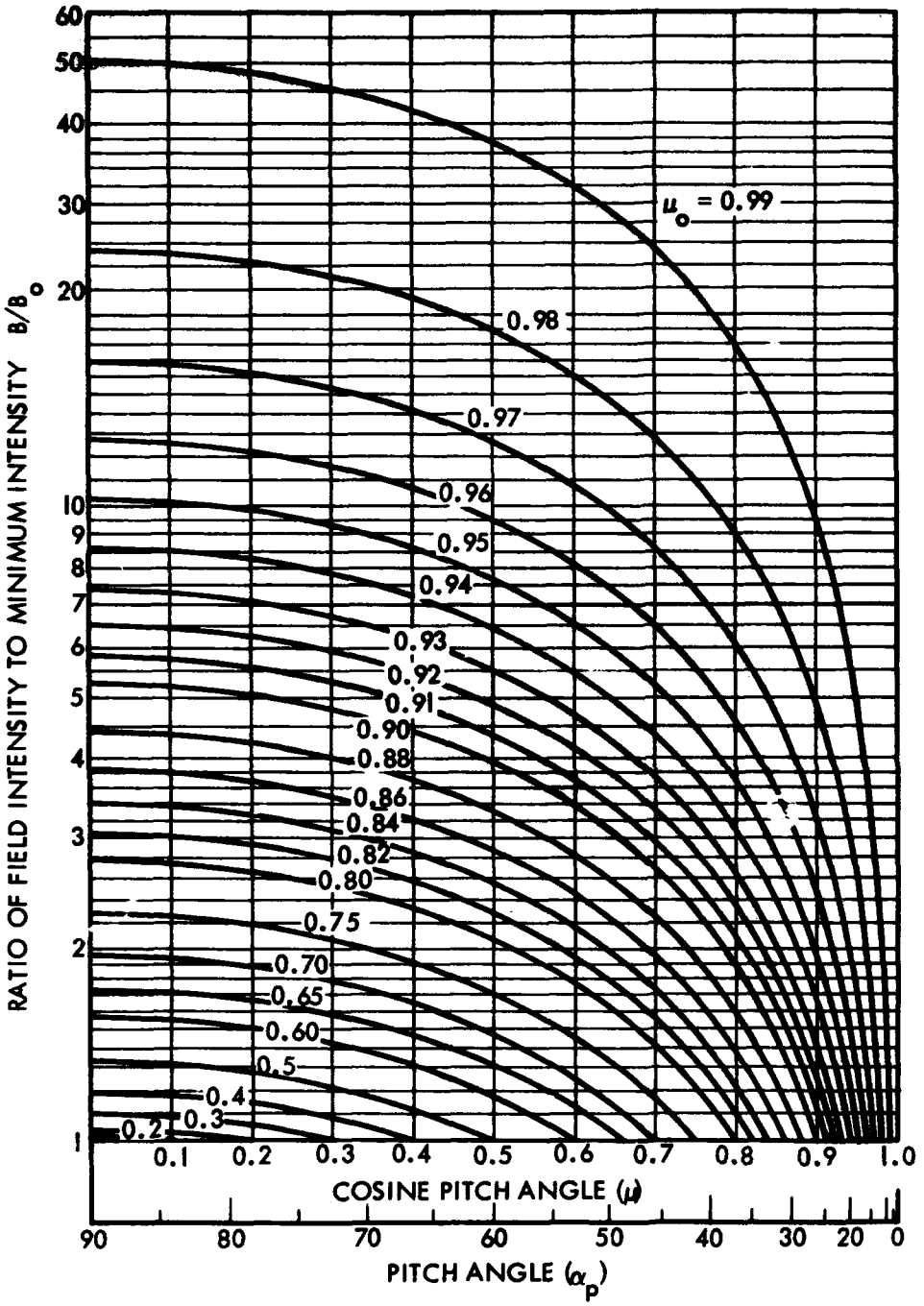

Figure 3B-2. Pitch angle as a function of field intensity.

Figure 3B-3 contains the mirror latitudes in a dipole field. In a strictly dipolar magnetic field, the equatorial pitch angle, α_o, is related to the latitude of the mirror point, λ_m, through the formula:

$$\sin^2 \alpha_o = B_o/B_m = \frac{\cos^6 \lambda_m}{\sqrt{4 - 3\cos^2 \lambda_m}} .$$

This formula is plotted in Figure 3B-3 (also see Table 3B-1). For particles mirroring near the equator ($\alpha_o \sim 90$ degrees), a simplified approximation:

$$\lambda_m \sim \frac{\sqrt{2}}{3} (90° - \alpha_o) \approx 0.4714 (90° - \alpha_o)$$

can be used.

To find the pitch angle α'_p at any latitude λ' given α_o read α'_o from the graph corresponding to λ'. The sine of α'_p is

$$\sin \alpha'_p = \sin \alpha_o \left(\frac{B}{B_o} \frac{\sin \alpha_o}{\sin \alpha'_o} \right) .$$

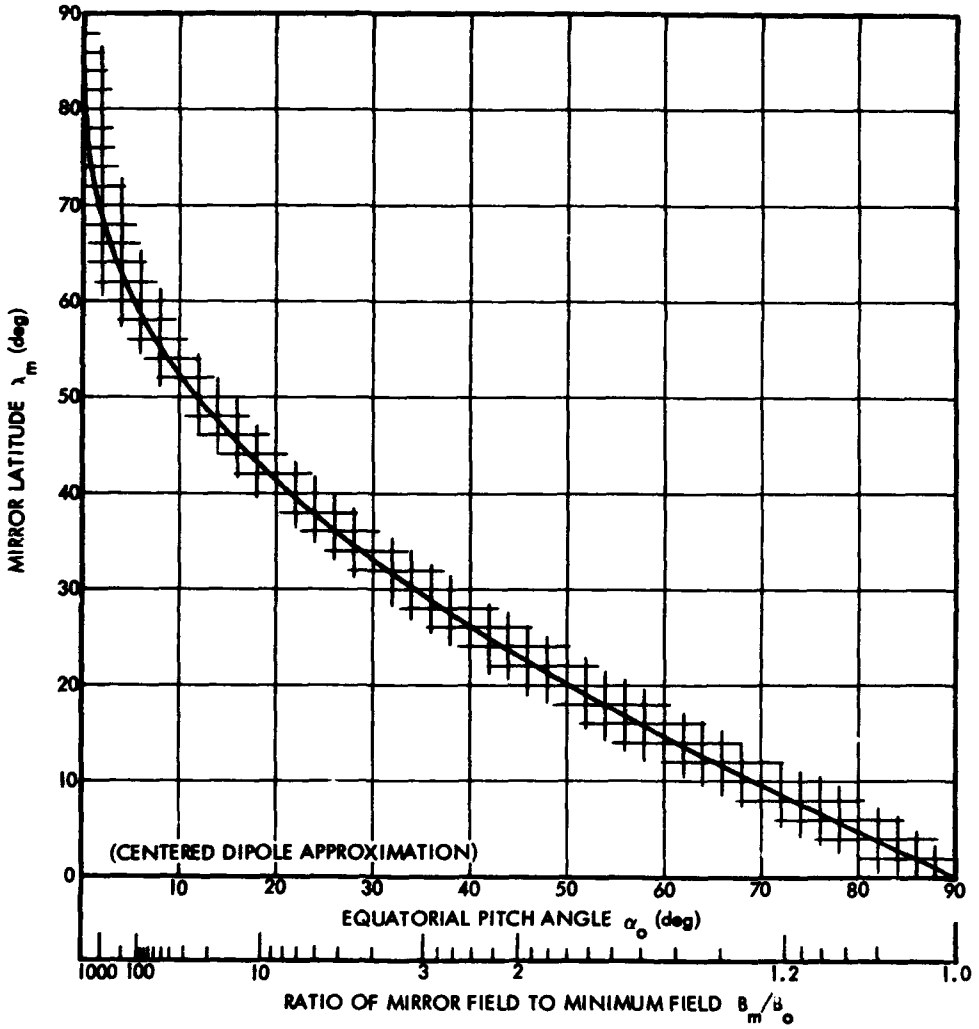

Figure 3B-3. Mirror latitudes in a dipole field.

Figure 3B-4 shows the atmospheric cutoff pitch angle. Particles with very small pitch angles cannot be trapped in the earth's field because they are rapidly lost in the atmosphere. The equatorial pitch angles of particles that mirror at an altitude of 100 kilometers are plotted in the figure as a function of $L = R_o/R_E$. Below $L = 1.5$, the distortion of the geomagnetic field is great enough to render inaccurate the results on this graph.

The variation of the cutoff pitch angle with altitude also is shown. The cutoff pitch angle corresponding to an arbitrary mirror altitude h is

$$\alpha_c \approx \alpha_c\,(100\text{ km}) + \frac{d\alpha_c}{dh}\left[\frac{h(\text{km}) - 100}{10^5}\right],$$

provided that h is not very much larger than 100 kilometers.

The latitude of the intersection of the field line with the earth's surface (the invariant latitude, see Section 2.2.2) is shown in the upper right of Figure 3B-4.

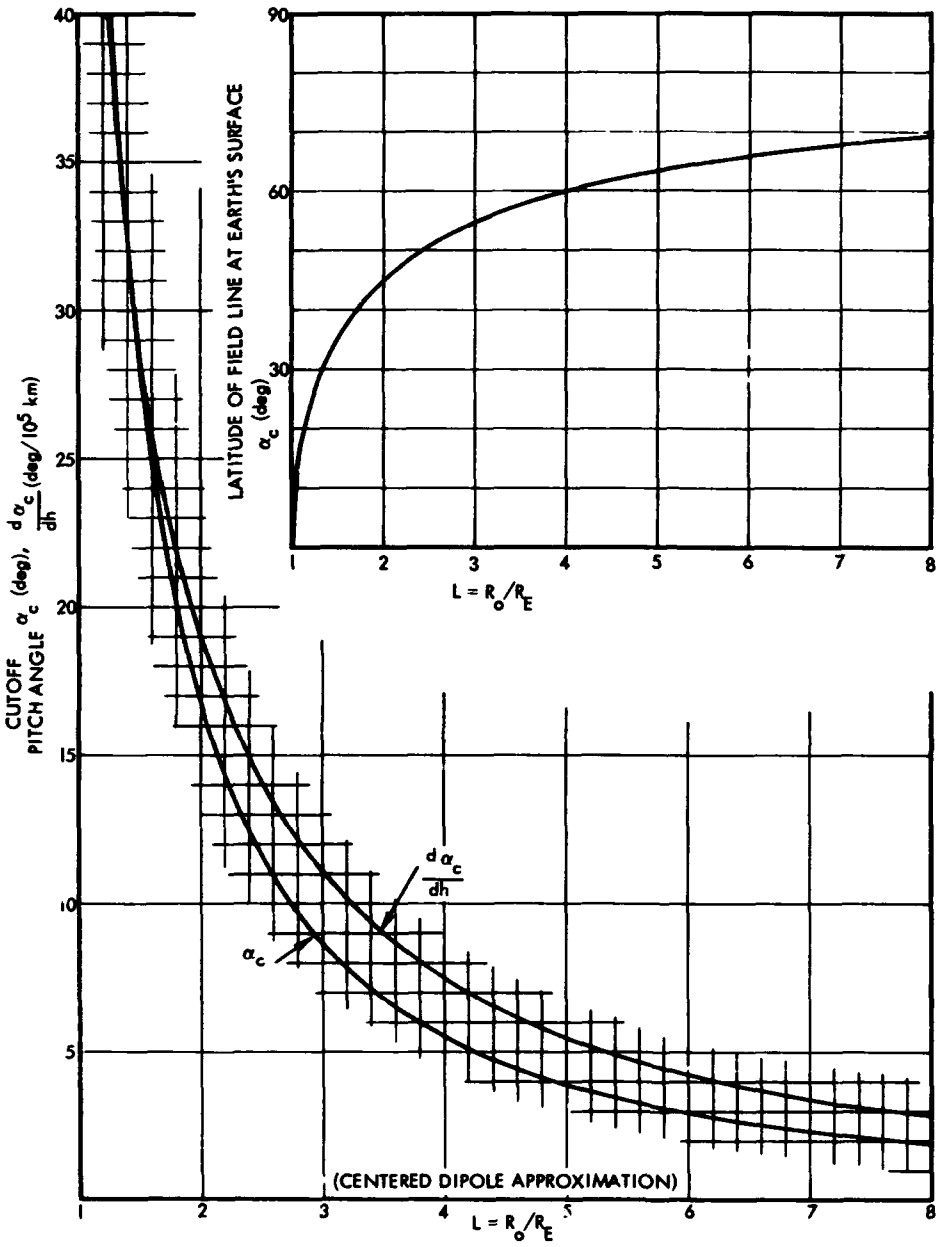

Figure 3B-4. The atmospheric cutoff pitch angle.

Figure 3B-5 shows mirror point altitude as a function of equatorial pitch angle. On low L-shells, the cutoff pitch angle varies considerably according to how deeply the trapped particles can penetrate the atmosphere. The variation of mirror point altitude with equatorial pitch angle is shown for a symmetric dipole field. In the actual distorted geomagnetic field, the curves in this figure would be shifted laterally by an amount that depends on longitude. When accuracy is essential, the data of Section 2 should be used.

Figures 3B-6 and 3B-7 give relativistic corrections to velocity and momentum. As the kinetic energy of a particle increases, the simple relations $T \sim 0.5\ mv^2$ and $p \sim mv$ become invalid. The exact relativistic formulas (Equations 3-10 and 3-11) are plotted here over limited ranges that should include most of the trapped radiation belt particles. Momentum p is given in the customary units MeV/c or GeV/c. At extremely high energies, the numerical magnitudes of momentum and kinetic energy are nearly identical.

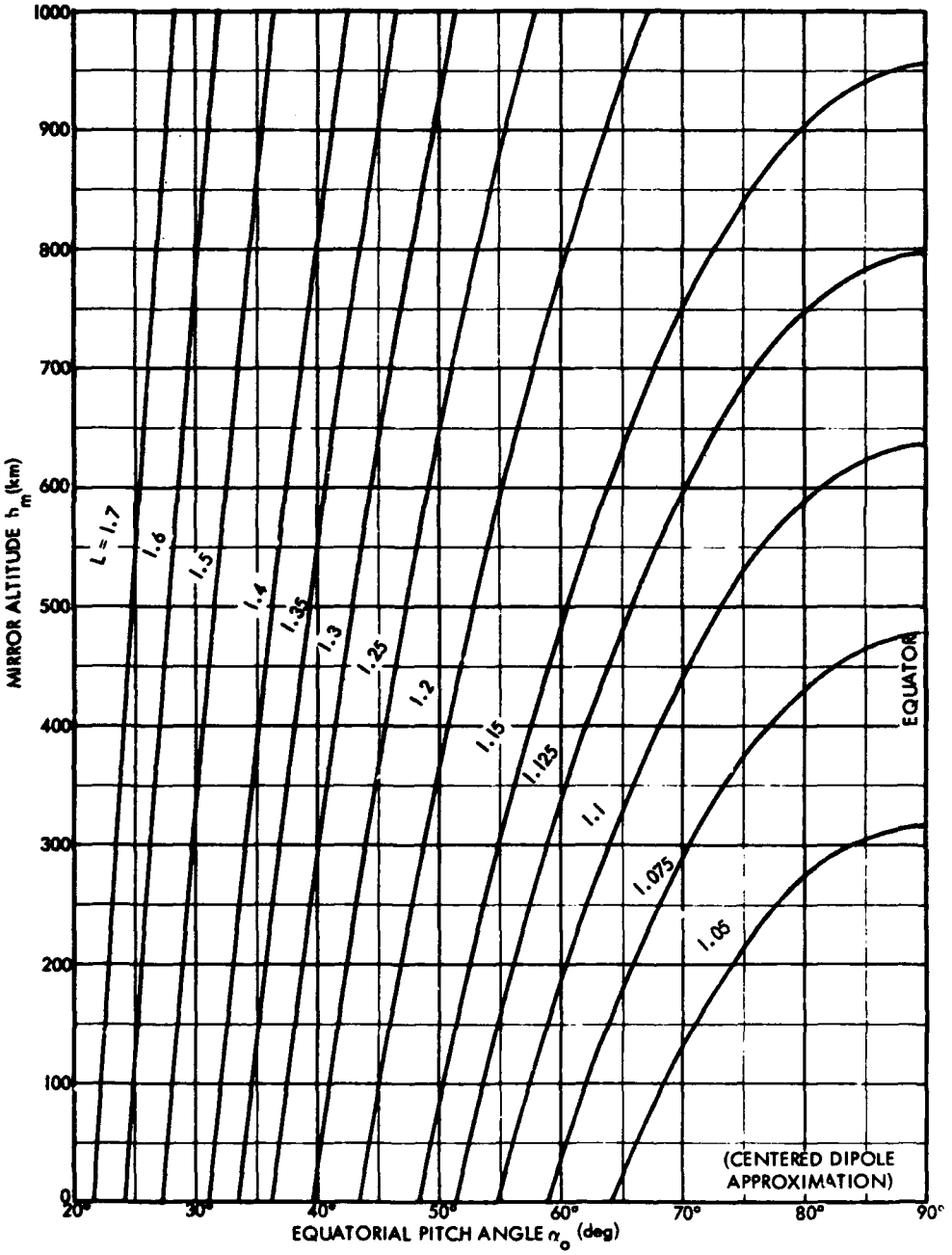

Figure 38-5. Mirror point altitude as a function of equatorial pitch angle.

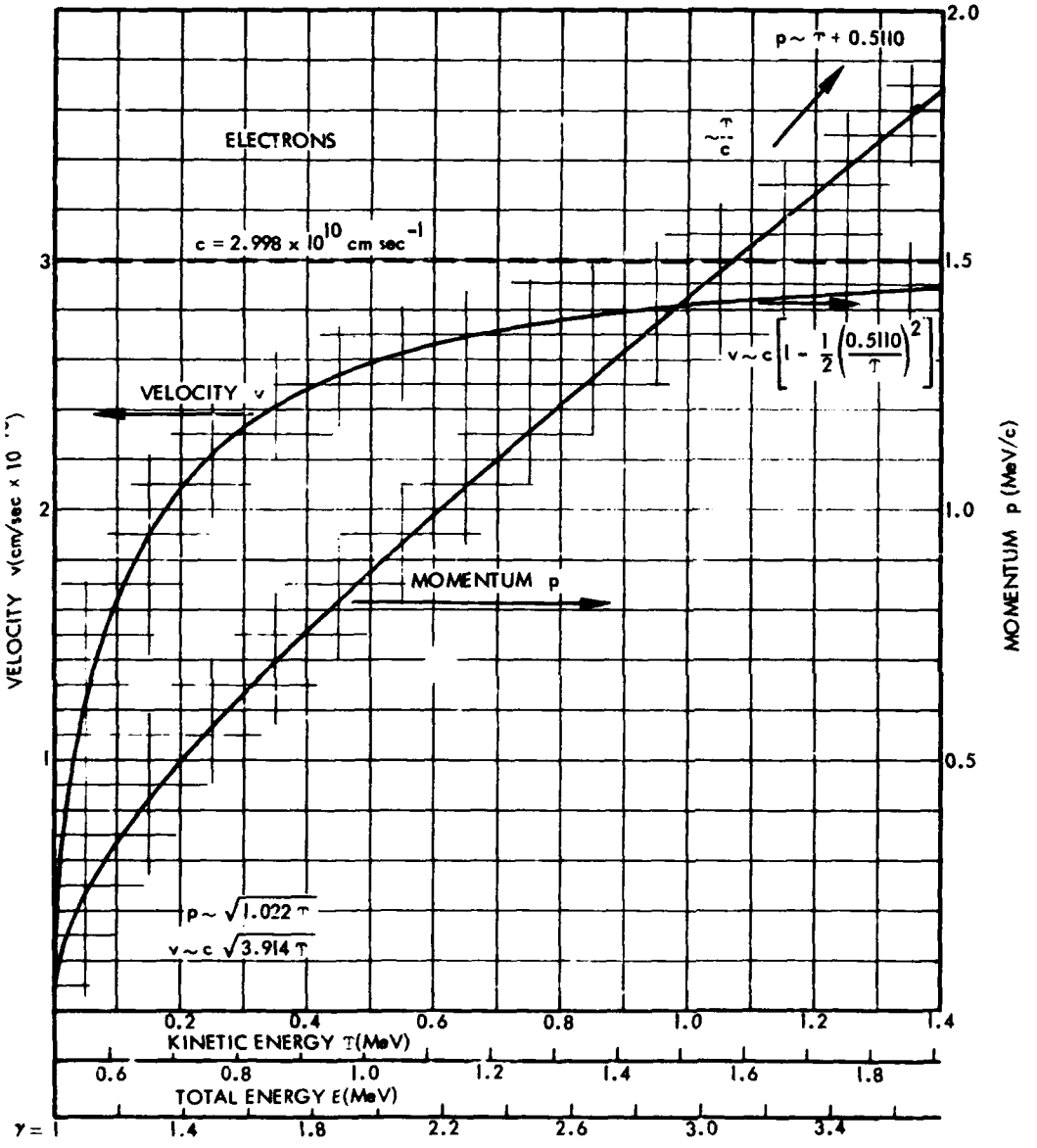

Figure 3B-6. Relativistic corrections to velocity and momentum.

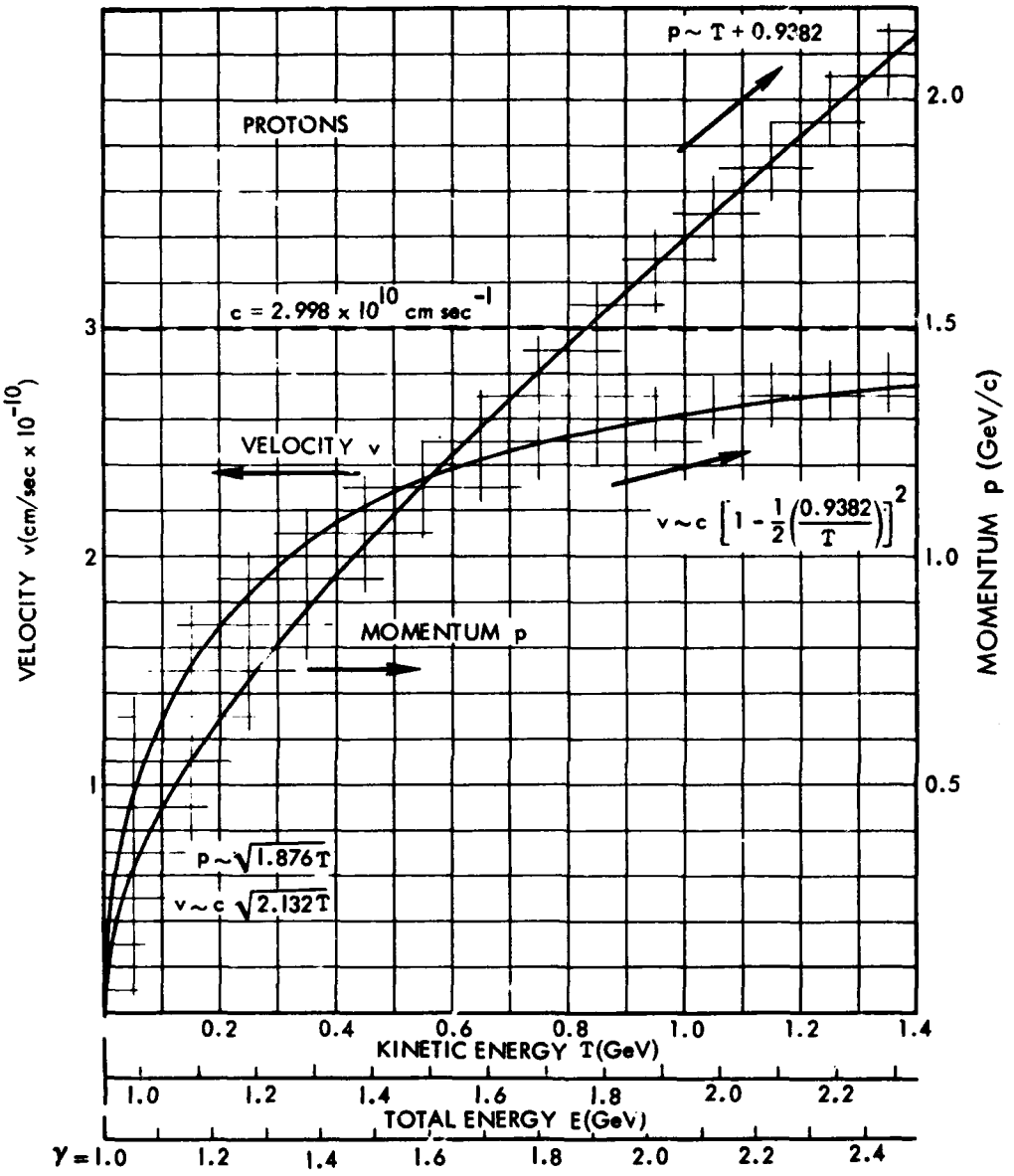

Figure 3B-7. Relativistic corrections to velocity and momentum.

Figure 3B-8 shows the magnetic moment of a charged particle as a function of kinetic energy. At low energies, the magnetic moment (first adiabatic invariant) of a charged particle is nearly equal to the kinetic energy divided by the mirror point field B_m. The correct energy dependent factor is plotted for particles with relativistic velocities (Equation 3-46). Division of the ordinate by the mirror field intensity yields the magnetic moment in MeV per gauss or GeV per gauss. The ordinate and abscissa have the same units. The lower dashed curve is just the kinetic energy—for comparison with the proper factor, $p^2/2m$.

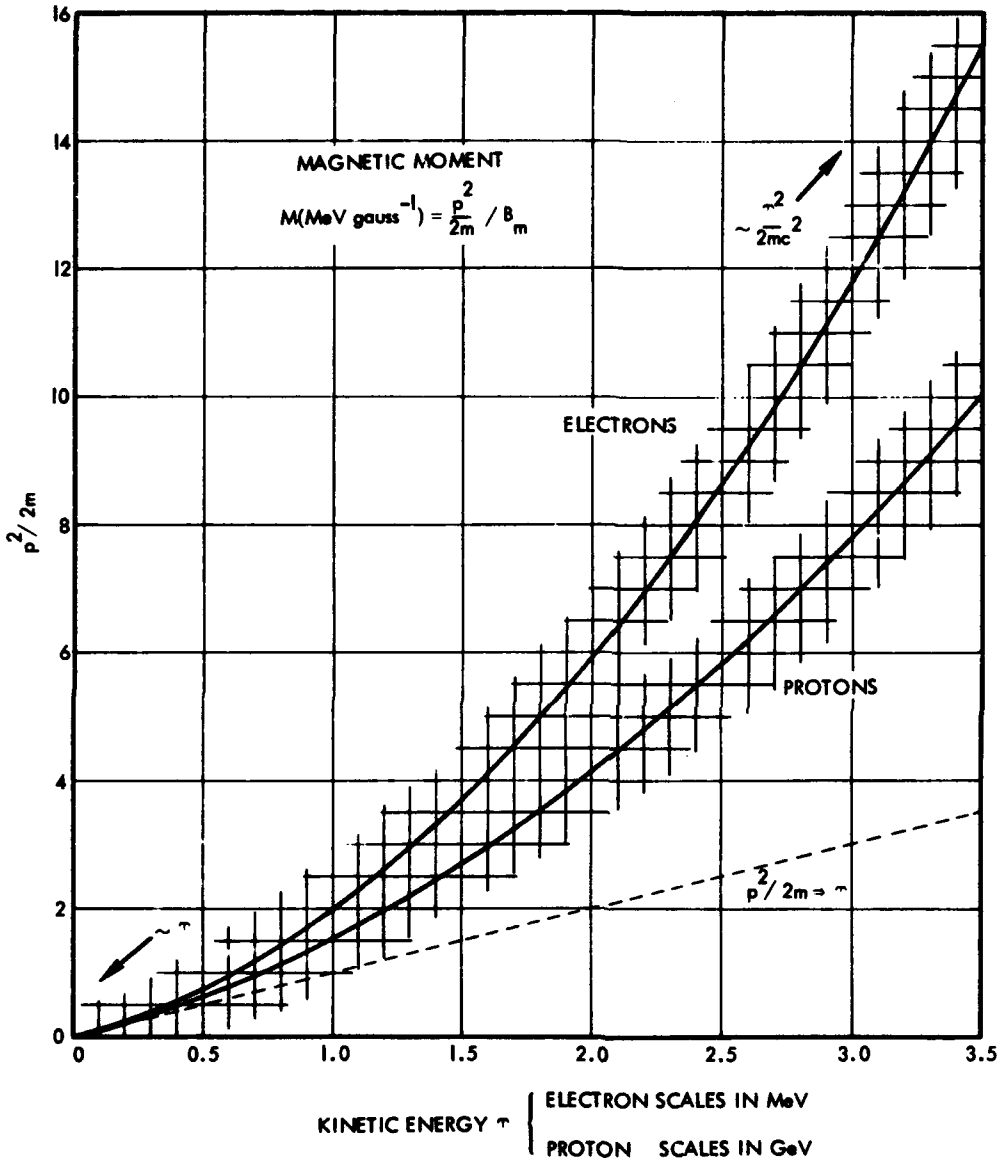

Figure 3B-8. Magnetic moment of a charged particle as a function of kinetic energy.

Figure 3B-9 contains the gyro-period of a charged particle in the geomagnetic field. The gyro-period $t_c = 2\pi mc/eB$ is plotted here for electrons and protons as a function of altitude in the earth's magnetic field. The gyro-periods of relativistic particles are increased by the factor

$$\gamma = \sqrt{1 + \frac{p^2}{m^2 c^2}} \quad .$$

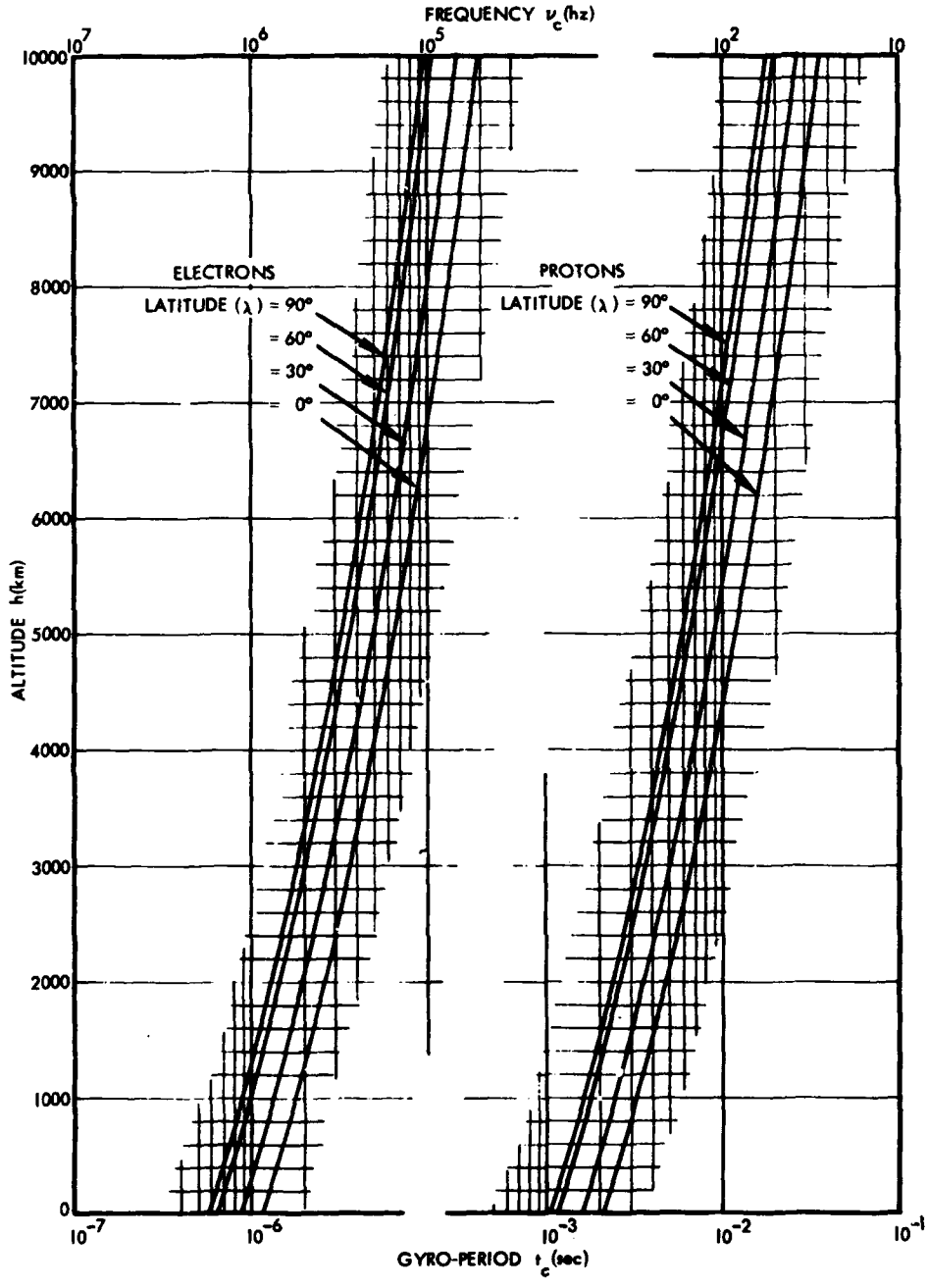

Figure 3B-9. The gyro-period of a charged particle in the geomagnetic field.

Figure 3B-10 shows the bounce periods of particles trapped in radiation belts. The bounce periods of trapped particles are plotted as a function of their velocities. The bounce periods vary directly with the total lengths of the trajectories, so the ordinate must be multiplied by $L = R_o/R_E$ to obtain the period in seconds. At relativistic energies (beyond 1 MeV for electrons and 2 GeV for protons), the velocity dependence is slight and usually may be ignored. The bounce periods of fast particles mirroring near the equator are about 0.07 L seconds.

For example: For a 1-MeV electron with an equatorial pitch angle of 30 degrees, the ordinate is 0.09. If the electron is trapped at L = 2, the bounce period is 0.09 L = 0.18 second.

Figure 3B-11 shows the bounce period and the second adiabatic invariant as functions of equatorial pitch angle. The bounce period t_b and the second adiabatic invariant J contain, respectively, the integrals

$$\mathcal{g} \equiv \frac{4}{R_o}\int_0^{S_m} dS/\mu$$

and

$$\mathcal{J} \equiv \frac{4}{R_o}\int_0^{S_m} \mu dS \quad ,$$

integrated along the field line from the equator to the mirror point. The factor of 4 accounts for a complete bounce period (Equations 3-47 and 3-75). These integrals are shown in this figure (also in Table 3B-1). The length, S, of a field line would yield a curve $4S/R_o$ falling between and passing through zero-ordinate at 90 degree pitch angle.

The complete J integral is

$$J = R_o \mathcal{J} p = L R_E \mathcal{J} p$$

and the bounce period is

$$t_b = R_o \mathcal{g}/v = L R_E \mathcal{g}/v \quad .$$

The momentum p and velocity v can be found from Figures 3B-6 and 3B-7. Any of several units may be employed for J. The most common are cgs units or mixed units—(MeV/c) cm, or (MeV/c) (earth radii). A third alternative, MeV sec, is less useful. The appropriate numerical conversion is J(MeV second = 0.02125 Lp(MeV/c).

For example: A 1-MeV electron has a velocity 2.8×10^{10} centimeters per second (Figure 2B-5). If the equatorial pitch angle is 30 degrees and L = 2, the ordinate $\mathcal{S}$ is 4.0 and the bounce period is $t_b = 6.37 \times 10^8 \times 2.0 \times 4.0/2.8 \times 10^{10} = 0.18$ second. The momentum is 1.4 MeV/c. The second adiabatic invariant is therefore $J = 2 \times 1.8 \times 1.4 = 5.0$ (MeV/c) R_E. The degenerate adiabatic invariant is $\mathcal{J} = J/p = 3.6\ R_E$.

The velocity of a 1-MeV proton is only 1.4×10^9 centimeters per second (Figure 3B-7). If the pitch angle and L are the same as for the electron in the first example, the proton's bounce period is $t_b = 6.37 \times 10^8 \times 2 \times 4.0/1.4 \times 10^9 = 3.6$ seconds. The corresponding gyro-periods of electrons and protons at L = 2 on the equator are 9×10^{-6} seconds and 1.7×10^{-2} seconds, respectively (Figure 3B-9).

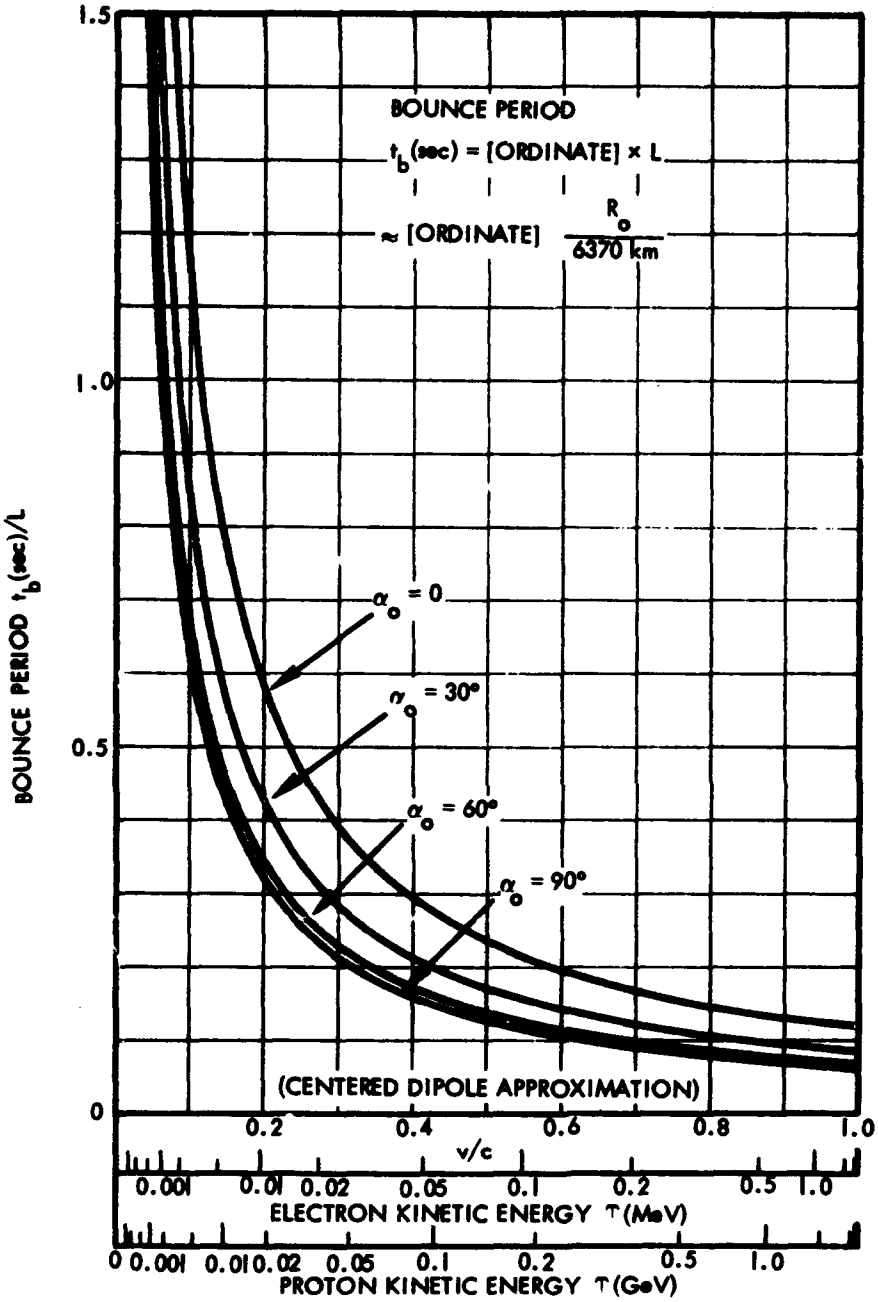

Figure 3B-10. Bounce periods of particles trapped in radiation belts.

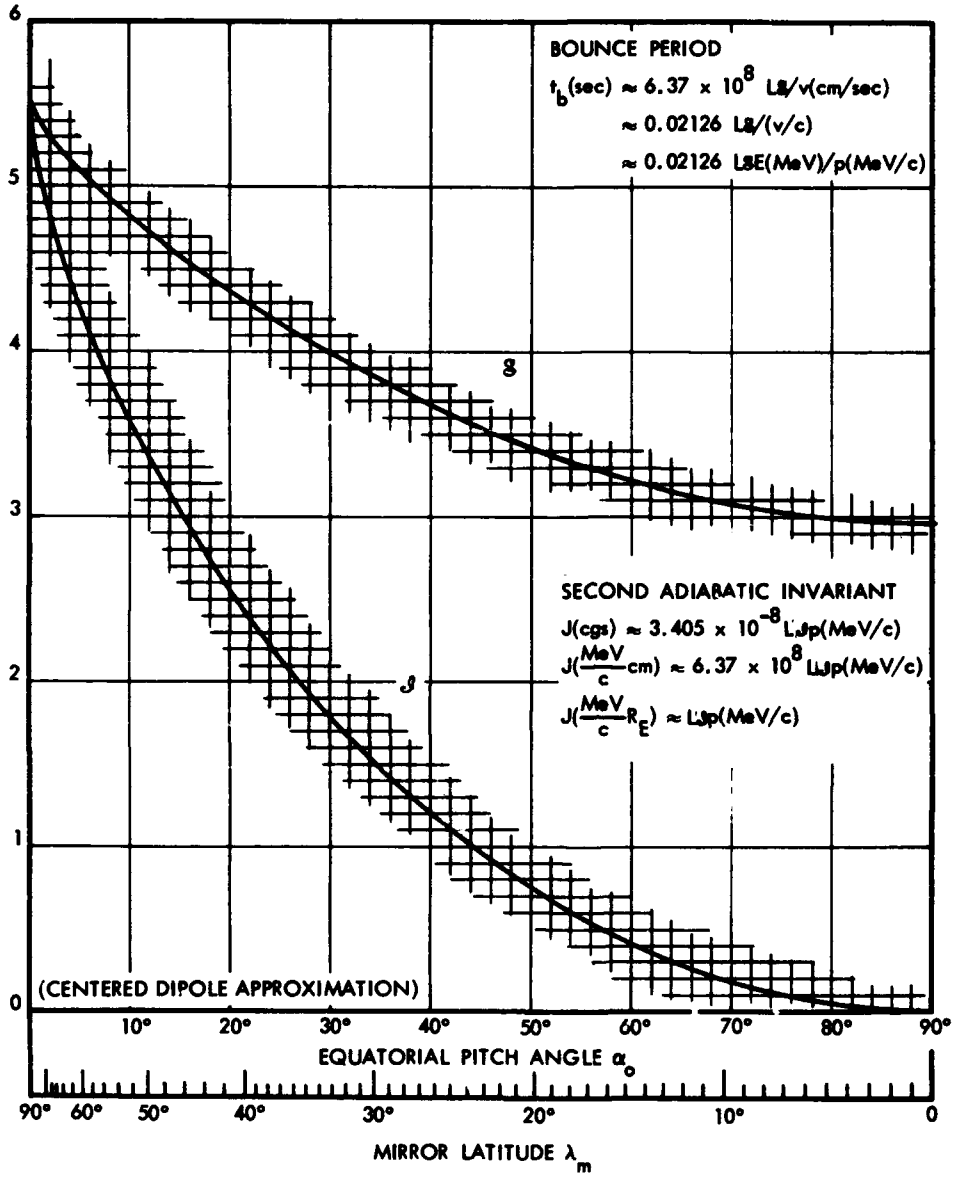

Figure 3B-11. The bounce period and second adiabatic invariant as functions of of equatorial pitch angle.

Figure 3B-12 shows azimuthal drift periods as a function of kinetic energy. The inhomogeneity of the earth's magnetic field results in an azimuthal drift of trapped charged particles with a period that varies approximately with the inverse first power of kinetic energy. This figure gives the energy dependence of the drift period. The period in seconds is obtained after division of the ordinate by L (Equation 3-50). The divergence of proton and electron curves is a result of relativistic effects as the electrons approach the speed of light. The energy-dependent factor $p^2/\gamma m = E(v^2/c^2)$ is approximately equal to $2T$ at low energies and approximately equal to T at very high energies. Only two pitch angles α_o are represented here. More exact drift periods can be found from succeeding figures.

For example: For a 1-MeV electron with an equatorial pitch angle near 90 degrees, the ordinate is 4×10^3. At L = 2, the drift period is $4 \times 10^3 / L = 2 \times 10^3$ second = 0.6 hour.

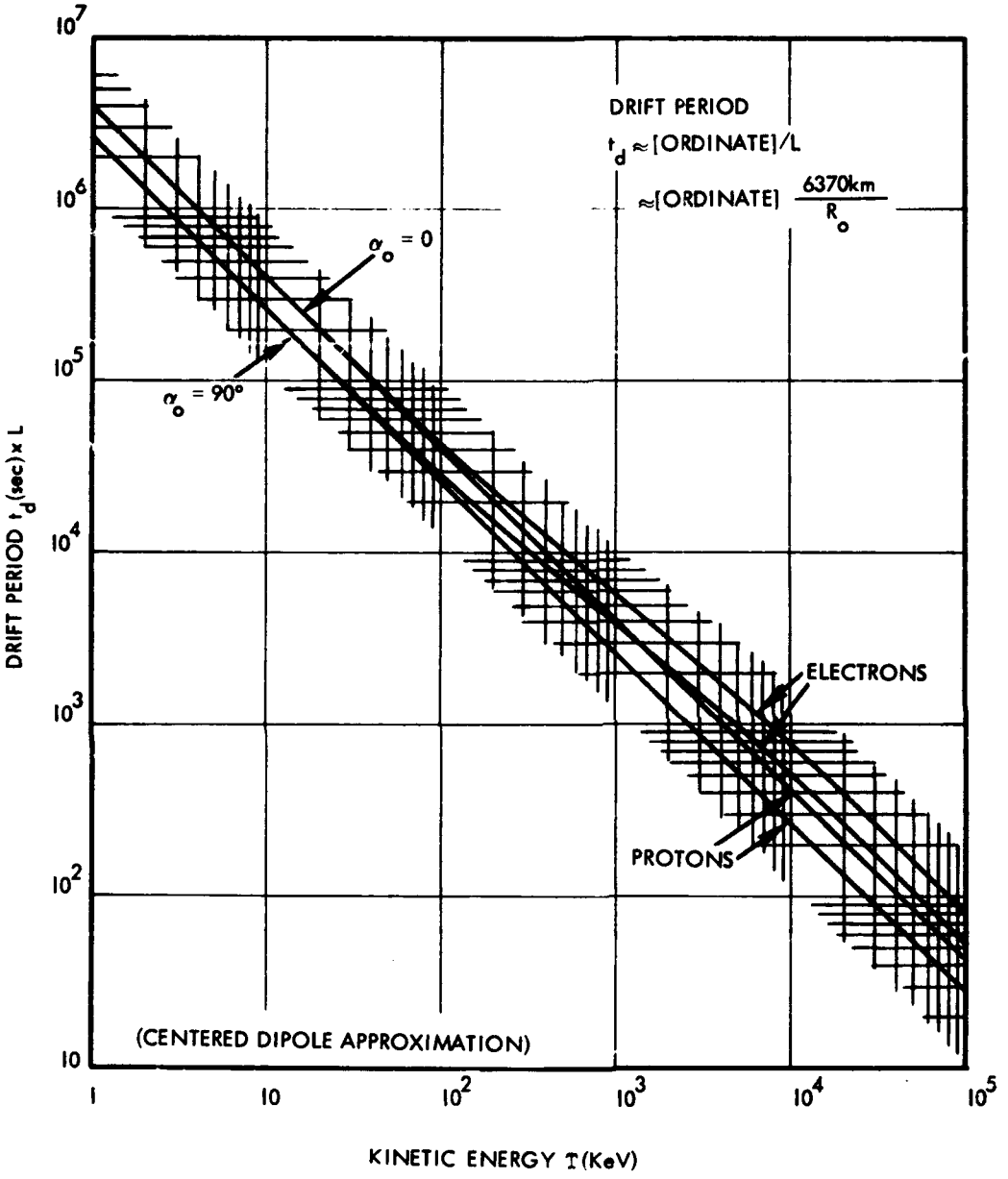

Figure 3B-12. Azimuthal drift periods as a function of kinetic energy.

Figure 3B-13 presents the azimuthal drift period as a function of the equatorial pitch angle in the earth's field. This figure, together with Figure 3B-14, which provides the energy-dependent factor, can be used to determine the azimuthal drift periods of particles trapped in the earth's magnetic field (Equation 3-50). The average angular drift velocity is simply

$$\omega_d = \frac{2\pi}{t_d} = \frac{2\pi L E(v^2/c^2)}{\mathcal{D}}$$

The drift velocity at the equator is the angular drift velocity multiplied by the equatorial radius $R_o = LR_E$ or

$$V = \frac{2\pi L^2 R_E E(v^2/c^2)}{\mathcal{D}} \quad .$$

For example: The energy-dependent factor for a 1-MeV electron is $E(v^2/c^2) = p^2/\gamma m = 1.3$ MeV (Figure 3B-14). If the electron has an equatorial pitch angle of 30 degrees, the ordinate of this graph is 6,250, which, at L = 2, results in a drift period $t_d = 6,250/2 \times 1.3 = 2,400$ seconds = 0.67 hour. The average angular drift rate is $2\pi/2,400 = 0.0026$ radian per second = 0.15 degree per second or 0.83 degree per bounce (Figure 3B-10). The average drift velocity is $V = 4.0 \times 10^4 \times (2)^2 \times 1.3/6,250 = 33$ kilometers per second.

For a 1-MeV proton, the ordinate of Figure 3B-14 is so small that the approximation $E(v^2/c^2) \approx 2$ may be used. If the pitch angle and L-value are the same as for the electron in the first example, the drift period is $t_d = 6,250/2 \times 2 = 1,560$ seconds = 0.43 hour.

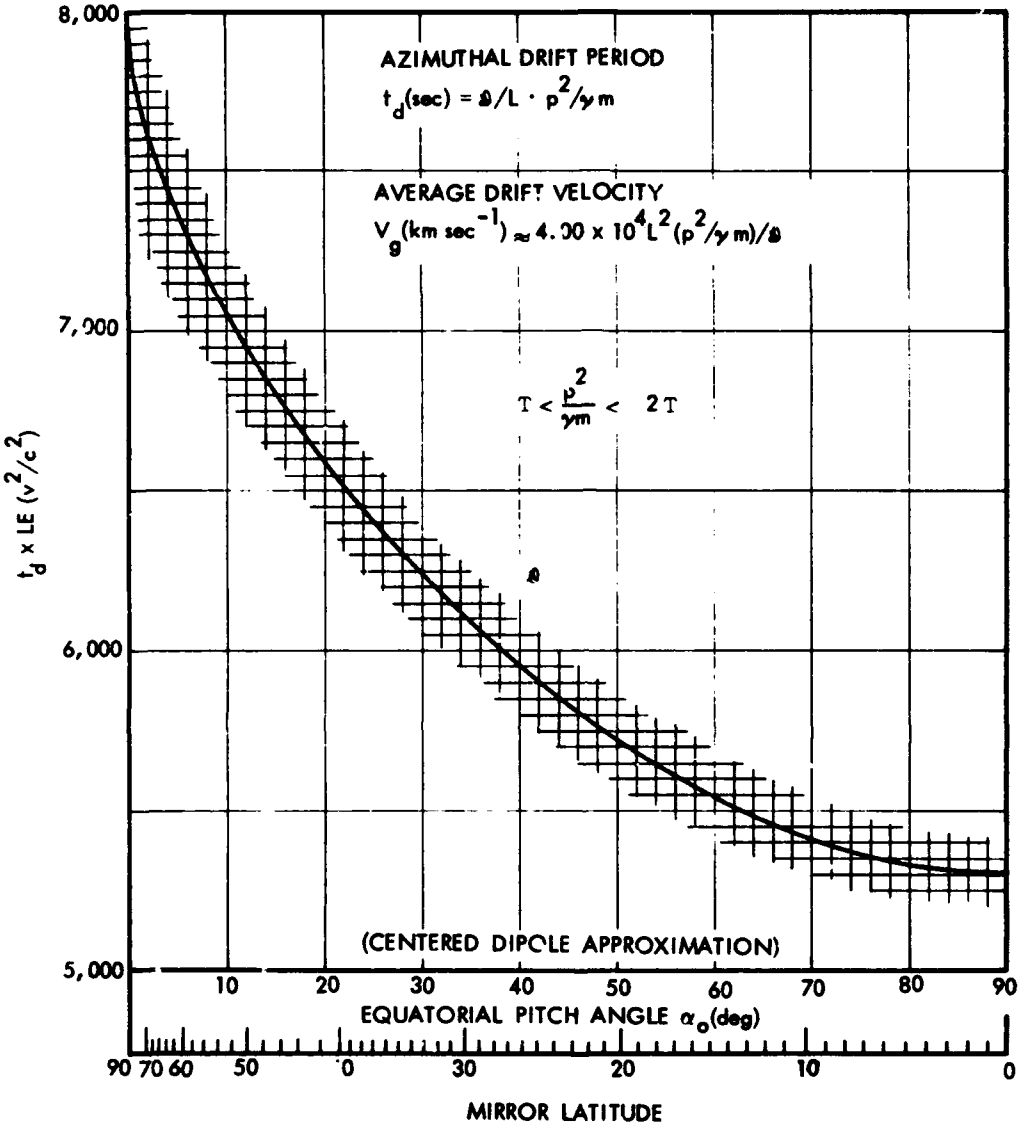

Figure 3B-13. Azimuthal drift period as a function of the equatorial pitch angle in the earth's field.

Figure 3B-14 contains the energy-dependent factor employed in azimuthal drift computations. The square of particle momentum divided by γ (or total energy multiplied by velocity squared) occurs frequently, particularly in computations relating to particle drift motions. For nonrelativistic particles, this factor is nearly equal to 2T. Accurate values at higher energies can be found from the formula:

$$p^2/\gamma m = \frac{T(T + 2mc^2)}{T + mc^2}$$

or from Figure 3B-14. The ordinate and abscissa are in the same units.

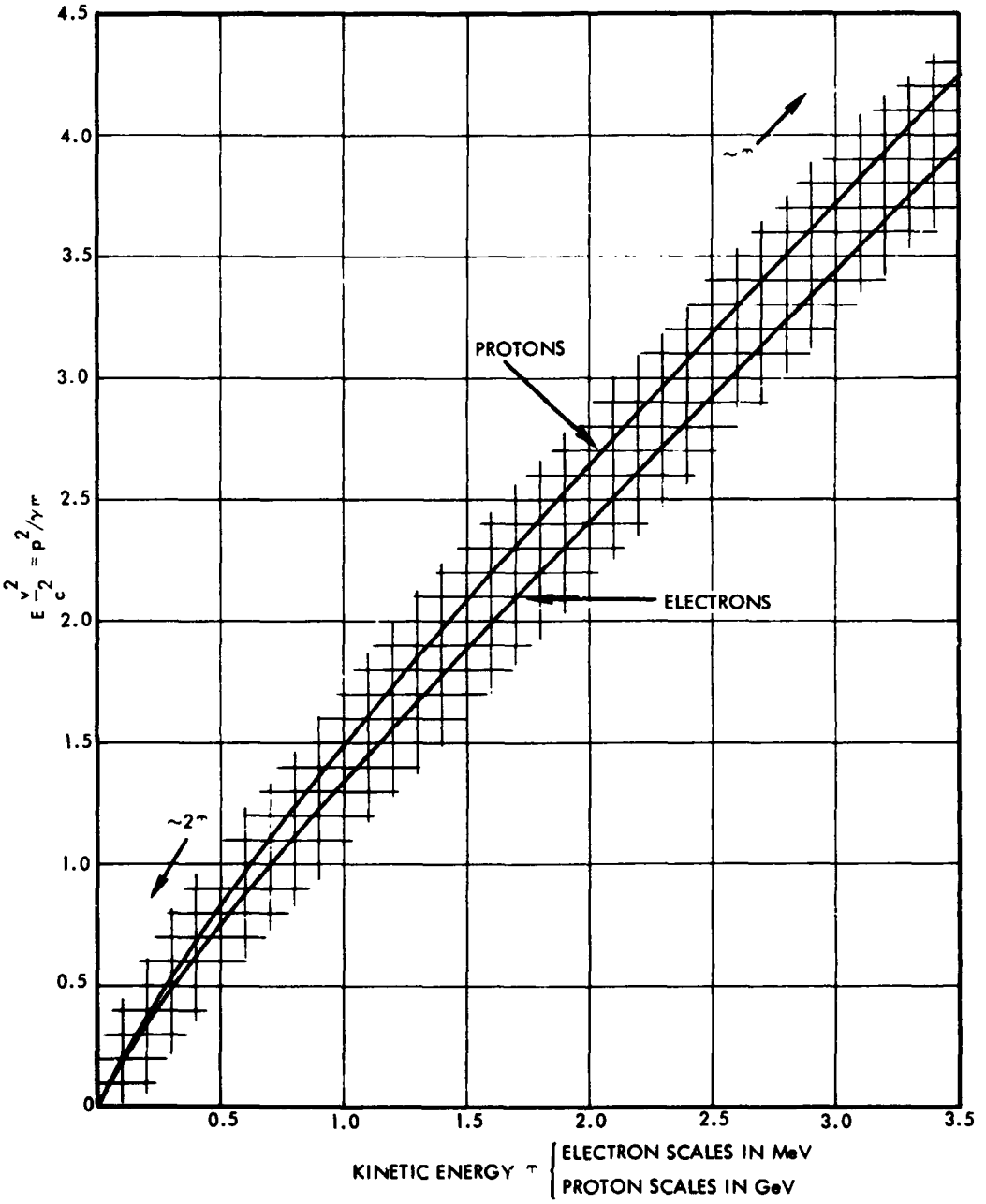

Figure 3B-14. Energy-dependent factor employed in azimuthal drift computations.

Figure 3B-15 shows constant-$\mathcal{J}$ curves in a dipole field. The upper half of this figure shows some selected contours of constant degenerate adiabatic invariant, $\mathcal{J} = J/p$ (in units of earth radii, R_E) in a dipole field. These curves contain the mirror points of all particles having a particular value of $\mathcal{J}$. The constant-$\mathcal{J}$ surfaces, constructed by rotating these curves about the polar axis are open and funnel shaped. The curves are labeled with the value of $\mathcal{J}$ in R_E. Several dipole field lines also are shown.

The constant-$\mathcal{J}$ curves are not the mirror point traces of particles that preserve adiabatic invariants while drifting across L-shells. The constant adiabatic invariant curves, labeled with the values of $J^2/Mm \propto \mathcal{J}^2 B_m$ in gauss square centimeters or gauss R_E^2, are shown in the lower part of the figure.

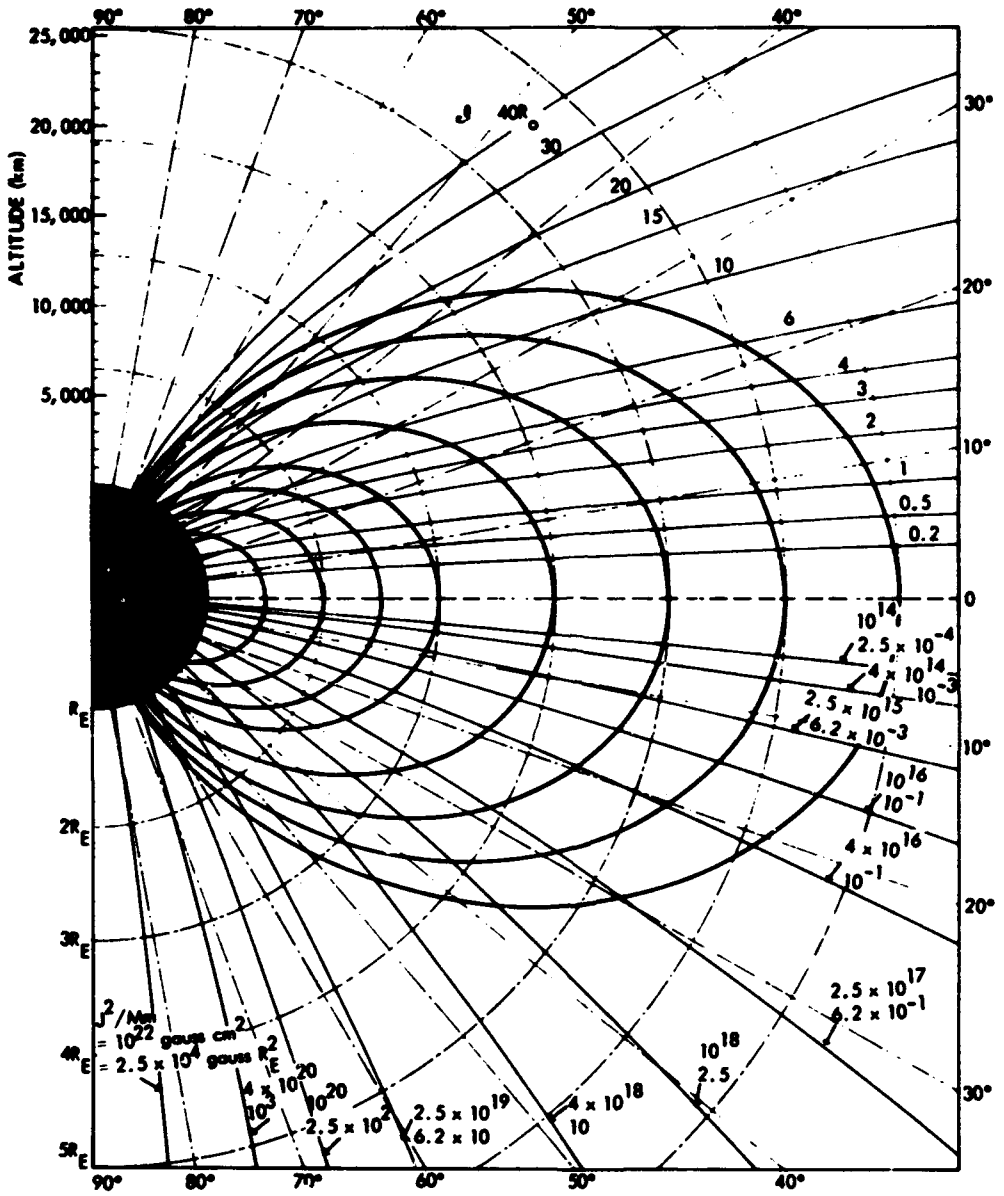

Figure 3B-15. Constant adiabatic invariant curves in a dipole field.

Figure 3B-16 contains constant adiabatic invariant curves in B, L coordinates. Constant J^2/Mm contours, such as in the lower part of Figure 3B-15, are shown in Figure 3B-16 in B, L coordinates. The mirror point of a particle drifting across L-shells while preserving the first two adiabatic invariants will follow a trajectory such as these.

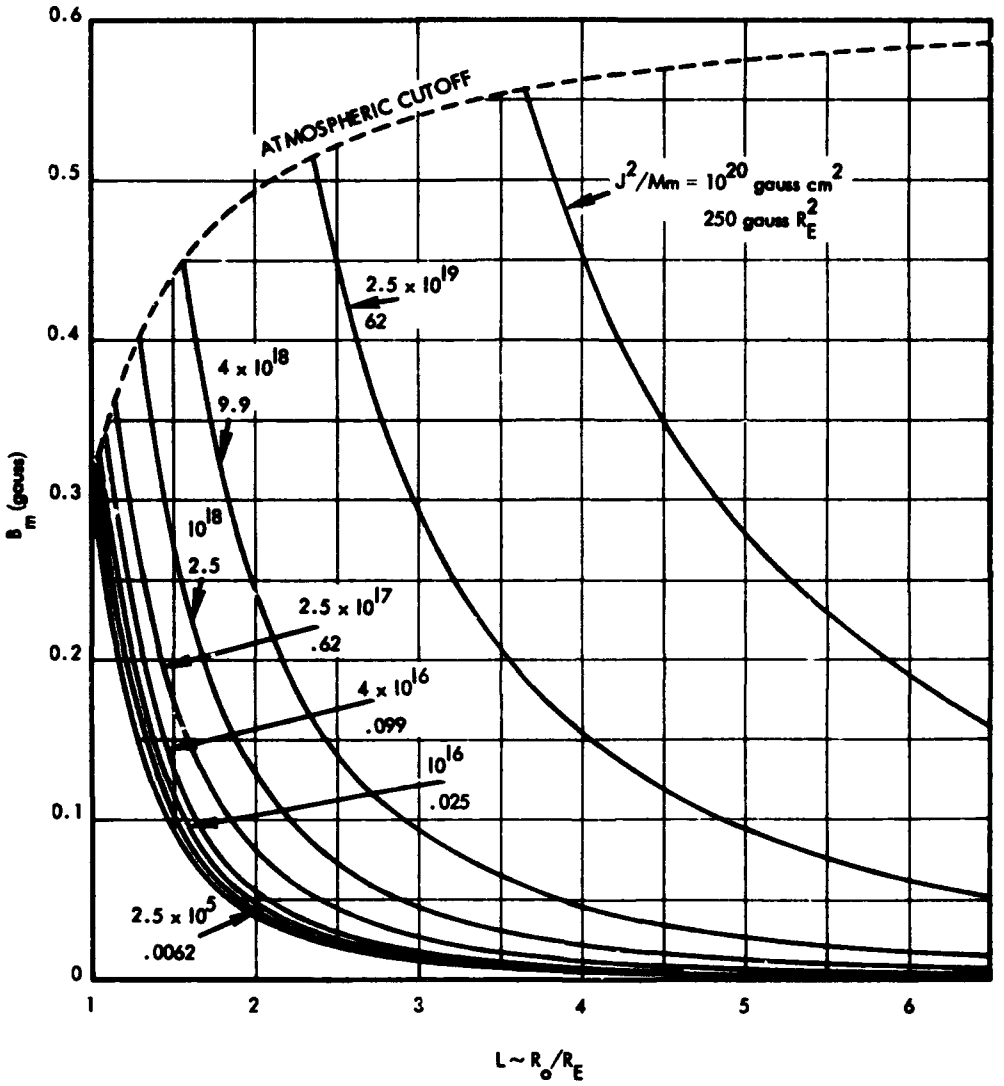

Figure 3B-16. Constant adiabatic invariant curves in B, L coordinates.

Figure 3B-17 presents adiabatic invariants of particles entering the atmosphere. The quantity J^2/Mm is shown as a function of L for particles entering the atmosphere mirroring at 100-kilometers altitude. J, M, and m may be in cgs units, or J may be in MeV/c cm, M in MeV/gauss, and M in MeV.

For example: A 1-MeV electron mirrors at 100-kilometers altitude on L = 2. From this figure, the ratio of its adiabatic invariants is $J^2/Mm = 30$ gauss R_E^2. If the electron started at L = 6 and drifted across L-shells while preserving its adiabatic invariants, the ratio of initial and final mirror fields, Bm, can be found from Figure 3B-19. The ratio is $B_m(LJ^2/Mm = 180)/B_m(LJ^2/Mm = 60) = 1.3 \times 10^{-6}/1.8 \times 10^{-5} = 0.07$. The constancy of the magnetic moment ensures that the ratio of initial and final momentum squared is the same as the ratio of the B_m's. When observed on L = 2, $p^2/2m$ was 2 MeV (Figure 3B-8). Initially, $p^2/2m$ must have been $2 \times 0.07 = 0.14$ MeV. The initial energy was approximately the same (0.14 MeV).

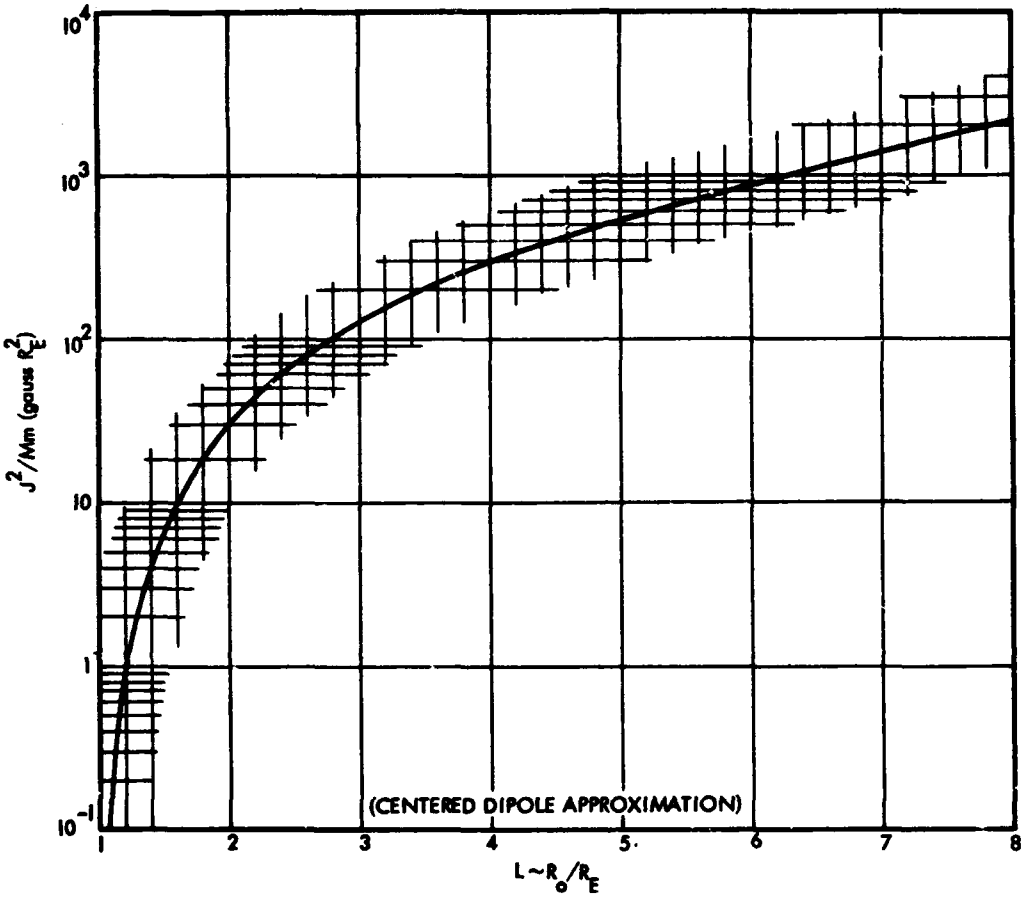

Figure 38-17. Adiabatic invariants of particles entering the atmosphere.

Figure 3B-18 contains an equatorial pitch angle as a function of L for constant adiabatic invariants. The equatorial pitch angle α_o varies so slowly with L that this figure has been folded over many times. The value of L can be found by multiplying the coordinate on the lower scale by the factor above the appropriate segment of the curve and dividing by J^2/Mm. The dimensions of J, M, and m are the same as in the preceding figures. If J^2/Mm is an integral power of 10, for example 10^n, L and α_o may be read directly from the curve labeled $\times 10^n$.

Small changes in α_o can be computed accurately by using the average slopes given on the right side together with the formula:

$$\alpha_o = [\text{constant}] + [\text{slope}] \times \log_{10} L \quad .$$

For example: A trapped particle is initially at L = 6 with an equatorial pitch angle of 50 degrees. The abscissa of this figure is at $LJ^2/Mm = 6 \times 10^{-1}$ gauss R_E^2. Therefore, J^2/Mm is 10^{-1} gauss R_E^2. The L-values may be read directly from the scale at the bottom. If the particle drifts to L = 2 while preserving its adiabatic invariants, the new equatorial pitch angle is 57.8 degrees. When the preceding simplified formula is used, the new pitch angle is computed to be

$$\alpha_o = 50 \text{ degrees} + (-16.1) \log_{10} \frac{L=2}{L=6} = 57.7 \text{ degrees} \quad .$$

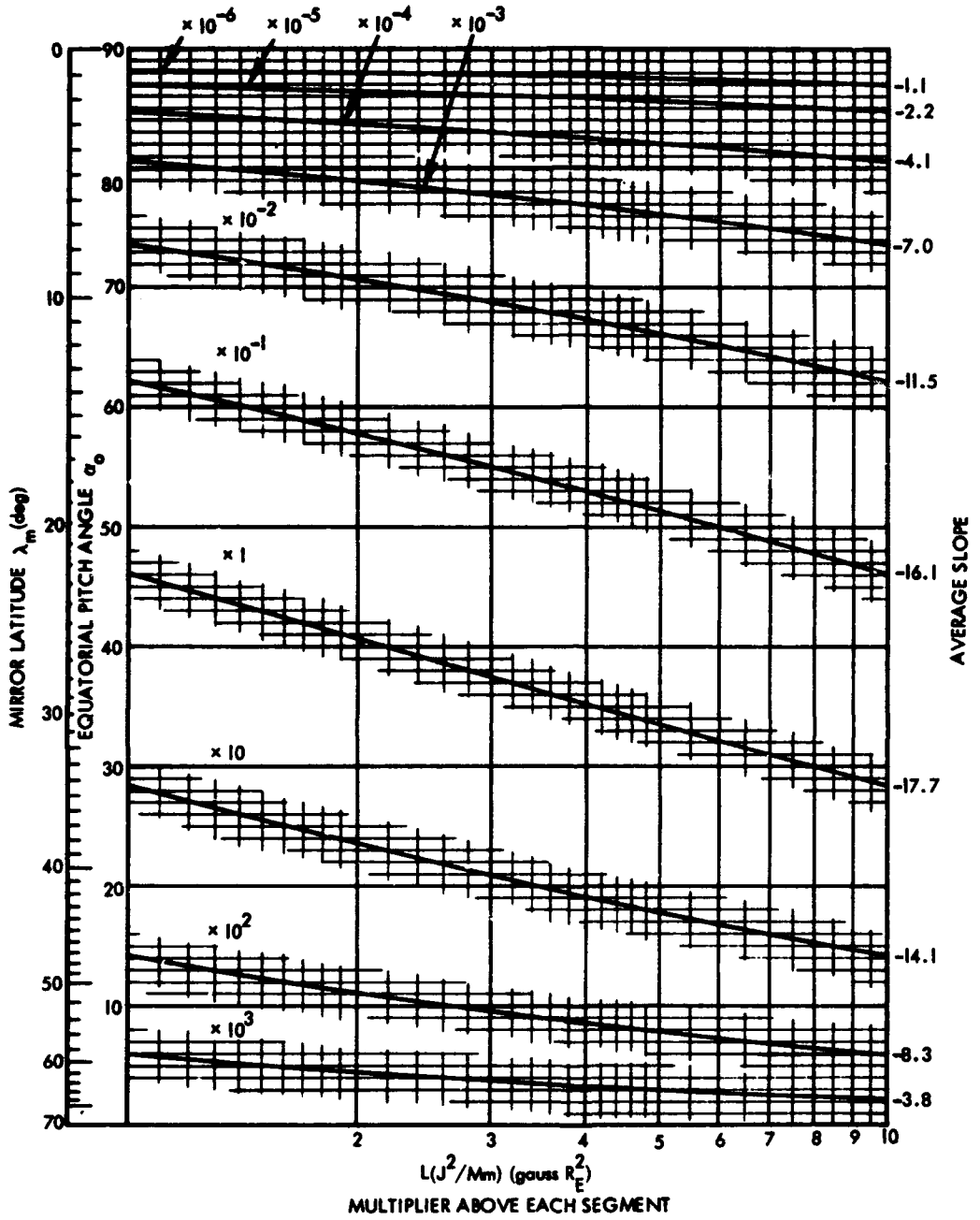

Figure 38-18. Equatorial pitch angle as a function of L for constant adiabatic invariants.

Figures 3B-19a and 3B-19b show a mirror point field as a function of L for constant adiabatic invariants. These figures contain essentially the same information as the last several figures, except that P_m has been multiplied by $(Mm_o)^3/J^6$ to obtain a unique function of L (J^2/Mm). The parameter J^2/Mm common to the ordinate and abscissa may be computed or, alternatively, determined from the preceding figure. If J^2/Mm is an integral power of 10, for example 10^n, L may be read directly from the curve labeled $x10^n$.

Constancy of the magnetic moment requires that $p^2/2m$ varies directly with B_m. The kinetic energy can be found, therefore, from Figure 3B-8.

Small changes in B_m can be computed with the aid of the average slopes at the right side and the formula:

$$\log_{10} B_m \cong [\text{constant}] + [\text{slope}] \times \log_{10} L \quad .$$

The figure has not been continued beyond $L = 10^{-3}$ because, for smaller L values ($\alpha_o > 80$ degrees), B_m is given quite accurately by the simple formula:

$$B_m \propto L^{-3} \quad .$$

For example: The equatorial pitch angle and L of a trapped particle are 50 degrees and 6, respectively. From the preceding figure, J^2/Mm is 10^{-1} gauss R_E^2. The mirror field may be read directly from the curve labeled 10^{-1} (after multiplication of the ordinate by 10^{-3}). If the particle drifts to L = 4 while preserving adiabatic invariants, the mirror field changes from $B_m = 0.0024$ gauss to $B_m = 0.0076$ gauss. If the particle is an electron with initial energy of 1 MeV, $p^2/2m$ is about 2 MeV (Figure 3B-8). The momentum squared is proportional to the mirror field if the magnetic moment is preserved. Finally, $p^2/2m$ is $2.0 \times (0.0076/0.0024) = 6.3$ MeV. The final kinetic energy is about 2.2 MeV. The energy of a trapped proton is more nearly proportional to B_m. If the drifting particle were a proton, its energy change would be from 1.0 MeV to $1.0 \times (0.076/0.024) = 3.2$ MeV.

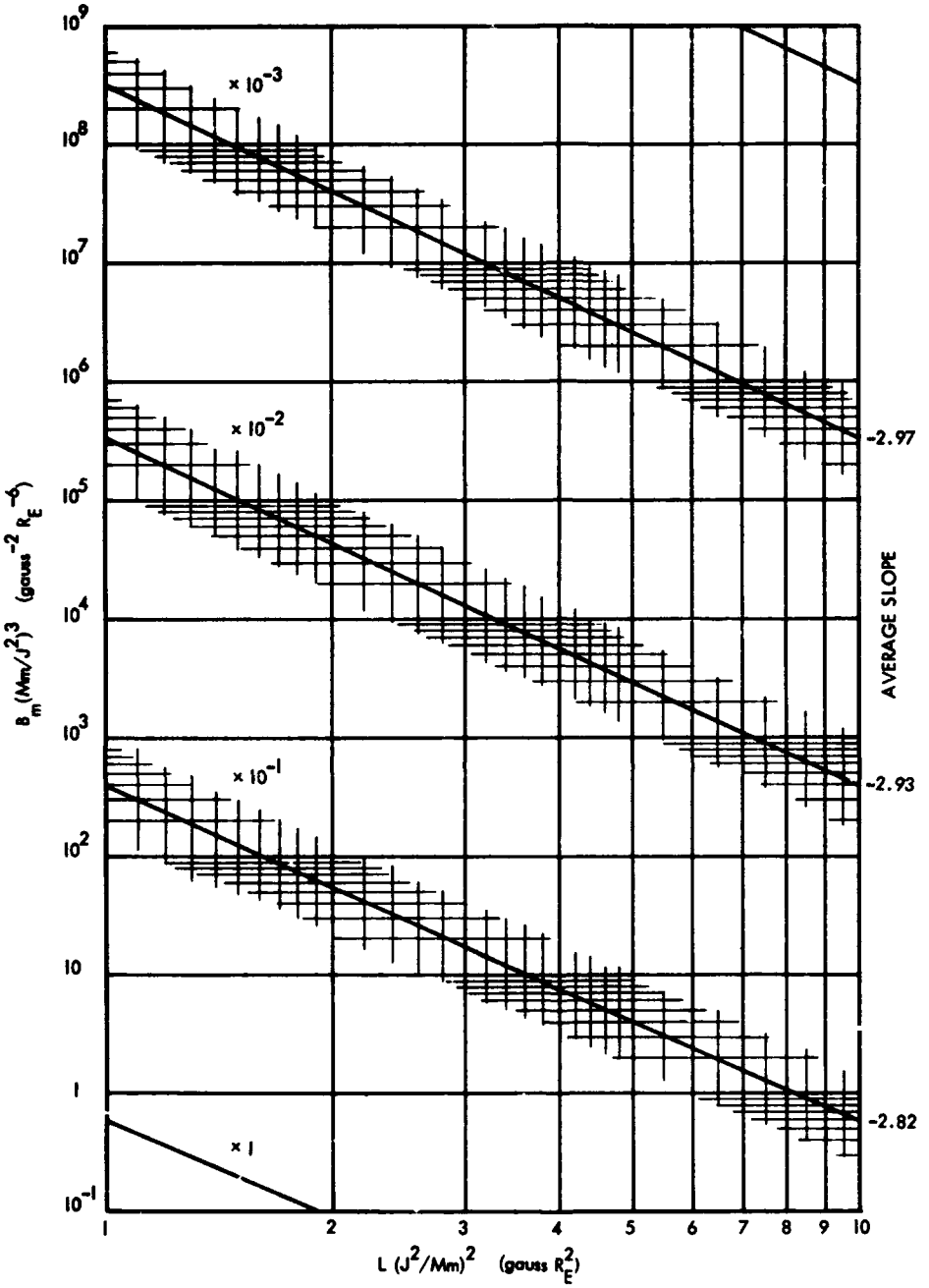

Figure 3B-19a. Mirror point field as a function of L for constant adiabatic invariants.

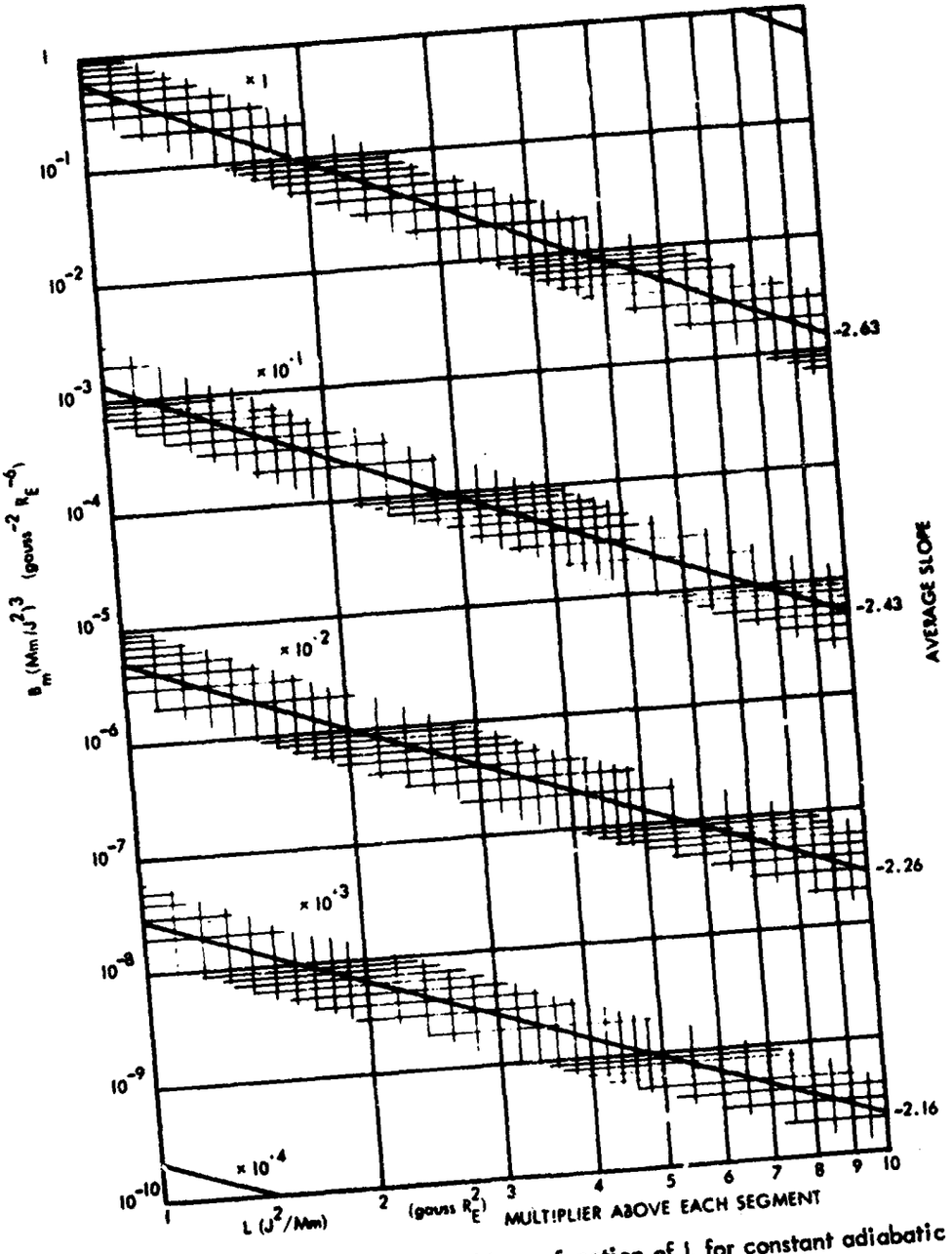

Figure 3B-19b. Mirror point field as a function of L for constant adiabatic invariants.

REFERENCES

1. L. Spitzer. Physics of Fully Ionized Gases, 102, Interscience, New York, 1956.

2. J. L. Delcroix. Introduction a la théorie des gas ionisés, Dunod, Paris, 1959, trans.: Introduction to the Theory of Ionized Gases, 146, trans. by Ben Daniel Clark, Interscience, New York, 1960.

3. H. Goldstein. Classical Mechanics, 383, Addison Wesley, Cambridge, 1950.

4. H. Alfvén and C.-G. Fälthammar. Cosmical Electrodynamics Fundamental Principles, Oxford U. Press, London, 1963.

5. H. Alfvén. Cosmical Electrodynamics, 232, Clarendon Press, Oxford, 1950.

6. L. Davis and D. B. Chang. "On the Effect of Geomagnetic Fluctuations on Trapped Particles," J. Geophys. Res., 67, 2169-2179, 1962.

7. C.-G. Fälthammar. "Effects of Time-Dependent Electric Fields on Geomagnetically Trapped Radiation," J. Geophys. Res., 70, 2503-2516, 1965.

8. H. Alfvén. "On the Electrical Field Theory of Magnetic Storms and Aurorae," Tellus, 7, 50-64, 1955.

9. H. Alfvén. "On the Theory of Magnetic Storms and Aurora," Tellus, 10, 104-116, 1958.

10. L. Block. "The Present State of the Electric Field Theory of Magnetic Storms and Aurorae," IAU Symposium 6, 58, 1956.

11. C. Störmer. The Polar Aurora, 392, Clarendon Press, Oxford, 1955.

12. P. Lanzano. "Analytic Contributions to the Störmer Problem," Astphys. Sp. Sci., 2, 319-333, 1968.

13. S.F. Singer. Bull. Am. Phys. Soc., Ser. II 1, 229, abs., 1956.

14. J.W. Chamberlain. "Motion of Charged Particles in the Earth's Magnetic Field," Geophysics the Earth's Environment, 141-174, ed. by C. DeWitt, J. Hieblot, and A. Lebeau, Gordon and Breach, New York, 1963.

15. G. Hellwig. "Über die Bewegung geladener Teilchen in schwach veränderlichen Magnetfeldern," Zeit. Naturforsch, 10a, 508-516, 1955.

16. E.C. Ray. "On the Motion of Charged Particles in the Geomagnetic Field," Ann. Phys., 24, 1-18, 1963.

17. K.S. Viswanathan and P. Venkatarangan. "The Geomagnetic Cavity and the Van Allen Radiation Belts, Pl. Sp. Sci., 14, 641-647, 1966.

18. V.P. Shalimov and I.N. Svachunov. "The Use of Störmer's Method for the Investigation of the Motion of Charged Particles in the Field of a Magnetic Dipole Situated in an External Magnetic Field II," Kosm Issled, 4, 394-403, 1966, trans: Cos Res 4, 350-357, 1966.

19. D. Stern. "Störmer Theory and Euler Potentials," Pl. Sp. Sci., 15, 1525-1530, 1967.

20. S. Chandrasekhar. Plasma Physics, 214, U. of Chicago, 1960.

21. T.G. Northrop. The Adiabatic Motion of Charged Particles, 105, Interscience, New York, 1963.

22. P.O. Vandervoort. "The Relativistic Motion of a Charged Particle in an Inhomogeneous Electromagnetic Field," Ann. Phys., 10, 401-453, 1960.

23. D.R. Bates. "The Temperature of the Upper Atmosphere," P.R.S. Lon, B64, 805-821, 1951.

24. F.S. Johnson. "Temperature in the High Atmosphere," Ann. Geophys., 14, 94-108, 1958.

25. L.H. Brace, N.W. Spencer, and A. Dalgarno. "Electrostatic Probe Data and Interpretation," Trans. Am. Geophys. U., 45, 82, 1964.

26. F.S. Johnson. "Structure of the Upper Atmosphere," Satellite Environment Handbook, 1-20, second ed, ed. by F.S. Johnson, Stanford Press, Stanford, Calif. 1965.

27. W.B. Hanson. "Structure of the Ionosphere," Satellite Environment Handbook, 21-49, ed. by F.S. Johnson, Stanford Press, Stanford, Calif. 1965.

28. S.F. Singer. "Radiation Belt and Trapped Cosmic-Ray Albedo," Phys. Rev. Letters, 1, 171, 1958, trapped albedo theory of the radiation belt, Phys. Rev. Letters, 1, 181, 1958.

29. R.C. Wentworth, W.M. MacDonald, and S.F. Singer. "Lifetimes of Trapped Radiation Belt Particles Determined by Coulomb Scattering," Phys. Fluids, 2, 499-509, 1959.

30. M. Walt and W.M. MacDonald. "The Influence of the Earth's Atmosphere on Geomagnetically Trapped Particles," Rev. Geophys., 2, 543-577, 1964.

31. J.G. Linhart. Plasma Physics, 274, North Holland, Amsterdam, 1960.

32. W.B. Thompson. An Introduction to Plasma Physics, 247, Pergamon Press, Oxford, London, 1962.

33. D.A. Hamlin, R. Karplus, R.C. Vik, and K.M. Watson. "Mirror and Azimuthal Drift Frequencies for Geomagnetically Trapped Particles," J. Geophys. Res., 66, 1-4, 1961.

34. J.S. Lew. "Drift Rate in a Dipole Field," J. Geophys. Res., 66, 2681-2686, 1961.

35. A.M. Lenchek, S.F. Singer, and R.C. Wentworth. "Geomagnetically Trapped Electrons From Cosmic Albedo Neutrons," J. Geophys. Res., 66, 4027-4046, 1961.

36. L.L. Newkirk and M. Walt. "Longitudinal Drift Velocity of Geomagnetically Trapped Particles," J. Geophys. Res., 69, 1759-1763, 1964.

37. E.N. Parker. "Disturbance of the Geomagnetic Field by the Solar Wind," Physics of Geomagnetic Phenomena, II, 1153-1202, ed. by S. Matsushita and W.H. Campbell, Academic Press, New York, 1967.

38. T.G. Cowling. Magnetohydrodynamics, 112, Interscience, New York, 1957.

39. W.A. Newcomb. "The Motion of Magnetic Lines of Force," Princeton U. Observ., Tech. Rept. No. 1, 1955.

40. K.M. Watson. "Use of the Boltzmann Equation for the Study of Ionized Gases of Low Density I," Phys. Rev., 102, 12-19, 1956.

41. K.A. Brueckner and K.M. Watson. "Use of the Boltzmann Equation for the Study of Ionized Gases of Low Density II," Phys. Rev., 102, 19-27, 1956.

42. G.F. Chew, M.L. Goldberger, and F.E. Low. "The Boltzmann Equation and the One-Fluid Hydromagnetic Equations in the Absence of Particle Collisions," Proc. Roy. Soc., A236, 112-118, 1956.

43. H. Grad and H. Rubin. Proceedings of the Second United Nations Conference on the Peaceful Use of Atomic Energy, 31, 190, U.N., Geneva, 1958.

44. T.G. Northrop and E. Teller. "Stability of the Adiabatic Motion of Charged Particles in the Earth's Field," Phys. Rev., 117, 215-225, 1960.

45. D.P. Stern. "The Motion of Magnetic Field Lines," Sp. Sci. Rev., 6, 147-173, 1966.

46. D. P. Stern. "Geomagnetic Euler Potentials," J. Geophys. Res., 72, 3995-4010, 1967.

47. D. P. Stern. Euler Potentials and Geomagnetic Drift Shells, GSFC Document X-641-67-329, 1967.

48. D. P. Stern. "Euler Potentials and Geomagnetic Drift Shells," J. Geophys. Res., 73, 4373-4378, 1968.

49. J. B. Taylor. "Equilibrium and Stability of Plasma in Arbitrary Mirror Fields," Phys. Fluids, 7, 767-773, 1964.

50. C. S. Gardner. "Adiabatic Invariants of Periodic Classical Systems," Phys. Rev., 115, 791-794, 1959.

51. D. Ter Haar. "Adiabatic Invariance and Adiabatic Invariants," Contemp. Physics, 7, 447-458, 1966.

52. G. F. Chew, M. L. Goldberger, and F. E. Low. The Individual Particle Equations of Motion in the Adiabatic Approximation, Los Alamos Rept. LA-2055, T-759, 1955.

53. M. Kruskal. The Spiraling of a Charged Particle, Princeton U. Project, Materhorn Rept. PM-S-33, NYO-7903, March 1958.

54. M. Kruskal. "Assymptotic Theory of System of Ordinary Differential Equations With All Solutions Nearly Periodic," The Theory of Neutral and Ionized Gases, 277-284, ed. by C. DeWitt and J. F. Detoeuf, Wiley, New York, 1960.

55. S. Chandrasekhar, A. N. Kaufman, and K. M. Watson. "Properties of an Ionized Gas of Low Density in a Magnetic Field, IV," Ann. Phys. 5, 1-25, 1958.

56. G. F. Chew, M. L. Goldberger, and F. E. Low. An Adiabatic Invariant for Motion Along the Magnetic Lines of Force, Los Alamos Rept. LA-2055, T-767, September 1955.

57. R. L. Kauffmann. "Conservation of First and Second Adiabatic Invariants," J. Geophys. Res., 70, 2181-2186, 1965.

58. J.D. Roederer. "On the Adiabatic Motion of Energetic Particles in a Model Magnetosphere," J. Geophys. Res., 72, 981-992, 1967.

59. C.E. McIlwain. "Coordinates for Mapping the Distribution of Magnetically Trapped Particles, J. Geophys. Res., 66, 3681-3691, 1961.

60. E.C. Stone. "The Physical Significance and Application of L, B_O, and R_O to Geomagnetically Trapped Particles," J. Geophys. Res., 68, 4157-4166, 1963.

61. A.M. Lenchek, S.F. Singer, and R.C. Wentworth. "Geomagnetically Trapped Electrons from Cosmic Ray Albedo Neutrons," J. Geophys. Res., 66, 4027-4046, 1961.

62. W.N. Hess. The Radiation Belt and Magnetosphere, 63-66, Blaisdell, Waltham, Mass. 1968.

63. J.F. Denisse and J.L. Delcroix. Theorie des Ondes dans les Plasmas, Dunod, Paris, 1961, trans: Plasma Waves, 140, Interscience, New York, 1963.

64. T.H. Stix. The Theory of Plasma Waves, 268, McGraw-Hill, New York, 1962.

65. S. Chapman and T.G. Cowling. The Mathematical Theory of Non-Uniform Gases, 319-379, University Press, Cambridge, 1952.

66. D.C. Montgomery and D.A. Tidman. Plasma Kinetic Theory, 286, McGraw-Hill, New York, 1964.

67. H.B. Phillips. Vector Analysis, 215-231, Wiley, New York, 1933.

68. R.S. Cohen, L. Spitzer, and P. Routly. "The Electrical Conductivity of an Ionized Gas," Phys. Rev., 80, 230-238, 1950.

69. L. Spitzer and R. Härm. "Transport Phenomena in a Completely Ionized Gas," Phys. Rev., 89, 977-981, 1953.

70. M. Abraham and R. Becker. The Classical Theory of Electricity and Magnetism, 283, Hafner, New York, trans.

71. H. Lamb. Hydrodynamics, 730, Dover, N. Y., 1945; and Cambridge, 1879.

72. S. Chapman and J. Bartels. Geomagnetism, II, 609-669, Oxford U. Press, London, 1940.

73. S. Chapman. "The Electrical Conductivity of the Ionosphere, A Review," Nuovo Cimento, 4, 1385-1412, 1956.

74. J.A. Fejer. "Atmospheric Tides and Associated Magnetic Effects," Rev. Geophys., 2, 275-309, 1964.

SECTION 4

TRAPPED RADIATION POPULATION

J.I. Vette, NASA—Goddard Space Flight Center

4.1 INTRODUCTION

In this section, a description is given of the distribution of charged particles within the earth's magnetosphere. This is done most conveniently by giving the flux of electrons and protons as functions of time, particle energy, spatial position, and orientation of the measuring device. In those cases where the particle motion obeys the adiabatic invariants, the orientation and position are connected through these invariants. In the usual cases, then, one attempts to describe functions of 4 or 5 variables. This is very difficult to do quantitatively in a concise manner because the fluxes depend heavily on all these variables and no coherent theory exists to unify the diverse behavior of the various components.

Fortunately, a large number of satellite measurements have been made in the past few years. These have provided enough observational data to form a good phenomenological picture of magnetospheric processes. Some of these processes are discussed in Sections 1, 3, and 5, and certain dominant ones also will be mentioned in the course of this section's description. Several books and proceedings of symposia now are available for those interested in becoming acquainted with many of the observations (References 1 through 5). Since all these contain references to most of the original work responsible for the present general ideas, no attempt will be made in this section to provide an extensive bibliography.

As conditions in the interplanetary medium change (such as solar wind density, velocity, temperature, or the interplanetary magnetic field), the shape of the magnetosphere changes and the particle fluxes undergo dramatic perturbations within the cavity. This section's purpose is to describe many of these changes and to present the quasi-static picture as well. Within the radiation belts are electrons and protons ranging in energy from the thermal plasma in the eV region up to several MeV electrons and several hundred MeV protons. The magnetic fields are well ordered and of great enough strength to

control the particles. This control is determined mainly by the energy density balance. If magnetic energy density ($B^2/8\pi$) is greater than the particle kinetic energy density [$nm(V^2/2)$] as discussed in Section 5, the particles are constrained by the magnetic field. Where the reverse is true such as in the interplanetary medium, the magnetic field is swept along with the particle flow.

In the magnetosheath region, as well as in parts of the geomagnetic tail, the balance of control seems to fluctuate between particles and fields. Electric fields are also important in the distant regions of the cavity. In the neutral sheet (Figure 1-2), energetic plasmas with densities ~ 1 particle per cubic centimeter frequently are found. Typical electron energies vary from 0.1 to 10 KeV and protons from 1 to 20 KeV. On both sides of the neutral sheet for a distance for ~ 6 R_E, low-energy plasma and nonthermal energetic particles are seen from time to time, but the flux values at any given point in space vary greatly with time, as do the average energies of the particles.

If adiabatic particle motion is computed in a staticly distorted magnetosphere, it becomes clear that regions of the magnetosphere exist in which particles cannot execute complete drift paths around the earth. Roederer (Reference 6) calculated locations of the regions of pseudotrapping in a model magnetosphere that included a tail field. Particles mirroring inside those regions are unable to complete a 180-degree drift around the earth. Those injected into the left or noon side will be lost into the tail; those injected into the right or tail side will abandon the magnetosphere through the boundary on the day side.

A picture of this situation for the noon-midnight meridian plane is shown in Figure 4-1. The pseudotrapping regions nearly always contain particles with energies $\lesssim 100$ KeV, but time variations are considerable and the flux values are generally a factor of 10 or more less than the stably trapped particles near the boundary between these regions.

Because the particle population and time behavior are different in many parts of the magnetosphere and because the appropriate coordinate system for the best description varies, dissecting the magnetosphere into the several different zones will be convenient:

- Inner radiation
- Electron slot
- Outer radiation

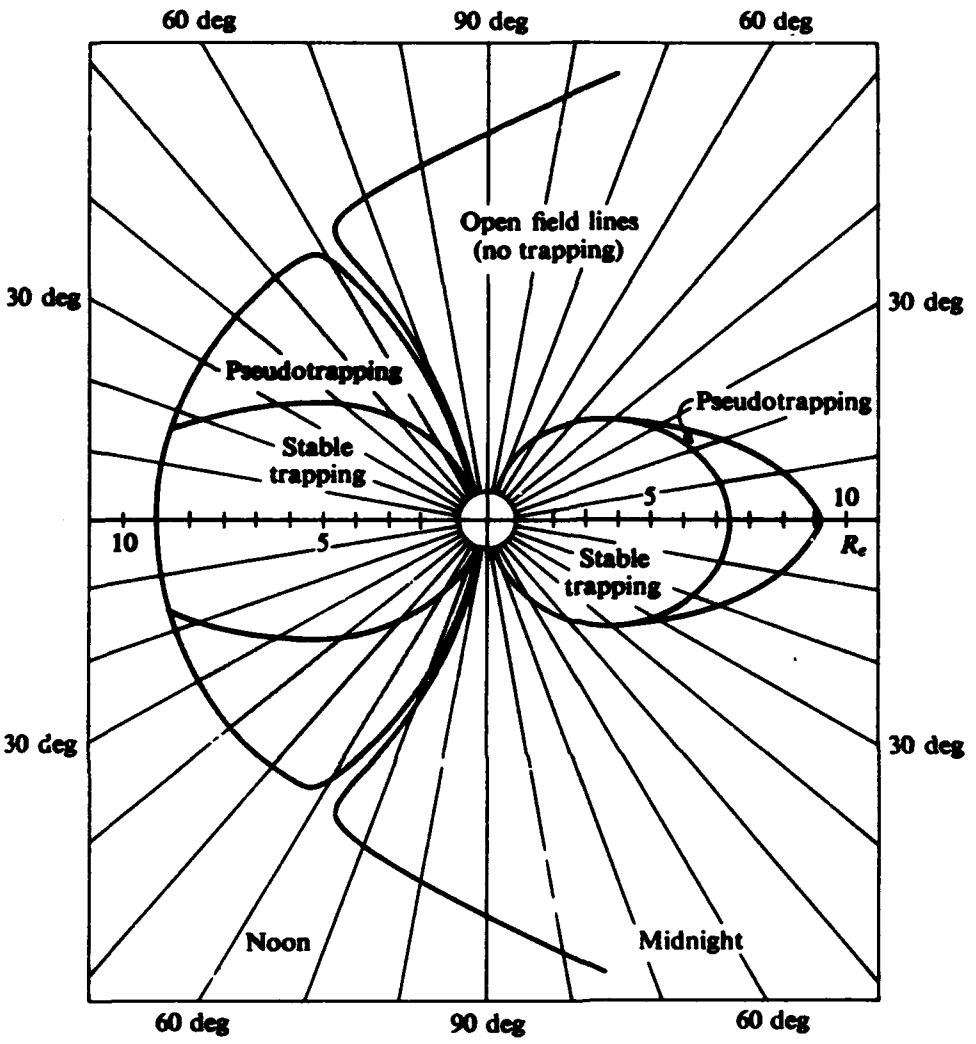

Figure 4-1. Trapping regions for a model magnetosphere.

- Pseudotrapped
- Geomagnetic tail
- Low altitude.

Each of these will be discussed in more detail to characterize the particle population for quantitative or semiquantitative work. Some of the important physical processes that are known to be effective in magnetospheric physics are discussed in other sections.

4.2 INNER RADIATION ZONE

The inner radiation zone is considered to be the region above 500 kilometers in altitude and enclosed by the McIlwain L-shell equal to 1.8 earth radii. The particle motion can be described by the invariants, and the B, L coordinates form a good system. Protons have been measured in this region from approximately 1 to several hundred MeV and are fairly stable with time. Proton model environments have been produced (References 7, 8, and 9) by merging much of the satellite data taken between 1958 and 1965. To produce a semiquantitative description without too much complexity, the integral energy regime has been broken into four separate bands: 0.1 to 4, 4 to 30, 30 to 50, and > 50 MeV. The description is then given as the omnidirectional flux J above energy E by:

$$J(>E, B, L) = F(B, L) \exp\left[(E_1 - E)/E_0(B, L)\right] \quad . \tag{4-1}$$

or, in the case of the 4 to 30 MeV band, as:

$$J(>E, B, L) = F(B, L)\,(E/E_1)^{-P(B, L)} \quad . \tag{4-2}$$

The quantities $F(B, L)$, $E_0(B, L)$, and $P(B, L)$ are given as tabular functions. These quantities for the most current proton environments AP1, AP3, AP5, and AP6 are presented in Figures 4-2 through 4-9. In Figure 4-2, the distribution function $J(>E, B, L)$ is shown as a contour map of constant flux lines. For AP5, $E_1 = 0.4$ MeV. In Figure 4-3, the spectrum is of the form:

$$J(>E, B, L) = J(>E_1, B, L) \exp\left[(E_1 - E)/E_0(B, L)\right] \quad .$$

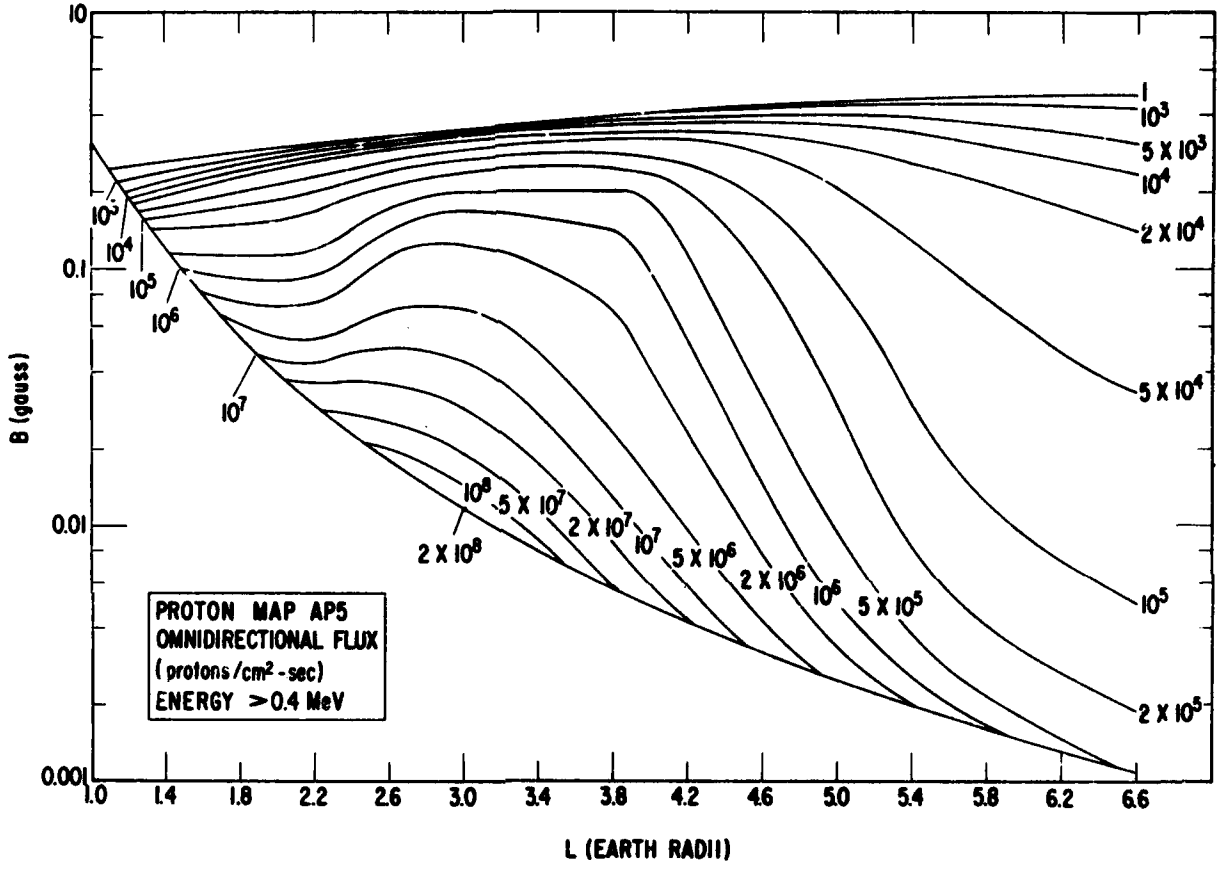

Figure 4-2. Log B, L flux map of the AP5 environment.

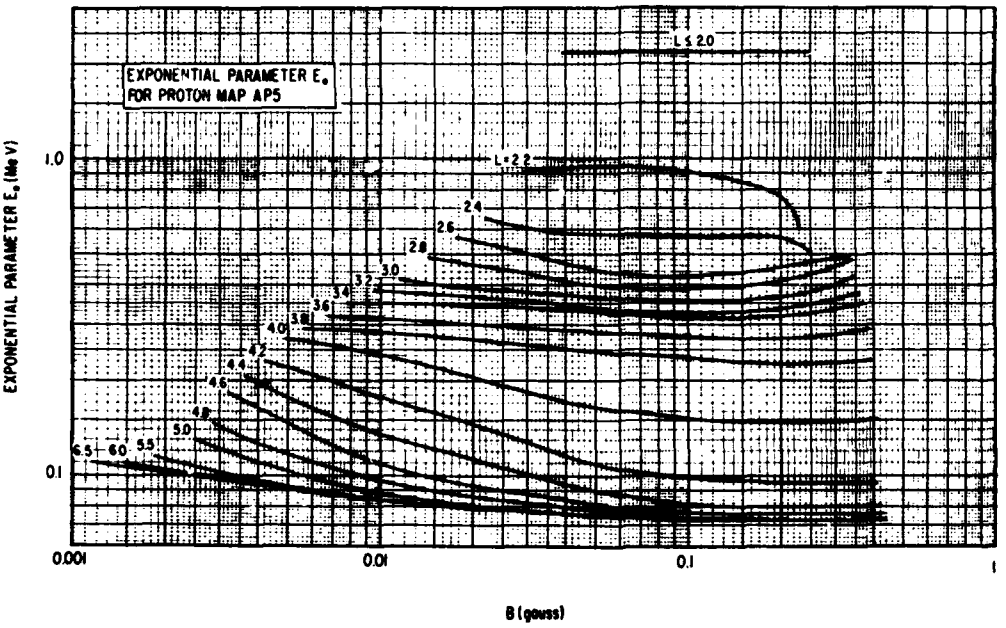

Figure 4-3. Spectral parameter E_0 used in the AP5 environment.

In Figure 4-4 for AP6, $E_1 = 4.0$ MeV. In Figure 4-5, the spectrum is of the form:

$$J(> E, B, L) = J(> E_1, B, L)\,(E/E_1)^{-P(B, L)} \quad .$$

One can look on these environments as representing a summary of the many different measurements made by numerous investigators. More details of the construction of the models and the comparison with the actual data may be found in References 7, 8, and 9.

The approximate distribution of protons at the geomagnetic equator is shown in Figure 4-10. The curves in Figure 4-10 were obtained from the proton model environments AP5 and AP6 as well as from some recent high-energy data from the OV3-4 satellite. It can be seen from the figure that the peak intensity of protons with energies above 4 MeV lies within our defined inner radiation zone. A subsidiary peak around 2.2 R_E first seen in 1963 has moved gradually

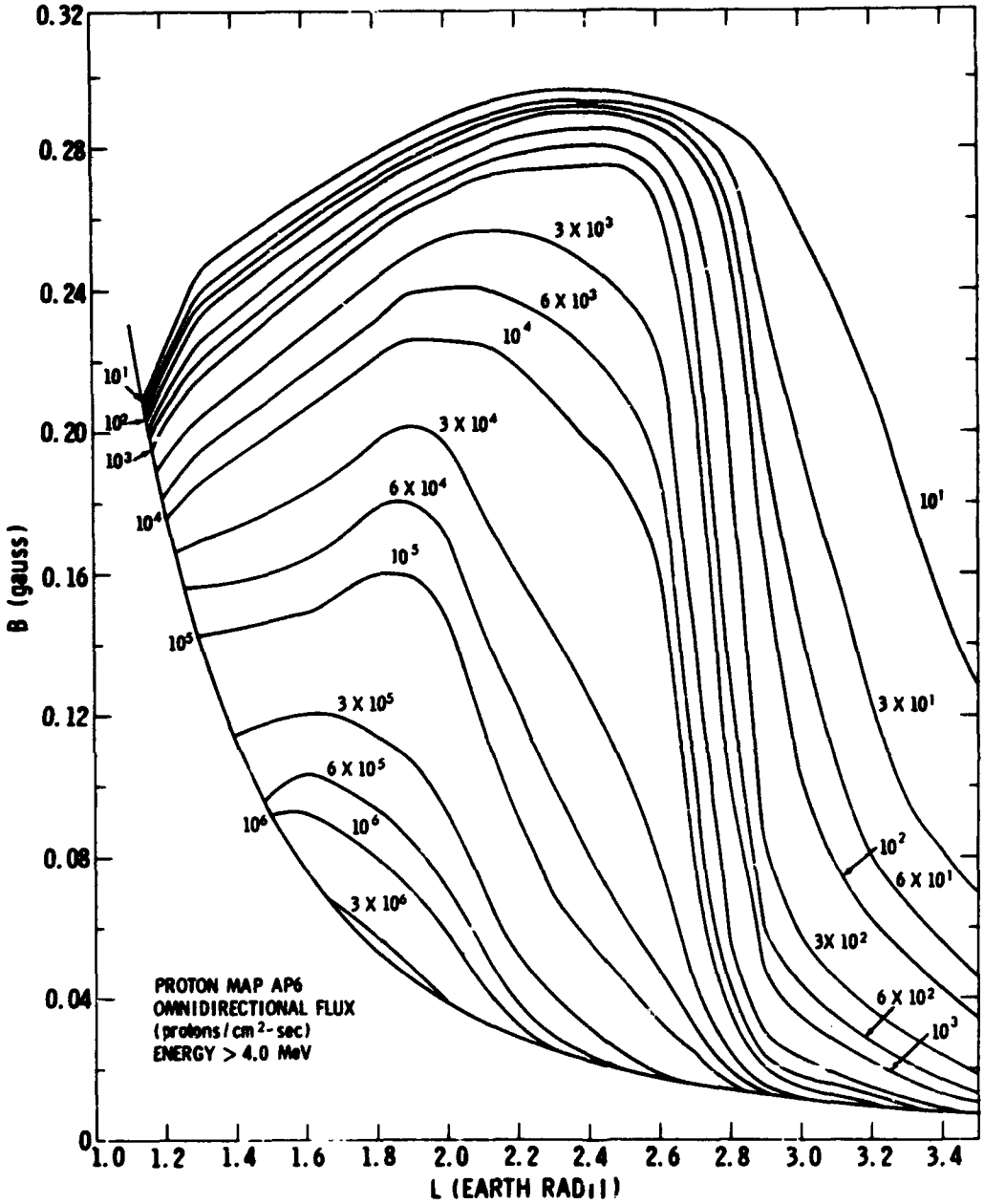

Figure 4-4 Log B, L flux map of the AP6 environment.

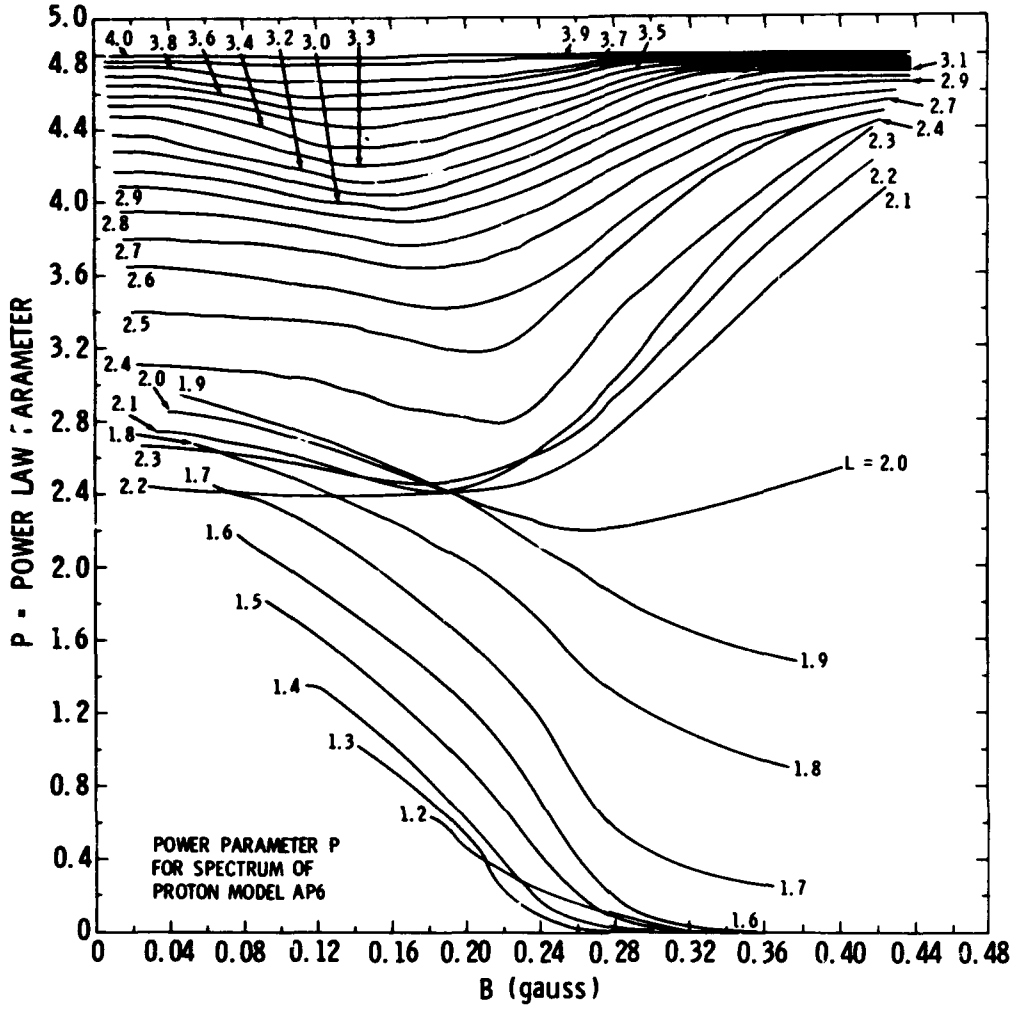

Figure 4-5. Spectral parameter P used in the AP6 environment.

inward and is no longer discernible. Perhaps some of the best demonstrations of the stability of inner-zone protons are given in Figures 4-11 and 4-12. These measurements were made continually by an experiment (Reference 10) on 1963 38C, an extremely long-lived satellite. In Figure 4-11, the points are 10-day averages of measurements in selected B intervals. These intervals are 0.18 to 0.19 gauss for L = 1.20, 0.175 to 0.185 for L = 1.35, 0.205 to 0.225 for L = 1.90, 0.21 to 0.23 for L = 2.20, and 0.215 to 0.235

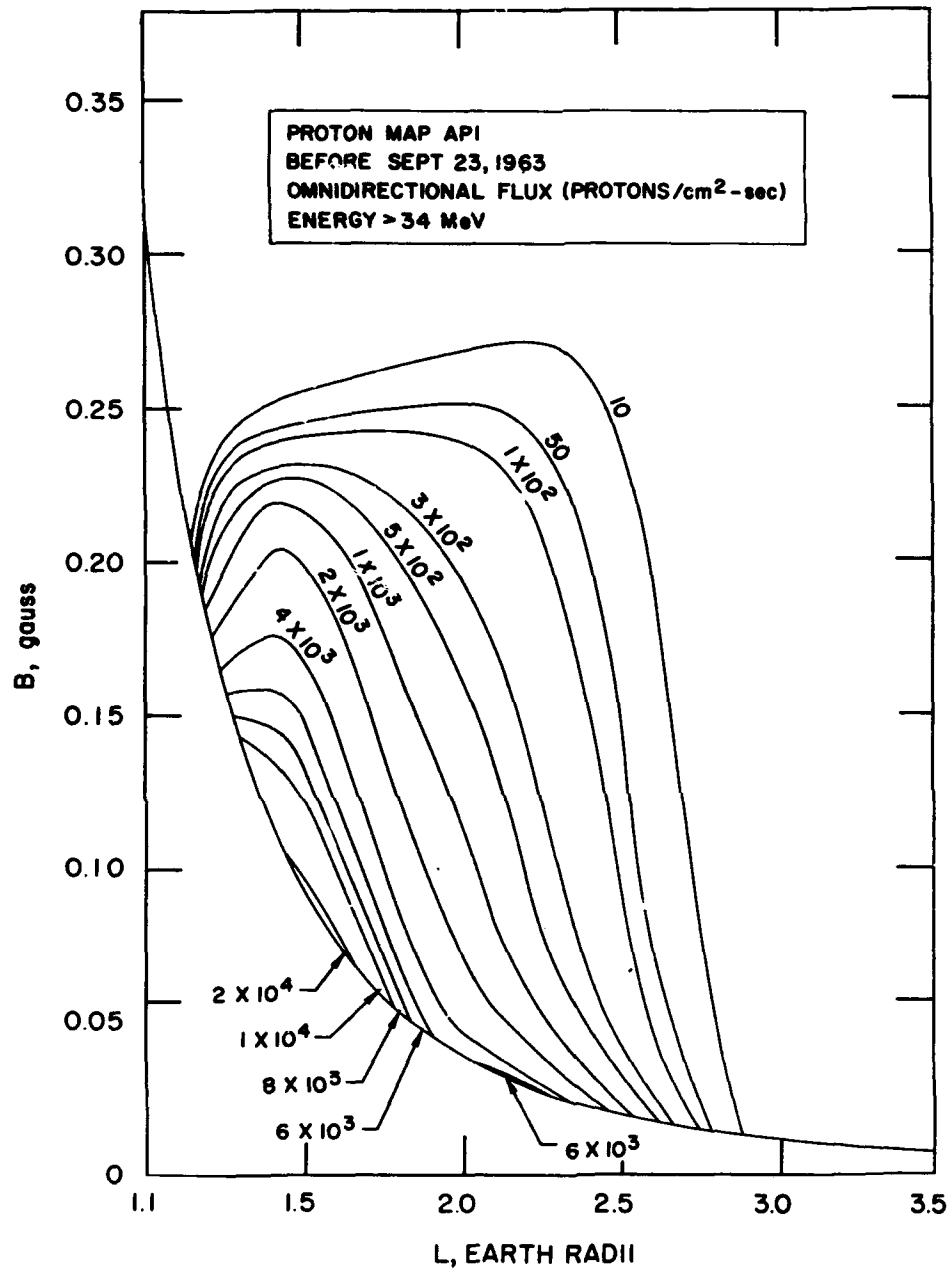

Figure 4-6. The B, L flux map of the API environment for the API E_1 = 34 MeV.

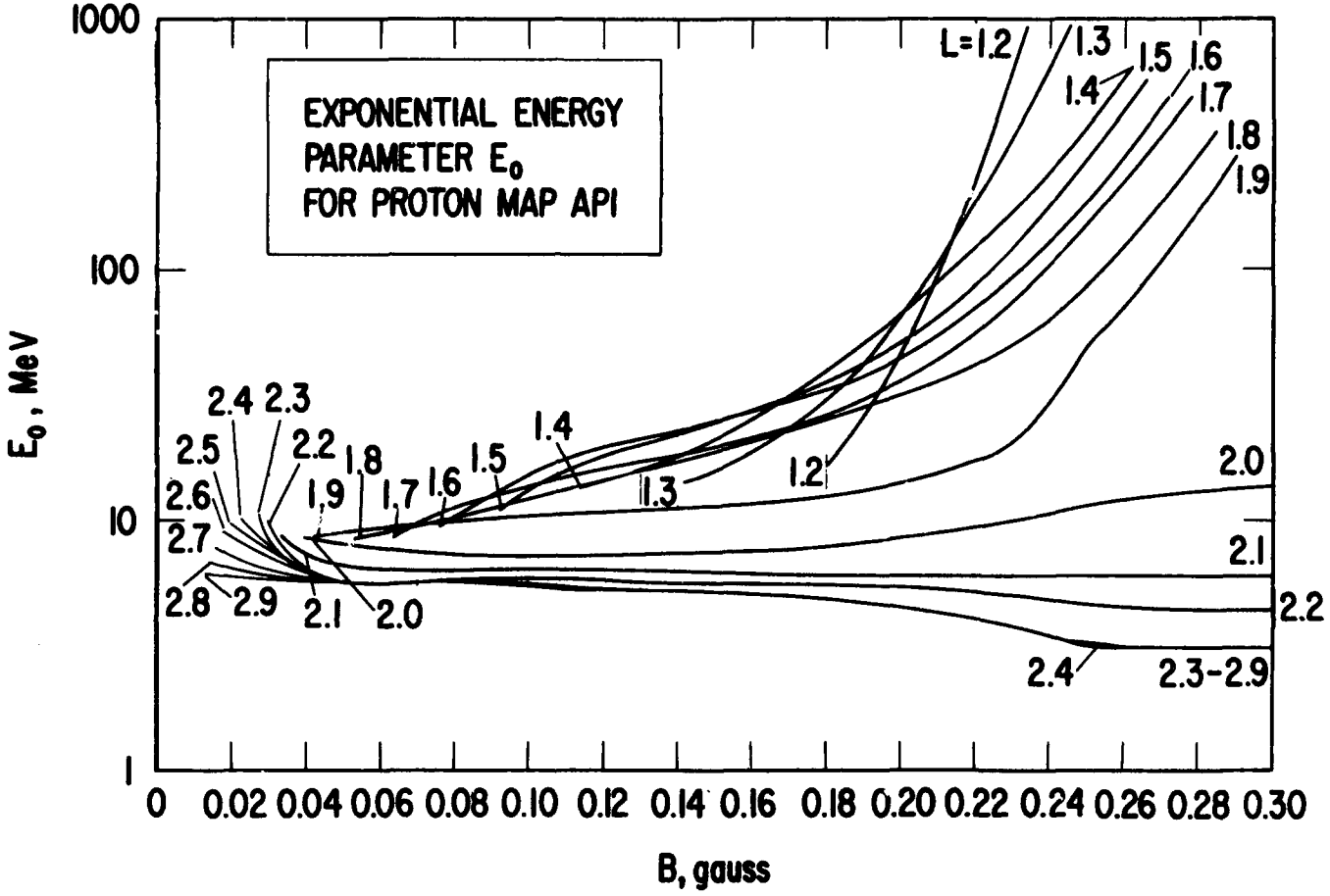

Figure 4-7. Spectral parameter E_0 used in the AP1 environment.
(See page 4-4 for definition.)

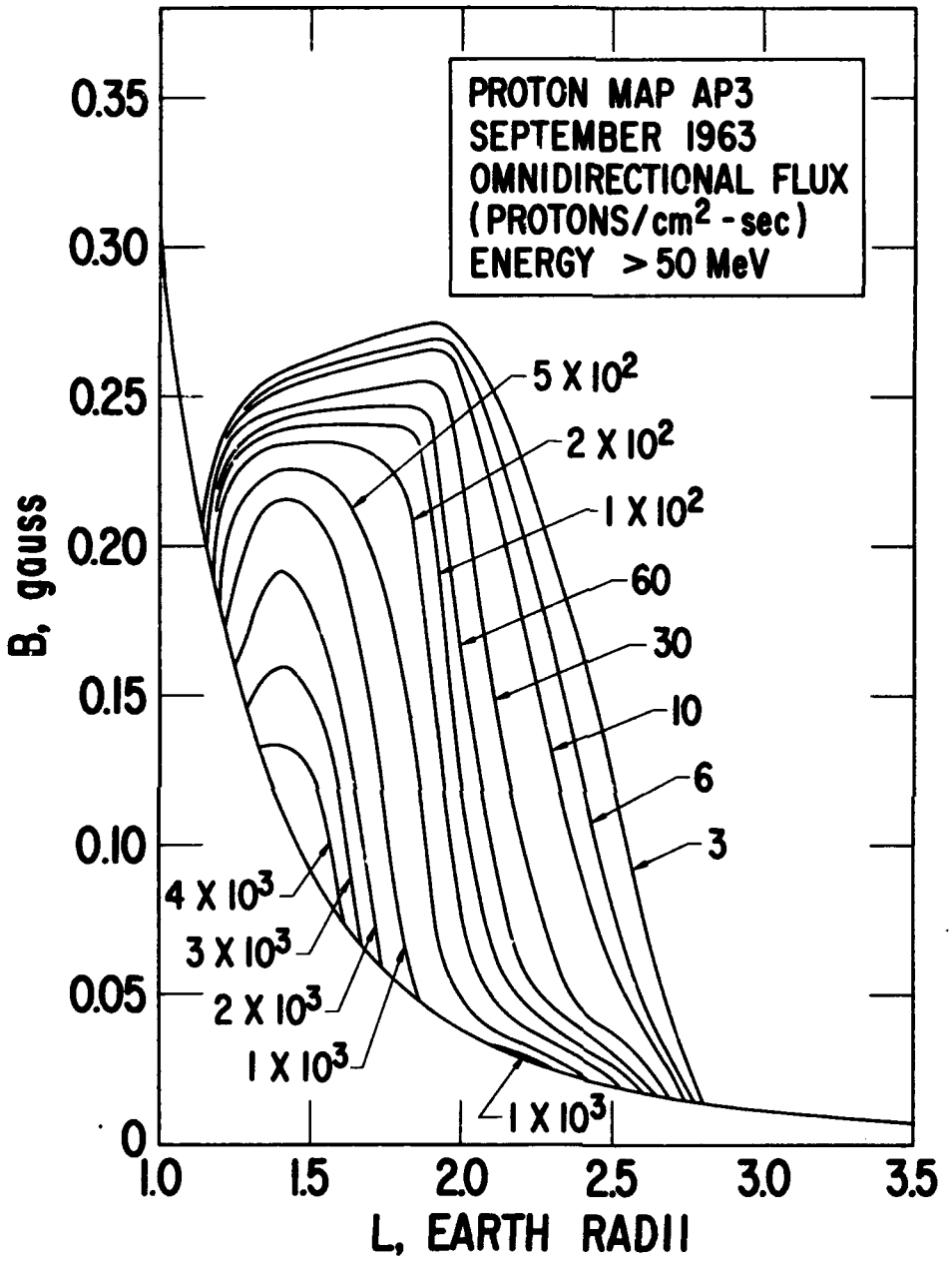

Figure 4-8. The B, L flux map of the AP3 environment for AP3 E_1 = 50 MeV.

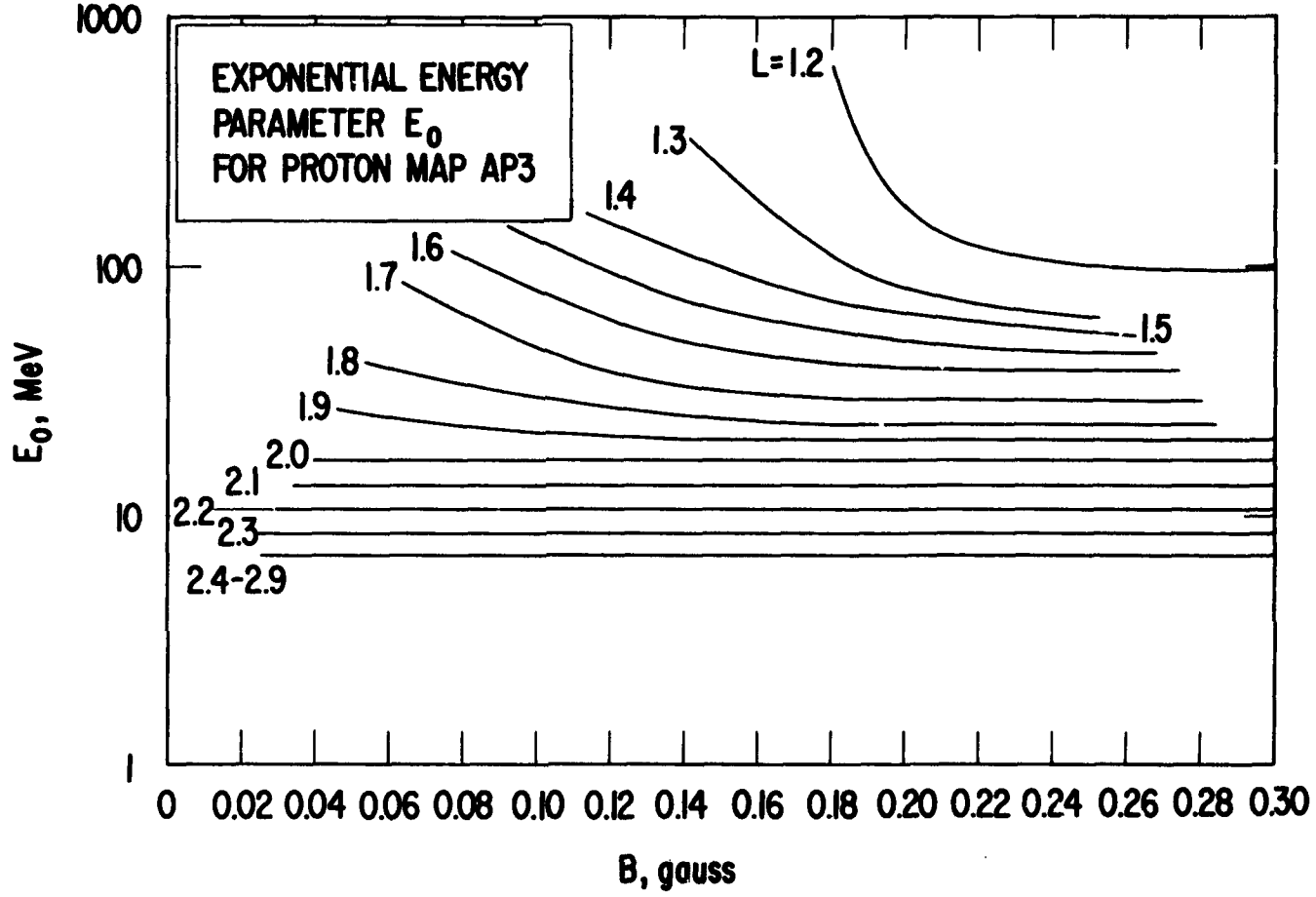

Figure 4-9. Spectral parameter E_0 used in the AP3 environment.
(See page 4-4 for definition.)

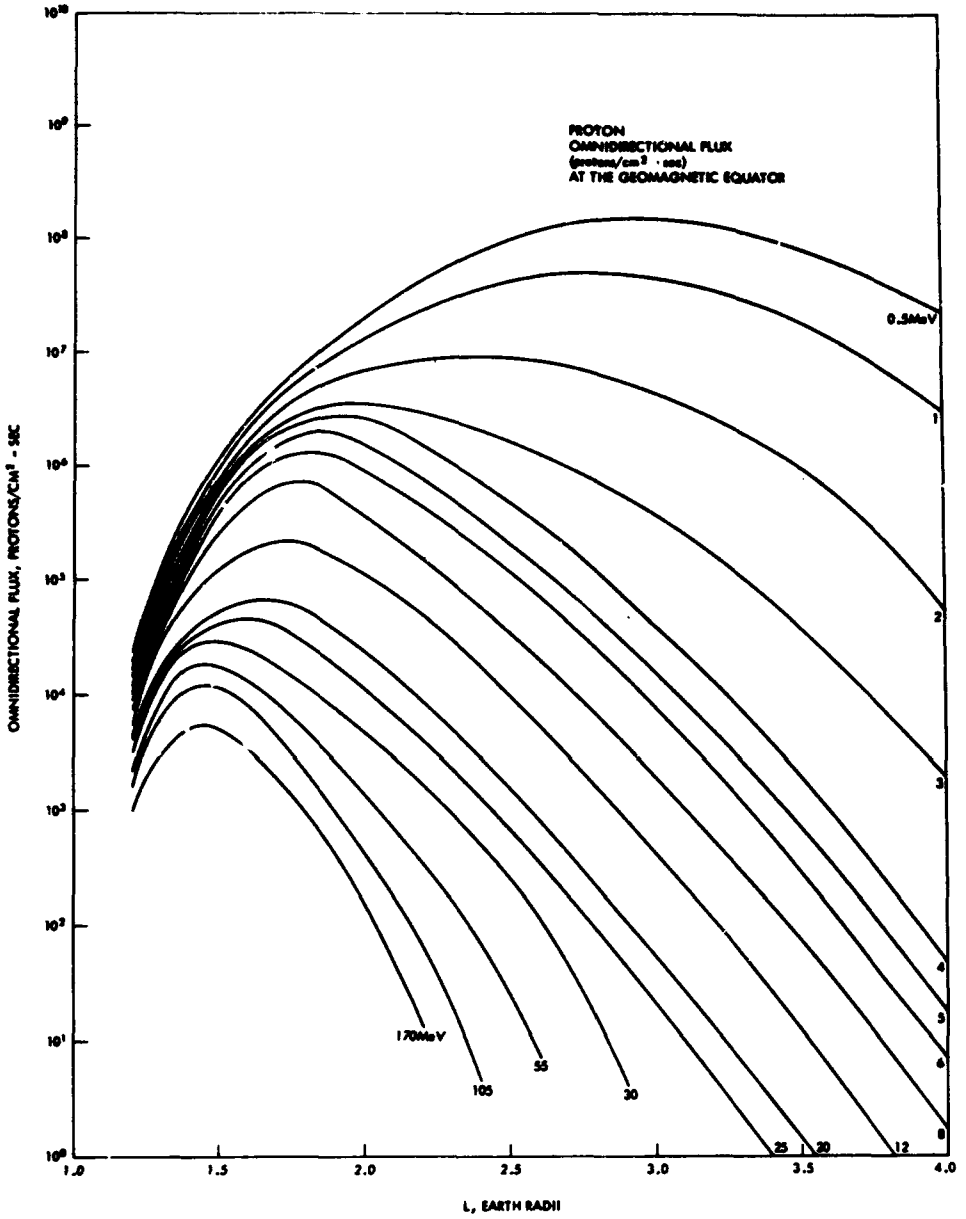

Figure 4-10. Equatorial, omnidirectional, proton flux profile.

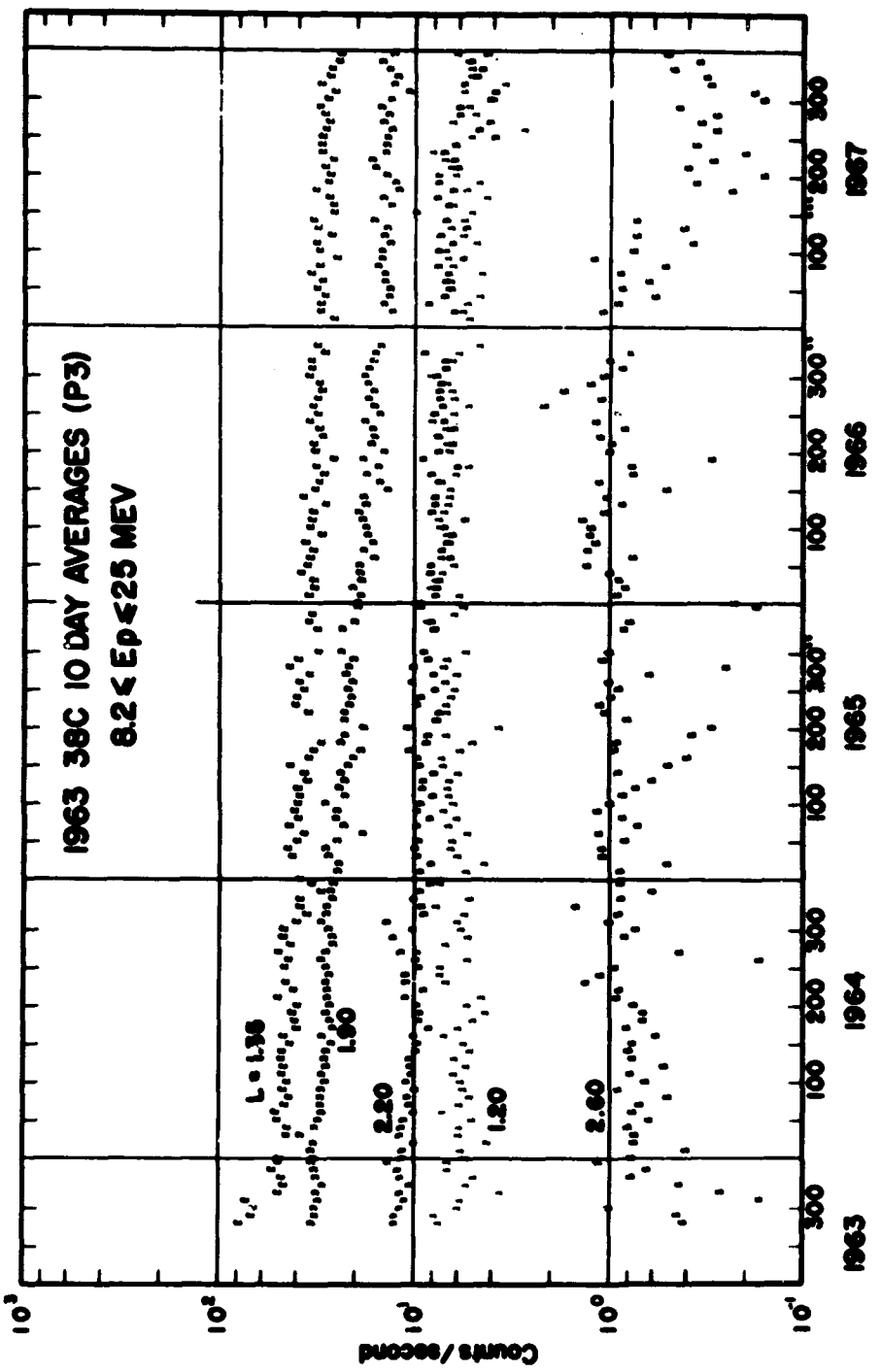

Figure 4-11. Time behavior of medium-energy protons (Reference 10).

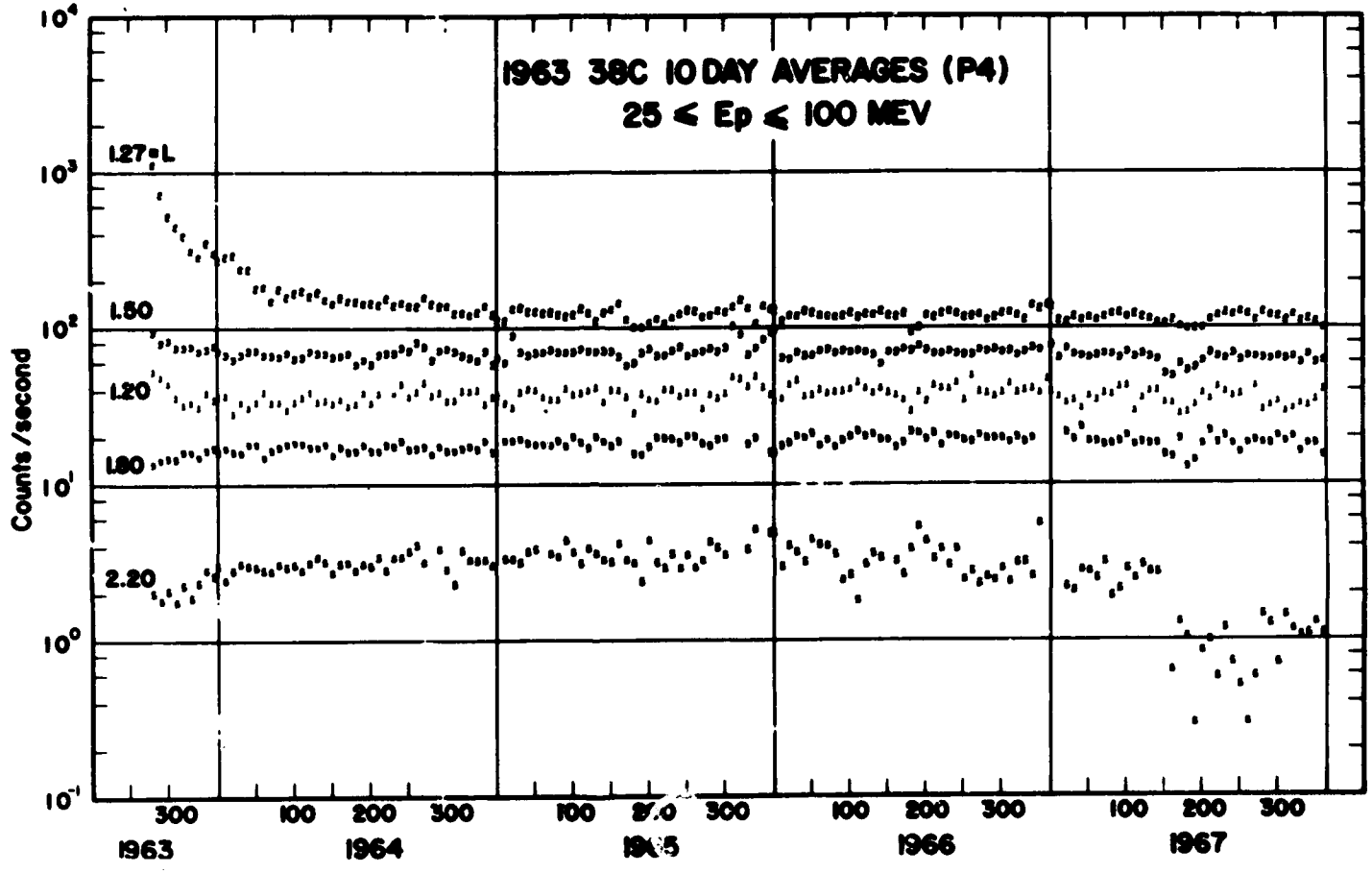

Figure 4-12. Time behavior of high-energy protons (Reference 10).

for L - 2.60. The minimum altitude for these intervals is high enough that atmospheric effects should not be important. Figure 4-12 contains results similar to those presented in Figure 4-11. The B-intervals for the various L-values are those given above for L = 1.2 and 2.2. For the other L-values, they are 0.16 to 0.17 gauss for L = 1.27, 0.19 to 0.20 for L = 1.5, and 0.20 to 0.21 for L = 1.8. The decrease at L = 1.27 during late 1963 and early 1964 has not yet been investigated in detail, but may be related to the 23 September 1963 magnetic storm.

Measurements of protons above 50 MeV have been very sparse near the equator. Consequently, the errors in the models may be larger than normal in this region. Recently, some detailed proton measurements from the OV3-4 satellite for energies above 15, 30, 55, 105, and 170 MeV have been presented (Reference 11). The three highest energy maps are shown in Figures 4-13, 4-14, and 4-15. The results of these three figures were obtained by the OV3-4 satellite and are in reasonable agreement with the models below 30 MeV. However, at the higher energies, about a factor of 3 difference exists in the equatorial regions. These new data are probably more correct above 40 MeV and should be used for estimating radiation damage effects until a new high-energy model can be generated. These newer data have been used in producing the equatorial radial profiles shown in Figure 4-10.

The electron population in the inner zone is somewhat more complicated than that for protons. On 9 July 1962, the Starfish Prime* nuclear detonation injected many energetic electrons into the region. Unfortunately, many experimenters prior to this event were unable to measure the electrons in the inner zone in the presence of the energetic protons. Consequently, little is known of the electron population prior to 1962. An electron model environment, AE1, was constructed from the data measured between January and September 1963 (Reference 7). This map is shown in Figure 4-16 for electrons >500 KeV and represents the electrons injected by the Starfish nuclear detonation. Although the lifetime of protons in the inner zone is many years, the effective lifetime of electrons is much less than this (Section 5). When they are injected into the radiation belts either by artificial means such as Starfish or by natural events, the electrons are observed to decay approximately exponentially with time.

* The Starfish Prime event on 9 July 1962 is referred to as the Starfish event throughout the remainder of this handbook.

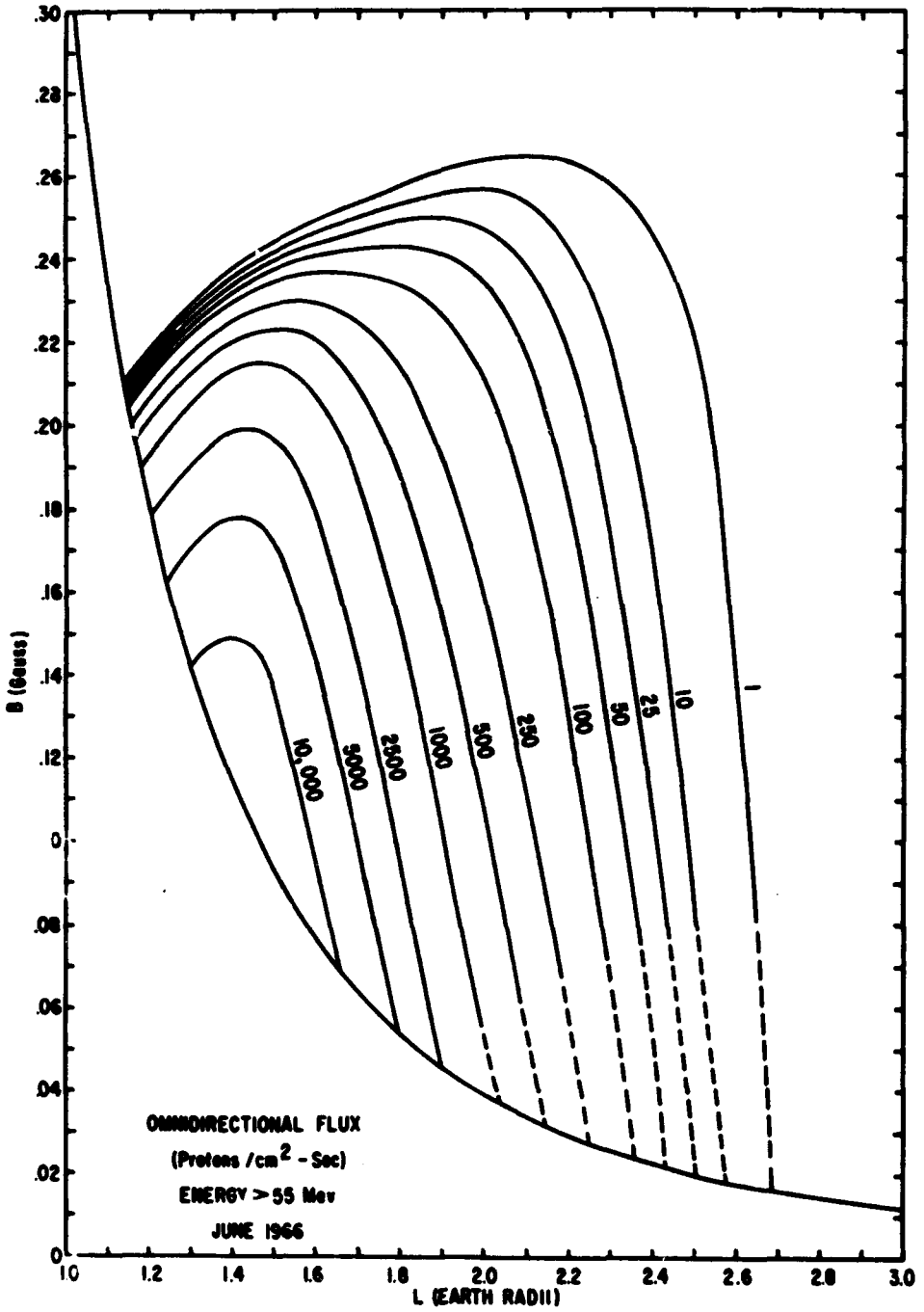

Figure 4-13. Omnidirectional proton B, L flux map for E > 55 MeV from OV3-4 measurements (Reference 11).

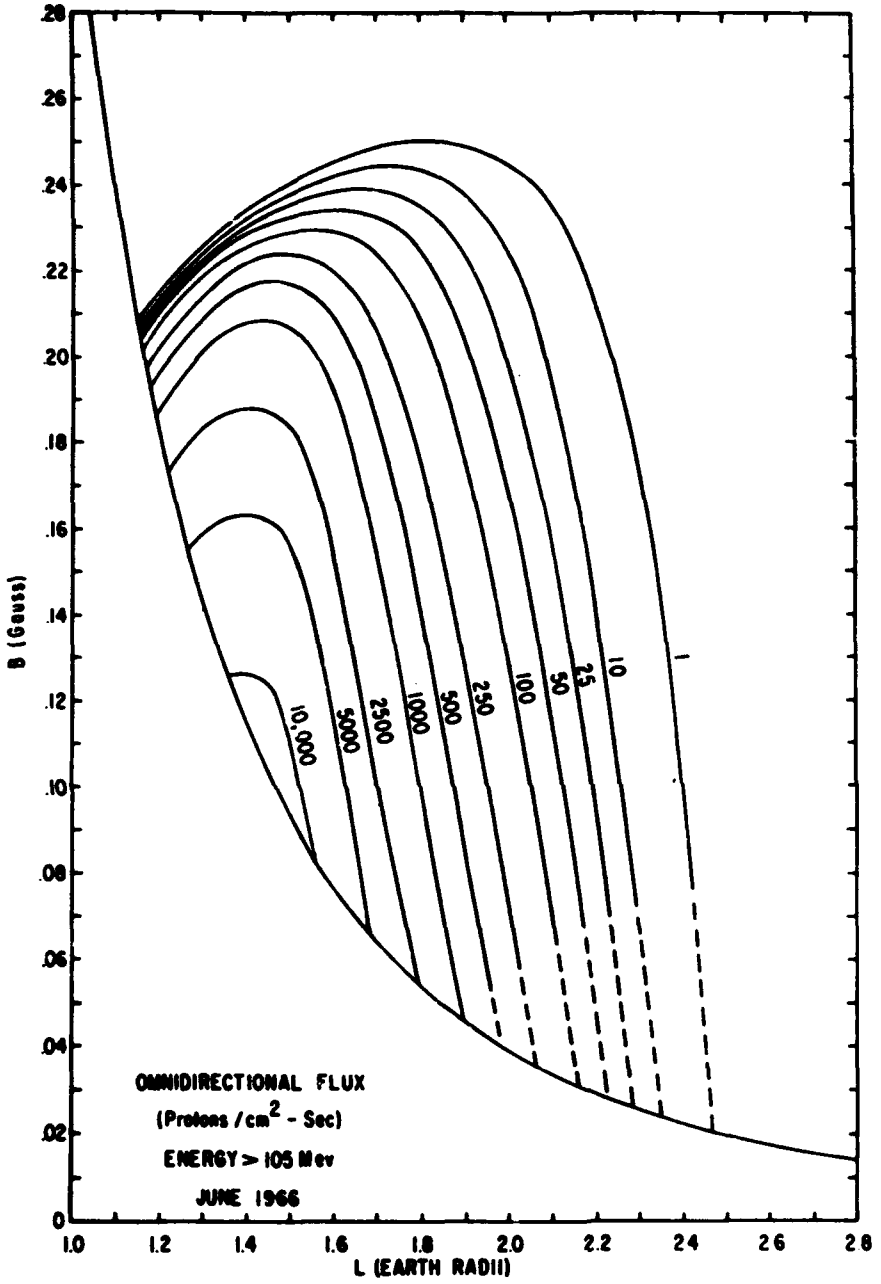

Figure 4-14. Omnidirectional proton B, L flux map for E > 105 MeV from OV3-4 measurements (Reference 11).

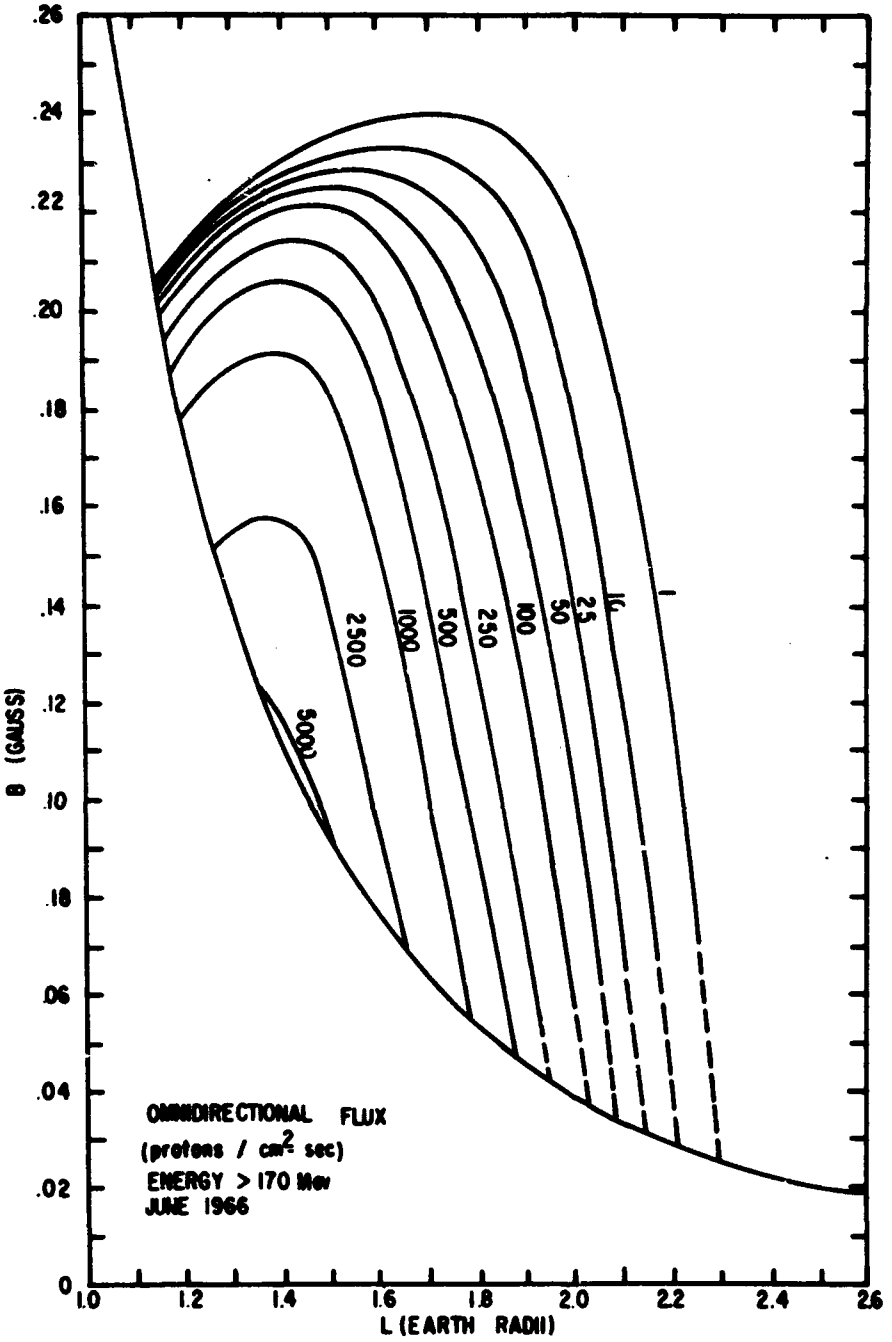

Figure 4-15. Omnidirectional proton B, L flux map for E > 170 MeV from OV3-4 measurements (Reference 11).

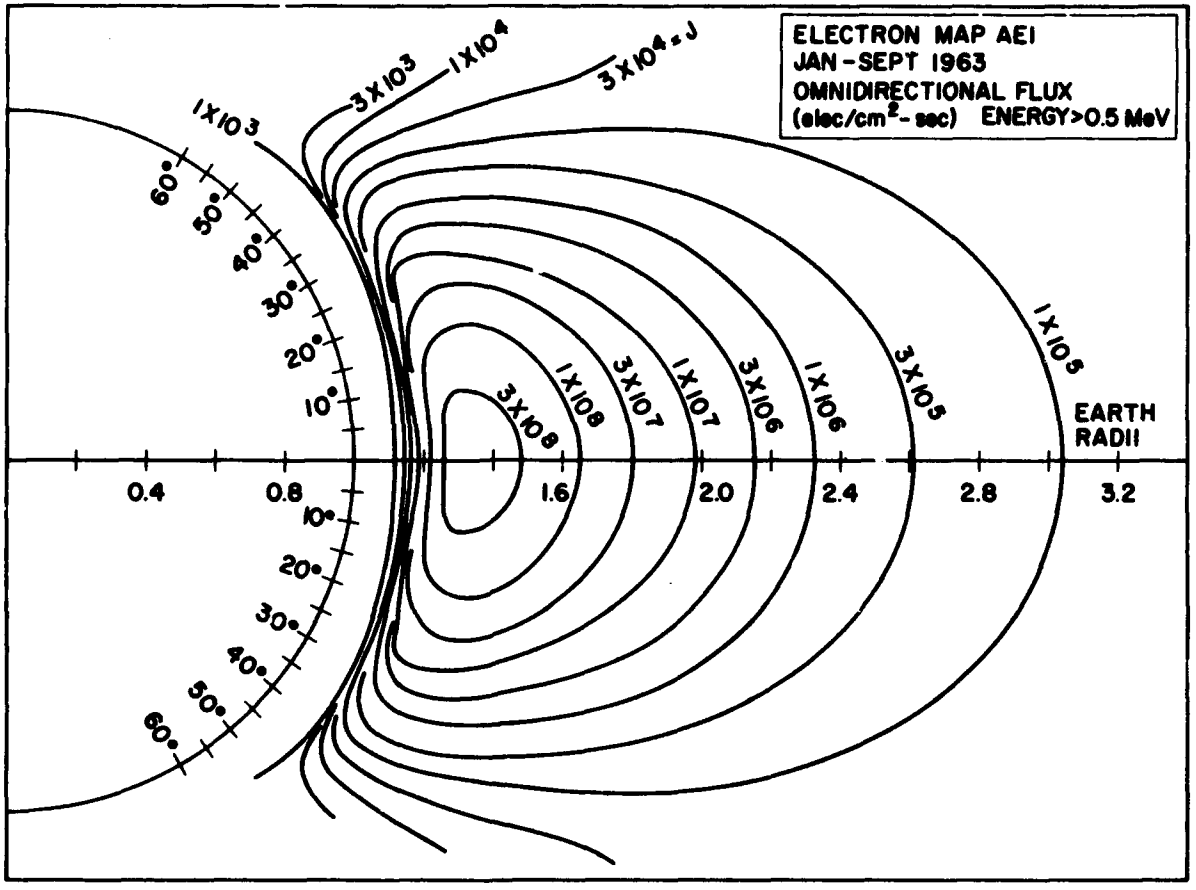

Figure 4-16. Post-Starfish electron flux map.

Walt (Reference 12) has compiled the electron lifetime obtained by various experiments. The results are shown in Figure 4-17. References to the individual measurements shown in the figure can be obtained from Reference 12. The theoretical curve by Walt assumes atmospheric scattering as the only loss mechanism. The lifetimes are approximately 300 days in the heart of the inner zone. In fact, the rapid drop in lifetime around L = 1.8 may be largely responsible for the production of an inner electron zone. The rapid fall off at lower L-values is caused by the increasing density of the earth's atmosphere. The solid curve represents the theoretical lifetimes obtained by Walt due to pitch angle scattering of the electrons produced by Coulomb interactions with the atmospheric atoms. This process is the dominant one at low L-values. However, above L = 1.25, other processes that are not well understood theoretically must become dominant. A discussion of these processes is given in Section 5.

Empirically, the long-term decay of the Starfish electrons is shown in Figures 4-18 and 4-19. In Figure 4-18, the points are 10-day averages of measurements by Bostrom and co-workers in selected B-intervals. These intervals for each L-value have been given in Section 4.2 A measurement of D_{st} for large magnetic storms is given near the bottom of the figure. At L = 2.20, the response to magnetic storms is quite apparent. The results in Figure 4-19 are similar to those given in Figure 4-18. The B-intervals not already given are 0.165 to 0.175 gauss for L = 1.3, 0.18 to 0.19 for L = 1.4, and 0.195 to 0.205 for L = 1.6. No discernible changes occur in conjunction with magnetic storms. The electrons > 1.2 MeV have decayed monotonically since the detonation. The same is not true of the lower energy electrons. Although the general behavior is one of exponential decay, definite increases occurred during the large magnetic storms in September 1966 and May 1967. Pfitzer and Winckler (Reference 13) have observed these same increases for electrons > 690 KeV. Based on these latest observations, large magnetic storms appear to produce electrons with energies not exceeding 700 KeV in the inner radiation zone. Thus, all higher energy electrons present are the residue of Starfish.

At much lower flux levels, electrons up to 780 KeV must be produced by neutron decay. Beall and co-workers (Reference 14) report increases in the electron flux > 0.28 MeV between October 1963 and March 1964. As will be seen when the outer zone is discussed,

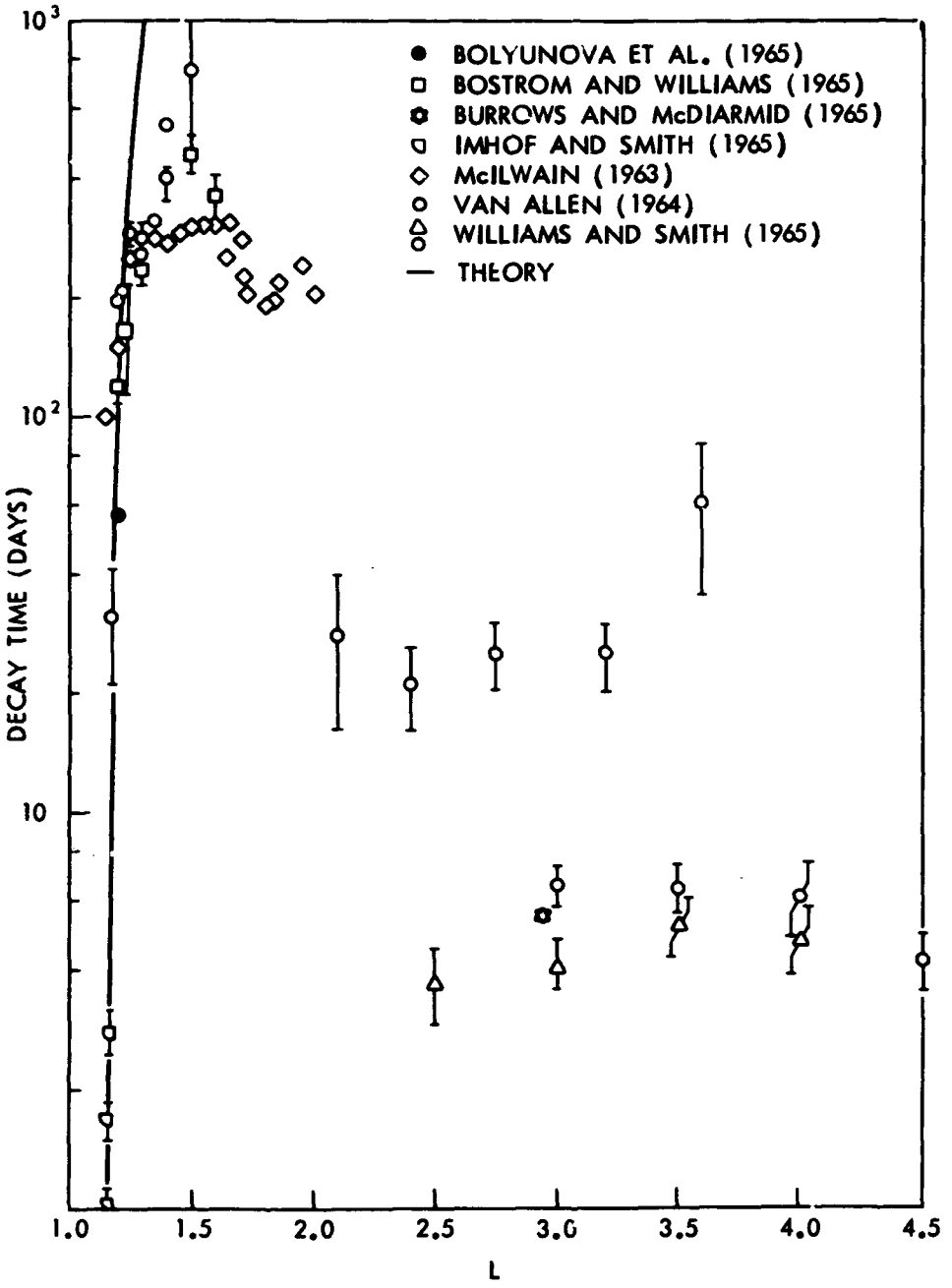

Figure 4-17. Lifetime of electrons in the radiation belts (Reference 12).

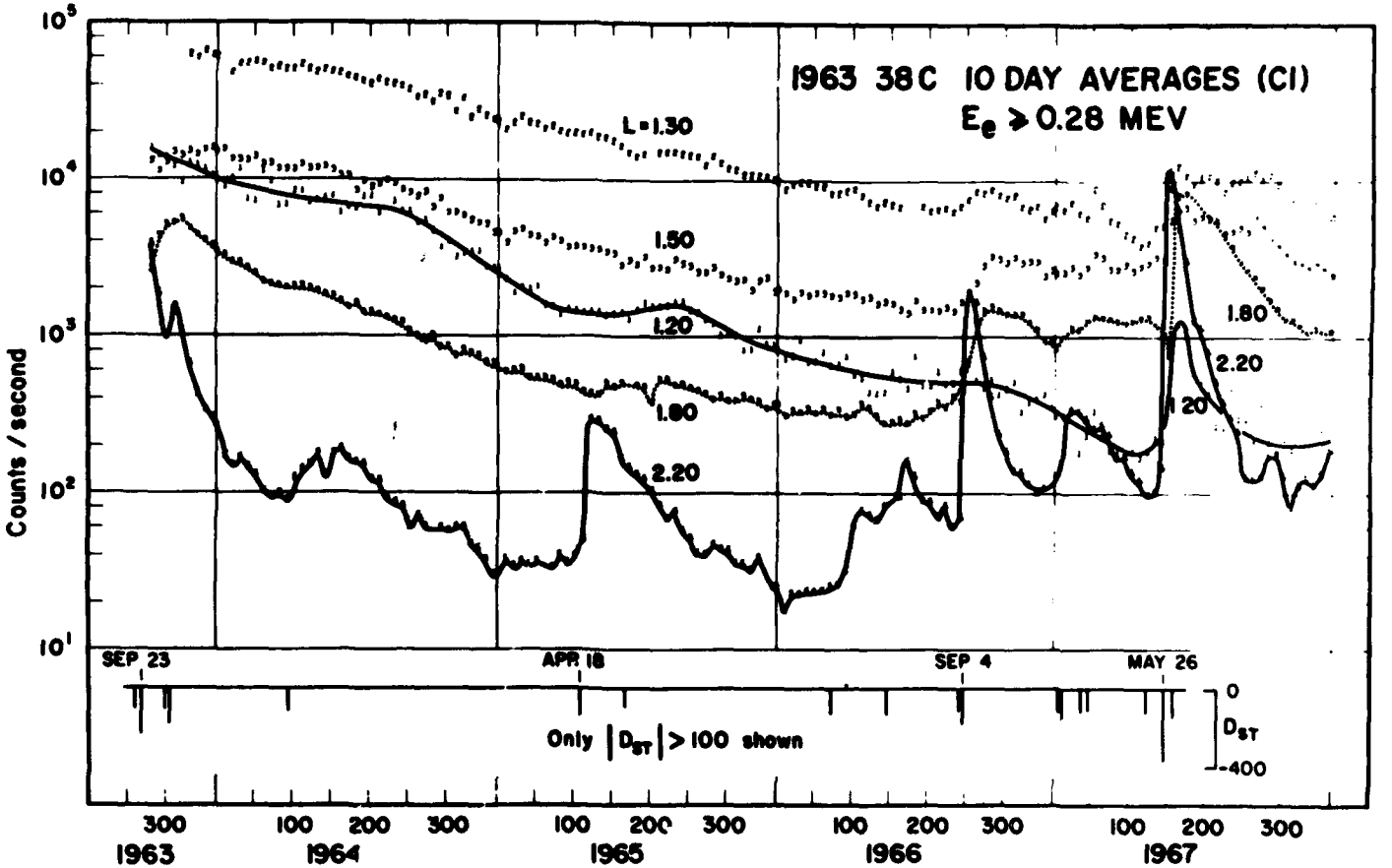

Figure 4-18. Time behavior of >280-KeV electrons (Reference 12).

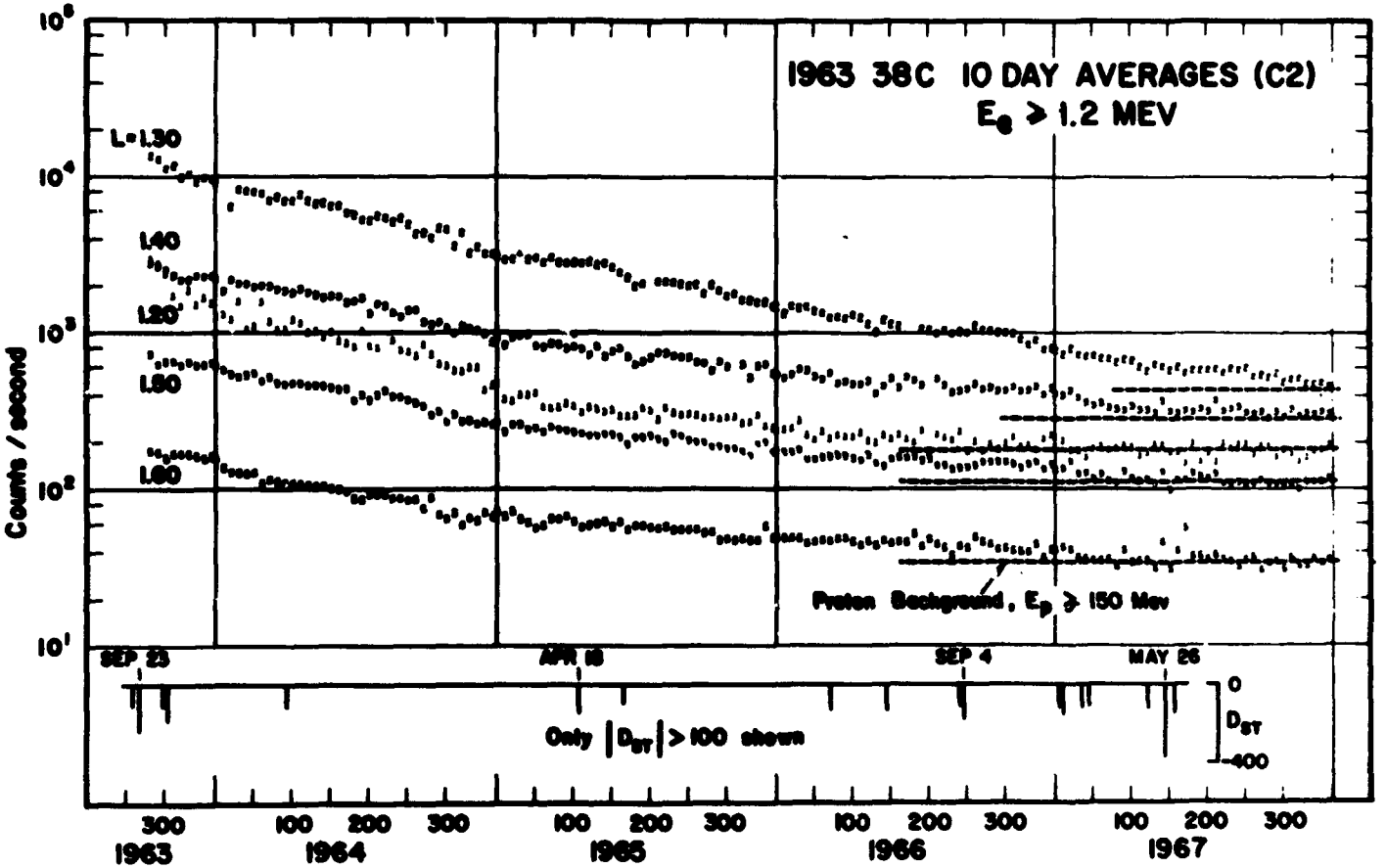

Figure 4-19. Time behavior of >1.2-MeV electrons in the inner radiation zone (Reference 12).

electrons of all energies change rapidly with time in response to magnetic perturbations. However, only the large perturbations produce effects on the inner-zone electrons. Between 1963 and 1966, the electrons injected by Starfish dominated the whole inner-electron zone. By mid-1966, however, electrons below 700 KeV had decayed to the point where natural effects became apparent. For higher energies, the electrons continue to decay.

The latest model electron environment to be produced is AE2 for the epoch August 1964. This environment is similar to the proton environments discussed earlier. However, the energy spectrum is presented as a tabular function in E and L since the B-dependence of the electron spectrum is very small. Thus:

$$J(> E, B, L) = F(B, L)\, N(> E, L) \quad . \tag{4-3}$$

The functions F(B, L) and N(E, L) are presented in Figures 4-20 through 4-23. N(E, L) is normalized so that:

$$\int_{0.5\ \mathrm{MeV}}^{\infty} N(E, L)\, dE = 1 \quad .$$

The points are experimental data used in constructing the environment. More details of this model are given in Reference 15. The slot and outer-zone portions of AE2 will be discussed in following sections.

The inner-zone portion of AE2 may be altered as a function of time using the observed decay constants. This is done by assuming that the decay is independent of energy. The value of decay constants that have been used by Stassinopoulos (Reference 16) in existing computer programs is shown in Table 4-1. However, to be precise, one should point out that the decay is energy-dependent over the L-range observed by Beall and others (Reference 14), with the higher energy particles decaying faster. This probably is caused by a diffusion of the particles across field lines as discussed in Section 5. Below L = 1.35, the decay is also B-dependent. The values of τ_2 were derived from the data presented by Beall (Reference 14); those of τ_1 were derived from a projected electron environment for December 1968 that was presented by Vette and others (Reference 15). This projected environment used data from Reference 14, but attempted to extrapolate in time in a slightly different fashion.

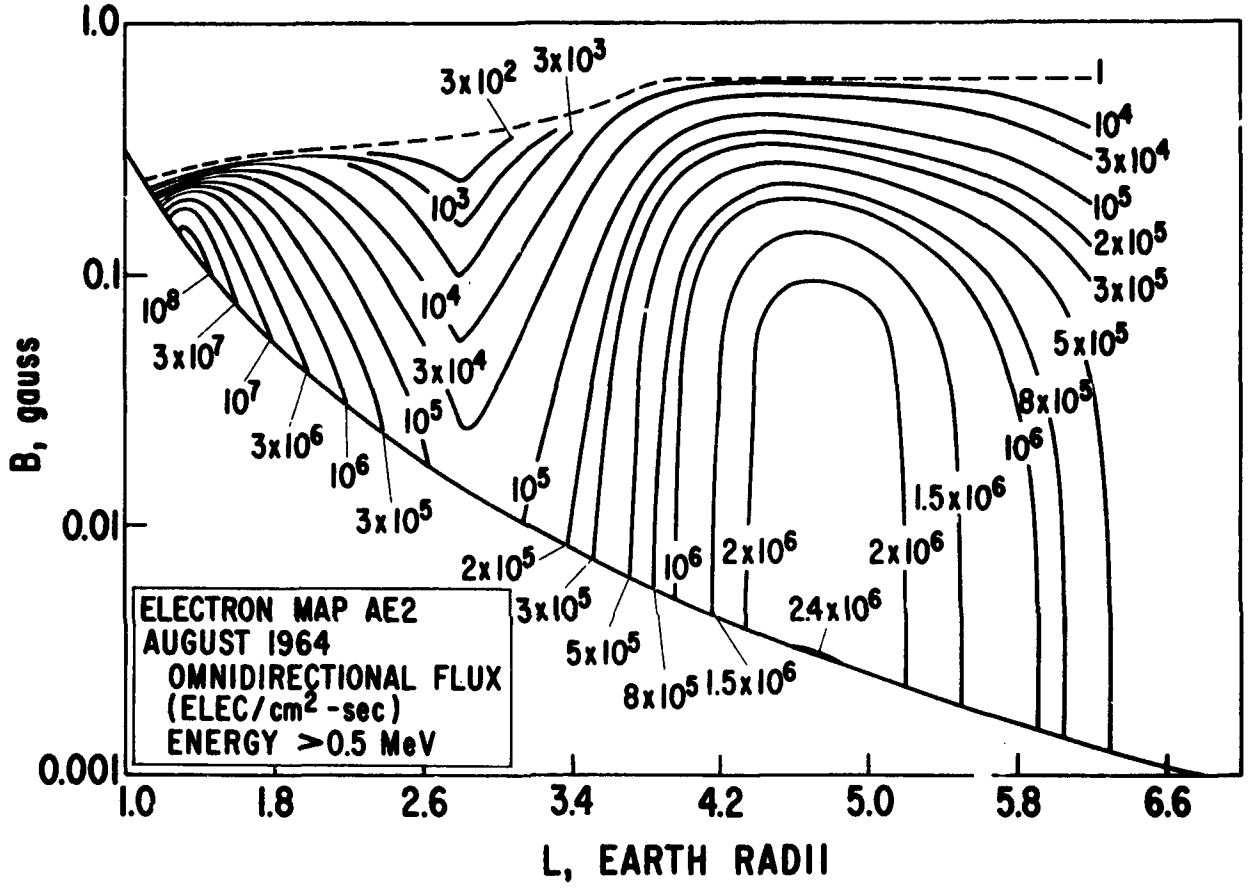

Figure 4-20. Log B, L flux map of the AE2 environment for AE2 E_1 = 0.5 MeV.

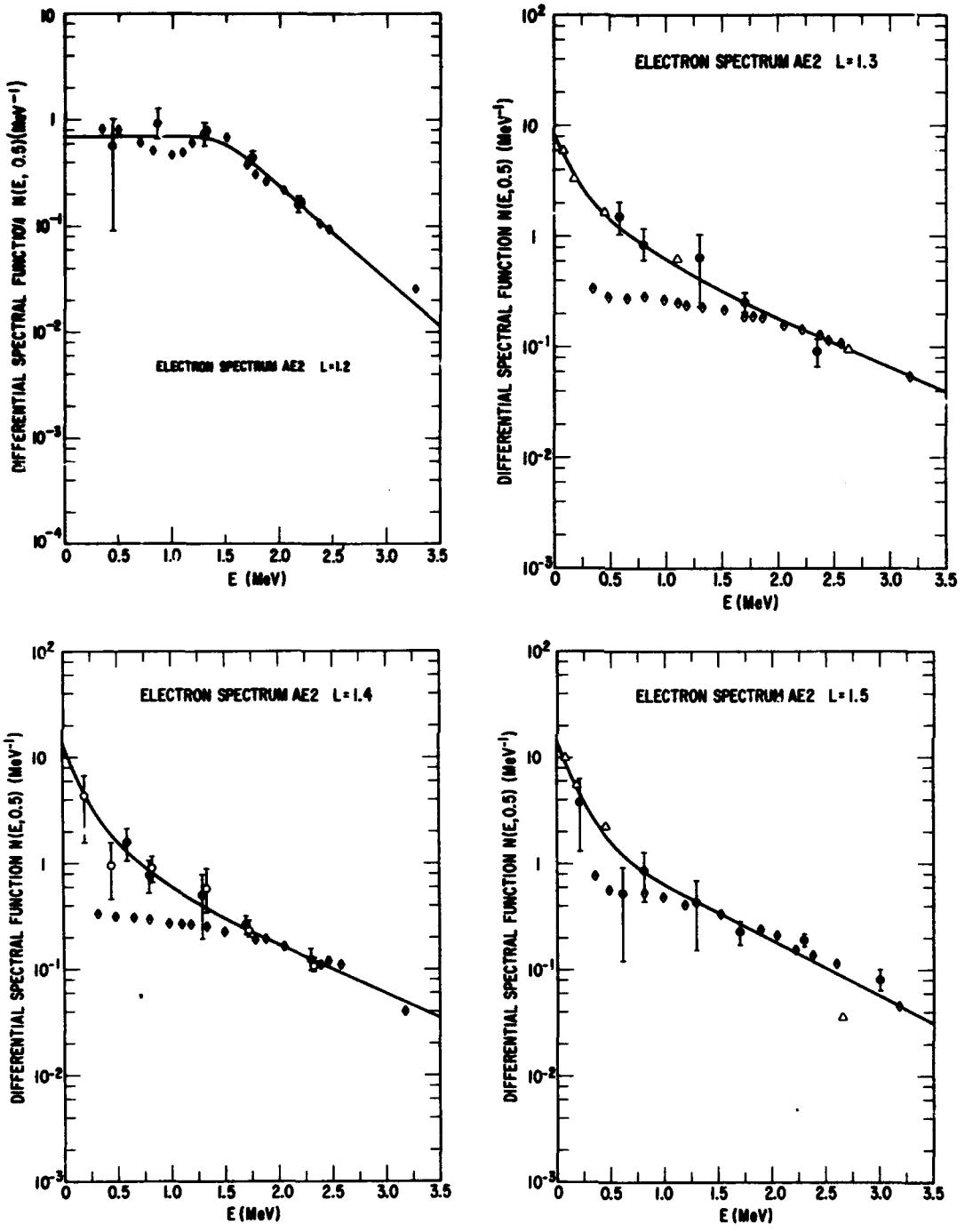

Figure 4-21. Differential spectral function N(E, L) used in the AE2 environment.

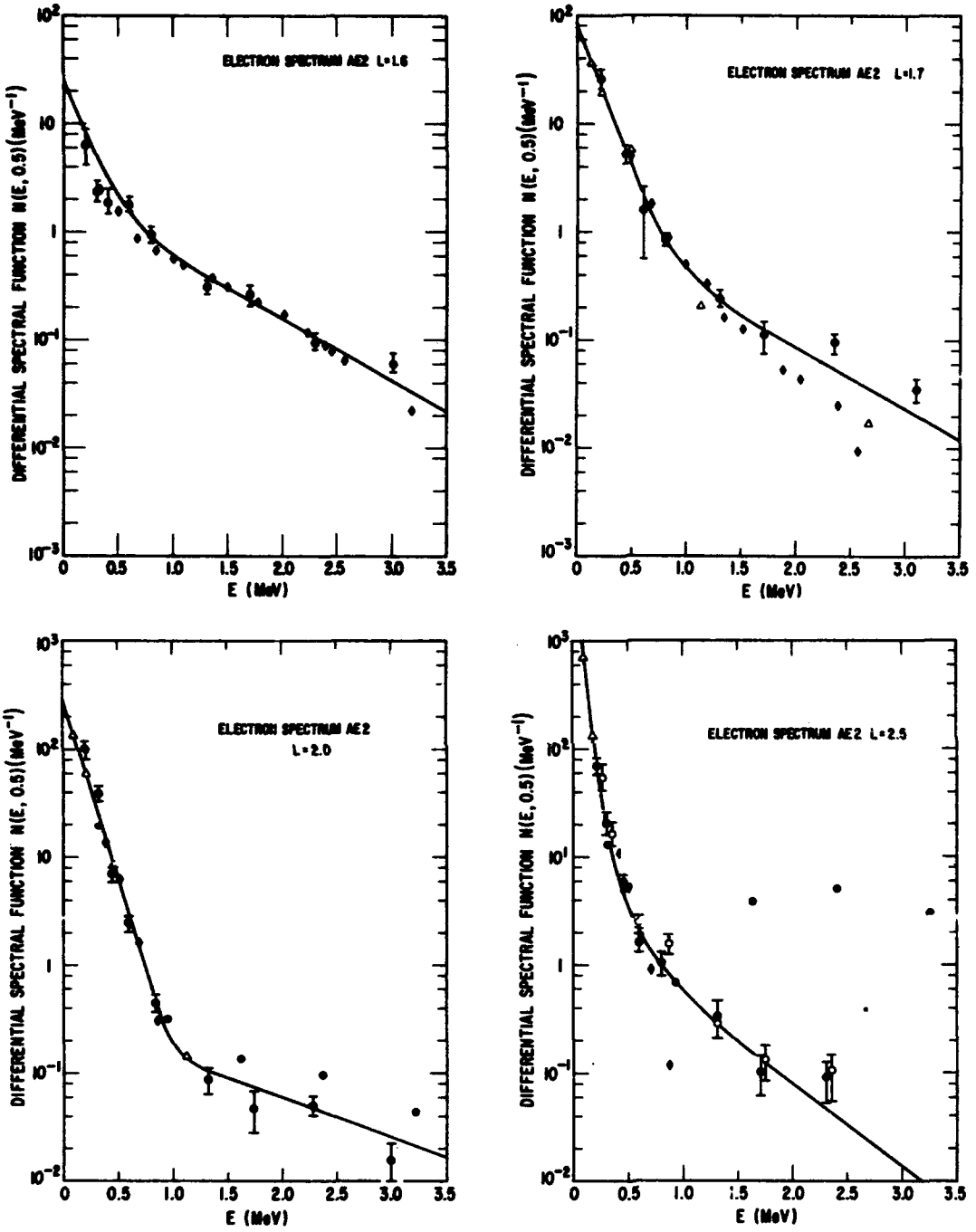

Figure 4-22. Differential spectral function N(E, L) used in the AE2 environment.

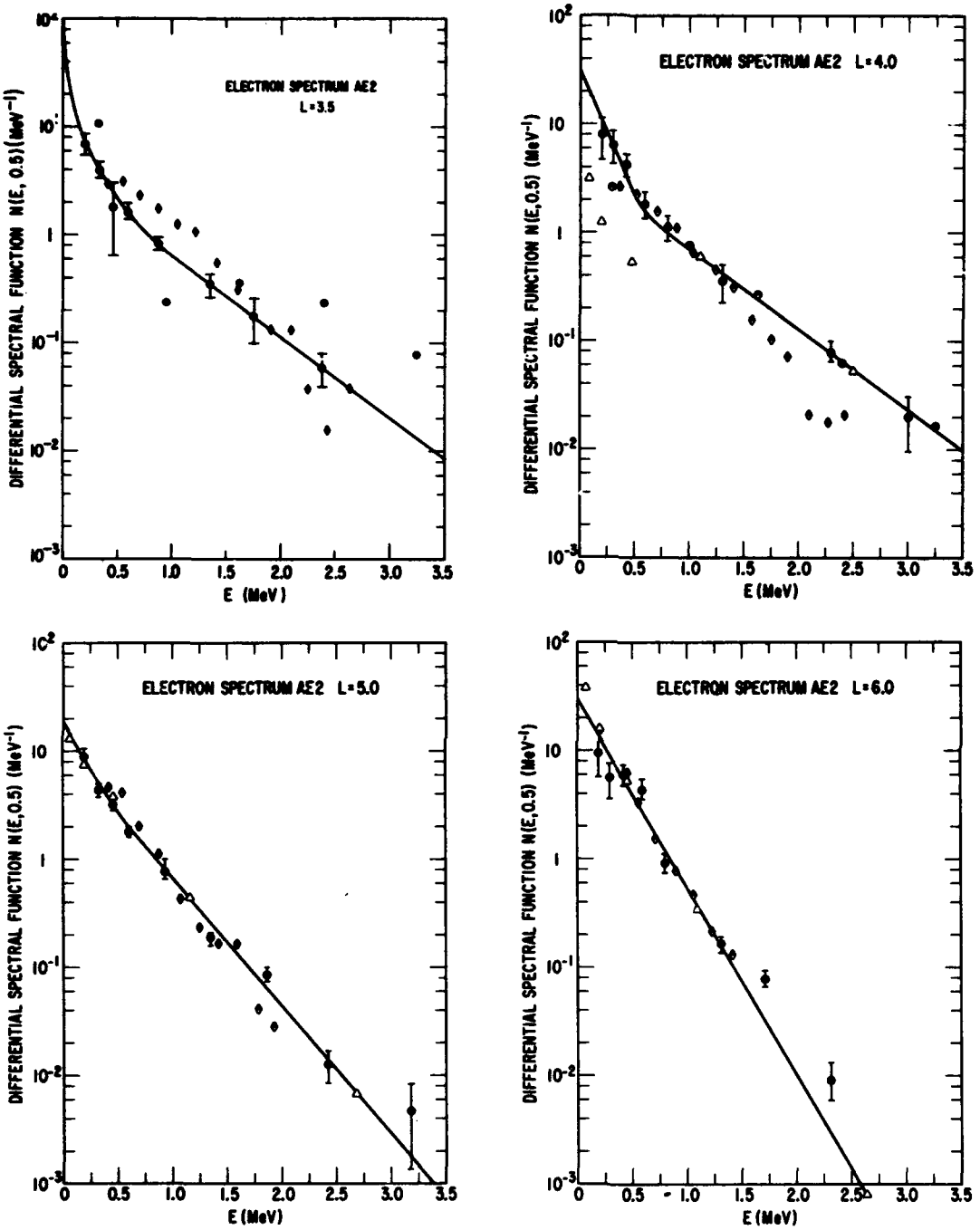

Figure 4-23. Differential spectral function N(E, L) used in the AE2 environment.

Table 4-1. Electron decay constants.

L (R_E)	τ_1 (days)	τ_2 (days)
1.15	75	50
1.17	300	155
1.18	328	190
1.20	356	230
1.23	373	273
1.25	382	295
1.27	388	325
1.30	396	352
1.35	404	386
1.40	412	410
1.45	418	431
1.50	429	443
1.55	460	447
1.60	686	452
1.65	970	488
1.70	1457	2000
1.75	3000	10^6
1.80	10^6	10^9

Because of these complexities, the best way to obtain a good model is to put all the data in a fixed time period. This work is in progress for a later time period than AE2, but it is not available at the present time. Since the number of magnetic storms that affect the inner zone is small, one cannot use a statistical treatment that does seem feasible for the outer zone. For those inner-zone electrons > 700 KeV, an exponential decay continuing to near-zero flux levels seems appropriate.

4.3 SLOT REGION

The slot region derives its name from an examination of the electron radial profiles. These profiles are shown in Figure 4-24. The curves in the figure were obtained from the electron model environment AE2 for the epoch August 1964. Decay of the fluxes below L = 2.0 has been considerable since that time. However, the general character of an inner and outer zone with a slot region in between still prevails. A minimum exists at all electron energies. It generally lies between L = 2.0 and 3.0. The position of this minimum is known to vary with the solar activity cycle. Frank and Van Allen (Reference 17) presented results based on their own measurements between 1958 and 1964. Vernov and co-workers (Reference 18) have given the L-value of this minimum for a more extensive set of satellites, including those of Frank and Van Allen. These results are presented in Figure 4-25 along with the L-position of the electron intensity maximum of the outer radiation zone. The figure shows the change of these parameters in going from near solar maximum into solar minimum conditions. The numbers denote measurements obtained from these satellites: 1—Explorer 4; 2—Pioneer 3; 3—Explorer 6; 4—Luna 2; 5—Explorer 7; 6—Spaceship-satellite 2, 3; 7—Explorer 12; 8—Cosmos 4, 7, 9; 9—Explorer 15; 10—Injun 3; 11—Explorer 14; 12—1963 38C; 13—Electron 1, 2, 3, 4; 14—OGO-1; 15—Explorer 26 (Reference 18).

The low-energy protons between 0.1 and 4 MeV show a radial peak in the electron slot region, as can be seen in Figure 4-10. Thus, the slot region represents a minimum for electrons of all energies and a maximum for the low-energy protons. The more energetic protons also have their outer edge within this region. As discussed in Section 5, this edge is produced by the breakdown of trapping conditions where the gyro-radius of the proton is very large in the weaker geomagnetic field.

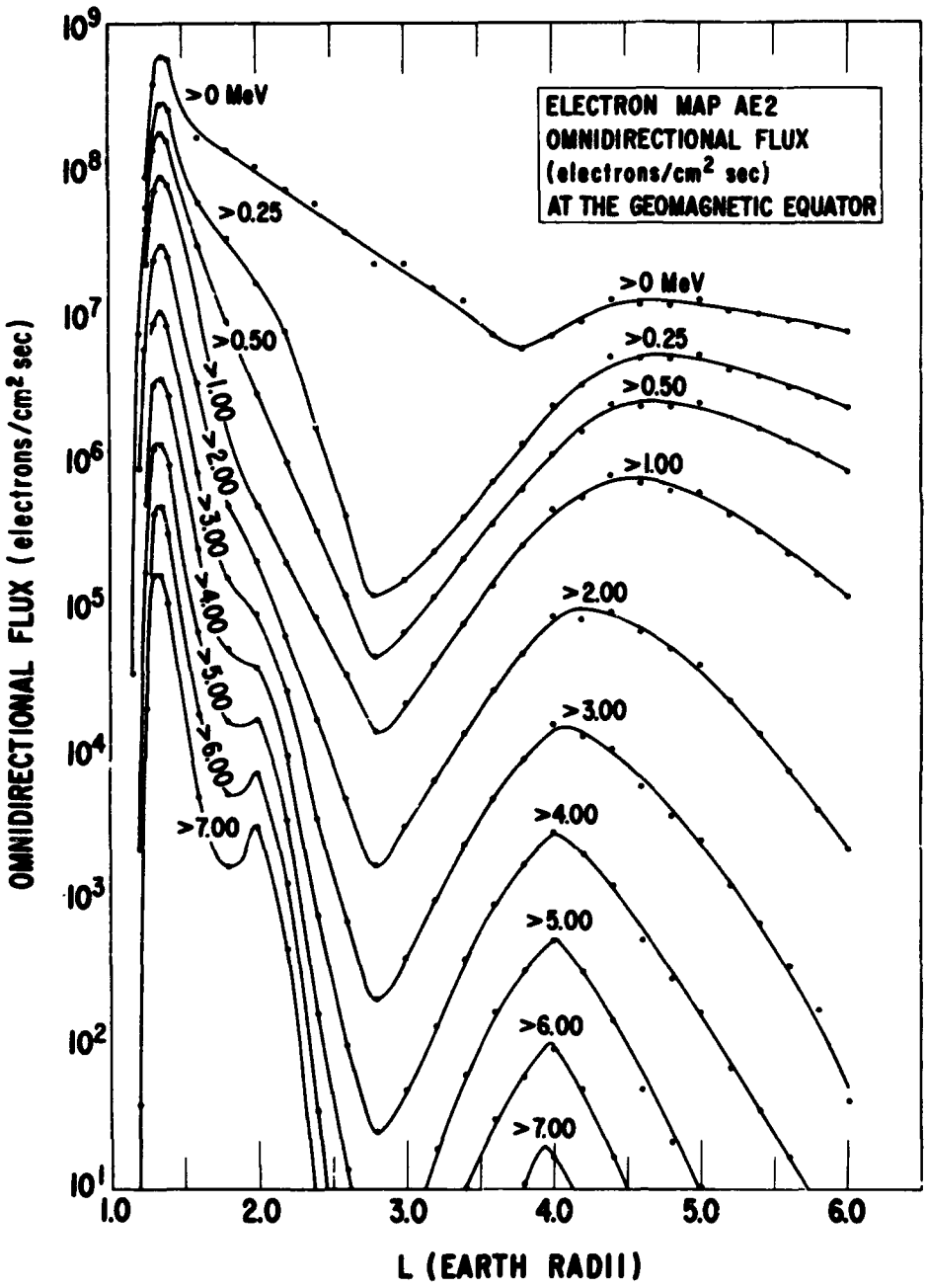

Figure 4-24. Equatorial, omnidirectional, electron flux profile.

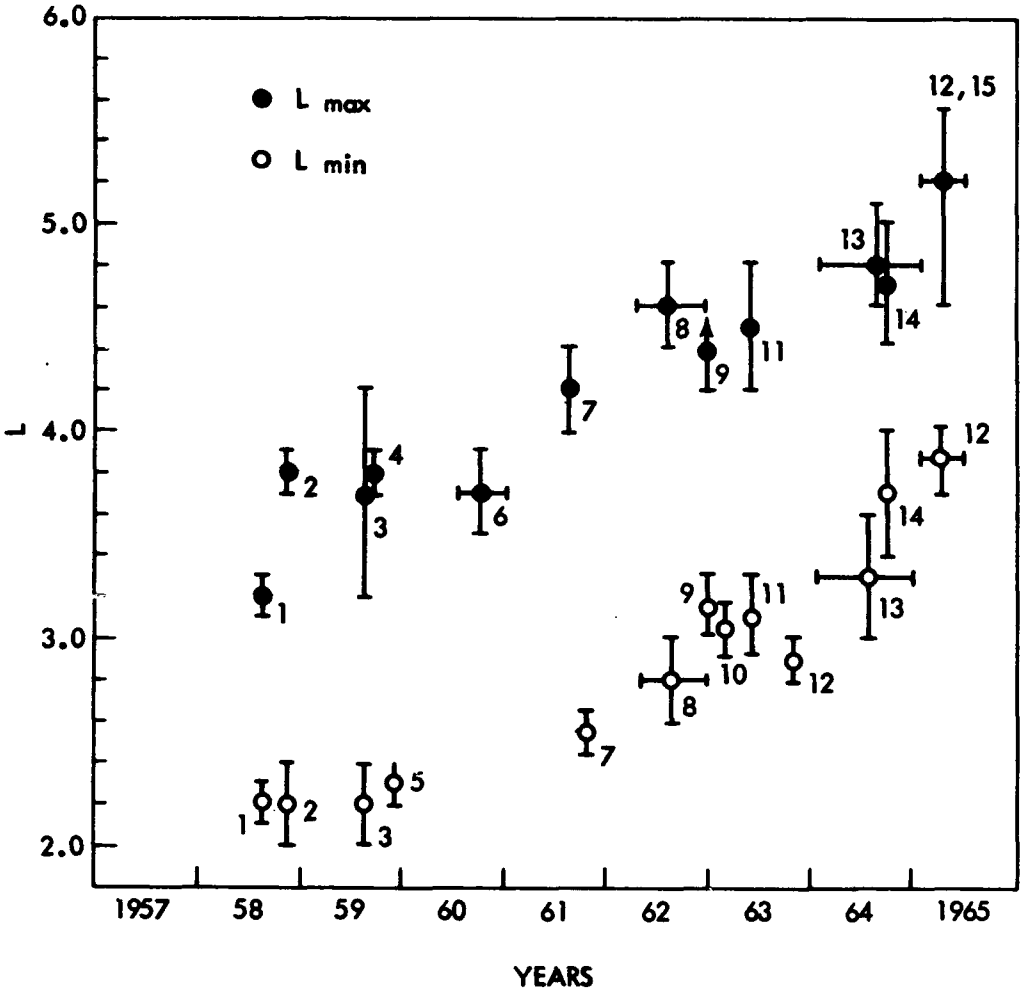

Figure 4-25. Position of the electron slot minimum and outer-zone maximum (Reference 18).

The time behavior of both protons and electrons becomes progressively more chaotic toward higher L-values. This can be seen by comparing the L = 2.2 curve in Figure 4-18 with the electrons at the lower L-shells. Fluctuations of protons in this region are much smaller than fluctuations of electons and do not occur as often. Large perturbations in the magnetic field produce changes even in the high energy proton distributions in this region. McIlwain (Reference 19) has reported on the redistribution of > 34 MeV protons during the 23 September 1963 magnetic storm. An example of the results are presented in Figure 4-26. This figure shows stable proton fluxes changed irreversibly during the 23 September 1963 magnetic storm. No effects occurred inside L = 1.8. For more details on this event, see Reference 19.

The long-term behavior of protons in the $2.2 \geq Ep \geq 8.2$ MeV range are shown in Figure 4-27. These are results similar to those presented in Figures 4-11 and 4-12. The B-interval for L = 3.0 is 0.225 to 0.245 gauss. The other intervals are defined in Section 4.2. The behavior of the protons is fairly steady until a large magnetic storm such as that in May 1967 perturbs the fluxes for several months. The main injection of protons of these energies occurs at L = 2.2, with depletions in the neighboring regions. Since these large events are rare, a static proton model in this region seems adequate for most work. However, the character of electrons is very similar to that in the outer zone and really should be handled in a statistical fashion.

4.4 OUTER RADIATION ZONE

This zone is considered to extend from L = 3.0 to the edge of the stable trapping region. This boundary of trapping extends out to 10 to 12 R_E at the subsolar point and to $\sim$ 7 R_E on the midnight side. However, because the magnetopause seems to be in constant motion, this boundary also moves in and out. In one extreme case, this trapping boundary moved in past 6.6 R_E on the sunward side (Reference 20). Of course, near the midnight meridian, the boundary does move in to 4.5 to 5.0 R_E on numerous occasions.

Although the average motion of the particles in this region is well understood by adiabatic motion in the distorted geomagnetic field, the dominant behavior is one of large time variations within a few weeks.

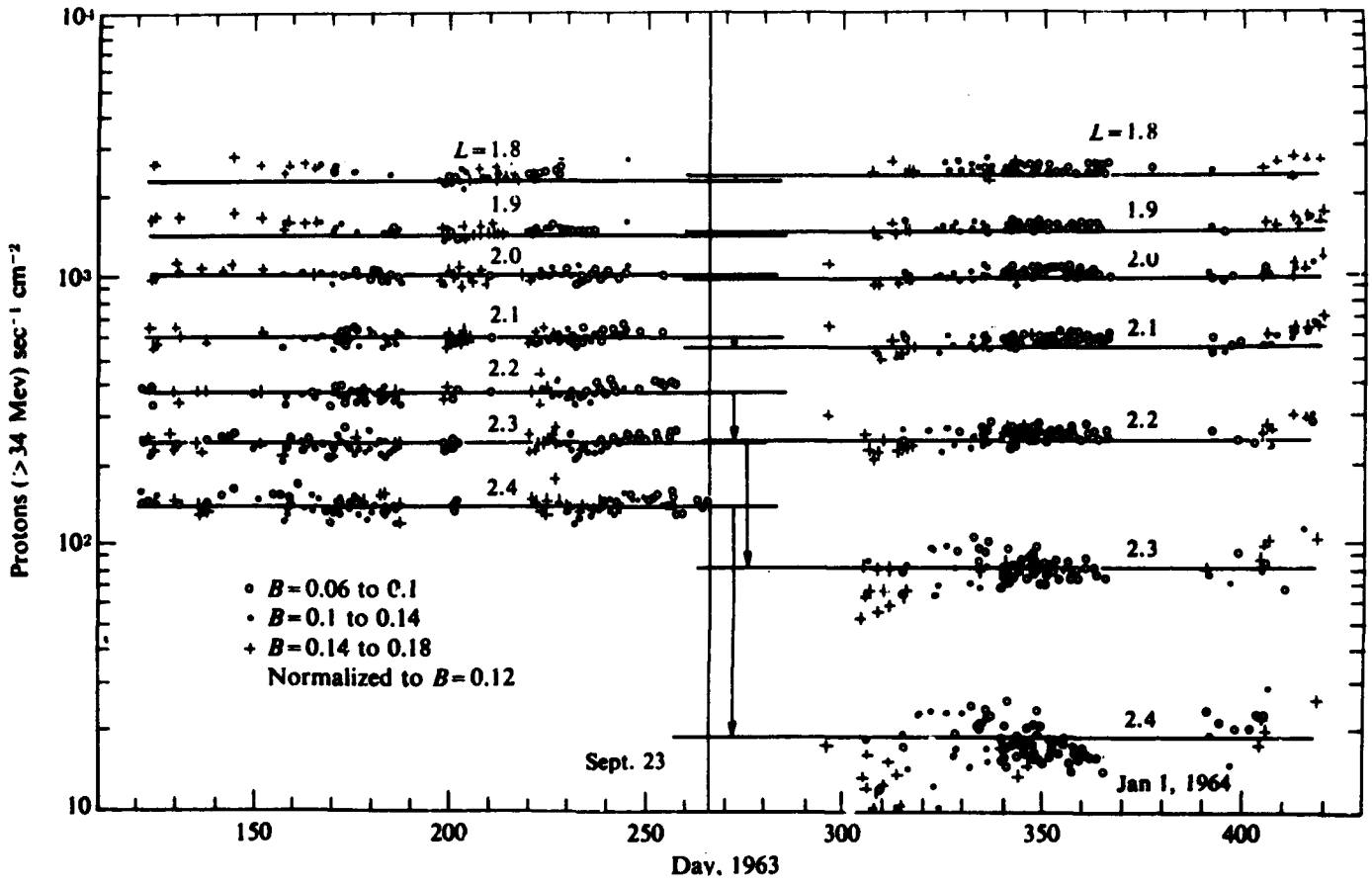

Figure 4-26. Nonadiabatic changes in the >34-MeV proton population that occurred during the 23 September 1963 storm (Reference 19).

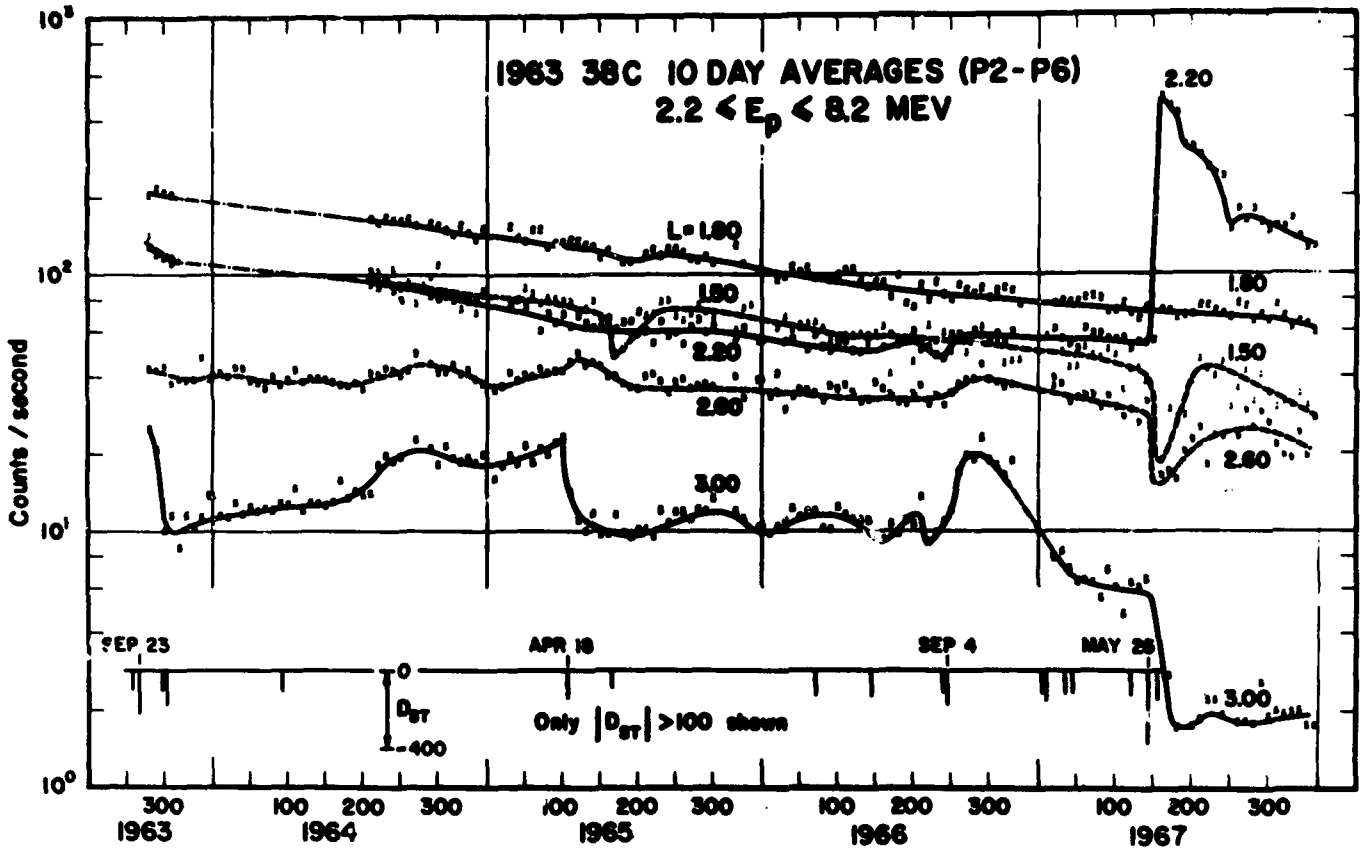

Figure 4-27. Time behavior of low-energy protons in the electron slot region. The initial increase at L=2.2 is contaminated by electrons which, 20 days later, have decayed to where they do not contribute to the count rate.

Electrons show much larger and more frequent changes than do protons. To illustrate this behavior, the electron flux ~ 300 KeV from two separate detectors during the first half of 1965 is given in Figure 4-29. The Explorer 26 measures particles near the equator while 1963 38C measures them at altitudes of 1,100 kilometers or very near the end of the field line (Reference 21). At L = 3.0 and 3.5, the Explorer 26 detector is contaminated by protons. On this time scale, the behavior of the two fluxes is similar. However, small time differences exist in the response of the electrons to magnetic perturbations. Below the data are plotted the D_{st} and Kp values. The character of the variations can be seen to be one of abrupt increases followed by approximately exponential decay. This is true all along the field line. As the L-value increases, one can see more time structure. In a gross sense, these changes are brought about by changes in the interplanetary plasma parameters. Changes also are observed in the magnetic field at the earth's surface and at satellite altitudes. The nearer the particles are to the boundary, the smaller the perturbations have to be to produce effects on the particle populations. The same conditions are true of the higher energy electrons as well, as can be seen in Figure 4-29. The results are similar to those shown in Figure 4-28. The increases are first observed well within the trapping region, and the electrons diffuse inward and outward. Particle loss occurs along the field lines by pitch angle diffusion. These particles eventually are lost into the atmosphere. A description of these loss patterns will be given in the section discussing low altitude.

An example of the time behavior of the protons that populate the outer zone (Reference 22) is given in Figure 4-30. These curves are for protons mirroring at the equator for eight integral energy measurements. The different curves are marked with letters running from A to H corresponding to the energies 98, 134, 180, 345, 513, 775, 1,140, and 1,700 KeV. The curves are displaced in order to avoid overlap, and the values read from the curves A to H must be multiplied by 10 raised to these exponents: -1.25, -1, -0.75, -0.50, -0.25, 0.25, 0.25, and 0.25 to get the integral intensity above a certain energy in protons $cm^{-2}\ sec^{-1}\ ster^{-1}$. Below the proton data are plotted hourly D_{st} values. This figure covers the same time period as that given in Figures 4-28 and 4-29 (Reference 22). One sees that the protons have much less change than electrons, although the effects are similar when changes do occur. The lower energy proton fluxes are increased during events whereas the higher energy fluxes show a depression and recovery. Part of the changes seen here represent the

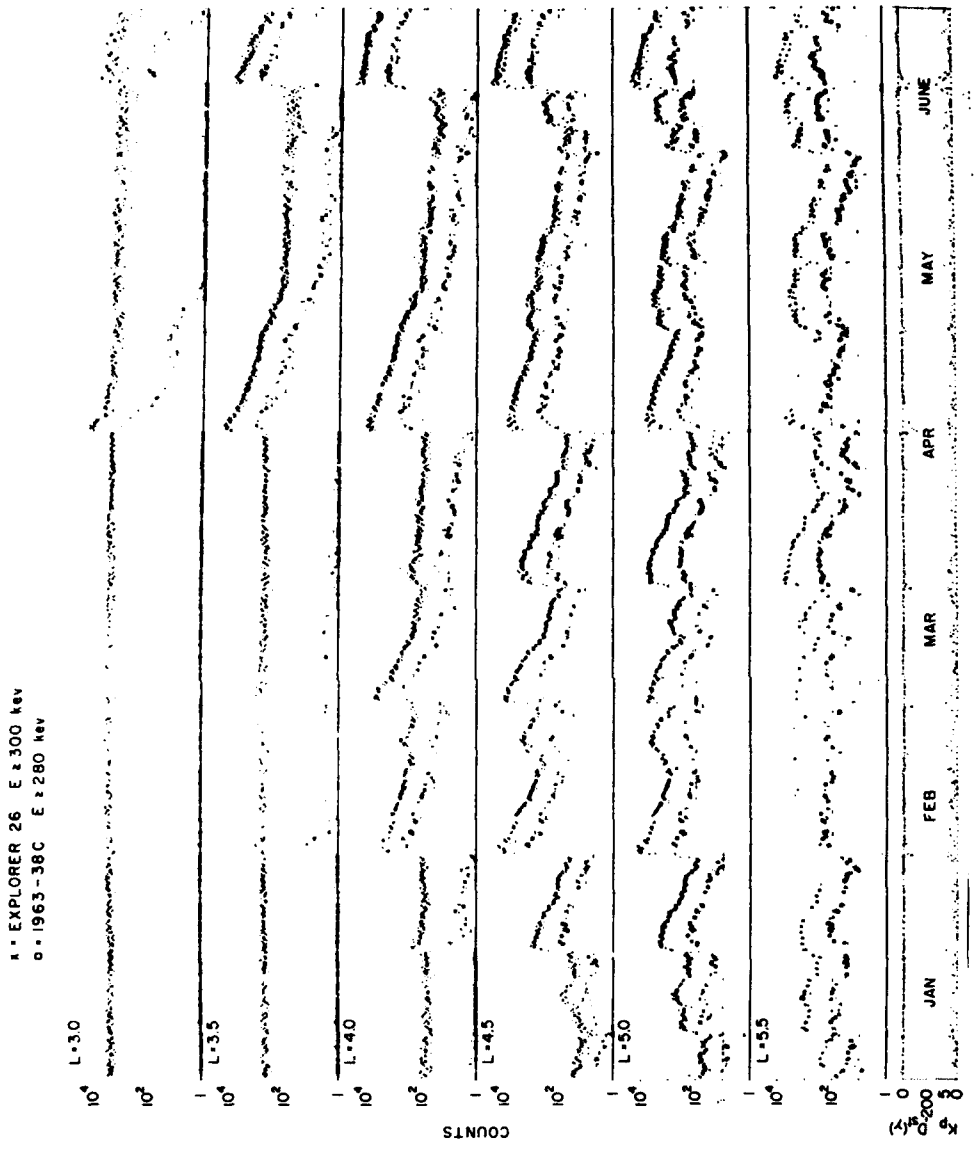

Figure 4-26. Time behavior of ~300-KeV electrons in the outer radiation zone (Reference 21).

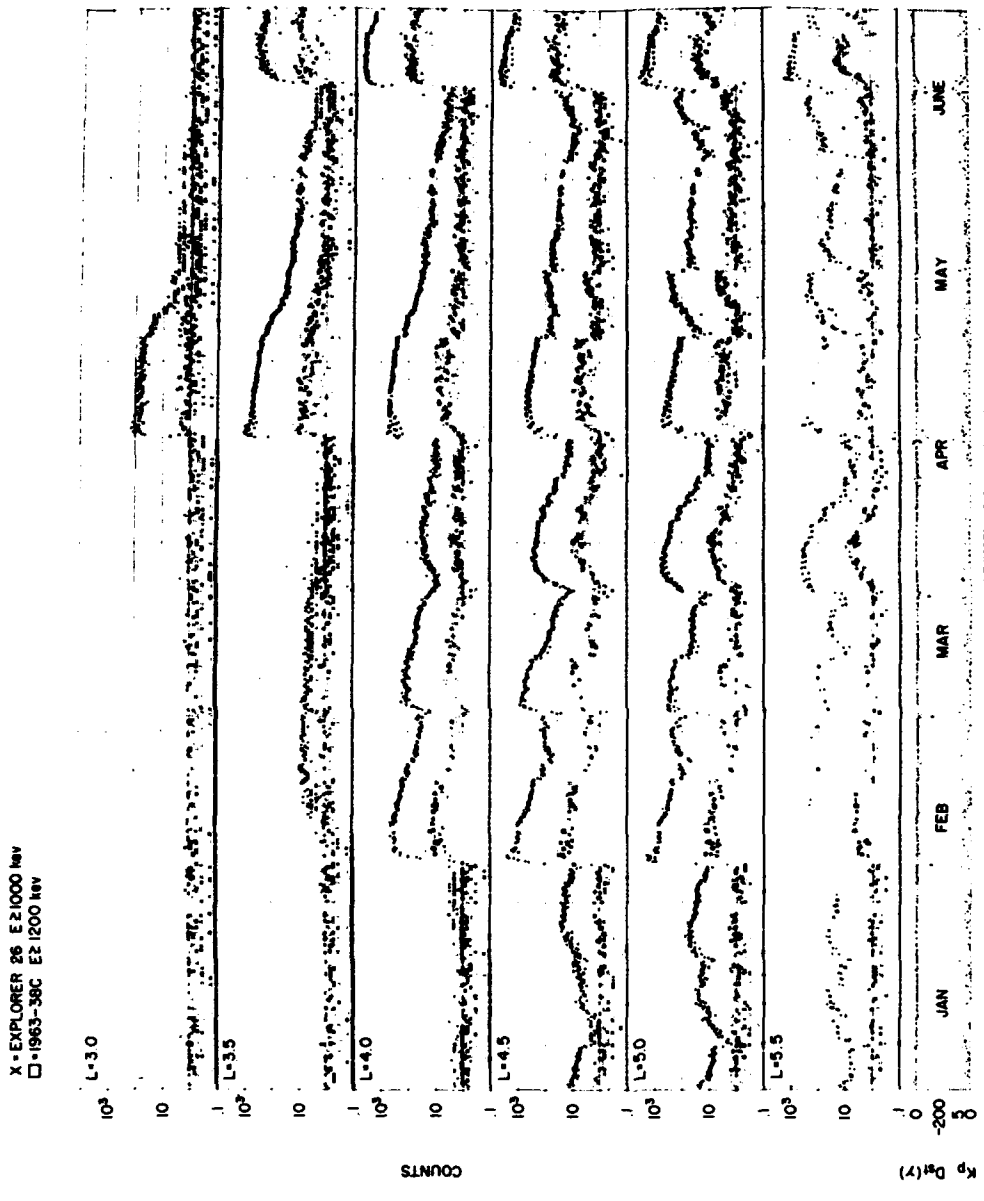

Figure 4-29. Time behavior of ~1-MeV electrons in the outer radiation zone. (Reference 21).

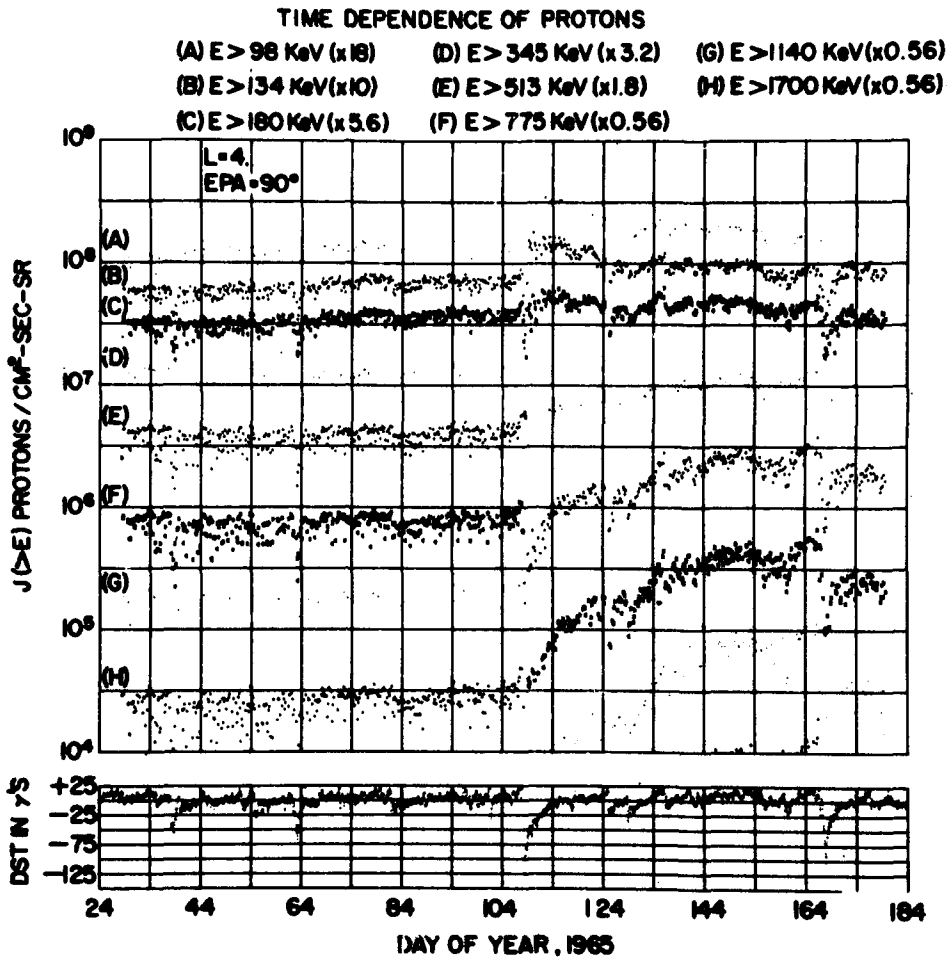

Figure 4-30. Time behavior of low-energy protons at L = 40. The curves are displaced to avoid overlap, and values for curves A to H must be multiplied by 10 raised to the exponents: -1.25, -1, -0.75, -0.50, -0.25, 0.25, 0.25, and 0.25 to get the integral intensity (Reference 22).

adiabatic changes of the fluxes consistent with magnetic field changes during the events (Reference 22). A measure of this field D_{st} also is shown in Figure 4-30.

Clearly, the causes of these variations are produced by events on the sun with subsequent changes in the interplanetary medium. Much detailed work has been done to show the relationship between outer-zone trapped radiation fluxes and other geophysical parameters such as Kp, D_{st}, solar wind mach number, solar wind density, and the direction of the interplanetary magnetic field. The two periodic effects associated with the sun are the 11-year solar cycle and the 27-day synodic rotation period. Both these periods are apparent in geophysical phenomena. However, the occurrence of solar geophysical events viewed over a large number of events can be described statistically.

For other than the primary studies to understand the dominant physical processes, the main use of the particle environment is to be able to determine the fluxes for some future time period. A statistical approach here is very useful. For any time period exceeding several months, a number of magnetic storms will occur. Consequently, the average flux is the most meaningful quantity for these longer periods. On the other hand, if one is considering a short-term mission that is highly sensitive to the radiation environment, one needs to have the time variations expressed in a quantitative way. A good way of doing this is to express the probability that the flux will exceed a certain level at any random time. Unfortunately, a model of the outer zone incorporating this approach has not been produced yet. However, on the $L = 6.6\ R_E$ shell, Vette and Lucero (Reference 23) have produced such an electron environment. They showed that the quantity:

$$y = \log (\text{FLUX}) \tag{4-4}$$

could be described approximately. The probability at any random time $T_1 < t < T_2$ that the variable y would exceed the value y_1 could be expressed as:

$$P(y > y_1) = \frac{1}{\sqrt{2\pi}\sigma} \int_{y_1}^{\infty} \exp\left[- \frac{(z - \mu)^2}{2\sigma} \right] dz \tag{4-5}$$

where

$$\mu = \int_{T_1}^{T_2} \frac{y(t)dt}{T_2 - T_1} \tag{4-6}$$

$$\sigma^2 = \int_{T_1}^{T_2} \frac{[y(t) - \mu]^2 \, dt}{T_2 - T_1} \quad . \tag{4-7}$$

Thus, y has a Gaussian distribution. The time-averaged omnidirectional flux for energy greater than E was given by:

$$J(> E, B/B_0, \phi) = CA(\phi) \, (B/B_0)^{-b} \, E^{n(\phi)} \, e^{-E/E_0} \quad . \tag{4-8}$$

The values of the parameters as well as more details about the environment are given in Reference 23. The probability distribution for various energies at the geomagnetic equator are given in Figures 4-31 and 4-32. The abscissa is the probability that the flux will exceed J_1 or the fraction of the time that the flux exceeds J_1.

In describing the outer-zone environment, the standard B, L coordinate system that is so successful in ordering fluxes in the inner zone must be abandoned. The reasons for this are twofold. In the distorted magnetosphere, the real lines of force are no longer coincident with the constant L-shells. Furthermore, the distortions of the cavity are changing constantly so that the exact shape at any given time is not necessarily known. Consequently, it is impossible to compute, a priori, a coordinate system based on the three invariants.

At geocentric distances in excess of 5 R_E, the main distortion of the cavity is an elongation in the antisolar direction. Consequently, a useful coordinate system that can be calculated for the outer zone is the B, L, ϕ system where ϕ is the local time of the measurement and B, L are computed in the usual way from a harmonic expansion of the field based on surface or low-altitude measurements of the vector-B field. Actually, the B/B_0, L, ϕ system is more convenient for presentation purposes.

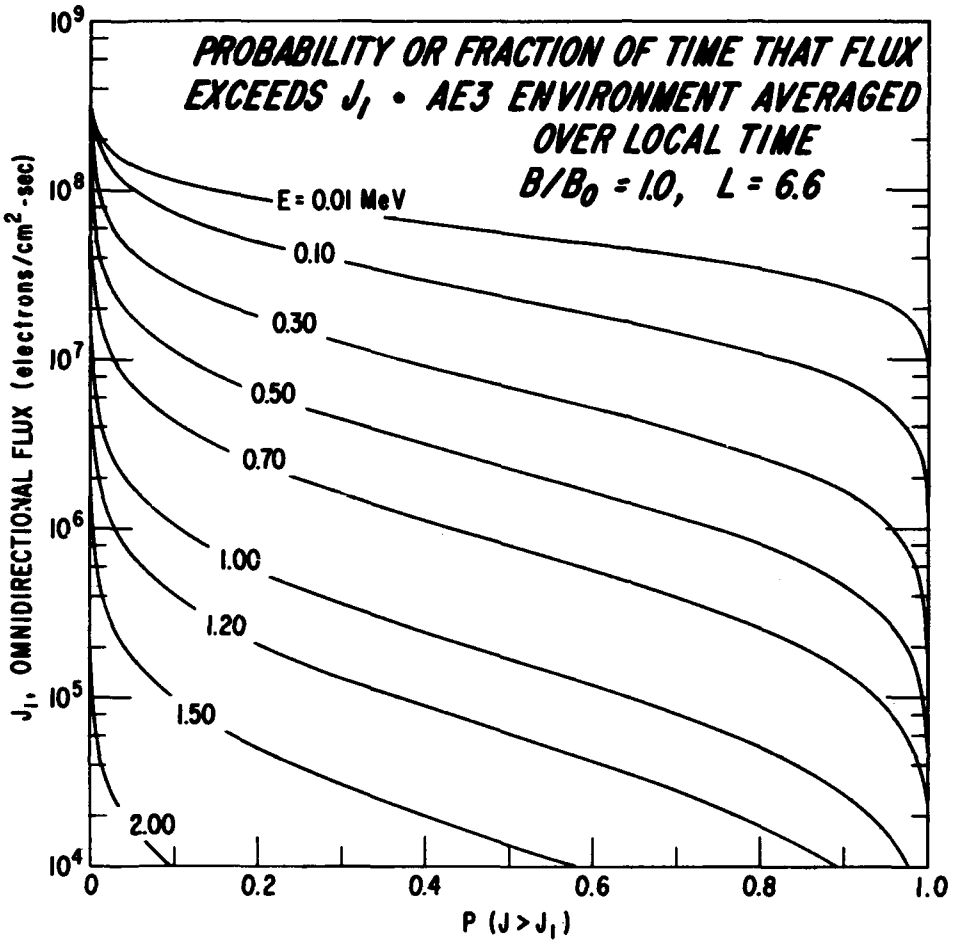

Figure 4-31. A statistical presentation of the AE3 environment averaged over local time—low and medium energies.

As indicated previously, no good statistical model yet exists for the outer zone. The last detailed model was AE2, which has been discussed. However, AE2 only purports to represent the approximate geometric mean of the outer-zone fluxes. Without having a complete description yet in hand, showing some of the statistical parameters that have been derived from existing data will have to suffice.

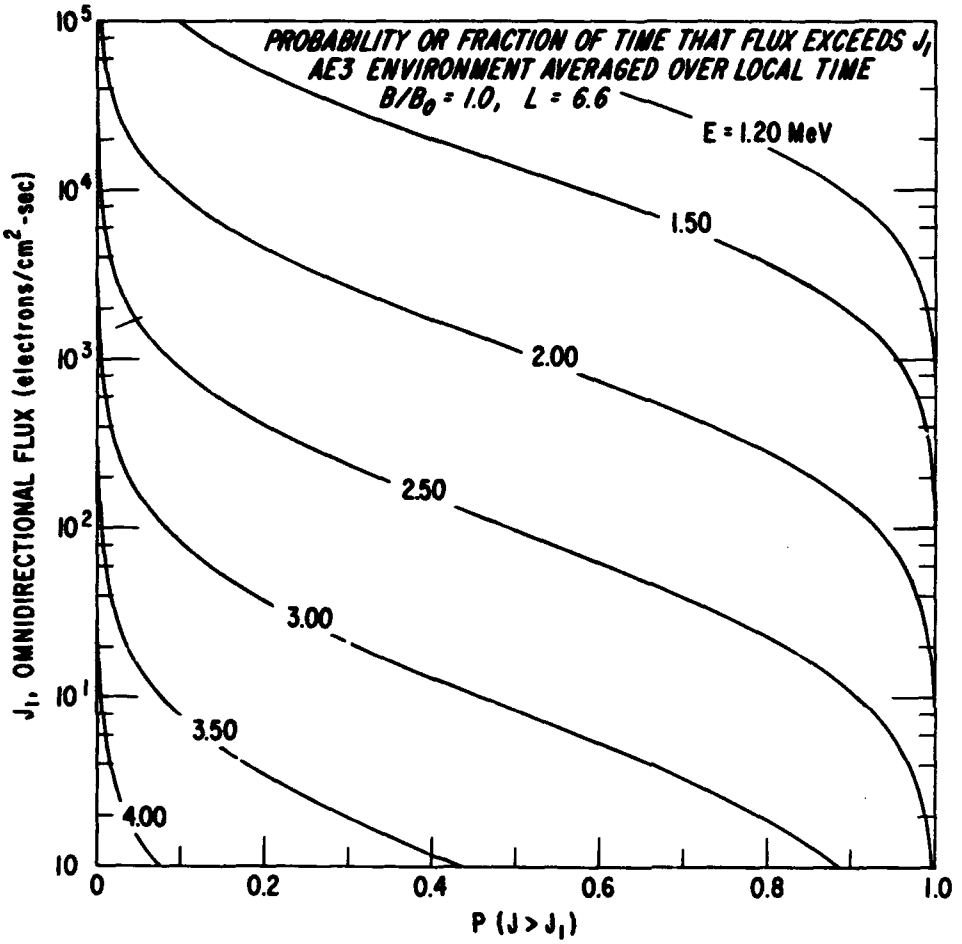

Figure 4-32. A statistical presentation of the AE3 environment averaged over local time—high energies.

The quantities of interest are:

(a) The average flux above energy E, $J_{avg}(> E, B, L, \phi)$

(b) The average of $y = \log_{10} J$, $\mu(> E, B, L, \phi)$

(c) The standard deviation of y, $\sigma(> E, B, L, \phi)$.

Under the assumption that a Gaussian distribution is adequate to describe the statistical situation, this relationship holds:

$$\mu + 1.17\sigma^2 = \log_{10} J_{avg} . \qquad (4\text{-}9)$$

All work so far shows this assumption to be a valid one.

Except at $L = 6.6\ R_E$, where several satellites carrying radiation detectors have been placed in orbit, the data on outer-zone L-shells can be obtained only by elliptical orbiting satellites that cross these shells at varying time intervals. Since many of these satellites have had apogees varying from 12 to 40 R_E, the number of data points in any given time interval is rather sparse. Consequently, the best that generally can be done to demonstrate the functional behavior of μ and σ is to present these variables averaged over B/B_0 or ϕ .

Some plots of μ, σ, and J_{avg} are presented in Figures 4-33, 4-34, and 4-35, respectively. The results in Figure 4-33 were taken near the equator and are averages over these time periods: Explorer 6, August to September 1959; Explorer 14, October 1962 to August 1963; and ERS-13, July to December 1964. Changes during the solar cycle are seen clearly. The results in Figure 4-34 were taken near the equator and cover the same time periods noted in Figure 4-33. The maximum variations for all energies except the > 40 KeV occur around L = 6.0 to 7.0. Although this is near the pseudotrapping boundary on the night side of the magnetosphere, the ERS-13 data were taken only on the daylight side. The Explorer 14 data spanned all local times and the Explorer 6 data were taken on the night side. No clear-cut solar cycle effects exist in this parameter. Figure 4-35 shows the movement of the electron maximum over the solar cycle and its possible enhancement during solar maximum.

Figure 4-25 shows the position of the maximum changes throughout the solar cycle. As the solar activity builds up, the outer belt maximum and the slot minimum move closer to the earth. It appears that the fluxes at the maximum of the outer belt also increase with solar activity. Although limited data are available to make this comparison, the increase appears to be about a factor of 3 to 4 for energies around 500 KeV.

The proton fluxes in the outer zone are given by the flux map AP5, which combines the results of many measurements, particularly those

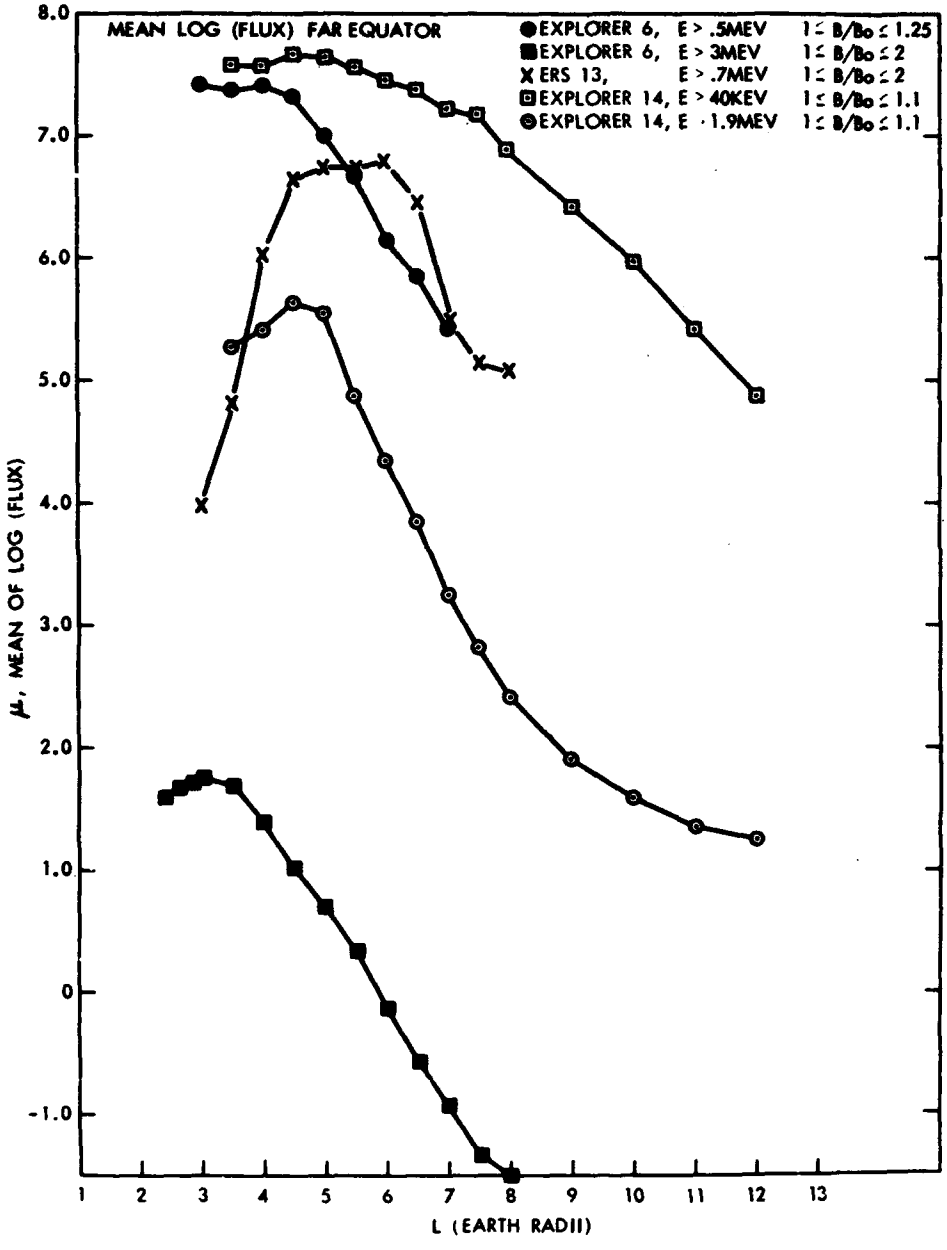

Figure 4-33. Radial behavior of the parameter μ in the outer radiation zone. Results pertain to different time periods. (See text.)

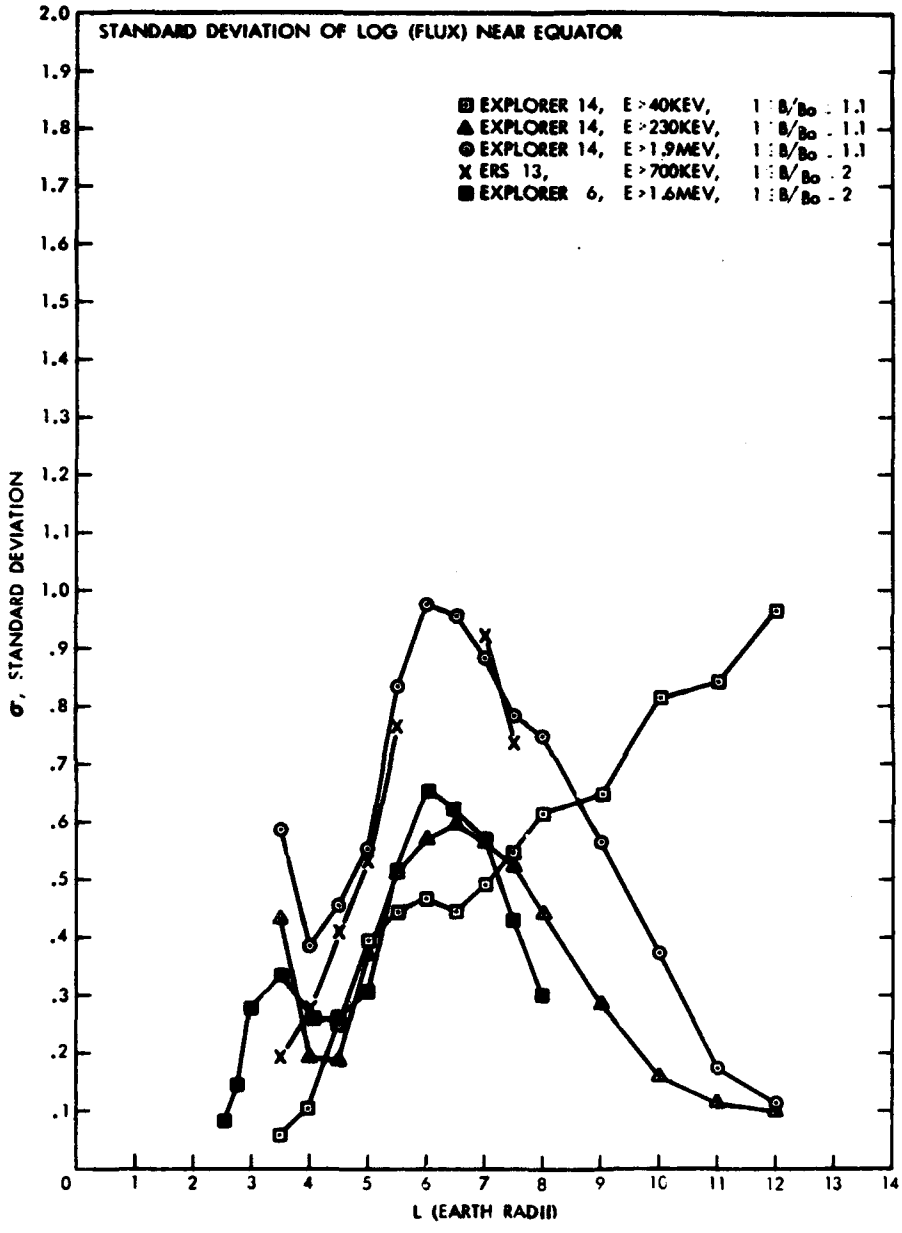

Figure 4-34. Radial behavior of the parameter σ in the outer radiation zone. Results pertain to different time periods. (See text.)

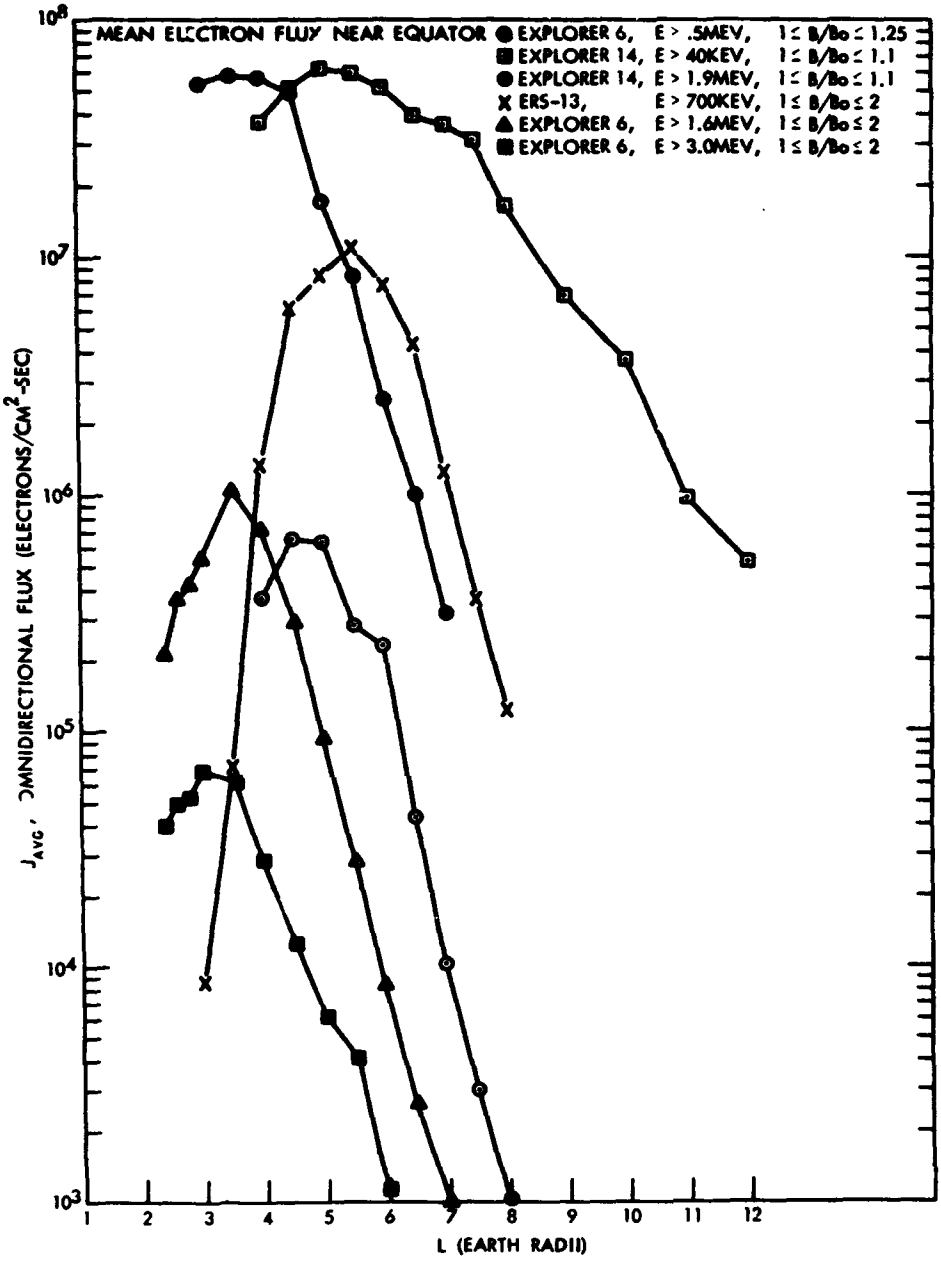

Figure 4-35. Radial behavior of the time-average omnidirectional electron flux in the outer radiation zone. Results pertain to different time periods. (See text.)

of Davis and Williamson (References 24 and 25). The proton distributions are much more stable than those of electrons, as discussed previously. However, large geomagnetic storms such as that of 18 April 1965 do produce significant changes that take some months to recover. Not enough storms produce a large enough effect to use a statistical approach. Consequently, static models are adequate except during periods following large magnetic storms. Whether one can determine the fluxes to better than a factor of 2 with realistic models is doubtful. The monitoring of low-energy protons over the solar cycle has not been extensive enough to determine whether any long-term effects occur. At low altitudes, the fluxes show more irreversible effects. The behavior of low-energy protons in the slot region is shown in Figure 4-36. The measurements are similar to those presented in Figures 4-11, 4-12, and 4-27 but cover lower energy protons. The initial proton response at L = 2.2 to the 26 May magnetic storm is contaminated by electrons.

The definitive observation of protons and electrons between 0.2 to 50 KeV in the radiation belts was begun by Frank (Reference 26) with instrumentation flown on OGO-3. During magnetic storms, the production of the disturbed magnetic fields (the main phase) attributed to ring currents in the magnetosphere is due mainly to the protons in this low-energy region. The behavior of the protons during the July 1966 storm is shown in Figure 4-37. Protons in this energy range and below are largely responsible for the ring currents produced during magnetic storms. This figure shows the increase in intensity and inward motion of the peak during the magnetic storm of 9 July 1966 (Reference 26). Although a detailed mapping over a long time period has not yet been presented, the approximate distribution during the main phase of the magnetic storm is shown in Figure 4-38 which gives an R-λ presentation of some of the results shown in Figure 4-37.

Finally, in connection with the outer zone, the existence of alpha particles, which were first clearly detected in the energy range around 2 to 15 MeV (Reference 27), should be mentioned. These particles show a peak in the radial distribution around L = 3.0. Later measurements (Reference 28) confirmed the existence of these particles and that the alpha-to-proton ratio for the same energy per nucleon lay between 10^{-3} and 10^{-4}. This experimental ratio as a function of L for various values of B/B_0 is shown in Figure 4-39. This ratio varies with L-value but seems to be independent of B/B_0 over the outer zone. The radial peak in the 0.5 MeV

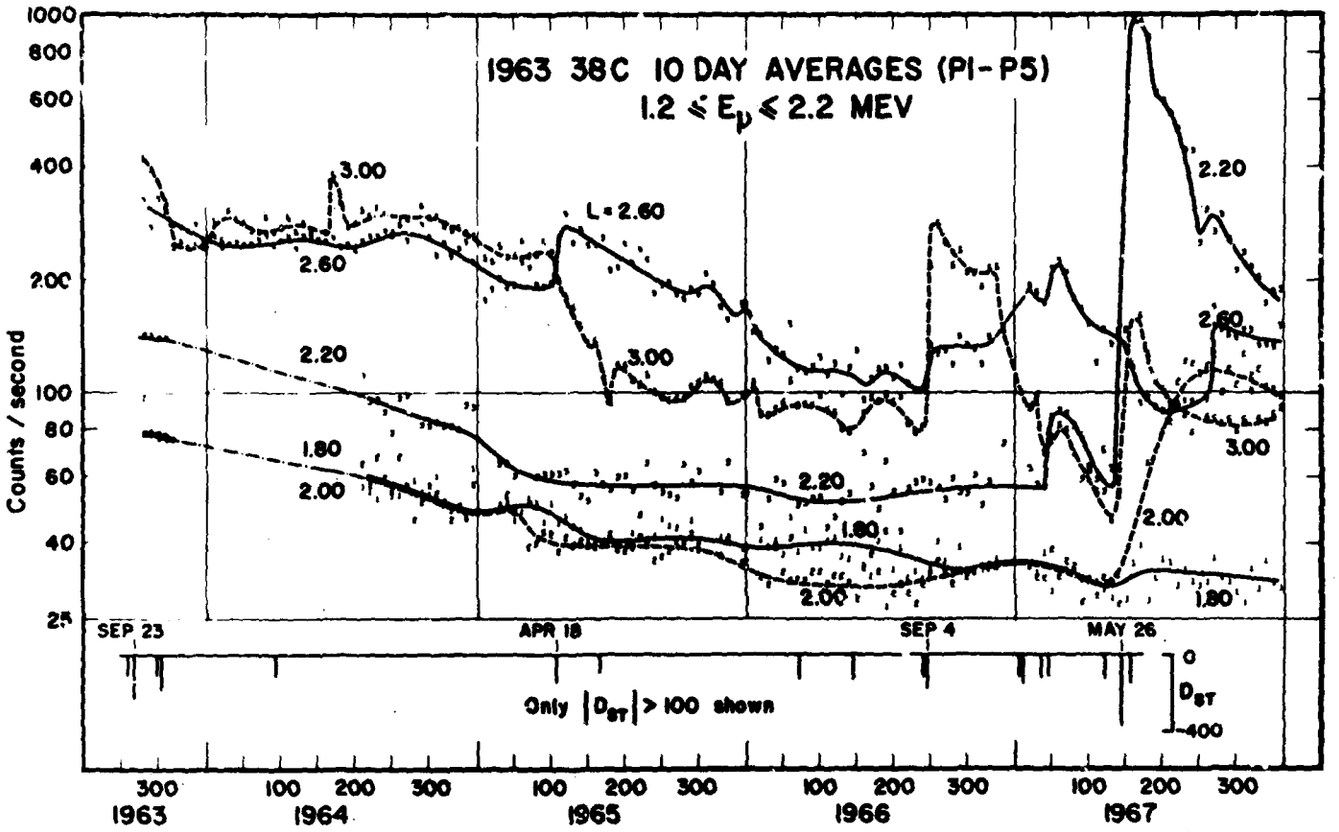

Figure 4-36. Time behavior of low-energy protons.

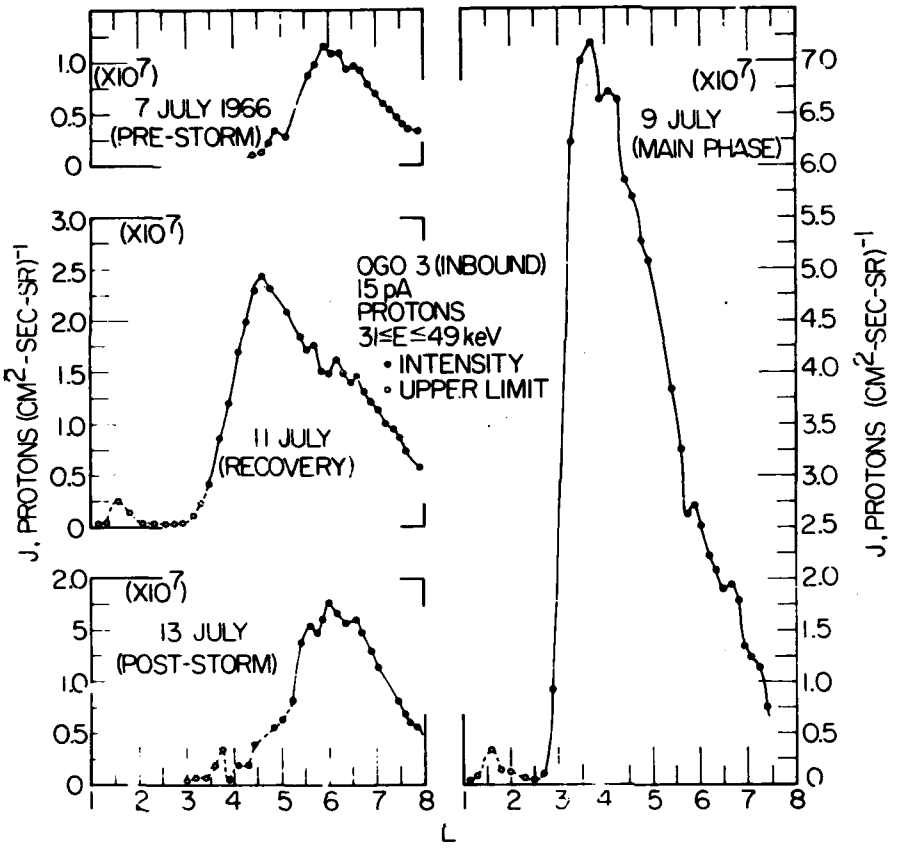

Figure 4-37. Variation of 31- to 49-KeV protons during a magnetic storm (Reference 26).

per nucleon alpha particles occurs around L = 3.1, the same place as the 0.5 MeV protons.

4.5 PSEUDOTRAPPED REGION

A qualitative picture of the extent of this region has been given in Figure 4-1. This was obtained by considering adiabatic particle motion in a distorted magnetosphere. Because it is confined closer to the geomagnetic equatorial plane on the dark side of the earth than it is on the sunward side, this region has been given two different names. The sunward portion is known as the skirt and actually

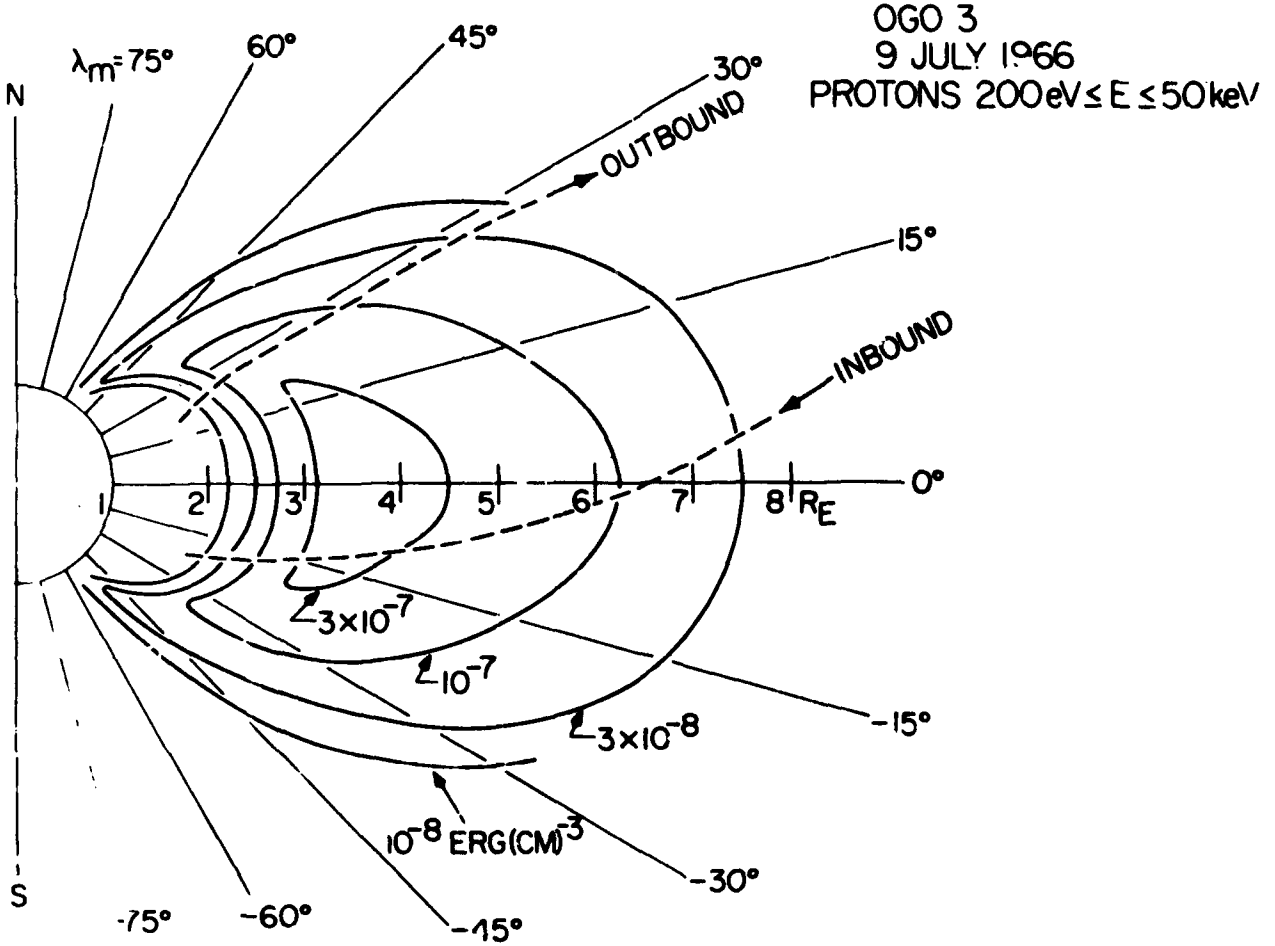

Figure 4-38. Distribution of very low-energy protons during a magnetic storm.

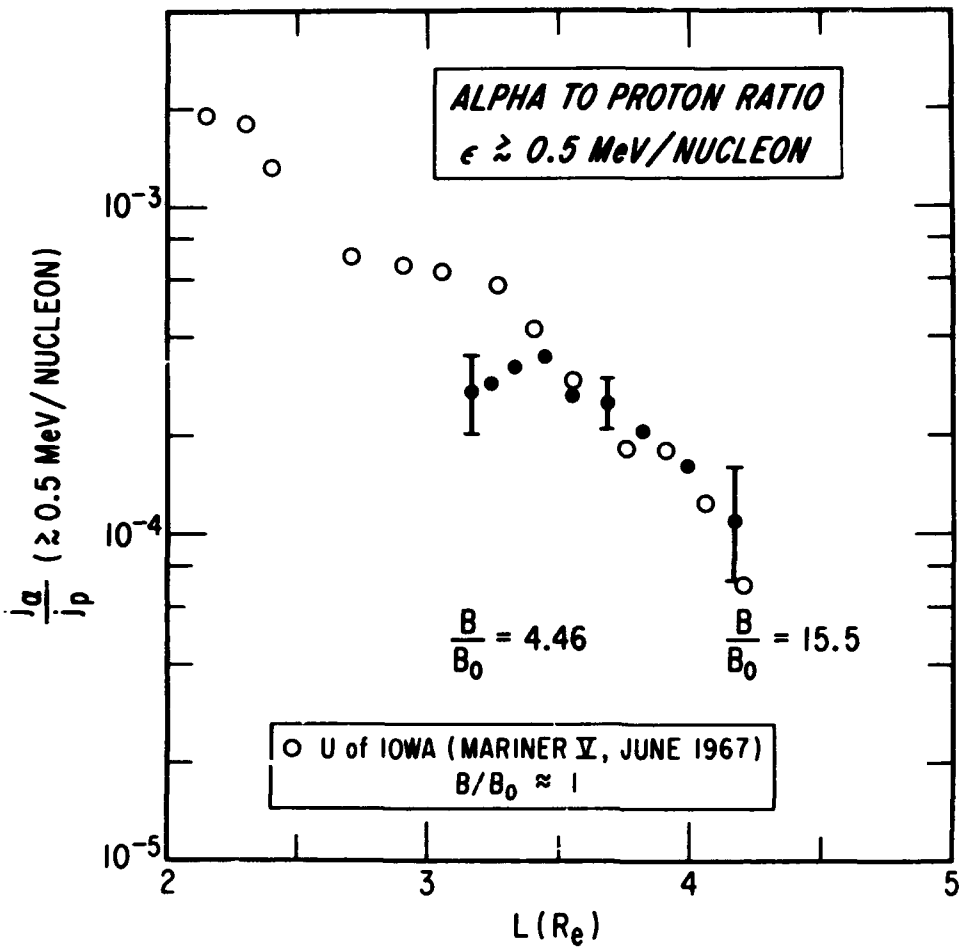

Figure 2-39. Ratio of alpha particles to protons (Reference 28).

covers the local time region 0400 to 2000. The region within ±4 hours of local midnight is called the cusp. A plot of the counting rates of two detectors on the ERS-17 satellite showing the various particle regions is shown in Figure 4-40. This figure illustrates the outer zone, the pseudotrapping region, and the motion of the magnetopause. The radial distance and B/B_0 calculated from a nondistorted magnetosphere are shown at the bottom. The periodic variations seen in the outer zone for the electrons > 100 KeV are due to the directional character of the detector rather than any periodic time variations of the flux. A projection of this orbit onto the model magnetosphere shown in Figure 4-1 suggests the satellite returns to the stable trapping region before encountering the magnetospheric boundary.

ERS-17 DETECTOR COUNTING RATES (10-13-65)

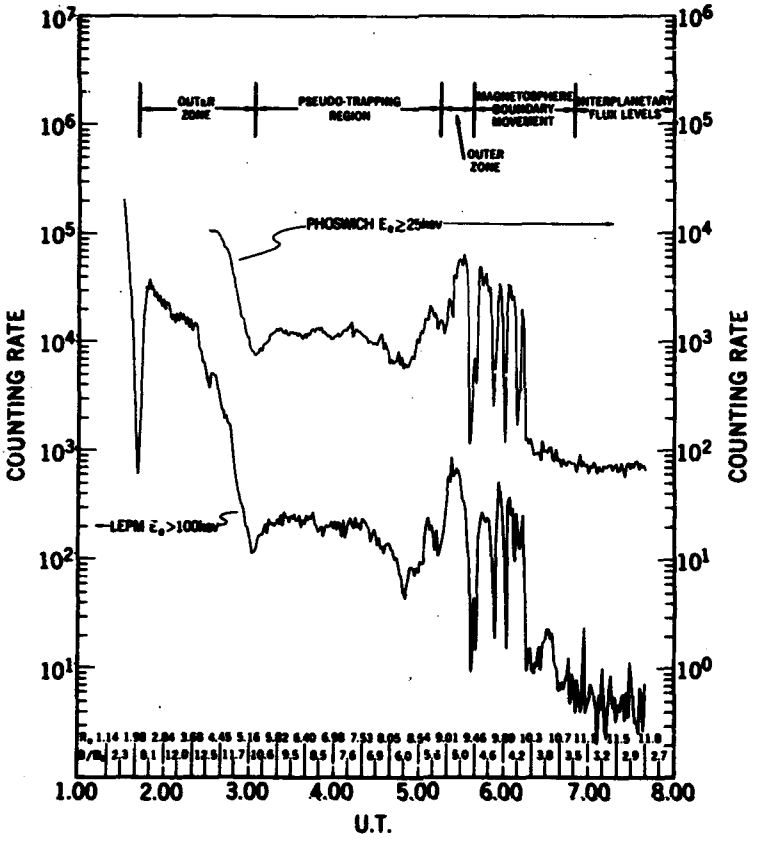

Figure 4-40. Typical satellite pass through the daylight magnetosphere.

Although discussions about the nature of this region have been held (References 29 through 33), detailed measurements of the boundaries on the midnight side have not been given. Typical flux values for electrons > 40 KeV are 10^4 to 10^6 cm^{-2} sec^{-1}. The edge of the particle trapping boundary determined by Explorer 14 is presented in Figure 4-41; by ERS-17, in Figure 4-42; and by Explorer 6, in Figure 4-43. This boundary can be considered the outer edge of the pseudotrapping region. Although the precise detection of the magnetopause requires a magnetometer, the boundary inferred by low-energy electron measurements on the daylight side corresponds very closely with that determined by magnetic measurements. The results of Figure 4-41 were obtained with electrons > 40 KeV. The inbound passes are close to the geomagnetic equator and the outbound passes are 15 to 30 degrees south (Reference 30). No difference in boundary distance

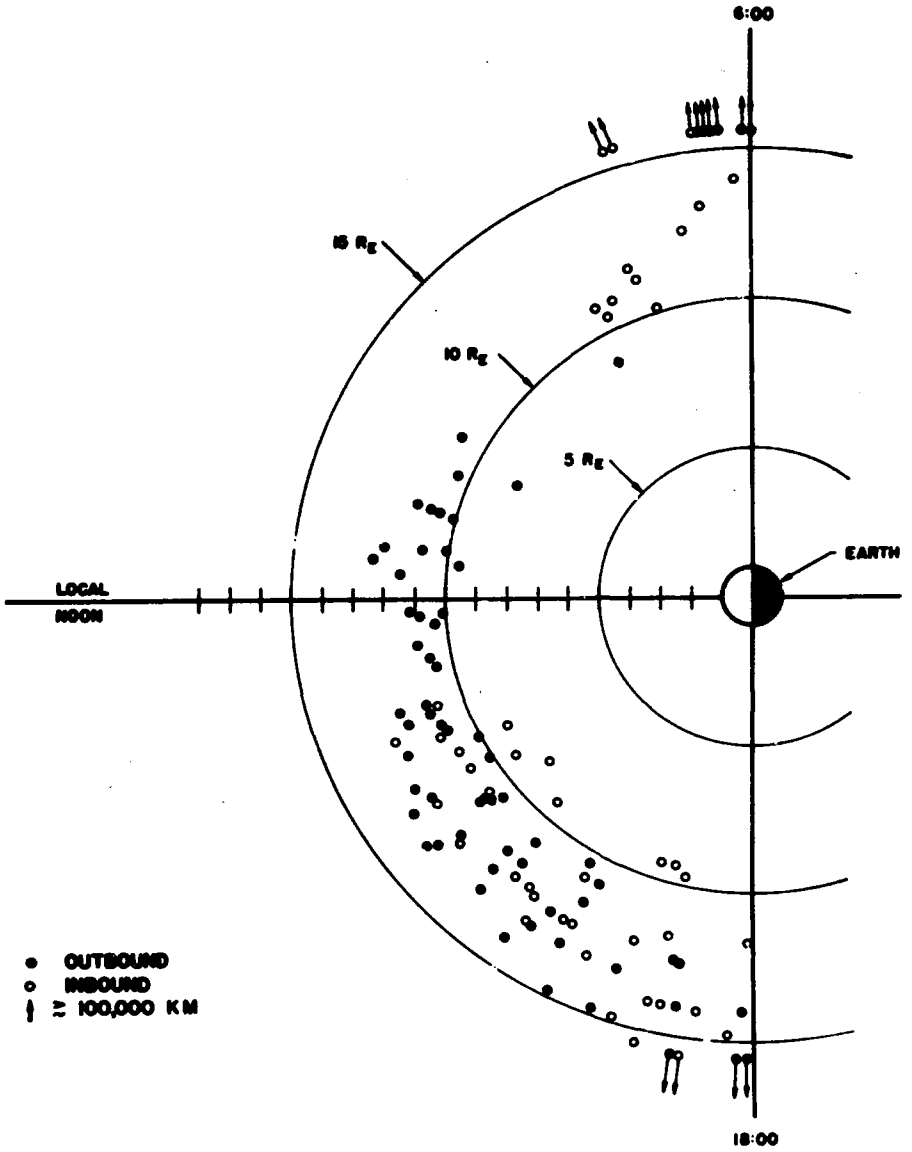

Figure 4-41. Particle trapping boundary measured by Explorer 14. E > 40 KeV (Reference 30).

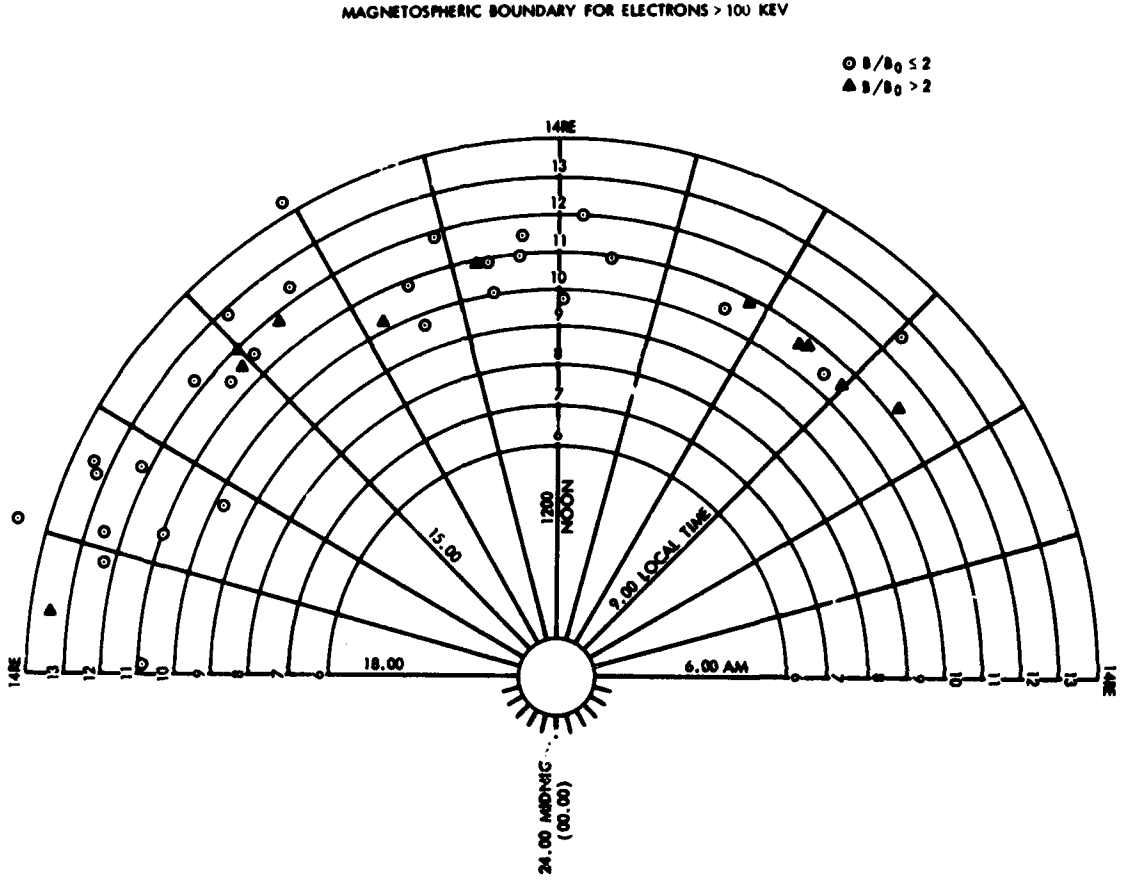

Figure 4-42. Particle trapping boundary measured by ERS-17.

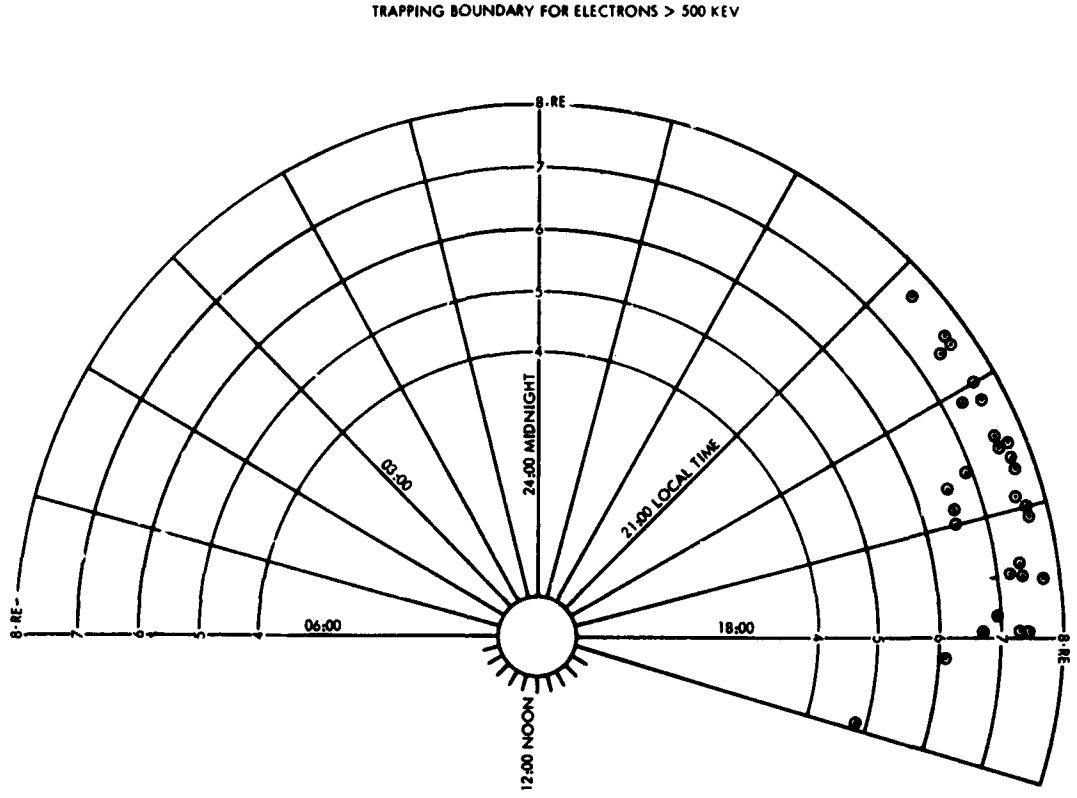

Figure 4–43. Particle trapping boundary measured by Explorer 6.

between the two types of passes seems to exist; thus, the cavity shape is roughly hemispherical in the front. The results in Figure 4-42 are similar to those given in Figure 4-41. The electrons are somewhat higher in energy (> 100 KeV) but also populate the daylight magnetosphere out to the boundary. No difference exists between the high-latitude and low-latitude boundaries. The highest magnetic latitudes reached by this satellite are approximately 45 degrees. In Figure 4-43, the effective boundary for these higher energy electrons does not seem to be the same as for the 40- and 100-KeV electrons. These measurements were made in 1959, and the boundary variations over the solar cycle are not yet known (Reference 34).

These satellites were active at different times in the solar cycle. Unfortunately, not enough data from all the various satellites have been studied to determine the average boundary change over the solar cycle. Change between 1962 and 1965 on the sunward side seems to be very little.

A measure of the inner pseudotrapping boundary determined by ERS-17 is given in Figure 4-44. This shows the variation of the boundary as a function of geomagnetic latitude (or B/B_0), although not enough points exist to present a clear picture. These boundaries were determined by > 100 KeV electrons using the ERS-17 measurements. Although the pseudotrapping results are rather sparse, the radial distance of this boundary depends on magnetic latitude (or B/B_0) in qualitative agreement with Figure 4-1. Furthermore, near the equator, the pseudotrapping boundary lies close to the magnetopause. In contrast to Figure 4-1, the northern and southern pseudotrapping regions seem to be closed by a thin band at the magnetopause. Much more data will have to be presented from the various satellites that have made measurements in this region before characteristics can be described in detail.

4.6 GEOMAGNETIC TAIL

On the sunward side of the magnetosphere, the radial extent of energetic particles is limited to about 10 to 14 R_E by the magnetospheric boundary. However, the tail of the magnetosphere extends for great distances, and particle fluxes have been seen on occasion as far as the moon (Reference 35). A wide variety of behavior is seen, depending upon the energy of the particles and the intensity threshold of the observing instruments. A radial profile has been obtained using detectors sensitive to electrons $\gtrsim$ 30 to 45 KeV with an intensity limit of

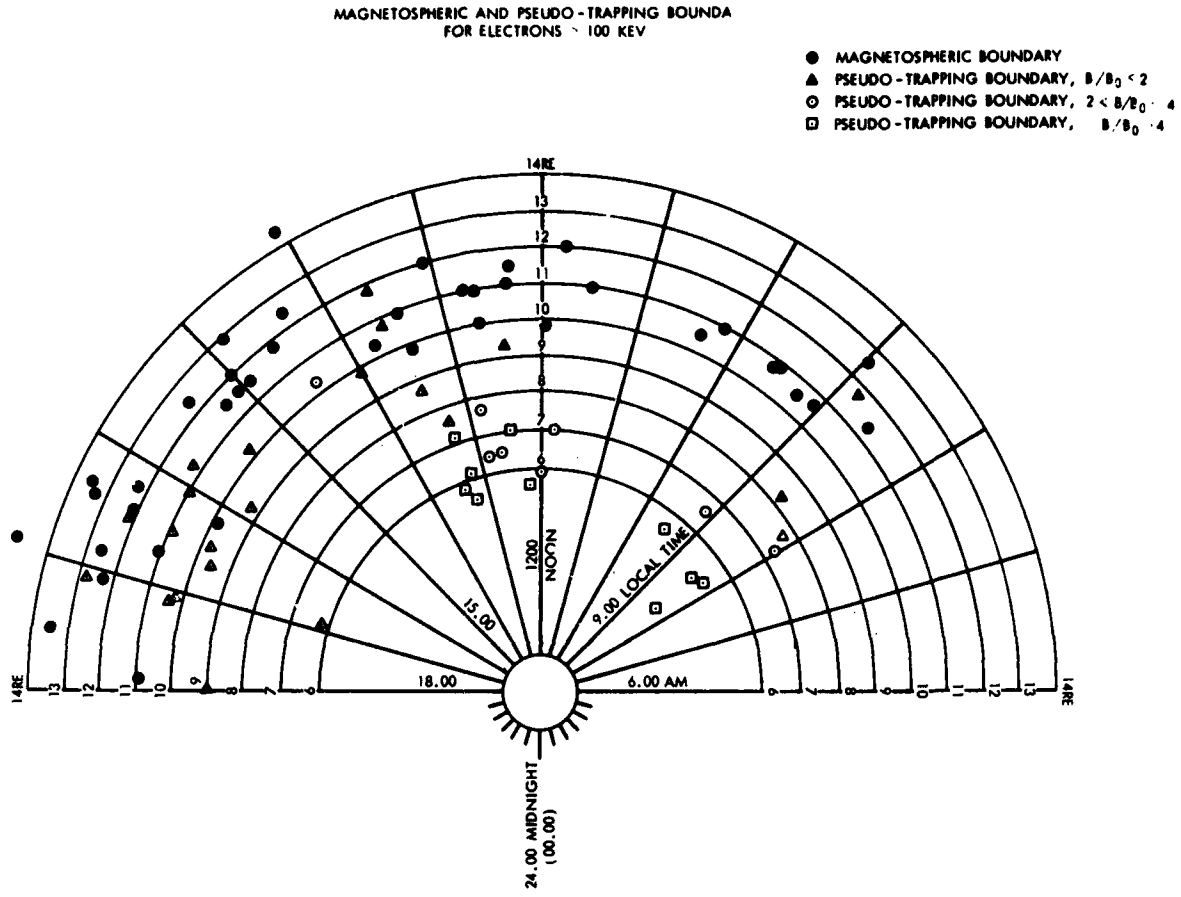

Figure 4-44. Comparison of magnetopause and pseudotrapping boundary.

$\sim 10^4$ cm ^{2}sec^{-1}. With these instruments, many times no fluxes are observed past ~7R_E. When they are observed, the events are called islands (exhibiting fluxes up to 10^7cm^{-2} sec^{-1}), which are nearly as intense as those in the radiation belts. The majority of these events show a fast rise time and a slow decay leading to the suggestion that these variations are temporal and not spatial (Reference 33). A typical observation obtained by a satellite passing out through the magnetotail is shown in Figure 4-45. In the figure, the islands of flux, as measured by > 45-KeV electron detectors, are shown clearly. This is an inbound pass of the Explorer 18 satellite. The typical sharp rise and slower fall of these island events are seen. The occurrence and intensity of these events do not depend very strongly on radial distance.

The occurrence of these island events has been shown (Reference 36) to be independent of the radial distance but to be strongly correlated with the distance above and below the neutral sheet. In fact, most electrons are confined to within a few earth radii of the sheet. The frequency of events increases with magnetic activity. Detailed observations (Reference 37) at 17 R_E give a fairly good picture of the whole geomagnetic tail since the dependence of fluxes with radial distance is small. The frequency of occurrence of electron fluxes > 64 KeV is shown as a function of solar magnetospheric coordinates in Figure 4-46. This earth-centered coordinate system is defined in this manner: The X-axis points toward the sun; the X, Z plane contains the earth's dipole magnetic moment vector; and the Y-axis is chosen to form a right-handed coordinate system. In the figure, the various shaded blocks represent the frequency of occurrence of fluxes greater than 83 electrons per cm^2 sec-ster in percent for the 5- x 5-degree solar magnetic angular areas. The outer dotted lines represent the average position for the standing shock wave and the inner dotted lines represent the average position of the magnetopause at 17 R_E. Notice the electrons are not confined to the magnetosphere near the dawn side and exist quite frequently in the magnetosheath. Consequently, near the dawn meridian, low-energy electron measurements are not good to determine the magnetospheric boundary (Reference 37).

Figure 4-46 shows that the presence of electrons is asymmetrical in longitude and that electrons are seen more frequently near the dawn side of the magnetosphere. As the intensity threshold is increased, only the region around 200- to 300-degrees longitude is populated. The energy spectrum of these electrons can be represented

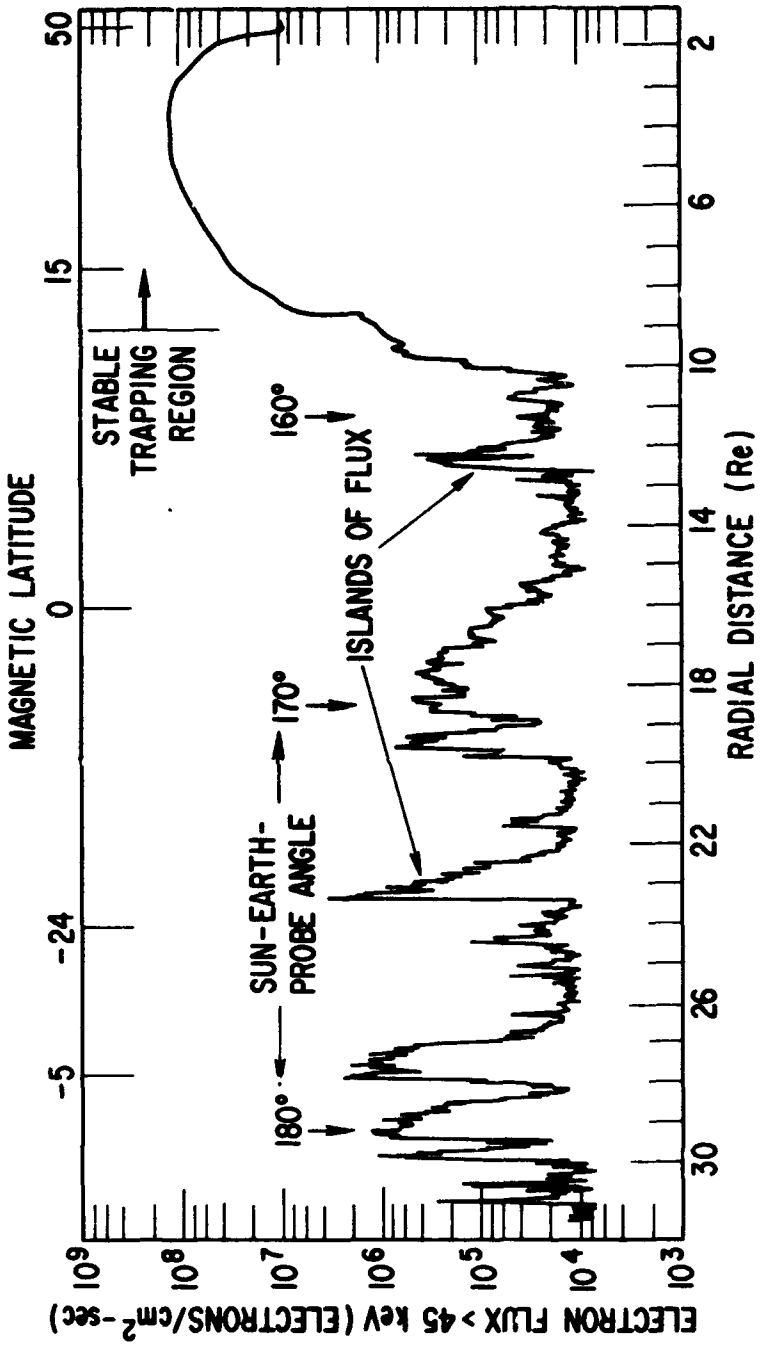

Figure 4-45. Typical satellite pass through the magnetotail.

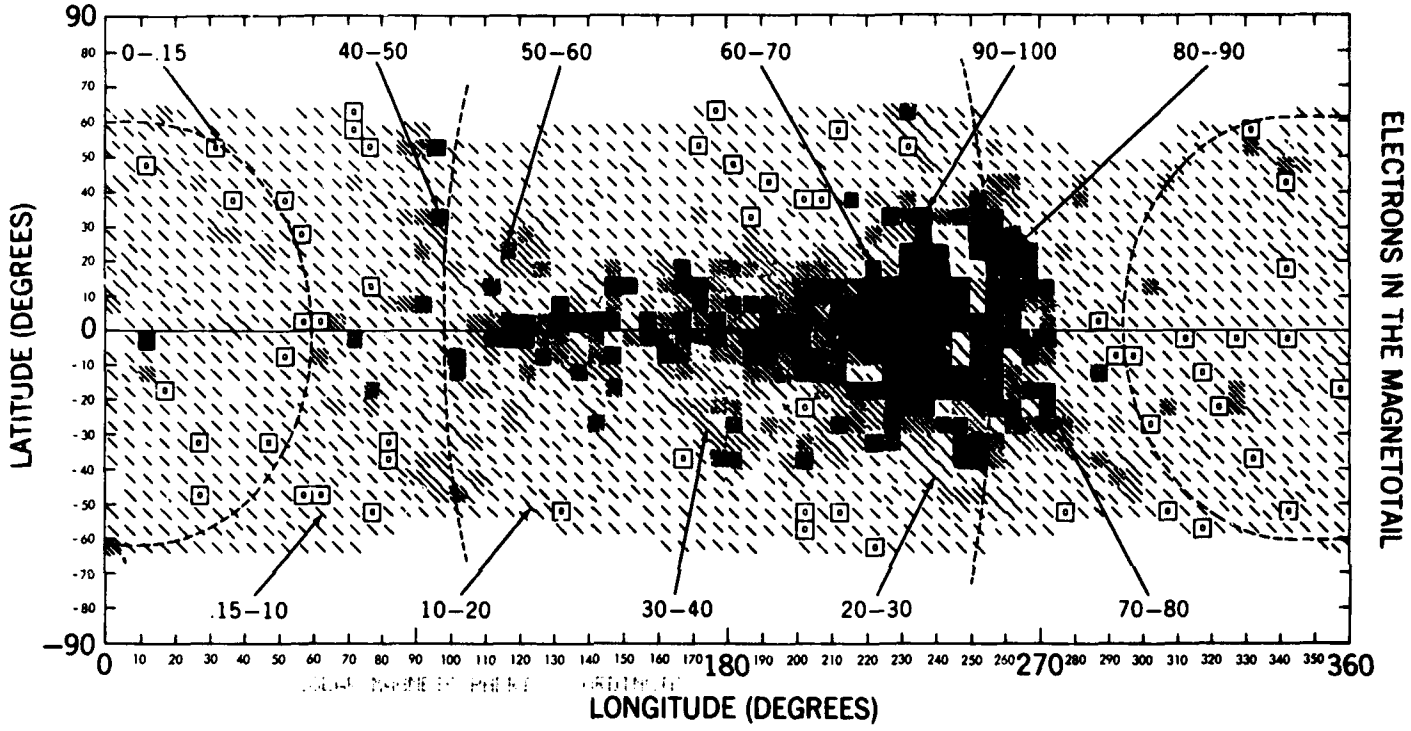

Figure 4-46. Frequency of occurrence of >64-KeV electron fluxes in the magnetotail (Reference 37).

fairly well by a spectrum of power law with a slightly harder spectrum in the region of most frequent occurrences as measured by > 64-KeV particles. The average exponent varies between 3 and 4.

These higher energy electrons really represent the tail of a lower energy electron distribution with energies between 0.2 to 12 KeV (Reference 38). The spectrum of these electrons is quasi-thermal and generally peaks between 1 and 10 KeV. This plasma sheet is present almost continuously and extends from the night-side boundary of the radiation belt outward to great distances (> 31 R_E). The sheet is 4- to 6-R_E thick with the approximate plane of symmetry being the magnetic neutral sheet shown in Figure 1-2. Omnidirectional fluxes > 100 eV extend to above 10^9 cm^{-2} sec^{-1}. Toward the dawn and dusk boundaries, this sheet flares out to 8 to 12 R_E in thickness with higher average energies near the dawn side. The observations of higher energy electrons > 45 KeV represent an increase in the energy of these lower energy particles, not a new cloud of electrons. Whenever the islands are seen, low-energy electrons always are present.

Protons with energies about a factor of 10 greater than the electrons also are found always in the plasma sheet with a similar peaked spectrum. Proton islands with intensities ~ 10^5 protons cm^{-2} sec^{-1} and energies > 125 KeV have been reported (Reference 39). These energetic protons have a spectrum that can be fit by a power law with an exponent lying between 4.9 to 7.8, which is much steeper than that for electrons. The nature of the proton islands is very similar to that of the electrons and may be caused by an energization of the lower energy protons. Typical values of the electron and proton parameters in the magnetotail are given in Table 4-2 (Reference 40)

Besides the average energy changes observed within the plasma sheet, evidence exists that the sheet moves around in space as the magnetospheric shape changes. However, the plasma sheet always appears to be present, but the particle temperature is usually so low that the more energetic particles are seen only sporadically. A picture of the plasma sheet shown in or near the equatorial plane is given in Figure 4-47. The plasmasphere shown is the region around the earth that contains low-energy thermal plasma generally confined to within 3 to 5 R_E (Sections 1.6 and 11.3.2). The region between the inner boundary of the plasma sheet and the trapping boundary is the cusp or pseudotrapping region where the electron energies are on the average much higher than in the plasma sheet. The density of dots is intended to convey a qualitative idea of the flux of electrons with energies between 100 eV and several KeV. The shaded region is that in which no good coverage has been obtained.

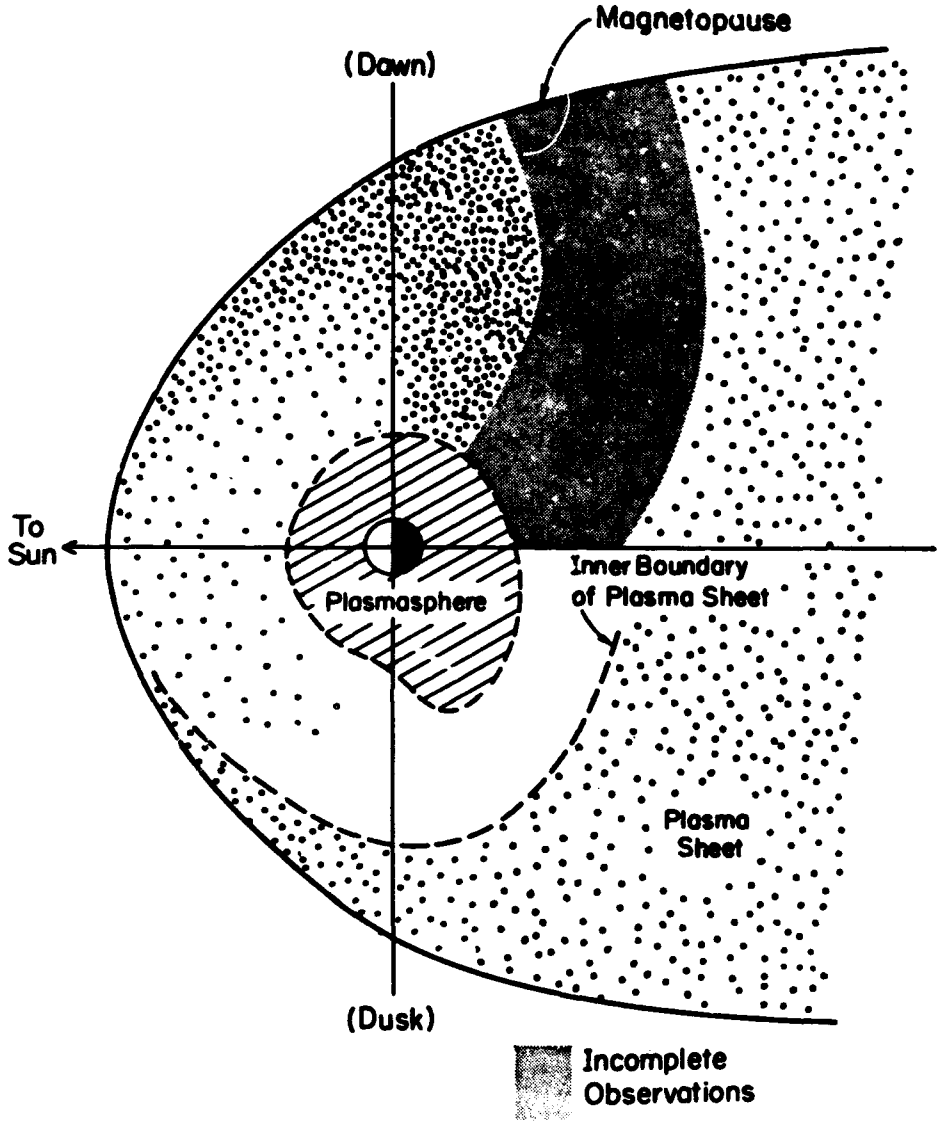

Figure 4-47. Distribution of 100-eV electrons in the magnetosphere. (Reference 41).

Table 4-2. Typical values of plasma parameters measured at 18 R_E.

Description of Particles	Particle Density (cm^{-3})	Range	Average Energy (KeV)	Range	Energy Density (KeV/cm^3)	Range
Electrons in High-Latitude Magnetotail	0.1	?	0.1	?	0.01	?
Protons in High-Latitude Magnetotail	0.1	?	1	?	0.1	?
Electrons in Plasma Sheet	0.5	0.1 to 3	0.6	0.1 to 10	0.3	0.01 to 2
Protons in Plasma Sheet	0.5	0.1 to 3	5	1 to 20	2.5	0.1 to 7

4.7 LOW ALTITUDE

The earth's atmosphere is responsible for producing the inner boundary of the radiation belts. As discussed in Section 5, charged particles interact with the atmosphere through Coulomb scattering, nuclear interactions, and energy loss by collision. The net result is that they eventually disappear from the trapped regions. The lifetime of the particles changes rapidly with altitude. For example, at 400 kilometers during solar minimum a 132-MeV proton lives about 5 years. At 250 kilometers, it lives about 3 months (Reference 42). The main interaction for these protons is energy loss by collision.

For electrons, on the other hand, Coulomb scattering dominates and the lifetime of 1.34-MeV electrons is about 4 to 2 days in this same region of space (Reference 43). Other mechanisms are responsible for transporting electrons to mirror points of approximately 500 kilometers, but then the atmospheric effects become dominant. Because of the asymmetry of the geomagnetic field, trapped particles that drift around the earth on constant L-shells and mirror at fixed B-values will encounter different atmospheric densities at different longitudes.

The regions of B, L space that are affected are shown in Figure 4-48 (also see Figures 2-10 to 2-19). The curves show lines of constant minimum altitude in B, L coordinates. Measurements in the B, L regions below 1,000 kilometers should show solar cycle effects because of the change in atmospheric density and composition. The general location where a given B, L point will reach its lowest altitude is around 45°W, 25°S in the region of the South American anomaly (Reference 44). The electron map, AE2, has been averaged over longitude so that a geographic latitude-altitude flux contour map could be displayed. This is shown in Figure 4-49. The outer-zone fluxes can be seen plunging into the atmosphere in the northern latitudes between 50 and 70 degrees. The South American anomaly pulls the flux contours to lower altitude in the 30°S to 50°S region and, thus, blends in with the southern outer-zone fluxes. Since electrons scatter readily in the atmosphere, those electrons that are lost to the lower atmosphere are replenished by scattering at slightly higher altitudes. These contours are representative of August 1964, and considerable decay has taken place since then.

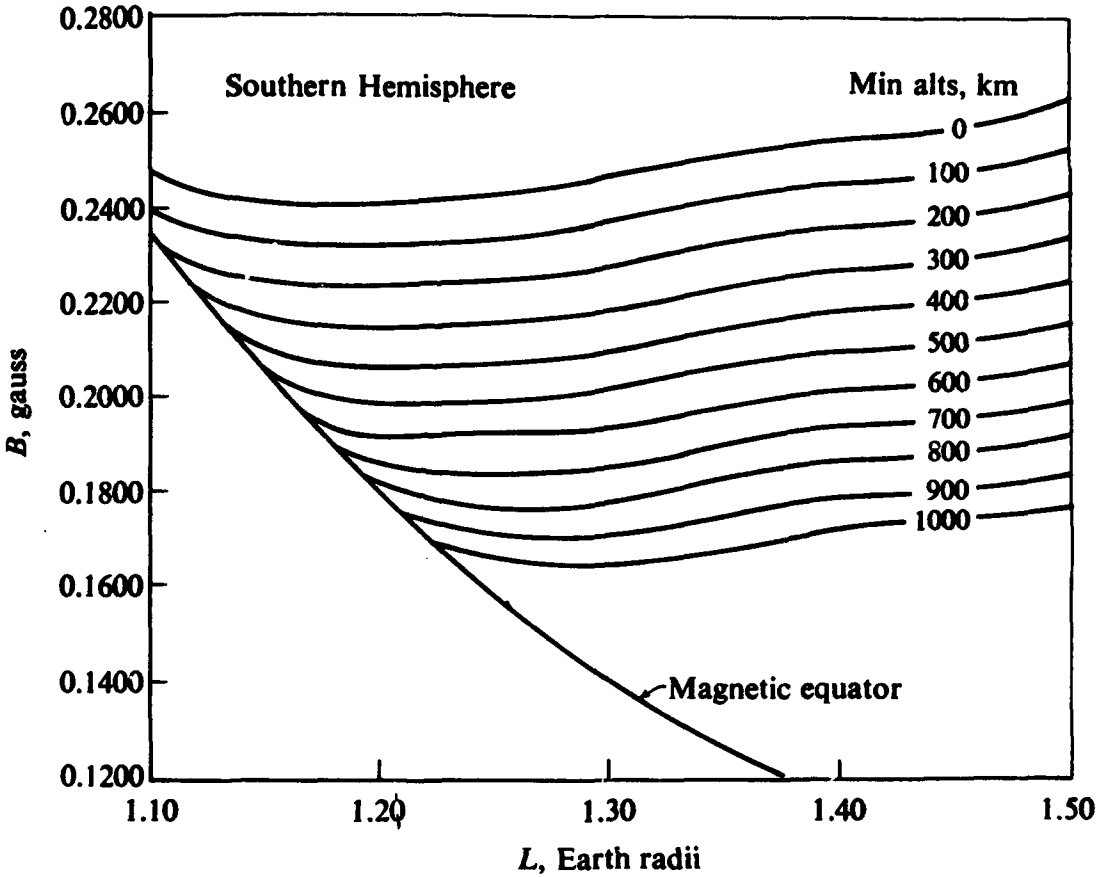

Figure 4-48. Minimum altitude curves.

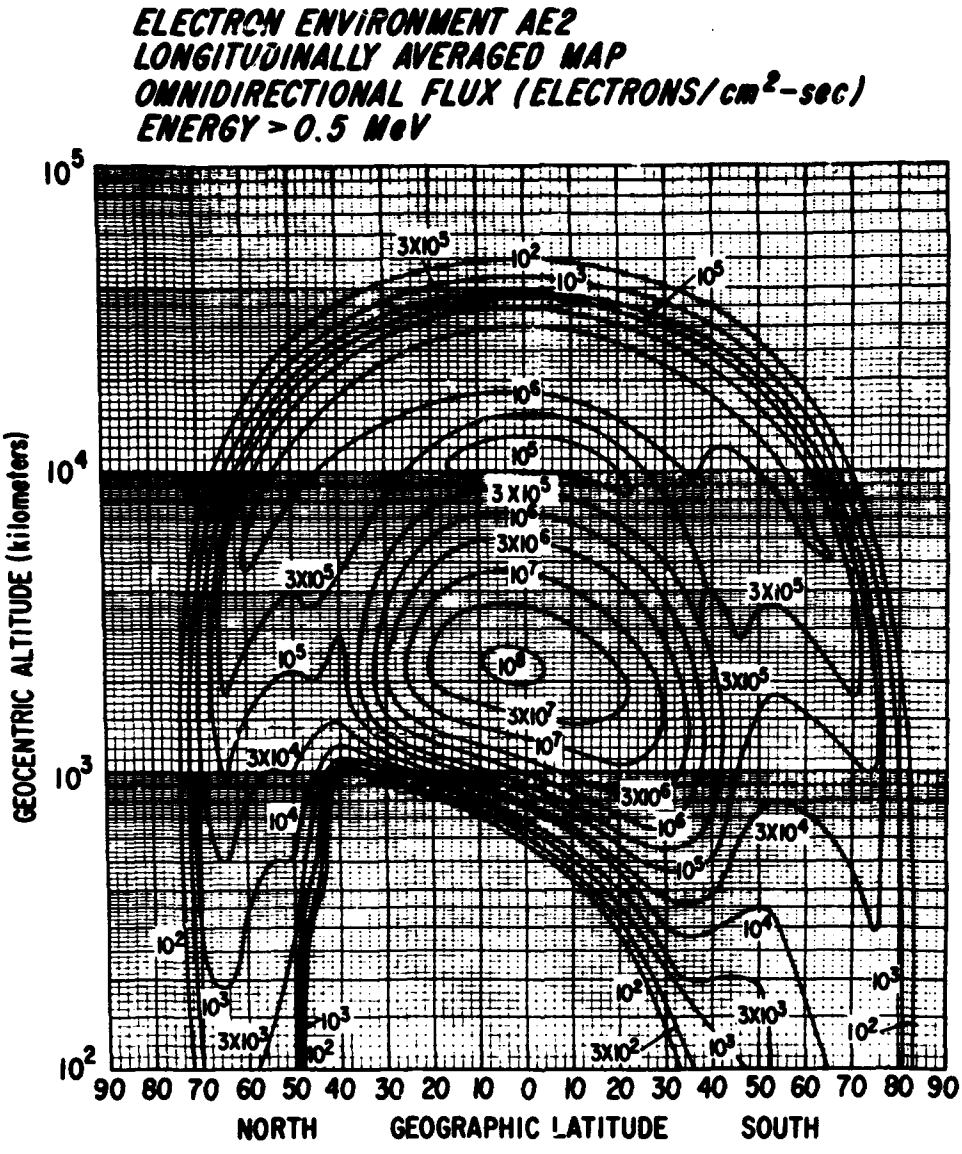

Figure 4-49. Longitudinally averaged electron flux map.

At altitudes below 350 kilometers, electrons are scattered so rapidly that longitudinal variations appear in the fluxes. The electrons that mirror at high B-values west of the anomaly will be wiped off as they drift through the anomaly as a result of scattering. Other electrons will diffuse to replenish those that are lost. Most of this replenishment should occur on the eastern slope of the anomaly. Calculations of this effect (Reference 45) predict the longitudinal behavior shown in Figure 4-50.

However, the qualitative picture of this longitudinal buildup (Reference 46), shown in Figure 4-51, shows some differences. These results show much less symmetry about the minimum point than the theoretical curves. The experimental measurements (Reference 46) were on 1963 38C, which can measure electrons above L = 2.0 at low enough minimum altitudes. B* represents the value of B that reaches altitudes between 200 and 350 kilometers in the anomaly. For $B > B^*$, all the electrons (> 280 KeV) are lost in the anomaly. For $B < B^*$, the electrons can drift through without being affected greatly. Clearly, a correct representation of the radiation environment at altitudes below 350 kilometers altitude should show longitudinal variations. However, no detailed models have been produced that incorporate this effect. Since no mechanisms exist to redistribute protons on time scales of the order of the drift period, protons do not show any longitudinal effects.

At the low altitudes between 100 and 500 kilometers, the density of the atmosphere will change over the solar cycle due to the change in ultraviolet heating (Section 11.3; Reference 47). If the particle sources change slowly in comparison, the equilibrium fluxes observed at these altitudes should change in accordance with the reciprocal of the density. Calculations of this effect on protons (Reference 48) were made assuming a cosmic ray albedo neutron source and the model atmosphere of Harris and Priester (References 45 and 46). In general, the measurements are not in good quantitative agreement with these calculations.

Heckman, Filz, and co-workers (References 42 and 50) have been monitoring high-energy protons at low altitude by flying recoverable nuclear emulsions on satellites. An increase in protons was observed following the Starfish detonation. This was caused by a redistribution of existing trapped protons, not by the injection of bomb-produced protons. The decay of this impulsive injection was consistent

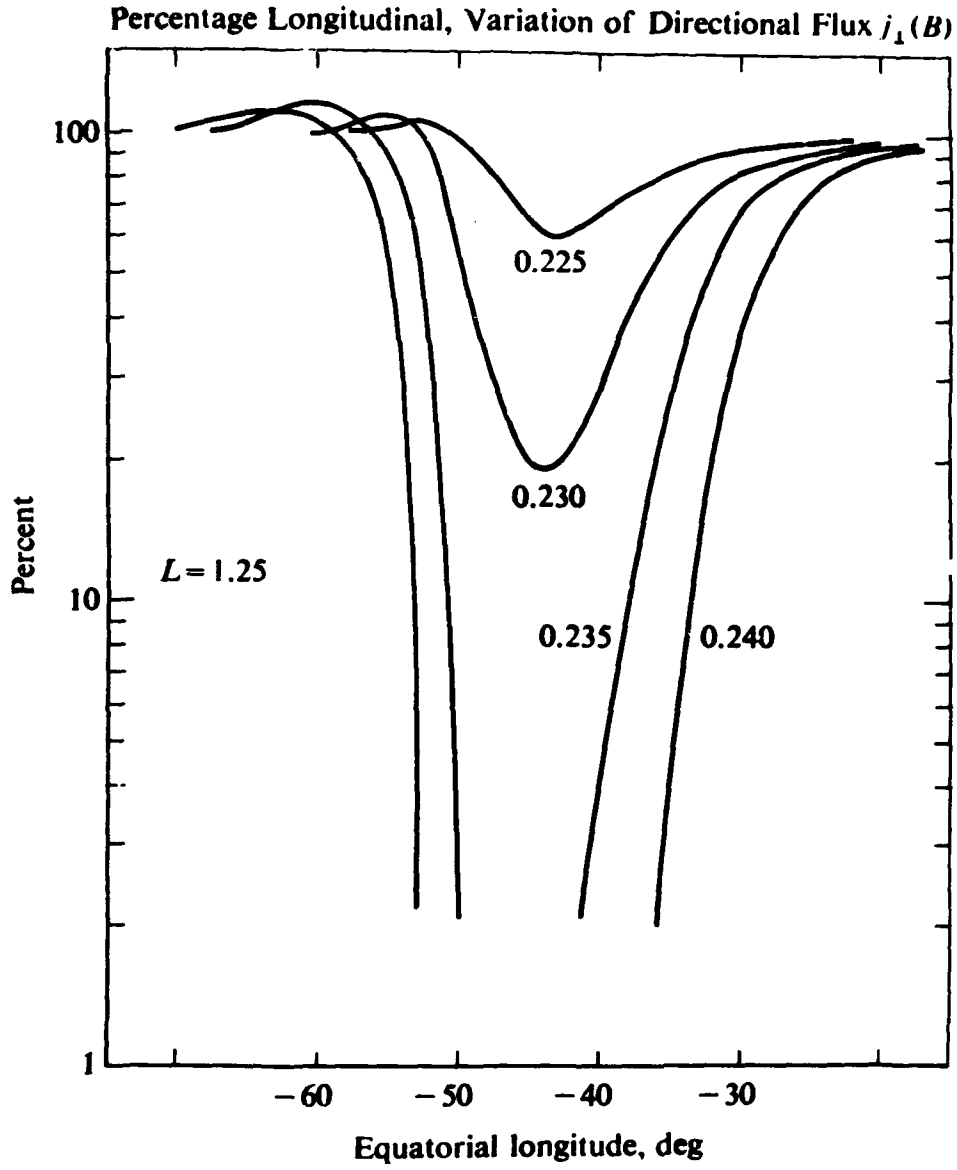

Figure 4-50. Longitudinal variation of low-altitude electron fluxes predicted from atmospheric scattering theory (Reference 45).

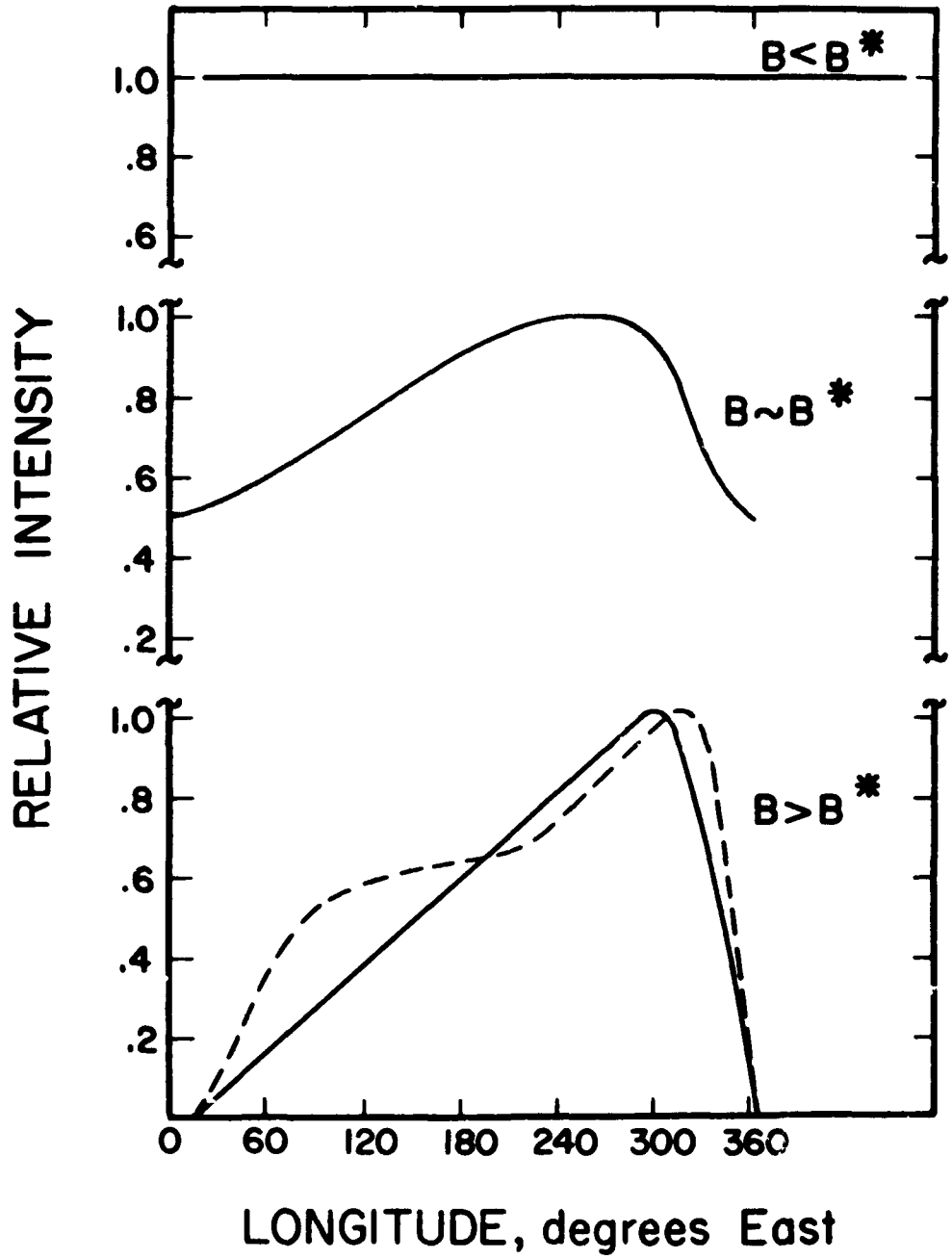

Figure 4-51. Longitudinal variation of low-altitude electron fluxes—experimental. B* is the value of B which reaches altitudes between 200 and 350 km in the anamoly (Reference 46).

with that expected from atmospheric interactions. From November 1962 to June 1966 the fluxes have been constant. However, later measurements (Reference 51) have indicated some apparent time changes in qualitative agreement with the calculations of Blanchard and Hess.

The results of these two series of measurements are shown in Figures 4-52 and 4-53. The results in Figure 4-52 were obtained by recoverable nuclear emulsions that integrate particles over the whole satellite orbit (Reference 50). For each flight, a weighted mean minimum altitude can be assigned. The sudden increase in 1962 is attributed to a redistribution of protons by the Starfish detonation on 9 July 1962. The decay curve through the points is that computed from atmospheric effects. The theoretical solar cycle effect computed by Blanchard and Hess (Reference 48) also is shown in the upper graph. The fractional change in the flux is plotted in Figure 4-53. The quantity j_c is the average flux over the time period November 1962 to June 1966. The decrease after mid-1966 is in qualitative agreement with the predicted solar cycle effect. These results were obtained by Nakano and Heckman (Reference 51) using nuclear emulsions. The results in both figures were obtained from integration throughout the orbits of the satellites. Although all the flux is accumulated in the South American anomaly, assigning a given B, L value to the measurement is impossible. The altitude profile for these series of measurements has been reproducible over the period August 1961 to November 1967 and can be expressed by:

$$J(E = 63 \text{ MeV}) = k(h_{min})^n \qquad (4\text{-}10)$$

where k is a constant, h_{min} is the effective minimum altitude that the measured protons encounter, and $n = 4.67 \pm 0.08$. The value of n depends on the gradient of the atmospheric density. The fact that n has remained constant over the observing time of 6 years indicates either that the upper atmosphere has not changed significantly over that portion of the solar cycle or that the particle motion is nonadiabatic. A diffusion of protons across L-shells in these regions is possible. Secular changes in the earth's magnetic field cause a given geographic point to have different B, L values at different times. This effect has not yet been properly taken into account in comparing proton fluxes at different time periods. All these factors make determining the actual time behavior of the low-altitude protons in B, L space difficult at this time.

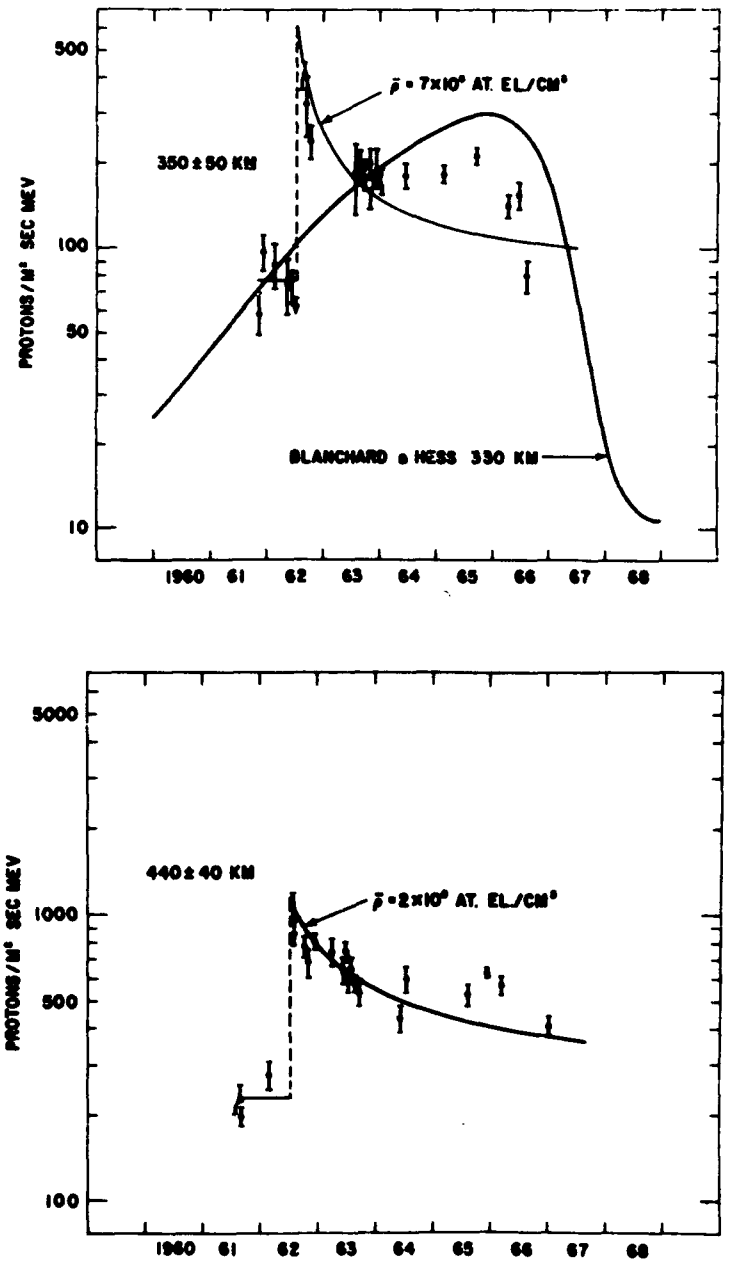

Figure 4-52. Time variation of 55-MeV protons at low altitude. (Reference 50).

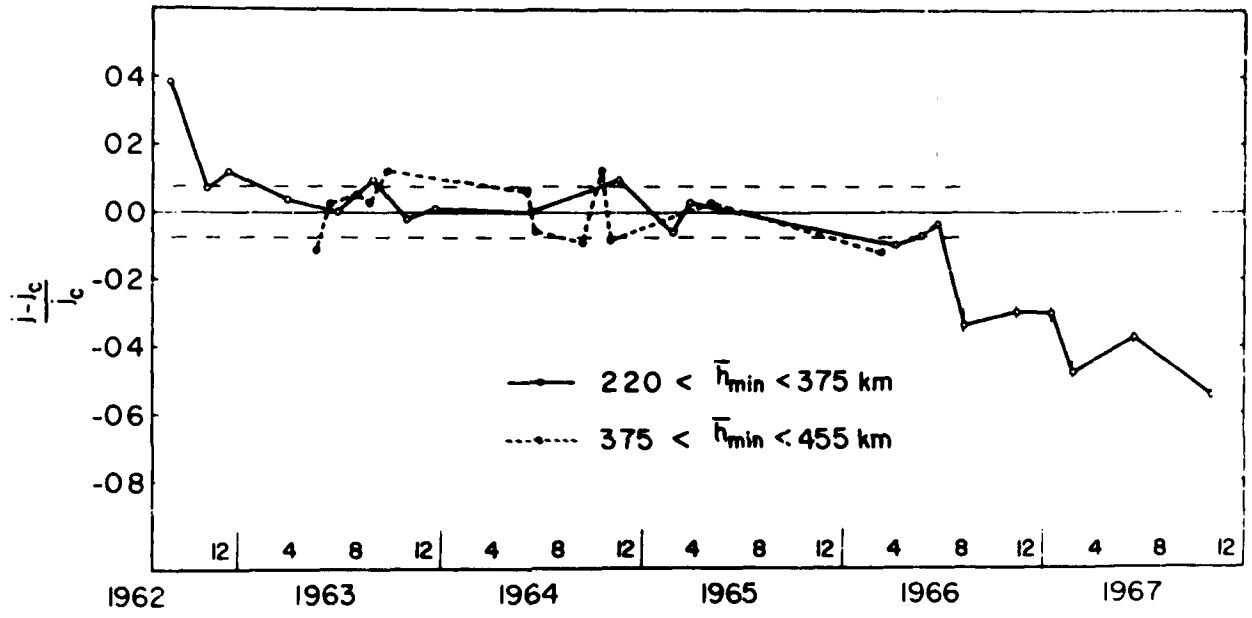

Figure 4-53. Time variation of 63-MeV protons at low altitude. The quantity j_c is the average flux over the time period November 1962 to June 1966 (Reference 51).

Two impulsive electron injections at low altitude following magnetic storms have been observed (Reference 43). These particles decayed in accordance with calculations based on atmospheric interactions. However, the long-term effective decay time of the electrons for those L-shells is much greater. Consequently, other source and loss mechanisms must be present. The main results of the long-term study of electrons at low L-values are given in Figures 4-54 and 4-55. The results in Figure 4-54 show the long-term decay after Starfish with an increase in the fluxes during a magnetic storm in October and November 1963. The references to the individual sets of measurements can be found in Reference 43. In Figure 4-55, the short-term measurements were obtained after two different electron increases during the 30 October to 3 November 1963 time period. The results are in good agreement with the theoretical results using atmospheric scattering as the loss mechanism. The much longer decay time for the long-term measurements implies additional sources and, possibly, additional loss mechanisms. Both the electron and proton data suggest that particle diffusion across L-shells is a possible source for the particles found near the inner edge of the radiation belt.

Since all of the magnetic field lines contained within the magnetosphere intersect the surface of the earth, all the magnetospheric regions described earlier can be observed at low altitudes. However, the magnetic field is not known sufficiently well to trace the field lines from the surface to distant regions. Consequently, assuring that one understands the detailed correspondence between low-altitude and high-altitude observations is difficult.

The invariant latitude of the field line at the earth's surface is commonly used to analyze high-latitude, low-altitude data. The invariant latitude is discussed in Section 3. As noted above, the particle fluxes in the outer zone, the pseudotrapping region, and the geomagnetic tail exhibit rather dynamic behavior. It should not be surprising, then, to learn that particles frequently are seen plunging down field lines to be lost in the atmosphere. An example of high-latitude precipitation zones is shown in Figure 4-56 (Reference 52). The zones were obtained by one short-lived satellite in November 1965. These are typical positions for the zones but much more data are needed to produce a good statistical study. This whole range of latitudes is known as the auroral zone where visible auroras have been seen and studied for many years. On the basis of several workers' measurements, a typical electron spectrum for precipitating auroral electrons has been prepared by Hess (Reference 1). This is shown in Figure 4-57. In the figure, E_0 is the e-folding rate in KeV.

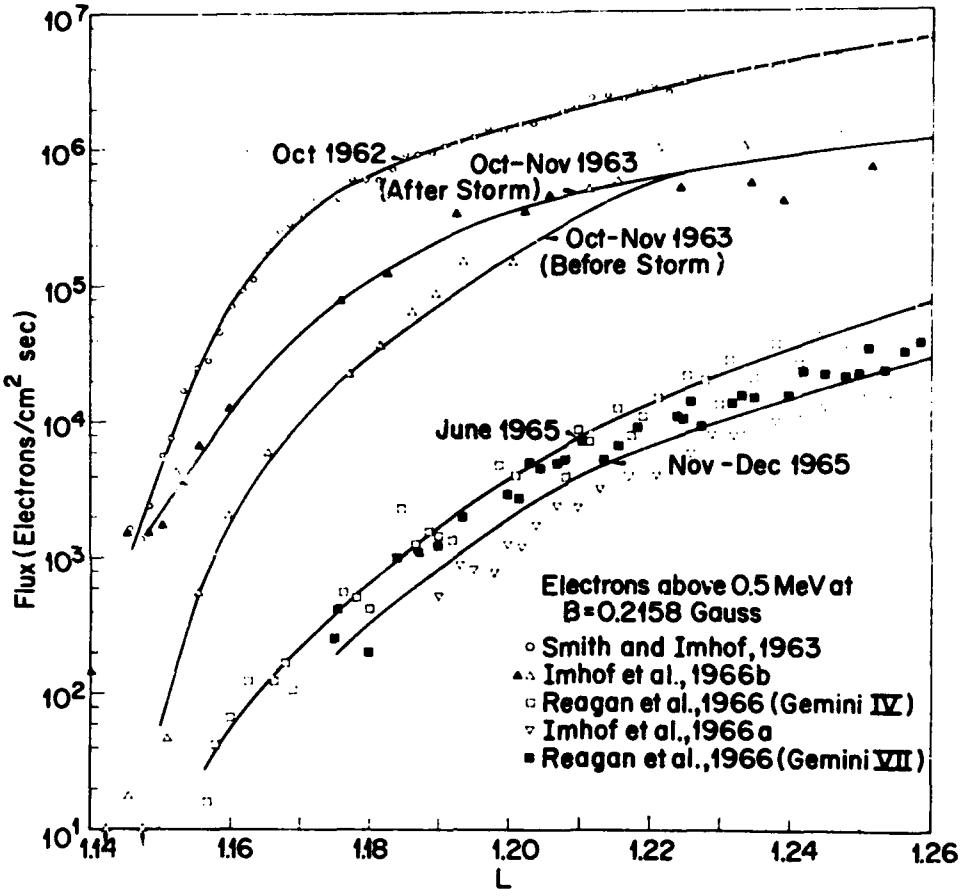

Figure 4-54. Time behavior of electrons at low L-values (Reference 43).

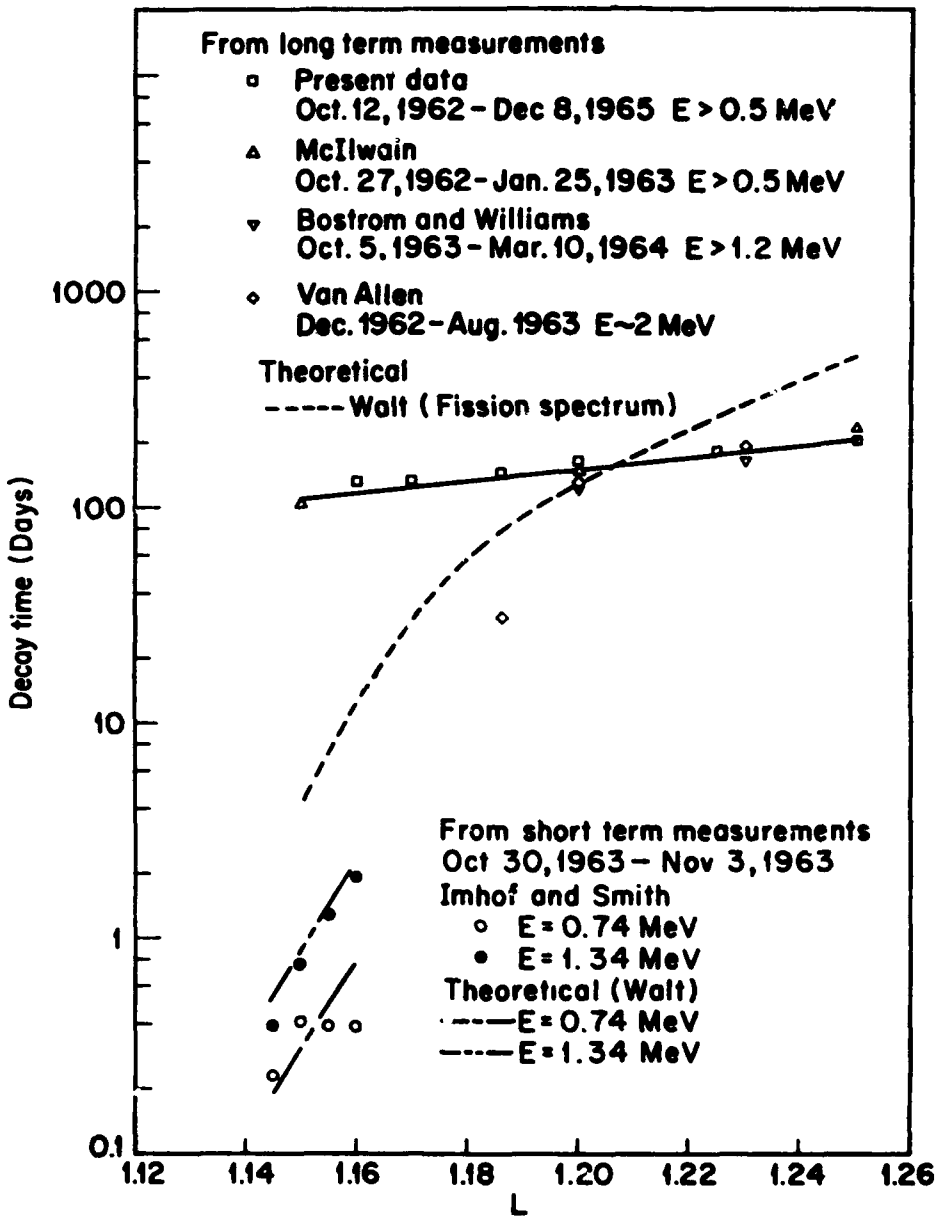

Figure 4-55. Best-fit trapped electron decay times (Reference 43).

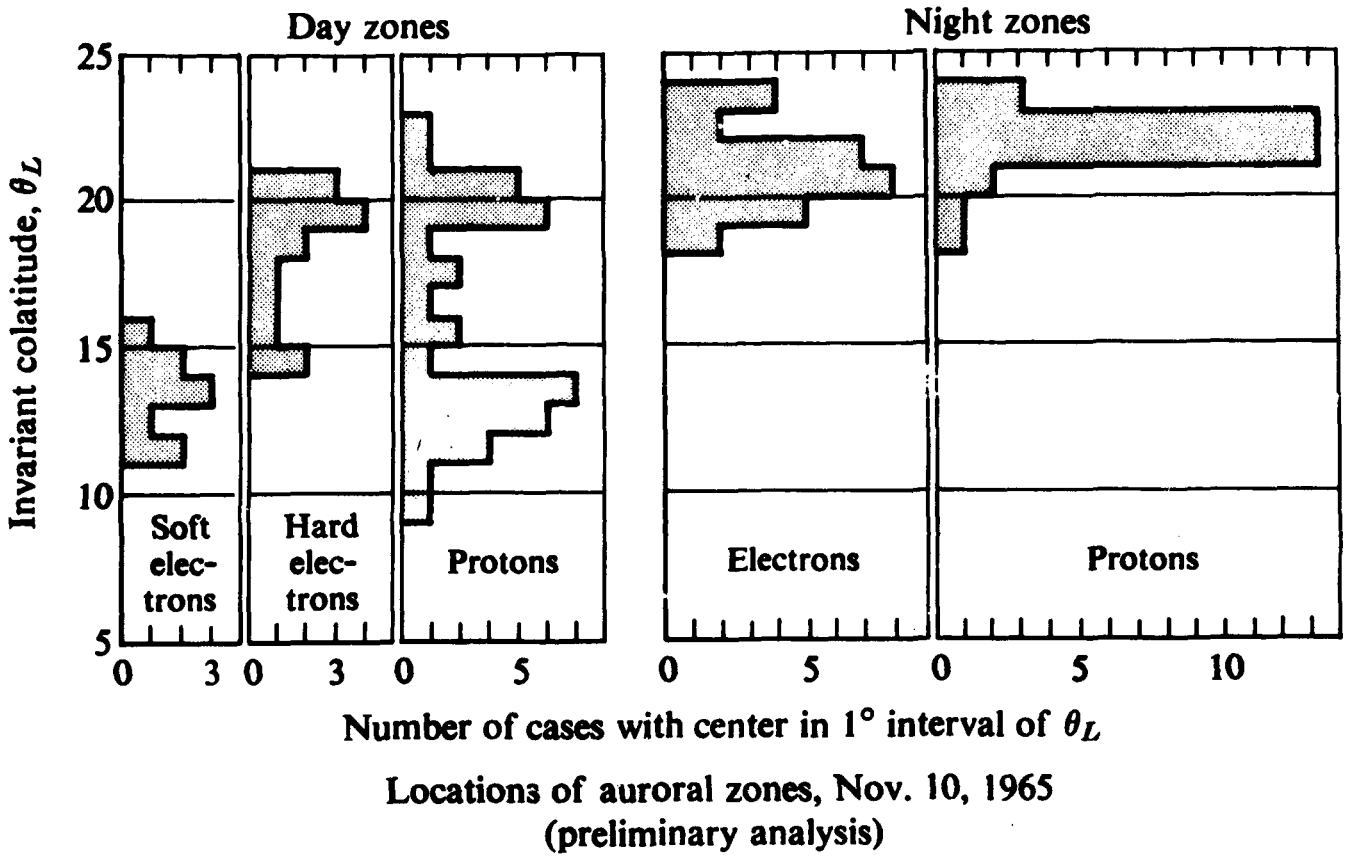

Figure 4-56. Particle precipitation zones in the auroral zone (Reference 52).

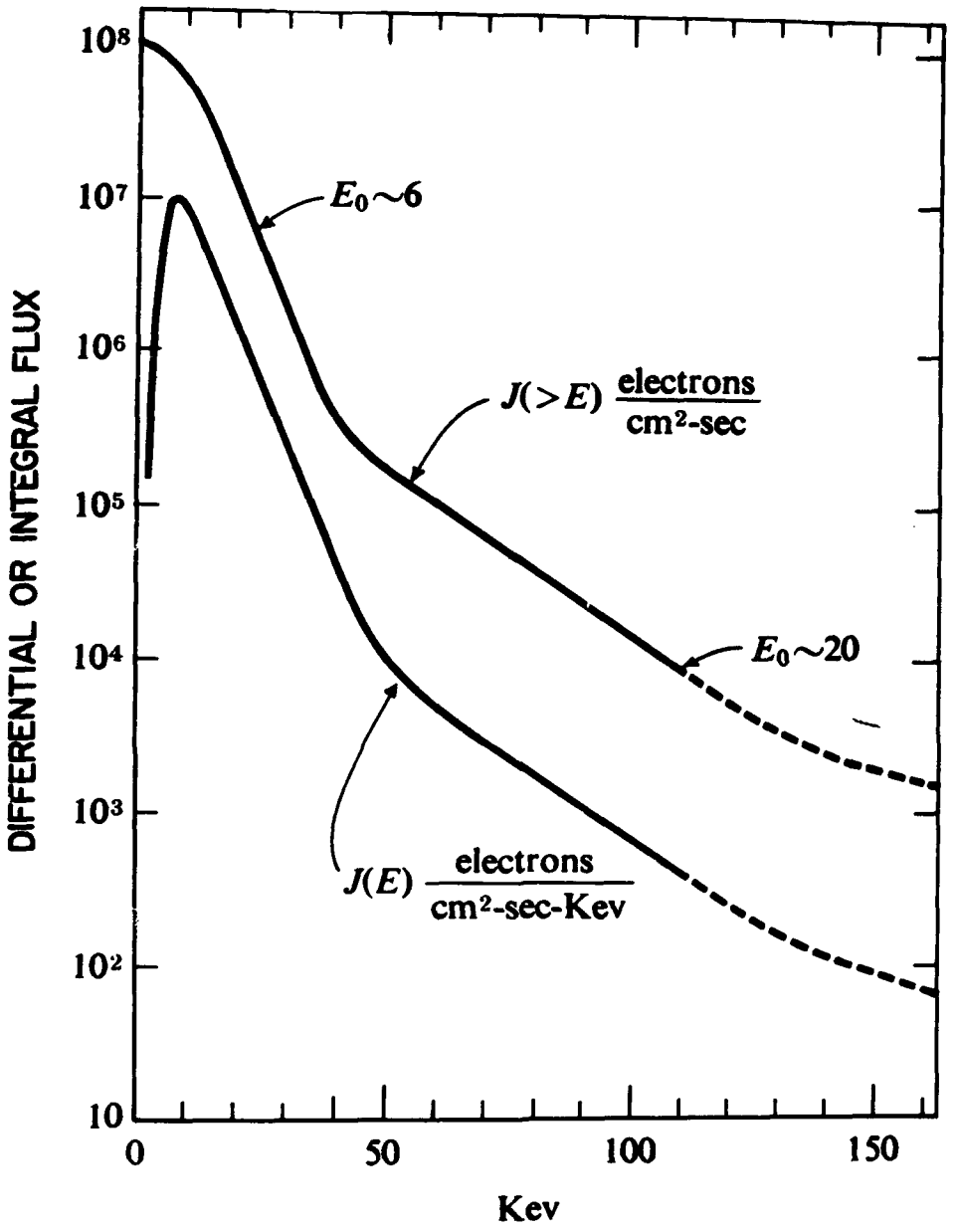

Figure 4-57. Typical energy spectra of precipitating auroral electrons. E_0 (KeV) is the e-folding rate (Reference 1).

These spectra are based on various experimental data but do not represent the output of a detailed statistical compilation. Both a differential and integral spectra are shown. The high-energy region shown by the dotted lines is not yet well known. It should be noted that the electron energy spectra differ in the two daytime zones shown in Figure 4-56.

Also, low-energy, precipitating protons with energies similar to those of electrons occur. Although no detailed models of the auroral zone precipitating particles exist, observations clearly show that this precipitation nearly always is present, although it fluctuates considerably. Consequently, a statistical approach seems desirable when enough data become available.

The particle boundaries have been seen by many low-altitude polar-orbiting satellites. Burrows and McDiarmid (Reference 53) have made detailed studies with Alouette 2 using two different detectors with electron energy thresholds of 35 KeV and 3.9 MeV. They have defined 3 types of boundaries: (1) a backgound boundary where the detector rate first drops to the cosmic ray background, (2) a smooth boundary where the 35-KeV electron profile shows a marked change in time behavior, and (3) a sharp boundary where the 35-KeV electron profile shows a sudden intensity drop of more than a factor of 10 within a latitude interval of 0.5 degrees. One result of their study is shown in Figure 4-58. They associate the smooth boundary and the 3.9-MeV background boundary with that of the stable region, the 35-KeV background boundary with the outer edge of the skirt and cusp in the tail and the trapping boundary elsewhere, and the sharp boundary with the inner edge of the cusp. The polar cap regions are intersected by the magnetic field lines, which do not normally contain particles because they are swept way back into the tail and constantly are being perturbed by changes in the interplanetary plasma parameters. However, following certain solar flares that accelerate protons and electrons, these solar particles can be seen over the polar caps as well as in interplanetary space.

4.8 SUMMARY

Section 4 has given a brief picture of the charged particles within the magnetosphere. In general near the magnetopause and in the magnetotail, the particles have energies in the 1- to 100-KeV range. Closer to the earth, these energies increase. Electrons with energies up to about 7 MeV are present around 3 earth radii, but the inner

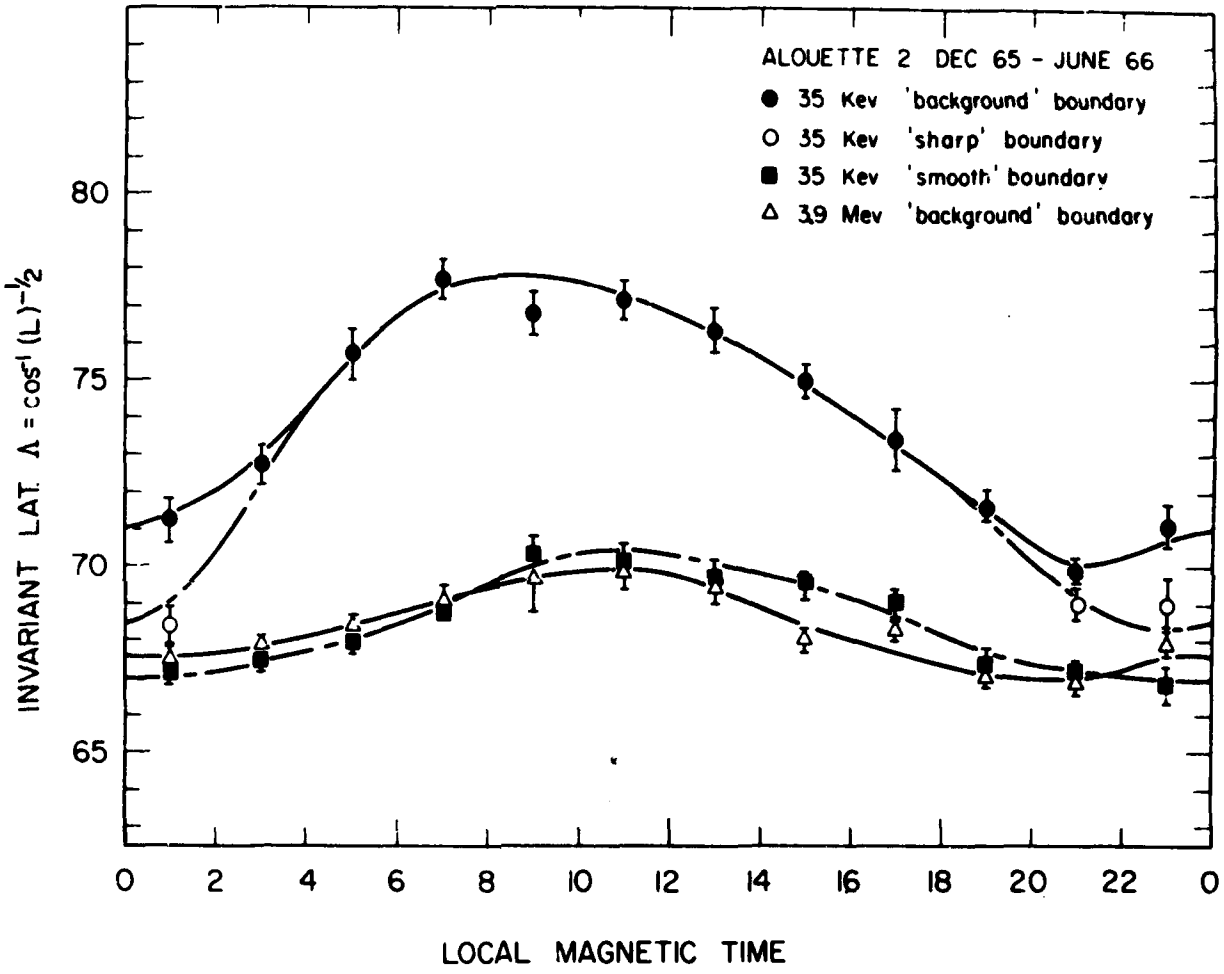

Figure 4-58. Local time variation of various outer-zone radiation boundaries that are associated with appropriate magnetospheric regions defined in the text (Reference 53).

zone does not seem to have any strong sources for electrons above 700 KeV. On the other hand, energetic protons up to several hundred MeV are present around 1.3 earth radii. Toward higher L-values maximum proton energies are observed to decrease monotonically.

In general, electrons show a much more dynamic behavior with flux levels changing by one or two orders of magnitude as the magnetosphere is perturbed by changes in the solar wind parameters. In order to discuss the particle behavior in some detail, the magnetosphere was broken into six separate regions: inner radiation, electron slot, outer radiation, pseudotrapped, geomagnetic tail, and low altitude.

REFERENCES

1. W. N. Hess. The Radiation Belt and Magnetosphere, Blaisdell Publishing Co., Waltham, Mass., 1968.

2. Introduction to Space Science, Second Edition, Gordon and Breach, Science Publishers, New York, 1968.

3. Radiation Trapped in the Earth's Magnetic Field, Proceedings of the Advanced Study Institute, Bergen, Norway, 16 August to 3 September 1965, ed. by B. M. McCormac, D. Reidel Publishing Co., Dordrecht, Holland, 1966.

4. Earth's Particles and Fields, Proceedings of the NATO Advance Study Institute, Freising, Germany, 13 July to 11 August 1967, ed. by B. M. McCormac, Reinhold Book Corp., New York, 1968.

5. "Proceedings of the International Symposium on the Physics of the Magnetosphere," Washington, D. C., 3 to 13 September 1968, Rev. Geophys., 7, 1-459, 1969

6. J. G. Roederer. "On the Adiabatic Motion of Energetic Particles in a Model Magnetosphere," J. Geophys. Res.., 72, 981-992, 1967.

7. J. I. Vette. Models of the Trapped Radiation Environment, Vol. I: Inner Zone Protons and Electrons, NASA SP-3024, 1966.

8. J. H. King. Models of the Trapped Radiation Environment, Vol. IV: Low Energy Protons, NASA SP-3024, 1967.

9. J. P. Lavine and J. I. Vette. Models of the Trapped Radiation Environment, Vol. V: Inner Belt Protons, NASA SP-3024, 1969.

10. C. O. Bostrom, D. S. Beall, and J. C. Armstrong. Trapped Particles in the Inner Zone, 1963 through 1967, presented at the International Symposium on the Physics of the Magnetosphere, Washington, D. C., 3 to 13 September 1968.

11. A. L. Thede. OV3-4 Dose Rate and Proton Spectral Measurements, AFWL-TR-128, January 1969.

12. M. Walt. "Loss Rates of Trapped Electrons by Atmospheric Collisions," Radiation Trapped in the Earth's Magnetic Field, Proceedings of the Advanced Study Institute, Bergen, Norway, 16 August to 3 September 1965, ed. by B. M. McCormac, D. Reidel Publishing Co., Dordrecht, Holland, 593-609, 1966.

13. K. A. Pfitzer and J. R. Winckler. "Experimental Observation of a Large Addition to the Electron Inner Radiation Belt after a Solar Flare Event," J. Geophys. Res., 73, 5792-5797, 1968.

14. D. S. Beall, C. O. Bostrom, and D. J. Williams. "Structure and Decay of the Starfish Radiation Belt, October 1963 to December 1965," J. Geophys. Res. 72, 3403-3424, 1967.

15. J. I. Vette, A. B. Lucero, and J. A. Wright. Models of the Trapped Radiation Environment, Vol. II: Inner and Outer Zone Electrons, NASA SP-3024, 1966.

16. E. G. Stassinopoulos. Computer Program to Calculate Radiation Belt Decay Factors, NASA Technical Note, TN D-2874, July 1965.

17. L. A. Frank and J. A. Van Allen. "Correlation of Outer Radiation Zone Electrons ($E_e \sim 1$ MeV) with the Solar Activity Cycle," J. Geophys. Res., 71, 2697-2700, 1966.

18. S. N. Vernov, E. V. Gortchakov, S. N. Kuznetsov, Yu. I. Logatchev, E. N. Sosnovets, and V. G. Stolpovsky. "Particle Fluxes in the Outer Geomagnetic Field," Rev. Geophys., 7, 257-280, 1969.

19. C. E. McIlwain. "Redistribution of Trapped Protons During a Magnetic Storm," Space Research V, Proceedings of the 5th International Space Science Symposium, Florence, 8 to 20 May 1964, ed. by P. Muller, D. G. King-Hele, and G. Righini, North-Holland Publishing Co., Amsterdam, 374-391, 1965.

20. A. G. Opp. "Penetration of the Magnetopause Beyond 6.6 R_E during the Magnetic Storm of January 13-14, 1967: Introduction," J. Geophys. Res., 73, 5697-5698, 1968. See also the succeeding seven papers in that issue.

21. D. J. Williams, J. F. Arens, and L. J. Lanzerotti. "Observations of Trapped Electrons at Low and High Altitudes," J. Geophys. Res., 73, 5673-5696, 1968.

22. F. Söraas and L. R. Davis. Temporal Variations of the 100 KeV to 1700 KeV Trapped Protons Observed on Satellite Explorer 26 During the First Half of 1965, NASA-GSFC-X-612-68-328, August 1968 (to be published).

23. J. I. Vette and A. B. Lucero. Models of the Trapped Radiation Environment, Vol. III: Electrons at Synchronous Altitudes, NASA SP-3024, 1967.

24. L. R. Davis and J. M. Williamson. "Low Energy Trapped Protons," Space Res. III, Proceedings of the 3rd International Space Science Symposium, Washington, D. C., 2 to 8 May 1962, ed. by W. Priester, North-Holland Publishing Co., Amsterdam, 365-375, 1962.

25. L. R. Davis and J. M. Williamson. "Outer Zone Protons," Radiation Trapped in the Earth's Magnetic Field, Proceedings of the NATO Advaned Study Institute, Bergen, Norway, 16 August to 3 September 1965, ed. by B. M. McCormac, D. Reidel Publishing Co., Dordrecht, Holland, 215-230, 1966.

26. L. A. Frank. "On the Distributions of Low-Energy Protons and Electrons in the Earth's Magnetosphere," Earth's Particles and Fields, Proceedings of the NATO Advanced Study Institute, Freising, Germany, 31 July to 11 August 1967, ed. by B. M. McCormac, Reinhold Book Corp., New York, 67-87, 1968.

27. S. M. Krimigis and J. A. Van Allen. "Distribution and Energy Spectrum of Alpha-Particles in the Radiation Zones," Earth's Particles and Fields, Proceedings of the NATO Advanced Study Institute, Freising, Germany, 31 July to 11 August 1967, ed. by B. M. McCormac, Reinhold Book Corp., New York, 127-140, 1968.

28. G. A. Paulikas, J. B. Blake, and S. C. Freden. Trapped Energetic Alpha Particles in the Outer Radiation Belt, Aerospace Corp., TR-0200(4260-20)-03, November 1968.

29. L. A. Frank, J. A. Van Allen, and E. Macagno. "Charged-Particle Observations in the Earth's Outer Magnetosphere," J. Geophys. Res., 68, 3543-3554, 1963.

30. L. A. Frank. "Survey of Electrons E > 40 KeV Beyond 5 Earth Radii with Explorer 14," J. Geophys. Res., 70, 1593-1626, 1965.

31. L. A. Frank and J. A. Van Allen. "Measurements of Energetic Electrons in the Vicinity of the Sunward Magnetospheric Boundary with Explorer 14," J. Geophys. Res., 69, 4923-4932, 1964.

32. K. A. Anderson, H. K. Harris, and R. J. Paoli. "Energetic Electron Fluxes in and Beyond the Earth's Magnetosphere," J. Geophys. Res., 70, 1039-1050, 1965.

33. K. A. Anderson. "Energetic Electron Fluxes in the Tail of the Geomagnetic Field," J. Geophys. Res., 70, 4741-4764, 1965.

34. A. Rosen. "Radiation Belt Boundary Near Solar Cycle Maximum as Determined from the Trapping of Energetic Electrons," J. Geophys. Res., 70, 4793-4816, 1965.

35. J. H. Wolfe, R. W. Silva, D. D. McKibbin, and R. H. Mason. "Preliminary Observations of Geomagnetospheric Wake at 1000 Earth Radii," J. Geophys. Res., 72, 4577-4581, 1967.

36. T. Murayama. "Spatial Distribution of Energetic Electrons in the Geomagnetic Tail," J. Geophys. Res., 71, 5547-5558, 1966.

37. M. D. Montgomery. "Observations of Electrons in the Earth's Magnetotail by Vela Launch 2 Satellites," J. Geophys. Res., 73, 871-890, 1968.

38. S. J. Bame, J. R. Asbridge, H. E. Felthauser, E. W. Hones, and I. B. Strong. "Characteristics of the Plasma Sheet in the Earth's Magnetotail," J. Geophys. Res., 72, 113-130, 1967.

39. A. Konradi. "Electron and Proton Fluxes in the Tail of the Magnetosphere," J. Geophys. Res., 71, 2317-2376, 1966.

40. S. J. Bame. "Plasma Sheet and Adjacent Regions," Earth's Particles and Fields, Proceedings of the NATO Advanced Study Institute, Freising, Germany, 31 July to 11 August 1967, ed. by B. M. McCormac, Reinhold Book Corp., New York, 372-383, 1968.

41. V. M. Vasyliunas. "Low-Energy Electrons on the Day Side of the Magnetosphere," J. Geophys. Res., 73, 7519-7523, 1968.

42. H. H. Heckman and G. H. Nakano. Low-Altitude Trapped Protons During Solar Minimum Period, 1962-66, University of California, UCRL-18422, September 1968.

43. W. L. Imhof, J. B. Reagan, and R. V. Smith. "Long-Term Study of Electrons Trapped on Low L Shells," J. Geophys. Res., 72, 2371-2378, 1967.

44. W. F. Dudziak, D. D. Kleinecke, and T. J. Kostigen. Graphic Displays of Geomagnetic Geometry, RM63TMP-2, DASA 1372, April 1963.

45. J. G. Roederer and J. A. Welch. "Calculations of Longitude Dependence of Geomagnetically Trapped Electron Fluxes," Space Res. VI, Proceedings of the Sixth International Space Science Symposium, Mar Del Plata, Argentina, 11 to 19 May 1965, ed. by R. L. Rose-Smith, MacMillan and Co., Ltd., London, 148-164, 1966.

46. D. J. Williams and J. W. Kohl. "Loss and Replenishment of Electrons at Middle Latitudes and High B Values," J. Geophys. Res., 70, 4139-4150, 1965.

47. I. Harris and W. Priester. "Theoretical Models for the Solar-Cycle Variation of the Upper Atmosphere," J. Geophys. Res., 67, 4585-4591, 1962.

48. R. C. Blanchard and W. N. Hess. "Solar Cycle Changes in Inner-Zone Protons," J. Geophys. Res., 69, 3927-3938, 1964.

49. I. Harris and W. Priester. "Relation Between Theoretical and Observational Models of the Upper Atmosphere," J. Geophys. Res., 68, 5891-5894, 1963.

50. R. Filz. "Observations of Inner Zone Protons in Nuclear Emulsions, 1961 to 1966, "Earth's Particles and Fields, Proceedings of the NATO Advanced Study Institute, Freising, German, 31 July to 11 August 1967, ed. by B. M. McCormac, Reinhold Book Corp., New York, 15-22, 1968.

51. G. H. Nakano and H. H. Heckman. "Evidence for Solar-Cycle Changes in the Inner-Belt Protons," Phys. Rev. Letters, 20, 806-809, 1968.

52. R. D. Sharp and R. G. Johnson. "Satellite Measurements of Auroral Particle Precipitation," Earth's Particles and Fields, Proceedings of the NATO Advanced Study Institute, Freising, Germany, 31 July to 11 August 1967, ed. by B. M. McCormac, Reinhold Book Corp., New York, 113-125, 1968.

53. J. R. Burrows and I. B. McDiarmid. "Local Time Asymmetries Near the High Latitude Boundary of the Outer Radiation Zone," Earth's Particles and Fields, Proceedings of the NATO Advanced Study Institute, Freising, Cermany, 31 July to 11 August 1967, ed. by B. M. McCormac, Reinhold Book Corp., New York, 45-56, 1968.

SECTION 5

SOURCES AND LOSSES OF TRAPPED PARTICLES

G.T. Davidson, Lockheed Palo Alto Research Laboratory

5.1 INTRODUCTION

Most of the unsolved problems relating to the trapped radiation belts have to do with two broad question: (1) Where do such large numbers of energetic particles come from and (2) Why, after they have been trapped, do they disappear again? Only partial answers are available. The source of high-energy trapped protons has been ascribed with a fair degree of success to decay of cosmic-ray-produced albedo neutrons. The same mechanism is quite inadequate to explain trapped electrons and low-energy protons.

Observations of the decay of artificial radiation belts have shown that the principal loss mechanism on low L-shells ($L < 1.25$) must be collisions in the atmosphere. Some additional loss mechanism must certainly exist that affects particles on higher L-shells. A large amount of effort has been expended in analyzing the effects of diffusion of particles across L-shells, and limited success has been achieved for some special instances. Otherwise, the L-shell diffusion theory is far from complete.

Many interesting particular effects have been explained, but their relevance to the overall picture of trapping and losses is not well understood. A recent subject of much attention has been the interaction of plasma waves with trapped particles. This topic is still rather controversial.

The Sections 5.2 and 5.3 treat the pure loss or source mechanisms, such as loss through repeated collisions with atmospheric particles and the neutron decay injection theory. Succeeding subsections discuss more complicated processes that may be responsible not only for injection and removal of particles but also for redistribution within the trapping regions.

Unfortunately, space limitations prohibit citing all the important reference materials. The references in this section are intended

primarily as a guide to further reading. For a more extensive list of source materials see Reference 1, which is a satisfactorily thorough survey of the subject.

5.2 LOSSES IN THE ATMOSPHERE

5.2.1 Particle Collisions

Section 3 considered the motion of isolated particles. The results of Section 3 hold if particle collisions do not substantially alter the motions. Not obvious, however, is that collision effects can be ignored when dealing with large numbers of particles. In the lowest parts of the atmosphere, the air behaves as a collision-dominated fluid with only rare manifestations of plasma-like behavior. One should expect that intermediate regions exist in the high atmosphere in which the effects of collisions and electromagnetic fields are comparable.

A fast, charged particle in an un-ionized medium loses energy efficiently through collisions with atomic electrons and nuclei. Orbital electrons involved in a collision may be excited to higher energy states or may be removed completely from the parent atoms. The resulting energy lost per unit trajectory distance by a fast particle of charge $\pm e$ and velocity v encountering stationary particles of charge $\pm e$ is the stopping power (References 2, 3, and 4):

$$-\frac{dE}{ds} = -\frac{dT}{ds} = \frac{2\pi e^4}{m_r v^2} n \ln \frac{(\text{maximum energy exchange})}{(\text{minimum energy exchange})} . \qquad (5\text{-}1)$$

The energy loss is proportional to the number density of stationary charged particles, n. The mass that frequently appears in formulas related to collisions between two particles is the reduced mass (Reference 5):

$$m_r = \frac{m_1 m_2}{m_1 + m_2} . \qquad (5\text{-}2)$$

When both particles are electrons, the reduced mass is $m_e/2$. When both are protons, the reduced mass is $m_p/2$. Otherwise, if one particle is an electron and the other is much heavier, the reduced mass is nearly equal to the electron mass, m_e. Because the reduced mass in collisions with electrons is small, the slowing of heavy, charged particles is due almost entirely to collisions with bound and free electrons (Reference 1).

The maximum energy transfer is determined by the dynamics of the collision process. It corresponds to direct impact with a scattering angle $\Theta \approx 180$ degrees in the center of mass reference frame (Reference 5). The maximum momentum exchange is so great that a bound electron behaves as though it were free of the parent atom (Reference 1).

The minimum energy transfer should correspond to nearly zero deflection. However, no well-defined minimum energy transfer exists when the particles are interacting through their electrostatic forces. The electrostatic forces between charged particles decrease so slowly with their separation that charged particles situated at infinite distances would seem to make a finite contribution to the stopping power (References 3 and 4). But a minimum energy transfer equal to zero would yield a false result. Actually, outside an atom or molecule, the electric fields of the nucleus and orbital electrons are mutually cancelled. The minimum energy exchange occurs in a collision in which the distance of closest approach is somewhat greater than the effective atomic radius (References 3 and 4).

The stopping power for heavy particles colliding with atomic electrons is

$$-\frac{dT}{ds} = Cn_b \frac{c^2}{v^2}\left(\ln\frac{2m_e v^2\gamma^2}{I^*} - \frac{v^2}{c^2}\right) \tag{5-3a}$$

$$C \equiv \frac{4\pi e^4}{m_e c^2}$$

$$= 8.168 \times 10^{-3}\ \text{cgs} = 5.099 \times 10^{-19}\ \text{eV cm}^2 \tag{5-3b}$$

where I^* is a mean excitation-ionization potential of the atoms and n_b is the average bound electron density. The parameters v and γ (the relativistic dilation factor) pertain to the fast particle.

The collision of electrons and heavy particles is governed by the Rutherford cross section (References 4 and 5). Scattering of electrons by electrons is somewhat more complicated. The relevant cross section is the Møller cross section (References 6 and 7). The stopping power that results for fast electrons (Reference 3) is

$$-\frac{dT}{ds} = C n_b \frac{c^2}{v^2}\left[\frac{1}{2}\ln\frac{m_e c^2 v^2 \gamma^3}{2I^{*2}} - \frac{2\gamma-1}{2\gamma^2}\ln 2 + \frac{1}{2\gamma^2} + \frac{1}{16}\left(\frac{\gamma-1}{\gamma}\right)^2\right] \quad (5\text{-}4a)$$

$$= C n_b \frac{c^2}{v^2}\left[\frac{1}{2}\ln\frac{p^2(T+m_e c^2)}{2I^{*2} m_e c^2} - \frac{m_e c^2(2T+m_e c^2)}{2(T+m_e c^2)}\ln 2 + \frac{1}{2}\left(\frac{m_e c^2}{T+m_e c^2}\right)^2 + \frac{1}{16}\left(\frac{T}{T+m_e c^2}\right)^2\right]. \quad (5\text{-}4b)$$

Stopping power formulas must be applied with caution for those electrons that have only enough energy that they are deflected through large angles before undergoing noticeable energy degradation. Multiple deflections are discussed in Section 5.2.2.

In an ionized gas the electrons are not bound; therefore, the minimum collisional momentum transfer is independent of atomic parameters. Thermal fluctuations are responsible for the effective shielding of a charged particle at distances greater than the Debye length λ_D (Section 3.6.1; Reference 8). A stopping power relevant to heavy particles colliding with free electrons (Reference 9) is

$$-\frac{dT}{ds} = C n_e \frac{c^2}{v^2}\left(\ln\frac{2m_e v\gamma^2\lambda_D}{\hbar} - \frac{1}{2\gamma^2}\right) \quad (5\text{-}5)$$

where $h = 2\pi\hbar$ is Planck's constant. The fully relativistic stopping power of electrons in an ionized gas apparently has not been worked out; for most purposes, employing Equation 5-5 with the appropriate electron parameters (Reference 10) will be sufficient.

Because the Debye length is so very much greater than the dimensions of atoms, each free electron is several times as effective as an individually bound atomic electron in stopping fast charged particles. The ratio of Equations 5-3 to 5-5 is approximately the ratio of the logarithm terms. Even if fractional ionization is only 25 percent, the free electrons may be as important to slowing processes as bound electrons.

The range,

$$R(T) = \int_{T}^{0} \left(- \frac{ds}{dT} \right) dT \ , \qquad (5\text{-}6)$$

is a useful indicator of the lifetime of a fast charged particle (References 3 and 4). Computed ranges of electrons, protons, and alpha particles in the most important atmospheric constituents are presented in Figure 5-1. The figure is similar to one presented by Lenchek and Singer (References 11 and 12). The ranges (Equation 5-6) have been computed by Berger and Seltzer (Reference 13) and by Barkas and Berger (Reference 14) using stopping power formulas. The range in centimeters is obtained after a division by the mass density of the stopping material. On this scale, the ranges in oxygen or nitrogen are nearly indistinguishable from the range in air. Several mean path lengths for nuclear and atomic reactions involving fast protons also are shown. The data on nuclear collisions and charge-exchange reactions are derived from References 15 through 19 (Section 5.2.4).

The energy loss rate per unit time is just the stopping power multiplied by velocity. Numerical substitution in Equations 5-3 through 5-5 yields the loss rates for electrons and protons:

$$- \frac{dT}{dt} \left(\text{eV sec}^{-1} \right) \cong C' n_b \frac{c}{v} \left[3.34 + \log_{10} T(\text{MeV}) - \log_{10} I^{*} (\text{eV}) \right.$$

$$\left. - 0.65 \left(\frac{T}{m_p c^2} \right) + 1.25 \left(\frac{T}{m_p c^2} \right)^2 \right] \quad \left\{ \begin{array}{l} \text{protons } T \ll m_p c^2 \\ \text{atomic collisions} \end{array} \right. \qquad (5\text{-}7)$$

$$- \frac{dT}{dt} \left(\text{eV sec}^{-1} \right) \cong C' n_e \frac{c}{v} \left[5.43 + \frac{1}{2} \log_{10} T(\text{MeV}) + \frac{1}{2} \log_{10} T_e(\text{k}) / n_e(\text{cm}^{-3}) \right.$$

$$\left. + 0.98 \left(\frac{T}{m_p c^2} \right) - 0.90 \left(\frac{T}{m_p c^2} \right)^2 \right] \quad \left\{ \begin{array}{l} \text{protons } T \ll m_p c^2 \\ \text{free electron collisions} \end{array} \right. \qquad (5\text{-}8)$$

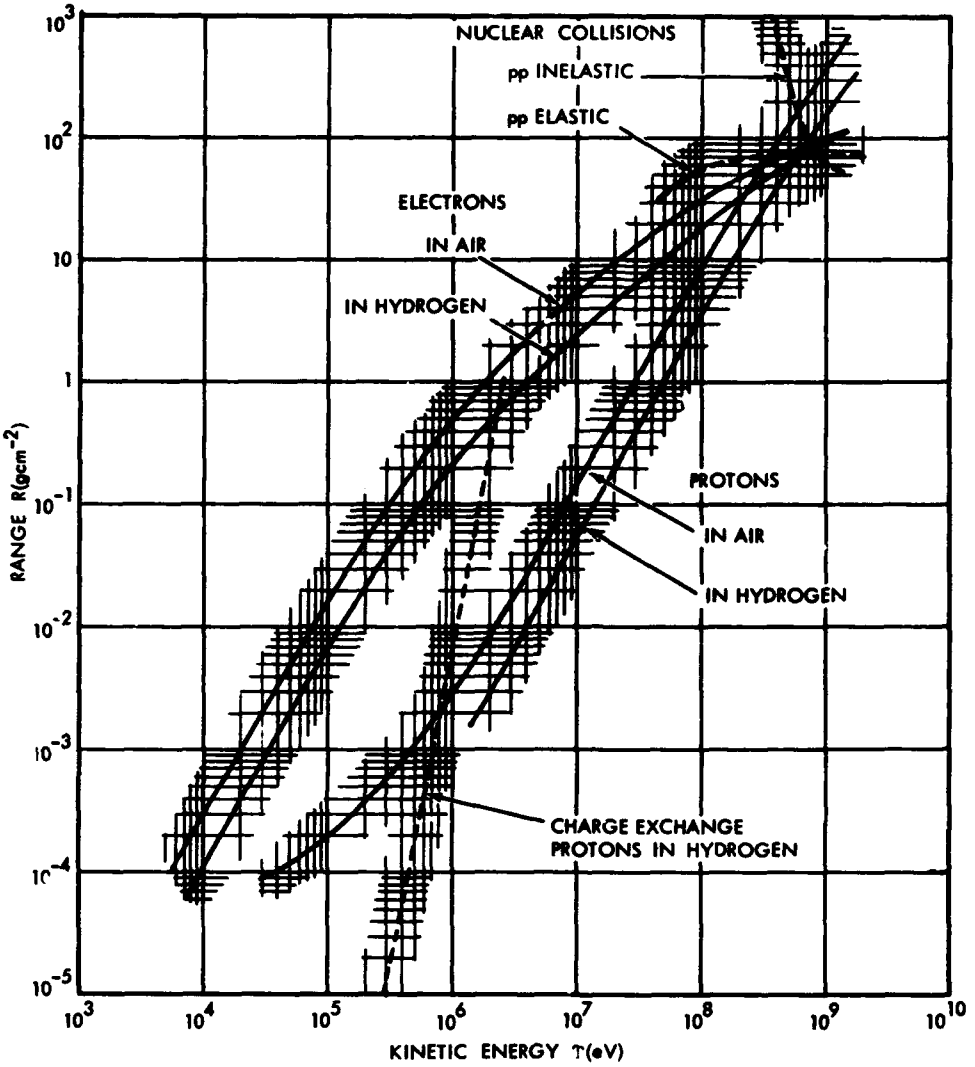

Figure 5-1. Ranges of electrons and protons in the air. This figure is similar to one presented by Lenchek and Singer (References 11 and 12). The ranges (Equation 5-6) have been computed by Berger and Seltzer (Reference 13) and by Barkas and Berger (Reference 14) using stopping power formulas. The range in centimeters is obtained after a division by the mass density of the stopping material. On this scale, the ranges in oxygen or nitrogen are nearly indistinguishable from the range in air. Several mean path lengths for nuclear and atomic reactions involving fast protons also are shown. The data on nuclear collisions and charge-exchange reactions are derived from References 15 through 19 (Section 5.2.4).

$$-\frac{dT}{dt}\left(\text{eV sec}^{-1}\right) \cong C' n_b \frac{c}{v}\left[5.92 + \frac{1}{2}\log_{10} T(\text{MeV}) - \log_{10} I^*(\text{eV}) - 0.11\left(\frac{T}{m_e c^2}\right) + 0.69\left(\frac{T}{m_e c^2}\right)^2\right] \quad \left\{\begin{array}{l}\text{electrons } T \ll m_e c^2 \\ \text{atomic collisions}\end{array}\right. \tag{5-9a}$$

$$-\frac{dT}{dt}\left(\text{eV sec}^{-1}\right) \cong C' n_b \frac{c}{v}\left[6.62 + \frac{3}{2}\log_{10} T(\text{MeV}) - \log_{10} I^*(\text{eV}) + 0.30\left(\frac{m_e c^2}{T}\right) + 0.21\left(\frac{m_e c^2}{T}\right)^2\right] \quad \left\{\begin{array}{l}\text{electrons } T \gg m_e c^2 \\ \text{atomic collisions}\end{array}\right. \tag{5-9b}$$

$$-\frac{dT}{dt}\left(\text{eV sec}^{-1}\right) \cong C' n_e \frac{c}{v}\left[10.0 + \frac{1}{2}\log_{10} T(\text{MeV}) + \frac{1}{2}\log_{10} T_e(k)/n_e\left(m^{-3}\right)\right] \quad \left\{\begin{array}{l}\text{electrons} \\ \text{free electron collisions}\end{array}\right. \tag{5-10}$$

$$C' = 3.520 \times 10^{-7}$$

The relevant electron densities (in electrons per cubic centimeter) are presented in Figure 5-2. The total density of bound electrons contributed by each constituent (usually) falls somewhere within the appropriate shaded region. The information is extracted principally from Section 12 (References 20, 21, and 22). This figure shows the extreme limits of n_e and n_b to be expected under all solar conditions and at all times of day. The 11-year solar cycle variation and the diurnal variation make up roughly equal parts of the entire range between upper and lower limits. The temporal variations are discussed more thoroughly in Section 12.

Some values of I^* and $\log_{10} I^*$ are given in Table 5-1 for representative atmospheric constituents. The contributions of individual constituents to the stopping power are additive. Generally one constituent prevails so it is only necessary to employ the total electron density and the average ionization-excitation potential of the dominant constituent.

When stopping powers are written as functions of velocities, only small differences occur between electron and proton formulas. In

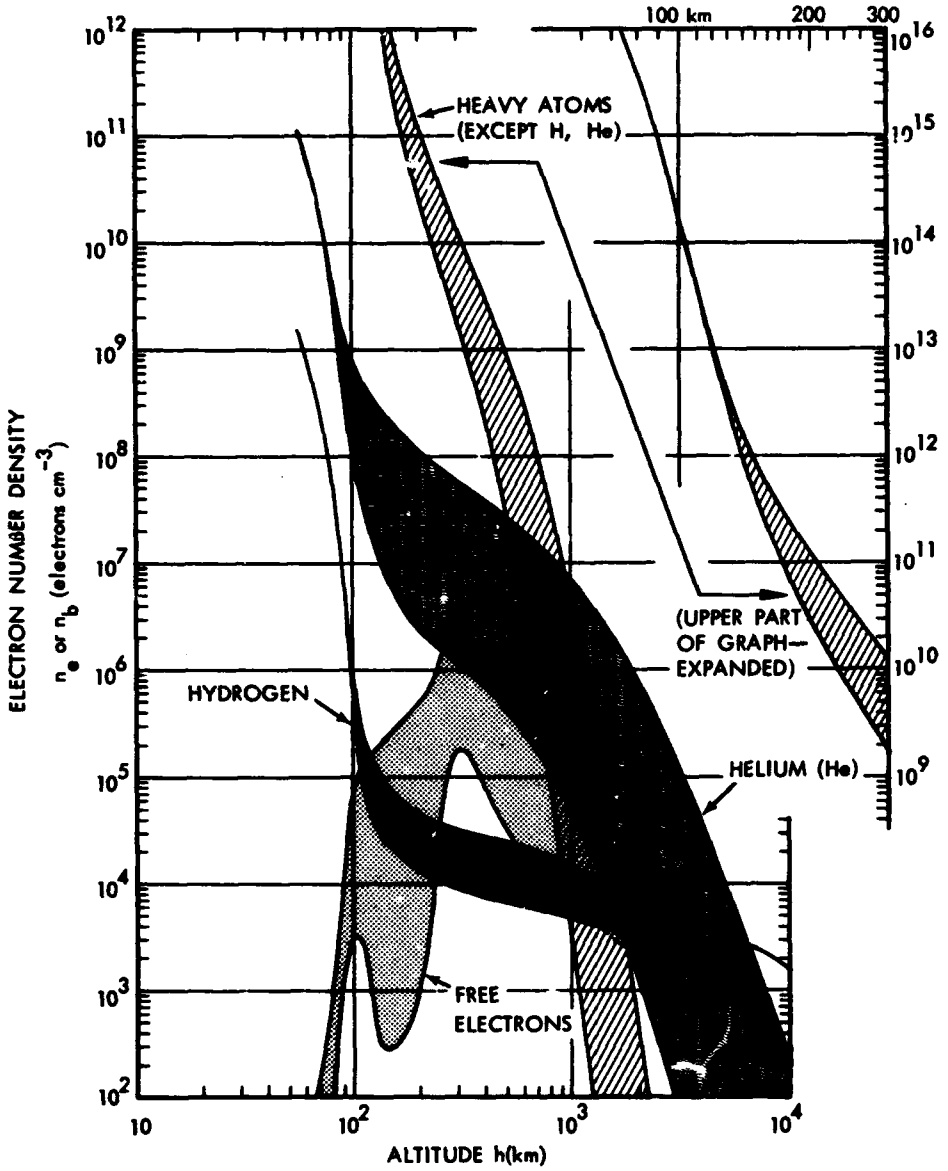

Figure 5-2. Electron number densities in the atmosphere. The total density of bound electrons contributed by each constituent (usually) falls somewhere within the shaded region.

Table 5-1. Excitation ionization potentials (Reference 23).

Material	I^* (eV)	$\log_{10} I^*$	Predominates in Altitude Range (km)
Air (nitrogen)	87	1.94	< 300
Oxygen	97	1.99	300 < h < 800
Helium	44	1.64	800 < h < 5000
Hydrogen	18	1.26	5000 < h

Equation 5-7, the first two terms in the square brackets become $6.60 + \log_{10}(m_e/m_p)T(\text{MeV})$. The difference between Equations 5-7 and 5-9b is only about 10 percent when particles of comparable velocities are considered.

The energy loss lifetime is of order

$$\tau_E \approx \frac{T}{(-dT/dt)} \quad . \tag{5-11}$$

In the upper part of the trapped radiation belts where the total average electron density may be of order 10^3 per cubic centimeter (References 20, 21, and 22), the predicted lifetimes of trapped electrons and protons would be of order 20 and 60 years, respectively. A particle of sufficient energy could very well remain trapped for a long time if the only effect of collisions were a degradation of kinetic energy.

5.2.2 Cumulative Deflections—the Fokker-Planck Equation

An energy loss formula is not quite adequate to describe the relaxation of charged particles in a plasma. The total accumulated deflections of a particle can become so great that eventually there is no longer a well-defined "forward" velocity. Additionally, the described stopping power formulas are not very accurate when the speed of the particle under scrutiny is not much greater than the thermal speed. A complete treatment of collision effects must include explicitly the random nature of individual collisions; the

expected deflection after many collisions should be related to the probable deflections in individual collision events. The Fokker-Planck equation satisfies these criteria quite neatly in predicting the evolution of a single-particle distribution function $f(\bar{x}, \bar{v}, t)$ according to the outcomes of many isolated events (References 24 through 27). Because confusion about its proper use is considerable, a brief derivation of the Fokker-Planck equation (Reference 28) is given. Suppose a probability $S(\bar{v}, \delta\bar{v}, t)\, d^3v\, \delta t$ exists that a test particle within the element of velocity space defined by $\bar{v}$ and d^3v (momentum space could as well be employed) experiences a small deflection $\delta\bar{v}$ sometime between t and $t + \delta t$. One may assume that S does not contain time as an explicit variable. This assumption defines a Markov process in which the expected behavior of a dynamical system does not depend on its past history (Reference 24). (Many interactions between particles are not Markovian, particularly if the test particle has internal energy states that may be excited during a collision.) During a time interval long enough to include a considerable number of collisions, the distribution function f evolves according to the formula:

$$f(u_i, t + \delta t)\, J(v, u) = \iiint_{[\text{all } \delta u_i]} f(u_i - \delta u_i, t)\, S(u_i - \delta u_i, \delta u_i)$$

$$J(\delta v, \delta u)\, J(v - \delta v, u - \delta u)\, d^3(\delta u_i)\, \delta t \quad . \qquad (5\text{-}12)$$

The velocity coordinates are generalized so that the components of $\bar{v}$ are linear functions of some set of u_i. The infinitesimal volume element $d^3(\delta\bar{v})$ is equivalent to $d(\delta u_1)\, d(\delta u_2)\, d(\delta u_3)$. The Jacobian (Reference 29):

$$J(v, u) = \frac{\partial(\delta v_x, \delta v_y, \delta v_z)}{\partial(\delta u_1, \delta u_2, \delta u_3)} = \text{Determinant} \begin{vmatrix} \frac{\partial(\delta v_x)}{\partial(\delta u_1)} & \frac{\partial(\delta v_y)}{\partial(\delta u_1)} & \frac{\partial(\delta v_z)}{\partial(\delta u_1)} \\ \frac{\partial(\delta v_x)}{\partial(\delta u_2)} & \frac{\partial(\delta v_y)}{\partial(\delta u_2)} & \frac{\partial(\delta v_z)}{\partial(\delta u_2)} \\ \frac{\partial(\delta v_x)}{\partial(\delta u_3)} & \frac{\partial(\delta v_y)}{\partial(\delta u_3)} & \frac{\partial(\delta v_z)}{\partial(\delta u_3)} \end{vmatrix} \qquad (5\text{-}13)$$

relates the δu_i to cartesian coordinates. A Taylor series expansion about $\delta u_i = 0$ gives to first order:

$$f(u_i, t) + \frac{\partial f(u_i, t)}{\partial t} \delta t \cong \left\{ \iiint \left[f(u_i, t)\, S(u_i, \delta u_i) - \sum_{j=1}^{3} \frac{\partial J(v,u)\, f(u_i, t)\, S(u_i, \delta u_i)}{\partial u_j} \frac{\delta u_j}{J(v,u)} + 1/2 \sum_{j=1}^{3} \sum_{k=1}^{3} \frac{\partial}{\partial u_j} \frac{\partial\, J(v,u)\, f(u_i, t)\, S(u_i, \delta u_i)}{\partial u_k} \frac{\delta u_j\, \delta u_k}{J(v,u)} \right] J(\delta v, \delta u)\, d^3(\delta u_i) \right\} \delta t \quad . \tag{5-14}$$

The probability S is normalized so that the total probability of a collision $\iiint S\, d^3(\delta \bar{v})$ is equal to 1 (including collisions that result in no deflection). The generalized Fokker-Planck equation may be written from Equation 5-14:

$$\frac{\partial f}{\partial t} = -\frac{1}{J} \sum_{j=1}^{3} \frac{\partial}{\partial u_j} \left(J f \langle \Delta u_j \rangle \right) + \frac{1}{2J} \sum_{j=1}^{3} \sum_{k=1}^{3} \frac{\partial}{\partial u_j} \frac{\partial}{\partial u_k} \left(J f \langle \Delta_j\, \Delta u_k \rangle \right) . \tag{5-15}$$

The Fokker-Planck coefficients represent averages of the probable deflections, and are defined as:

$$\langle \Delta u_i \rangle = \left[\iiint \delta u_j\, S(u_i, \delta u_i) J\, d^3(\delta u_i) \right] / \delta t \tag{5-16a}$$

$$\langle \Delta u_i\, \Delta u_k \rangle = \left[\iiint \delta u_j\, \delta u_k\, S(u_i, \delta u_i) J\, d^3(\delta u_i) \right] / \delta t \tag{5-16b}$$

$$= \begin{matrix} j, k \\ 1, 2, 3 \end{matrix}$$

In cartesian coordinates, the Fokker-Planck equation has a simple tensor form (Reference 26):

$$\frac{\partial f}{\partial t} = -\nabla_v \cdot f \langle \Delta \bar{v} \rangle + \frac{1}{2} \nabla_v \nabla_v : f \langle \Delta \bar{v}\, \Delta \bar{v} \rangle \quad . \tag{5-17}$$

The notation $\langle\ \rangle : \langle\ \rangle$ refers to dyadic multiplication (Reference 29). ∇_v is just the velocity space gradient.

Using a coordinate system with a symmetry exis that coincides with some special symmetry axis of the physical system often is convenient. No Fokker-Planck coefficients exist involving the azimuthal angle about the symmetry axis. In cylindrical coordinates, $\bar{v}$ is decomposed into parallel, $\bar{v}_{\parallel}$, and transverse, $\bar{v}_{\perp}$, components. The Jacobian is $2\pi v_{\perp}$. The Fokker-Planck equation that results is

$$\frac{\partial f}{\partial t} = \frac{\partial}{\partial v_{\parallel}} f\langle \Delta v_{\parallel}\rangle - \left(\frac{1}{v_{\perp}} + \frac{\partial}{\partial v_{\perp}}\right) f\langle \Delta v_{\perp}\rangle + \frac{1}{2}\frac{\partial}{\partial_{\parallel}^{2}}\langle f\,(\Delta v_{\parallel})^{2}\rangle + \left(\frac{1}{v_{\perp}}\frac{\partial}{\partial v_{\parallel}} + \frac{\partial^{2}}{\partial v_{\parallel}\,\partial v_{\perp}}\right) f\langle \Delta v_{\parallel}\,\Delta v_{\perp}\rangle + \left(\frac{1}{v_{\perp}}\frac{\partial}{\partial v_{\perp}} + \frac{1}{2}\frac{\partial^{2}}{\partial v_{\perp}^{2}}\right) f\langle (\Delta v_{\perp})^{2}\rangle . \tag{5-18}$$

In velocity v and pitch angle α_p coordinates (spherical coordinates), the Jacobian is $2\pi v^2 \sin\alpha_p$. The corresponding Fokker-Planck equation is

$$\frac{\partial f}{\partial t} = -\left(\cot\alpha_p + \frac{\partial}{\partial \alpha_p}\right) f\langle \Delta \alpha_p\rangle - \left(\frac{2}{v} + \frac{\partial}{\partial v}\right) f\langle \Delta v\rangle + \frac{1}{2}\left(-1 + 2\cot\alpha_p\frac{\partial}{\partial \alpha_p} + \frac{\partial^{2}}{\partial \alpha_p^{2}}\right) f\langle (\Delta\alpha_p)^{2}\rangle + \left(\frac{2}{v}\cot\alpha_p + \cot\alpha_p\frac{\partial}{\partial v} + \frac{2}{v}\frac{\partial}{\partial \alpha_p} + \frac{\partial^{2}}{\partial v\,\partial \alpha_p}\right) f\langle \Delta\alpha_p\,\Delta v\rangle + \left(\frac{1}{v^{2}} + \frac{2}{v}\frac{\partial}{\partial v} + \frac{1}{2}\frac{\partial^{2}}{\partial v^{2}}\right) f\langle (\Delta v)^{2}\rangle . \tag{5-19}$$

The cosine of the pitch angle, μ, is usually a convenient variable, in which case the Jacobian is $2\pi v^2$ and the Fokker-Planck equation in velocity-pitch angle cosine coordinates becomes

$$\frac{\partial f}{\partial t} = -\frac{\partial}{\partial \mu} f\langle \Delta\mu \rangle - \left(\frac{2}{v} + \frac{\partial}{\partial v}\right) f\langle \Delta v \rangle$$
$$+ \frac{1}{2}\frac{\partial^2}{\partial \mu^2} f\langle (\Delta\mu)^2 \rangle + \left(\frac{2}{v}\frac{\partial}{\partial \mu} + \frac{\partial^2}{\partial \mu\, \partial v}\right) f\langle \Delta\mu \Delta v \rangle$$
$$+ \left(\frac{1}{v^2} + \frac{2}{v}\frac{\partial}{\partial v} + \frac{1}{2}\frac{\partial^2}{\partial v^2}\right) f\langle (\Delta v)^2 \rangle \ . \qquad (5\text{-}20)$$

In the last equation, the velocity could have been replaced by the kinetic energy with a resulting Jacobian of just 2π (the number of particles in $dT d\mu$ is $2\pi f(T, \mu)\, dT d\mu$). The Fokker-Planck equation in energy-cosine pitch angle coordinates is

$$\frac{\partial f}{\partial t} = -\frac{\partial}{\partial \mu} f\langle \Delta\mu \rangle - \frac{\partial}{\partial T} f\langle \Delta T \rangle + \frac{1}{2}\frac{\partial^2}{\partial \mu^2} f\langle (\Delta\mu)^2 \rangle$$
$$+ \frac{\partial^2}{\partial \mu\, \partial T} f\langle \Delta\mu \Delta T \rangle + \frac{1}{2}\frac{\partial^2}{\partial T^2} f\langle (\Delta T)^2 \rangle \ . \qquad (5\text{-}21)$$

The Fokker-Planck equation represents a diffusion in velocity space (References 24 and 26). Particles starting in a group at one point in velocity space eventually will become difficult to identify as members of the original group. However, after a finite time interval, the particles that were originally traveling together have not only different velocities but also different spatial positions. It is necessary to define the distribution function so that it is spatially invariant when collisions are ignored. This requirement is not always trivial. Usually, the distribution of velocities at a fixed point (or surface) is adequate to determine the behavior of the entire ensemble (Section 3.6).

CUMULATIVE DEFLECTIONS IN AN IONIZED GAS. Parallel and transverse deflections may be decomposed either with respect to the direction of the initial velocity or to the direction of the magnetic field. A particle traversing an ionized medium will experience small random deflections every time it comes near enough to an electron to be influenced by the field around that electron. Figure 5-3 shows the trajectory of a charged particle in a fully ionized plasma. The dots represent electrons; the dashed circles represent the Debye spheres with a radius equal to the Debye length. (Actually,

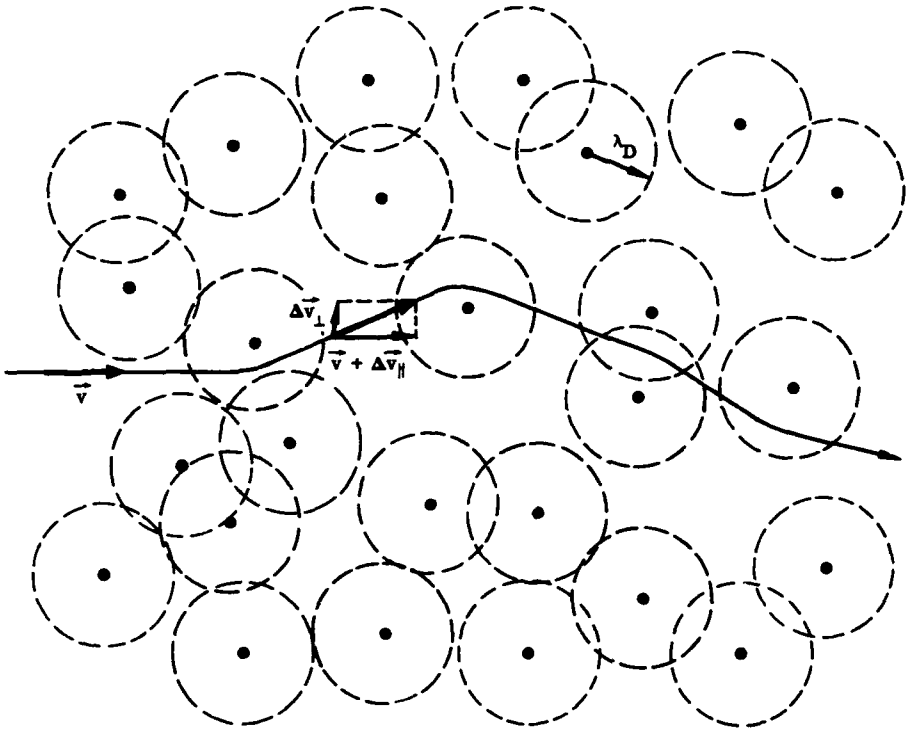

Figure 5-3. The path of a light-charged particle (an electron) in a fully ionized gas.

many electrons might be found within any individual Debye sphere.) A fast charged particle is affected by the nearly stationary electrons only when it penetrates their respective Debye spheres.

The first Fokker-Planck coefficient $\langle \Delta v_\parallel \rangle$ is equivalent to a gradual loss of kinetic energy. It usually is called the dynamical friction coefficient (References 30 and 31). The averages of $\langle \Delta v_\perp \rangle$ and $\langle \Delta v_\parallel \Delta v_\perp \rangle$ in a uniform medium are expected to be zero because a transverse velocity increment is equally probable in any direction about the symmetry axis. The effects of random deflections are contained in the remaining coefficients $\langle (\Delta v_\parallel)^2 \rangle$ and $\langle (\Delta v_\perp)^2 \rangle$.

Chandrasekhar has computed Fokker-Planck coefficients for inverse square-type forces (Reference 31). The significant (nonrelativistic) coefficients for the slowing of a particle of mass m_1 and velocity v by free electrons (Equation 5-3b defines C, also see Reference 32) are

$$\langle \Delta v_{\parallel} \rangle = -2C\, n_e \frac{m_e^2}{m_1 m_r 2kT_e} G\left(\sqrt{\frac{m_e v^2}{2kT_e}}\right) \ln \Lambda \qquad (5\text{-}22)$$

$$\langle (\Delta v_{\parallel})^2 \rangle = 2C\, n_e \frac{m_e}{m_1^2 v} G\left(\sqrt{\frac{m_e v^2}{2kT_e}}\right) \ln \Lambda \qquad (5\text{-}23)$$

$$\langle (\Delta v_{\perp})^2 \rangle = C\, n_e \frac{m_e}{m_1^2 v} \left[\operatorname{erf}\left(\sqrt{\frac{m_e v^2}{2kT_e}}\right) - G\left(\sqrt{\frac{m_e v^2}{2kT_e}}\right) \right] \ln \Lambda \qquad (5\text{-}24)$$

The function G is related to the error function:

$$\operatorname{erf}(x) = \frac{2}{\sqrt{\pi}} \int_0^x \exp(-y^2)\, dy \qquad (5\text{-}25)$$

through the definition:

$$G(x) = \frac{\operatorname{erf}(x) - x \frac{d}{dx} \operatorname{erf}(x)}{2x^2} \quad . \qquad (5\text{-}26)$$

Figure 5-4 gives numerical values of G and erf . The parameter Λ is related to the number of elecrons in a Debye sphere. Generally, $\ln \Lambda$ may be set equal to:

$$\ln \Lambda = \ln\left(\lambda_D \frac{3kT}{e^2}\right) \approx 15 - 20 \quad . \qquad (5\text{-}27)$$

If more accuracy is desired, the tabulations of $\ln \Lambda$ by Spitzer (Reference 32) may be found useful.

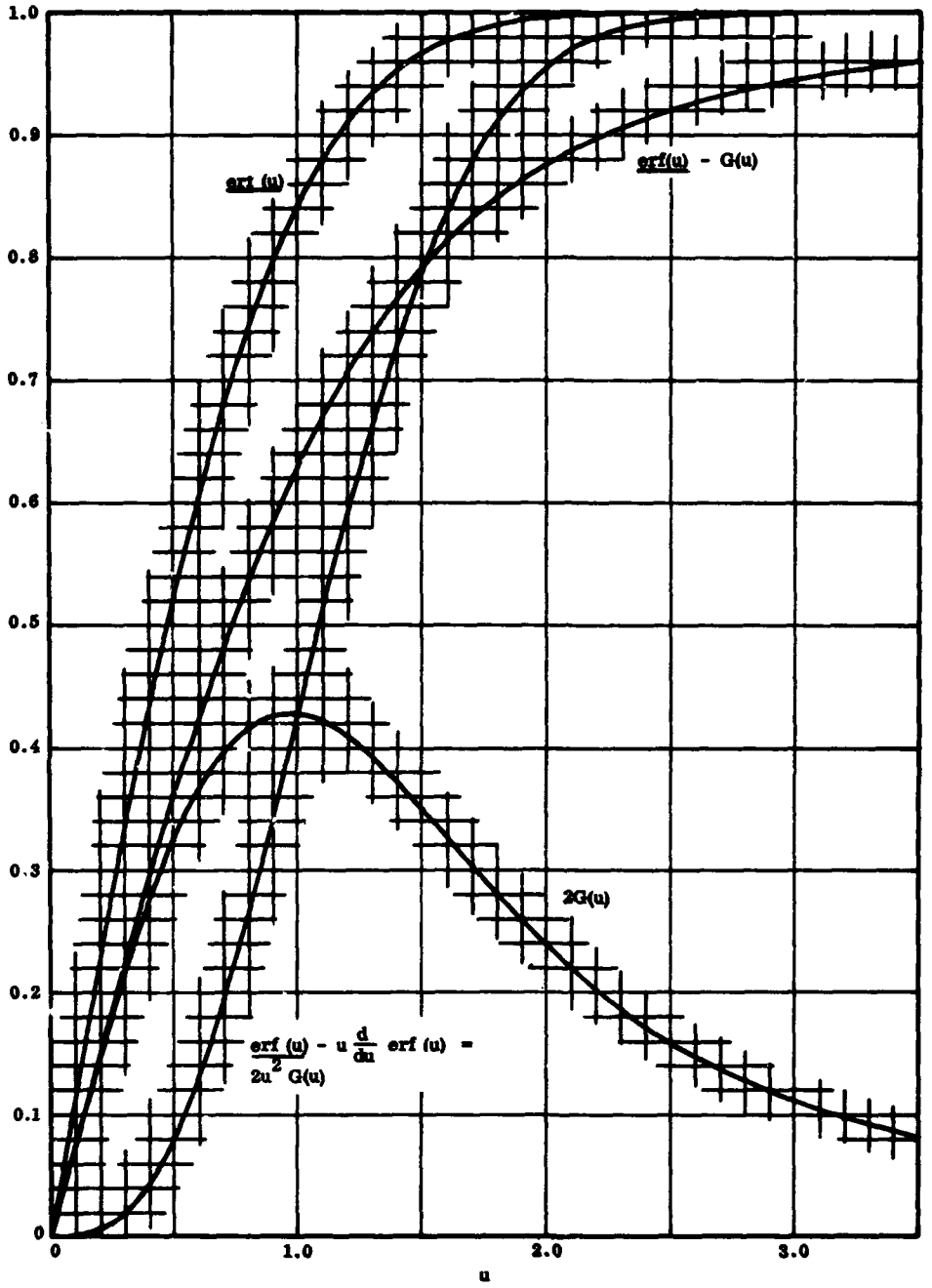

Figure 5-4. Functions used in computing Fokker-Planck coefficients for the slowing and deflection of a charged particle in an ionized gas.

The Fokker-Planck coefficients for moderately high velocities are approximately

$$\langle \Delta v_{\parallel} \rangle \cong - C n_e \frac{m_e}{m_1 m_r} \frac{c^2}{v^2} \ln \Lambda \qquad (5\text{-}28)$$

$$\langle (\Delta v_{\parallel})^2 \rangle \cong C n_e \frac{kT}{m_1^2 c} \frac{c^3}{v^3} \ln \Lambda \qquad (5\text{-}29)$$

$$\langle (\Delta v_{\perp})^2 \rangle \cong C n_e \frac{m_e c}{m_1^2} \frac{c}{v} \ln \Lambda . \qquad (5\text{-}30)$$

The similarity between Equations 5-28 and 5-5 is readily apparent; the numerical magnitudes of the logarithmic terms are actually quite close. At incident particle velocities greater than about 4 times the thermal electron speed, the two formulas give nearly identical results. Only for very slow particles is Equation 5-28 preferred over Equation 5-5 (which is also correct at relativistic velocities).

The ratio of the "diffusion" coefficient $\langle (\Delta v_{\perp})^2 \rangle$ to the dynamical friction $\langle \Delta v_{\parallel} \rangle$ is proportional to m_r/m_1. For protons passing through free electrons, the ratio m_r/m_1 is only 1/1,836; but for electrons passing through a gas of free electrons, the ratio is 1/2. Generally, deflections are much more important for electrons than for fast, heavy particles (Section 5.2.1).

A useful measure of the lifetime of a particle in a plasma is the average time required to deflect the initial velocity through 90 degrees. A deflection relaxation time (Reference 32) might be defined as:

$$\tau_D = \frac{v^2}{\langle (\Delta v_{\perp})^2 \rangle} = \frac{mv}{8\pi} n_e e^2 (\text{erf} - G) \ln \Lambda \qquad (5\text{-}31a)$$

$$\approx 0.002 \frac{m^2 v^3}{n_e e^4} . \qquad (5\text{-}31b)$$

The deflection relaxation time is usually less than the energy relaxation time, τ_E, for electrons. The deflection relaxation lifetime of electrons in the outer trapping regions is on the order of 10 to 100 years.

5.2.3 Collisions in the Earth's Atmosphere

A trapped particle is effectively removed if it loses enough energy in successive collisions that it is no longer distinguishable from low-energy ambient particles ($T \approx 1,000$ to $2,000$ K). A trapped particle also is lost if its trajectory is altered by collisions so that it enters a low-altitude region of the atmosphere where it may be stopped within a small fraction of its bounce period. Although a single violent collision would suffice to substantially alter the pitch angle, a large number of successive small deflections can have the same effect.

The earth's atmospheric density, ρ, decreases with altitude, h, roughly according to the hydrostatic equation:

$$\frac{d\rho}{dh} \cong -\frac{\rho}{H} \exp(-h/H) \quad . \tag{5-32}$$

The parameter H is called the scale height. The scale height in the lower atmosphere is of the order 7 kilometers, so the number of molecules and atoms per cubic centimeter falls from about 10^{20} at the surface to less than 10^{11} above 120 kilometers. The scale height increases in the upper atmosphere, but the number density still is generally less than 10^{6} atoms per cubic centimeter at 1,000-kilometer altitude. Generally, trapped particles can be found with mirror altitudes down to 120 to 150 kilometers. Below 120 kilometers the atmospheric density increases so fast that stably trapped particles never are found there. Further details regarding atmospheric parameters are in Section 12.

If it is trapped so that it never comes below several thousand kilometers altitude, a charged particle will spend its life in what is essentially a tenuous vacuum. Its lifetime is much greater than its gyro-period, bounce period, drift period, and other time parameters.

5.2.4 Loss of Trapped Protons in the Earth's Atmosphere

The loss of trapped heavy particles is analytically and conceptually simpler than the loss of electrons because the effects of deflections can be ignored. A further simplification can be achieved in neglecting the effects of free electrons below several thousand kilometers altitude. Many more bound electrons exist than free electrons in this region (Figure 5-6). At most altitudes, one constituent of the atmosphere predominates over all the others. In the important altitude range of 200 to 800 kilometers, most of the slowing of fast particles

is due to exygen atoms. For rough computational purposes, the average excitation potential of oxygen, $I^* \approx 97.5$ eV, may be used in Equation 5-3 or Equation 5-7. The total number of bound electrons is about eight times the total number of oxygen atoms. Where an appreciable fraction of the atmosphere is molecular and atomic hydrogen, the appropriate excitation potential is 13.9 eV. Below 200 kilometers, an acceptable average excitation potential is $I^* \approx 87$ eV (the average for air).

Protons with large kinetic energies can be involved in nuclear interactions (References 11, 12, and 15). This is the dominant loss process at very high kinetic energies, above 300 to 500 MeV. The range of protons in air is compared in Figure 5-1 with the mean free paths for nuclear interactions. The relative energy dependence of the competing slowing processes is such that, at energies only slightly below 300 MeV, nuclear interactions are virtually insignificant.

At kinetic energies below 1 MeV, a proton is susceptible to charge-exchange reactions with hydrogen and oxygen atoms. After picking up an orbital electron, the neutralized proton–now a hydrogen atom–likely will escape the trapping region before being reionized. Because of the accidental equality of their ionization potentials, oxygen and hydrogen have a resorance in the charge exchange reaction with protons (References 18 and 19). The charge-exchange cross sections for protons in hydrogen or oxygen is of order 10^{-15} to 10^{-14} square centimeter up to 10 KeV (References 16 and 17). At higher energies, charge-exchange rates fall rapidly. The mean path for charge exchange is shown in Figure 5-1. Clearly, charge exchange must be the dominant loss process for protons with energies less than 100 KeV. Above 1 MeV, charge exchange is negligible. (Alternating neutralization and ionization of protons mirroring at low altitudes might result in a diffusion across field lines (References 33 and 34). This process is not likely to be significant except for protons that penetrate so deeply in the atmosphere that they are already near the ends of their trapped lifetimes.)

The total rate of removal of protons from a volume in phase space (References 11 and 12) is

$$\frac{\partial f(T)}{\partial t} = \frac{\partial}{\partial T}\left[f(T)\frac{dT}{dt}\right] - f(T)\, v \sum_k n_k \sigma_k^{[loss]} . \qquad (5\text{-}33)$$

The first term on the right of the equal sign in Equation 5-33 is due to the gradual energy loss. The last term on the right takes account of violent interactions (nuclear reactions or charge exchange). $\sigma_k^{[loss]}$ is the cross section for the reaction and n_k is the number density of the reacting atoms (or nuclei) of species k. Lifetimes for trapped protons predicted according to Equation 5-33 are shown in Table 5-2.

Table 5-2. Energy loss lifetimes of trapped particles with pitch angles near 90 degrees (References 11 and 12).

Trapped Particles	L = 1.2 (days)	L = 1.6 (years)	L = 3 (years)
300 KeV Electron	10	6	20
2 MeV Electron	100	60	200
10 MeV Proton	50	30	100
100 MeV Proton	1825	1000	(not trapped)

In equilibrium, the trapped proton loss rate must be balanced by the production rate. The production rate will include an external source of strength q (per eV per cubic centimeter per second) plus the production rate of secondary protons originating in nuclear reactions. The secondary production rate can be written in terms of a cross section for secondary production $\sigma_k^{[sec]}$ and the fractional probability $W(T', \mu_o' \rightarrow T, \mu_o)$ that a reaction induced by a proton with energy T' and equatorial pitch angle cosine μ_o' will yield a proton with energy T and equatorial pitch angle cosine μ_o. The loss and production rates should be averaged over the particle trajectories and equated. The result is the steady state equation (References 11, 12, and 35):

$$\frac{\partial}{\partial T}\left[j_o(T, \mu_o)\,\overline{\frac{dT}{ds}}\right] - \overline{j_o(T, \mu_o) \sum_k n_k \sigma_k^{[loss]}} + \overline{q(T, \mu_o)}$$

$$+ \int_T^\infty dT' \int_{-1}^{1} d\mu_o'\; j_o(T', \mu_o') \overline{\sum_k n_k \sigma_k^{[sec]}\, W_k(T', \mu_o' \rightarrow T, \mu_o)} = 0 \,. \quad (5\text{-}34)$$

$f_o(T, \mu_o)v$ has been replaced by the equatorial intensity $j_o(T, \mu_o)$.

The horizontal bars denote trajectory averages, i.e.,:

$$\bar{x} \equiv \frac{\oint x\, ds}{\oint ds} = \frac{\int_{-S_m}^{S_m} x \frac{dS}{\mu}}{\int_{-S_m}^{S_m} \frac{dS}{\mu}} . \qquad (5\text{-}35)$$

A solution of Equation 5-33 for the case of negligible secondary production (Reference 35) is

$$j_o(T, \mu_o) = \left(\overline{\frac{dT}{ds}}\right)^{-1} \int_T^{\infty} dT' \, \overline{q(T', \mu_o)} \cdot \exp\left[- \int_T^{T'} dT'' \left(\frac{dT}{ds}\right)^{-1} \overline{\sum_k n_k \sigma_k^{[loss]}} \right] . \qquad (5\text{-}36)$$

The exponential function accounts for nuclear collisions. This factor can be significant only for particles with high kinetic energies and pitch angles sufficiently small that they will dip low into the atmosphere and encounter many nuclei with large cross sections, $\sigma^{[loss]}$. If the source q is fairly uniform, the form of j_o is determined primarily by the variation of $\overline{dT/ds}$ due to the atmospheric density distribution. In fact, j_o should be roughly inversely proportional to the total number of electrons encountered along the orbit. Therefore, on low L-shells, j_o and f_o should be strongly dependent on pitch angle.

That j_o depends very strongly on mirror latitude means that the omnidirectional flux J_o on the equator should increase rapidly with L on low L-shells. The actually observed altitude dependence of J_o is consistent with atmospheric collisions being the predominant loss mechanism for protons below L = 1.4 (References 11 and 35).

Actually, on low L-shells, nearly all the trapped-particle depletion occurs within the South American anomaly region (Section 2.4.2; References 35 and 36). Therefore, the trajectory averages (Equation 5-35) should be average also over longitude.

EAST-WEST ASYMMETRY. The spatial-gradient of proton fluxes at low altitudes results in an excess of protons moving eastward. This is simply because protons moving toward the east have

guiding centers above the point observation. Protons moving toward the west have guiding centers below that point. The particles with the lower guiding centers are trapped on lower field lines and, consequently, are lost more rapidly to the atmosphere. The ratio of eastward-to-westward intensities (References 37 and 38) is

$$\frac{j(\text{east})}{j(\text{west})} = \exp\left(2\rho_c \cos I/H\right) \tag{5-37}$$

where ρ_c is the gyro-radius and I is the field-line inclination. The east-west asymmetry has been utilized to derive scale heights H within the upper atmosphere (Reference 39).

(The current that results from the inequality of fluxes in opposite directions is analogous to the current in Equation 3-101, which depends on the gradient of particle pressure.)

5.2.5 Loss of Trapped Electrons in the Atmosphere

The depletion of the trapped-electron belts must be treated as a diffusion in energy, pitch angle space (T, μ_o space). The Fokker-Planck coefficients of the diffusion equation (References 10 and 35) are

$$\langle \Delta T \rangle = \frac{\overline{dT}}{dt} \tag{5-38}$$

$$\langle \Delta \mu_o \rangle = -C \frac{m_e c^2}{p^2 v} \frac{1-\mu_o^2}{\mu_o} \left[\frac{\mu^2}{\mu_o^2(1-\mu^2)} - 1\right] \sum_k n_k Z_k^2 \ln \Theta_{k[\min]}^{-1} \tag{5-39}$$

$$\langle (\Delta \mu_o)^2 \rangle = C \frac{m_e c^2}{p^2 v} \frac{(1-\mu_o^2)^2}{\mu_o^2} \frac{\mu^2}{1-\mu^2} \sum_k n_k Z_k^2 \ln \Theta_{k[\min]}^{-1} \tag{5-40a}$$

$$\equiv \frac{T + m_e c^2}{[T(T+2m_e c^2)]^{3/2}} (1-\mu_o^2)\, Y(\mu_o) \tag{5-40b}$$

$$\langle \Delta T \Delta \mu_o \rangle = 0 \tag{5-41}$$

$$\langle (\Delta T)^2 \rangle \approx 0 \ . \tag{5-42}$$

The number of orbital electrons in an atom of species k has been denoted by Z_k. Only the dynamical friction (Equation 5-38) is proportional to the total number of bound electrons—the other coefficients contain an extra Z-factor. The minimum scattering angle in the center of mass frame is $\theta_{[min]}$. The logarithm terms of Equations 5-39 and 5-40 are essentially similar to the terms in the square brackets of Equations 5-4 and 5-5(for the cases of collisions with bound or with free electrons).

The complete Fokker-Planck diffusion equation reduces to a trapped electron loss rate equation (Reference 10)

$$\frac{\partial N_o(T, \mu_o)}{\partial t} = \frac{\partial}{\partial T}\left[N_o(T, \mu_o)\,\overline{\frac{\partial T}{\partial t}}\right] + \frac{\pi c}{T(T + 2mc^2)}\,\frac{\partial}{\partial \mu_o}\left[t_b(1 - \mu_o^2)\,Y(\mu_o)\,\frac{\partial f(T, \mu_o)}{\partial \mu_o}\right] \quad (5\text{-}43)$$

where t_b is the bounce period. For convenience, the first terms in Equation 5-43 have been written with f_o replaced by the total number of particles in a magnetic flux tube per unit μ_o, per unit cross-sectional area at the equator:

$$N_o(T, \mu_o) = 2\pi f_o(T, \mu_o)\, v\, \mu_o\, t_b \quad . \quad (5\text{-}44)$$

The third Fokker-Planck coefficient (Equation (5-40) has been written in terms of $Y(\mu_o)$ because this artificial function is nearly independent of μ_o except when the pitch angle is near the atmospheric cutoff. The slowing rate $\overline{dT/dt}$ behaves similarly. However, near the cutoff, μ_c, both $\overline{dT/dt}$ and $Y(\mu_o)$ are extremely sensitive to μ_o. It is primarily this fact which has prohibited adequate analytic solutions of Equation 5-43; the solutions have been generally through numerical computations (References 10, 35, 36, 40, and 41). The results of a sample calculation, assuming injection strongly concentrated at one energy and pitch angle, are shown in Figure 5-5. In the figure, injection into the trapped radiation belts was concentrated at an equatorial pitch angle α_o = arc sin μ_o = arc sin 0.25 and a kinetic energy of T = 1.5 MeV. The successive views represent "snapshots" at the times 90, 190, 365, and 900 days after the initial injection event. The flux intensity j(cm^{-2} sec^{-1} MeV^{-1} $ster^{-1}$) is given as a function of μ

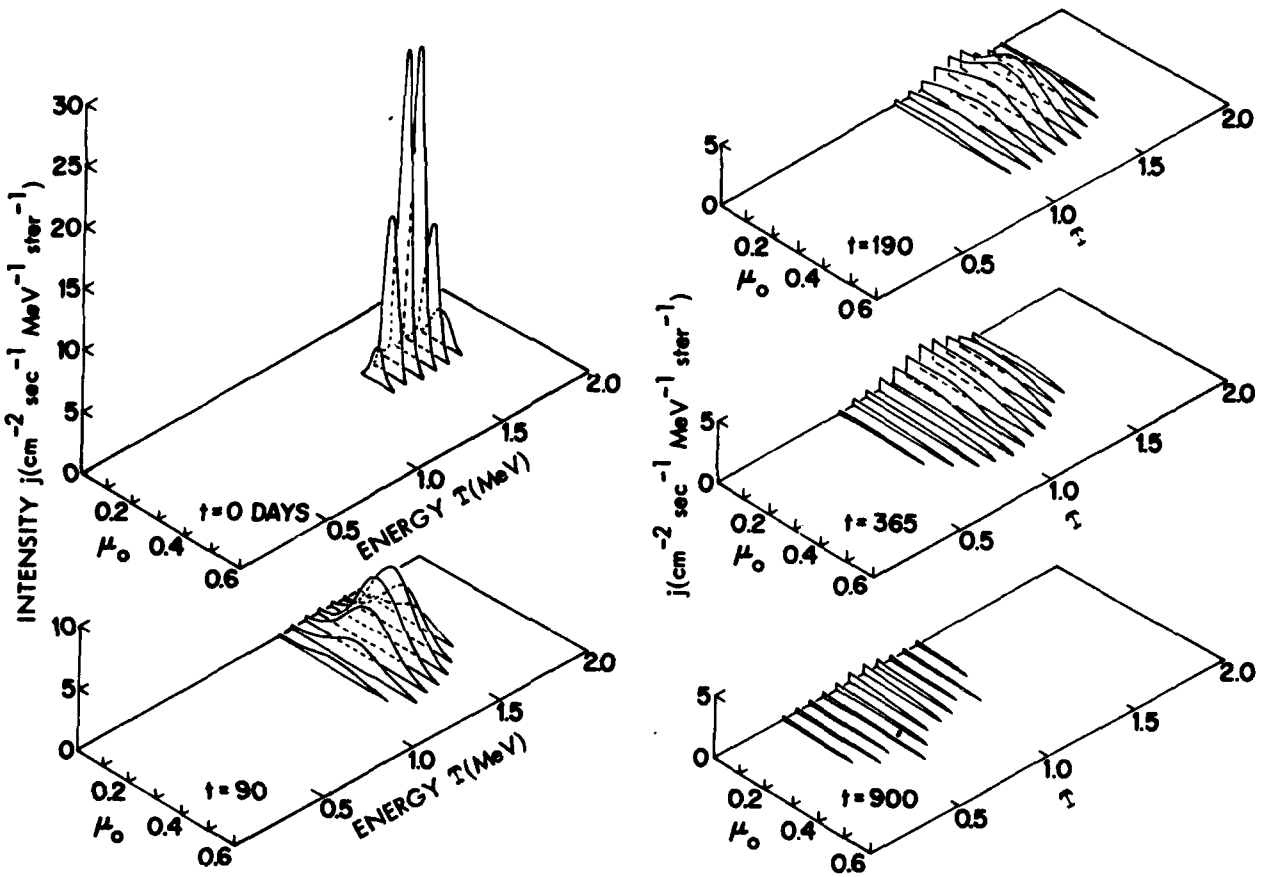

Figure 5-5. Diffusion of a group of electrons in energy, pitch angle space (Reference 40). Injection into the trapped radiation belts was concentrated at an equatorial pitch angle α_o = arc sin μ_o = arc sin 0.25 and a kinetic energy of T = 1.5 MeV. The successive views represent "snapshots" at the times 90, 190, 365, and 900 days after the initial injection event. The flux intensity j(cm^{-2} sec^{-1} MeV^{-1} ster^{-1}) is given as a function of μ and kinetic energy T.

and kinetic energy T. The effect of collisions is to broaden the distributions and degrade the energy. Eventually, of those injected at an intermediate pitch angle, the only trapped particles remaining have mirror points near the equatorial plane.

Below $L \approx 1.25$, agreement of theory and observation leaves little doubt that, during periods of weak geomagnetic activity, electrons are lost primarily through atmospheric collisions. The electron fluxes resulting from the Starfish high-altitude nuclear explosion decayed by as much as an order of magnitude within the first few days. During this time, several competing loss mechanisms may have been effective. After several weeks, the major irregularities in the pitch angle distributions disappeared and the decay leveled off to a nearly exponential behavior. By that time, the exponential decay rates were about the same everywhere on any L-shell. Observed and predicted decay rates are shown later in this section (Figure 5-13).

Above $L \approx 1.25$, the decay after several weeks was exponential but the observed fluxes lay somewhat above the theoretical predictions. This seems to imply either an additional steady source of electrons or displacement of electrons toward lower L-shells (Reference 42). Diffusion of particles across L-shells seems to be the likeliest explanation. This topic is discussed in Section 5.4.

In the outer part of the trapped radiation belts, intensity variations occur over short time intervals that cannot be reconciled with slow diffusion and atmospheric loss. Lifetimes of some outer-belt particles may be as short as several days. Although the depletion of trapped-particle belts through atmospheric collisions is always effective, additional loss processes of comparable importance must be considered.

5.3 INJECTION OF TRAPPED PARTICLES THROUGH NUCLEAR DECAYS

5.3.1 Injection of Trapped Particles

The source term, $q(T, \mu_0)$, in Equation 5-34 represents the instantaneous appearance of trapped particles with a given energy and pitch angle. Charged particles may be introduced in many ways—as products of fission fragment decays (the decay of fission fragments is discussed in Section 12), as products of neutron decays, as products of ionization, or as products of charge-transfer reactions (between atoms and ions). The decay of a neutron leaves behind a fast proton and a fast electron. This mechanism, which will be discussed in

Section 5.3.2, therefore would appear a likely source of either kind of trapped particle.

The rate of injection $q(T, \mu, S, \psi)$ generally depends not only on energy, T, and pitch angle, μ, but also on location on the field line, S, and on azimuthal angle, ψ, referred to the field line. The rate of increase in $f(T, \mu, S)$ (averaged over ψ) due to injection in a segment δS of the field line is

$$\frac{df(T, \mu, S)}{dt} = \frac{\left[\int_0^{2\pi} q(T, \mu, S, \psi) d\psi\right] \delta S}{\pi \mu v t_b} . \qquad (5\text{-}45)$$

Note the factor μ in the denominator—isotropic injection does not result in isotropic trapping. With the aid of Liouville's equation (Equation 3-82) the rate of increase in $f_o(T, \mu_o)$ at the equator due to injection everywhere on the field line can be found. The result is

$$\frac{df(T, \mu_o)}{dt} = \frac{\oint \frac{dS}{\mu} \int_0^{2\pi} d\psi q(T, \mu, S, \psi)}{2\pi \oint \frac{dS}{\mu}} . \qquad (5\text{-}46)$$

The integration must follow a particle trajectory. If the injection rate is independent of ψ, the rate of increase is just $\overline{q(T, \mu_o)}$, as discussed in Section 5.2.4.

5.3.2 The Cosmic Ray Albedo Neutron Theory of Trapped Radiation Belt Formation

The albedo neutron theory of the trapped particle belts may be briefly outlined thus (References 11, 12, 43, and 44): Cosmic rays colliding with atmospheric nuclei produce neutrons; some of these neutrons, the albedo neutrons, leave the atmosphere, whereupon they decay leaving in their place charged particles that can be trapped. The expected numbers of trapped particles depend on the rates at which neutrons leave at the top of the atmosphere. The outgoing neutron flux is very uncertain though it appears that a substantial portion of the high-energy trapped protons below $L \approx 1.5$ may be accounted for by decay of albedo neutrons (References 11 and 12).

Neutrons are produced by cosmic rays in (p, n) and similar reactions (References 45 and 46). The neutrons may decay in flight, with a half life of about 11 minutes or, more probably, may be lost in

atmospheric collisions (Reference 47). Very few neutrons reach low enough altitudes that they can be easily detected. Direct observations of fast neutron fluxes is hindered by experimental difficulties so the neutron flux at high altitudes is poorly known. Most estimates of albedo neutron fluxes have been derived from the basic processes affecting neutrons rather than from extrapolations of observations (References 46 and 48 through 52). The number escaping, which is not a large fraction of the number produced, is therefore very uncertain.

High-energy neutrons, say at kinetic energies greater than 50 MeV, are deflected only slightly in the atmosphere. Therefore, the fast-neutron component of the albedo flux escapes nearly tangential to the horizon—being produced by cosmic rays with paths that do not intersect the earth's surface. The angular spread of the emergent beam of neutrons is determined primarily by the angular distribution of particles produced in cosmic ray "stars" (Reference 45). Fast secondary particles in turn may interact with other atomic nuclei; about three-fourths of all neutron-generating interactions are due to secondary particles. Most of the albedo neutrons with kinetic energies greater than 1 GeV are in a beam less than 10 degrees wide. Only below 60 MeV is the width of the beam more than 60 degrees.

There is a latitude variation in the energies of cosmic rays which can penetrate the atmosphere; this is a consequence of the fact that cosmic rays cannot enter the forbidden regions discussed in Section 3.2.3. At latitudes beyond 60 to 70 degrees, solar cosmic rays can penetrate the atmosphere and contribute to the neutron albedo. The kinetic energies involved are moderate, 10 to 100 MeV, and the neutron production rates are expected to vary throughout the 11-year solar cycle. Neutrons are produced nearly isotropically in the center of mass reference frame. The angular distribution of albedo neutrons is therefore fairly broad (References 11 and 12).

Each neutron decay releases a proton with a kinetic energy nearly equal to that of the neutron. High-energy protons can be injected only when the projection of the initial velocity vector is tangent to the top of the atmosphere. The rate of injection can be approximated by:

$$\frac{df(T, \mu_o)}{dt} \cong \overline{q}(T) \quad \frac{\oint \eta(\mu, S) \frac{dS}{\mu}}{\oint \frac{dS}{\mu}} \qquad (5\text{-}47)$$

where η is the fraction of the trajectory over which injection is possible and $\overline{q'}$ is an equivalent isotropic injection rate. Figure 5-6 shows how the pitch angle cone of halfwidth α_p at any point on a field line intersects the earth's atmosphere. Only within the shaded strip of the figure can neutrons be emitted (from the top of the atmosphere) that can decay at point P, thus releasing protons with the pitch angle α_p. Some pitch angle cones intersect the earth at all azimuthal angles; others do not intersect the earth anywhere (e.g. small pitch angles near the equator. It is evident that only a very small

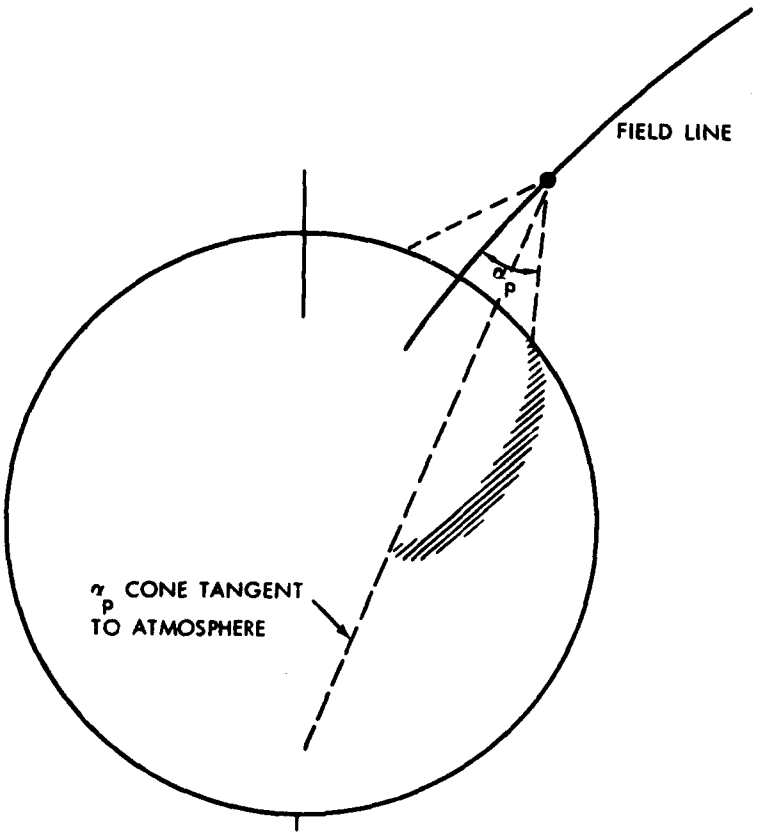

Figure 5-6. The intersection of a pitch angle cone with the earth's surface.

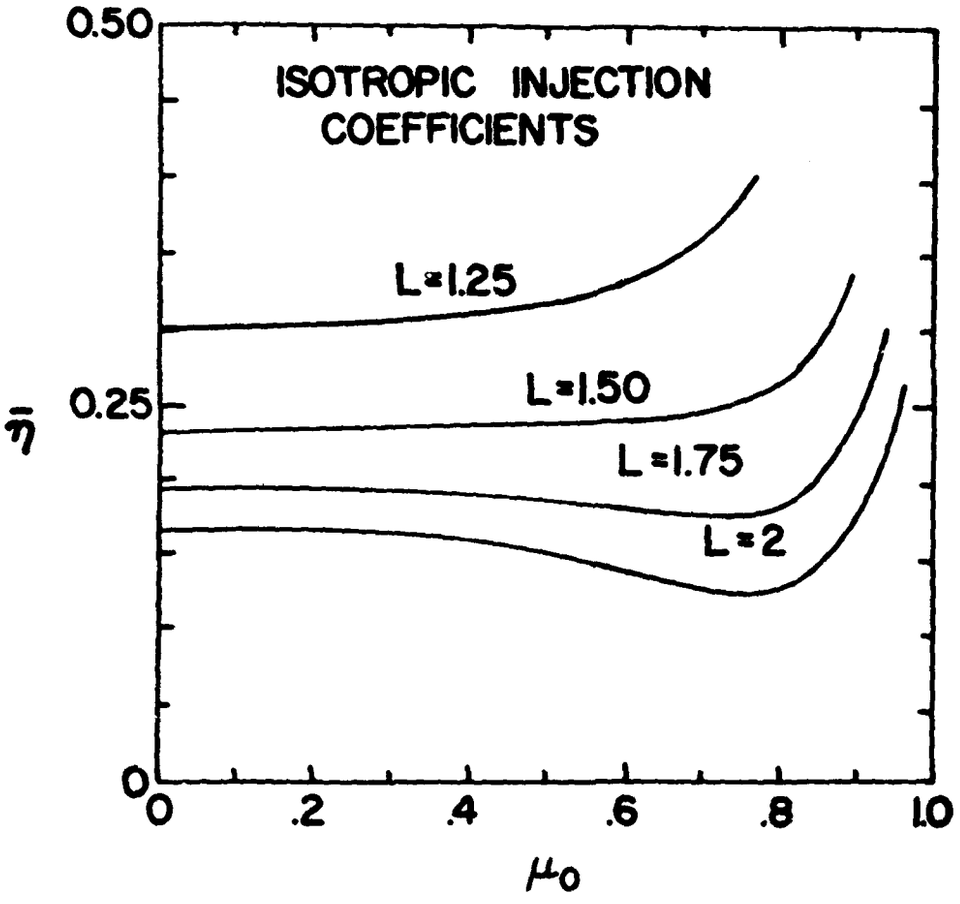

Figure 5-7. Equatorial pitch angle dependence of the average injection coefficient $\bar{\eta}$ for an isotropic neutron flux emerging from the atmosphere (References 11 and 12).

part of the pitch angle cone is within several degrees of being tangential to the atmosphere. Low-energy protons ($T \lesssim 50$ MeV) are injected nearly isotropically; η is then just the fraction of the pitch angle cone that intersects the earth. Some computed values of η are shown in Figures 5-7 and 5-8. In Figure 5-8, above $T \approx 50$ MeV, the effect of the finite width of the albedo neutron beam is included. The pitch angle dependence is nearly the same as in Figure 5-7.

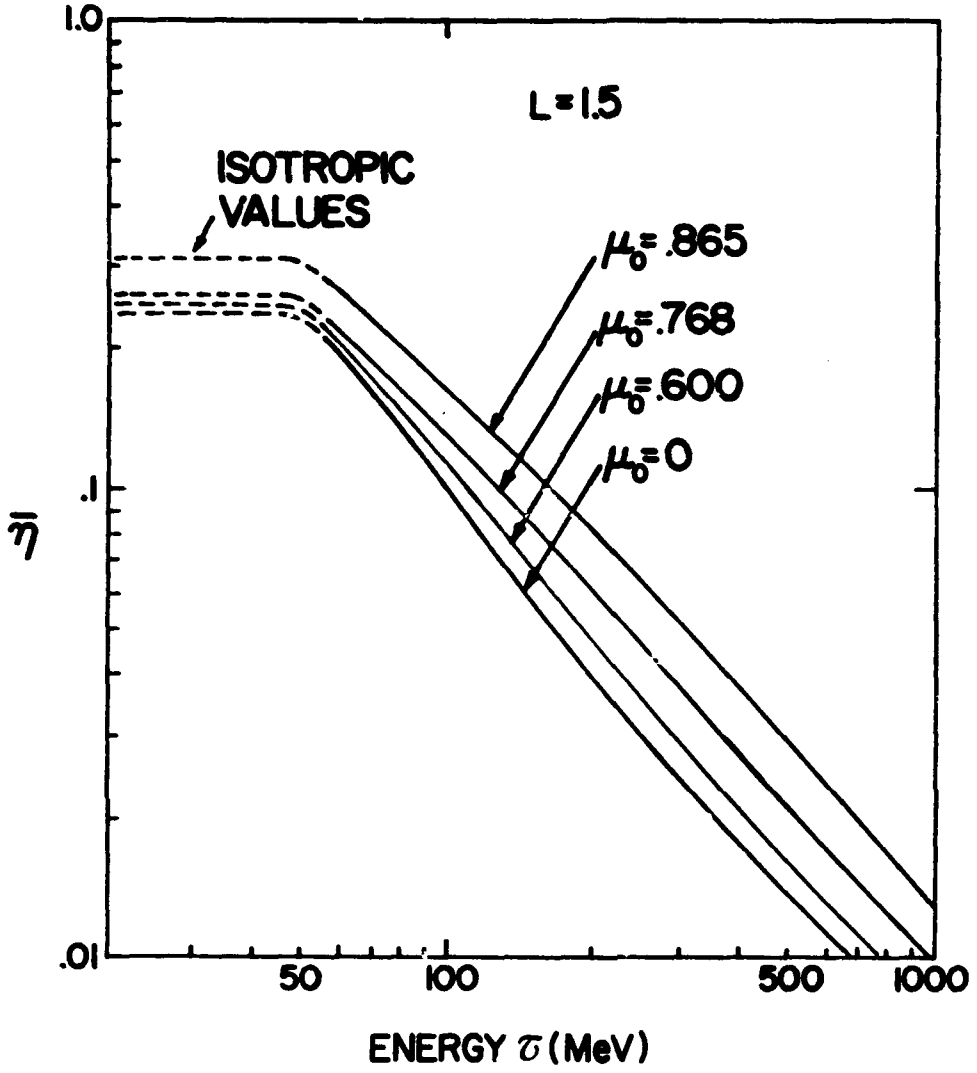

Figure 5-8. Energy dependence of average albedo neutron injection coefficient (References 11 and 12). Above $T \approx 50$ MeV, the effect of the finite width of the albedo neutron beam is included. The pitch angle dependence is nearly the same as in Figure 5-7.

The high-energy protons of the lower trapped radiation belt are fairly well accounted for by the albedo neutron-decay theory (Reference 12). The slope of the observed energy spectrum above 50 MeV is matched well by the predicted spectrum (Section 4.2). Some recent studies combining neutron decay and radial diffusion are discussed in Section 5.4.4. At lower kinetic energies, the numbers of trapped protons are much too great to be attributed solely to decay of fast neutrons. The low-energy albedo neutrons produced by solar cosmic rays might yield appreciable numbers of low-energy protons. However, these solar cosmic ray albedo neutrons cannot reach the equator at low altitudes; they cannot be responsible for an enhancement of trapping of protons with large pitch angles.

LOW ENERGY ALBEDO NEUTRONS. High-energy trapped protons can be attributed to decays of fast neutrons. The same source is relatively ineffective in producing trapped electrons; the low-energy trapped electron number density is nearly everywhere much larger than the trapped proton density. It has been suggested that the electrons could be injected by low-energy albedo neutrons (References 43 and 44). However, neutrons with kinetic energies below 1 MeV are deflected appreciably within the atmosphere. For that reason, considering a diffusion-type problem is necessary to obtain the albdeo flux.

For any quantity that is transported through a material medium, in this case j (the number of neutrons per square centimeter per ster per second), a Boltzmann-type equation can be formulated. The Boltzmann equation (Equation 3-91) gives the rate of change of a number density in a volume element that follows the flow. The general transport equation for j in a plane-layered medium (References 53, 54, and 55) is

$$\zeta \frac{\partial j(T, \zeta, h)}{\partial h} + j(T, \zeta, h)\, n\sigma(T, \zeta) = q(T, \zeta, h) + \int_T^\infty dT' \int_{-1}^{1} d\zeta'\, j(T', \zeta', h)\, n\sigma(T', h)\, W(T', \zeta' \rightarrow T, \zeta) \tag{5-48}$$

where h is the depth measured perpendicular to the layers. The first term on the left denotes the rate of depletion (or augmentation) of a stream of particles moving at an angle arc cos ζ from the normal to the plane (note the similarity to Equation 5-34 when ζ is replaced by μ_o). The second term is the rate of loss by collisions, σ is the

total cross section, and n is the number density of scatterers. Particles are added to the stream by a source of strength q, or by scattering, with a fractional probability W, from all other energies, T', and angles, arc cosine ζ'. Slow neutrons scatter almost isotropically, in which case the scattering probability σW is equal to the product of a constant σ_s (which, of course, must be less than or equal to σ) and $W(T' \rightarrow T)$.

When Equation 5-48 is integrated over ζ, a simplified equation is obtained in terms of the omnidirectional neutron flux J and the flux across a constant-h surface F (Section 3.5.2; Reference 53):

$$4\pi \frac{\partial F(T)}{\partial h} + J(T)\, n\sigma = Q(T,h) + \int_{T}^{\infty} dT'\, J(T')\, n\sigma_s\, W(T' \rightarrow T) \qquad (5\text{-}49)$$

where Q now represents an average source strength:

$$Q(T,h) = \frac{1}{2} \int_{-1}^{1} d\zeta\, q(T, \zeta, h) \; . \qquad (5\text{-}50)$$

Equation 5-49 can be solved by standard numerical methods (References 48, 53, 54, 55, and 56).

Equation 5-49 has a form that resembles a conventional diffusion equation. In the lower atmosphere, where the mean path lengths are so short that j is nearly independent of ζ, the first term in Equation 5-49 may be replaced by

$$\frac{\partial}{\partial h}\left(D \frac{\partial J}{\partial h}\right) \; .$$

D is a diffusion coefficient (References 46, 51, 52, and 54). Unfortunately, the free paths of neutrons near the top of the atmosphere are large compared with other dimensional parameters. Consequently, the anisotropies are great enough that the diffusion equation solution does not give entirely reliable results for the flux at the top of the atmosphere.

An additional complication is that neutrons of energies much less than 1 eV cannot leave the earth's gravitational field. This has the effect of increasing the rate of neutron decays near the earth, though the albedo is diminished only slightly (Reference 46).

Various solutions to the neutron-transport problem have appeared. They are all normalized to measured fluxes of neutrons of cosmic rays observed at low altitudes. Figure 5-9 shows computed rates of neutron decays near the earth. These should be the same as the rates of electron injection (References 44, 45, and 46). The electrons released from slow neutron decays above the atmosphere are injected into the trapping regions nearly isotropically.

Albedo neutron decay is definitely inadequate as the sole source of trapped electrons (References 35, 43, and 44). Additionally, it is significant that the energy spectrum of trapped electrons is much different from that of the neutron decay component (Reference 57).

5.4 NONCONSERVATION OF THE THIRD ADIABATIC INVARIANT

5.4.1 Hydromagnetic Stability of Trapped Radiation

Simple two-particle interactions are inadequate to explain all the observations relevant to trapped particle sources and losses. The remainder of this chapter is concerned with the effects of plasma oscillations and collective behavior of large numbers of particles. A first consideration is whether the trapped radiation belts are always stable against gross instabilities, primarily involving violation of the third adiabatic invariant Φ.

The $\bar{J} \times \bar{B}$ term in the mechanical force equation (Equation 3-100) can be simplified readily with the aid of Maxwell's Equations (Equation 3-108). The result is

$$\bar{J} \times \bar{B} = -\nabla \frac{B^2}{8\pi} + \nabla \cdot \frac{\bar{B}\bar{B}}{4\pi} \quad . \tag{5-51}$$

The expression on the right of Equation 5-51 may be identified with the divergence of the Maxwell stress tensor (Reference 58):

$$\bar{\bar{T}} = \frac{1}{4\pi} \begin{bmatrix} \frac{1}{2}B_x^2 + \frac{1}{2}B_y^2 + \frac{1}{2}B_z^2 & -B_xB_y & -B_xB_z \\ -B_yB_x & \frac{1}{2}B_x^2 - \frac{1}{2}B_y^2 + \frac{1}{2}B_z^2 & -B_yB_z \\ -B_zB_x & -B_zB_y & \frac{1}{2}B_x^2 + \frac{1}{2}B_y^2 - \frac{1}{2}B_z^2 \end{bmatrix} \tag{5-52}$$

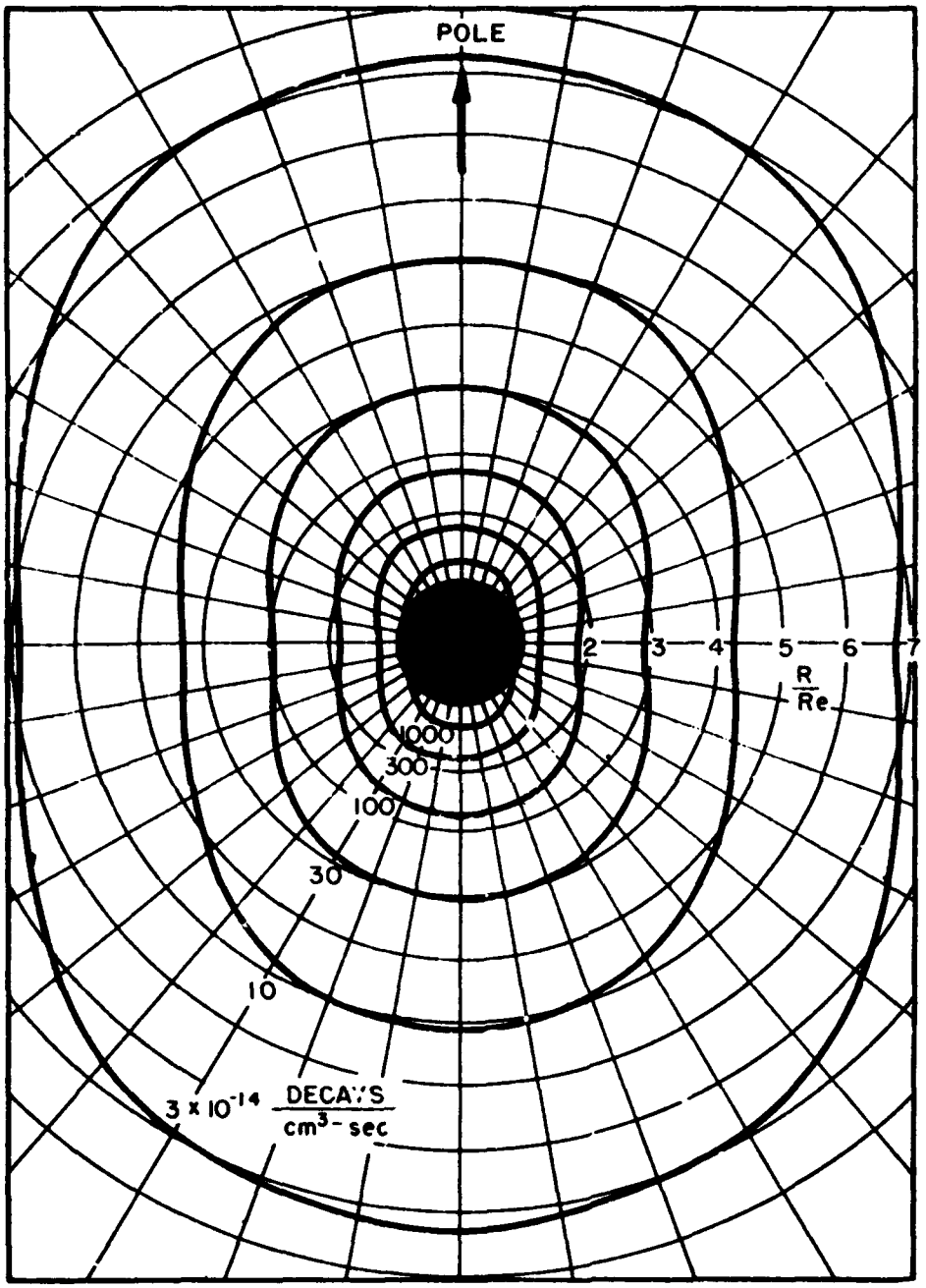

Figure 5-9. Neutron decay rate contours near the earth (Reference 46).

The mechanical force equation then can be written in the concise form:

$$\rho \frac{\partial \bar{v}}{\partial t} = - \nabla \cdot (\bar{\bar{T}} + \bar{\bar{P}}) \ . \qquad (5\text{-}53)$$

The magneto-mechanical stresses are equivalent to a pressure $B^2/8\pi$ transverse to the field lines and a tension $B^2/8\pi$ along the field lines (References 32, 58, and 59).

The ratio of the transverse particle pressure to the magnetic pressure is a useful criterion of the relative importance of particles versus field (Reference 60). If the ratio

$$\beta_P = \frac{\sum_{[\text{all particles}]} \gamma m v_\perp^2}{B^2/8\pi} \qquad (5\text{-}54)$$

is much greater than unity, the medium behaves as a classical fluid and the magnetic field has little effect on the gross motion. Conversely, if β_P is extremely small, so little energy is contained in the particles that the effects of collective behavior are likely to be insignificant. When β_P is extremely small, so little energy is contained in the particles that the effects of collective behavior are likely to be insignificant. When β_P is computed for observed naturally trapped particles, the result is generally much less than 1. If β_P (in any part of the radiation belts) should ever exceed about 0.1, the radiation belts would very likely exhibit all the types of plasma instabilities observed in mirror machines in the laboratory (References 60, 61, and 62).

The parameter β_P is nearly the ratio of kinetic energy density to magnetic energy density. The total magnetic energy within a shell of field lines is shown in Figure 5-10. (The unit of energy in the figure is equivalent megatons of TNT explosive energy; 1 MT = 4.2×10^{22} erg = 4.2×10^{15} joule.) The magnetic energy represented is the total magnetic energy in the field between the earth's surface and the shell at any specified L-parameter. The total kinetic energy of the particles trapped in the same region is not expected to exceed appreciably the magnetic field energy.

Usually β_P varies considerably along a field line (in most cases where stable trapping is observed, the largest β_P occurs at the equator). The largest β_P can be used to estimate the saturation fluxes for any assumed pitch angle distribution. Actually, even the largest β_P should be somewhat less than unity. A limit of 0.1 probably would be

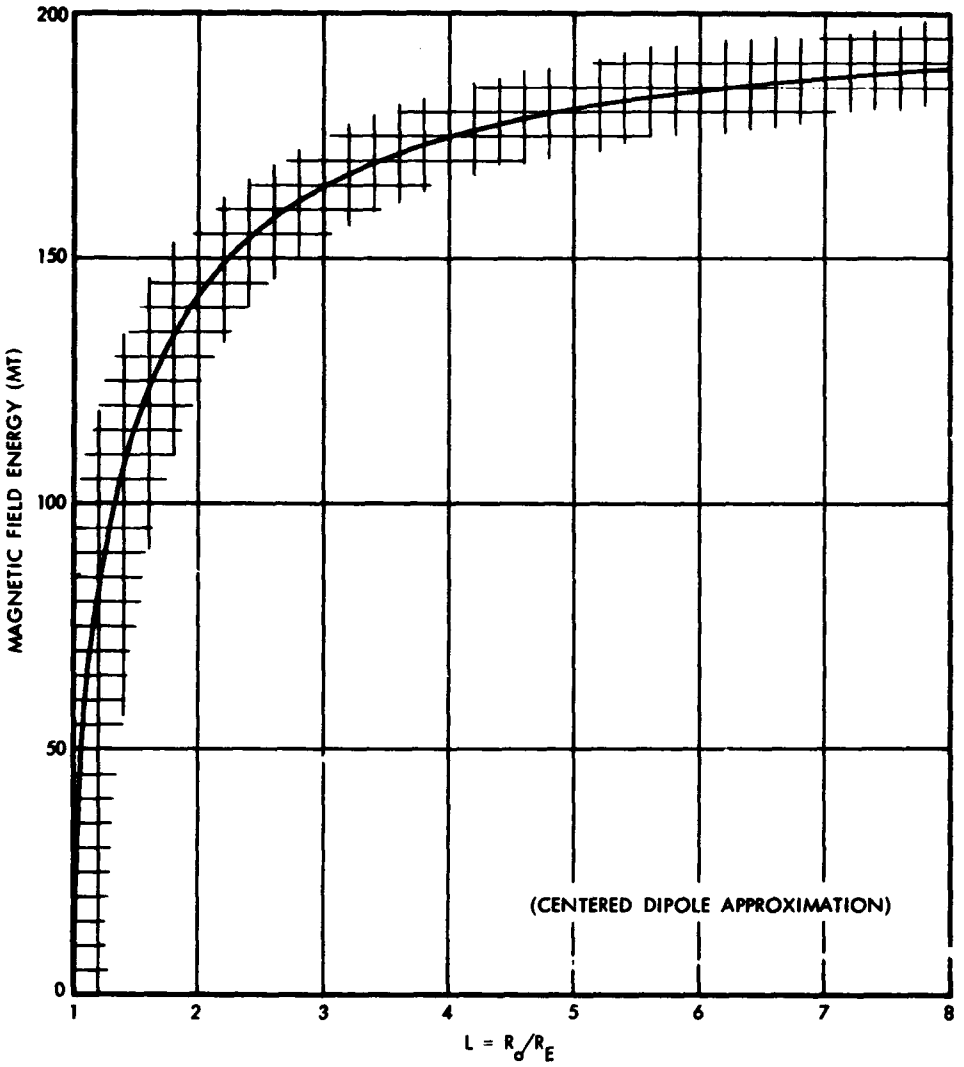

Figure 5-10. Total magnetic field energy in the volume contained between the earth's surface and a shell of field lines at $L = R_o/R_E$. The unit of energy in the figure is equivalent megatons of TNT explosive energy; 1 MT = 4.2×10^{22} erg = 4.2×10^{15} joule.

reasonable for most practical cases. The limit on β_P is invoked in Section 7.3.2 to predict the maximum trapped fluxes that might occur following a high-altitude nuclear detonation.

Computing β_P is fairly straightforward when all particles have the same energy and the pitch angle distribution has a simple form such as

$$j_o = \frac{n+1}{2n\mu_c} J_o \left[1 - \left(\frac{\mu}{\mu_c}\right)^n\right] \Bigg\} \; |\mu| < \mu_c ; \; n > 0 . \qquad (5\text{-}55)$$

The omnidirectional flux in the equatorial plane is J_o. In terms of the pressure ratio, the maximum flux is

$$J_o = \beta_P \frac{3B_E^2(n+3)}{16\pi pL^6} \Big/ \left[(n+4) + \frac{n+1}{2L^3\sqrt{4 - 3/L}}\right] \qquad (5\text{-}56)$$

where the atmospheric cutoff has been substituted for μ_c. For an isotropic distribution ($n \sim \infty$), the flux limit is

$$J_o(cm^{-2}sec^{-1}) \leq 1.09 \times 10^{20} \frac{\beta_P}{p(MeV/c)} \Big/ \left[L^6 + \frac{L^3}{2\sqrt{4 - 3/L}}\right]. \qquad (5\text{-}57)$$

In this case, the largest β_P does occur at the equator. Equations 5-56 and 5-57 should give reasonably reliable results for the total allowed trapping.

5.4.2 Interchange Instability in the Outer Trapping Regions

A plasma may be expected to be confined by a magnetic field that provides a sufficiently great magnetic pressure on the exterior to counteract the particle pressure of the plasma that is seeking to escape. This is not always possible, though. The instability that results if two fluids (in the present case, a plasma and a magnetic field) can exchange positions with a consequent decrease in total energy is known as the Rayleigh-Taylor instability (Reference 58). This instability is well known from early laboratory studies where it was called the fluting or interchange instability because a plasma boundary tends to break up into grooves or "flutes" as the plasma leaks out, carrying along the field lines (References 60, 61, and 63). Generally, whenever field lines at the plasma boundary are convex to the exterior, an instability results (Reference 63).

The criterion for stability at an interior point is rather complicated. Though the field lines may be convex in a direction toward which the particle density decreases, the plasma may be stable everywhere except on the extreme outer boundary. The plasma particle pressure in the exterior region may be greater than the interior pressure; the growth of instabilities thereby is restrained.

The total energy of all the particles on a field line is proportional to $\int H(M, J, \alpha, \beta)\, f(M, J, H)\, dMdJ$ where H is the Hamiltonian and M and J are the first two adiabatic invariants (References 64, 65, and 66). The Euler potentials, α and β (Section 3.4.1), are especially useful in treating hydromagnetic stability. The plasma is stable only if any exchange of two field lines and their associated trapped particles results in an increase in the total energy. With the assumptions that the adiabatic invariants M and J are preserved and that the Hamiltonian depends on only one spatial coordinate α, the necessary and sufficient criterion for stability (Reference 66) is

$$\int dM, dJ \left(\frac{\partial H}{\partial \alpha}\right)^2 \left(\frac{\partial f}{\partial H}\right)_{M, J} < 0 \quad . \tag{5-58}$$

The notation $(\partial / \partial H)_{MJ}$ refers to a partial derivative in which M and J are held fixed. Often the sufficiency criterion alone:

$$\left.\left(\frac{\partial f}{\partial H}\right)_{M, J} < 0 \quad \right\} \text{all } M, J \tag{5-59}$$

need be considered.

The stability criterion would be satisfied for almost any particle distribution if a minimum with respect to α and β existed in H. All the particles in such an energy well would have minimum energy and escape from the well would not be possible. In a dipole field, no energy wells occur, so examining the details of the distribution function is necessary to determine whether Equation 5-59 is satisfied.

The assumption that f depends only on one spatial coordinate is entirely justified for a geomagnetic field that has a high degree of axial symmetry. The particle distribution function must be related, however, to the distribution in T, μ_o, L or T, B, L coordinates if meaningful comparisons are to be made with actually observed particle fluxes or intensities. Some of the details of the transformation are given because the intermediate results may be of general utility.

The distribution function f can be replaced by $N(M, J, \alpha)$, the number crossing the equator per unit magnetic flux, $d\alpha d\beta$. The total number of particles per energy interval and per μ_o interval in a magnetic flux tube of cross section $R_o dR_o d\phi$ is

$$N(T, \mu_o, R_o)\, R_o dR_o d\phi = J\, N(M, J, \alpha)\, d\alpha\, d\beta \ . \tag{5-60}$$

The adiabatic invariants are related to energy and pitch angle through the Jacobian

$$J \equiv \frac{\partial(M, J)}{\partial(T, \mu_o)} = \left[\frac{\partial M}{\partial T}\,\frac{\partial J}{\partial \mu_o} - \frac{\partial M}{\partial \mu_o}\,\frac{\partial J}{\partial T}\right] \tag{5-61}$$

$$= \frac{\gamma p}{B_o}\, R_o \mu_o\, g(\mu_o) \tag{5-62}$$

where $g(\mu_o)$ is just vt_b/R_o, as defined in Equation 3-47. Now the coordinate β may be chosen equal to ϕ, the azimuthal angle or longitude. The corresponding α is $-M_E/R_o$ on the equator, where the magnetic flux element is

$$d\alpha\, d\beta = B_o R_o\, dR_o\, d\phi \ . \tag{5-63a}$$

The relation between the previously defined two distribution functions is

$$N(T, \mu_o, R_o) = R_o\, \gamma p \mu_o\, g(\mu_o)\, N(M, J, \alpha) \ . \tag{5-63b}$$

The left-hand side of Equation 5-63b is related to the intensity (Equation 5-44). The relation between intensity and total number of trapped particles reduces to (References 68 and 69):

$$N(M, J, \alpha) = 2\pi m\, \frac{j_o(T, \mu_o)}{p^2} = \frac{N(M, J, R_o)}{B_o R_o} \tag{5-64a}$$

$$\sim \pi \frac{j_o(T, \mu_o)}{T} \Bigg\} \text{ low energies} \ . \tag{5-64b}$$

The partial derivative with respect to H in the stability criterion can be replaced with a partial derivative with respect to R_o by the (not obvious) relation (Section 3.4.1; Reference 67):

$$\frac{\partial}{\partial R_o} = B R_o \frac{\partial}{\partial \alpha} = B R_o \frac{e}{c} \frac{\partial \beta}{\partial t} \left(\frac{\partial}{\partial H} \right)_{M, J} . \qquad (5\text{-}65)$$

However $R_o \partial\beta/\partial t$ is just the azimuthal drift velocity; therefore, $(e/c)\partial\beta/\partial t$ is always negative regardless of the sign of the electrical change. Finally, the interchange stability criterion (Equation 5-59) is

$$\left(\frac{\partial}{\partial L} \frac{j_o(T, \mu_o)}{p^2} \right)_{M, J} > 0 \quad \Bigg\} \text{all } M, J \quad . \qquad (5\text{-}66)$$

In the natural trapped radiation belts, most of the energy is retained by fast protons. If the protons by themselves are stable, the trapped electrons should not be able to overcome the inertia of the protons. It is probably safe to assert that the entire trapped particle belts are stable against interchange of field lines. The proton intensities are not well known for all values of M; however, all the available data indicate that the natural trapped radiation is stable as far out as $L \approx 5$ to 6 (References 67 through 71). That $N(M, J, \alpha)$ increases with radial distance may be taken as good evidence that particles are being added continually from outside (Reference 70). If particles were not continually added, the outer boundary would be subject to instabilities and the consequent loss of particles would lead to a reversal of the gradient (Equation 5-66).

The artificial electron belts resulting from the Starfish high-altitude nuclear explosion are another matter entirely. When a simplified model of the artificial electron distribution is constructed and $\partial(j_o/p^2)/\partial L$ is integrated over J, the necessary stability criterion (Equation 5-58) clearly is not satisfied (Reference 69). The results of such a computation are depicted in Figure 5-11. How a plasma behaves following the onset of instability is not very well understood. If indeed the electrons are subject to instability and the resulting hydromagnetic motion preserves M and J, then electrons might be expected to move outward with a softening of their energy spectrum. A softening of the energy spectrum of the Starfish trapped electrons may have been observed, though an interpretation on the basis of hydromagnetic instabilities is uncertain (Reference 69).

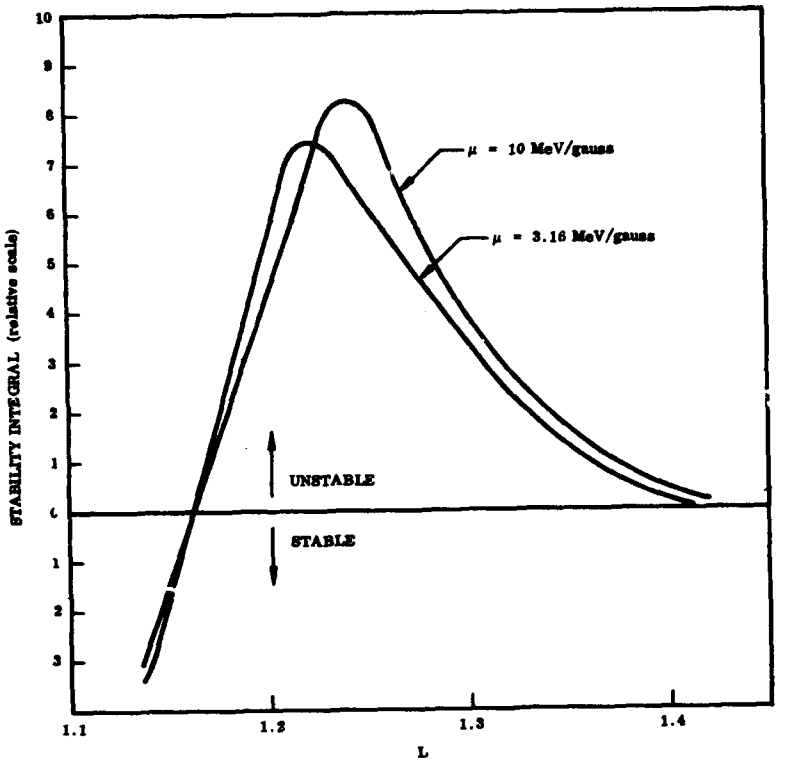

Figure 5-11. The stability function, $d(j_o/p^2)/dL$, integrated over J, the second adiabatic invariant, for the Starfish trapped electron belts (Reference 69).

The preceding discussion of hydromagnetic stability was incomplete because currents flowing in the ionosphere were ignored. In the trapped radiation belts, the field lines are effectively "frozen" into the material. If an entire field line is to exchange its position with another, the finite transverse conductivity in the ionosphere results in a relative motion of material and field lines at the lower ends of the lines. Equations 3-100 and 3-101 relate the velocity with which field lines are dragged through a plasma to the induced currents; thus:

$$\bar{J} = \bar{\bar{\sigma}} \cdot \bar{v} \times \bar{B} \qquad (5\text{-}67)$$

where $\bar{\bar{\sigma}}$ is the conductivity tensor. Substituting this in Equation 3-100, however, gives a force:

$$\bar{F} = (\bar{\bar{\sigma}} \cdot \bar{v} \times \bar{B}) \times \bar{B} \qquad (5\text{-}68)$$

contrary to the direction of motion. This force is thought to be adequate to restrain the field lines and prevent interchange.

The stability of the earth's radiation belts retaining the electric fields induced by plasma motion in the ionosphere has been analyzed (Reference 71). The energetic trapped protons can be stabilized by the ionospheric conductivity during the day, even if the simple stability criteria were violated. At night, when ionospheric electron densities are low, the ionosphere cannot be very effective in preventing instabilities.

5.4.3 Radial Motion of Trapped Particles as a Consequence of Nonadiabatic Behavior—Resonant Acceleration

The interchange instability leads to nonconservation of the third adiabatic invariant, Φ. If the instability occurs in a dipole field, trapped particles tend to move outwards, initially preserving the adiabatic invariants M and J. But, the stability criterion (Equation 5-67) now seems to be well satisfied in the trapped radiation belts. The interior (particle) pressure is counterbalanced by more than sufficient exterior (particle) pressure so that any mixing of particles on different L-shells might be expected to result in particles being transported inward by diffusion (References 68, 70, and 72 through 75). In fact, any process that involves nonconservation of Φ could result in inward (or outward) motion of trapped particles. Here then is a relatively uncomplicated mechanism for maintaining the radiation belts against atmospheric and other losses. Enough particles exist in the solar wind to supply all the trapped particles, provided they can get down to low enough altitudes.

Invariance of Φ requires that magnetic and electric fields do not change appreciably within the particles' drift periods (Section 3; References 64 and 65). If the fields fluctuate in a regular fashion, some particles possibly can be accelerated—somewhat as particles are accelerated in a cyclotron or betatron. Several instances have been noted in which a recurring geomagnetic fluctuation apparently resulted in acceleration of trapped electrons (References 69 and 76).

The requirements for an accelerating field seem to be met by a coherent worldwide magnetic variation with periods of about 1 hour, sometimes referred to as Dp2 or DP2 variations (References 77 and 78). Intense groups of nearly monoenergetic electrons in the lower

radiation belt were observed to be associated with several such fluctuations (Reference 76). The drift periods of these electrons were similar to the periods of the fluctuations, which exhibited several complete cycles.

Whenever the magnetic fluctuation fields are known, the electric fields in the ionosphere can be derived with the aid of known ionospheric conductivities. The majority of the electric field in the DP2 fluctuations appears to be a curl-free field ($\nabla \times \bar{E} = 0$)—derivable from a potential field (References 78 and 79). Conductivities along field lines are very large, which in turn leads to potential gradients that are nearly transverse to the field above the ionosphere. One component of the electric field will be in an azimuthal (ϕ) direction. This component is primarily responsible for particle acceleration (Reference 76). A particle with the proper drift period and phase is in resonance and experiences an accelerating force on each circuit of the earth. The situation is not exactly equivalent to the acceleration of charged particles in a cyclotron. Instead, a particle drifts inward and the resulting increase of kinetic energy is a consequence of conservation of M and J .

TRAJECTORIES OF PARTICLES CONSERVING ONLY THE FIRST AND SECOND ADIABATIC INVARIANTS. If the first and second adiabatic invariants are preserved, this simple relation (Reference 80):

$$\Phi = \pi\left(\frac{J^2}{Mm}\right)\left(\frac{\sin \alpha_o}{\mathcal{J}(\alpha_o)}\right)^2 \qquad (5\text{-}69)$$

results from Equations 3-46, 3-75, and 3-76. $\mathcal{J}(\alpha_o)$ is just that part of J that depends on the pitch angle. Equation 5-69 relates the equatorial pitch angle α_o to the flux invariant Φ. Equation 5-69 alternatively may be regarded as a relation between L and the pitch angle:

$$L = 2B_E R_E^2 \left(\frac{Mm}{J^2}\right)\left(\frac{\mathcal{J}(\alpha_o)}{\sin \alpha_o}\right)^2 \quad . \qquad (5\text{-}70)$$

Once L and α_o are known, the mirror field B_m can be found immediately. Since M is assumed constant, the momentum squared must be proportional to B_m as a trapped particle moves across L-shells. Numerical relations between L, α_o, and B_m are given in Figures 3B-15 through 3B-19. Those figures are plotted for arbitrary values of the parameter $J^2/Mm = 2I^2 B_m$.

Of course, the distribution function $N(M, J, \alpha)$ is conserved for a group of particles that moves inward or outward together with changes in the geomagnetic field (this is because the flux $d\alpha d\beta$ is conserved). The intensity j_o therefore is seen from Equation 5-64 to be proportional to momentum squared.

When the equatorial pitch angle is large, the momentum squared is nearly inversely proportional to L^3 as a particle crosses L-shells. For mirror latitudes less than about 20 degrees, the momentum squared is nearly (within an error of less than 1 percent):

$$p^2 \cong \frac{2mB_E M}{L^3}\left[1 + \frac{3}{2\pi R_E}\sqrt{\frac{LJ^2}{B_E Mm}}\right]. \qquad (5\text{-}71)$$

Or, in terms of the initial mirror latitude λ_{m1},

$$p^2 \cong p_1^2\left(\frac{L_1}{L}\right)^3\left[1 + \frac{q}{2}\sin\lambda_{m1}\left(\sqrt{\frac{L}{L_1}} - 1\right)\right]. \qquad (5\text{-}72)$$

The subscripts 1 refer to the specified initial values.

At low energies, the square of momentum may be replaced by the kinetic energy. Equations 5-71 and 5-72 then give directly the energy gain or loss resulting from cross L-shell drift.

5.4.4 Stochastic Acceleration and L-Shell Diffusion

Most geomagnetic fluctuations are not obviously periodic (except for the daily variation). They are randomly distributed in time, with characteristic periods from fractions of a minute up to many hours. A schematic representation of the power spectrum of geomagnetic fluctuations observed on the earth's surface was presented in Figure 2-7.

That random, isolated magnetic disturbances can cause irreversible changes in the particle distribution is demonstrated readily for the type of disturbance known as a sudden commencement. During a sudden commencement, the geomagnetic field is rapidly compressed (Section 2.6.2), especially on the sunlit side of the earth. Particles continue to drift adiabatically in the distorted field, but now those that were previously all on a single L-shell may be on quite different

invariant surfaces. The end result is that, if the compressed field is released sufficiently slowly, trapped particles will be spread over a finite range of L-shells (Reference 75). Repeated compressions and expansions of the geomagnetic field thereby can result in diffusion of particles.

Any magnetic field fluctuation with a characteristic period near the drift period can cause nonconservation of the third adiabatic invariant Φ, and acceleration of particles. The acceleration of a charged particle by random electromagnetic field fluctuations is called stochastic acceleration (References 73 and 81). Again (as in the treatment of particle collisions), a Fokker-Planck-type equation is useful in describing a process that is determined by the outcomes of many random events. The Fokker-Planck diffusion equation, for the number of particles trapped in a magnetic flux tube at R_o per unit area in the equatorial plane $N(M, J, R_o)$, is expected to be of the form:

$$\frac{\partial N(M, J, R_o)}{\partial t} = -\frac{\partial}{\partial R_o}\left[\langle \Delta R_o \rangle \, N(M, J, R_o)\right] + \frac{1}{2}\frac{\partial^2}{\partial R_o^2}\left[\langle (\Delta R_o)^2 \rangle \, N(M, J, R_o)\right] + \bar{Q} \qquad (5\text{-}73a)$$

$$\equiv -\frac{\partial}{\partial R_o}\left[D_1 \, N(M, J, R_o)\right] + \frac{1}{2}\frac{\partial^2}{\partial R_o^2}\left[D_2 \, N(M, J, R_o)\right] + \bar{Q} \qquad (5\text{-}73b)$$

A source $\bar{Q}$ has been included here. A one-dimensional diffusion equation is valid if the diffusion proceeds with a time scale that is large compared to all other time parameters. If at any point on a field line they are transferred to another field line, the particles are rapidly "smeared" over a new invariant surface. Only on very high L-shells need the invariant surfaces be specified by more than one parameter. In the extreme outer radiation belts, a two-dimensional diffusion equation involving R_o or L and some other coordinate (such as pitch angle α_o or mirror point field B_m) would be necessary (References 28, 82, and 83).

A particular solution of Equation 5-73 is available for the case when the distribution function $N(M, J, \alpha, \beta)$ is constant everywhere. Liouville's theorem must apply to N. It is only necessary that particles should follow dynamical trajectories (Φ need not be conserved) in order that N remain unchanged after the exchange of particles between two invariant surfaces. The stability criterion (Equation 5-58)

guarantees that energy is not lost or gained. When the distribution function $B_o R_o N(M, J, \alpha)$ (Section 5.4.2) is inserted in the Fokker-Planck equation, the time rate of change must be zero. A solution (References 28, 82, 86, and 87) is:

$$D_1 = \frac{R_o^2}{2} \frac{\partial}{\partial R_o}\left(\frac{D_2}{R_o^2}\right) . \tag{5-74}$$

The relation between the two Fokker-Planck coefficients should hold when sources and losses are included in the diffusion equation. Therefore, only one coefficient need be computed:

$$D = \frac{1}{2} D_2 . \tag{5-75}$$

The simplified radial, or cross-L, diffusion equation may be rewritten:

$$\boxed{\frac{\partial N(M, J, R_o)}{\partial t} = -\frac{\partial}{\partial R_o}\left\{\frac{D}{R_o^2} \frac{\partial}{\partial R_o}\left[R_o^2 N(M, J, R_o)\right]\right\} + \bar{Q}} \tag{5-76}$$

The motion of a particle during a geomagnetic disturbance should be derivable directly from the equations of motion of an individual particle. The drift velocity is perpendicular to the field lines. The rate of change of R_o must be a single-valued function of the meridian plane component of the drift velocity V_D (References 81, 84, 88, 89, and 90):

$$\frac{dR_o}{dt} = V_{D[\text{meridian plane}]} \frac{\sqrt{1 + 3\sin^2\lambda}}{\cos^3\lambda} \tag{5-77}$$

where λ is the latitude of the particle at the instant an electric field is applied.

The diffusion coefficient D for a dipole field may be computed after breaking the disturbance field B into symmetric (S) and asymmetric (A) parts:

$$\begin{aligned}\bar{B}_1 = {} & [-S(t)\cos\theta - A(t)\, r \sin 2\theta \cos\phi]\,\hat{r} \\ & + [S(t)\sin\theta - A(t)\, r \cos^2\theta \cos\phi]\hat{\theta} + [A(t)\, r \cos\theta \sin\phi]\hat{\phi}\end{aligned} \tag{5-78}$$

where $\hat{r}$, $\hat{\theta}$, and $\hat{\phi}$ are the unit vectors in an earth-centered spherical coordinate system and θ is the polar angle or colatitude. The spherical harmonic expansion of $\bar{B}_1$ has been terminated at the first-order terms. The induced electric field $\bar{E}_1$, associated with the magnetic disturbance, is (Equation 3-107)

$$\bar{E}_1 = \frac{1}{7} r^2 \frac{dA}{dt} \sin\theta \sin\phi \hat{r} - \frac{2}{7} r^2 \frac{dA}{dt} \cos\theta \sin\phi \hat{\theta}$$

$$+ r\left[\frac{1}{2} \frac{dS}{dt} \sin\theta - \frac{2}{21} r \frac{dA}{dt} (3 - 7 \sin^2\theta) \cos\phi\right] \hat{\phi} \quad . \qquad (5\text{-}79)$$

The time average of the displacement is complicated; the computation has been performed with the result (Reference 89):

$$D_{[mag]}(L, \lambda_m) = 2\pi^2 \left(\frac{5}{7}\right)^2 \Gamma(\lambda_m) \frac{R_E^2 L^{10}}{B_E^2} \left[\nu^2 P_A(\nu)\right]_{\nu = 1/t_d} \qquad (5\text{-}80a)$$

$$= 16.55\, \Gamma(\lambda_m)\, R_E^2\, L^{10} \left[\nu^2 P_A(\nu)\right]_{\nu = 1/t_d} \quad . \qquad (5\text{-}80b)$$

The power spectrum is evaluated at the drift frequency. The function $\Gamma(\lambda_m)$ is presented in Figure 5-12. As might have been expected, $D_{[mag]}$ depends only on the asymmetric A part of the fluctuations. The magnetic fluctuations have been decomposed by Fourier analysis so that the power spectrum $P_A(\nu)$ is the Fourier transform of the average of $A(t)\, A(t + t')$:

$$P_A(\nu) = 4 \int_0^\infty dt' \overline{[A(t)\, A(t + t')]} \cos 2\pi\nu t' \quad . \qquad (5\text{-}81)$$

the flux of energy transported by magnetic fluctuations between the frequencies ν and $\nu + d\nu$ is proportional to $P_A(\nu)d\nu$.

A similar result follows for curl-free electric fields. When the disturbance field $\bar{E}_1$ is everywhere normal to the static magnetic field, the diffusion coefficient (References 82, 88, and 89) is

$$D_{[el]}(L, \lambda_m) = \frac{L^6}{8B_E^2} \sum_k \left[P_k(L, \nu)\right]_{\nu = 1/t_d} \quad . \qquad (5\text{-}82)$$

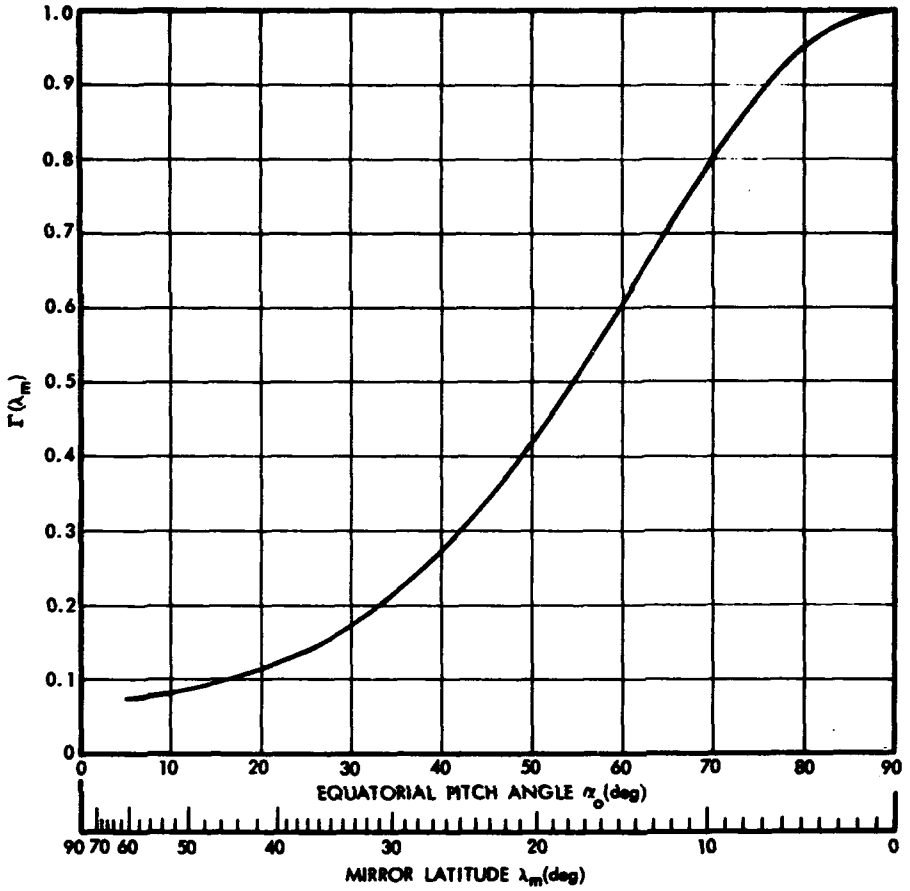

Figure 5-12. Latitude-dependent part of the radial diffusion coefficient (Reference 89).

The power spectrum, $P_k(L, \nu)$, here an explicit function of L, corresponds to the k'th component of the harmonic analysis of the electric field:

$$E_{\phi\,1}(L, \phi, t) = \sum_{k=0}^{\infty} E_{k\phi}(L, t) \cos\left(k\phi + \psi(L, t)\right) \qquad (5\text{-}83)$$

where ψ is merely a phase correction. The electric field diffusion coefficient $D_{[el]}$ depends on the mirror latitude only through the drift period t_d. The variation of drift period with mirror latitude is so slight (Equation 3-50) that $D_{[el]}$ is quite insensitive to mirror

latitude. Generally, the magnetic fluctuation diffusion coefficient $D_{[mag]}$ is much more sensitive to mirror latitude than is the electric field diffusion coefficient $D_{[el]}$. The magnetic diffusion coefficient falls so rapidly with increasing mirror latitude that magnetic acceleration effects are most important near the equatorial plane.

The magnetic fluctuation diffusion coefficient might be computed from a knowledge of magnetic disturbances observed on the earth's surface (Section 2.7). But the asymmetric part of the disturbance is proportional to radial distance, so ground-based magnetometers are sensitive primarily to S-variations. The relation between A and S is provided by the model chosen for the magnetic field. Some theoretical models have been constructed (References 89 and 91). Observational data collected with artificial satellites may be employed to further refine the models (Reference 92). Attempts have been made recently (References 93 and 94) to perform direct measurements of electric fields in the magnetosphere.

The spectral behavior of magnetic variations is not known with any more certainty than is the spatial dependence. The crude spectrum of Figure 2-17 is proportional, below about 1 hertz, approximately to the -2 power of frequency. A $P \propto \nu^{-2}$ frequency dependence is in agreement with most computations based on sudden commencements and other disturbances with a fast rise time succeeded by a slow recovery. For this special case, the diffusion coefficient is independent of drift period and is just proportional to L^{10}. Other assumed types of magnetic fluctuations yield quite different diffusion coefficients. Generally, for a power spectrum of the form:

$$P_A(\nu) \propto \nu^{-n} \tag{5-84a}$$

the diffusion coefficient (Reference 89) is

$$D_{[mag]} \propto L^{6+2n} M^{2-n} \propto L^{12-n} p^{4-2n} . \tag{5-84b}$$

EMPIRICAL COMPUTATIONS OF DIFFUSION COEFFICIENTS FROM OBSERVATIONAL DATA. The observation of an uncomplicated, unequivocal example of radial diffusion remains elusive. Because the motions of individual particles cannot be traced, observations of temporal changes in the trapped particle distribution must be relied on. But a radial motion of a group of particles is subject to being interpreted as a convective fluid motion of the entire group. On the other hand, a decay of the trapped particle flux at a single, isolated location perhaps could be explained by some other, yet undiscovered, loss process.

That the Liouville distribution function $N(M, J, \alpha)$ increases with L is suggestive of radial transport but is hardly conclusive evidence. The most compelling evidence for radial diffusion perhaps should be sought in the lower L-shells where the sources and losses are best understood. It has been noted that the artificial Starfish electron belts near L = 1.25 did not decay as rapidly as predicted from atmospheric losses alone. Computed and observed decay times are compared in Figure 5-13. Below $L \approx 1.2$, the observed decay time τ and the decay time predicted from atmospheric loss time τ_a differ enough that a cross L-diffusion coefficient can be computed. The atmospheric loss is well understood. The apparent discrepancy could only be explained by the addition of electrons diffusing from higher L-shells. The decay of the Starfish electrons can be represented by a simple empirical relation:

$$\frac{\partial N(M, J, R_o, t)}{\partial t} = - \frac{N(M, J, R_o, t)}{\tau} \tag{5-85a}$$

where τ is the time required for a decrease by a factor $1/e = 0.368$. The diffusion equation for this case can be solved analytically with the result (Reference 42):

$$D = \frac{\int_{R_{o1}}^{R_{o2}} \left[\frac{1}{\tau_a} - \frac{1}{\tau}\right] N(M, J, R_o, t)\, dR_o}{\left[\frac{1}{R_o^2} \frac{\partial}{\partial R_o}\left(R_o^2 N(M, J, R_o t)\right)\right]_{R_{o1}}^{R_{o2}}} \tag{5-85b}$$

where τ_a is the predicted atmospheric loss decay time. The momentum of particles is nearly proportional to B_o, so the relation between n and measured intensity j (Equations 5-64 and 5-72) is

$$N(M, J, R_o) \cong \frac{\pi R_o\, j_o(T, \mu_o)}{M\left[1 + \frac{3}{2\pi}\sqrt{R_o \frac{J^2}{Mm} \frac{B_E}{R_E^3}}\right]} . \tag{5-86}$$

Computations thus far have been practical only for particles with orbits restricted to the equatorial plane (where J = 0).

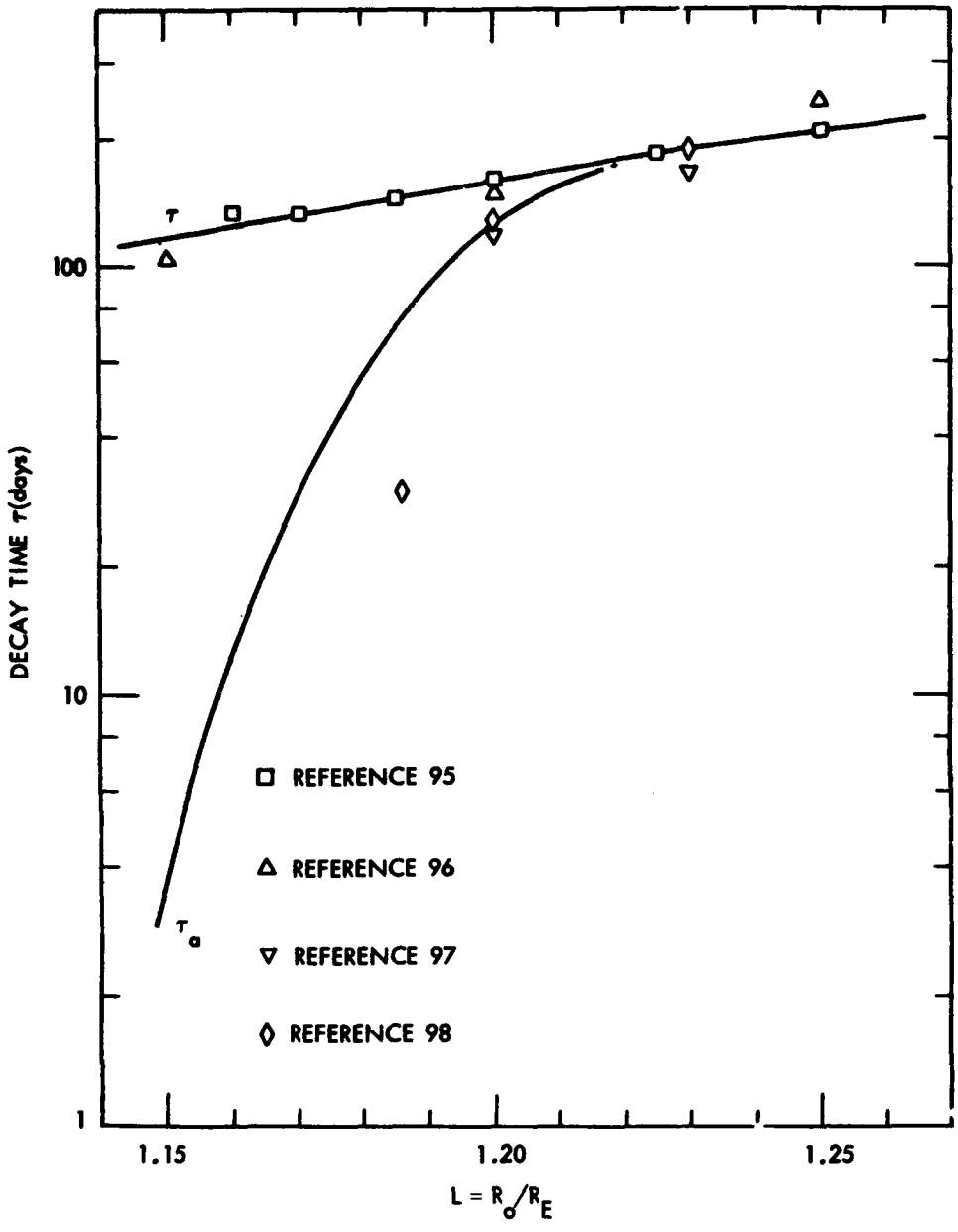

Figure 5-13. Decay time constants of the Starfish trapped electron belts (Reference 42). τ is the actual measured lifetime while τ_a is that computed for atmospheric losses alone.

Near the lower edge of the artificial radiation belts the intensity is approximately proportional to exp(138 x L). In this same region, τ_a drops very rapidly with decreasing altitude. τ and τ_a are compared in Figure 5-13. The computed diffusion coefficient (Figure 5-14) has a strong inverse dependence on L (Reference 42). This result is not easily reconciled with Equation 5-85. Perhaps a very large positive exponent in the magnetic fluctuation power spectrum is not necessary if the diffusion at low altitudes is principally due to curl-free electric fields, particularly the fields associated with recurring fluctuations (Section 5.4.3). Indeed, the particles noted in Section 5.4.3 that presumably had been accelerated by recurring field fluctuations were at $L \approx 1.15$ (Reference 76), below most of the trapped radiation regions. In the higher parts of the trapped electron belts, the decay time constants of Figure 5-15 have to be explained. The estimated intrinsic uncertainties, except where indicated in the figure, are generally of an order of magnitude comparable with the scatter of individual points. The data points attributed to Reference 98 are anomalously high because they include the effects of artificial electron belts. The higher characteristic energy of electrons released after a nuclear detonation results in lifetimes enhanced by a factor of 2 to 5. The higher set of data points attributed to Reference 104 represents only the electrons with more than 1-MeV kinetic energy. The solid curve at the left refers to computations of atmospheric losses (Reference 41). It should be evident from this figure that atmospheric decay cannot account for more than a small fraction of particle losses above $L \approx 1.5$. The trapped electrons resulting from the USSR high-altitude nuclear explosion of 1 November 1962 exhibited a radial spreading that can be explained by radial diffusion (References 106 and 107). When electrons restricted to the equatorial plane are considered, the resulting diffusion coefficient is represented by the single point at L = 1.8 in Figure 5-14. The L-dependence of the diffusion coefficients in the lower left of Figure 5-14 is so extreme that a nearly vertical line (with a negative slope) appears. Elsewhere, the diffusion coefficients agree with Equation 5-85. The individual points at L = 1.7, 2.1, and 2.2 were computed from observations on the decay of artificial electron belts (Section 6). The curve attributed to Reference 75 pertains to the diffusion of trapped protons.

An interesting case that seems to be attributable to radial diffusion was observed (References 108 and 109) in the outer radiation belts. There the electron distribution was greatly disturbed by a magnetic storm. After the storm, certain features of the radial distribution seemed to drift inward. Figure 5-16 illustrates how the perturbation in the

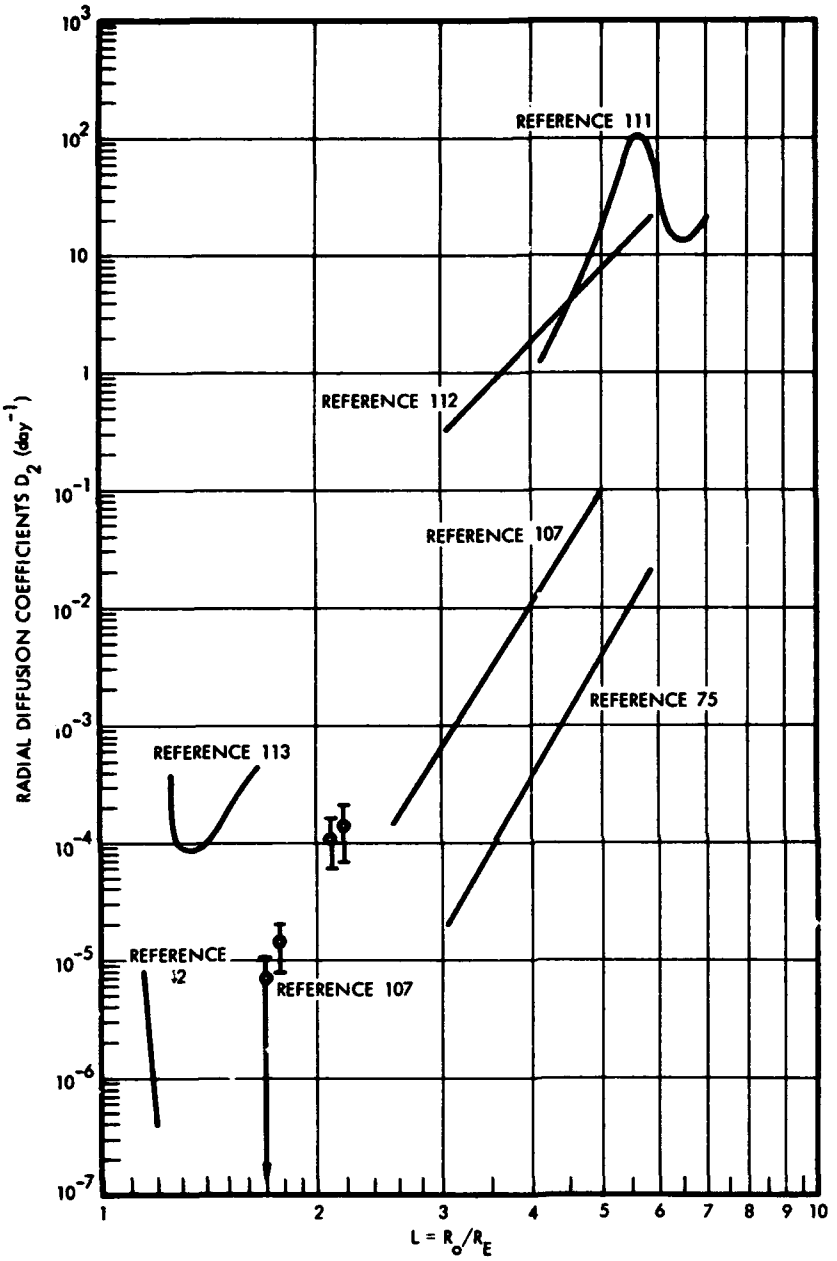

Figure 5-14. Radial diffusion coefficients for electrons with 90-degree equatorial pitch angles (Reference 110). The L-dependence of the diffusion coefficients in the lower left of Figure 5-14 is so extreme that a nearly vertical line (with a negative slope) appears. Elsewhere, the diffusion coefficients agree with Equation 5-85. The individual points at L = 1.7, 2.1, and 2.2 were computed from observations on the decay of artificial electron belts (Section 6). The curve attributed to Reference 75 pertains to the diffusion of trapped protons.

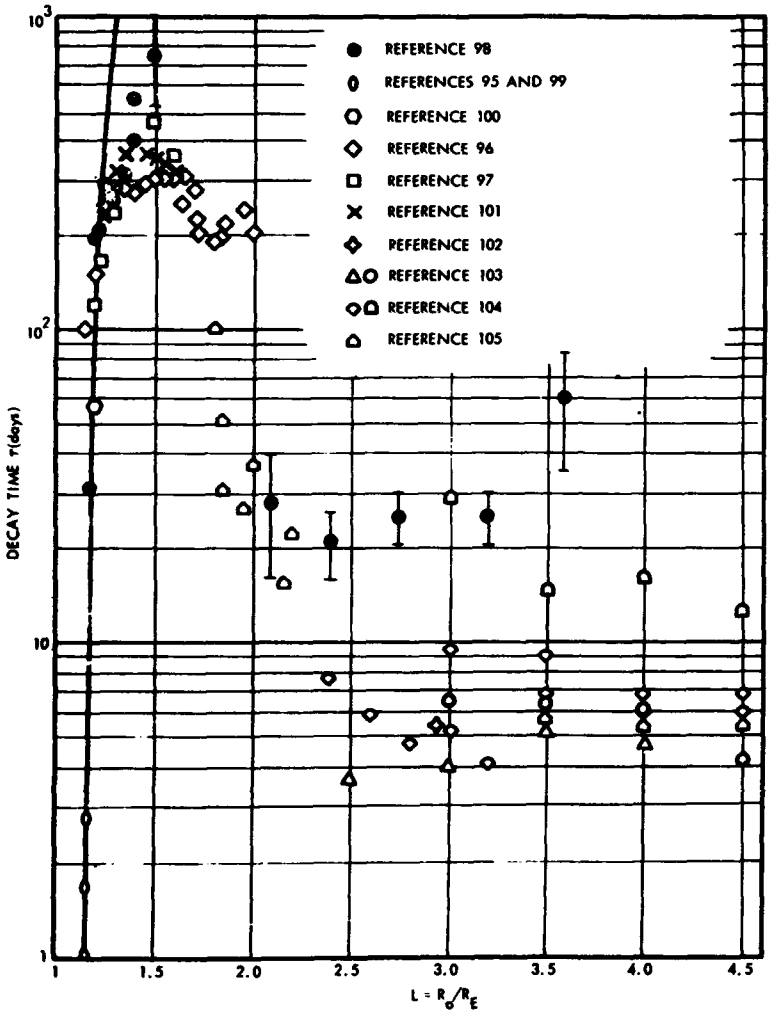

Figure 5-15. Decay time parameters for trapped electrons on intermediate L-shells. The estimated intrinsic uncertainties, except where indicated in the figure, are generally of an order of magnitude comparable with the scatter of individual points. The data points attributed to Reference 98 are anomalously high because they include the effects of artificial electron belts. The higher characteristic energy of electrons released after a nuclear detonation results in lifetimes enhanced by a factor of 2 to 5. The higher set of data points attributed to Reference 104 represents only the electrons with more than 1-MeV kinetic energy. The solid curve at the left refers to computations of atmospheric losses (Reference 41).

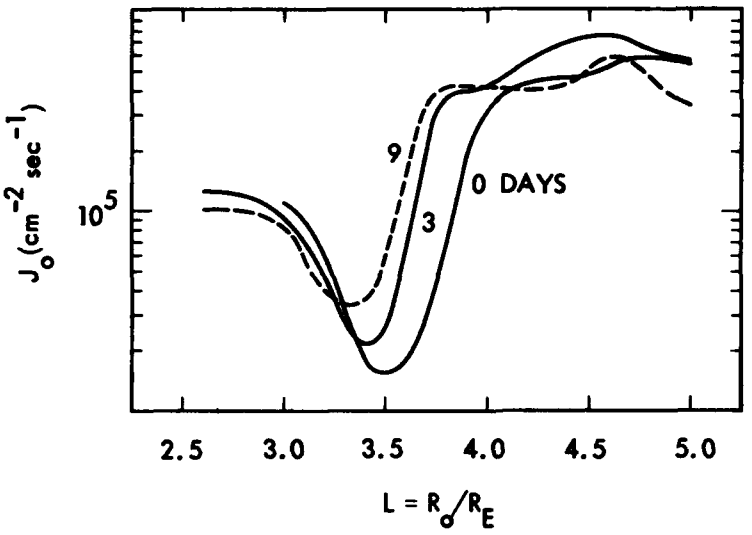

Figure 5-16. Inward motion of trapped electrons during a period of 9 days.

distribution moved inward while preserving its general shape. The omnidirectional fluxes on the equator of electrons with energies above 1.6 MeV are shown in Figure 5-16 (Reference 108). Though this is not obviously the result of pure radial diffusion, the inward motion can be described by a diffusion equation with the coefficients shown in Figure 5-14 (Reference 107).

The remainder of diffusion coefficient determinations have been primariiy attempts to explain steady-state features of the trapped electron and proton belts (Reference 114). Most electron diffusion coefficients computed for the region between $L \approx 1.8$ and $L \approx 5$ exhibit the expected L^{10} form.

The low-energy trapped proton distributions seem to be consistent with the hypothesis that these protons originate in the outer magnetosphere and are transported by diffusion to lower L-shells (References 68, 75, and 115). Recent examination of the higher energy protons (Reference 116) indicates that radial diffusion plays an important part in determining the distribution of these particles below L = 2. When the albedo neutron source, atmospheric loss mechanisms, and radial diffusion are combined, the resulting distribution is consistent with the observed distribution of protons above

several MeV. Because of the scarcity of definitive measurements, the radial (L) dependence of proton diffusion coefficients is not yet certain to be at all near L^{10}.

5.5 NONCONSERVATION OF THE FIRST AND SECOND ADIABATIC INVARIANTS

5.5.1 Trapping Limits

That geomagnetic fluctuations and large-scale electric fields can alter the third adiabatic invariant has been demonstrated adequately. If Φ is not conserved in the trapped radiation belts, changes in the first and second adiabatic invariants might also be expected (References 28 and 89). The power density of geomagnetic fluctuations observed on the earth's surface falls rapidly with increasing frequency, but energy in moderately high-frequency oscillations near the gyrofrequency and bounce frequency is still sufficient to affect trapped particle motions. Properly, the Fokker-Planck diffusion equations for radial diffusion and pitch angle diffusion should include terms resulting from failure of all the adiabatic invariants (Reference 28).

One possible consequence of nonadiabatic behavior is that stable trapping of protons and heavy particles becomes less likely as the particles' kinetic energies increase. Section 3.2.3 noted that on any L-shell a maximum energy occurs above which trapped orbits are not possible. Actually, the maximum energies of protons observed in the trapped radiation belts seems to be somewhat lower than predicted by the simple theory (References 11 and 117). It has been suggested that this is because inhomogeneities in the magnetic field may be about the same size as the particles' gyro-radii. Therefore, M and perhaps J might not be strictly invariant (Reference 11). Analysis of naturally trapped proton data leads to an empirical formula for the maximum momentum of protons on any L-shell:

$$p(\mathrm{MeV/c}) \leqslant \frac{1800}{L^2} \quad . \tag{5-87}$$

This momentum limit is about 10 times lower than the limit derived from Störmer's theory for orbits in a strictly dipolar field (Equation 3-28). Protons with greater momenta presumably are not trapped with lifetimes comparable to their predicted lifetimes for energy loss in the atmosphere.

5.5.2 Nonconservation of the Second Adiabatic Invariant—Fermi Acceleration

If a trapped particle is to have its adiabatic invariants altered, the fluctuation fields must be aligned in such a fashion that particle acceleration can occur. Section 5.4.4 noted that only certain components of the fluctuation fields had any effect on the third adiabatic invariant, e.g., only the azimuthal component of a large-scale electric field can accelerate particles. Because the second invariant J depends on the longitudinal component of momentum, $\bar{p}_{\parallel}$, only the parallel part of the fluctuating electric field, $\bar{E}_{1\parallel}$, should be expected to cause nonconservation of J.

A change in $\bar{p}_{\parallel}$ does not necessarily involve a change in J, however. For example: When a dipolar magnetic field is compressed, the field lines are shortened. Hence, the distance between mirror points, $|S_{m2} - S_{m1}|$, is decreased. But if the adiabatic invariant

$$J = 2 \int_{S_{m1}}^{S_{m2}} p_{\parallel} \, ds$$

is to be preserved, $p_{\parallel}$ must increase enough to offset the shortening of the trajectory. The resultant increase in the total momentum is a consequence of invariance of the magnetic moment invariant M. It has been called Fermi acceleration because a similar effect was invoked by Fermi in an attempt to explain cosmic ray acceleration (References 32 and 65). A simple explanation of Fermi acceleration may be constructed by referring to a charged particle spiralling about a field line as it enters a region where the field converges. In a static field, the particle is reflected with no change in its kinetic energy (Section 3.3.2). But, if the turning point is moving with a longitudinal velocity V_m toward the gyrating particle, a stationary observer would, after reflection, measure an increase by an amount of $2V_m$ in the particle's longitudinal velocity.

The energy gain (Fermi acceleration) in a single encounter with a moving magnetic mirror is (Reference 118)

$$\delta E = 2p_{\parallel}\left\{\frac{(1-v_{\parallel}^2/c^2)}{(1-v^2/c^2)}\,V_m + \left[\frac{(1-v_{\parallel}^2/c^2)}{(1-v^2/c^2)}(1-3v_{\parallel}^2/c^2) + 3\,\frac{(1-v_{\parallel}^2/c^2)}{(1-v^2/c^2)}\,\frac{v_{\parallel}^2}{c^2}\right]V_m^2 v_{\parallel}\right\} \qquad (5\text{-}88a)$$

$$\cong 2p_{\parallel}\,(V_m + V_m^2/v_{\parallel})\ . \qquad (5\text{-}88b)$$

This formula is valid when the velocity of the moving mirror is considerably less than the speed of light. The mirror velocity is to be taken positive in head-on collisions and negative in collisions in which the mirror overtakes the particle.

The effects of hydromagnetic waves are equivalent to the accelerations incurred in many random encounters with moving magnetic mirrors. If some average frequency of encounters ν_m exists, the Fokker-Planck coefficients for the alteration of the parallel part of the momentum (Reference 119) are

$$\langle \Delta p_{\parallel} \rangle \approx \frac{2\gamma^2 m^2 V_m^2}{p_{\parallel}}\,\nu_m \qquad (5\text{-}89)$$

$$\langle (\Delta p_{\parallel})^2 \rangle \approx 4\gamma^2 m^2 V_m^2\,\nu_m\ . \qquad (5\text{-}90)$$

If particle motions are influenced primarily by resonant encounters, then the frequency ν_m is equal to the bounce frequency or approximately $v_{\parallel}/S$, where S is the distance between mirror points. The Fokker-Planck coefficients thus are found to be related simply:

$$\langle \Delta p_{\parallel} \rangle = \frac{1}{2}\,\frac{d}{dp_{\parallel}}\,\langle (\Delta p_{\parallel})^2 \rangle\ . \qquad (5\text{-}91)$$

This equation has been derived elsewhere in other contexts and appears to be a general result for bounce resonant interactions between trapped particles and electromagnetic disturbances (References 105 and 120). The same relation could be obtained (as in Section 5.4.4) by presuming that the distribution function $f(p_{\parallel})$ = constant is highly stable against instabilities that derive their growth energy from the parallel momentum.

The order of magnitude of the diffusion coefficients can be estimated for general magnetic disturbances. The mirror velocity is nearly

$$V_m \cong 2\pi R_o \nu \frac{B_{||}}{B_o} \frac{\cos^8 \lambda_m (1 + 3 \sin^2 \lambda_m)}{9 \sin \lambda_m (1 + \frac{5}{3} \sin^2 \lambda_m)} \tag{5-92}$$

where $B_{||}$ is the parallel part of the disturbance amplitude and ν is the frequency. This formula is valid only when the mirror latitude λ_m is not too near zero. Since a continuous wave power spectrum must be presumed, particles out of resonance by an amount $\delta\nu$ clearly can interact only with a given train of waves for a time $\delta t \approx 1/2\,\delta\nu$. The change in the particles' momentum during the same time is

$$\delta p_{||} = 2\gamma m V_m \frac{\delta t}{t_b} \quad . \tag{5-93}$$

Averaged over time, this gives the Fokker-Planck coefficient

$$\left\langle (\Delta p_{||})^2 \right\rangle \approx \frac{16\pi^2}{9^2} \frac{R_E^2}{B_E^2} \frac{L^8 \cos^{16} \lambda_m}{\sin^2 \lambda_m} \frac{B_{||}^2}{2\delta\nu} \quad . \tag{5-94}$$

It can be shown (Reference 121) that, where δB is the average amplitude of waves in a narrow frequency band of width $\delta\nu$, the power spectral density is

$$P(\nu) \sim \frac{(\delta B)^2}{2\delta\nu} \quad . \tag{5-95}$$

The strength of geomagnetic fluctuations with periods of about 1 second can be estimated by presuming that disturbances originate on the exterior of the trapped radiation region (References 119 and 122 through 126). The trapped plasma behaves as an elastic medium; magnetic disturbances propagate inward by hydromagnetic waves. A hydromagnetic wave travels with the Alfvén velocity (References 59 and 63):

$$V_A = \frac{c}{\sqrt{1 + 4\pi\rho c^2/B^2}} \quad . \tag{5-96}$$

The Alfvén velocity increases with decreasing altitude until the density of the atmosphere ρ begins to increase faster than B . If hydromagnetic waves are not absorbed strongly, the amplitude of the waves above $r \approx 1.5\ R_E$ must increase with altitude. The amplitude of fluctuations on any L-shell above $L \approx 1.5$ is therefore likely to be greatest near the equator. The amplitude of hydromagnetic waves can be represented roughly as

$$B_{II} \sim B'_{II} \frac{L \cos^6 \lambda}{6} \tag{5-97}$$

where B'_{II} is the amplitude at L = 6 (Reference 119) (in $MeV^2/c^2/sec$). The corresponding Fokker-Planck diffusion coefficient is

$$\left\langle (\Delta p_{II})^2 \right\rangle \approx 34 \frac{[p(MeV/c)]^4}{\gamma^2} \frac{L^6 \cos^{20} \lambda_m}{\sin^2 \lambda_m} P'_{II}(\nu)_{\nu = 1/t_b} \quad . \tag{5-98}$$

Using measured power spectra in the outer magnetosphere (Reference 127), an approximate lifetime of 1 MeV electron at $L \approx 6$ can be found with the aid of Equation 5-91:

$$\tau \approx \frac{p_{II}}{\left\langle \Delta p_{II} \right\rangle} \approx 2\ yr \quad . \tag{5-99}$$

Apparently, the Fermi acceleration bounce resonance process is significant only for particles mirroring very near the equatorial plane at times when the power density of magnetic fluctuations is far above the normal values. A similar result follows for other bounce-resonant interactions (Reference 120). That this is the most important mechanism for depletion of trapped particles in any region is therefore unlikely.

Some attempts have been made to include nonconservation of J in radial diffusion computations (Reference 28). The experimental evidence on radial diffusion has not yet, however, been adequate to test cases other than $J \approx 0$ ($\alpha_o \approx 90$ degrees).

Whether longitudinal components of curl-free electric fields with periods near 1 second result in trapped particle losses is uncertain. Electric fields play such important roles in current auroral acceleration and precipitation theories that significant effects on trapped particle populations might be presumed. This is almost surely a valid conclusion in the outer parts of the magnetosphere (Section 5.6).

5.5.3 Nonconservation of the First Adiabatic Invariant—Wave Particle Interactions

The magnetic moment invariant M involves only the transverse part of the momentum. It does not follow, however, that changes in $\bar{p}_\perp$ and $\bar{p}_{||}$ (and hence in M and J), are always independent. The effects of electromagnetic waves near the trapped particle's gyrofrequencies are somewhat more complicated than the effects of relatively slow magnetic fluctuations.

Electromagnetic waves of moderately high frequencies are propagated quite efficiently along magnetic field lines. While traveling from one "end" to the other along a field line, a wave has an opportunity to interact with many particles on the associated L-shell. Also, the wave might be reflected by the ionosphere and make several traversals of the field line before dying away. A wave propagating along a field line can be represented by the solutions to Maxwell's equations (in rectangular coordinates)(Reference 128):

$$\bar{E}_1 = \hat{x}\, E_\perp \cos\psi \pm \hat{y}\, E_\perp \sin\psi + \hat{z}\, E_{||} \cos\psi \qquad (5\text{-}100a)$$

$$\bar{B}_1 = \mp\, \hat{x}\, B_\perp \sin\psi + \hat{y}\, B_\perp \cos\psi \qquad (5\text{-}100b)$$

$$\bar{J}_1 = \hat{x}\, J_\perp \sin\psi \mp \hat{y}\, J_\perp \cos\psi + \hat{z}\, J_{||} \sin\psi \ . \qquad (5\text{-}100c)$$

The z-axis here is along the field line. The phase angle ψ is $\omega t - kz$ where k, the wave number, is equal to 2π divided by the wave length. Maxwell's equations (Equations 3-105 through 3-108) for the perturbed field of the wave reduce to:

$$B_\perp = \frac{kc}{\omega} E_\perp \qquad (5\text{-}101a)$$

$$J_\perp = \frac{1}{4\pi c} E_\perp \left(\omega - \frac{k^2 c^2}{\omega} \right) \qquad (5\text{-}101b)$$

$$J_{||} = \frac{\omega}{4\pi c} E_{||} \ . \qquad (5\text{-}101c)$$

(E and B are in conventional gaussian units, and J is in emu, see Appendix 3A). There is an arbitrariness in the sign of some components of the field vectors. Clearly, the upper signs pertain to a right-handed circularly polarized wave that rotates in the same sense as the gyrating electrons. The other signs yield a left-handed, circularly polarized wave. The relative phases of the rotating transverse wave

vectors are depicted in Figure 5-17. The wave vectors are depicted there as seen by a stationary observer looking in the negative z direction. The field components should be considered rotating clockwise (upper diagram) or counterclockwise (lower diagram) as viewed by a stationary observer looking in a direction contrary to the unperturbed magnetic field. The shaded area labelled f_1 represents the perturbation in the electron distribution function.

Longitudinal oscillations can be separated from transverse oscillations if propagation is strictly along the direction of the magnetic field. The mixture of transverse and longitudinal oscillations that would result from nonparallel propagation leads to elliptical polarization. Only purely circular polarization is considered here.

Gyrating particles interact with all components of an electromagnetic wave. If a wave consists entirely of longitudinal oscillations, the only force acting on a charged particle is along the direction of propagation. If it is moving along a field line with nearly the velocity of a longitudinal wave but slightly out of phase, the particle will be accelerated by the longitudinal electric field $\bar{E}_{1,\parallel}$. Given sufficient time, the gyrating particles adjust their speeds to the phase velocity of the wave so that they will eventually ride along in the "troughs" or "crests." The mechanism by which the transverse part of the velocity is altered in wave-particle interactions is considerably more complicated. When gyrating particles encounter circularly polarized waves, the $\bar{v} \times \bar{B}_1$ term in the equation of motion (Equation 3-3) has both longitudinal and transverse components.

An observer moving with a circularly polarized electromagnetic wave would sense no rotation of the field vectors. $\bar{E}_{1\perp}$ and $\bar{B}_{1\perp}$ would appear to maintain a fixed orientation with respect to the steady state field. But, to particles moving with longitudinal velocities different from the wave phase velocity, the wave rotates at a doppler-shifted frequency. Particles overtaking the wave experience a perturbed field that rotates in a direction contrary to the actual polarization. When the relative longitudinal velocity of wave and particle is just great enough that the particle senses a wave field rotating at its own gyro-frequency, the particle is in <u>resonance</u> with the wave. A particle that is just slightly out of resonance can be accelerated in a manner analogous to the acceleration by longitudinal oscillations. Only particles that are very near to resonance can be affected strongly

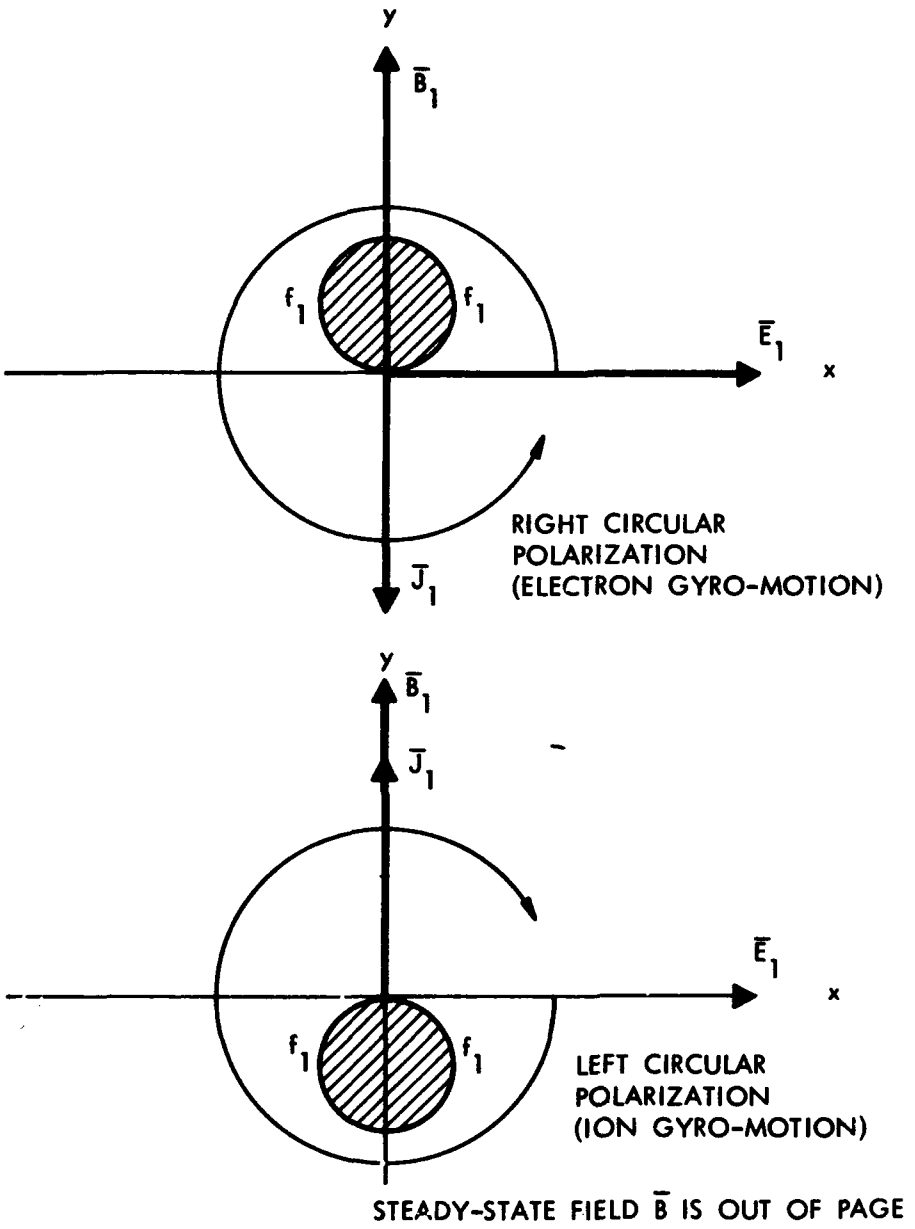

Figure 5-17. Relative phases of wave field vectors in a circularly polarized wave. The shaded area labeled f_1 represents the perturbation in the electron distribution function.

by wave particle interactions. Usually, positively and negatively charged particles may be in resonance with the same wave, although their longitudinal velocity components are entirely different. The longitudinal velocities of resonant particles are related to the wave phase velocities:

$$V_p = \frac{\omega}{k} \tag{5-102}$$

by the doppler frequency shift condition (Reference 129) for electrons:

$$v_{\parallel} = V_p \frac{\omega - \omega_e}{\omega} \tag{5-103a}$$

and for protons

$$v_{\parallel} = V_p \frac{\omega + \omega_i}{\omega} \quad . \tag{5-103b}$$

ω_e and ω_i are the gyro-frequencies, which include a factor of the inverse of the relativistic dilation factor γ. These two equations are valid for right-handed waves—rotating in the same sense as the electrons. They can be employed for waves of either polarity if ω is regarded as negative for left-handed waves.

From Equations 5-103, the rather odd result follows that a wave rotating in the same sense as the electrons but at a frequency below the electron gyro-frequency will be in resonance with electrons moving in a direction opposite to the wave. Protons in resonance with the same wave must be moving in the same direction as the wave but slightly faster.

In a coordinate frame moving together with a circularly polarized wave at the phase velocity V_p, the $\bar{v} \times \bar{B}_1/c$ force appears to be cancelled by the $\bar{E}_{\perp}$ force. The force on a resonant particle in this coordinate frame is zero; therefore, its total energy remains constant (References 129 through 132). The momentum relative to the moving reference frame, which also must be conserved, is

$$p_W = \sqrt{p_{\perp}^2 + \gamma_W^2 (p_{\parallel} - m\gamma V_p)^2} \tag{5-104a}$$

$$\gamma_W^2 \equiv \frac{1}{\sqrt{1 - V_p^2/c^2}} \approx 1 \quad . \tag{5-104b}$$

Because some radiation belt particles have velocities near the speed of light, a fully relativistic formulation has been retained. When making the transition to a nonrelativistic formulation, both γ_W and the mass dilation factor γ must become nearly equal to 1. The phase velocity of most plasma waves is actually so small that γ_W seldom differs appreciably from 1 .

According to Equation 5-104, an infinitesimal alteration of the transverse momentum $\delta p_\perp$ is related to an infinitesimal change in the longitudinal momentum $\delta p_{||}$ or:

$$p_\perp \left[1 - \gamma_W^2 \left(p_{||} - m\gamma V_p \right) \frac{V_p}{m\gamma c^2} \right] \delta p_\perp = - \gamma_W^2 \left(p_{||} - m\gamma V_p \right) \left(1 - \frac{p_{||} V_p}{m\gamma c^2} \right) \delta p_{||} \quad . \tag{5-105}$$

In the nonrelativistic limit, this reduces to a much simpler formula (References 131, 133, and 134):

$$p_\perp \delta p_\perp \cong - \left(p_{||} - m V_p \right) \delta p_{||} \quad . \tag{5-106}$$

Figures 5-18a and 5-18b illustrate the velocity space trajectories of protons interacting with waves at the proper phase velocities. In constructing these relations between $v_{||}$ and $v_\perp$ Equation 5-121 was utilized since it provides, in conjunction with Equations 5-103 and 5-105, a relation between phase velocity and frequency. At high velocities, these trajectories are very nearly circular; this means that the alteration of the particles' kinetic energies is slight. The corresponding velocity space trajectories would be indistinguishable from circles for most radiation belt electrons.

From the preceding equations, a simple relation follows for the change in the transverse part of the momentum relative to the change in the total momentum of electrons:

$$\frac{\delta p_\perp^2}{\delta p^2} \cong \frac{\omega_e}{\omega} \tag{5-107a}$$

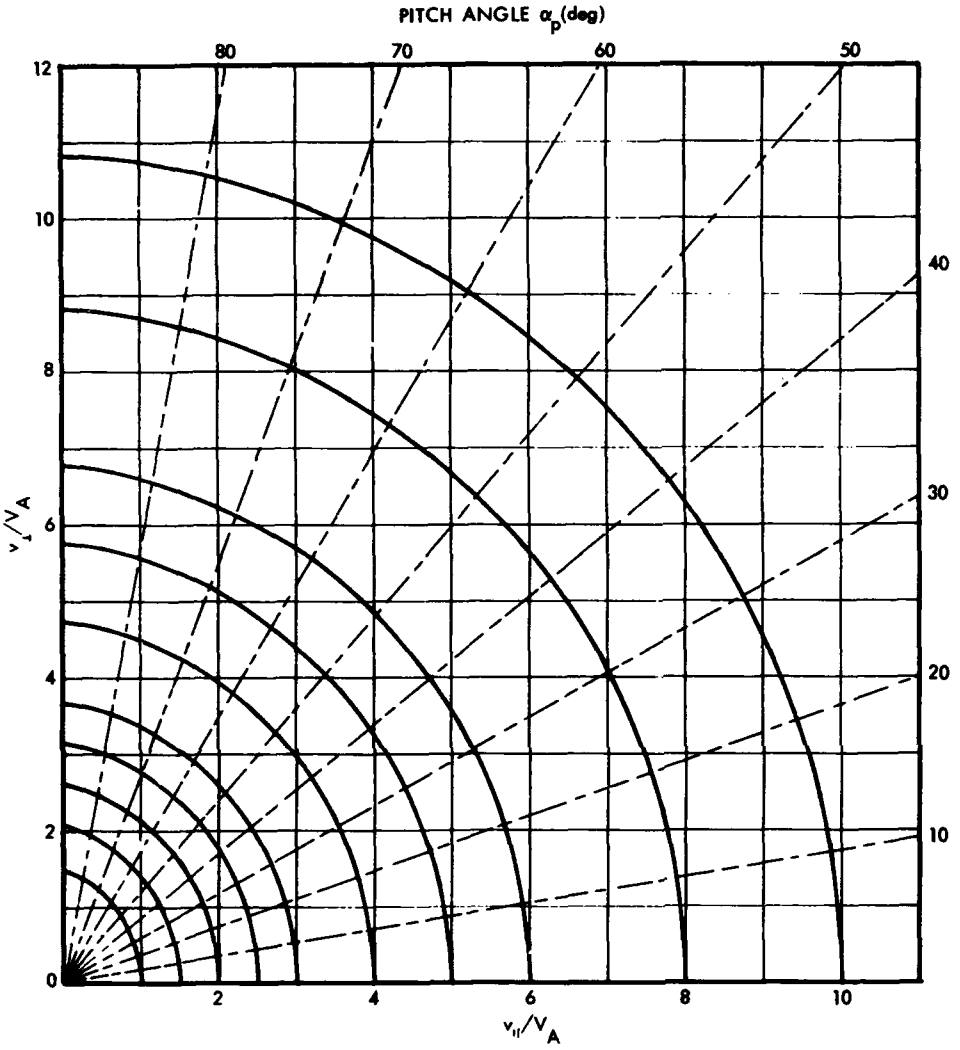

Figure 5-18a. Velocity space trajectories of a proton interacting with circularly polarized waves—velocity components are relative to the Alfvén velocity V_A.

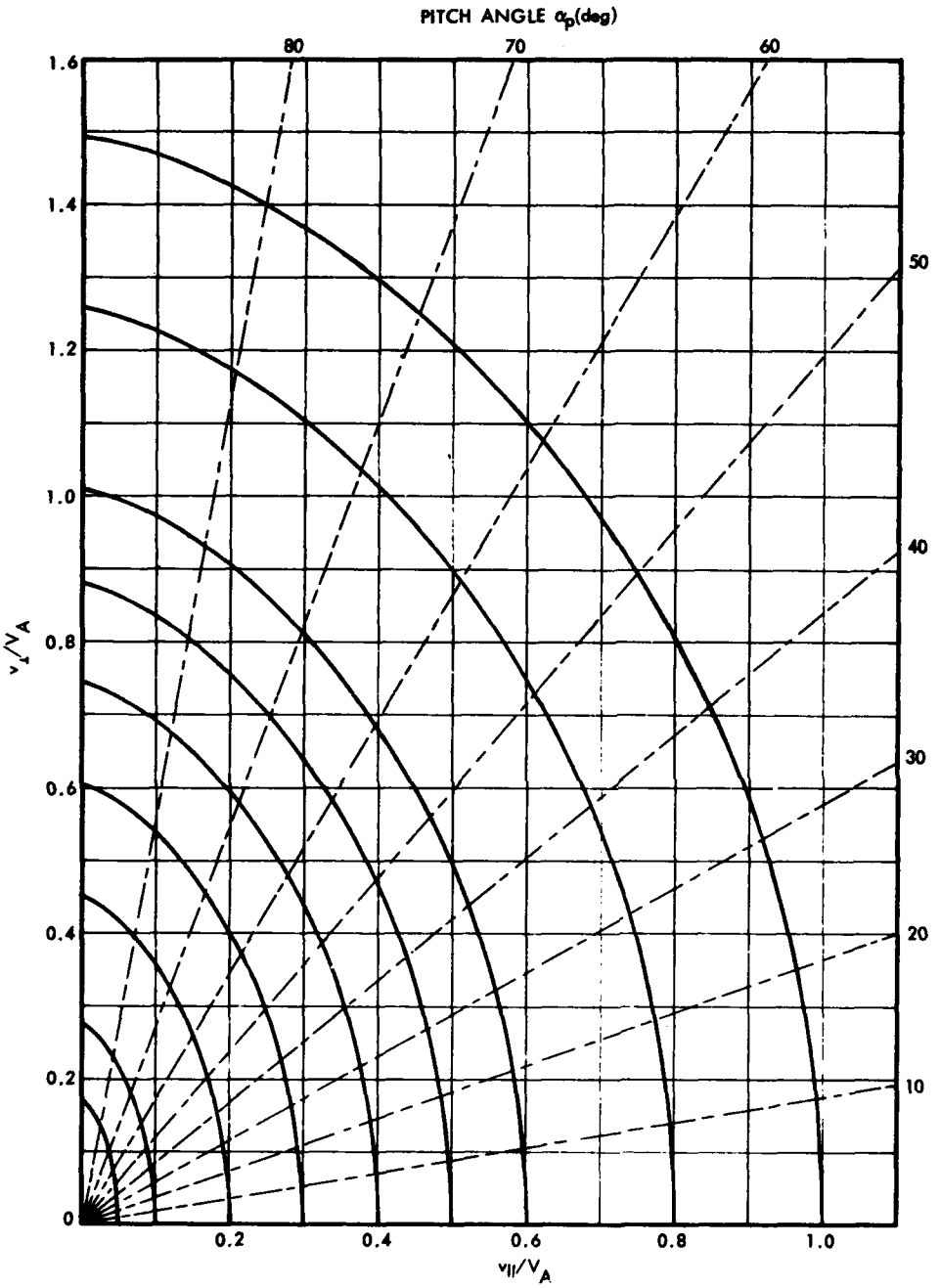

Figure 5-18b. Velocity space trajectories of a proton interacting with circularly polarized waves—velocity components are relative to the Alfvén velocity V_A.

or of protons or positive ions:

$$\frac{\delta p_\perp^2}{\delta p^2} \cong - \frac{\omega_i}{\omega} \quad . \tag{5-107b}$$

Clearly, deflections of gyrating particles are much more important than changes in the total momentum whenever the frequency of the waves is much lower than the particles' gyro-frequencies. Also, oppositely charged particles are deflected in quite different directions by the same wave.

PITCH ANGLE DIFFUSION. The scattering of trapped particles by electromagnetic waves very much resembles the scattering by bound and free electrons in the atmosphere. Fokker-Planck coefficients can be derived for the wave-particle interactions and included in the pitch angle diffusion Equation 5-21. The Fokker-Planck equation for wave-particle interactions, neglecting energy losses, has just two coefficients: $\langle \Delta \mu \rangle$ and $\langle (\Delta \mu)^2 \rangle$ (References 133 through 136). As in Section 5.4.4, a simple relation can be constructed between two Fokker-Planck coefficients if a particular solution of the diffusion equations is known. An isotropic pitch angle distribution [$f(T, \mu)$ independent of μ] is a steady state solution of the pitch angle diffusion equation. This is essentially because, near resonance, as many particles would be subject to acceleration as subject to deceleration (Section 5.5.4; Reference 26). The rate of change of the distribution function f is therefore zero, and the Fokker-Planck equation reduces to a simple differential equation relating two diffusion coefficients. After some simplification, the diffusion equation for the pitch angle distribution of trapped particles is

$$\frac{\partial f(\mu)}{\partial t} = \frac{\partial}{\partial \mu} \left[D \frac{\partial f(\mu)}{\partial \mu} \right] \tag{5-108a}$$

$$D \equiv \frac{1}{2} \langle (\Delta \mu)^2 \rangle \quad . \tag{5-108b}$$

The single diffusion coefficient D can be estimated if the variation in the pitch angle is known for a single interaction with a wave of known characteristics. The pitch angle alteration is found from the changes in the momentum components. From Equations 5-104 and 5-106, the relation between pitch angle and the longitudinal part of the momentum is

$$\delta \mu \cong \left(\frac{1}{p} - \frac{p_{||} m \gamma V_p}{p^3} \right) \delta p_{||} \quad . \tag{5-109}$$

The change in $p_{||}$ is just the acceleration $q\bar{v}\times\bar{B}_1/c$ multiplied by the time δt during which a particle is near resonance. A particle that is an amount δk away from exact resonance falls out of phase with the wave in a time roughly equal to $2/v_{||}\delta k$. With this substitution for δt and neglecting terms of order V_p/v, the diffusion coefficient becomes

$$D \approx \frac{m\omega_c^2(1-\mu^2)}{p\gamma\mu} \frac{B_\perp^2/\delta k}{B^2} \quad . \tag{5-110}$$

The factor $B_\perp^2/\delta k$ has the form of a power spectrum (amplitude squared per unit wave number, Section 5.5.2; Equation 5-95). It represents the magnetic fluctuation energy in a band of width:

$$\delta\omega \approx \frac{\omega}{k}\,\delta k = V_p\,\delta k \quad . \tag{5-111}$$

As in the case of radial diffusion and bounce resonance diffusion, all that is needed to fully determine the effects of pitch angle scattering is a knowledge of the spectrum of waves. In practice, the major obstacle in this approach is the difficulty of measuring the amplitudes of waves that are not readily transmitted through the ionosphere and atmosphere. The spectrum of whistlers and very low frequency (VLF) noise observed on the ground is largely irrelevant because these waves already may have lost significant amounts of energy to the trapped particles (Reference 123).

When the energy exchanged between waves and particles is not negligible, the energy diffusion terms in the Fokker-Planck equation also must be taken into account. But because energy and pitch angle are interrelated, the Fokker-Planck equation should transform to an equation in one variable. The differential operators are generally of the form (Reference 119):

$$\frac{\delta}{\delta p} \equiv p_W\left(\frac{\partial p_W}{\partial p_\perp}\frac{\partial}{\partial p_{||}} - \frac{\partial p_W}{\partial p_{||}}\frac{\partial}{\partial p_\perp}\right) \tag{5-112a}$$

$$\cong p_\perp \frac{\partial}{\partial p_{||}} - \left(p_{||} - m\gamma V_p\right)\frac{\partial}{\partial p_\perp} \quad . \tag{5-112b}$$

When the distribution function is a function of p_W and some other variable, for example x, the differential operator (Equation 5-112) is just

$$\frac{\delta}{\delta p} = p_W \left(\frac{\partial p_W}{\partial p_\perp} \frac{\partial x}{\partial p_\parallel} - \frac{\partial p_W}{\partial p_\parallel} \frac{\partial x}{\partial p_\perp} \right) \frac{\partial}{\partial x} \quad . \tag{5-113}$$

In terms of the pitch angle cosine μ:

$$\frac{\delta}{\delta p} = \frac{p_\perp}{p} \left[\frac{p_\perp^2}{p^2} + \gamma_W^2 \left(p_\parallel - m\gamma V_p \right) \left(\frac{p_\parallel}{p^2} - \frac{V_p}{m\gamma c^2} \right) \right] \frac{\partial}{\partial \mu} \tag{5-114a}$$

$$\cong \frac{p_\perp}{p} \left(1 - \frac{p_\parallel m\gamma V_p}{p^2} \right) \frac{\partial}{\partial \mu} \quad . \tag{5-114b}$$

The diffusion equation properly should have the form

$$\frac{\partial f}{\partial t} \approx \frac{p_W^4}{p^4} \left(1 - \frac{m V_p p \mu}{\partial p_W^2} \right) \frac{\partial}{\partial \mu} \left[D \left(1 - \frac{m V_p p \mu}{\partial p_W^2} \right) \frac{\partial f}{\partial \mu} \right] \quad . \tag{5-115}$$

(p and γ are not constants, but functions of p_W and μ). The diffusion coefficient D is the same as was given in Equation 5-110 (Reference 134 contains another derivation of D). However, when the momentum space trajectories differ appreciably from true circles, the V_p terms are not negligible and Equation 5-115 has no longer the form of a simple diffusion equation, such as Equation 5-108.

Actually, the pitch angle diffusion equation for the geomagnetic field also is complicated by the possibility that the various factors may not be constant along the field lines. If D can be averaged along the particle trajectories, a diffusion equation can be established in which μ is replaced by its equatorial value μ_o . This difficulty is avoided usually by assuming that most wave-particle interactions occur near the equator (Reference 133).

Scattering of particles by waves tends to flatten the pitch angle distribution of trapped particles (References 132, 133, and 137). If no loss cone existed, the ultimate steady state would be an isotropic distribution, $f(\mu_o)$ = constant. The impossibility of trapping particles that have very small pitch angles leads to a smoothing of the $f(\mu_o)$ contour near the atmospheric cutoff μ_c . Any discontinuity in the pitch angle distribution would be removed rapidly through pitch angle diffusion. The principal difference between scattering by atmospheric electrons and scattering by waves is that waves are likely to

be effective at very high altitudes. Even particles restricted by large pitch angles to the equatorial regions could be subject to rapid diffusion due to wave particle interactions.

5.5.4 Propagation of Waves in a Plasma

In the preceding section, the diffusion of trapped particles was considered on the presumption that the wave power spectrum in the trapping region is known. An alternative approach is to consider how charged particles absorb or amplify waves passing through the trapping region. Some restrictions thereby may be placed on the trapped particle distribution if wave intensities are to be consistent with what is known about absorption and reflection in the ionosphere.

Equations 5-100 and 5-101 merely describe the electric and magnetic fluctuations in a wave. The equation of motion of the wave that accounts for the interaction with particles has not yet been introduced. The distribution function f might be represented by a steady state part f plus a perturbed part f_1. When $f + f_1$, $\bar{E}_1$ and $\bar{B} + \bar{B}_1$ are inserted in the Boltzmann equation (Equation 3-91), the result, to first order in perturbed quantities (neglecting collisions), the Boltzmann-Vlasov equation, is (Reference 26)

$$\frac{\partial f_1}{\partial t} + \frac{1}{m\gamma}\,\bar{p}\cdot\nabla f_1 + \frac{\omega_c}{\gamma}(\bar{p}\times\hat{z})\cdot\nabla_p f_1 + q\left[\bar{E}_1 + \frac{1}{m\gamma c}\,\bar{p}\times\bar{B}_1\right]\cdot\nabla_p f = 0\,. \tag{5-116}$$

The wave field may be represented by the oscillatory parts of Equations 5-100, and f_1 may be represented by a function of the form $g\sin(\phi \pm \psi)$.

The equations for longitudinal and transverse oscillations are separable for the special case of propagation along the direction of the steady part of the magnetic field. Substitution of f_1 into the current equation:

$$\bar{J}_1 = \frac{q}{c}\iiint d^3p\,\bar{v}\,f_1 \tag{5-117}$$

facilitates the elimination of g, $E_\perp$, and $E_\parallel$. The result (after a partial integration of the longitudinal part, Equation 5-118b) is the dispersion equation relating frequency and wave number (Reference 138) for circular polarization:

$$\omega^2 - k^2c^2 = -\sum_{\substack{\text{electrons}\\ \text{and ions}}} \omega^2_{p(e,i)} \iiint d^3p \, \frac{p_\perp}{2\gamma}$$

$$\cdot \frac{1}{(\omega \pm \omega_c - kp_{||}/m\gamma)} \left[\left(\omega - \frac{kp_{||}}{m\gamma} \right) \frac{\partial f/n}{\partial p_\perp} + \frac{kp_\perp}{m\gamma} \frac{\partial f/n}{\partial p_{||}} \right] \quad (5\text{-}118a)$$

$$\omega = \sum_{\substack{\text{electrons}\\ \text{and ions}}} \omega^2_{p(e,i)} \iiint d^3p \, \frac{\omega}{\gamma^2} \frac{1}{(\omega - kp/m\gamma)^3}$$

$$\cdot \left(1 + \frac{p_\perp^2}{m^2c^2} \right) \frac{f}{n} \quad . \quad (5\text{-}118b)$$

Note that the gyro-frequency contains a factor $1/\gamma$. The upper signs pertain to right-handed waves, and the lower signs pertain to left-handed waves. The electron and ion plasma frequencies (References 32, 58, and 128) are

$$\omega_p = \sqrt{\frac{4\pi ne^2}{m}} \quad (5\text{-}119a)$$

for electrons:

$$\omega_{pe}(\text{sec}^{-1}) = 5.641 \times 10^4 \sqrt{n_e(\text{cm}^{-3})} \quad (5\text{-}119b)$$

and for protons:

$$\omega_{pi}(\text{sec}^{-1}) = 1.317 \times 10^3 \sqrt{n_i(\text{cm}^{-3})} \quad . \quad (5\text{-}119c)$$

The ratio of electron plasma frequency to electron gyro-frequency throughout the upper atmosphere is shown in Figure 5-19. The plasma frequency is essentially identical with the electron plasma frequency. Plasma oscillations are insignificant at low altitudes where the ratio falls to zero. The electron densities used in Figure 5-19 were those shown in Figure 5-2.

Consider waves traveling in a plasma with an isotropic, low-temperature, particle velocity distribution. Since electrical neutrality requires equality of the numbers of ions and electrons,

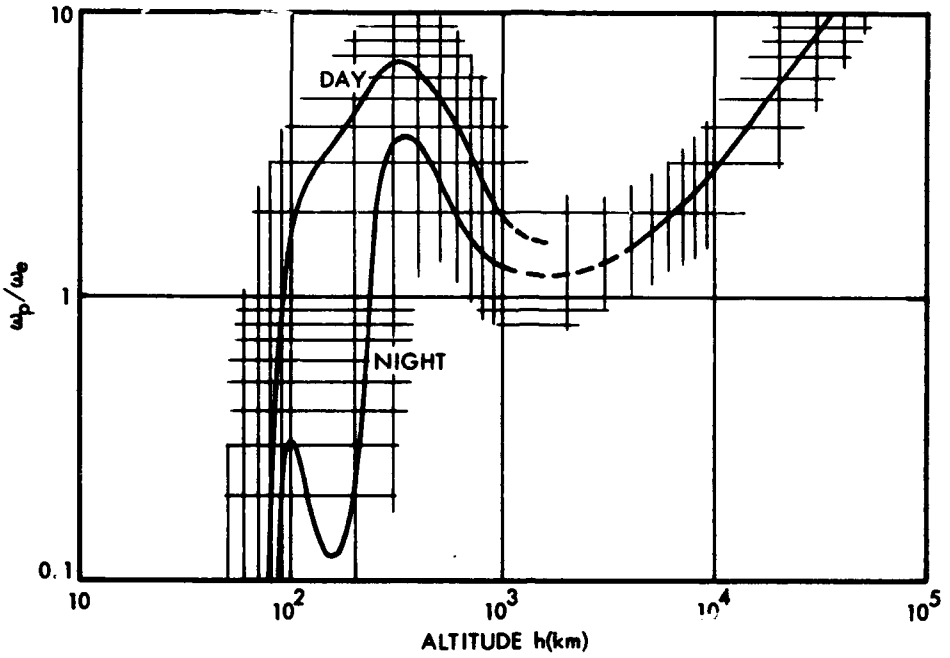

Figure 5-19. The ratio of plasma frequency to electron gyro-frequency throughout the atmosphere and trapped radiation regions. Plasma oscillations are insignificant at low altitudes where the ratio falls to zero. (See Figure 5-2 for electron densities.)

the ion-plasma frequency is negligible compared with the electron-plasma frequency. The dominant terms in the longitudinal polarization dispersion, Equation 5-118b, are

$$\omega^2 = \omega_{pe}^2 + \omega_{pi}^2 \equiv \Omega_p^2 \approx \omega_{pe}^2 \quad . \tag{5-120}$$

That is, in a cold plasma, the only possible longitudinal waves are nonpropagating electrostatic oscillations at the plasma frequency (Reference 128).

The dispersion equation for circularly polarized transverse waves in a plasma consisting entirely of low-velocity particles is

$$\frac{c^2}{v_p^2} = \frac{k^2 c^2}{\omega^2} = 1 + \frac{\omega_{pe}^2}{\omega(\omega_e - \omega)} - \frac{\omega_{pi}^2}{\omega(\omega_i + \omega)} \qquad (5\text{-}121a)$$

$$= 1 + \frac{\Omega_p^2}{(\omega_e - \omega)(\omega_i + \omega)} \quad . \qquad (5\text{-}121b)$$

Again, one equation can be employed for both right-handed and left-handed waves if ω is regarded as a quantity that may be either positive or negative. The neglect of propagation in directions other than along $\bar{B}$ is fairly well justified because the dispersion equation for the most interesting waves (low frequencies) does not change drastically with small deviations from parallel propagation (Reference 128). Discussions of plasma waves with arbitrary propagation angles may be found in standard texts, notably References 128 and 139.

The dispersion equation near the electron gyro-frequency is shown graphically in Figure 5-20. The left-handed waves and the high-frequency right-handed waves have phase velocities greater than the speed of light. The low-frequency right-handed waves—the whistler mode—generally have phase velocities much lower than the speed of light. Because observed power spectra of geomagnetic fluctuations seem to fall rapidly with increasing frequency, electrons should be expected to interact most effectively with very slow waves in the whistler mode (References 129, 130, and 131).

Beyond the right edge of Figure 5-20 are other modes near the proton gyro-frequency. Rather than continuing toward zero-phase velocity at zero frequency, the whistler mode curve turns over near the ion gyro-frequency where the dispersion equation becomes approximately

$$\frac{c^2}{v_p^2} = \frac{k^2 c^2}{\omega^2} \cong \frac{\Omega_p^2}{\omega_2(\omega_i + \omega)} \qquad (5\text{-}122a)$$

$$\cong \frac{\omega_{pi}^2}{\omega_i(\omega_i + \omega)} \quad . \qquad (5\text{-}122b)$$

That part of the dispersion Equation 5-121a where the oscillation frequency is near the proton or ion gyro-frequency customarily is denoted the magnetosonic mode (References 128 and 139). A left-circularly polarized wave also can propagate at frequencies less than the

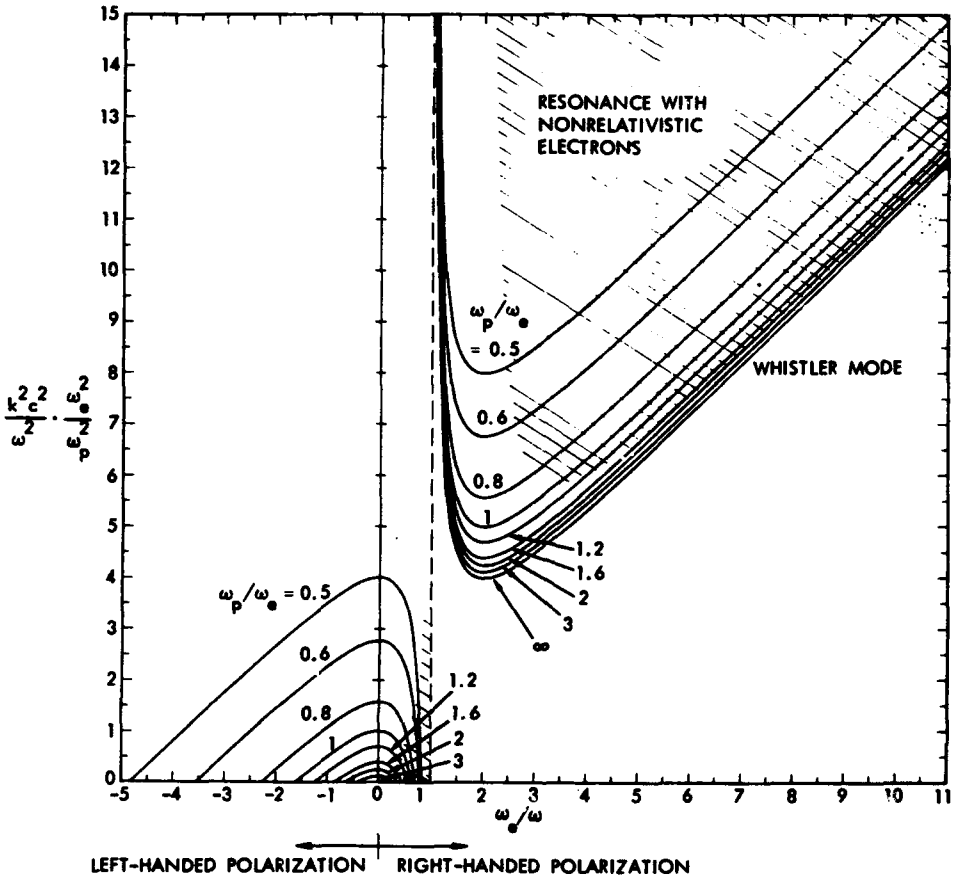

Figure 5-20. The dispersion equation for circularly polarized waves propagating along field lines in a low-temperature plasma. Generally, plotting some parameters other than frequency and wave number is convenient. Those chosen for the figure are proportional to the inverse of frequency and to the phase velocity. The remaining arbitrary parameter is the ratio of plasma frequency to electron gyro-frequency (Figure 5-19). Plasma waves in the shaded regions in Figure 5-20 can interact over the remainder of the diagram. There are only restricted bands of frequencies for which wave propagation is possible.

ion gyro-frequency. The dispersion equation for low-frequency left-handed waves is the same as Equation 5-115 with the distinction that ω is negative ($-\omega_i < \omega < 0$). This part of the dispersion equation is the ion-cyclotron mode; its relation to ions is analogous to the relation of the whistler mode to electrons.

INSTABILITIES—GROWING WAVES. When a plasma contains some components with finite average energies, the dispersion equations may not always be satisfied with purely real frequencies (or wave numbers). In Equations 5-118, the denominators of the integrands vanish for some values of $p_{\parallel}$. If f remains finite over a range of values of $p_{\parallel}$, the integrals are singular. A prescription for eliminating the singularity is to add a small imaginary part $i\epsilon$ to ω (References 58, 138, and 139). This amounts to a multiplication of the perturbed fields by factors involving $\exp(\epsilon t)$. The waves are amplified or damped according to the sign of ϵ. If the growth/damping rate ϵ is positive, the plasma is unstable and waves will grow until either the particles' kinetic energy is dissipated in waves or the waves are restrained by some means. The "streaming" instability in the longitudinal mode is well known (Reference 139). Instabilities in the transverse oscillation modes also should be expected to result from relative motions of the particles with finite energies. The differential operator in the integrand of Equation 5-112a is the same as the operator (Equation 5-112b) that appears in the Fokker-Planck equation. When the invariant momentum p_W is chosen as one variable, the integrand of the dispersion integral should contain derivatives only with respect to one variable. The distribution function might be factored in two parts (Reference 140), i.e.,

$$f = g(p_W)\, h(x) \qquad (5\text{-}123)$$

where x represents the remaining coordinate. It is then possible to derive an equilibrium solution for h(x) from the one-dimensional diffusion equation.

The energy source that is needed to sustain growing waves is just the kinetic energy of the faster particles. To obtain growth rates, splitting the particle distribution into two parts is usually advantageous: (1) an isotropic, low-temperature part and (2) a nonthermal part that may comprise only a small fraction η of the total number of particles. Then the dispersion equation can be separated into its real and imaginary parts. The real part is essentially the cold plasma dispersion equation, Equation 5-121a (except that the squares of the plasma frequencies properly should be multiplied by the factions $1 - \eta_e$ and $1 - \eta_i$

of low-temperature electrons and ions, respectively). The imaginary part of the dispersion equation is

$$\epsilon = \frac{W(\omega)}{\omega} \sum_{\substack{\text{ions} + \\ \text{electrons}}} \eta \omega_p^2 \iiint d_p^3 \frac{p_\perp}{2\gamma} \frac{\epsilon}{(\omega \pm \omega_e - kp_{||}/m\gamma)^2 + \epsilon^2}$$

$$\cdot \left[\mp \omega_c \frac{\partial f/n}{\partial p_\perp} + \frac{kp_\perp}{m\gamma} \frac{\partial f/n}{\partial p_{||}} \right] \qquad (5\text{-}124a)$$

$$W(\omega) \equiv \frac{(\omega \pm \omega_i)^2 (\omega \mp \omega_e)^2}{2(\omega \pm \omega_i)^2 (\omega \mp \omega_e)^2 + 2\omega_e \omega_i \Omega_p^2 \pm \omega \omega_e \omega_{pe}^2} . \qquad (5\text{-}124b)$$

When the growth rate ϵ is small, the integrand in Equation 5-124a is very sharply peaked at $p_{||} = (\omega \pm \omega_c) m\gamma/k$. The integration over the parallel momentum component can be reduced to a product of an integral of the form:

$$\int_{-\infty}^{\infty} \frac{dy}{1 + y^2} = \pi \qquad (5\text{-}125)$$

multiplied by the remainder of the integral evaluated at the peak. The growth rate is

$$\epsilon \cong W(\omega) \pi^2 \sum_{\substack{\text{ions} + \\ \text{electrons}}} \eta \omega_p^2 \left\{ \int_0^\infty dp_\perp \frac{kp_\perp^2 \gamma}{|k|(1 + p_\perp^2/m^2c^2 \pm \gamma \omega_c p_{||}/kmc^2)} \right.$$

$$\cdot \left[- p_{||} \frac{\partial f/n}{\partial p_\perp} + p_\perp \frac{\partial f/n}{\partial p_{||}} \right]$$

$$\left. + \int_0^\infty dp_\perp \frac{2m p_\perp^2 \gamma \omega}{|k|(1 + p_\perp^2/m^2c^2 \pm \gamma \omega_c p_{||}/kmc^2)} \frac{f}{n} \right\}_{p = p_R} \qquad (5\text{-}126)$$

The final term has been reduced by a partial integration. The absolute value of k must be used in the denominators. These formulas are relativistically correct if p_R is a solution of the equation:

$$p_R = \frac{\omega}{k}\sqrt{1 + \frac{p_\perp^2}{m^2c^2} + \frac{p_R^2}{m^2c^2}} \pm \frac{qB}{mck} \quad . \tag{5-127}$$

A growth rate in terms of the total momentum p and pitch angle cosine μ may be more convenient. The growth rate of transverse waves is then

$$\epsilon = W(\omega)\pi^2 \sum_{\substack{\text{ions} + \\ \text{electrons}}} \eta\omega_p^2 \int_{p_1}^{\infty} dp \left\{ p^2(1-\mu^2)\frac{k}{\gamma\omega|k|} \cdot \left[1 - \frac{\gamma^2\omega(\omega \pm \omega_c)m^2}{k^2p^2}\right]\frac{\partial f/n}{\partial \mu} - \frac{2mp}{|k|}\left[1 - \frac{\omega(\omega \pm \omega_c)}{k^2c^2}\right]\frac{f}{n}\right\}_{\mu=(\omega\pm\omega_c)m\gamma/kp} \tag{5-128}$$

where p_1 is a solution of the equation:

$$p_1 = \frac{\omega}{k}\sqrt{1 + p_1^2/m^2c^2} \pm \frac{qB}{mck} \quad . \tag{5-129}$$

One should remember when applying these formulas that ω_c is minus ω_e for an electron stream.

A final reduction of the growth rate is of interest for the special case of trapped electrons. A Maxwellian momentum distribution may be assumed with $f \propto \exp(-p^2/p_o^2)$, and the pitch angle distribution may be assumed constant between $-\mu_c$ and $+\mu_c$, at which points the number of nonthermal particles drops to zero. The growth rate is

$$\epsilon \cong -W(\omega)\sqrt{\pi}\, m\eta\omega_{pe}^2 \left\{ \frac{\gamma^4 m^2}{2k^2|k|p_o}\frac{1-\mu_c^2}{\mu_c^5}\left[(1-\mu_c^2)\,\omega \mp \mu_c^2\omega_e\right] \cdot \frac{(\omega \mp \omega_e)^2}{\omega(\omega \mp \gamma^2\omega_e)} + \frac{p_o}{|k|\mu_e}\left[1 - \frac{\omega(\omega\mp\omega_e)}{k^2c^2}\right]\right\} e^{-p^2/p_o^2}\Big|_{p=p_R} \tag{5-130}$$

where p_R is a solution of the equation:

$$\mu_c = \frac{(\omega \pm \omega_c)\, m\gamma}{k\, p_R} \quad . \tag{5-131}$$

The result for trapped protons is similar except that $-\omega_e$ is to be replaced by $+\omega_i$. Other formulations of the growth rate can be found in References 132 and 133.

The second term in the integrand of Equation 5-128 is always negative. In an isotropic medium there is a consequent damping, the Landau damping, of waves (References 139, 141, and 142). The reason for the Landau damping effect is that more particles can absorb energy from a wave than can lose energy to the wave. But, when the particles' momentum, pitch angle distribution is sufficiently anisotropic, the $\partial f/\partial \mu$ term predominates and certain waves can experience a growth in amplitude.

In the trapped radiation belts, where $\partial f/\partial \mu$ is generally negative, growing waves under normal conditions can be excited only in those modes that rotate in the same sense as the trapped particles. Trapped electrons can excite the whistler mode at frequencies below the electron gyro-frequency. The limiting frequency could be found approximately by equating the right side of Equation 5-129 to zero and eliminating k with the aid of the dispersion equation, Equation 5-121. Trapped protons will excite only the ion-cyclotron mode at frequencies below their gyro-frequency. However, a beam of fast particles concentrated primarily along the direction of the field lines would cause unstable growing waves with a polarization opposite to the sense of gyration of the beam particles. An electron beam might excite high-frequency, left-handed waves although the growth rates are rather small—the denominator of $W(\omega)$ can be positive only if $2|\omega|(\omega_e + |\omega|)^2$ is greater than $\omega_e \Omega_p^2$. The amplification of waves by electron streams has been invoked as a source of some of the low-frequency radio noise that apparently originates above the ionosphere (References 144 through 147). Generation of magnetoionic mode waves (right-hand polarization) at frequencies around the proton gyro-frequency presumably would be due to a beam of protons.

That a beam of particles even with no transverse momentum could be unstable to transverse waves might be justified with the aid of Equations 5-107a and 5-107b. When the right-hand sides of these momentum-exchange conditions are negative, which is true of

particles interacting with waves polarized contrary to their gyrorotation, a loss of energy results in an increase in the transverse component of momentum. Therefore, any perturbation that tends to increase the pitch angle results in loss of energy to waves—the beam is unstable. The same argument could be employed to show why a bunch of particles with large pitch angles is unstable to waves that rotate in the same sense as the particles.

5.5.5 Wave Particle Interaction Limits on Particle Trapping

The growth rate of unstable waves can be used to obtain limits on the numbers of particles that can be trapped in outer L-shells (Reference 133). The greatest number of particles that can be trapped is just sufficient to maintain growing waves against absorption in the ionosphere or escape from the trapping region. A group of waves traveling along a field line experiences an amplitude increase by a factor $\exp(\epsilon t_W)$, where t_W is the time the wave spends in the region of interaction. In equilibrium, this is just balanced by the wave losses due to inefficient reflection at the ionosphere; the amplitude loss is just the inverse of the reflection coefficient R_W. The equilibrium condition is

$$\epsilon t_W \approx - \ln R_W \quad . \tag{5-132}$$

The logarithm of $1/R_W$ is an insensitive function of wave parameters. A reasonable value of $\ln R_W$ is probably between 2 and 10 (References 123, 133, and 147). The greatest uncertainty is in the interaction time t_W. An upper limit on t_W is the wave bounce-time. Actually, the varying conditions along the field line ensure that waves and particles fall out of resonance long before they have traversed the length of the field line.

When a group of trapped particles excites waves that can grow appreciably during a single bounce period (that is, $\epsilon t_b > 1$), the waves may be assumed to be deflected enough that most of them are lost immediately. A continually operating source of particles is presumed to replenish the trapped particles. Some limiting kinetic energy is likely above which growing waves are unable to appreciably alter the pitch angles within one or several bounce periods. Loss of electrons above $T \approx 1.6$ MeV does seem to be independent of what happens to lower energy particles (Reference 133). The limiting equatorial omnidirectional flux of electrons above $T \approx 40$ KeV is shown in Figure 5-21 as computed by Kennel and Petschek. The

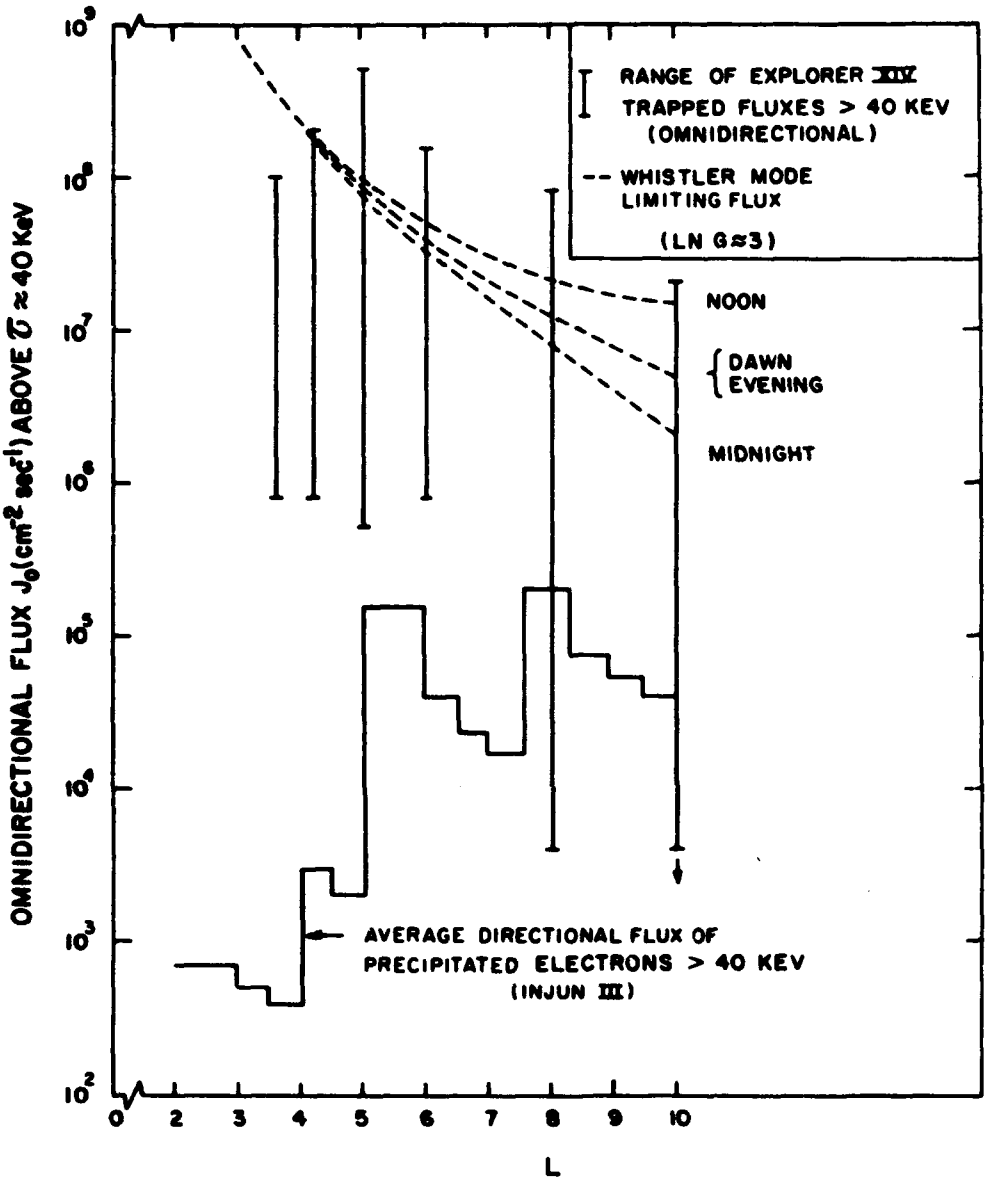

Figure 5-21. Limits on trapping of high-energy electrons (Reference 133).

observed data were obtained from References 108, 148, and 149. An assumed wave reflection coefficient of 0.1 percent was used. Some observed fluxes also are indicated on the figure. Clearly, the largest

observed fluxes approach the trapping limit. On L-shells below about $L \approx 3$ to 4, the numbers of trapped electrons must be determined by other processes.

The "slot" in the trapped electron distribution is a particular feature of the radiation belts that might be due to wave particle interactions. Since the earliest observations, trapped electrons have seemed to be distributed between two belts separated by a distinct gap between $L \approx 3$ and 5. The most plausible explanation yet offered for this slot is that it results from extremely efficient trapping of waves. If the reflection coefficient is near unity, the wave growth rates must be small. This necessitates that the number of densities of trapped particles that would sustain wave growth must be very low.

A suggestion has been made that nearly perfect wave reflection can occur as a wave deviates from propagation strictly parallel to the magnetic field direction (Reference 150). This can occur near the lower hybrid resonant frequency (Reference 124):

$$\omega_{LH} = \sqrt{\frac{(\omega_i^2 + \omega_{pi}^2)\,\omega_i \omega_e}{\omega_i(\omega_i + \omega_e) + \omega_{pi}^2}} \qquad (5\text{-}133)$$

Indeed, in the region of the slot the lower hybrid frequency at low altitudes is of the same order of magnitude as the frequency of the waves that might be excited near the equator by 10-KeV to 1-MeV electrons.

The relevance of unstable wave growth to trapped proton distributions is not so well understood. The pitch angle distribution of intermediate L-shell protons ($L \geq 3.8$) has been found to be consistent with removal by interaction with unstable waves (Reference 140). Some predicted pitch angle distributions are compared in Figure 5-22. The theoretical curves agree quite well with observations except near the equator. The arbitrary parameter U is related to the ratio of proton and Alfvén velocities. The proton flux is a function of L and $\ln R_W/\delta\lambda$ where $\delta\lambda$ is the latitudinal extent of the wave particle interaction region. A best fit to observed distributions is obtained when U is near unity. This is consistent with observed proton energies and Alfvén velocities derived from electron density data. A reflection coefficient near 10 percent brings the theoretical fluxes into close agreement with observed fluxes.

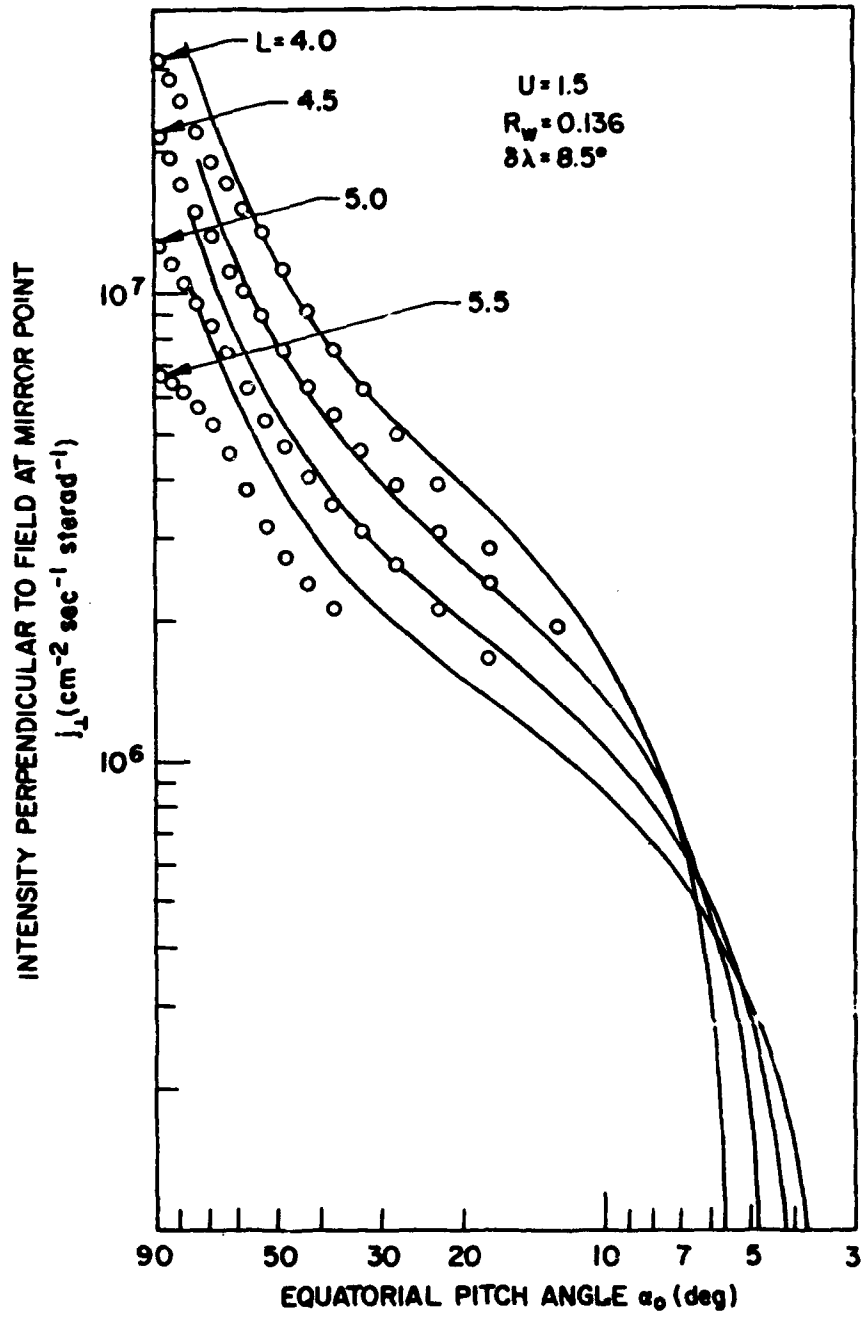

Figure 5-22. Pitch angle distribution of trapped protons predicted according to equilibrium between waves and particles (Reference 140).

RING CURRENT AND THE OUTER RADIATION BELTS. It has recently become apparent that the ring current that operates during periods of geomagnetic disturbance (Reference 151) may have an important relationship to the more stable, trapped particle belts. The ring current is established in a time that may be as short as 1 hour. During this time, protons of energies less than 100 KeV must enter the magnetosphere and be transported as far inward as $L \approx 3$. One mechanism that will accomplish this is Bohm diffusion (References 152 and 153), which is essentially the maximum possible rate. Particles subject to Bohm diffusion are displaced by one gyro-radius within one gyro-period. The rapid alterations in the ring current may be taken as evidence of intense wave turbulence during geomagnetic storms—intense enough that the slow radial diffusion discussed in Section 5.4.4 is no longer valid.

The rapid decay of ring current protons may be due to the rapid increase of plasma density at the edge of the plasmasphere (Reference 153). Inside a region beginning normally at about $L \approx 6$, the total electron density is several orders of magnitude higher than outside. The electron density inside the plasmasphere is apparently sufficient to cause rapid loss of protons through wave growth followed by pitch angle diffusion. During geomagnetic storms, the plasmasphere shrinks and the ring current moves inward simultaneously. The ring current protons are of too low energies to contribute to the stable trapped proton belts, but the formation and decay processes may have relevance to the higher energy particle belts.

5.6 CONVECTION IN THE OUTER MAGNETOSPHERE AS A SOURCE OF TRAPPED PARTICLES

Much of the kinetic energy possessed by trapped particles now appears to have been acquired after their introduction into the magnetosphere. The solar wind is a likely source of charged particles, but solar wind particles have rather low energies, compared with the thousands or millions of electron volt energies of trapped particles. A number of investigators have attempted to explain injection at the outer part of the trapping region through a two-step process: Convection of low-energy plasma down to the trapping region followed by (or concurrent with) in situ acceleration of the charged particles (References 154 through 159).

Most convection theories embody the presumptions that, within the plasmasphere ($L \sim 3$-4), the plasma is constrained effectively to rotate with the earth and that the outer edge of the magnetosphere remains fixed with respect to the sun and solar wind. The basic

convective mechanism has been described in Section 1. One model is sketched in Figure 5-23 (Reference 154). The upper sketch in the figure refers to the situation that would prevail if the plasmasphere were stationary. In the lower sketch, the plasmasphere is rotating with respect to the solar wind orientation and a shear exists throughout the outer magnetosphere. In the upper half of the figure is shown an equatorial plane cross section of the postulated circulation of plasma in the magnetosphere. The solar wind is assumed to drag the plasma back along the outer boundary, thus establishing two closed convection cells. If a shear motion due to the rotation of the inner plasmasphere is introduced, the convection cells are distorted as in the lower half of Figure 5-23. The convective motion brings charged particles down to the trapping region and also results in the establishment of complicated electric fields that can accelerate the particles. Details of this and other convective processes are to be found in the previously cited references.

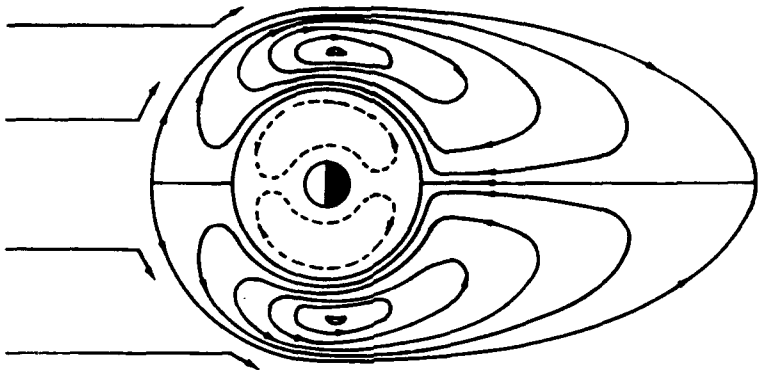

NO ROTATION OF PLASMASPHERE

SUN

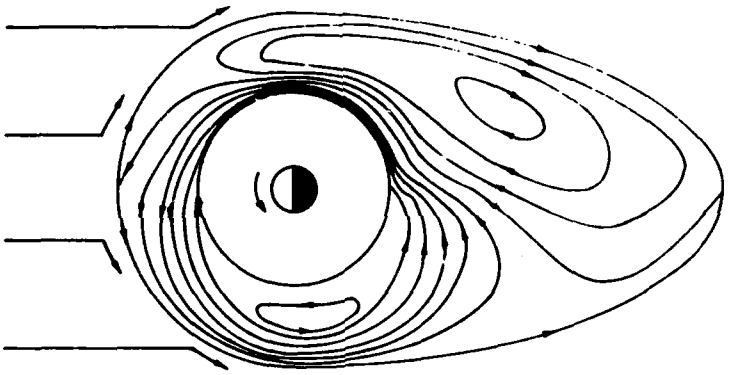

INCLUDING DRAG ON ROTATING PLASMASPHERE

Figure 5-23. Convection in the equatorial plane of the magnetosphere (Reference 154). The upper sketch in the figure refers to the situation that would prevail if the plasma sphere were stationary. In the lower sketch, the plasma sphere is rotating with respect to the solar wind orientation and a shear exists throughout the outer magnetosphere.

REFERENCES

1. W.N. Hess. The Radiation Belt and Magnetosphere, Blaisdell, Waltham, Mass., 1968, 541 pp.

2. H. Bethe. "Quantenmedranik der Ein-und Zwei-Electronenproblem," Hbd. Phys., 2nd ed., ed. by Smekal, Springer, Berlin, 273-560, esp. 515-524, 1933.

3. H. Bethe and J. Askin. "Passage of Radiation Through Matter," Experimental Nuclear Physics, I, ed. by E. Segré, Wiley, New York, 166-357, 1953.

4. R.D. Evans. The Atomic Nucleus, McGraw-Hill, New York, 1955, 567-599.

5. H. Goldstein. Classical Mechanics, Addison Wesley, Cambridge, Mass., 1950, 383 pp, esp. 58-92.

6. C. Møller. Ann. d. Phys., 14, 531, 1932.

7. N.F. Mott and H.S.W. Massey. The Theory of Atomic Collisions, 3rd ed., Oxford, London, New York, 1965, 840 pp.

8. J.L. Delcroix. Introduction à la théorie des gaz ionisés, Dunod, Paris, 1959, trans. Introduction to the Theory of Ionized Gases, Interscience, New York, 1960, 146 pp.

9. B. Kwal. J. Phys. Rad., 12, 805, 1951.

10. W.M. MacDonald and M. Walt. "Distribution Function of Magnetically Confined Electrons in a Scattering Atmosphere," Ann. Phys., 15, 44-62, 1961.

11. A.M. Lenchek and S.F. Singer. "Geomagnetically Trapped Protons from Cosmic-Ray Albedo Neutrons," J. Geophys. Res., 67, 1263-1287, 1962.

12. A.M. Lenchek and S.F. Singer."The Albedo Neutron Theory of Geomagnetically Trapped Protons," Plan. Sp. Sci., 11, 1151-1208, 1963.

13. M.J. Berger and S.M. Seltzer. Tables of Energy Losses and Ranges of Electrons and Protons, NASA, SP-3012, 1964.

14. W.H. Barkas and M.J. Berger. Tables of Energy Losses and Ranges of Heavy Charged Particles, NASA, SP-3013, 1964.

15. W.N. Hess. "Summary of High Energy Nucleon-Nucleon Cross Section Data," Rev. Mod. Phys., 30, 368-401, 1958.

16. W.L. Fite, R.T. Brackman, and W.R. Snow. "Charge Exchange in Proton-Hydrogen Atom Collisions," Phys. Rev., 112, 1161-1169, 1958.

17. D.R. Bates and A. Dalgarno, "Electron Capture 3, Capture into Excited States in Encounters Between Hydrogen Atoms and Fast Protons," Proc. Phys. Soc. Lon., A66, 972, 1953.

18. R.F. Stebbings, W.L. Fite, and D.G. Hummer, "Charge Transfer Between Atomic Hydrogen and N^+ and O^+," J. Chem. Phys., 33, 1226- , 1960.

19. D. Rapp and I.B. Ortenburger. "Interchange of Charge Between Gaseous Molecules," J. Chem. Phys., 33, 1230- , 1960.

20. A.D. Anderson and W.E. Francis. "The Variation of the Neutral Atmospheric Properties With Local Time and Solar Activity from 100 to 10,000 km," J. Atm. Sci., 23, 110-124, 1966.

21. W.B. Hansen, "Structure of the Ionosphere," Satellite Environment Handbook, ed. by F.S. Johnson, Stanford Press, Stanford, Calif., 21-49, 1965.

22. H.C. Brinton, R.A. Pickett, and H.A. Taylor. "Thermal Ion Structure of the Plasmasphere," Plan. Sp. Sci., 16, 899-909, 1968.

23. A. T. Nelms. Energy Loss and Range of Electrons and Protons, NBS, circular 577, 1956.

24. S. Chandrasekhar. "Stochastic Problems in Physics and Astronomy," Rev. Mod. Phys., 15, 1-89, 1943.

25. M. N. Rosenbluth, W. M. MacDonald, and D. L. Judd. "Fokker-Planck Equation for an Inverse-Square Force," Phys. Rev., 107, 1-6, 1957.

26. D. C. Montgomery and D. A. Tidman. Plasma Kinetic Theory, McGraw-Hill, New York, 1964, 286 pp.

27. E. N. Parker. Interplanetary Dynamical Processes, Interscience, New York, 1963.

28. G. Haerendel. "Diffusion Theory of Trapped Particles and the Observed Proton Distribution," Earth's Particles and Fields, ed. by B. M. McCormac, Reinhold, New York, 171-191, 1968.

29. H. B. Phillips. Vector Analysis, Wiley, New York, 1933, 231 pp.

30. S. Chandrasekhar. Principles of Stellar Dynamics, U. Chicago, Chicago, 1942; Dover, New York, 1960, 248 pp.

31. S. Chandrasekhar. "Dynamical Friction I General Considerations: The Coefficient of Dynamical Friction," Ap. J., 97, 255-262, 1943.

32. L. Spitzer. Physics of Fully Ionized Gases, Interscience, New York, 1956, 102 pp.

33. A. Omholt. "Studies on the Excitation of Aurora Borealis 1, The Hydrogen Lines," Geophys. Publ. Geophysica Norvegica, 20, 1, 1958.

34. G. T. Davidson. "Expected Spatial Distribution of Low-Energy Protons Precipitated in the Auroral Zones," J. Geophys. Res. 70, 1061-1068, 1965.

35. M. Walt and W. M. MacDonald. "The Influence of the Earth's Atmosphere on Geomagnetically Trapped Particles," Rev. Geophys., 2, 543-577, 1964.

36. W. M. MacDonald and M. Walt. "Diffusion of Electrons in the Van Allen Belt, 2 Particles with Mirroring Points at Low Altitude," J. Geophys. Res., 67, 1962, 5025-5033.

37. A.M. Lenchek and S. F. Singer. "Effects of the Finite Gyroradii on Geomagnetically Trapped Protons," J. Geophys. Res., 67, 4073-4075, 1963.

38. S. E. Vernov, E. V. Gorchakov, P. I. Shavrin, and K. N. Sharvina. "Radiation Belts in the Region of the South Atlantic Anomaly," Sp. Sci. Rev., 7, 490-533, 1967.

39. H.H. Heckman and G. H. Nakano. "East-West Asymmetry in the Flux of Mirroring Geomagnetically Trapped Protons," J. Geophys. Res., 68, 2117-2120, 1963.

40. M. Walt. "The Effects of Atmospheric Collision on Geomagnetically Trapped Electrons," J. Geophys. Res., 69, 3947-3958, 1964.

41. M. Walt. "Loss Rates of Trapped Electrons by Atmospheric Collisions," Radiation Trapped in the Earth's Magnetic Field, ed. by B. M. McCormac, Reidel, Dordrecht, Holland, 337-351, 1966.

42. L.L. Newkirk and M. Walt. "Radial Diffusion Coefficient for Electrons at Low L-Values," J. Geophys. Res., 73, 1013-1017, 1968.

43. W. N. Hess, J. Killeen, C. Y. Fan, P. Meyer, and J. A. Simpson. "The Observed Outer-Belt Electron Distribution and the Neutron Decay Hypothesis," J. Geophys. Res., 66, 2313-2314, 1961.

44. W. N. Hess and J. Killeen. "Spatial Distribution of Electrons from Neutron Decay in the Outer Radiation Belt," J. Geophys. Res., 66, 3671-3680, 1961.

45. B. Rossi. High Energy Particles, Prentice Hall, New York, 1952, 561 pp.

46. W. N. Hess, E. W. Canfield, and R. E. Lingenfelter. "Cosmic Ray Neutron Demography," J. Geophys. Res., 66, 665-677, 1961.

47. W. F. Libby. Radiocarbon Dating, U. Chicago, Chicago, 1952.

48. L. L. Newkirk. "Calculation of the Low-Energy Neutron Flux in the Atmosphere by the S_n Method," J. Geophys. Res., 68, 1825-1833, 1963.

49. R. E. Haymes. "Fast Neutron in the Earth's Atmosphere, 1. Variation With Depth," J. Geophys. Res., 69, 841-852, 1964.

50. R. E. Haymes. "Fast Neutrons in the Earth's Atmosphere, 2. Time Variation at High Altitudes," J. Geophys. Res., 69, 853-859, 1964.

51. R. E. Lingenfelter. "The Cosmic Ray Neutron Leakage Flux," J. Geophys. Res., 68, 5633-5640, 1963.

52. R. E. Lingenfelter and E. J. Flamm. "Neutron Leakage Flux from Interactions of Solar Protons in the Atmosphere," J. Geophys. Res., 69, 2199-2207, 1964.

53. S. Chandrasekhar. Radiative Transfer, Dover, New York, 1960, 385 pp, esp. 54-69.

54. E. H. Bareiss. "A Survey and Classification of Transport Theory Calculation Techniques," Second UN Int. Con. Peaceful Uses of At. Energy, 1958.

55. B. G. Carlson. "The Numerical Theory of Neutron Transport," Methods in Computational Physics, I, ed. by B. Adler, S. Fernbach, and M. Rothenberg, Academic Press, New York, 1-42, 1963.

56. B. G. Carlson and G. I. Bell. "Solution of the Transport Method," Second UN Conf. on Peaceful Uses of At. Energy, 1958.

57. M. Walt and W. M. MacDonald. "Energy Spectrum of Electrons Trapped in the Geomagnetic Field," J. Geophys. Res., 66, 2047-2052, 1961.

58. S. Chandrasekhar. Plasma Physics, U. of Chicago, Chicago, 1960, 214 pp.

59. T. G. Cowling. Magnetohydrodynamics, Interscience, New York, 1957, 112 pp.

60. R. F. Post. "Some Observations on Plasma Instabilities in the Mirror Machine," Plasma Hydromagnetics, ed. by D. Bershader, Stanford U., Stanford, Calif., 1-39, 1962.

61. N. Rostoker. "Plasma Stability," Plasma Physics in Theory and Application, ed. by W. B. Kunkel, McGraw-Hill, New York, 120-146, 1966.

62. K. M. Watson. Stability of Trapped Electron Belts, Aerospace Corp., TR-1001, S2855-40-1; Air Force, BSD-TR-328, 1966, 28 pp.

63. J. G. Linhart. Plasma Physics, North Holland, Amsterdam, 1961, 214 pp.

64. T. G. Northrop and E. Teller. "Stability of the Adiabatic Motion of Charged Particles in the Earth's Field," Phys. Res., 117, 215-225, 1960.

65. T. G. Northrop. The Adiabatic Motion of Charged Particles, Interscience, New York, 1963, 105 pp.

66. J. B. Taylor. "Equilibrium and Stability of Plasma in Arbitrary Mirror Fields," Phys. Fluids, 7, 767-773, 1964.

67. J. W. Dungey. "Effects of Electromagnetic Perturbations on Particles Trapped in the Radiation Belt," Sp. Sci. Rev., 4, 199-222, 1964.

68. J. W. Dungey, W. N. Hess, and M. P. Nakada. "Theoretical Studies of Protons in the Outer Radiation Belt," Sp. Res., 5, 399-403, 1965.

69. J. B. Cladis, G. T. Davidson, W. E. Francis, L. L. Newkirk, L. R. Tepley, M. Walt, and R. C. Wentworth. Search for Possible Loss Processes for Geomagnetically Trapped Particles, Lockheed M.S.C., M-57-65-1, DASA 1713, 1965, 128 pp.

70. M. P. Nakada, J. W. Dungey, and W. N. Hess. "On the Origin of Outer-Belt Protons 1," J. Geophys. Res., 70, 3529-3532, 1965.

71. D. B. Chang, L. D. Pearlstein, and M. N. Rosenbluth. "On the Interchange Stability of the Van Allen Belt," J. Geophys. Res., 70, 3085-3097, 1965.

72. E. N. Parker. "Geomagnetic Fluctuations and the Form of the Outer Zone of the Van Allen Radiation Belt," J. Geophys. Res., 65, 3117-3130, 1960.

73. L. Davis, Jr., and D. B. Chang. "On the Effect of Geomagnetic Fluctuations on Trapped Particles," J. Geophys. Res., 2169-2179, 1962.

74. B. A. Tverskoy. "Dynamics of the Radiation Belts of the Earth, 2.," Geomag. Aeron., 3, 351-366, 1964.

75. M. P. Nakada and G. D. Mead. "Diffusion of Protons in the Outer Radiation Belt," J. Geophys. Res., 70, 4777-4791, 1965.

76. W. L. Imhof, J. B. Cladis, and R. V. Smith. "Observation of an Energy-Selective Redistribution in the Inner Radiation Belt," Plan. Sp. Sci., 14, 569-577, 1966.

77. G. L. Pai and V. A. Sarabhai. "Periodic Fluctuations in the Geomagnetic Field During Magnetic Storms," Plan. Sp. Sci., 12, 855-865, 1964.

78. A. Nishida. "Geomagnetic DP2 Fluctuations and Associated Magnetospheric Phenomena," J. Geophys. Res., 73, 1795-1803, 1968.

79. T. Obayashi and A. Nishida. "Large-Scale Electric Field in the Magnetosphere," Sp. Sci. Rev., 8, 3-31, 1968.

80. R. L. Kauffmann. "Conservation of First and Second Adiabatic Invariants," J. Geophys. Res., 70, 2181-2186, 1965.

81. C.-G. Fälthammar. "Effects of Time Dependent Electric Fields on Geomagnetically Trapped Radiation," J. Geophys. Res., 70, 2503-2516, 1965.

82. J. G. Roederer. "Shell Splitting and Radial Diffusion of Geomagnetically Trapped Particles," Earth's Particles and Fields, ed. by B. M. McCormac, Reinhold, New York, 193-208, 1968.

83. G. Haerendel. "On the Violation of the Second and Third Adiabatic Invariants," J. Geophys. Res., 71, 1857-1868, 1966.

84. T.J. Birmingham, T.G. Northrop, and C.-G. Fälthammar. "Charged Particle Diffusion by Violation of the Third Adiabatic Invariant," Phys. Fluids, 10, 2389-2398, 1967.

85. A.T. Nelms. Energy Loss and Range of Electrons and Protons, NBS, circular 577, 1956.

86. J.W. Dungey. "Effects of Electromagnetic Perturbations on Particles Trapped in the Radiation Belts," Sp. Sci. Rev., 4, 199-222, 1965.

87. C.-G. Fälthammar. "On the Transport of Trapped Particles in the Outer Magnetosphere," J. Geophys. Res., 71, 1487-1491, 1966.

88. C.-G. Fälthammar. "Coefficients of Diffusion in the Outer Radiation Belt," Radiation Trapped in the Earth's Magnetic Field, ed. by B.M. McCormac, Reidel, Dordrecht, Holland, 398-402, 1966.

89. C.-G. Fälthammar. "Radial Diffusion by Violation of the Third Adiabatic Invariant," Earth's Particles and Fields, ed. by B.M. McCormac, Reinhold, New York, 157-169, 1968.

90. Al Ershkovich, G.A. Skuridin, L.S. Chesalin, and V.P. Shalimov. "Transport of Charged Particles in a Dipole Magnetic Field under the Influence of Electromagnetic Impulses," Kosm. Issled., 5, 792-795, 1967, trans: Cos. Res., 5, 673-675, 1967.

91. B.J. Conrath. "Radial Diffusion of Trapped Particles With Arbitrary Pitch Angle," J. Geophys. Res., 72, 6069-6076, 1968.

92. A. Nishida and L.J. Cahill, Jr. "Sudden Impulses in the Magnetosphere Observed by Explorer 12," J. Geophys. Res., 69, 2243-2255, 1964.

93. G. Haerendel and R. Lüst. "Electric Fields in the Upper Atmosphere," Earth's Particles and Fields, ed. by B.M. McCormac, Reinhold, New York, 271-285, 1968.

94. G. Haerendel, R. Lüst, and E. Reiger. "Motion of Artificial Ion Clouds in the Upper Atmosphere," Pl. Sp. Sci., 15, 1-18, 1967.

95. W. L. Imhof, J. B. Reagan, and R. V. Smith. "Long Term Study of Electrons Trapped on Low L-Shells," J. Geophys. Res., 72, 2371-2377, 1967.

96. C. E. McIlwain. "The Radiation Belts, Natural and Artificial," Science 142, 355- , 1963.

97. C. O. Bostrom and D. J. Williams. "Time Decay of the Artificial Radiation Belt," J. Geophys. Res., 70, 240-242, 1965.

98. J. A. Van Allen. "Lifetimes of Geomagnetically Trapped Electrons of Several MeV Energy," Nature 203, 1006- , 1964.

99. W. L. Imhof and R. V. Smith. "Longitudinal Variations of High Energy Electrons at Low Altitudes, J. Geophys. Res., 70, 569-577, 1965.

100. A. D. Bolyunova, O. L. Vaisberg. Yu. Galpernin, B. P. Polapov, V. V. Temny, and F. K. Shuyskaya. "Investigations of Corpuscles on the Electron-1 and Electron-2 Satellites," Space Research, North Holland, Amsterdam, 649-661, 1966.

101. D. S. Beall, C. O. Bostrom, and D. J. Williams. "Structure and Decay of the Starfish Radiation Belt, October 1963 to December 1965," J. Geophys. Res., 72, 3403-3427, 1967.

102. J. R. Burrows and I. B. McDiarmid. "A Study of Beta Decay Electrons Injected into the Geomagnetic Field in October 1962," Can. J. Phys., 42, 1529-1547, 1964.

103. D. J. Williams and A. M. Smith. "Daytime Trapped Electron Intensities at High Latitudes at 1100 Kilometers," J. Geophys. Res., 70, 541-556, 1965.

104. D. J. Williams, J. F. Arens, and L. J. Lanzerotti. "Observation of Trapped Electrons at Low and High Altitudes," J. Geophys. Res., 73, 5673-5696, 1968.

105. C. S. Roberts. "Cyclotron-Resonance and Bounce-Resonance Scattering of Electrons Trapped in the Earth's Magnetic Field," Earth's Particles and Fields, ed. by B. M. McCormac, Reinhold, New York, 317-336, 1968.

106. W. L. Brown. "Observations of the Transcient Behavior of Electrons in the Artificial Radiation Belts," Radiation Trapped in the Earth's Magnetic Field, ed. by B.M. McCormac, Reidel, Dordrecht, Holland, 610-633, 1966.

107. L. L. Newkirk and M. Walt. "Radial Diffusion Coefficient for Electrons at 1.76 < L < 5," J. Geophys. Res., 73, 7231-7236,

108. L. A. Frank, J. A. Van Allen, and H. K. Hills. "A Study of Charged Particles in the Earth's Outer Radiation Zone with Explorer 14," J. Geophys. Res., 69, 2171-2191, 1964.

109. L. A. Frank. "Inward Radial Diffusion of Electrons Greater than 1.6 Million Electron Volts in the Outer Radiation Zone, J. Geophys. Res., 70, 3533-3540, 1965.

110. M. Walt. "Radial Diffusion of Trapped Particles," Particles and Fields in the Magnetosphere, ed. by B.M. McCormac, D. Reidel, Dordrecht, Holland, 410-415, 1970.

111. L. D. Kavanaugh, Jr. "An Empirical Evaluation of Radial Diffusion Coefficients for Electrons of 50-100 keV Form L = 4 to L = 7," J. Geophys. Res., 73, 2959-2965, 1968.

112. T. J. Birmingham. "Convection Electric Fields and the Diffusion of Trapped Magnetospheric Radiation," J. Geophys. Res., 74, 2169-2181, 1969.

113. T. A. Farley. "Radial Diffusion of Starfish Electrons," J. Geophys. Res., 74, 3591-3600, 1969.

114. J. G. Roederer. "Experimental Evidence on Radial Diffusion of Geomagnetically Trapped Particles," Earth's Particles and Fields, ed. by B.M. McCormac, Reinhold, New York, 143-155, 1968.

115. F. Söraas. Comparison of Post Storm Non-Adiabatic Recovery of Trapped Protons With Radial Diffusion, Goddard Space Flight Center, Z-612-69-241, 1969.

116. T. A. Farley, A. D. Tomassian, and M. Walt. "The Source of High Energy Protons in the Van Allen Radiation Belt," to be published (1970).

117. C.Y. Fan, P. Meyer, and J.A. Simpson. "Dynamics and Structure of the Outer Radiation Belt," J. Geophys. Res., 66, 2607-2640, 1961.

118. P. Morrison. "The Origin of Cosmic Rays," Hdb. d. Phys., 45/1, ed. by S. Flügge, Springer, Berlin. 1-87, esp. 24-30, 1961.

119. E.N. Parker. "Effect of Hydromagnetic Waves in a Dipole Field on the Longitudinal Invariant," J. Geophys. Res., 66, 693-708, 1961.

120. C.S. Roberts and M. Schulz. "Bounce Resonant Scattering of Particles Trapped in the Earth's Magnetic Field," J. Geophys. Res., 73, 7361-7376, 1968.

121. S.O. Rice. "Mathematical Analysis of Random Noise," Bell System Tech. J., 23, 24; Selected Papers on Noise and Stochastic Processes, ed. by N. Wax, Dover, New York, 130-294, 1954.

122. A.J. Dessler, W.E. Francis, and E.N. Parker. "Geomagnetic Storm Sudden-Commencement Rise Times," J. Geophys. Res., 65, 2715-2719, 1960.

123. W.E. Francis and R. Karplus. "Hydromagnetic Waves in the Ionosphere," J. Geophys. Res., 65, 3593-3600, 1960.

124. D.G. Wentzel. "Hydromagnetic Waves and the Trapped Radiation, 1. Breakdown of the Adiabatic Invariance," J. Geophys. Res., 66, 359-363, 1961.

125. D.G. Wentzel. "Hydromagnetic Waves and the Trapped Radiation, 2. Displacement of the Mirror Points," J. Geophys. Res., 66, 1641-1649, 1961.

126. A.J. Dragt. "Effect of Hydromagnetic Waves on the Lifetime of Van Allen Radiation Protons," J. Geophys. Res., 66, 1641-1649, 1961.

127. R.E. Holzer, M.G. McLeod, and E.J. Smith. "Preliminary Results from the OGO 1 Search Coil Magnetometer, Boundary Positions and Magnetic Power Spectra," J. Geophys. Res., 71, 1481-1486, 1966.

128. J. F. Denisse and J. L. Delcroix. Theorie des Ondes dans les Plasmas, Dunod, Paris, 1961, trans: Plasma Waves, Interscience, New York, 1963, 140 pp.

129. N. M. Brice. "Fundamentals of Very Low Frequency Emission Generation Mechanisms," J. Geophys. Res., 69, 1251-1258, 1964.

130. J. W. Dungey. "Loss of Van Allen Electrons Due to Whistlers," Plan. Sp. Sci., 11, 591-596, 1963.

131. J. W. Dungey. "Resonant Effect of Plasma Waves on Charged Particles in a Magnetic Field," J. Fluid Mech., 15, 74-82, 1963.

132. J. M. Cornwall. "Scattering of Energetic Trapped Electrons by Very-Low-Frequency Waves," J. Geophys. Res., 69, 1251-1258, 1964.

133. C. F. Kennel and H. E. Petschek. "Limit on Stably Trapped Particle Fluxes," J. Geophys. Res., 71, 1-28, 1966.

134. R. Gendrin. "Pitch Angle Diffusion of Low Energy Protons Due to Gyroresonant Interaction With Hydromagnetic Waves," J. Atm. Terr. Phys., 30, 1313-1330, 1968.

135. P. A. Sturrock. "Stochastic Acceleration," Phys. Rev., 141, 186-191, 1966.

136. D. E. Hall and P. A. Sturrock. "Diffusion, Scattering, and Acceleration of Particles by Stochastic Electromagnetic Fields," Phys. Fluids, 10, 2620-2628, 1967.

137. D. B. Chang and L. D. Pearlstein. "On the Effect of Resonant Magnetic Moment Violation on Trapped Particles," J. Geophys. Res., 70, 3075-3083, 1965.

138. T. F. Bell and O. Buneman. "Plasma Instability in the Whistler Mode Caused by a Gyrating Electron Stream," Phys. Rev., A 133, 25-26, 1964.

139. T. H. Stix. The Theory of Plasma Waves, McGraw-Hill, New York, 1962, 268 pp.

140. G. Haerendel. "On the Balance Between Radial and Pitch Angle Diffusion," Particles and Fields in the Magnetosphere, ed. by B.M. McCormac, D. Reidel, Dordrecht, Holland, 416-428, 1970.

141. D.A. Tidman and R.K. Jaggi. "Landau Damping of Transverse Waves in the Exosphere by Fast Particle Fluxes," J. Geophys. Res., 67, 2215-2221, 1962.

142. F.E. Scarf. "Landau Damping and the Attenuation of Whistlers," Phys. Fluids, 5, 6-13, 1962.

143. R.L. Dowden. "Doppler Shifted Cyclotron Generation of Exospheric Very-Low-Frequency Noise ('hiss')," Plan. Sp. Sci., 11, 361-369, 1963.

144. N.M. Brice. "An Explanation of Triggered VLF Emissions," J. Geophys. Res., 68, 4626-4628, 1963.

145. K. Maeda and I. Kimura. "Origin and Mechanism of VLF Emissions," Space Res., 3, 310-323, 1963.

146. D.B. Chang. "Amplified Whistlers as the Source of Jupiter's Sporadic Decameter Radiation," Astrophys. J., 138, 1231-1241, 1963.

147. J.A. Jacobs and T. Watanabe. "Amplification of Hydromagnetic Waves in the Magnetosphere by a Cyclotron Instability Process With Applications to the Theory of Hydromagnetic Whistlers," J. Atm. Terr. Phys., 28, 235-253, 1966.

148. L.A. Frank. "A Survey of Electrons E 40 KeV Beyond 5 Earth Radii With Explorer 14," J. Geophys. Res., 70, 1593-1626, 1965.

149. B.J. O'Brien. "High Latitude Geophysical Studies With Satellite Injun 3, 3. Precipitation of Electrons into the Atmosphere," J. Geophys. Res., 69, 13-44, 1964.

150. C.T. Russell and R.M. Thorne. "On the Structure of the Inner Magnetosphere," to be published (1969).

151. S. I. Akasofu and C. I. Meng. "A Study in Polar Magnetic Storms," J. Geophys. Res., 74, 293-313, 1969.

152. J. M. Cornwall. "Diffusion Processes Influenced by Conjugate Point Wave Phenomena," Radio Sci., 3, 740- , 1968.

153. J. M. Cornwall, F. V. Coroniti, and R. M. Thorne. "Turbulent Loss of Ring Current Protons, to be published (1970)

154. W. I. Axford and C. O. Hines. "A Unifying Theory of High-Latitude Geophysical Phenomena and Geomagnetic Storms, Can. J. Phys., 39, 1433-1464, 1961.

155. W. I. Axford, H. E. Petschek, and G. L. Siscoe. "Tail of the Magnetosphere," J. Geophys. Res., 70, 1231-1236, 1965.

156. W. I. Axford. "Some Aspects of the Structure and Dynamics of the Terrestrial Magnetosphere," Natural and Electromagnetic Phenomena Below 30 kc/s., ed. by D. F. Bleil, Plenum Press, New York, 5-32, 1964.

157. J. W. Dungey. "The Reconnection Model of the Magnetosphere," Earth's Particles and Fields, ed. by B. M. McCormac, Reinhold, New York, 385-392, 1968.

158. H. E. Taylor and E. W. Hones. "Adiabatic Motion of Auroral Particles in a Model of the Electric and Magnetic Fields Surrounding the Earth," J. Geophys. Res., 70, 3605-3628, 1965.

159. J. H. Piddington. "The Magnetospheric Radiation Belt and Tail Plasma Sheet," Pl. Sp. Sci., 16, 703-716, 1968.

SECTION 6

HISTORY OF ARTIFICIAL RADIATION BELTS

M. Walt, Lockheed Palo Alto Research Laboratory

6.1 INTRODUCTION

A number of artificial radiation belts have been created by high-altitude nuclear detonations. In these events, some of the radioactive fission fragments from the bomb reached altitudes high enough that the beta decay electrons were injected into trapped orbits. A list of these events is given in Table 6-1 along with unclassified values* of the pertinent characteristics of each of the belts. The decay times are the approximate times for the flux to decrease by a factor of 1/e and are estimated for the longest lived portion of each of the artificial belts. Detailed descriptions of the events are given in following sections, along with references to the original reports.

Teak and Orange were low-latitude detonations occurring at altitudes of 77 and 43 kilometers, respectively. Few trapped electrons were injected by these two bursts. Furthermore, the burst locations were in the Pacific Ocean where the surface magnetic field is relatively high—this longitude effect contributed to the low-injection efficiency. On the other hand, the three Argus tests were designed primarily to test the geomagnetic trapping theory. Therefore, to maximize the injection efficiency, the detonations were made at an altitude as high as practical and in a region of low-magnetic field over the Atlantic Ocean. Starfish, a low-latitude, high-altitude burst in the Pacific, was not implemented with trapping in mind; thus, the intensity and persistency of the radiation belt was a surprise. The long lifetime of electrons from Starfish was unexpected, considering the rapid decay of the Argus tests at $L \approx 2$. The three Russian tests in 1962 led to significant trapping, but, because the injection was at $L > 1.7$, the fluxes decayed more rapidly than at the center of the Starfish belt.

*Throughout this report, the values for detonation, altitude, yield and time have been taken from unclassified sources and do not represent official DNA figures.

Table 6-1. High-altitude nuclear detonations.

Event	Altitude (km)	Time (U.T.)	Date	Latitude	Longitude	Approximate L-Value of Detonation	Yield	Characteristics of Band	Approximate Decay Time
Teak	76.8	10:50:05	1 Aug 1958	17°N	169°W	1.12	MT Range	Low Altitude	~few days
Orange	42.97	10:30:08	12 Aug 1958	17°N	169°W	1.12	MT Range	Low Altitude	~1 day
Argus 1	~200	2:30:00	27 Aug 1958	38°S	12°W	1.7	1-2 KT	Narrow Band	0-20 days
Argus 2	~250	3:20:00	30 Aug 1958	50°S	8°W	2.1	1-2 KT	Narrow Band	10-20 days
Argus 3	~500	22:10:00	6 Sept 1958	50°S	10°W	2.0	1-2 KT	Narrow Band	10-20 days
Starfish	400	09:00:029	9 July 1962	16.7°N	190.5°E	1.12	1.4 MT	Wide Distribution	1-2 years
USSR 1	—	03:40:46	22 Oct 1962	—	—	~1.8	—	Wide Distribution	~30 days
USSR 2	—	04:41:18	28 Oct 1962	—	—	~1.8	—	Wide Distribution	~30 days
USSR 3	—	09:13:	1 Nov 1962	—	—	1.75	—	Narrow Band	~30 days

In discussing the trapped electrons resulting from a nuclear detonation, three categories of the electron flux should be distinguished:

1. Untrapped electrons that make one pass through the equatorial plane and are absorbed in the atmosphere at the conjugate point.

2. Transiently trapped electrons that initially mirror above the atmosphere in both northern and southern hemispheres but that intersect the dense atmosphere during their eastward drift (these electrons do not execute a complete drift around the earth).

3. Long-term trapped electrons whose initial orbits place their mirror points above the atmosphere at all longitudes.

In general, the most intense fluxes of trapped electrons occurring after a nuclear detonation are those of the first category. A satellite located on the field line of the explosion will be subjected to these intense fluxes. However, the diameter of the initial "beta tube" is generally between 100 to 1,000 kilometers. The passage of a given satellite through this region is unlikely during the short time period of the most intense fluxes. The beta-tube fluxes persist as long as fission fragments are high enough (~50 kilometers) that the upward-directed electrons leave the atmosphere, but the intensity will decay approximately as $t^{-1.2}$.

In the remainder of this section, attention will be directed to the long-term trapping phenomena observed following high-altitude nuclear explosions.

6.2 TEAK AND ORANGE*

6.2.1 Introduction

Evidence of trapped particle enhancement (Reference 1) resulting from Teak and Orange has not received wide attention partly because

*Sections 6.2.1, 6.2.2, 6.2.3, 6.2.4, 6.3.1, and 6.3.2 were contributed by the group at St. Louis University. We are grateful to Drs. A. H. Weber, D. J. Manson, J. F. Fennell, J. A. George, J. L. Hickerson, R. T. Hoverter, and G. V. Maldonado for carrying out the work described here.

the report was declassified only recently and partly because of the theoretical improbability of substantial trapping from detonations at such low altitudes. Coordinates available from the open literature for the two events are summarized in Table 6-1.

A careful reexamination of Explorer 4 data acquired at Lima (12.0°S, 77.1°W), Johnston Island (16.7°N, 169.5°W), Singapore (1.2°N, 256.8°W), and Johannesburg (25.9°S, 332.3°W) tracking stations indicates that Teak produced a shell of trapped electrons (the unidirectional scintillation counter, Channel 2, indicated count-rate modulation above natural background at twice the tumble frequency) lasting several days and centered at $L \approx 1.2$.

Visual, geomagnetic, and electrical effects of Teak and Orange are discussed in Reference 2. Radar backscatter observations have been quoted indicating that, 5 hours after Teak, the debris cloud of fission products was centered some 600 kilometers west-northwest of Johnston Island and that it had dimensions of several hundred kilometers, at an altitude between 100 and 200 kilometers (Reference 1). At 200 kilometers, the L-shells in the region of the observed enhancement ($L = 1.1$ to 1.2) would have intersected the debris cloud at a magnetic field value B of approximately 0.32 gauss.

Data from Teak are presented in Figures 6-1, 6-2, and 6-3 as true counts per second, corrected only for counter deadtimes. A description of Explorer 4 instrumentation and references to calibration information are presented in the discussion of the Argus events (Section 6.3.2). All data available for these two events from the tracking stations specified—Channels 1($E > 5$ MeV), 2($E > 580$ KeV), and 3($E > 3$ MeV) (Reference 3)—were searched for enhancement or lack of enhancement in the region $L = 1.1$ to 1.3, and all results are summarized in Tables 6-2 and 6-3. A brief inspection of the data presented will indicate the data's fragmentary nature and the hazards of attempting conclusions. Enhancement from the Orange event was not sufficient to warrant separate study and is presented in Table 6-3 only for the sake of augmenting the understanding of Teak.

6.2.2 Presentation of Data

Three examples of the Teak intercepts are presented in Figures 6-1 to 6-3, which show the enhanced fluxes at 0.3, 24.0, and 48.0 hours after the detonation. The numbered data points (numerals are centered on points) refer to the three channels noted previously;

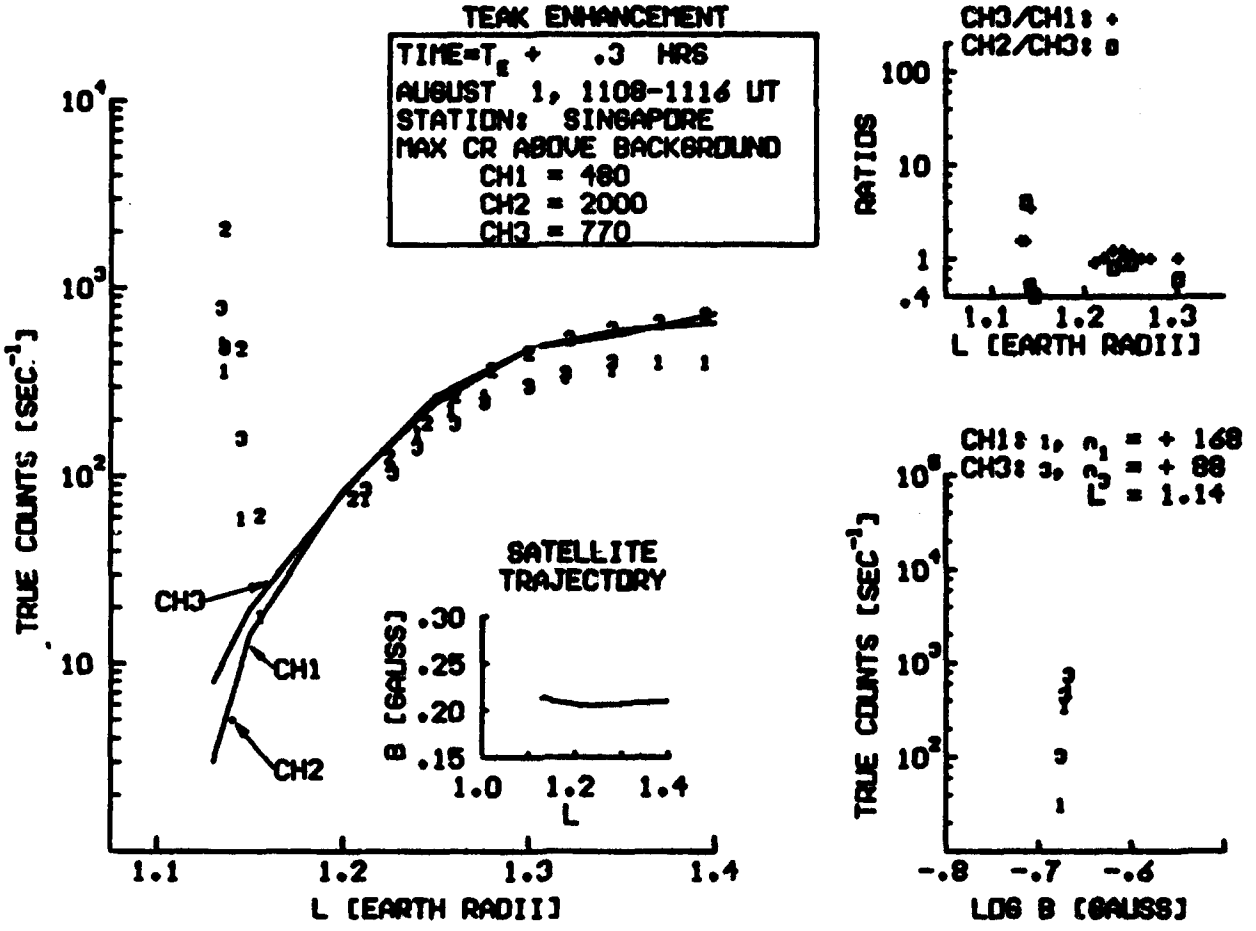

Figure 6-1. Time sequence of measurements of (1) true counts versus L, (2) count rate ratios versus L, and (3) true counts versus log B for the Teak enhancement 0.3 hours after the detonation. Numerals centered on data points refer to measurements by channels 1, 2, and 3 counters, respectively. Solid lines or dots represent measured pre-Teak background for the same B and L positions.

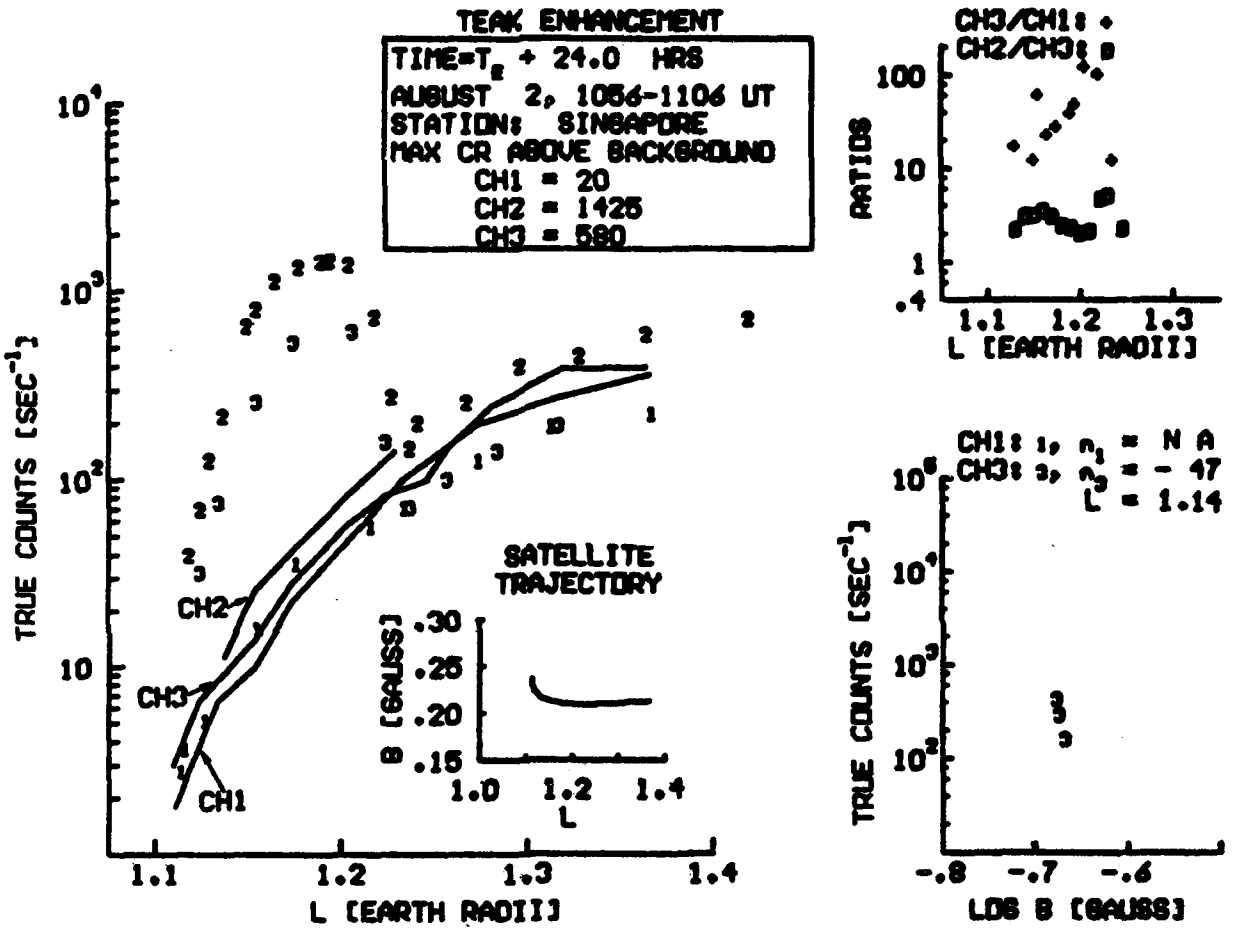

Figure 6-2. Time sequence of measurements of (1) true counts versus L, (2) count rate ratios versus L, and (3) true counts versus log B for the Teak enhancement 24 hours after the detonation. Numerals centered on data points refer to measurements by channels 1, 2, and 3 counters, respectively. Solid lines or dots represent pre-Teak background for the same B and L positions.

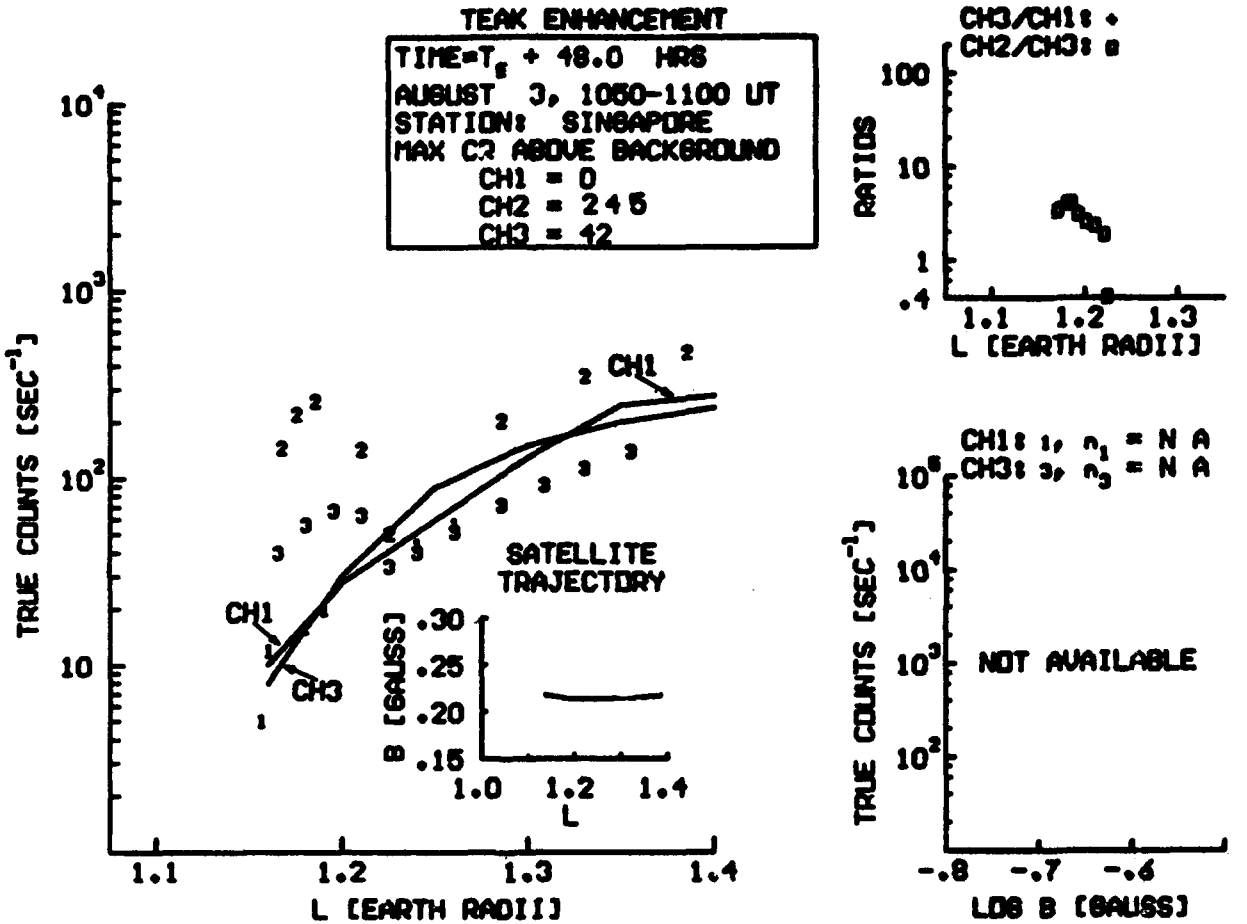

Figure 6-3. Time sequence of measurements of (1) true counts versus L, (2) count rate ratios versus L, and (3) true counts versus log B for the Teak enhancement 48 hours after the detonation. Numerals centered on data points refer to measurements by channels 1, 2, and 3 counters, respectively. Solid lines or dots represent pre-Teak background for the same B and L positions.

Table 6-2. Summary of Teak data at times after the event time T_E.

T_E +	Station	L (earth radii)	L (gauss)	Max. Trans Count-Rate CH 1 Above Background (sec^{-1})	Max. Trans Count-Rate CH 2 Above Background (sec^{-1})	Max. Trans Count-Rate CH 3 Above Background (sec^{-1})	Ratio CH 1/CH 2 Average	Ratio CH 2/CH 3 Average	Flux Density E>.5 MeV CH 1 Above Background ($cm^{-2}sec^{-1}$)	Flux Density E>.5Mh MeV CH 2 Above Background ($cm^{-2}sec^{-1}$)	Flux Density E>.5 MeV CH 3 Above Background ($cm^{-2}sec^{-1}$)
.3 hrs	Singapore	1.165 1.155	.2100 .2240	480	1960	770	1.3	1.1	795	4.9×10^6	1283
6.9 hrs	Johnston Island	1.175 1.180	.2495 .2512	300	3650	4400	11.7	2.0	498	1.42×10^5	6666
8.9 hrs	Johnston Island	1.170 1.250	.2280 .2280	38	NA	40	1.5	NA	53	---	67
18.7 hrs	Johnston Island	1.185 1.215	.1795 .1858	NA	8400	2800	NA	1.9	---	1.11×10^5	4666
22.3 hrs	Singapore	1.130 1.200	.2050 .2171	30	NA	1200	32.1	NA	50	---	1833
23.3 hrs	Lima	1.195 1.220	.2753 .1959	NA	NA	2300	NA	2.1	---	---	3833
24.8 hrs	Singapore	1.130 1.225	.2020 .2150	20	1040	580	77	2.9	33	3.53×10^6	966
29.3 hrs	Johannesburg	1.200 1.210	.1772 .1923	NA	NA	1000	NA	NA	---	---	1666
30.5 hrs	Johnston Island	1.180 1.200	.2030 .2305	18	NA	200	7.3	NA	30	---	333
47.0 hrs	Lima	1.200 1.215	.2753 .1959	0	4040	1500	NA	NA	0	1.06×10^5	2500
48.0 hrs	Singapore	1.165 1.220	.2130 .2230	0	265	92	NA	3.0	0	6.25×10^3	70
53.3 hrs	Johannesburg	1.130 1.220	.1697 .1885	NA	NA	900	NA	NA	---	---	1500
54.6 hrs	Johnston Island	1.185 1.270	.2030 .2700	4.5	NA	85	5.2	NA	7.5	---	91.6
64.3 hrs	Johnston Island	1.150 1.210	.1702 .1915	NA	NA	1100	NA	NA	---	---	1833
80.1 hrs	Johnston Island	1.185 1.215	.1800 .2150	0	NA	800	NA	NA	0	---	1333
112.1 hrs	Johnston Island	1.150 1.205	.1800 .2150	0	NA	300	NA	NA	0	---	480

Table 6-3. Summary of Orange data at times after the event time T_E.

T_E +	Station	L (earth radii)	B (gauss)	Max. True Count-Rate CH 1 Above Background (sec^{-1})	Max. True Count-Rate CH 2 Above Background (sec^{-1})	Max. True Count-Rate CH 3 Above Background (sec^{-1})	Ratio CH 3/CH 1 Average	Ratio CH 2/CH 3 Average	Flux Density E_p>5 MeV CH 1 Above Background ($cm^{-2}sec^{-1}$)	Flux Density E_p>500 KeV CH 2 Above Background ($cm^{-2}sec^{-1}$)	Flux Density E_p>3 MeV CH 3 Above Background ($cm^{-2}sec^{-1}$)
3.9 hrs	Johannesburg	1.14 ↑ 1.38	.1827 ↓ .2089	0	NA	0	NA	NA	0	NA	0
8.6 hrs	Singapore	1.08 ↑ 1.62	.2350 ↓ .2550	0	NA	0	NA	NA	0	NA	0
10.5 hrs	Singapore	1.07 ↑ 1.20	.2220 ↓ .3000	0	0	0	NA	NA	0	0	0
15 hrs	Johnston Island	1.11 ↑ 1.20	.2180 ↓ .2850	20	180	86	4.3	1.8	33.2	4.5×10^3	143
16 hrs	Johannesburg	1.17 ↑ 1.25	.1683 ↓ .1943	0	0	0	NA	NA	0	0	0
20.4 hrs	Singapore	1.05 ↑ 1.15	.2621 ↓ .2710	4	NA	NA	NA	NA	6.6	NA	NA
27.8 hrs	Johannesburg	1.14 ↑ 1.22	.1927 ↓ .2090	0	0	0	NA	NA	0	0	0
32.4 hrs	Singapore	1.15 ↑ 1.56	.2300 ↓ .2500	0	0	0	NA	NA	0	0	0
38.7 hrs	Johnston Island	1.07 ↑ 1.09	.2240 ↓ .2530	8.5	NA	4	1.7	NA	4.2	NA	6.6
39.8 hrs	Johannesburg	1.17 ↑ 1.26	.1638 ↓ .2005	0	0	0	NA	NA	0	0	0
44.1 hrs	Singapore	1.02 ↑ 1.12	.2670 ↓ .3150	0	0	0	NA	NA	0	0	0
76.5 hrs	Johnston Island	1.24 ↑ 1.46	.2340 ↓ .3180	0	0	0	NA	NA	0	0	0

Channels 1 and 3 are omnidirectional and 2 is unidirectional. Channel 2 points represent a numerical average over one tumble period of 6.7 seconds. The labeled solid lines represent background data measured at the same B and L positions a few days (in some cases, a few hours) before the Teak event. Motion of the satellite in B, L space during the times of data acquisition is indicated by the satellite trajectory curves in the boxes of the figures. True count rate versus log B is presented for the average value of L indicated. L is assumed constant for that portion of the trajectory in which B changed rapidly.

Ratios of count rate versus L also are presented for true counts above background in the enhanced regions and for background ratios in the natural radiation regions (unity or near unity ratios). Ratios of unity are considered indicative of the high-energy protons in the natural belt. All pre-Teak ratio measurements in the region L = 1.1 to 1.3 yielded ratios near unity for all counters (Channels 1, 2, and 3). In a fission spectrum electron flux, the ratio of Channel 3 to Channel 1 would be about 100.

In Tables 6-2 and 6-3, the maximum flux densities above background (electrons per square centimeter per second above 5, 0.58, and 3 MeV for Channels 1, 2, and 3, respectively) are presented for three sample intercepts using these geometric factors: 0.6 cm^2 for channel 1; 0.04 cm^2 ster for channel 2; and 0.6 cm^2 for channel 3.

6.2.3 Buildup and Decay of Teak Radiation

Figure 6-4 gives the maximum true count rates (channel 3 GM counter; E > 3 MeV) above the background versus time after Teak at the B and L values indicated. Points were corrected to common B-values using the measured variations of count rate as a function of B at nearly constant L. Data were acquired as close as possible in time to the times of acquisition of the data being corrected. Where sufficient data were available, the points were fitted by the solid straight lines. For Johnston Island data at L = 1.2 and B = 0.181, the radiation decayed one order of magnitude in 11.6 days. A fit to the t^{-n} expression gives n = 0.31. At the nearby position L = 1.1 and B = 0.260, the radiation decays one order of magnitude in 1.61 days, and n = 2.0. On the L = 1.2 shell, the low flux value at T_E+ 5 hours measured at Johannesberg indicates that the worldwide buildup of trapped flux at L = 1.2 was not immediate.

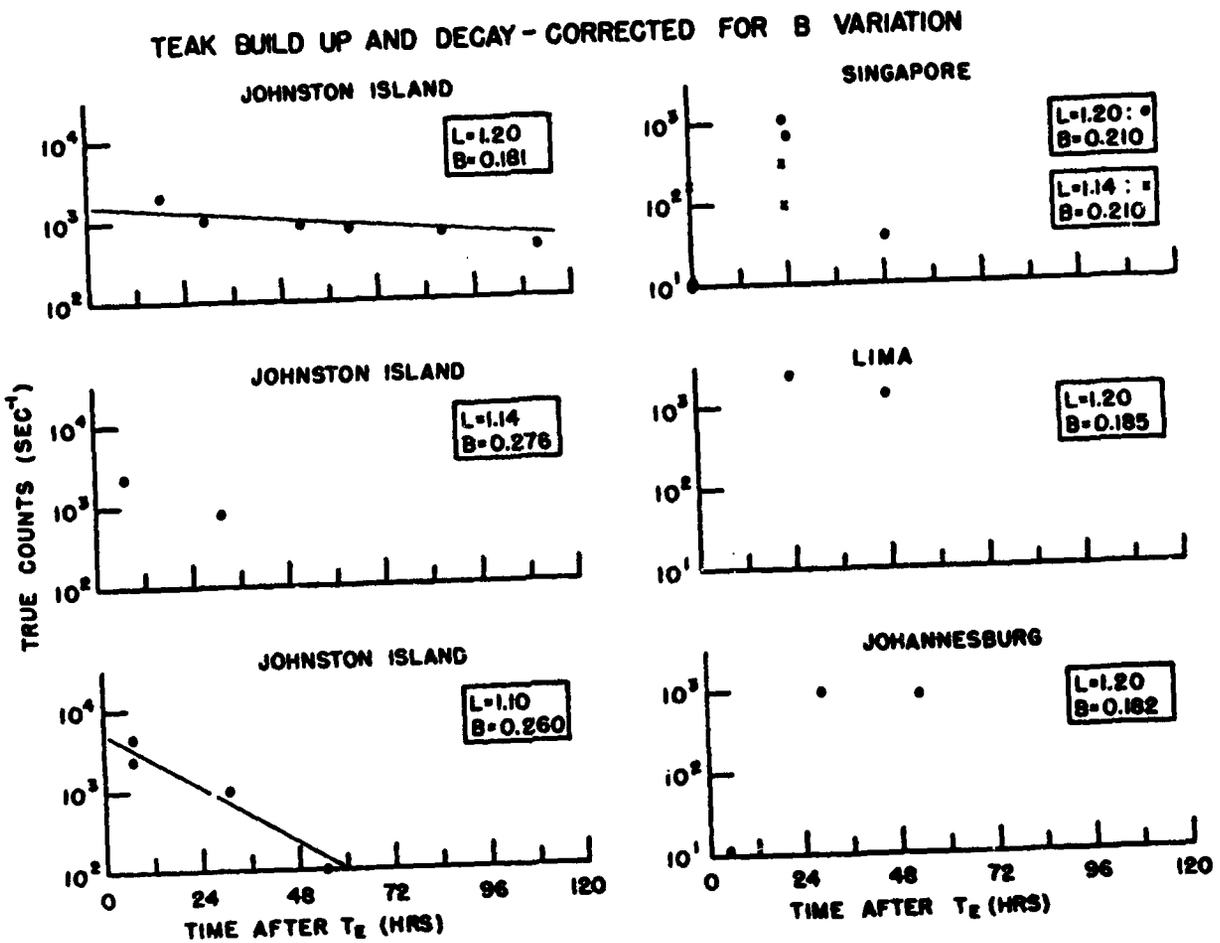

Figure 6-4. Buildup and decay of Teak enhancement.

6.2.4 Interpretation of Teak Data

Because of the appearance of enhancements at several closely grouped L-positions during the initial 18 hours after T_E and the indicated slow buildup of the shell at L = 1.2, separately discussing data acquired in the first few hours after T is desirable. The measurement over Singapore 18 minutes after detonation is anomalous in that the slope of log (count rate) versus log B is positive and the count rate ratios are too low for representation as a fission spectrum. These data suggest that the particles are energetic electrons early arrived from the Teak blast location. The early data from Singapore (Figure 6-1) also could represent a mixture of protons displaced from the natural belt with those fission electrons that would reach Singapore 18 minutes after detonation.

A pass at Johnston Island 6.9 hours after T_E indicates that the maximum of the shell is located at L = 1.14. The ratios Channel 3 to Channel 1 ($\approx$10) are suggestive of a fission-electron spectrum and are nearly constant as the satellite passed over the detonation site. Count rate modulations obtained with Channel 2 were observed throughout the enhancement at approximately twice the tumble frequency, thus indicating that increased flux was due to trapped particles rather than gamma radiation. During this early pass over Johnston Island, the flux was found to decrease with decreasing B. This suggested that the directional distribution of particles would be of the "butterfly" type, i.e., most of the particles had low mirroring points.

Table 6-2 indicates the worldwide nature of the trapping at the L = 1.2 shell, and Channel 3 to Channel 1 ratios, where available, indicate a fission-electron spectrum. The observed profile of the shell, of course, depends on the B-location and manner in which the satellite traverses the shell. The picture at Singapore (Figure 6-2) where the satellite follows an almost constant-B trajectory is perhaps the most striking. This figure shows the enhancement maximum at $L \approx 1.19$, although the earlier pass (Figure 6-1) showed the maximum at $L \lesssim 1.14$ and no significant increase at $L \geq 1.2$. The rapid decay of electron fluxes trapped at $L < 1.14$ is understandable. However, the delayed injection at $L \approx 1.2$ still is not explained.

The decay of the Teak radiation (Figure 6-4) is quite dependent on the L-shell and B-value of the measurement location: Where B-corrected data were sufficient, the times for 1/e decay were found to be approximately 4 days for L = 1.20 (22 to 110 hours after T_E) and approximately 14 hours at L = 1.10 (6.9 to 55 hours after T_E). These

values agree fairly well with theoretical atmospheric scattering losses (Reference 4).

Because of the time delay just noted and the fragmentary nature of the data, several rough approximations are necessary to estimate the electron inventory. Using Singapore data (Figure 6-2), (1) the half width at half maximum (HWHM) for the directional distribution was estimated from the average slope of log (true count rate) versus log B plots for data acquired at several tracking stations, (2) mean bounce periods were calculated for the electrons counted by each detector based on an estimate of the mean energy for the portion of the time-dependent fission spectrum above the counter threshold, (3) Channel 2 data were corrected for decay by assuming the same decay rate as for Argus 1, (4) Channel 3 data were corrected for decay by assuming the same decay rate as observed at Johnston Island, (5) correction was made for the estimated portion of the fission spectrum at energies below the counter thresholds.

These approximations, paralleling the procedure outlined in Section 6.3.2, yielded, for the total number of electrons of all energies trapped in the Teak shell at T + 1 hour (neglecting all particles mirroring between the satellite latitude and the magnetic equator), 6×10^{20} and 5×10^{19} for Channels 2 and 3 data, respectively. The estimate based on Channel 3 data is probably more reliable because of the more accurate decay correction.

6.3 ARGUS EXPERIMENTS

6.3.1 Introduction

The Argus experiments, consisting of three high-altitude detonations, were carried out in 1958 (Table 6-1) to test whether electrons could be trapped by the geomagnetic field. Locations for the detonations were chosen in the South Atlantic where the traces of mirroring points have their closest approach to the earth. Brief histories of the Argus experiments are given in References 5 and 6.

Measurements of the trapped radiation from all three Argus events were made by the satellite Explorer 4, and data also were obtained for the second event by sounding rockets. Analyses of the satellite results are published in DASA reports and in open literature (References 7 through 13). The sounding rocket results are given in References 14, 15, and 16.

Following the three high-altitude detonations, narrow bands of trapped electrons were detected and observed to decay for several weeks. Since the L-values of the three detonations differed slightly, the time decay and latitude spread of the individual bands could be studied separately.

6.3.2 Explorer 4 Measurements

Explorer 4 contained instrumentation specifically intended to observe the trapped radiation from the Argus experiments. It was launched 26 July 1958 into an orbit with an apogee of 2,200 kilometers, a perigee of 260 kilometers, and a 51-degree inclination.

Information concerning the body motion, emphemerides, calibrations and description of detectors, telemetry, and location of ground stations for Explorer 4 has been published (References 17 through 20). The present summary of Explorer 4 data relies on count rates obtained from three detectors whose characteristics are cited in Table 6-4.

Table 6-4. Characteristics of three Explorer 4 detectors.

Channel	Detector	Electron Threshold (MeV)	Dead Time (μsec)	Geometric Factor
1	Omnidirectional GM	5	62.5	0.6 cm^2
2	Directional Scintillator	0.58	91	0.04 cm^2 ster
3	Omnidirectional GM	3	62.5	0.6 cm^2

Figures 6-5 and 6-6 show the Argus 1 shell in relation to natural radiation for two penetrations, 1.80 hours (Huntsville, Pass 414; Table 6-5) and 25.48 hours (Huntsville, Pass 427) after the event. Observed count rates C_{obs} are presented versus real time, and the B, L coordinates are indicated. Channel 1 points have been plotted only in the Argus region where the Channel 1 count rates differed from Channel 3. Figures 6-5 and 6-6 show the narrow band of artificially injected radiation at L = 1.72. The extended region of high

Table 6-5. Summary of unidirectional data for Argus 1 and Argus 2.

Date (1958)	Event, Pass	Max Flux j (θ)* (cm^{-2} sec^{-1} $ster^{-1}$)	HWHM (deg)	B, L (gauss, earth radii)	Latitude (deg)	East Longitude (deg)	Altitude (km)	Time UT(min)
27 Aug	1 + 1.8 hr; 414	1.5×10^6	20	0.221, 1.68 (256 UT)	17.6 (256 UT)	285.5 (256 UT)	1518 (256 UT)	256.083 to 256.209
	415	1.0×10^6	21	0.24, 1.70	21	262	1437	367.5 to 368.0
28 Aug	1 + 25.48 hr; 427a	1.46×10^5	18	0.2132, 1.675	16.3	285.8	1578	236.0 to 236.5
	427b	2.56×10^5	28	0.2174, 1.710				236.5 to 236.68
	427c	5.42×10^5	18	0.2195, 1.739				236.69 to 236.85
	427d	1.68×10^5	30	0.220, 1.748				236.871 to 237.0
	427e	1.44×10^5	22	0.2224, 1.757	18.6	287.6	1531	237.0 to 237.162
29 Aug	440	1.65×10^5	18	0.22, 1.7	16.7	286.5	1615	216.0 to 217.0
30 Aug	2 + 1.87 hr; 454	5.28×10^5	13	0.274, 2.12	28.8	270.8	1394.5	310.279 to 310.333

Note:

* Background subtracted.

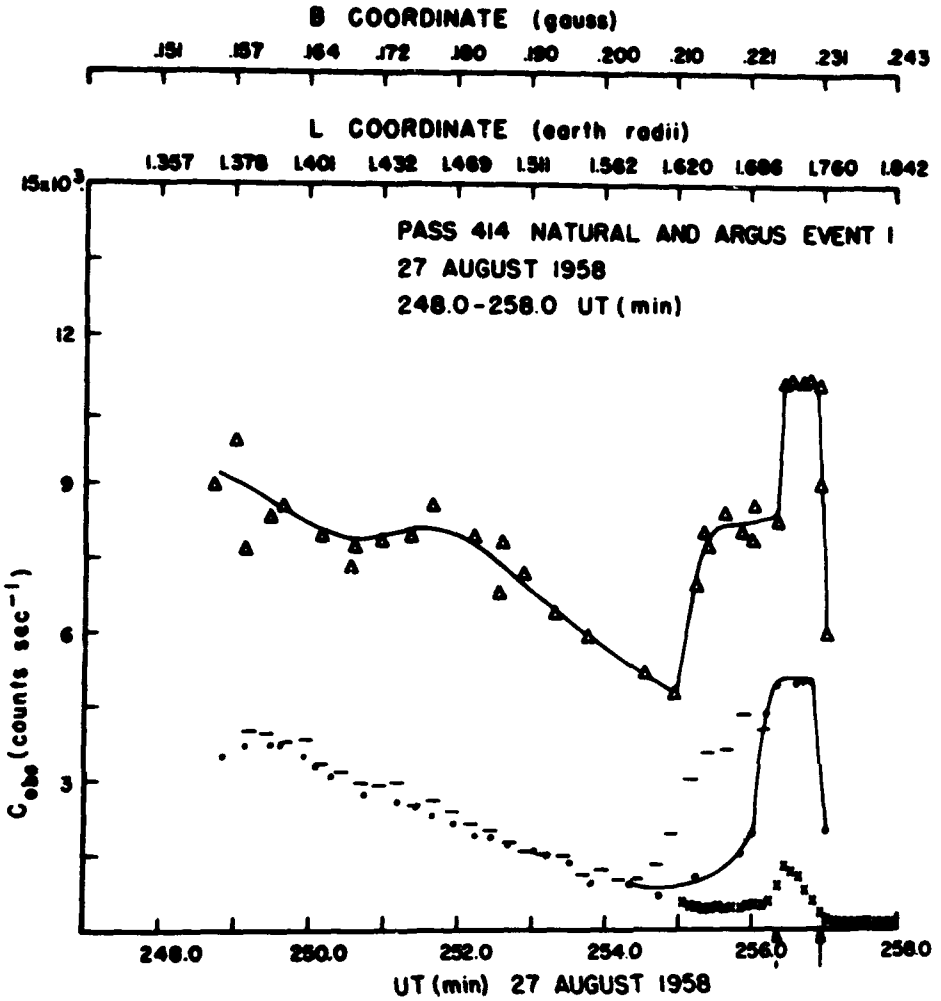

Δ Channel 2—maximum observed count rate when directional counter was perpendicular to B.

— Channel 2—minimum observed count rate when directional counter was parallel to B.

• Channel 3—20-second average.

x Channel 1—7-second average.

Figure 6-5. Argus 1 trapping 1.80 hours after T_E; data were acquired at Huntsville.

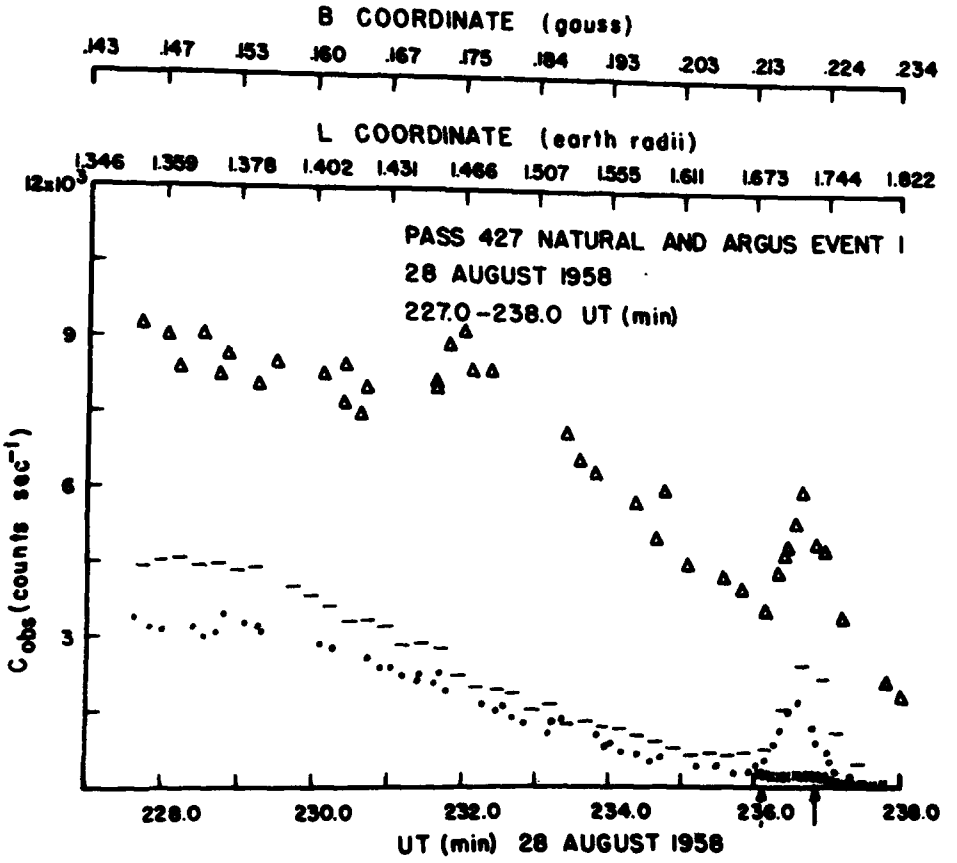

Figure 6-6. Argus 1 trapping 25.48 hours after T_E; data were acquired at Huntsville. Symbols are defined in Figure 6-5.

counting rate $L < 1.5$ denotes the inner-radiation belt. The shoulder of the central band seen at $L = 1.68$ with Channel 2 also appears when the Channel 2 directional detector is oriented parallel to the magnetic field. This feature may be caused by gamma rays from the fission debris cloud. Arrows on the time axis of Figure 6-5 indicate the region in which the unusual distributions of Figure 6-7 were acquired. Channel 2 maximum count rates are near saturation at the center of the shell, $L = 1.72$. Arrows on the time axis of Figure 6-6 indicate the spatial region in which the distributions of Figure 6-7 (measured one day earlier) have become normal (Figure 6-8).

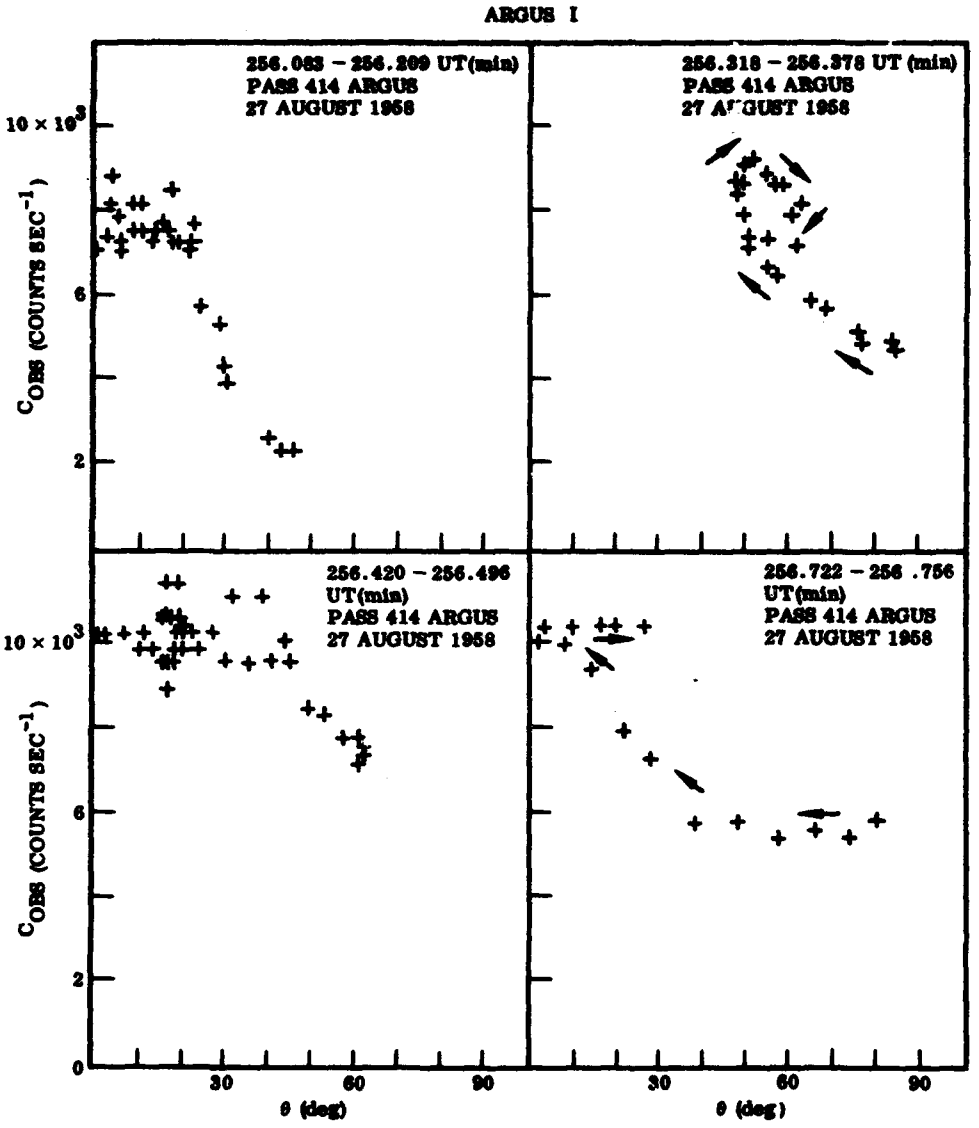

Figure 6-7. Sample of observed unidirectional count rate versus θ (angle between counter axis and plane perpendicular to B)—Argus 1, 1.80 hours after T_E.

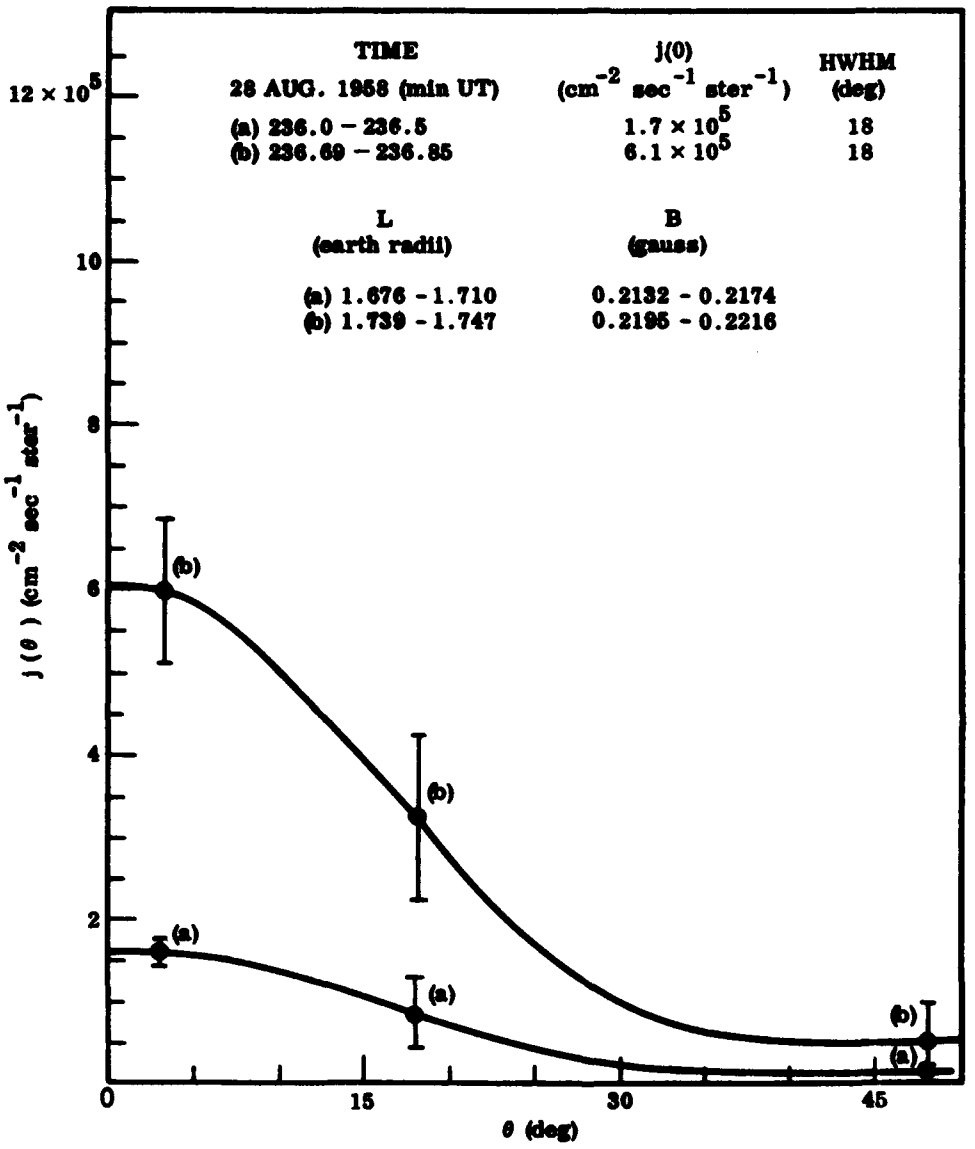

Figure 6-3. Unidirectional flux density versus θ [angle between j(θ) and plane perpendicular to B]—distributions for Argus 1, T_E + 25.48 hours.

Pitch angle distributions corresponding to these two penetrations are shown in Figures 6-7 and 6-8, respectively. In Figure 6-7, samples of observed count rate versus θ (the angle between counter axis and a plane perpendicular to geomagnetic field direction) are plotted for the shell penetration 1.8 hours after T_E. Plots have been selected from a sequence made for each rotation of the satellite to illustrate the different distributions observed. Arrows in Figure 6-7 indicate direction of time of data acquisition. Unusual shapes may be caused by injection from nearby debris cloud. Abnormally high penetrating component (counter nearly parallel to B: tail of distributions in upper and lower right of figure) could indicate gamma radiation from debris cloud. The angular distributions observed in this early period are unusual since the flux varies appreciably during one rotation period of the vehicle, and appreciable fluxes are found at large pitch angles. Analysis of these data to obtain true angular distributions is difficult because of rapidly varying fluxes and because the detector saturates at about 10^4 counts per second. The distributions become more normal as time progresses. For example, the distributions at T_E + 25.48 hours (Figure 6-8) are normal and not markedly different from those observed in the inner Van Allen belt. Analysis of Event 2 (pass 454, T_E + 1.87 hours; Table 6-5) indicated only normal distributions. Channel 2 was inoperative for all Argus 3 measurements.

In Figure 6-8 (Huntsville, Pass 427 and one day later than the data of Figure 6-7), the flux j (θ) versus θ is plotted, where θ is the angle between j (θ) and a plane perpendicular to the geomagnetic field. Distributions in Figure 6-8 are normal and similar to those observed in the natural (inner Van Allen) belt. Each solid curve represents averages over several satellite tumble periods for the time intervals indicated, which were chosen at two intensity levels as the satellite crossed the shell. Table 6-5 summarizes the directional data from Argus 1 and 2. The decay of the maximum unidirectional flux density at the L = 1.72 position for Argus 1 is plotted in Figure 6-9. Data were for peak intensities in the shell (L = 1.72) and at times when the scintillation counter (Channel 2) was perpendicular to the geomagnetic field. Data uncorrected for B-variation (solid circle points) were acquired at slightly differing B-values. Corrections for each point to two constant B-values (triangle and open circle points) made by using mirror point flux density versus B plots are included also.

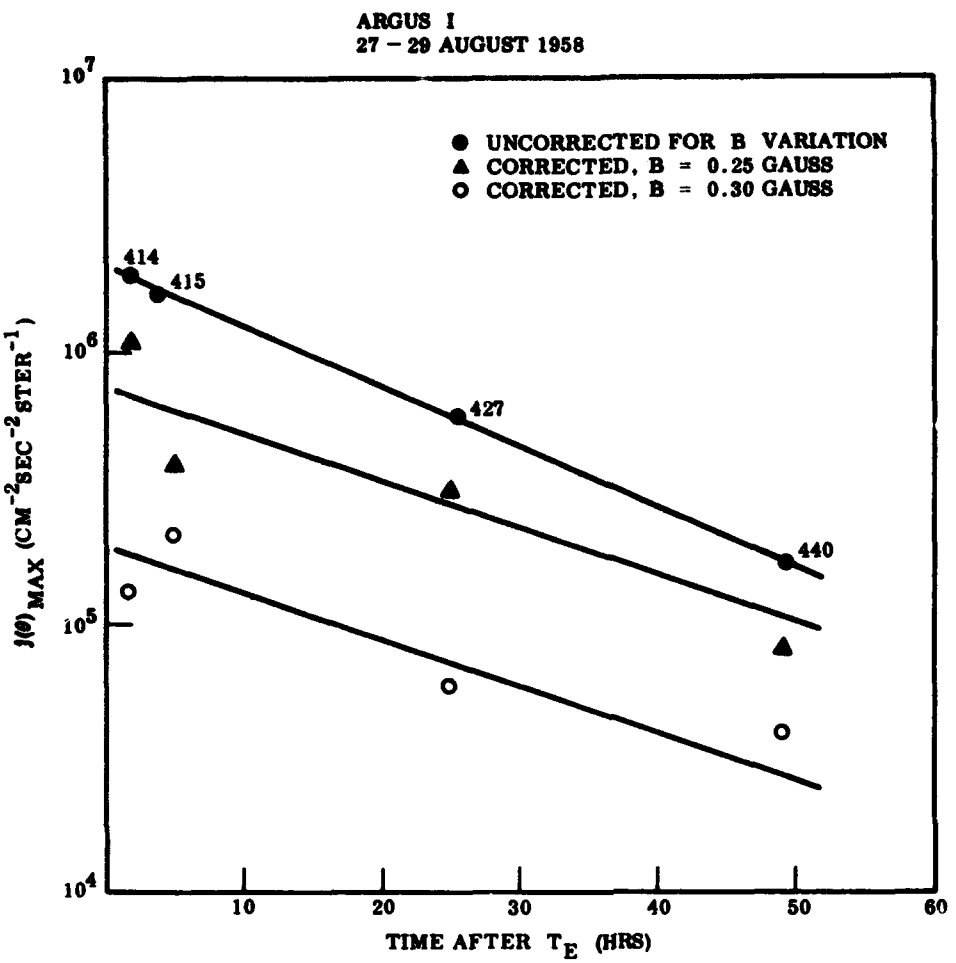

Figure 6-9. Decay of unidirectional peak flux density $j(\theta)_{max}$ perpendicular to B for Argus 1.

Omnidirectional data for Argus 1, 2, and 3 are summarized for each event in Figures 6-10 through 6-12 (Reference 21). The data presented were reduced from a fresh set of playback records (carefully filtered to eliminate noise) made from a selected group of telemetry tapes acquired by the Huntsville tracking station. A portion of Event 3 data was obtained from the University of Iowa reports (References 9 and 10). Natural background has been subtracted using McIlwain's Explorer 4 data (Reference 22).

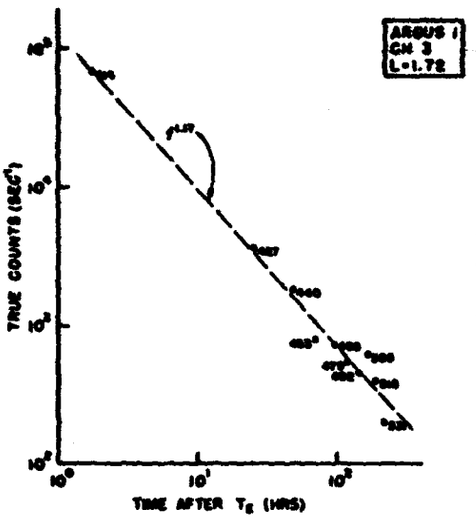

(a) DECAY

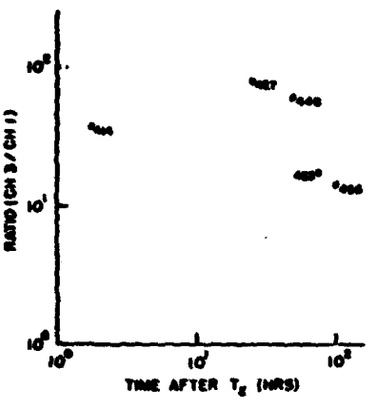

(b) CHANNEL 3 (E > 3 MeV) ÷ CHANNEL 1 (E > 5 MeV) RATIOS

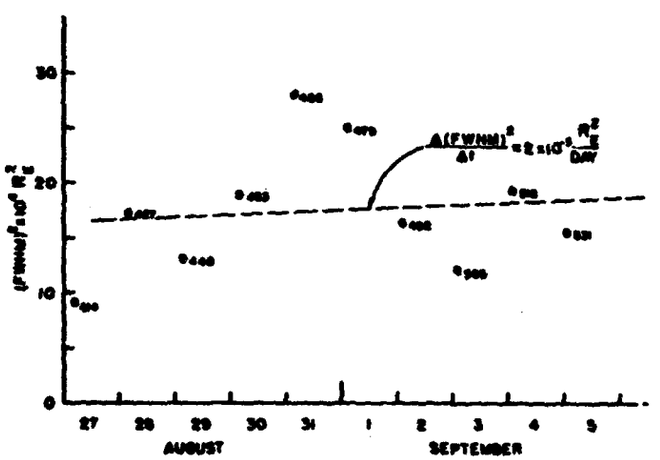

(c) SHELL DIFFUSION FOR ARGUS 1.

Figure 6-10. Summary of omnidirectional data for Argus 1.

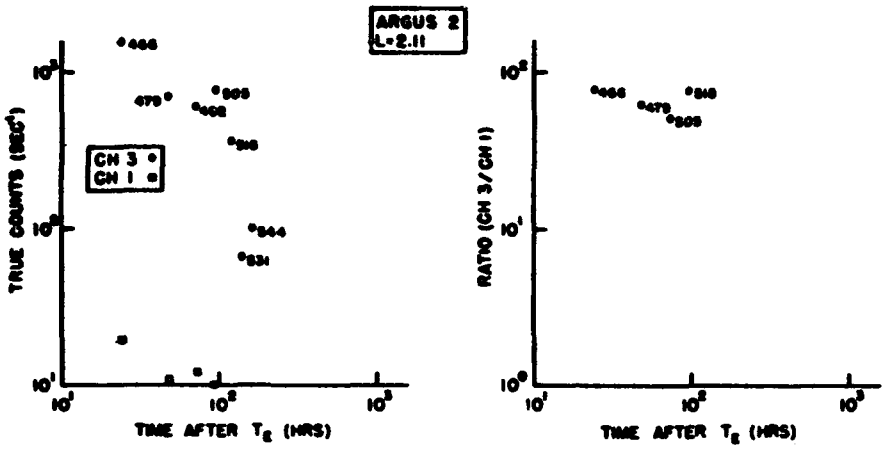

(a) DECAY

(b) CHANNEL 3 (E > 3 MeV) ÷ CHANNEL 1 (E > 5 MeV) RATIOS

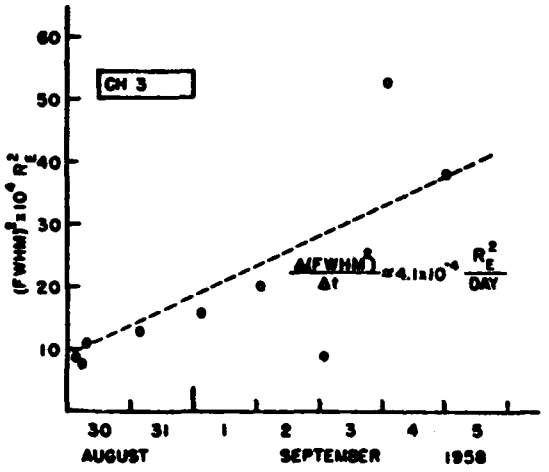

(c) SHELL DIFFUSION FOR ARGUS 2 (SIMILAR TO FIGURE 6-10)

Figure 6-11. Summary of omnidirectional data for Argus 2.

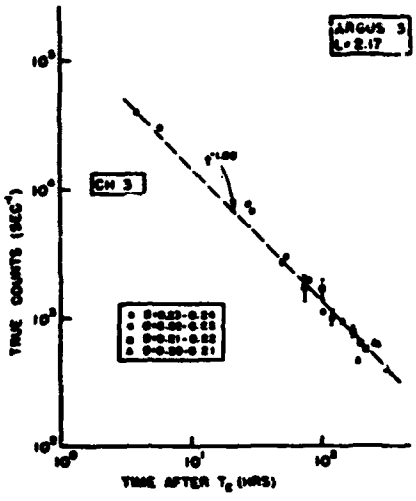

(a) DECAY

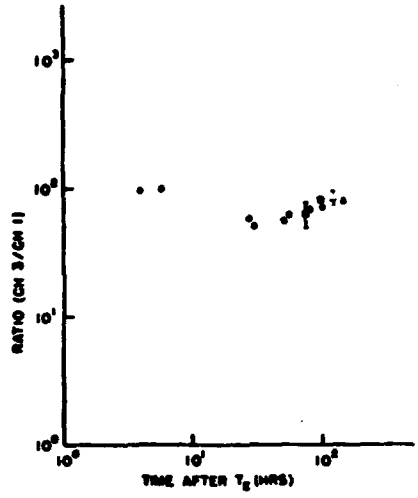

(b) CHANNEL 3 (E > 3 MeV) ÷ CHANNEL 1 (E > 5 MeV) RATIOS

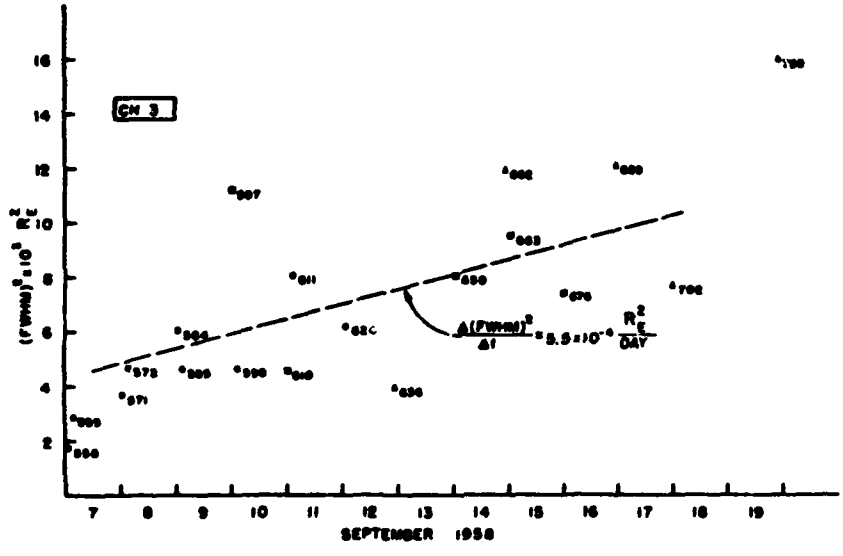

(c) SHELL DIFFUSION FOR ARGUS 3 (SIMILAR TO FIGURE 6-10)

Figure 6-12. Summary of omnidirectional data for Argus 3.

Figure 6-10a is a plot of count rate versus time after T_E. The slope of the decay (t^{-n} law) yields n = 1.17. Figure 6-10b is a plot of Channel 3 to Channel 1 peak count rate ratios at L = 1.72 versus time after T_E. This ratio serves as a spectral index and should give values near 100 in a fission-electron spectrum. Ratio data terminate at Pass 466 because the Channel 1 count rate decreased to background. Figure 6-10c is a plot of the square of the full width at half maximum (FWHM) for the shell versus time, indicating the amount of diffusion across L. Any appreciable motion of electrons from one L-value to another should be apparent in a widening of the shell. Data were obtained from smoothed plots of count rate versus L, background was subtracted, and a least squares fit (dashed line) made to the data.

Figures 6-11 and 6-12 present similar data for Argus 2 and Argus 3. In Figure 6-11, B-values range from 0.248 (Pass 466) to 0.222 gauss (Pass 531). A least squares fit to the count rate decay data was not made because of the scatter of the data. In Figure 6-12, the range of B-values is indicated. The time decay of the count rate is proportional to $t^{-1.09}$. All three shells of trapped particles appeared to be quite stable. Maximum flux densities were observed consistently at the same L-values (Argus 1, L = 1.72; Argus 2, L = 2.11; Argus 3, L = 2.17). Radial diffusion coefficients $\Delta(\text{FWHM})^2/\Delta t$ are noted in Figures 6-10c, 6-11c, and 6-12c. These values may be compared with the value $7 \times 10^{-5} R_E^2$ per day found (Reference 23) for the third USSR test in November 1962 at L = 1.77.

The decay of the Argus shells was observed to have a t^{-n} time dependence. For Argus 1, n = 1.17 (Figure 6-10a); for Argus 3, n = 1.09 (Figure 6-12a). For Argus 2 (Figure 6-11a), the t^{-n} law was not applied because of the large scatter of the satellite data (Section 6.3.3). Count rate ratios were roughly constant with time for the time spans included by the data and are roughly as expected for a fission-electron spectrum. Ratios for Argus 1 may indicate slightly harder radiation than for Argus 2 and Argus 3. The decay of Argus 2 may have been increased by some dumping on the magnetically disturbed days 3 to 5 September, as indicated by the apparent change in slope after Pass 505 (Figure 6-11a).

An apparent mean lifetime was found for Argus 1 and Argus 3 Events for energies E > 3 MeV. If an exponential decay is approached asymptotically in the time interval 70 < (time after T_E) < 200 hours, the time required for the electron flux to decrease by a factor of 1/e is approximately 6 days at L = 1.72. A similar analysis for Argus 3 yields a

decay time of approximately 10 days at L = 2.17 for the time interval 100 < (time after T_E) < 320 hours.

6.3.3 Sounding Rocket Measurements

A series of rocket soundings also was made to assess the trapping from the Argus experiments. Originally designed as a backup to the satellite measurements, the rockets provided valuable additional information on the second explosion. The sounding rocket program consisted of a total of 19 launches—3 test launches and 16 actual measurements. The rockets were five-stage vehicles with nominal apogees of about 800 kilometers and were launched from Wallops Island, Virginia; Patrick Air Force Base, Florida; and Ramey Air Force Base, Puerto Rico. Because the first Argus event was at too low an L-value to be observed easily from these launch positions, the majority of the rockets were launched to sample the second event.

Table 6-6 lists the launch location, time of launch after burst, and performance. With these vehicles, data were obtained in the interval between 0.5 hour and about 90 hours after the second detonation.

The instrumentation in each payload consisted of eight GM counters with various shield thicknesses and dynamic ranges. Channels 1, 2, 3, 4, 6, 7, and 8 had thresholds of about 0.2, 0.15, 1.0, 1.0, 4.5, 0.5, and 0.4 MeV, respectively, and Channel 5 was a duplicate of Channel 1. Examples of the data obtained are shown in Figure 6-13, which gives the counting rates of the various counters versus flight time for the launch from Wallops Island 4 hours after Event 2 (Reference 16).

The maximums observed in all counting rates approximately 775 seconds after launch denote passage through the artificial radiation belt. The earlier maximums seen on Channels 1 and 2 at about 450 seconds result from the rocket passing through apogee at that point. As the vehicle falls, the flux decreases until passage into the intense Argus band at 775 seconds. Both north and south of the central band is a region of enhanced radiation from the bomb. For example, in Figure 6-13, the natural background for Channel 3 at 36-degrees latitude is about 30 counts per second, and the entire region between the band and 36 degrees contains fission electrons.

A determination of the energy spectrum from the counting rates of the various threshold detectors indicated that the spectrum was indistinguishable from a fission spectrum. Furthermore, detailed investigations of the ratios of the count rates of the various detectors at

Table 6-6. Sounding rocket launches.

Item	Launch Site	Flight Number	Date (1958)	Time After Burst (hr:min)	Performance
Background					
	Patrick	1822	15 Aug		OK
	Ramey	1841	20 Aug		Failure
	Wallops	1859	25 Aug		Failure
Event 1			27 Aug		
	Patrick	1909	27 Aug	1:03	OK
	Ramey	1914	27 Aug	1:54	Failure
	Ramey	1917	27 Aug	4:12	OK
	Wallops	1913	27 Aug	4:59	Failure
Event 2			30 Aug		
	Wallops	2019	30 Aug	0:28	OK
	Patrick	2022	30 Aug	1:11	OK
	Wallops	2021	30 Aug	1:58	OK
	Ramey	2023	30 Aug	2:32	OK
	Patrick	2025	30 Aug	3:16	OK
	Wallops	2024	30 Aug	4:01	OK
	Wallops	2027	30 Aug	18:42	OK
	Ramey	2026	30 Aug	19:43	Failure
	Patrick	2020	31 Aug	20:47	OK
	Ramey	2041	2 Sept	87:42	Failure
	Wallops	2042	2 Sept	88:43	OK
	Patrick	2043	2 Sept	90:55	OK

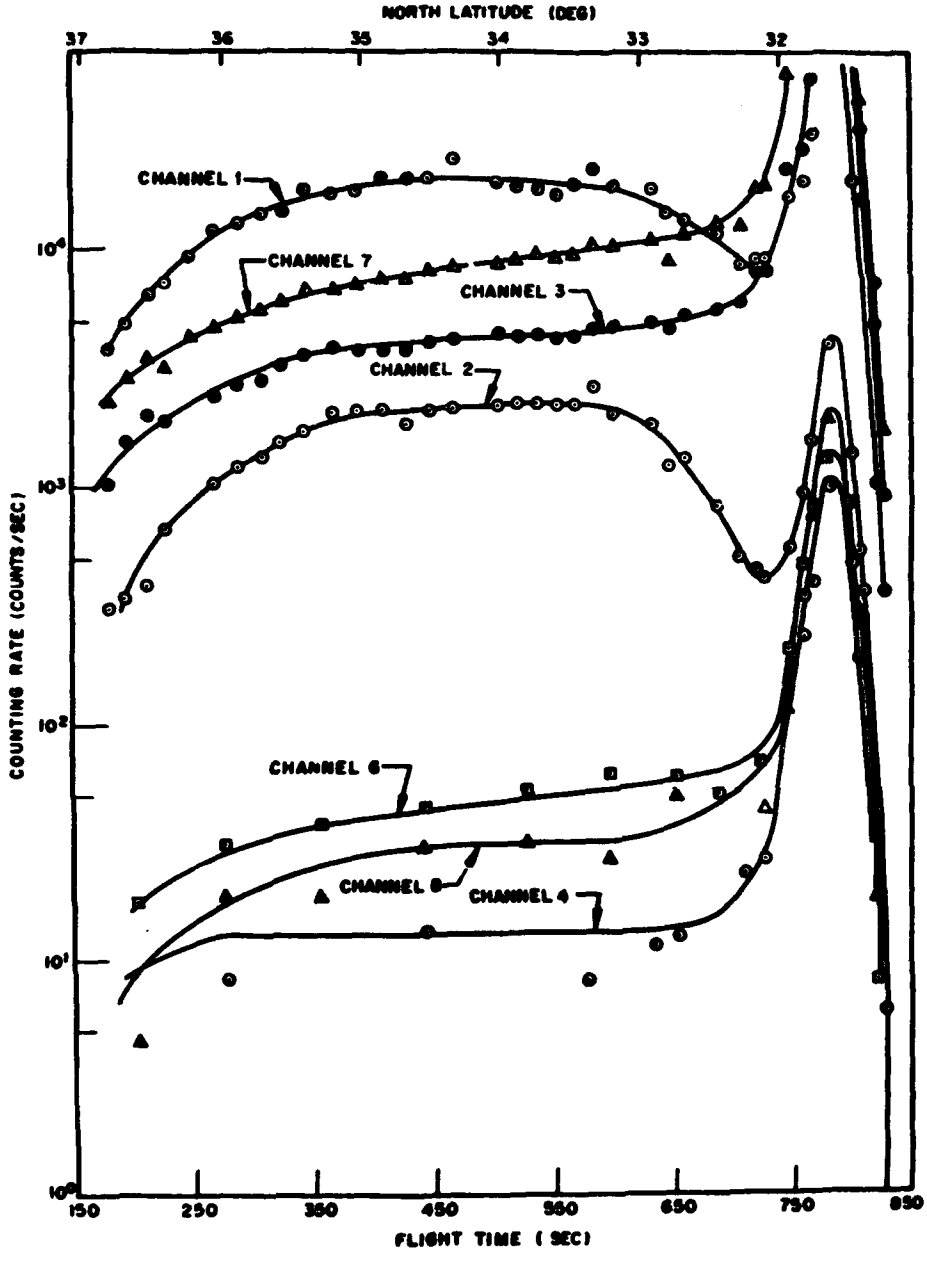

Figure 6-13. Counting rates of detectors on rocket flight 2024 versus flight time.

different times and at different locations showed that the spectrum did not change appreciably with time or position.

The decay rate of the artificial radiation belt was estimated by comparing the count rates of the various flights as they passed through comparable positions in invariant space. Figure 6-14 illustrates the data of Event 2 in the form of count rate ratios for the various pairs of vehicles. If it is assumed that the decay rate is a power law (flux $\propto t^{-n}$), then $n = 1.15 \pm 0.03$ (Reference 16).

6.3.4 Summary of Argus Experiment Results

The Argus experiments demonstrated conclusively that electrons could be injected into the geomagnetic field and, for a time, would behave as predicted by adiabatic theory. The narrow shells formed were very stable and, although some widening with time was found by detailed analysis, the increase is not far outside experimental error. Broad regions of less intense radiation were found outside the central band on Argus 2. The origin of these wings is not understood, although they may have been produced by neutral fission fragments passing across field lines. Their appearance immediately (within 30 minutes) after the detonation suggests a different origin from the extended radiation observed at L = 1.2 following Teak. Within experimental errors, the energy spectrum corresponded to that for fission-spectrum electrons and was constant in space and time.

The time decay of the Argus radiation was more rapid than expected, the effective lifetime being on the order of 1 week, depending on the time period considered. This decay is much too rapid to be caused by scattering of the electrons by the ambient atmosphere.

Estimates of the electron inventories and injection efficiencies for the Argus experiments are very uncertain primarily because measurements were made only at relatively low altitudes and could not detect electrons mirroring above Explorer 4. Hence, the injection efficiencies based on the number of trapped electrons actually observed are lower limits to the true injection efficiencies. Efficiencies thus computed from Explorer 4 data are shown in Table 6-7 and are less than 1 percent. Errors in these values are appreciable, a factor of 10 disagreement existing, for example, between the results of Channels 2 and 3 for Argus 2. A very rough estimate of the total number of electrons injected can be made by assuming the Argus electrons are distributed along magnetic field lines in the same way that the natural radiation belt electrons are. The resulting estimates of total

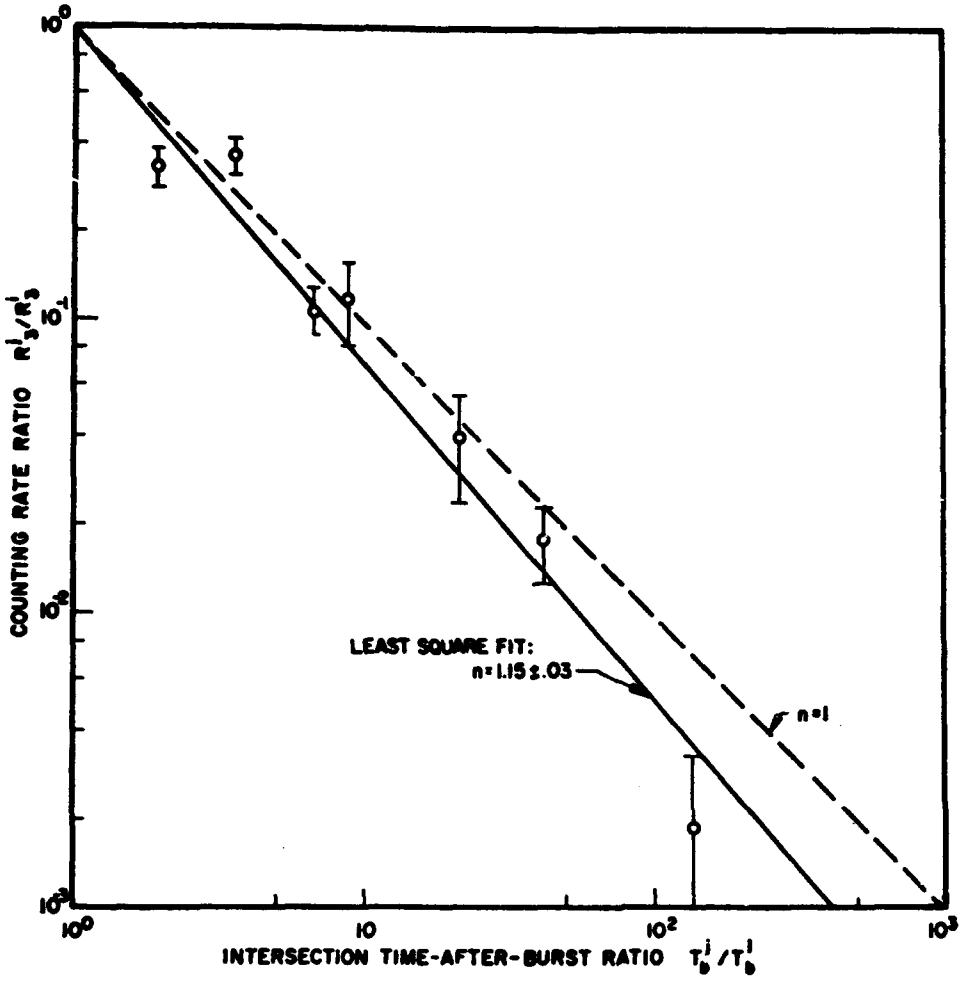

Figure 6-14. Time rate of decay of electron flux for Event 2.

Table 6-7. Argus injection efficiencies.

Item	Argus 1		Argus 2		Argus 3, Channel 3
	Channel 2	Channel 3	Channel 2	Channel 3	
Observed injection efficiency for electrons mirroring below Explorer 4 (percent)	0.6	0.25	0.14	0.012	0.3
Estimated total injection efficiency (percent)	12	5.0	27	2.3	11

injection efficiency also are given in Table 6-7. Because the extrapolation of Argus fluxes from Explorer 4 altitudes to the equatorial plane is extremely questionable, these latter numbers should be used with caution.

6.4 STARFISH

6.4.1 Introduction

The Starfish nuclear event on 9 July 1962 consisted of a detonation yield of about 1.4 megaton at an altitude of 400 kilometers above Johnston Island, 16.7°N, 190.5°E. Because of its intensity and long-term persistence, the radiation belt created by this event dramatically demonstrated the vulnerability of satellites to artificial radiation belts.

6.4.2 Satellite Measurements

At the time of the detonation, a number of satellites, including Injun I, Traac, Ariel 1, and Cosmos 5, were in orbit. Unfortunately, none of these satellites had detectors designed for the intensity and energy spectrum encountered, and the orbits were too low (~1,000 kilometers) to sample the full extent of the belt. Consequently, knowledge of the initial spatial distribution is incomplete, and the energy spectrum at early times is largely unknown. On 10 July, Telstar was launched into a more favorable orbit. However, since the launch of Telstar was after the explosion, no unambiguous means existed to determine the natural background for Telstar detectors, and the energy selectivity of the instruments was not designed to distinguish fission-spectrum electrons from electrons in the natural radiation belts. Ariel 1 and Traac were short lived in the new radiation belt and only provided data on the initial distribution. Injun I operated for 50 days following the detonation, and Telstar continued for many months.

On 2 October, Explorer 14 was placed in a highly eccentric orbit. The Department of Defense (DoD) satellite Starad (1962 βK) was launched on 26 October and Explorer 15 was launched on 27 October. Explorer 15 and Starad had detectors specifically designed for fission-spectrum electrons so that satisfactory coverage of the Starfish belt was obtained following their launches. Additional information also has been provided by Injun 3, launched 13 December 1962. The very long-term decay of the belt has been observed by the satellite 1963 38C, which has taken data continuously from 28 September 1963 to the present time. A number of DoD satellites also made measurements

in late 1962 and 1963 in low-altitude orbits. However, these data are not particularly useful because of the restricted spatial coverage and short satellite life.

Table 6-8 lists the satellites that, to date, have given the most valuable information on the Starfish belt. Because of the widespread distribution of Starfish electrons and their long lifetimes, many other measurements of the belt have been made in conjunction with other space experiments.

6.4.3 Characteristics of the Starfish Belt

The complete description of the Starfish radiation belt perhaps never will be known since some of the needed early-time experimental data are lacking. This summary, which is based primarily on satellite observations of trapped particles, will present all available information in a concise form. Comments on the injection mechanisms will be given in Section 6.4.5.

Following the Starfish explosion, an intense radiation belt was formed. The contours of the belt (Figure 6-15) as determined by

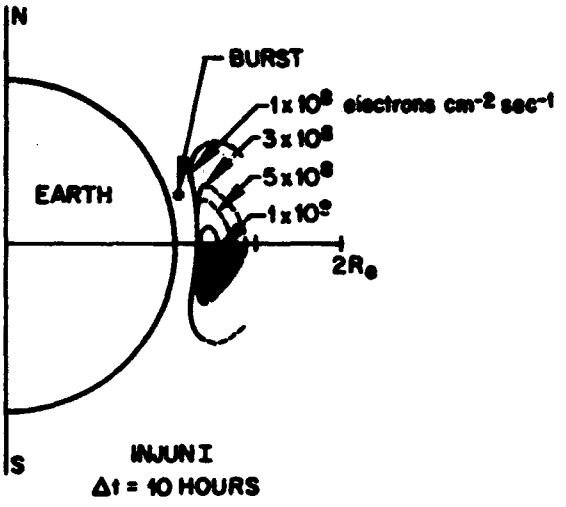

Figure 6-15. Flux contours 10 hours after Starfish, as determined from Injun I data.

Table 6-8. Principal Starfish measurements.

Satellite Designation	Launch Date	End of Active Life	Apogee (km) Perigee (km) Inclination (deg)	Comments	Pertinent References
Injun 1	29 June 1961	Aug 1962	1,010 890 67	Low altitude; principal data from a single bremsstrahlung detector	24, 25, 26
Cosmos 5	28 May 1962		1,600 204 49	Incomplete data available	27, 28
Ariel	26 April 1962	~12 July 1962	1,200 400 54	Low dynamic range; poor energy discrimination	29, 30, 31
Traac	15 Nov 1961	12 Aug 1962	1,110 951 32.4	Low altitude; short lifetime	32
Telstar	10 July 1962	21 Feb 1963	5,630 955 44.7	Good orbit; long active period; poor background knowledge	23, 33, 34
Alouette	29 Sept 1962		1,040 993 80	Low altitude	35
Explorer 14	2 Oct 1962	8 Oct 1963	98,533 292 33	High apogee	36, 37
Starad (1962 β K)	26 Oct 1962	18 Jan 1963	5,580 198 71	Good orbit; good energy discrimination; difficult data-reduction problems	38, 39, 40
Explorer 15	27 Oct 1962	9 Feb 1963	17,300 310 18	Good orbit	23, 41
Injun 3	13 Dec 1962	3 Nov 1963	2,785 237 70.4	Instrumentation comparable to Injun 1; higher altitude orbit	25
1963 39C	28 Sept 1963		1,140 1,867 89.9	Long term, low-altitude coverage	42, 43, 44

Injun I (References 24 and 25) show the flux concentrated in a narrow crescent, centered on $L \approx 1.2$. These Injun I data were obtained by a heavily shielded detector (the so-called SpB), which responded primarily to bremsstrahlung produced by electrons over a broad energy range between 1 and 5 MeV. The numbers identifying the contours are the fluxes of fission-spectrum electrons needed to give the observed counting rates. Although the absolute values of the fluxes are uncertain by perhaps a factor of 2, the relative values should be much better except in the area of the dashed lines, which are extrapolations of measured data and, hence, are very uncertain.

From detailed measurements made by Traac shortly after the detonation (References 29 and 32), a very narrow, enhanced region also was found at $L \approx 1.16$. This maximum probably resulted from the electrons emitted by fission fragments that remained on the field lines passing through the explosion location.

The other satellites in orbit at the time of the detonation gave results in essential agreement with the Injun I results of Figure 6-15. However, since these satellites were at low altitude, the flux could not be observed at $L \gtrsim 1.3$ except at high latitude, and the large region depicted by the dashed lines could not be measured directly. The latitude extent to which increases in counting rates were observed was very large. Cosmos 5 (References 27 and 28) registered increased rates at the maximum L-value of its orbit which was $L = 2.3$, and Ariel (Reference 30) showed substantial increases in trapped flux as high as $L = 7$. However, the electron flux detected at these high L-values was 3 orders of magnitude lower than that observed in the center of the belt, indicating that the number of electrons involved was not large.

On the day following Starfish, Telstar (Reference 23) was launched and obtained the flux contours shown in Figure 6-16. The numbers in the figure are the intensities (cm^{-2} sec^{-1}) of fission-spectrum electrons required to give the observed counting rates of the Telstar solid state detector having a threshold of about 400 KeV. Since Telstar was launched after Starfish, no substraction of the natural background was possible. Identification of Figure 6-16 with Starfish distributions requires the assumption that the natural background was a negligible fraction of the observed fluxes. The Telstar contours clearly extend to much greater L-values and involve more electrons than are implied by the Cosmos 5 and Injun I data.

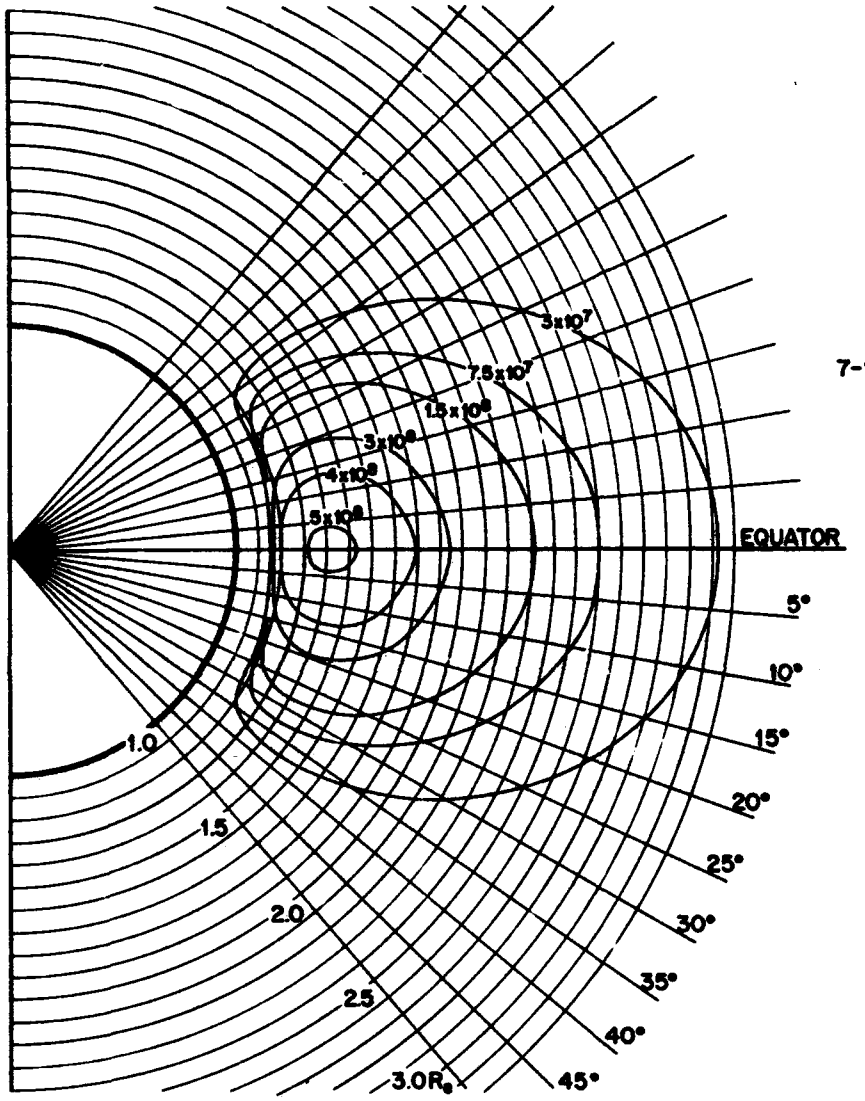

Figure 6-16. Flux contours 2 days after Starfish, as determined from Telstar data by Newkirk and Walt (unpublished).

The discrepancy between the Injun I and Telstar measurements of the Starfish belt at early times has been one of the most puzzling features of the experiment. By the time additional measurements could be made with Explorer 14, Starad, and Explorer 15, the discrepancy largely had vanished because of the rapid decay of fluxes at $L \gtrsim 1.7$. To reconcile the Injun I and Telstar measurements requires one or more of the following assumptions:

1. The Telstar detectors registered primarily natural radiation belt electrons at $L \geq 1.5$. These electrons had been injected by some geophysical disturbance before 9 July 1962 and their subsequent decay was observed by Telstar.

2. The extrapolations of low-altitude Injun I data to high altitudes were incorrect.

3. The electrons observed by Telstar at $L > 1.5$ had lower energies than expected for fission-spectrum electrons and were counted more efficiently by Telstar than by Injun I.

From the observed monotonic decay of the electrons seen by Telstar subsequent to 10 July, these fluxes probably were injected impulsively by Starfish. Conceivably, the injection was a geophysical phenomena; such variations have been observed at times of magnetic storms. However, this explanation is unlikely since the magnetic activity indices several months prior to 9 July show no large activity. Although the extrapolations of Injun I data to $L = 1.5$ on the equator are indeed uncertain, significant differences exist between the flux contours of Injun I and Telstar even over the region of common data.

At the present time, the most likely explanation for the discrepancy between Injun I and Telstar is that the spectrum of injected electrons varied with L, the electrons being less energetic at larger L-values. Physical processes that could lead to this situation are discussed in Section 6.4.5. Some direct experimental evidence for this "softening" of spectra with increasing L was obtained several months after Starfish and is presented in Figure 6-17. The figure shows the omnidirectional flux in the equatorial plane versus L as measured with various instruments several months after Starfish. These instruments are the 0.5- and 5.0-MeV threshold detectors on Explorer 15 (References 41 and 45), and the Telstar detector with threshold at ~0.4 MeV. The shaded areas that are shown represent an upper limit to the natural background flux, the estimate being obtained from measurements made by OV1-2 in December 1965 (Reference 46). For the present comparison, this background is negligible. The curve for

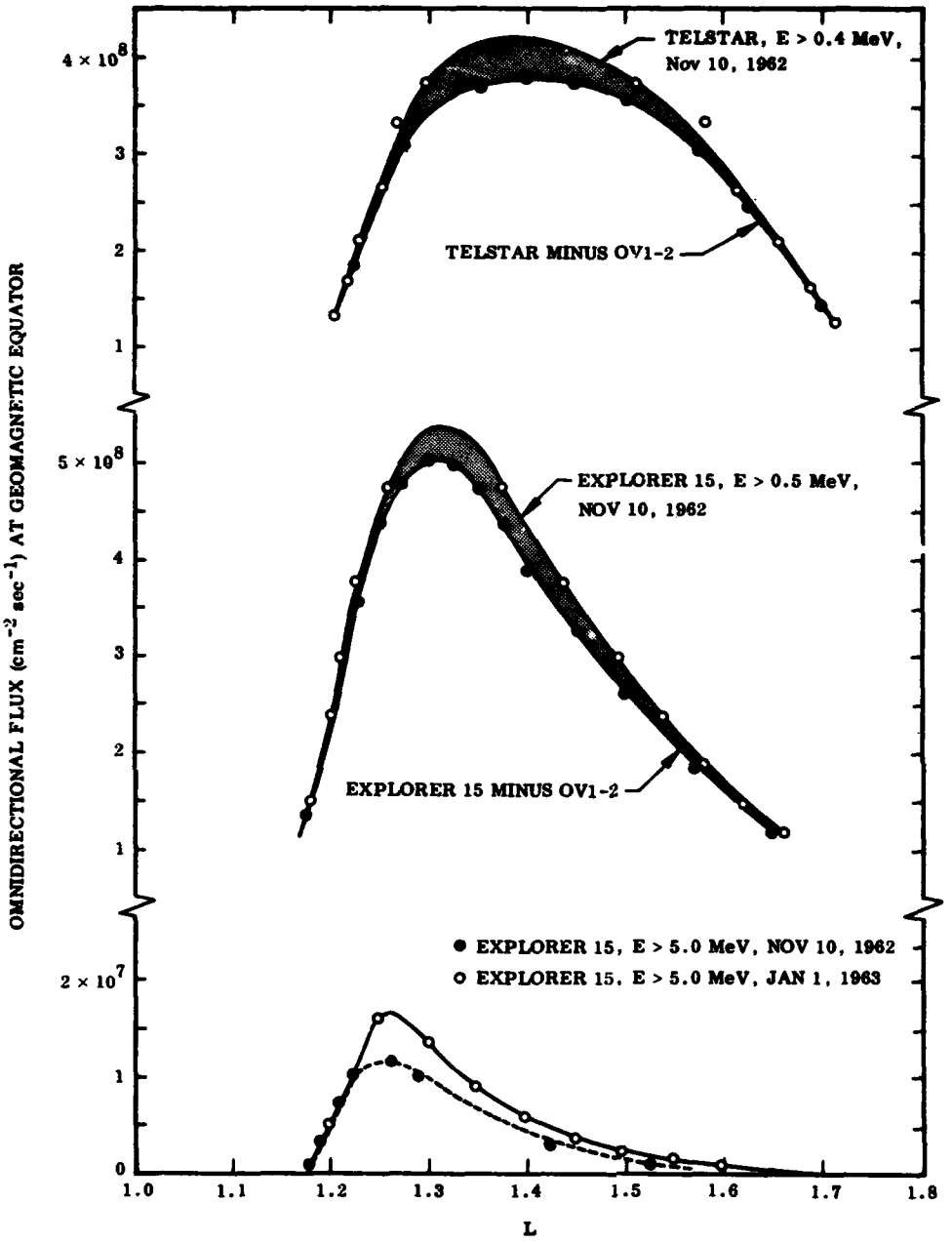

Figure 6-17. Comparison of omnidirectional fluxes in the geomagnetic equatorial plane as a function of L, several months after Starfish.

Telstar was determined from Telstar data by Newkirk and Walt (unpublished). The salient feature of Figure 6-17 is that the distribution becomes more widespread in L as the energy threshold of the detector is decreased, i.e., the less energetic electrons are at larger L. Consequently, the differences between the initial distributions from Telstar and Injun I may well result from the spectrum variations with L.

This conclusion is borne out more explicitly by measurements made with Starad (References 47 and 48) in October and December of 1962. The instrument used was a multichannel magnetic spectrometer that obtained a five-point energy spectrum of the electrons at various L-values. The results are given in Figure 6-18 and show the progressive softening of the electron spectrum with increasing L. Although these data were taken several months after Starfish and a considerable decay of weapon-injected electrons probably has resulted, the spectrum changes appear too large to be attributed to a contamination by the naturally occurring radiation belt particles.

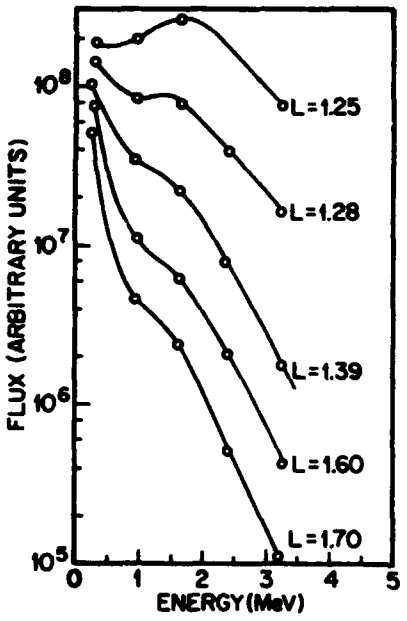

Figure 6-18. Experimental spectra of radiation belt electrons following Starfish (Reference 47).

The Cosmos 5 results do not support this explanation, however. The flux contours based on a low-energy electron detector (estimated energy sensitivity is in the range 15 to 50 KeV) show a very narrow maximum at about L = 1.2 and resemble the Injun I contours more closely than those of Telstar. The Cosmos 5 data have been discounted largely in the present analysis because (1) the energy sensitivity of the detector is uncertain, (2) the spatial coverage is very incomplete and some of the extrapolations performed by the original authors are clearly in error, i.e., assumption of flux independent of B , and (3) the incomplete nature of the published report makes it difficult to evaluate the probable errors in the smoothed results. The alleged maximum at L = 1.2 is based entirely on a 20-percent reduction in the flux in going from about L = 1.2 to 1.21. Thus, a 20-percent error in this region would vitiate the conclusion.

The various estimates of the inventory of electrons artificially added to the belts by the Starfish detonation are listed in Table 6-9. Choosing the best value for the total number of electrons injected by Starfish involves a subjective judgment. Furthermore, since some of the low-energy electrons may be ambient ionospheric electrons that were shock heated to relativistic energies, calculations of the injection efficiency may be meaningless. However, until further data are available, the inventory figure of 7.5×10^{25} recomputed from Telstar data is preferred as the best estimate of the actual inventory. Also, pending further theoretical analyses, the lower energy electrons at $L > 1.5$ are identified as fission electrons that were transported across L-shells by a flute instability or some other electromagnetic effect. Thus, the total number of injected electrons is taken to be 7.5×10^{25}, giving an injection efficiency of about 10 percent.

6.4.4 Decay of the Starfish Radiation Belt

The decay of the Starfish radiation belt has been studied extensively and an enormous body of data has been accumulated. From these data have come the best information to date on the dynamics of trapped electrons at $L \lesssim 2$. In general, the decay is complex—it is not a true exponential and changes more rapidly at early times. Examples of the observed decay are shown in Figure 6-19 from Injun I and Injun III data, and Figure 6-20 from Telstar data. Pre-Starfish background rates in Figure 6-19 are shown by the horizontal bars (Reference 25). Although the decay is not exponential, it has been convenient to approximate the time variation by an exponential function and to designate the lifetime as the time required for the flux to decrease a factor of 1/e. This

Table 6-9. Electron inventories for Starfish.

Starfish Electon Inventory	Satellite	Author	Reference
8×10^{24} > 40 KeV, 6 hours	Injun I	Van Allen, Frank, O'Brien	24
1.3×10^{25}, 10 hours	Injun I	Van Allen	25, 37
1.5×10^{25} E > 20 KeV, 1 hour	Cosmos 5	Galperin	28
2×10^{26}	Telstar	Hess	49
1.2×10^{26}	Telstar	Brown, Gabbe	34
8.8×10^{24} E > 0.5 MeV	Explorer 15	McIlwain	41
9.8×10^{22} E > 5.0 MeV (5 Nov 1962)	Explorer 15	McIlwain	41
$6.6 \pm 2 \times 10^{24}$ E > 500 KeV (Dec 1962)	Starad	West	48
7.5×10^{25}	Telstar	Newkirk, Walt	Recomputed from original data assuming a fission spectrum

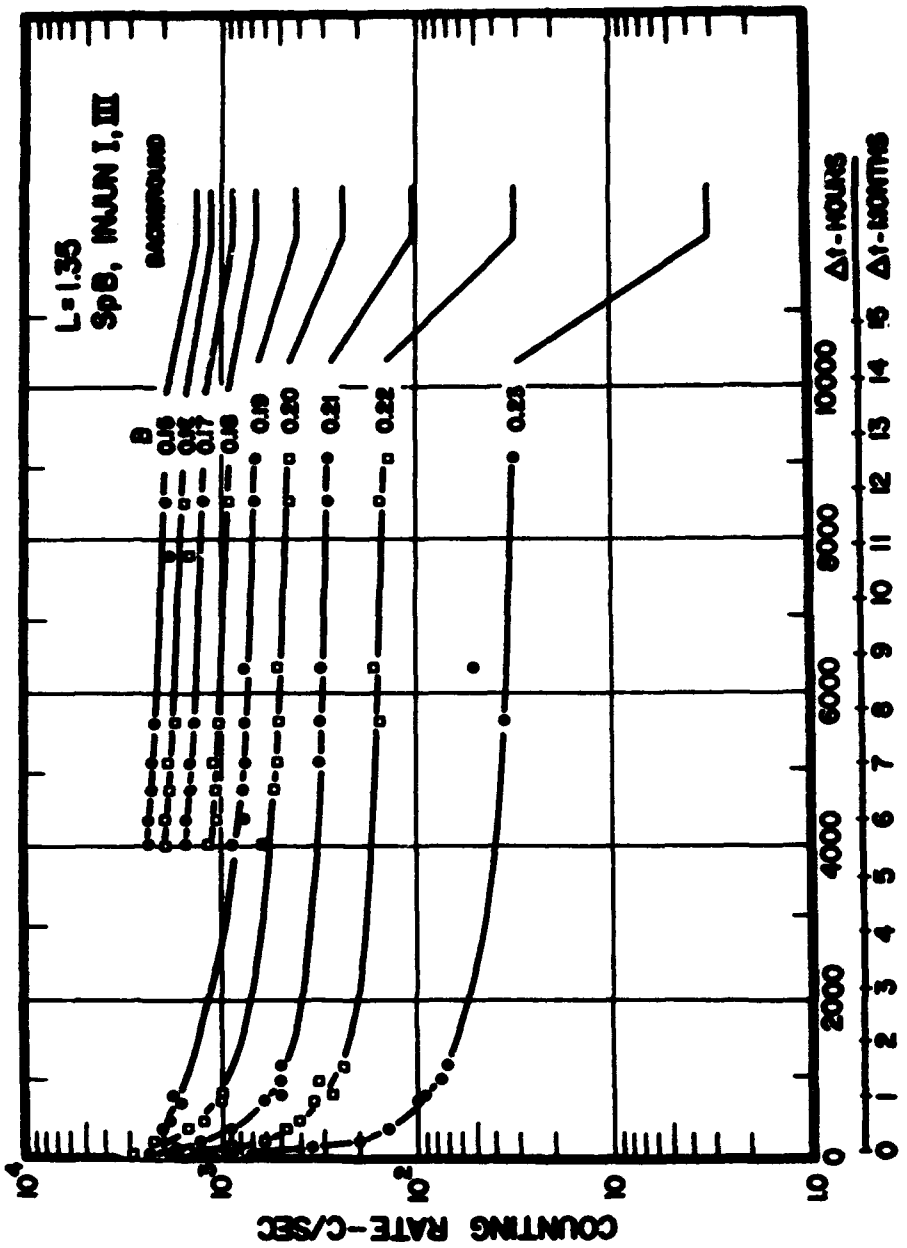

Figure 6-19. Counting rate data from Injun I and Injun III following Starfish.

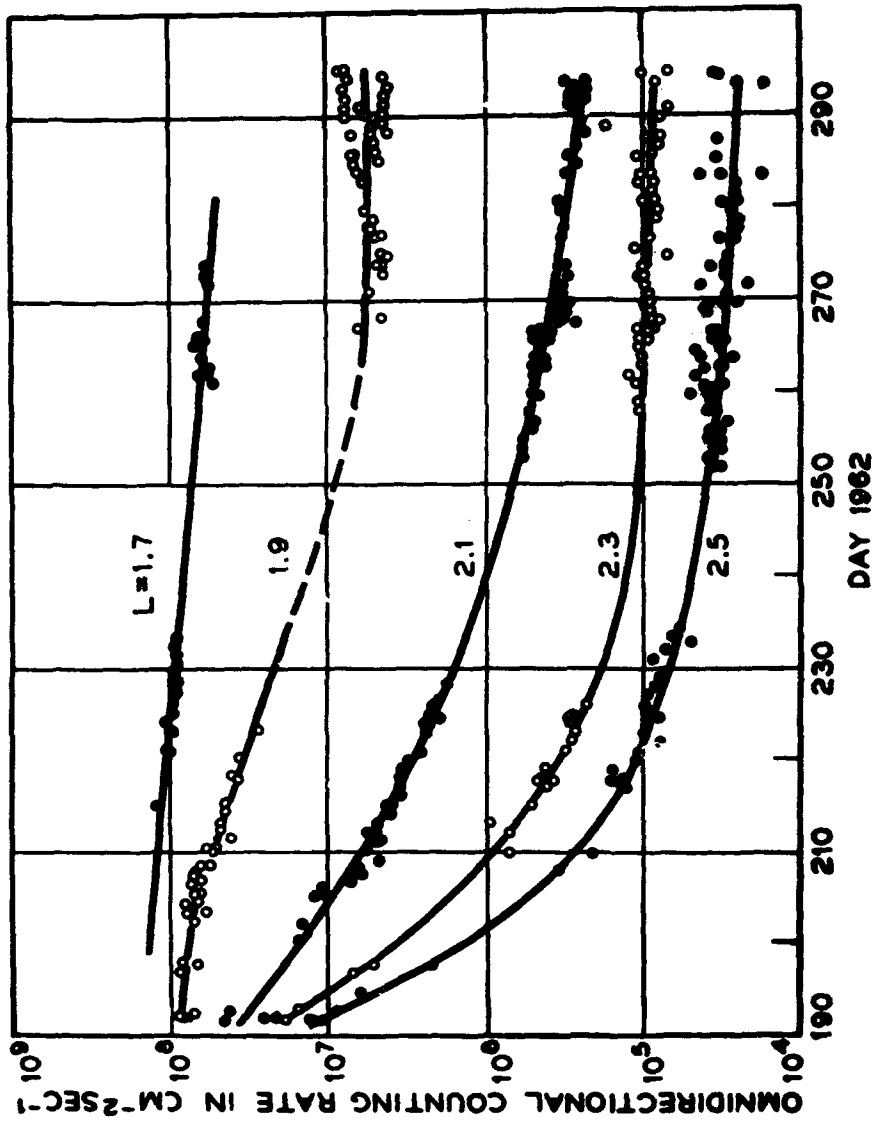

Figure 6-20. Omnidirectional counting rate data from Telstar following Starfish (Reference 23).

lifetime, as obtained by the Starfish decay, depends not only on position in B, L space but also on electron energy and the epoch considered.

The gross decay for $L \leq 1.25$ is well understood in terms of the interaction of electrons with the atmosphere. The agreement between theory and experiment is demonstrated in Figure 6-21. The lower sets of points for B = 0.20, 0.21, and 0.22 gauss have been corrected for the enhanced proton background observed by Filz and Holeman (Reference 51). For $L > 1.25$, the decay is more rapid than can result from this process, so other factors must be involved. Although the mechanism is unknown, empirical values for the apparent lifetime are available. A compilation of apparent electron lifetimes obtained from Starfish and other nuclear tests is given in Figures 5-13 and 5-14.

6.4.5 Interpretation of Starfish Injection

The following description of the formation of an artificial radiation belt by the Starfish detonation is based on the trapped electron populations, the observations of delayed gamma rays in space and in the atmosphere at the conjugate region, and the optical measurements of the expanding debris and the electron-excited aurora.

The geometry of the experiment is depicted in Figure 6-22, which shows the field lines in the meridian plane passing through Johnston Island. The dotted line is the locus of mirroring points of particles that, upon drifting around the earth, will mirror at minimum altitude of 100 kilometers when passing through the South American anomaly. Electrons emitted by fission fragments below this line can be trapped, only transiently, and the long-term trapped electrons must mirror above this line. The location of Starfish in Figure 6-22 is designated by an asterisk.

At detonation time, the debris moved outward and the major fraction was arrested at a distance of <500 kilometers perpendicular to the magnetic field. The debris moved fairly freely parallel to the magnetic field lines and the majority of it was deposited in the atmosphere in the northern and southern hemispheres. Measurements of the quantity of the debris at these locations are very inconclusive but the well-defined debris-excited aurora indicates that the motion of most of the debris was controlled by the field. Photographs of the detonation region show evidence that some of the material did not follow field lines to the south but jetted upward. (Reference 54). This material, perhaps as much as 10 percent of the total fission-fragment content, is expected to have contributed most of the trapped

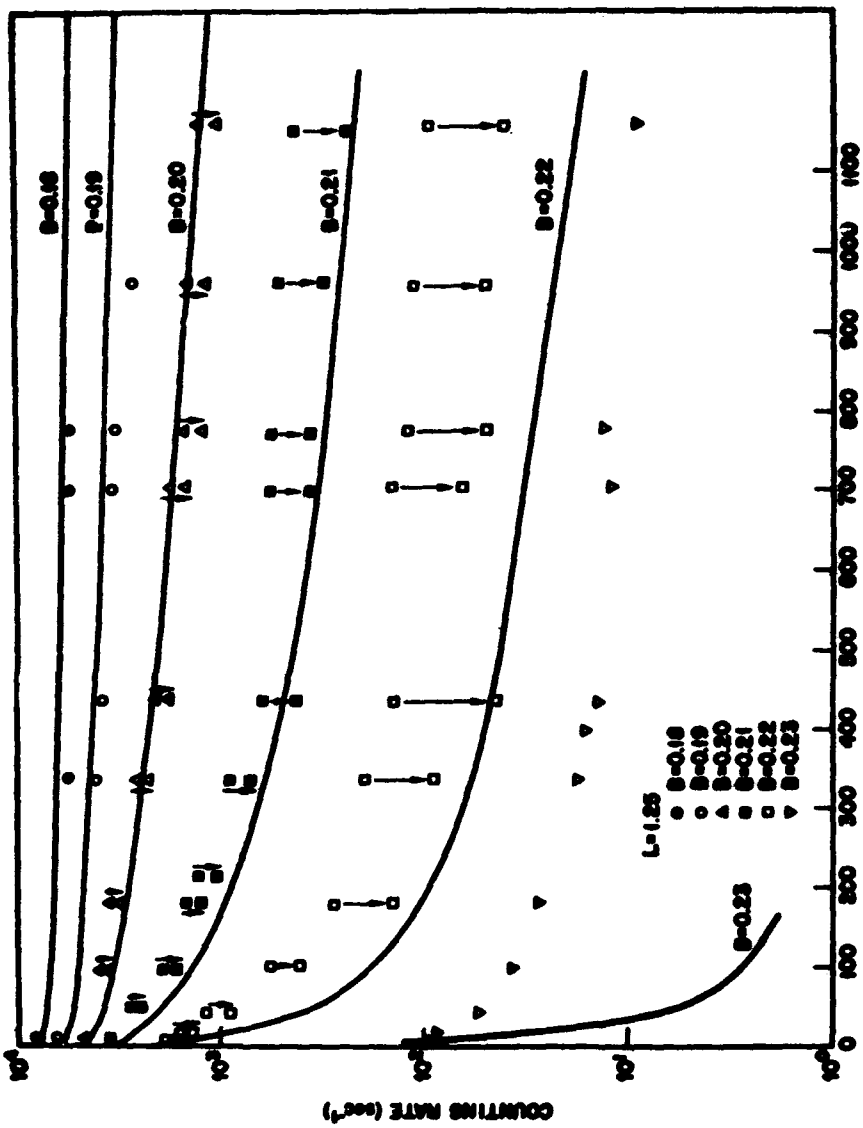

Figure 6-21. Comparison of experimental and theoretical values for the time decay of the Starfish radiation belt (Reference 50).

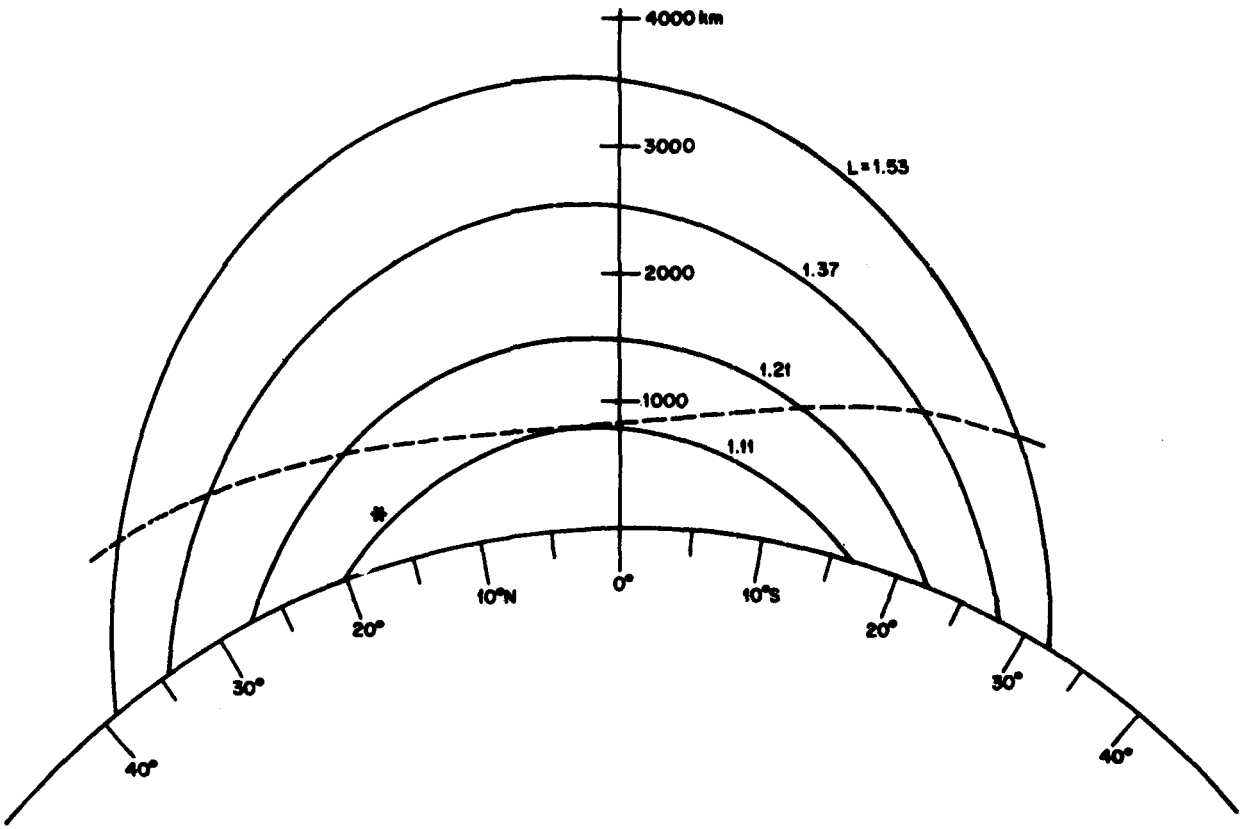

Figure 6-22. Field lines in the meridian plane passing through Johnston Island. The dashed line is the locus of the mirroring points of particles which will drift around the earth to mirror at 100 km altitude in the South American anomaly. The location of Starfish is designated by the asterisk.

electrons, although the jet's reaching L = 7 appears unlikely. Widespread trapped fluxes also could result from fission fragments that were electrically neutral and passed freely across field lines. The means by which trapped electrons were produced at L = 7 is not understood nor is the apparent softening of the electron energy spectrum with increasing L. Several explanations for this softening have been suggested and are discussed:

1. The electrons populating higher L-shells were emitted by fission fragments much later than the average emission time. Since the spectrum of electrons emitted by gross fission fragments becomes less energetic with time, the trapped population also will exhibit this spectrum change. Although this is a possible explanation, the effects being large enough to produce the Injun I and Telstar differences seems unlikely. However, the lack of early time spectral data makes this theory difficult to disprove.

2. The high L-electrons actually were injected at lower L-values but were transported to high L-values by electromagnetic processes that reduced their energy. Several electromagnetic processes—for example, the classical flute instability—are available for this transport. Furthermore, the energy spectrum changes accompanying the transfer to higher L of trapped electrons at constant magnetic moment and integral invariant appear to be adequate. Calculations of the stability of an azimuthally uniform trapped flux from Starfish indicate that the distribution is flute unstable (Reference 54). Also, detailed calculations of the motion of the early time debris tube show this motion to higher L.

3. The higher L-electrons are not fission electrons but are ambient electrons that were accelerated by the shock wave from the explosion. A highly approximate calculation (Reference 55) suggests that sufficient flux could be produced in this way. However, the energy of the electrons excited in this manner does not appear to be sufficient.

4. The electrons were emitted on the inside of the expanding magnetic bubble and were adiabatically decelerated as the bubble expanded. Since the bubble expansion is completed before more than about 5 percent of the electrons are emitted, this mechanism appears unlikely. Furthermore, the electrons would be injected near the burst point ($L \simeq 1.2$) and would not be distributed widely.

6.5 USSR DETONATIONS IN 1962

6.5.1 Introduction

In the fall of 1962, the Soviet Union conducted three high-altitude nuclear weapons tests that produced significant trapping of high-energy electrons. The dates and approximate times of these detonations are given in Table 6-1.

Data on the trapped electrons were obtained by a number of satellites including Telstar 1, Explorer 14, Alouette, Starad (1962 βK), and Explorer 15. Characteristics of these satellites are listed in Table 6-8. Since Starad and Explorer 15 were instrumented specifically to observe the fission-spectrum electrons from Starfish (which occurred on 9 July 1962), the information obtained on the USSR detonations with these two satellites is especially valuable. Unfortunately, both satellites were launched after the 22 October explosion and, therefore, give little information for that event.

Section 6.5.2 summarizes the available trapped electron information that resulted from these explosions. In Section 6.5.3, an assessment of the total inventory of trapped electrons is presented.

6.5.2 Summary of Trapped Particle Data

22 OCTOBER EVENT. Trapped electrons from the 22 October explosion were observed by Telstar, Alouette, and Explorer 14 soon after the detonation. The residual radiation was seen some days later by Explorer 15. Since the orbits of these vehicles were appreciably different, observations were made at significantly different altitudes. Alouette, being a circular polar orbit at $\sim$1,000 kilometers, intercepted the band at low altitude, whereas the Explorer 14 crossings were near the equatorial plane. Telstar, having moderate inclination, is perhaps the most favorably situated of the three. All three satellites had instruments designed to measure natural radiation. Consequently, the energy sensitivities were not optimum for fission-spectrum electrons.

According to measurements made by Alouette, a broad band of electrons was injected, extending from a sharp inner boundary at about $L = 1.8$ to $L = 6$. Explorer 14, on the other hand, did not observe an increase beyond about $L = 3.6$ to 4.2. However, because of the higher natural background experienced by Explorer 14 (due to lower detector thresholds and higher altitude of L-intercepts),

Explorer 14 would not have detected a flux of the magnitude seen by Alouette at $L > 3.6$. Hence, injection probably did occur to about $L = 6$. A double maximum in the L-profile of the belt was suggested by Alouette's data. This observation was confirmed by passes of Explorer 15 made shortly before the second Russian shot.

The most complete flux distributions for this event were derived from Telstar's counting rates (Reference 56). A plot of omnidirectional fluxes in R, λ coordinates is shown in Figure 6-23. The dotted

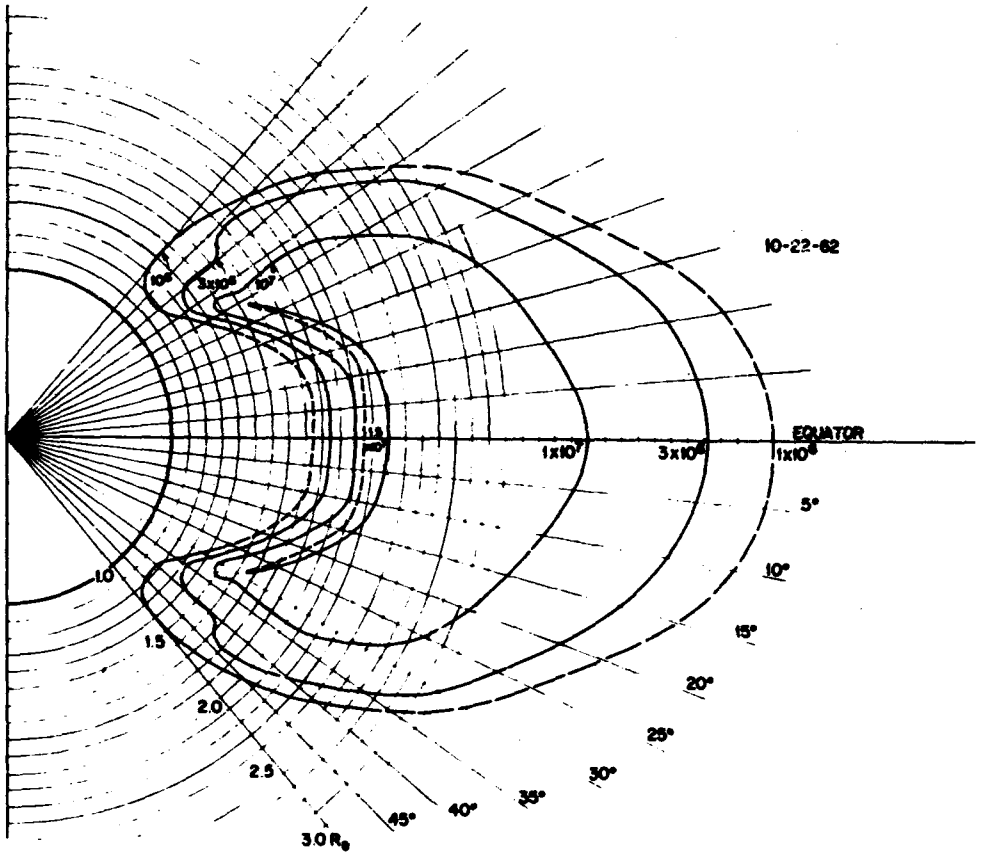

Figure 6-23. Omnidirectional flux (cm^{-2} sec^{-1}) contours (Telstar data) immediately following the Russian test of 22 October 1962 (Reference 56).

contours denote extrapolations based on the spatial derivatives of the flux in the measured regions (solid lines). The numbers shown represent the flux values immediately after injection.

28 OCTOBER EVENT. Because of the large number of radiation measuring satellites in orbit at the time of detonation, the trapped radiation from the 28 October event is better known than that of any other high-altitude nuclear explosion. In particular, the two satellites Explorer 15 and Starad were instrumented to measure energy spectra and angular distributions of fission-fragment electrons. Unfortunately, because the spin rate of Explorer 15 was larger than planned, angular distribution information was not recovered. In the case of Starad, the telemetry and timing system introduced noise and position errors, thereby reducing the value of that satellite. By careful study, some of these difficulties have been overcome, yielding a fairly complete analysis of some of the data from the 28 October test (Reference 38).

In many respects, the trapped radiation produced on 28 October resembled that produced on 22 October. The trapped band had a sharp inner boundary at $L \approx 1.8$ and extended to $L \approx 3.0$ as seen by Alouette and Explorer 15. A well-defined double maximum was apparent with peaks at $L \approx 1.82$ and $L \approx 2.17$ (values slightly E-dependent). A detailed analysis (Reference 38) was presented based on information from a directional spectrometer carried on Starad. From the pitch angle distribution (confirmed in Reference 57), it is clear that a major injection occurred at low altitudes. Several different experimenters report that the energy spectrum was not an equilibrium fission spectrum, at least at some positions. This result implies either that the debris motion extended over many minutes or that some electromagnetic effect altered the energy after the electrons were injected.

Omnidirectional fission-electron fluxes from Telstar also were computed for this event and are given in Figure 6-24 for time zero (Reference 56). In the analysis resulting in the figure, the energy spectrum was assumed to be a fission spectrum at all points, an assumption known to be incorrect. However, the Telstar detector (threshold ≈ 0.4 MeV) is not very sensitive to spectrum changes of the type observed. The contours in the region $L \approx 2$ show maximums off the equator in agreement with the conclusions of West that the injection was at low altitude.

1 NOVEMBER EVENT. The distribution of trapped electrons from the 1 November event was qualitatively different from the two previous

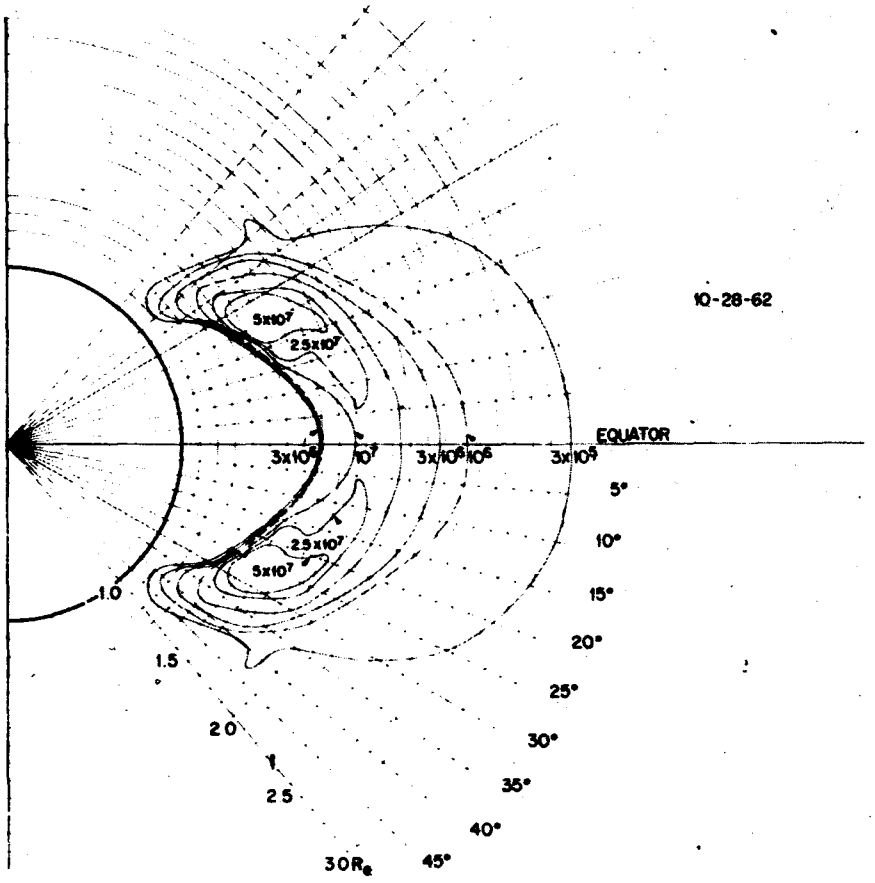

Figure 6-24. Omnidirectional flux (cm^{-2} sec^{-1}) contours (Telstar data) immediately following the Russian test of 28 October 1962 (Reference 56).

ones in that the injection was confined to a narrow band centered at L = 1.766 with a full width at half maximum in the equatorial plane of about 250 kilometers. The best readily available data describing the narrow band and its subsequent decay are given in Reference 23.

No pitch angle distributions have been published, but the observed B-independence of the omnidirectional flux measured by Explorer 15 implies (with some uncertainty) that injection occurred along the entire field line.

6.5.3 Electron Inventories

22 OCTOBER EVENT. Electron inventories for the 22 October event have been obtained from Explorer 14 and Telstar data, and a lower limit to the inventory has been estimated from Alouette data. From Explorer 14 results, Van Allen (Reference 26) estimated that 1.5×10^{24} electrons with energy greater than 230 KeV were trapped (also, see Reference 36). However, this number is questionable because of uncertainties in the geometric factor for fission-spectrum electrons, high natural background, and the restricted spatial coverage. Van Allen was unable to detect any injection above $L = 3.6$, whereas Alouette clearly indicated that high-energy electrons were present out to about $L = 6$.

The Alouette orbit was in the low regions of the radiation belts. However, if the omnidirectional flux is assumed to be constant along field lines, a lower limit to the inventory can be estimated. From the L-shell profile of orbit 316 published in Figure 5 of Reference 35, one derives $>1.15 \times 10^{23}$ electrons above 3.9 MeV or a total electron inventory $>2.9 \times 10^{24}$ electrons, assuming that 4 percent of the fission electrons are above the nominal detector threshold of 3.9 MeV.

The most complete spatial coverage for the 22 October event was given by Telstar (Figure 6-23). The total population derived from that figure is 4.8×10^{25} electrons.

28 OCTOBER EVENT. Similar analyses were made of the Alouette data and the Telstar count rates for the 28 October detonation. The data of Pass 298, shown in Figure 6 of Reference 35, were used for Alouette and gave an inventory of $>3.5 \times 10^{22}$ electrons above 3.9 MeV, or a total of $>8.8 \times 10^{23}$ electrons. The total inventory derived from Telstar data plotted in Figure 6-24 is 1.6×10^{25} electrons. West (Reference 38), using Starad results, obtains inventories of $2.0 \pm 1 \times 10^{25}$, $1.2 \pm 0.5 \times 10^{25}$, and $5.9 \pm 2 \times 10^{24}$ for electrons above 0.2, 0.5, and 1.0 MeV, respectively. From a separate instrument on the same satellite, 5×10^{24} electrons above 1.2 MeV were obtained as cited in Reference 39.

1 NOVEMBER EVENT. Computation of the electron inventory for the 1 November 1962 explosion were derived for three energy thresholds from the published electron fluxes of Brown (Reference 23):

- E > 0.5 MeV 5.6×10^{23} electrons
- E > 1.9 MeV 2.8×10^{23} electrons
- E > 2.9 MeV 8.5×10^{22} electrons .

The ratio of these values is in reasonable agreement with that of a fission source. The value for the 0.5 MeV threshold is rather inaccurate, however, because of the higher background at low energy.

The inventories for the three tests are summarized in Table 6-10, where the first column identifies the satellite, the second column shows the total number of electrons above the detector threshold, and the third column presents the total number of fission electrons detected, assuming that the energy distribution was an equilibrium fission spectrum. The last column includes an adjustment, where available, to correct for factors specified in the footnotes, and gives quantities that are to be compared. There are factors of 10 disagreement in the face values of the inventories for the first two USSR detonations.

The most probable values for the inventories were selected thus: For the 1 November event, the only data available are those of Brown (Reference 23). The internal consistency in his results for the 1 November event and the agreement between the spot checks of his Explorer 15 data with other data for the 28 October electron fluxes argues that the inventory is probably good to better than a factor of 2. Of the three inventory values, the 1.9 MeV threshold result is preferable. The >0.5 MeV channel had high background, and the >2.9 MeV channel contains such a small fraction of the fission spectrum that the inventory is critically dependent on the detector energy sensitivity.

For the 22 October detonation, most of the data has large uncertainties. The orbital period of Explorer 14 was too long for good sampling, and the background was so high that the bomb electrons were not discernible above L = 3.5. Alouette was in a low-altitude orbit and did not sample the most intense fluxes. Furthermore, the geometric factor of the >3.9 MeV detector on Alouette is probably very uncertain since the straggling of electrons in 1.4 grams per square centimeter of material is very difficult to estimate. Telstar has the best orbit but the detectors have poor energy selectivity for fission-spectrum electrons. However, in spite of the uncertainties

Table 6-10. Electron inventories for the USSR tests.

Satellite	Measured Value		Total Observed Electrons E > 0	Inventory Estimate
22 October				
Explorer 14	1.5×10^{24}	E > 230 KeV (L < 3.5)	1.8×10^{24}	4.5×10^{24}[a]
Alouette	1.15×10^{23}	E > 3.9 MeV	2.9×10^{24}	2.9×10^{24}
Telstar			4.8×10^{25}	4.8×10^{25}
28 October				
Explorer 14	1.5×10^{24}	E > 230 KeV	1.8×10^{24}	3.6×10^{24}[b]
Alouette	3.5×10^{22}	E > 3.9 MeV	8.8×10^{23}	8.8×10^{23}
Telstar			1.6×10^{25}	1.6×10^{25}
Starad (Reference 39)	5×10^{24}	E > 1.2 MeV (L > 1.9)	1.2×10^{25}	1.35×10^{25}[c]
Starad (Reference 38)	2.0×10^{25}	E > 200 KeV	2.3×10^{25}	2.3×10^{25}
	1.2×10^{25}	E > 500 KeV	1.7×10^{25}	1.7×10^{25}
	5.9×10^{24}	E > 1.0 MeV	1.2×10^{25}	1.2×10^{25}
1 November				
Explorer 15	5.6×10^{23}	E > 0.5 MeV	7.9×10^{23}	
	$2.8\ 10^{23}$	E > 1.9 MeV	1.19×10^{24}	1.2×10^{24}
	8.5×10^{22}	E > 2.9 MeV	8.0×10^{23}	

Notes:

[a] Increased by 25 percent for electrons at L > 3.5 on the basis of the Telstar distributions and increased by a factor of 2 to allow for a rapid decay in the 2 days between injection and sampling by Explorer 14.

[b] Increased by a factor of 2 to allow for the decay between the 28 October and the sampling period on ~ 30 October.

[c] Increased by 12 percent for electrons at L < 1.9 on the basis of the distributions measured with Telstar.

in the geometric factor of Telstar, the ratio of inventories for the 22 October and 28 October tests obtained by Telstar should be accurate. This ratio is about 3. The ratio of the 22 to 28 October test as computed from Alouette is also 3, although this agreement is probably fortuitous.

For the 28 October detonation, the inventory of $\sim 1.2 \times 10^{25}$ electrons appears to be the most accurate. This figure was obtained independently by two groups (References 38 and 39), using different instruments. Although West's three inventory determinations scatter by a factor of 2, the value associated with a threshold of 1.0 MeV was selected since the background is lowest at that energy. This inventory value obtained from Starad is in rather good agreement with the Telstar result of 1.6×10^{25}, a fact that supports the Telstar figure for the 22 October explosion. Since the absolute values of the Starad fluxes are probably better than those of Telstar, the Starad value for the 28 October test is accepted and the Telstar ratio of 22 to 28 October inventories is used to find the inventory for the 22 October explosion. The final results for total electron inventories, $E > 0$ are:

- Event 1—22 October, 3.6×10^{25} electrons
- Event 2—28 October, 1.2×10^{25} electrons
- Event 3—1 November, 1.2×10^{24} electrons .

The low values for inventories deduced from Alouette were disregarded because the low-altitude orbit did not sample the intense fluxes and because of uncertainties in the geometric factors. The assumption used in the inventory calculation (flux at constant-L is independent of B) is obviously wrong on the basis of the Telstar distributions.

A substantial disagreement still remains between the values from Explorer 14 and the final values selected, the difference being a factor of 8 for Event 1 and a factor of 3.5 for Event 2. In the case of Event 2, the concentration of flux off the equatorial plane (Figure 6-24) would result in a lower inventory being measured by Explorer 14. The discrepancy for Event 1 still is unresolved. However, since the Telstar orbit is much superior for sampling the artificial belt, the Explorer 14 data have been ignored in computing inventories.

REFERENCES

1. G. L. Johnson and R. B. Dyce. A Study of Explorer IV Records in the Pacific Area, Stanford Research Institute, FO-0-111, Menlo Park, Calif., 1960.

2. S. Matsushita. "On Artificial Geomagnetic and Ionospheric Storms Associated with High-Altitude Explosions," J. Geophys. Res., 64, 1149-1161, 1959.

3. J. A. Van Allen, C. E. McIlwain, and G. H. Ludwig. "Satellite Observations of Electrons Artificially Injected into the Geomagnetic Field," J. Geophys. Res., 64, 877-891, 1959.

4. M. Walt. "Loss Rates of Trapped Electrons by Atmospheric Collisions," Radiation Trapped in the Earth's Magnetic Field, ed. by B. M. McCormac, D. Reidel Publishing Co., Dordrecht, 336-351, 1966.

5. R. W. Porter. "Symposium of Scientific Effects of Artificially Introduced Radiations at High Altitudes," J. Geophys. Res., 64, 865-867, 1959.

6. N. C. Christofilos. "Sources of Artificial Radiation Belts," Radiation Trapped in the Earth's Magnetic Field, ed. by B. M. McCormac, D. Reidel Publishing Co., Dordrecht, 565-575, 1966.

7. J. A. Van Allen. ARGUS I Observations with Explorer IV Satellite, State University of Iowa, Report, Department of Physics, 1959.

8. J. A. Van Allen. ARGUS II Observations with Explorer IV Satellite, State University of Iowa, Report 59-14, 1959.

9. J. A. Van Allen. ARGUS III Observations with Explorer IV Satellite, State University of Iowa, Report 59-15A, 1959.

10. J. A. Van Allen. ARGUS III Observations with Explorer IV Satellite, Vol. II, State University of Iowa, Report 59-15B, 1959.

11. A. H. Weber, R. M. Delaney, J. F. Fennell, J. A. George, D. J. Manson, R. J. Ockersz, J. M. Paikeday, and J. K. Bock. Analysis of ARGUS/Explorer IV Records, DASA, Report 1613, Saint Louis University, Physics Department, 1965.

12. A. H. Weber, A. F. Brisken, M. E. Coughlin, J. F. Fennell, J. A. George, Wm. K. Kottmeyer, D. J. Manson, J. R. Ockersz, and J. M. Paikeday. Further Detailed Analysis of Telemetry Records Obtained by Explorer IV Satellite Concerning Geomagnetically Trapped Radiation, DASA, Report 1889, Saint Louis University, Department of Physics, 1966.

13. D. J. Manson, J. A. George, J. M. Paikeday, J. F. Fennell, R. M. Delaney, and A. H. Weber. Unidirectional and Omnidirectional Flux Densities of Trapped Particles in ARGUS Shells and the Inner Van Allen Belt, Explorer 4 Satellite Data, DASA, Report 2052-1, Saint Louis University, Physics Department, 1968.

14. L. Allen, J. L. Beavers, W. A. Whitaker, J. A. Welch, and R. B. Walton. "Project Jason Measurement of Trapped Electrons from a Nuclear Device by Sounding Rockets," J. Geophys. Res., 64, 893-907, 1959.

15. Analysis of Jason Data, Final Report, Lockheed Missiles & Space Company, AFSWC-TR-61-82, Palo Alto, Calif., 1961.

16. J. B. Cladis and M. Walt. "Behavior of Geomagnetically Trapped Electrons Injected by High-Altitude Nuclear Detonations," J. Geophys. Res., 67, 5035-5054, 1962.

17. Army Ballistic Missile Agency (Huntsville, Ala.) and Smithsonian Astrophysical Observatory (Cambridge, Mass.), "Explorer IV—1958 Epsilon," Orbital Data Series Issue 6, 6 Vols., 1959.

18. J. A. Van Allen, C. E. McIlwain, and G. H. Ludwig. "Radiation Observations with Satellite 1958 Epsilon," J. Geophys. Res., 64, 271-286, 1959.

19. E. O. Baicy, J. Bock, and T. R. Jeter. The ARGUS Experiment Calibration of Explorer IV Prototype, Defense Atomic Support Agency, Report WT-1671, Ballistic Research Laboratory, Aberdeen, Md., 1963.

20. D. J. Manson. Van Allen Radiation Belt and ARGUS Directional Flux Density Distributions, Explorer IV Satellite Data, Ph. D. dissertation, Saint Louis University, Department of Physics, 1966.

21. J. A. George. Omnidirectional Fluxes; Explorer IV Satellite Data, ARGUS Events 1 and 2, Ph. D. dissertation, Saint Louis University, Department of Physics, May 1966.

22. C. E. McIlwain. "Coordinates for Mapping the Distribution of Magnetically Trapped Particles," J. Geophys. Res., 66, 3681-3691, 1961.

23. W. L. Brown. "Observations of the Transient Behavior of Electrons in the Artificial Radiation Belts," Radiation Trapped in the Earth's Magnetic Field, ed. by B. M. McCormac, D. Reidel Publishing Co., Dordrecht, 610-633, 1966.

24. J. A. Van Allen, L. A. Frank, and B. J. O'Brien. "Satellite Observations of the Artificial Radiation Belt of July 1962," J. Geophys. Res., 68, 619-627, 1963.

25. J. A. Van Allen. "Spatial Distribution and Time Decay of the Intensities of Geomagnetically Trapped Electrons from the High Altitude Nuclear Burst of July, 1962," Radiation Trapped in the Earth's Magnetic Field, ed. by B. M. McCormac, D. Reidel Publishing Co., Dordrecht, 575-593, 1966.

26. J. A. Van Allen. State University of Iowa, Report SUI 63-67, Iowa City, Iowa, 1963.

27. Y. I. Galperin and A. D. Bolyunova. Space Research, 5, North-Holland Publishing Co., Amsterdam, 446-458, 1965.

28. Y. I. Galperin. "Physical Picture of the Origin of the Artificial Radiation Belt During the American High-Altitude Thermonuclear Explosion of 9 July 1962," Issled. Kosmich. Prost., Nauka, 388-393, 1965.

29. A. C. Durney, H. Elliot, J. J. Hynds, and J. J. Quenby. "Satellite Observations of the Energetic Particle Flux Provided by the High-Altitude Nuclear Explosion of July 9, 1962," Nature, 195, 1245-1248, 1962.

30. H. Elliot. "Some Cosmic Ray and Radiation Belt Observations Based on Data from the Anton 302 G-M Counter in Ariel I," Radiation Trapped in the Earth's Magnetic Field, ed. by B.M. McCormac, D. Reidel Publishing Co., Dordrecht, 76-100, 1966.

31. A.C. Durney, H. Elliot, R.J. Hynds, and J.J. Quenby. "The Artificial Radiation Belt Produced by the Starfish Nuclear Explosion," Proc. Roy. Soc. A, 281, 565-583, 1964.

32. G.K. Pieper. "A Second Radiation Belt from the July 9, 1962, Nuclear Detonation," J.Geophys.Res., 68, 651-657, 1963.

33. W.L. Brown, J.D. Gabbe, and W. Rosenzweig. "Results of the Telstar Radiation Experiments," Bell System Tech. J., 42, 1505-1559, 1963.

34. W.L. Brown and J.D. Gabbe. "The Electron Distribution in the Earth's Radiation Belts During July, 1962, as Measured by Telstar," J.Geophys.Res., 68, 607-619, 1963.

35. J.R. Burrows and I.B. McDiarmid. "A Study of Electrons Artificially Injected into the Geomagnetic Field in October, 1962," Can. Jour. Phys., 42, 1529-1547, 1964.

36. L.A. Frank, J.A. Van Allen, and H.K. Hills. "A Study of Charged Particles in the Earth's Outer Radiation Zone With Explorer 14," J.Geophys.Res., 69, 2171-2191, 1964.

37. J.A. Van Allen. Further Observations on the Starfish and Soviet Artificial Radiation Belts, State University of Iowa, Report SUI 63-37, Department of Physics, State University of Iowa, Iowa City, Iowa, 1963.

38. H.I. West, Jr. "Some Observations of the Trapped Electrons Produced by the Russian High-Altitude Nuclear Detonation of October 28, 1962," Radiation Trapped in the Earth's Magnetic Field, ed. by B.M. McCormac, D. Reidel Publishing Co., Dordrecht, 634-662, 1966.

39. W.L. Imhof, E.E. Gaines, D.R. King, G.H. Nakano, R.V. Smith, and F.J. Vaughn. Analysis and Evaluation of Measurements of Geomagnetically Trapped Electrons from High Altitude Nuclear Explosions, Lockheed Missiles & Space Company, Report 1540, Palo Alto, Calif., 1964, 119 pp.

40. Interim Results of Radiation Measurements from Air Force Satellite 1962, Air Force Cambridge Research Laboratories, Report 17, June 1963 (unpublished).

41. C.E. McIlwain. "Measurements of the Trapped Electron Intensities Made by the Explorer XV Satellite," Radiation Trapped in the Earth's Magnetic Field, ed. by B.M. McCormac, D. Reidel Publishing Co., Dordrecht, 593-610, 1966.

42. C.O. Bostrom and D.J. Williams. "Time Decay of the Artificial Radiation Belt," J.Geophys.Res., 70, 240-243, 1965.

43. D.J. Williams and A.M. Smith. "Daytime Trapped Electron Intensities at High Latitudes at 1100 km," J.Geophys.Res., 70, 541-557, 1965.

44. D.S. Beall, C.O. Bostrom, and D.J. Williams. "Structure and Decay of the Starfish Radiation Belt, October, 1963, to December, 1965," J.Geophys.Res., 72, 3403-3425, 1967.

45. C.E. McIlwain. "The Radiation Belts, Natural and Artificial," Science, 142, 355-361, 1963.

46. M.C. Chapman and T.A. Farley. "Absolute Electron Fluxes and Energies in the Inner Radiation Zone in 1965," J.Geophys. Res., 73, 6825-6835, 1968.

47. H.I. West, Jr., L.G. Mann, and S.D. Bloom. University of California, Report UCRL-7659, TID-4500, (29th Ed.), 1964.

48. H.I. West, Jr. "The Trapped Electron Spectra from the Starfish Detonation and from the Outer Belt in the Fall of 1962," Radiation Trapped in the Earth's Magnetic Field, ed. by B.M. McCormac, D. Reidel Publishing Co., Dordrecht, 663-666, 1966.

49. W.N. Hess. "The Artificial Radiation Belt Made on July 9, 1962," J.Geophys.Res., 68, 667-685, 1963.

50. M. Walt and L.L. Newkirk. "Addition to Investigation of the Decay of the Starfish Radiation Belt," J.Geophys.Res., 71, 3265-3266, 1966.

51. R.C. Filz and E. Holeman. "Time and Altitude Dependence of 55-MeV Trapped Protons, August, 1961, to June 1964," J.Geophys. Res., 70, 5807-5822, 1965.

52. J. A. Van Allen. Further Observations on the Starfish and Soviet Artificial Radiation Belts, State University of Iowa, Report SUI 63-37, Department of Physics, State University of Iowa, Iowa City, Iowa, 1963.

53. J. Zinn, H. Hoerlin, and A. G. Petschek. "The Motion of Bomb Debris Following the Starfish Test," Radiation Trapped in the Earth's Magnetic Field, ed. by B. M. McCormac, D. Reidel Publishing Co., Dordrecht, 671-693, 1966.

54. J. B. Cladis, G. T. Davidson, W. E. Francis, L. L. Newkirk, L. R. Tepley, M. Walt, and R. C. Wentworth. Search for Possible Loss Processes for Geomagnetically Trapped Particles, Lockheed Missiles & Space Company, Report M-57-65-1, DASA 1713, Palo Alto, Calif., 1965, 128 pp.

55. S. A. Colgate. "Energetic Electrons from Shock Heating in the Exosphere," Radiation Trapped in the Earth's Magnetic Field, ed. by B. M. McCormack, D. Reidel Publishing Co., Dordrecht, 693-703, 1966.

56. R. A. Berg, J. B. Cladis, G. T. Davidson, W. E. Francis, E. F. Gaines, L. L. Newkirk, and M. Walt. Trapping at High L Values of Beta Particles from Nuclear Explosions, Vol. I, Lockheed Missiles & Space Company, Report LMSC-BO39917, DASA 1984, Palo Alto, Calif., 1967, 78 pp.

57. L. D. Katz, D. Smart, F. R. Paolini, R. Giacconi, and R. J. Talbot. "Measurements on Trapped Particles Injected by Nuclear Detonations," Space Research, 4, North-Holland Publishing Co., 646-664, 1964.

SECTION 7

PARTICLE INJECTION BY NUCLEAR DETONATIONS

G.T. Davidson, Lockheed Palo Alto Research Laboratory
R.W. Hendrick, Jr., General Electric Company—TEMPO

7.1 INTRODUCTION

The particles injected by a high-altitude nuclear detonation into the earth's magnetic field are predominantly electrons (as was evident in the observational results discussed in Section 5), some protons, and perhaps a small number of other particles such as positrons, deuterons, tritons, and α-particles. The primary source of protons is neutron decay; usually the trapped protons contributed by the bomb are insignificant compared with the much more numerous naturally trapped protons. Positron production in the typical nuclear explosion is negligible; but by appropriate design, such as placing a shell of copper around the bomb, a significant yield of positrons could be produced. The positrons, being readily distinguishable from natural and artificial trapped electrons, might be a useful diagnostic tool in studying the earth's magnetic field and the decay processes of the trapped particles. The production of other particles, such as deuterons, is unimportant.

The injection of electrons by nuclear detonations into artificial radiation belts requires a source of electrons and a mechanism for trapping them. They may be injected directly into trapped orbits when they are produced as free electrons. Alternatively, they may experience perturbations that alter their trajectories so that ultimately they are trapped in stable orbits. Electron sources will be considered first, then trapping in general, radioactive debris motion, and, finally, the trapping that results from specific configurations.

7.2 SOURCES OF ELECTRONS

7.2.1 Decay of Fission Debris

Probably the most important source of electrons—certainly the most important source of electrons of energy greater than 1 MeV—is the radioactive debris remaining from the fission process. As they decay toward the stable isotropes, fission products provide large numbers of beta decay electrons. Pertinent properties of the

radioactive debris, such as mass distribution, beta decay rate, and beta energy spectra, are discussed in Section 11.2. The average energy of the beta electrons (Figure 1-2) declines with time after fission. Consequently, the initial energy spectrum of trapped electrons can vary according to the time required for the arrival of debris at a given point. The strength of this source can be appreciated by realizing that the total energy of the electrons produced by the debris from 1 megaton of fission yield is 1 to 2 orders of magnitude greater than the energy of electrons normally in the inner belt.

Free neutrons have a decay half-life of about 1,000 seconds. The resulting products of a single decay event are a proton, an electron (or beta ray), and an antineutrino. The proton retains most of the kinetic energy of the original neutron. The electron is left with an average of about 300 KeV of the total. Typically, neutron-decay electrons account for about 0.5 percent of the total yield. These electrons are emitted in the course of the neutron flight. Because neutrons decay slowly, only those traveling at speeds between 2 and 100 kilometers per second remain in the geomagnetic field long enough to contribute significantly to injection. Although some low-energy neutrons are produced by a nuclear detonation, the majority of slow neutrons are a result of thermalization and reflection of neutrons by the atmosphere. This source has been investigated previously (References 1 and 2). The decay of neutrons has been shown to contribute primarily to the outer Van Allen belt. A multi-megaton detonation conceivably could double the radiation intensity in the outer region. However, it should not be expected to create any "hot" spots of greatly enhanced dose rates.

Hydromagnetic compressions and shock waves may produce an acceleration of ambient electrons to higher energies, but evoking such processes to account for the nuclear test data has been unnecessary.

7.2.2 Debris Motion—Low-Altitude Detonations

So that the injected electron population may persist, injection must occur at hundreds or thousands of kilometers altitude. The processes that lead to the motion of debris toward high altitudes vary with detonation altitude. First consider low-altitude detonations. Radioactive debris and thermal radiation from the weapon are restrained by collisions with air atoms. The resulting fireball is small compared to the atmospheric scale height (Reference 3). In this case, the fireball rises only slightly and debris will not attain great enough altitudes for persistent trapping.

Hot fireballs formed by detonations are very buoyant, and the buoyancy and shock interactions can accelerate the fireballs to velocities of several kilometers per second. If little overlying air exists, this rise is not impeded appreciably, and the fireball can travel upward on a ballistic trajectory, expanding as it progresses, into a more tenuous atmosphere. An approximate criterion for this behavior can be obtained by considering the mass of air per unit area-the areal density - above and within a fireball that spans an atmospheric scale height. The ratio of masses is about 1:2. Consequently, even if all the air directly above the fireball were accelerated to the fireball velocity, the fireball would not extract much energy or momentum from the original fireball. Thus, if the fireball radius is at least comparable to the atmospheric scale height, this ballistic rise of fireball and debris will carry the radioactive debris rapidly upward to great heights.

Approximately half the energy of a detonation is radiated away and half remains in the fireball at a temperature of 6,000 to 8,000 K (Reference 4). The heat content of air is about 10^4 cal/gm at these temperatures. The fireball radius for a megaton detonation therefore will be greater than half a scale height—about 4 kilometers—if it is above about 60 kilometers.

The radioactive debris in rising fireballs can cause injection into the trapped radiation belts in two ways: (1) If the debris is carried sufficiently high, electrons emitted in the fireball may escape whereupon they can be trapped in the geomagnetic field (the air is sufficiently tenuous that beta rays lose little energy escaping the fireball). This mechanism applies to the bulk of the beta emitting debris. (2) Some individual debris particles may be able to escape the fireball even though the fireball proper may not reach the altitudes necessary for persistent electron trapping. An atom that undergoes beta decay recoils to conserve momentum. Typical recoil velocities are 3 to 5 km/sec, provided that the energy of the emitted electron is a few million eV. If it is near the edge of the fireball, a recoiling atom can escape and travel upwards with the recoil velocity. These atoms may still not be stable isotopes and, hence, may emit yet more decay electrons at higher altitudes where persistent trapping may occur. A recoiling atom itself may be trapped in the geomagnetic field and may travel a considerable distance along the field lines before emitting subsequent beta electrons.

The recoil process is inefficient because the collisional cross sections of atoms are excessive at energies of several eV. (Although

each species will have a different collisional cross section, atom-atom momentum-exchange cross sections at velocities of a few kilometers per second are of the order of 3×10^{-16} cm^2). No more than about 1 percent of recoil atoms are near enough to the surface of the fireball to escape.

DETONATIONS ABOVE 100 KILOMETERS. For very high detonations, the fireball material will not recombine but will remain ionized. It will rise as a radioactive diamagnetic sphere through ionosphere and geomagnetic field. The effects of interactions with the ambient geomagnetic field will be to (1) reduce the expansion perpendicular to the magnetic field, (2) produce a gross force (predominantly upward) on the diamagnetic fireball due to the gradient of the geomagnetic field, (3) cause freezing of local magnetic field lines into the fireball, (4) generate a horizontal electric field due to the eastward drift of the beta rays and the westward drift of the positive ions, and (5) cause the sloughing of an outer plasma magnetic field interaction zone.

These various effects will modify different aspects of electron injection into the geomagnetic field. The restriction of expansion across the field will result in injection over a limited range of L-parameter. The injection therefore is relatively intense. The extent of the intense-injection region will depend upon the motion of the ionized plasma, but it can be measured in terms of the diameter of the fireball when the internal gas pressure falls to equilibrium with the magnetic field pressure.

Diamagnetic and charge-separation forces will modify the trajectory of the fireball, causing deviation from a strictly ballistic trajectory. Diamagnetic forces can be significant compared to gravity only if the gas is very hot. The diamagnetic force will be several times the product of gas volume by the gradient of the magnetic field pressure. The exact factor depends upon the shape of the diamagnetic volume, but it is usually between 1 and 2 for reasonable shapes. For illustrative purposes, a value of 2 may be presumed.

The ratio of diamagnetic to gravitational force on the volume as a whole will be

$$\frac{F_d}{F_G} \approx \frac{2}{\rho g} \frac{B^2}{8\pi} \frac{6}{r} \qquad (7\text{-}1)$$

where r is the geocentric distance to the burst point, ρ is the gas density, g is the gravitational constant [$\approx 980(R_E/R_E + h)^2$ cm^2/sec], and B is the geomagnetic field intensity. The magnetic forces will not be significant until the gas pressure in the fireball decreases to the point where it attains equilibrium with the geomagnetic field (Section 5.4.1). In this situation, the internal particle energy density is nearly equal to the magnetic energy density $B^2/8\pi$. The particle energy density is of order $1/2\,\rho v_\perp^2$, where $v_\perp$ is the mean velocity perpendicular to the field. Equation 7-1 then becomes

$$\frac{F_d}{F_G} = \frac{6v_\perp^2}{gr} \quad . \tag{7-2}$$

If the diamagnetic force is to exceed the gravitational force, a mean velocity exceeding about 3.4 kilometers per second is required. This corresponds to a 1.6-eV temperature. At altitudes below about 200 kilometers, the radiation properties of air are such that temperatures can remain this high for only a few seconds. Consequently, diamagnetic forces could produce significant effects only for detonations above about 200-kilometers altitude. Even above 200 kilometers, the effects are important only while the fireball is intact—a period of several seconds at most.

The conductivity of a fireball plasma temporarily prevents those field lines that passed through the original fireball from leaving the fireball even though it moves. This freezing of magnetic field lines causes injection of electrons on the detonation field lines until those magnetic field lines can escape either by gradual diffusion or turbulent breakup of the fireball. During this frozen-in phase, beta decay electrons will be produced in the fireball in a region of low magnetic field strength. Substantial numbers appear susceptible to being trapped in an expanding magnetic bottle and could lose considerable energy before they are scattered sufficiently to escape the trap. After leaving the bottle, they may still have a very short life against loss in the atmosphere. In short, magnetic field freezing can prevent injection of electrons on elevated magnetic shells until this phase passes.

"Sloughing" will leave radioactive debris distributed in the wake of the fireball. This debris can later emit beta decay electrons. Between the fireball proper and the ambient exterior magnetic field is an interaction zone in which fireball, ambient gas, and magnetic

field materials are mixed. As the fireball rises, this interaction zone tends to be sloughed off by the retarding effect of the magnetic field. Sloughed material will continue along the magnetic field line until stopped by collisions with air molecules or gravity. It may still reach great heights but on L-shells quite different from the bulk of the fireball.

Some of the high-speed debris can escape as independent particles. The first portion to escape is that directed along the geomagnetic field. Above about 100 kilometers, coupling between the expanding bomb debris and the ambient air is through hydromagnetic interactions rather than through atom-atom momentum-exchange collisions as in lower altitude hydrodynamics (Reference 4). The weapon debris is ionized initially. The tendency of the expanding debris to "sweep" up the magnetic field is resisted by the inertia of other low-velocity air ions. The air ions may be preexisting ionospheric ions, ions produced by absorption of X rays from the detonation, or ions produced by interactions in the hydromagnetic shock wave driven by the debris. However, this mechanism is ineffective in the direction of the magnetic field, so atoms directed initially along the field may behave as independent particles.

Initial debris particle velocities are of the order of 10^8 cm/sec. At this speed, fission fragments with mass number near 100 have an energy of about 0.5 MeV and a range in air of several hundred micrograms/cm^2. Consequently, they can escape along the geomagnetic field from an altitude of about 100 kilometers if the magnetic field line inclination is large. These particles can reach altitudes conducive to persistent injection in a matter of a few seconds. They then will be guided by the geomagnetic field to the conjugate region and deposited there. During their traversal, they may emit beta decay electrons, which are injected into the radiation belts. Typically, the time of flight will be several tens of seconds. Thus, roughly half the potential beta yield from these atoms can be trapped in the geomagnetic field in a region containing the detonation L-shell.

DETONATIONS ABOVE 200 KILOMETERS. For detonations above several hundred kilometers altitude, insufficient material may exist above the detonation to restrain the upward-directed debris in its initial expansion. The mass per solid angle that is swept up by an expanding spherical surface in an atmosphere having a density that declines exponentially with a scale height H is

$$\frac{\Delta m}{\Delta \Omega} = 2\rho^* H^3 \qquad (7\text{-}3)$$

where ρ^* is the density at the origin of the expansion. If the mass of overlying atmosphere is less than about 100 times the debris mass per solid angle, the upward moving debris and intercepted air will continue at speeds greater than 10 kilometers per second (a hundredth of the initial velocity).

In a 1962 U.S. Standard Atmosphere, the overlying air is 10^7 g/ster at an altitude of 340 kilometers. If the debris mass were 1,000 kg (≈1 ton), this air would have a hundred times the debris mass per solid angle, and velocities of tens of kilometers per second would persist. Consequently, material will reach regions of efficient injection and trapping in times ranging from a fraction of a minute to a few minutes. A considerable portion of the total beta yield of this material may be trapped if the detonation is above about 340 kilometers.

If hydromagnetic interactions dominate the coupling of the debris to the ambient air, a phase may occur in which some air remains ionized and stays behind (Reference 4). If so, the high-speed fission debris may interact with neutral air atoms. One possible interaction is a charge-exchange reaction in which the air atom acquires the charge from the debris ion, which becomes a neutral atom. The debris atom may outrun any hydromagnetic shock structure and, being neutral, continue unimpeded into the geomagnetic field. The process competing with charge exchange is reionization, which once again will couple the debris to the magnetic field.

A simplified model of the atomic interactions is a stream of material consisting only of neutral and singly ionized material penetrating a neutral gas. If the charge-exchange cross section is σ_{10} and the ionization cross section is σ_{01}, the fraction of the stream that will be neutral is

$$Y = \frac{\sigma_{10}}{\sigma_{01} + \sigma_{10}} \left\{ 1 - \exp \left[- \frac{\rho (\sigma_{01} + \sigma_{10}) s}{m} \right] \right\} \qquad (7\text{-}4)$$

where s is the penetration depth and m is the mass of a single air atom. The stream is assumed singly charged at the start. Thus, the fraction that is neutral will be 63 percent of its ultimate value when $\rho s = m/(\sigma_{01} + \sigma_{10})$.

For the typical value of 10^{-15} cm^2 for σ_{01} (Reference 5), this will occur when the mass traversed is 2.5×10^{-8} g/cm^2. This is also approximately the mean range for reionization of a neutral particle. It also leads to a range of 10 kilometers at 320-kilometer altitude or an escape upward from a 440-kilometer altitude in a 1962 U.S. Standard Atmosphere. Consequently, unless the detonation were above about 400 kilometers, the probability is low that debris atoms could escape without undergoing many charge-exchange cycles. Moreover, each charge-exchange cycle will yield another low-velocity air ion that will couple to the hydromagnetic expansion and decelerate the mass of debris. In summary, for detonations in the altitude range of 350 to 500 kilometers, this mechanism will account for the escape of a moderate fraction of the debris at large velocities. This, in turn, leads to extensive injection into the trapped electron belts.

If the local magnetic field lines are not nearly vertical, the effect of charge-exchange will be more significant. A charged particle emitted directly upward is constrained to spiral about a field line if it is to escape the atmosphere. Thus, such an ion will have a much longer interaction path than an upward-traveling neutral, and, hence, the charged particle will have a greater probability of becoming neutralized and escaping.

Penetration of debris across the geomagnetic field may result in greatly enhanced trapping on magnetic shells above the detonation region. If there is little overlying air or if the air couples poorly to the expanding debris (as in the Starfish event), the magnetic field makes the major contribution to stopping the debris. A megaton of energy can produce an expansion of about 1,000 kilometers in a 0.5 gauss magnetic field. Furthermore, the magnetic field debris interface is susceptible to the Rayleigh-Taylor instability (Sections 5.4.1 and 5.4.2) so that the debris may break up into jets that penetrate very far into the geomagnetic field. This mechanism may result in a large fraction of the upwardly directed debris reaching altitudes of thousands of kilometers—altitudes producing large trapping efficiencies—within a few seconds. Jetting was clearly observed during the Starfish detonation (Reference 4).

If 1,000 kg of material were involved in the debris expansion, the transition to the magnetic field dominated case should be at altitudes of the order of 400 to 500 kilometers. At these altitudes, the air swept up per solid angle is but several times the original mass of debris.

TRAPPED FLUX COMPUTATIONS BASED ON THE JETTING MODEL. Section 8 (Figures 8-25 through 8-29) presents integrations along circular satellite orbits of the trapped electron flux resulting from nuclear explosions at various L-values, as a function of the altitude of the orbits at various inclinations. The radiation environment used in that work was computed from a jetting debris model of the fission-fragment motion (Reference 6). In this model, the fission fragments are assumed to propagate rectilinearly through the magnetosphere in a conical volume as they decay and inject beta electrons. The outer surface of the jet is assumed to be tangential to both the fully expanded magnetic bubble and the geomagnetic field lines in their undisturbed condition.

Figure 8-30 shows the orbital integrations given for the case of a field-saturation environment. This environment was computed by assuming that (1) electrons are injected by simultaneous nuclear detonations at latitudes corresponding to the range of L-values between 1.08 and 5.77, (2) the pitch angle distribution of the injected electrons is that given by the jetting debris model, and (3) the maximum flux is attained at each L-value when the particle pressure, determined from the pitch angle distribution at a point on the field line (Section 5.4.1), is equal to the undisturbed field pressure. The resultant flux contours are shown in Figure 7-1. The previously discussed assumptions overly simplify the problem. The actual saturation flux easily could be different by 1 order of magnitude at low L-values and as much as 2 orders of magnitude above L = 1.5.

7.3 TRAPPING EFFICIENCY

There will be a lowest altitude and corresponding maximum mirror magnetic field intensity, B_c, below which electron loss is rapid. If electrons are injected isotropically at a point where the field intensity is B', the fraction that mirrors above the minimum altitude is

$$\epsilon = \sqrt{1 - \frac{B'}{B_c}} \,. \qquad (7\text{-}5)$$

The immediate trapping fraction is shown in Figure 7-2 for injection at temperate latitudes. For latitudes from 30 to 90 degrees, the trapped fraction deviates less than 5 percent from the data presented here. Electrons were presumed to be injected isotropically from a point at latitude λ^* and altitude $h^* = h_c + \delta h'$.

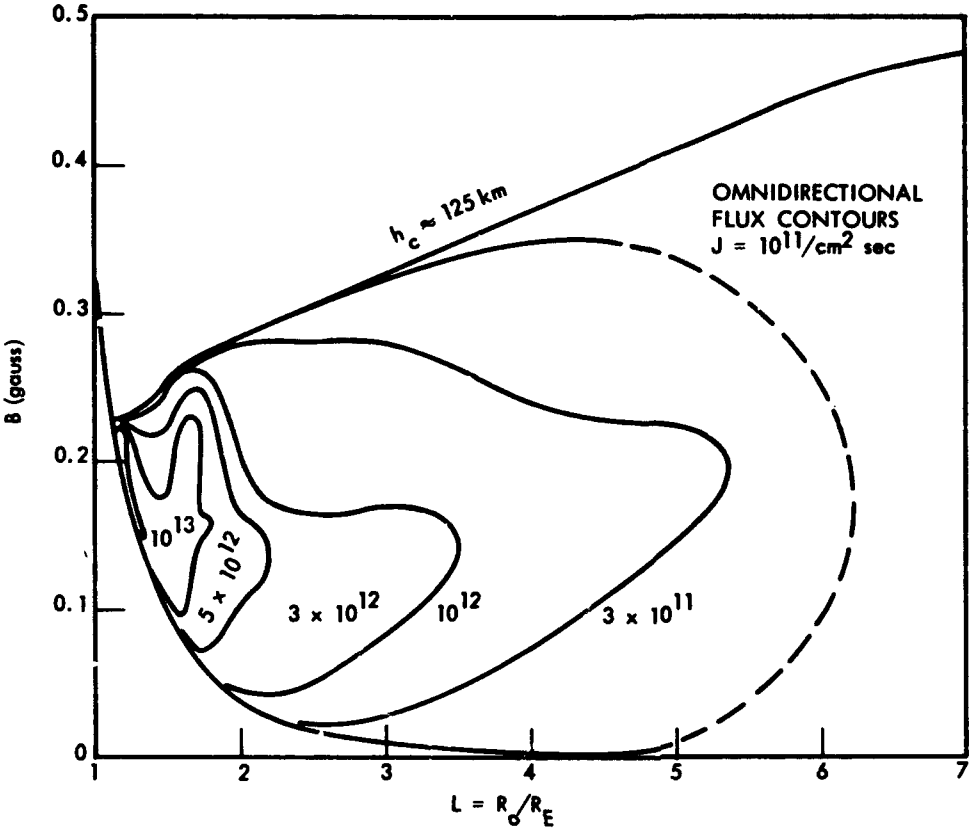

Figure 7-1. Contours of omnidirectional flux that would result from complete saturation of the closed trapping region (out to L ~ 6).

If injection is at an altitude $h' = h_c + \delta h << R_E$, slightly above the minimum mirror altitude, the trapping fraction can be approximated as

$$\epsilon \cong \sqrt{\frac{3\delta h}{R_E + h_c}} \left[1 + \frac{\cos^2 \lambda_c}{2(1 + 3 \sin^2 \lambda_c)} \right]^{1/2} \qquad (7\text{-}6)$$

where λ_c is the latitude of the critical mirror point. Thus, once the critical loss altitude h_c is exceeded, the trapping efficiency rises rapidly. As can be seen in Figure 7-2, if δh is as little as 100 kilometers, the trapping fraction exceeds 25 percent.

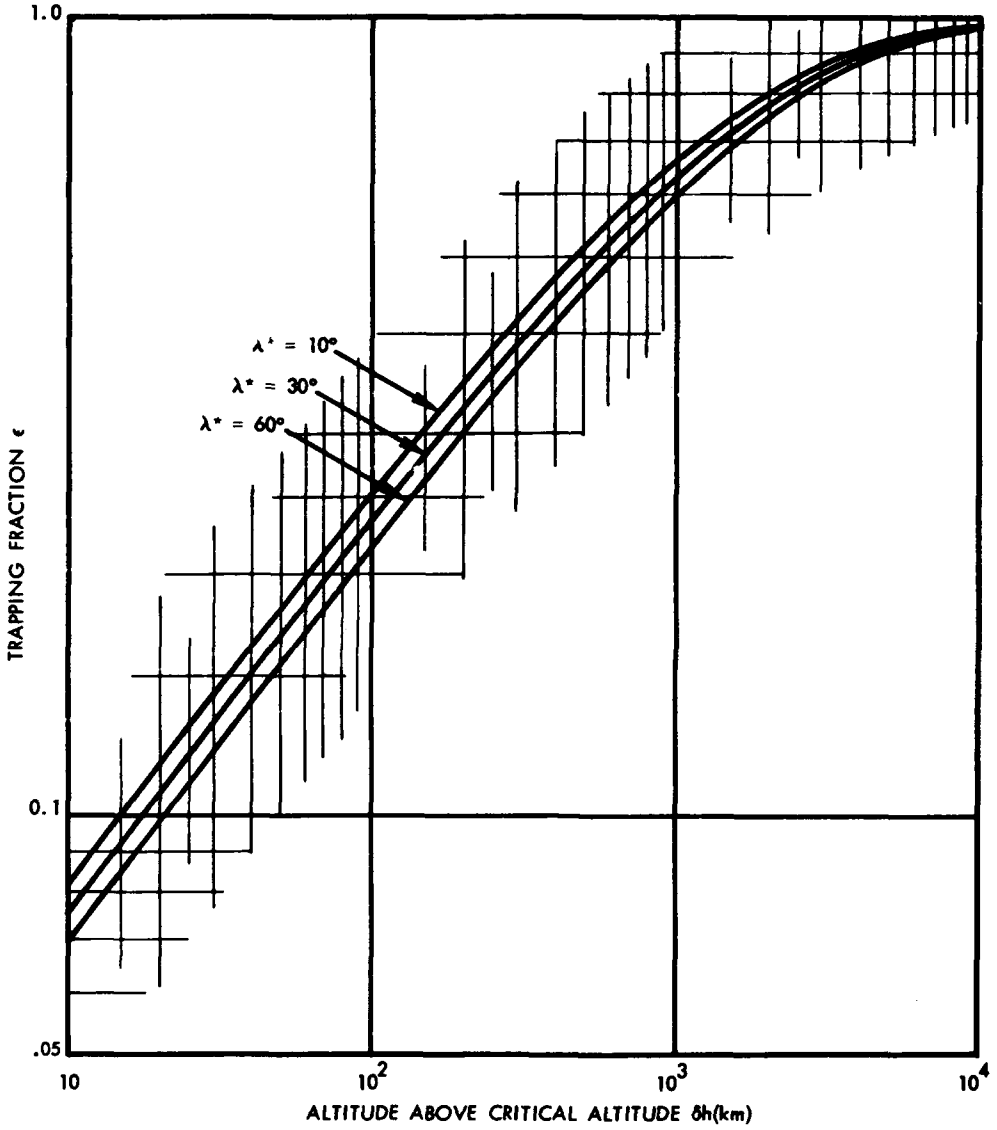

Figure 7-2. The trapping fraction as a function of injection altitude. Electrons were presumed to be injected isotropically from a point at latitude λ^* and altitude $h^* = h_c + \delta h'$.

The lowest allowable mirror altitude to be considered in trapping calculations will depend upon the required lifetime and the geographical coordinates of the mirror point. For problems related to temporary trapping near the point of injection, the primary consideration is the altitude of the critical mirror point at the local longitude. After they have drifted through the South American anomaly, the maximum mirror magnetic field intensity of trapped particles remains at the atmospheric cutoff field intensity in the anomaly region. The loss of trapped particles in the atmosphere is discussed in Sections 5.2.3, 5.2.4, and 5.2.5.

The eastward-drift velocity (Section 3.3.2) of the trapped betas is about 10 km/sec at low L-values. Consequently, the local field configuration dominates for lifetimes of the order of 100 seconds or less. Figures 2-10 to 2-19 show the altitudes of northern and southern mirror points as a function of longitude. In computing electron trapping after several bounce periods, the altitude corresponding to the lower of the two conjugate points should be used as the immediate loss altitude. In any particular L-shell, the minimum magnetic intensity at 150-kilometer altitude can be used with the data presented in Figure 7-2 to compute trapping efficiency.

The trapping fraction is a simple quantity that is useful in general, rough analysis of electron injection; but detailed computations require additional descriptors. One in general use is the mirror point density. This is the number of electrons that are reflected within a small interval δB about the mirror field B_m. The fraction of the total number of electrons emitted at B' is

$$\delta n = \frac{B' \delta B}{2B_m^2 \sqrt{1 - B'/B_m}} \quad . \tag{7-7}$$

If the distributions are put in this form, the contributions from injections at different field strengths can be added simply, and the decay of any particular portion of the distribution can be followed easily. This is often the most useful representation for computations pertaining to long-lived trapped particle shells.

7.4 TRAPPING PHENOMENOLOGY

After a nuclear detonation, several high-energy electron phenomena may be observed (depending upon the altitude of the beta decay electron injection). Three distinct time regimes of interest are

1. Immediately after injection, the particles still form a distinct group. During the first several seconds, the total azimuthal drift of hardly any particle exceeds 1 degree. A typical high-altitude nuclear explosion deposits debris over a region extending several degrees in longitude.

2. From about 5 to 10 seconds up to 1 or more hours, the artificial electrons are spreading over the entire trapping region.

3. After about 1 hour, the trapped particles are spread uniformly in longitude. The initial fluxes ultimately are reduced by a factor $\Delta\Phi/2\pi$, where $\Delta\Phi$ is the azimuthal angular extent of the injection region. The critical altitude must correspond to the South American anomaly region.

During the three time regimes following a nuclear detonation, the injected electrons exhibit quite different aspects. Initially, a tube containing all the upwardly emitted beta decay electrons will extend from the radioactive source to the conjugate electron loss regions in the atmosphere. This is referred to as the "beta tube". The untrapped electrons may make an appreciable contribution to the flux during the first few seconds after the detonation. They must be considered in addition to those electrons that remain trapped. If the radioactive debris is sufficiently high that significant numbers of trapped electrons persist for several bounce periods, the electrons drift eastward and begin spreading apart.

The region of intense, trapped electron flux to the east of the injection region is sometimes called the "arch". As the arch progresses eastward, the changing altitude of mirror points may cause removal of electrons from the arch by air scattering. Electrons not lost passing the South American anomaly gradually will spread to fill a magnetic shell. Only this shell will persist after the beta decay source is removed.

The intensity of electrons shortly after injection is given by Equation 5-47. The only necessity is to replace the source strength in that equation by the total number of electrons injected per volume element N, divided by 4π. Liouville's Equation (Equation 2-104) gives the intensity at any point in the field. Injections over a segment δS of the field line result in a contribution:

$$\delta J(B) = 2\int_{\mu'}^{\mu_c} d\mu \frac{N\delta S}{\sqrt{1 - (1 - \mu^2)B'/B}} \qquad (7\text{-}8)$$

to the omnidirectionally trapped flux where the field strength is B. μ is the cosine of the pitch angle at B and N is the source strength in electrons/m^3. A source at B′ provides particles in a restricted interval of pitch angles, between the atmospheric cutoff:

$$\mu_c = \sqrt{1 - B/B_c} \tag{7-9}$$

and the pitch angle corresponding to injection at 90 degrees:

$$\mu' = \sqrt{1 - B/B'} \quad . \tag{7-10}$$

When the observation point is below the injection point, μ' is set equal to zero. The flux of untrapped electrons in the debris region is computed similarly except that the pitch angle integration is over the range from μ_c to 1.

7.4.1 Beta Tube

In the beta tube, many electrons make a single traverse to the conjugate region. The flux of untrapped electrons (to which must be added the trapped flux of Equation 7-29) is

$$J(B, B_c) = \int_{h_c}^{\infty} dh' \frac{n}{\sin I} \sqrt{\frac{B}{B'}} \ln \frac{\sqrt{B_c}\,(\sqrt{B'} + \sqrt{B})}{\sqrt{B'}\sqrt{B_c - B} + \sqrt{B}\sqrt{B_c - B'}} \quad . \tag{7-11}$$

n is now the production rate (N in Equation 7-8 is nearly $\int_0^t$ ntd). The element of distance along the field line has been replaced by the altitude element:

$$dh' = \sin I \, dS \tag{7-12}$$

where I is the inclination of the field line at the injection point and B′ is the magnetic field at h′. For a thin injection layer of thickness $\delta h'$ at low altitude, Equation 7-11 reduces to:

$$J(B, L) \cong \left(\sqrt{\frac{1 - 3/4L}{1 - 1/L}} \sqrt{\frac{B}{B_c}} \ln \frac{\sqrt{B_c} + \sqrt{B}}{\sqrt{B_c - B}} \int_{h_c}^{h_c + \delta h'} \text{ndh} \right.$$

$$\left. - \sqrt{\frac{1 - 5/8L}{1 - 1/L}} \frac{B}{\sqrt{B_c (B_c - B)}} \int_{h_c}^{h_c + \delta h'} \text{ndh} \sqrt{\frac{3|h' - h_c|}{R_E}} \right) \quad . \tag{7-13}$$

If n is uniform over the injection layer, the integrals in Equation 7-13 may be replaced by:

$$\int_{h_c}^{h_c + \delta h'} ndh' = n\delta h' \qquad (7\text{-}14a)$$

$$\int_{h_c}^{h_c + \delta h'} ndh \sqrt{\frac{3|h' - h_c|}{R_E}} = n \frac{2}{\sqrt{3}} \sqrt{\frac{\delta h'}{R_E}}\, \delta h' \qquad (7\text{-}14b)$$

Figure 7-3 shows the dependence of J on B for very thin injection layers. A very thin source of thickness $\delta h'$ was assumed on each of the specified L-shells. The local critical field, B_c, must be used, corresponding to the atmospheric cutoff at the injection longitude. At early times, untrapped electrons predominate so it is only necessary to use Equation 7-13 or the numerical values in Figure 7-3 multiplied by the injection rate $n\delta h$ to obtain a reliable estimate of the prompt flux. The beta decay production rate after 10 seconds is about

$$n\delta h = \frac{2 \times 10^{16} Y_F}{At^{1.15}} \quad (\text{electrons/cm}^2/\text{sec}) \qquad (7\text{-}15)$$

where A is the area in square kilometers, transverse to the tube over which the debris is spread, Y_F is the fission yield in megatons, and t is time in seconds. The production rate varies somewhat, depending upon the fissionable isotope used, but this is a good representative value.

This source function ndh can be multiplied by the ordinate of Figure 7-3 to compute the omnidirectional flux in the tube. For instance, if the debris from a megaton of fission is spread over a region 100 kilometers in radius, at 60 seconds the source is 6×10^9 /cm^2 sec. The omnidirectional fluxes are then of the order 10^{10}/cm^2 sec near the detonation region or its conjugate (within several tens of kilometers). The flux from a single detonation is well within the stability limits of Section 5.

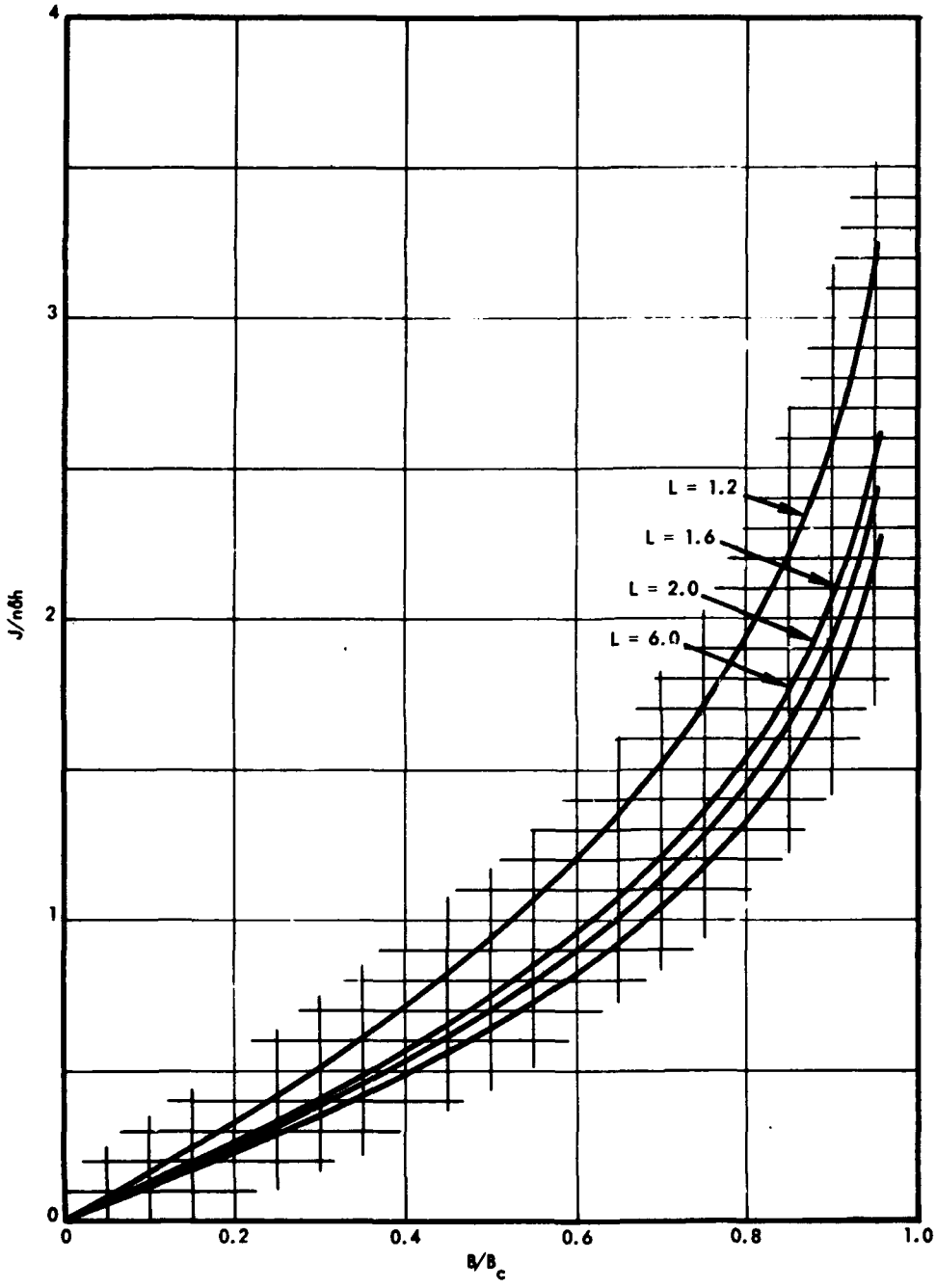

Figure 7-3. Omnidirectional flux of untrapped electrons in the beta tube as a function of location on the associated field lines. A very thin source of thickness $\delta h'$ was assumed on each of the specified L-shells. The local critical field, B_c, must be used, corresponding to the atmospheric cutoff at the injection longitude.

7.4.2 Drift Dilution of Trapped Electrons

Those electrons that are trapped begin immediately drifting eastward, away from the injection region. The treatment of the resultant azimuthal spreading is difficult. Some details are given here because the general method is not discussed in most readily available sources. As a particular group of particles with angular drift rate $\omega_d(E)$ passes from the geomagnetic longitude ϕ to longitude $\phi' = \phi + \omega_d(E)(t' - t')$ in the time $t' - t$, the distribution function $f(E, \phi, t)$ must remain constant, or:

$$f(E, \phi, t) = f(E, \phi', t') \quad . \tag{7-16}$$

Equation (7-16) is a special form of Liouville's theorem (Section 3.5). The total rate of change of the intensity per unit solid angle, j, in a tube drifting with the particles is

$$\frac{dj(B, E, \mu)}{dt} = \int dS' \frac{n(S', E, t)}{2\pi t_b \mu'} \tag{7-17}$$

where μ' is the pitch angle cosine at the point S′, which transforms to μ at the point B, or:

$$\mu' = \sqrt{1 - (1 - \mu^2)\, B(S')/B} \quad . \tag{7-18}$$

Integrations over time and pitch angle may be performed to obtain the omnidirectional flux from Equation 7-17. Since all actual flux measurement devices must observe only over a finite energy range, a practical solution to the injected flux problem also entails an energy integration. Customarily, the flux, $J(E > E_1)$, is measured above a given energy E_1. The integration here is carried out from E_1 to infinity. A simplified injection model is specified. A similar procedure could be followed in numerical computations for more complicated situations.

Assume an injection rate:

$$n(S', E, t') = N(S', t')\, R(t') \exp\left(\frac{E}{E_o}\right)/E_o \tag{7-19}$$

uniform between the longitudes Φ_1 and Φ_2. R represents the decay rate of fission debris and N is the distribution of the debris along a field line in units of total number of beta decays per cm^3. An exponential spectrum, $\propto \exp(-E/E_o)$ was assumed mainly for simplicity. The energy integration may be carried out first. Because of the discrete nature of the source, the energy integration at a given observation longitude (ϕ) and time (t) is performed over the function sketched in Figure 7-4 — the product of the exponential function by a number of "square functions." The result is

$$\int_{E_1}^{\infty} dE \text{ (square function) } e^{-E/E}/E_o = \sum_{n=0}^{\infty} \exp\left[-\frac{\phi - \Phi_2 + 2\pi m_2 + 2\pi n}{DE_o(t-t')}\right]$$

$$-\sum_{n=0}^{\infty} \exp\left[-\frac{\phi - \Phi_1 + 2\pi m_1 + 2\pi n}{DE_o(t-t')}\right] + (m_2 - m_1)\exp\left(-\frac{E_1}{E_o}\right) \tag{7-20a}$$

$$= \left\{\exp\left[-\frac{\phi - \Phi_2 + 2\pi m_2}{DE_o(t-t')}\right] \div \left\{1 - \exp\left[\frac{2\pi}{DE_o(t-t')}\right]\right\} - \exp\left[-\frac{\phi - \Phi_1 + 2\pi m_1}{DE_o(t-t')}\right]\right\}$$

$$+ (m_2 - m_1)\exp\left(-\frac{E_1}{E_o}\right) \equiv U(t-t', \phi). \tag{7-20b}$$

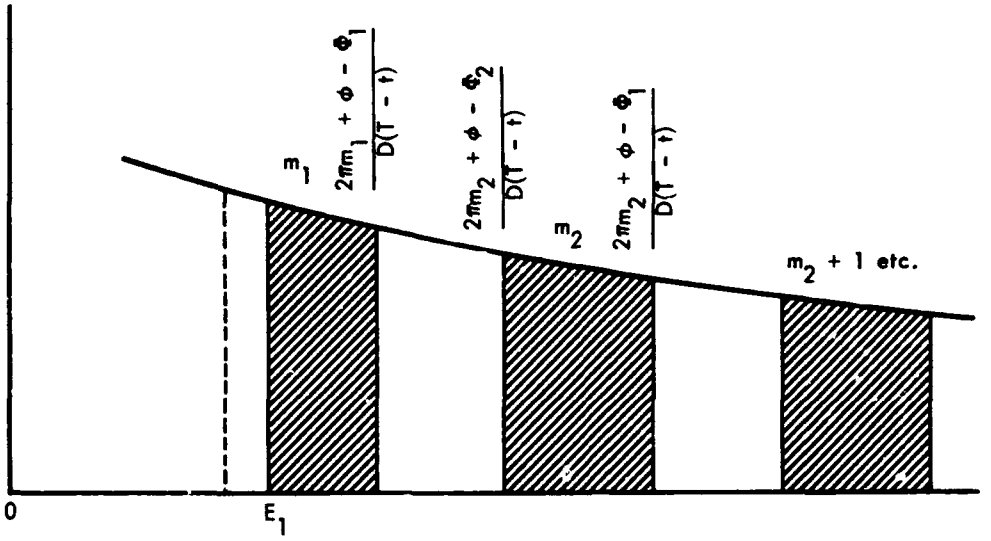

Figure 7-4. The integrand of Equation 7-20a.

An angular drift rate $\omega_d = DE$ independent of pitch angle has been presumed. This approximation is good (Equation 3-50) if the total energy $E = T + mc^2$, is employed. The m's are integers defined so that:

$$\frac{\phi - \Phi_1 + 2\pi m_1}{DE_1} \geq t - t' > \frac{\phi - \Phi_1 + 2\pi(m_1 - 1)}{DE_1} \tag{7-21a}$$

$$\frac{\phi - \Phi_2 + 2\pi m_2}{DE_1} \geq t - t' > \frac{\phi - \Phi_2 + 2\pi(m_2 - 1)}{DE_1} \quad . \tag{7-21b}$$

When the integration over pitch angle is completed, the result is

$$J(E > E_1, t, \phi) = 2\int_o^t dt' R(t') \int dS' \frac{N(S', t')}{t_b} \sqrt{\frac{B}{B'}}$$

$$\cdot \ln \frac{\sqrt{B'}\sqrt{B_c - B} + \sqrt{B}\sqrt{B_c - B'}}{\sqrt{B_c}\sqrt{|B' - B|}} \; U(t - t', \phi) \tag{7-22}$$

A useful further specialization is the case when N is a delta function of time. The flux is then

$$J(E > E_1, t, \phi) =$$

$$J(E > E_1, t \sim \infty) \cdot \left(\left\{ \exp\left[-(\phi - \Phi_2 + 2\pi m_2)/DE_o t \right] - \exp\left[-(\phi - \Phi_1 + 2\pi m_1)/DE_o t \right] \right\} \right.$$

$$\left. \div \left[1 - \exp\left(-2\pi / DE_o t \right) \right] + (m_2 - m_1) \exp\left(- \frac{E_1}{E_o} \right) \right) \quad . \tag{7-23}$$

As the width of the source approaches zero, the dilution factor U becomes

$$U(t, \phi) \sim \exp\left[-(\phi - \Phi^* + 2\pi m^*)/DE_o t \right] / \left\{ DE_o t \left[1 - \exp(-2\pi / DE_o t) \right] \right\} \quad . \tag{7-24}$$

where Φ^* is the center of the injection region and m^* is defined by the equation:

$$\frac{\phi - \Phi^* + 2\pi m^*}{DE_1} \geq t - t' > \frac{\phi - \Phi^* + 2\pi (m^* - 1)}{DE_1} \quad . \tag{7-25}$$

Some computed azimuthal flux distributions are shown in Figures 7-5 through 7-7 for selected L-shells. Several cases for various assumed injection region widths are shown in the figures. The sensitivity to the source characteristics decreases rapidly with elapsed time. In the figures, the initial flux is uniform over a segment of width $\Delta \Phi$. The ultimate steady state is denoted by the horizontal dashed line. An exponential

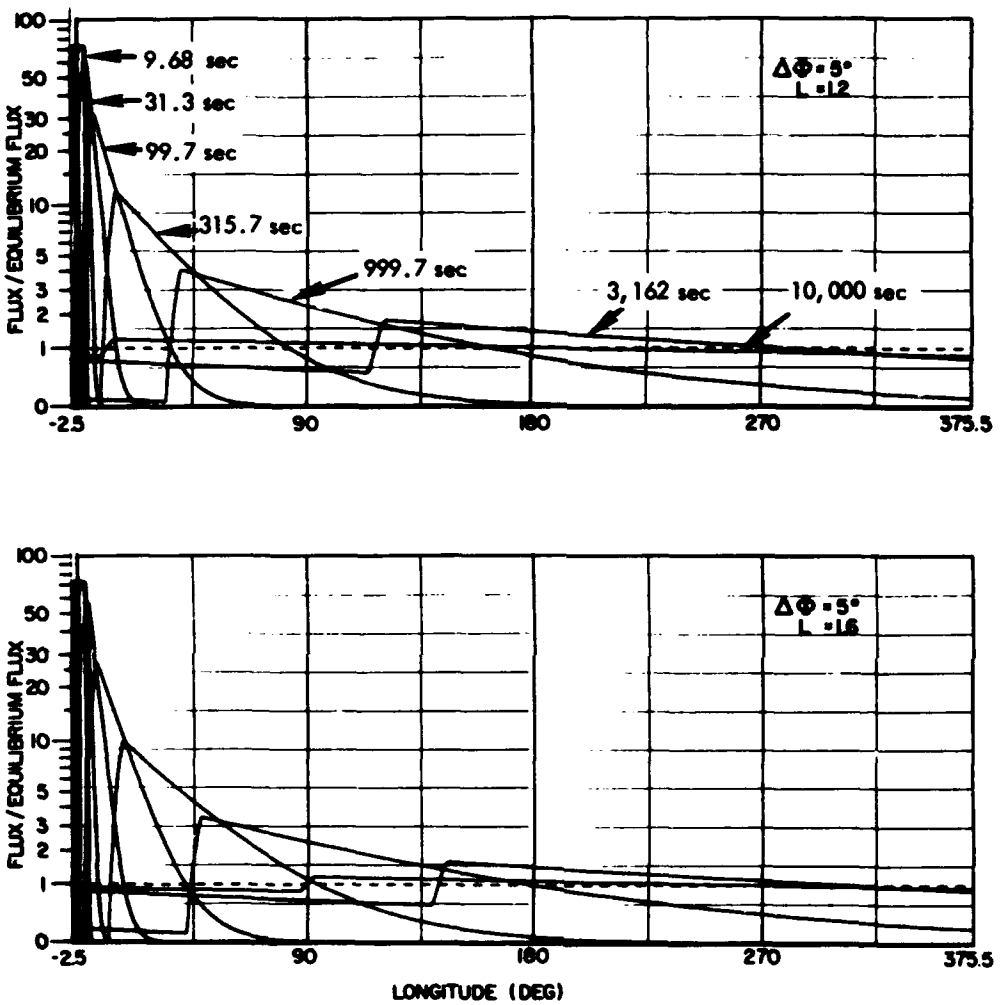

Figure 7-5a. The drift dilution of a group of electrons injected instantaneously in a longitudinal segment of finite width. In the figures, the initial flux is uniform over a segment of width $\Delta\Phi$. The ultimate steady state is denoted by the horizontal dashed line. An exponential energy spectrum with a mean energy of 1.2 MeV was assumed for all these figures. The longitudes are marked off at 45-degree intervals beginning in the center of the injection region. Individual curves are labeled with the time in seconds after the detonation. The same times are relevant to all the parts of Figures 7-5 through 7-7.

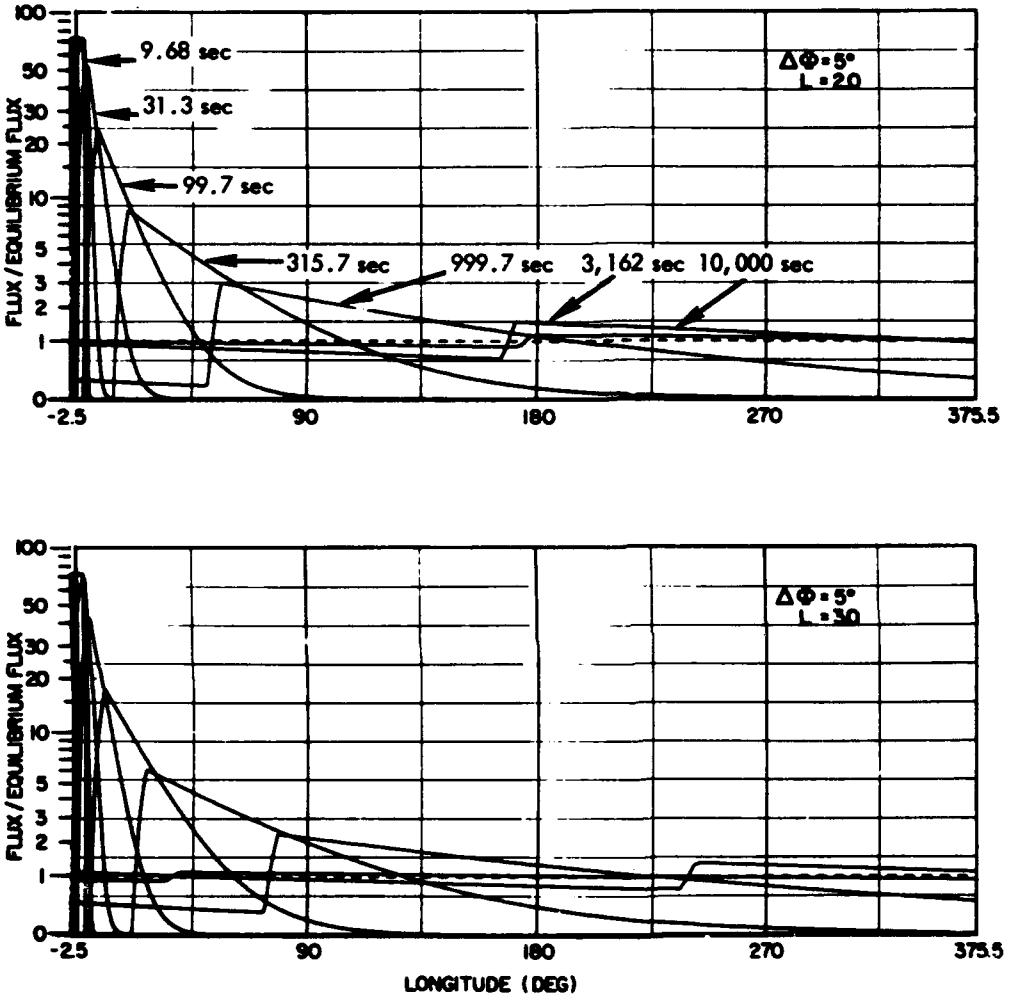

Figure 7-5b. The drift dilution of a group of electrons injected instantaneously in a longitudinal segment of finite width.

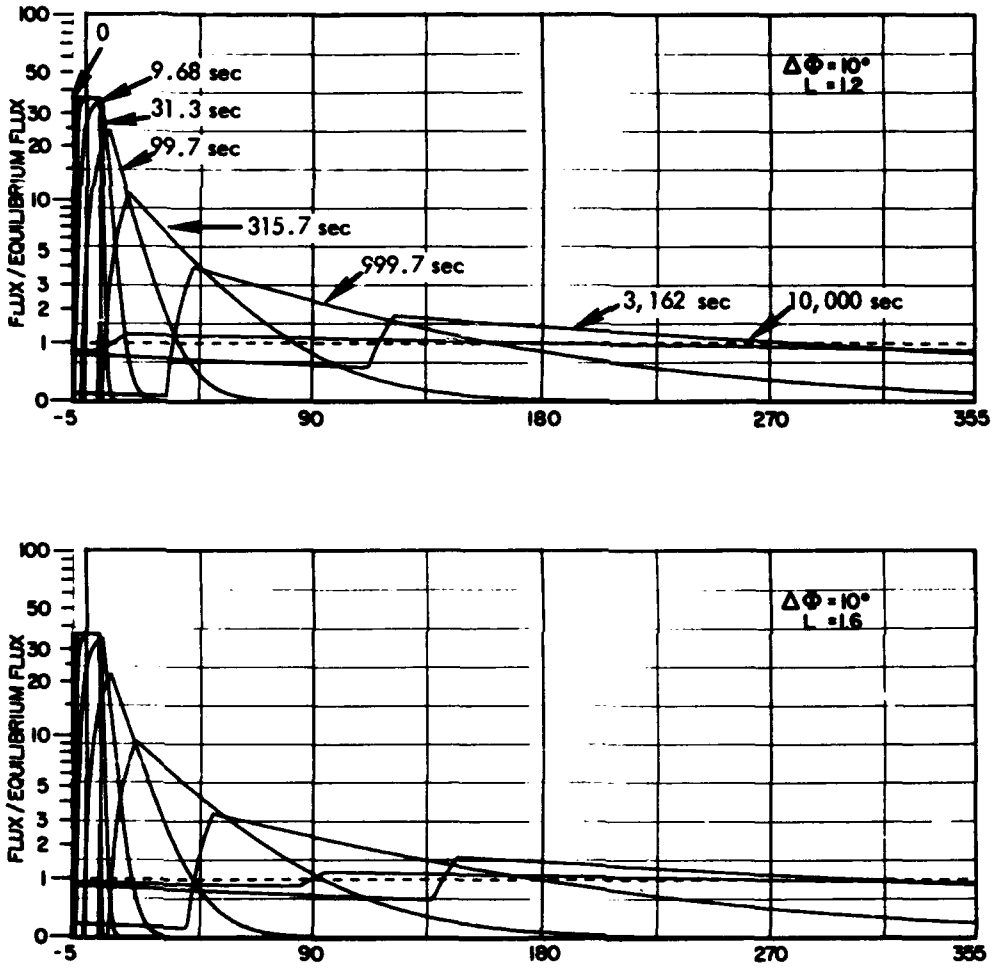

Figure 7-6a. The drift dilution of a group of electrons injected instantaneously in a longitudinal segment of finite width.

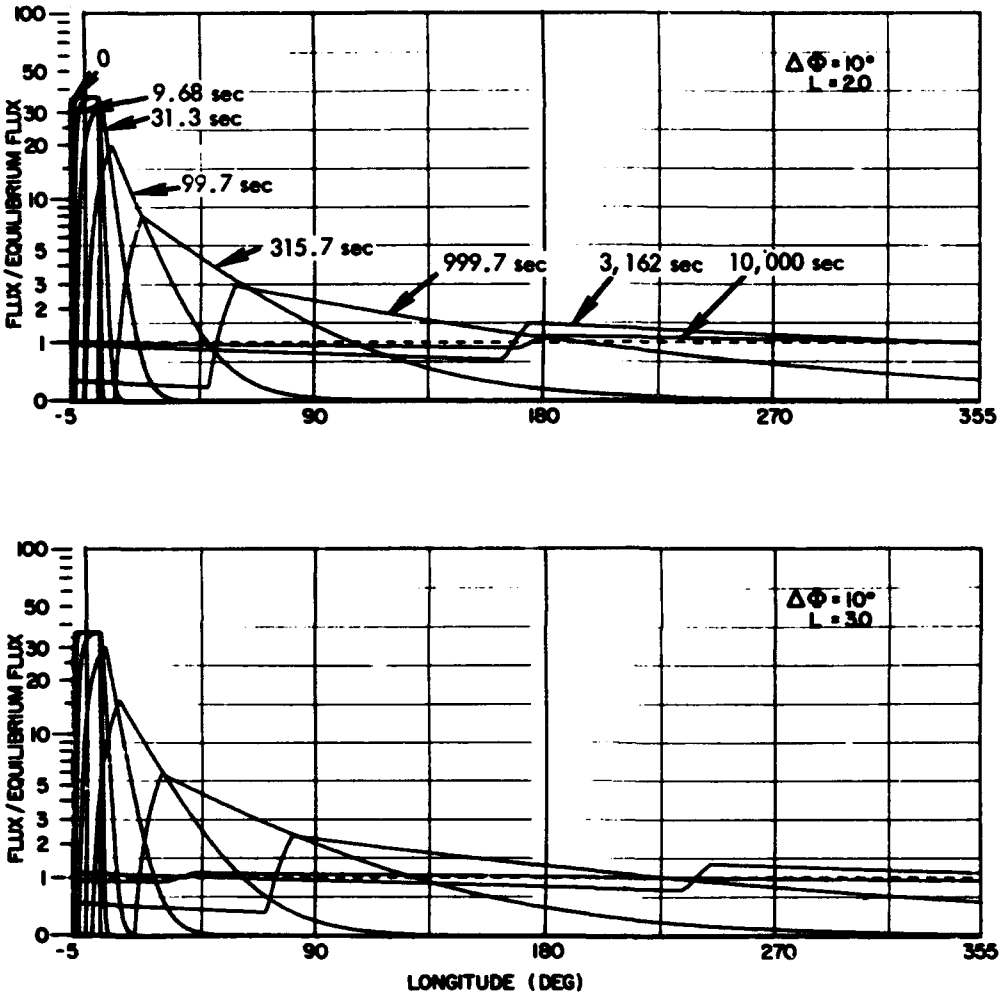

Figure 7-6b. The drift dilution of a group of electrons injected instantaneously in a longitudinal segment of finite width.

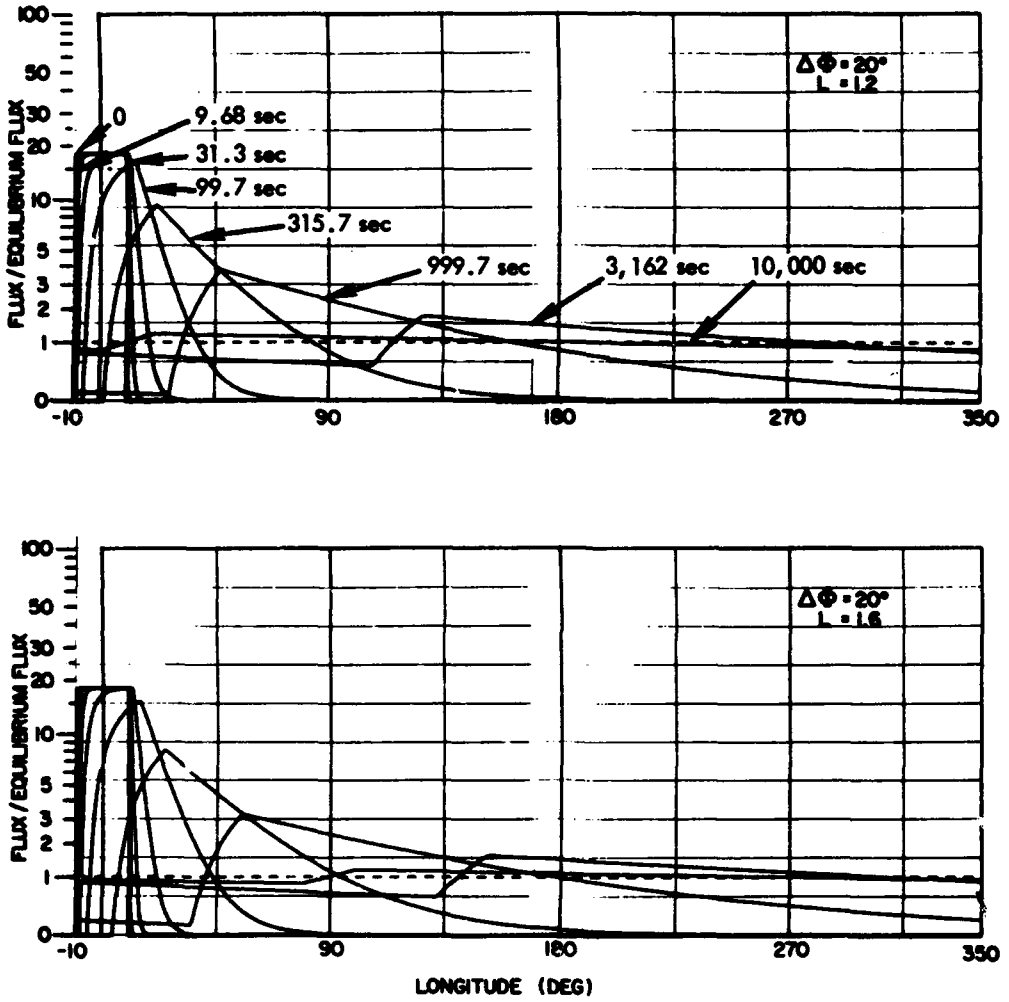

Figure 7-7a. The drift dilution of a group of electrons injected instantaneously in a longitudinal segment of finite width.

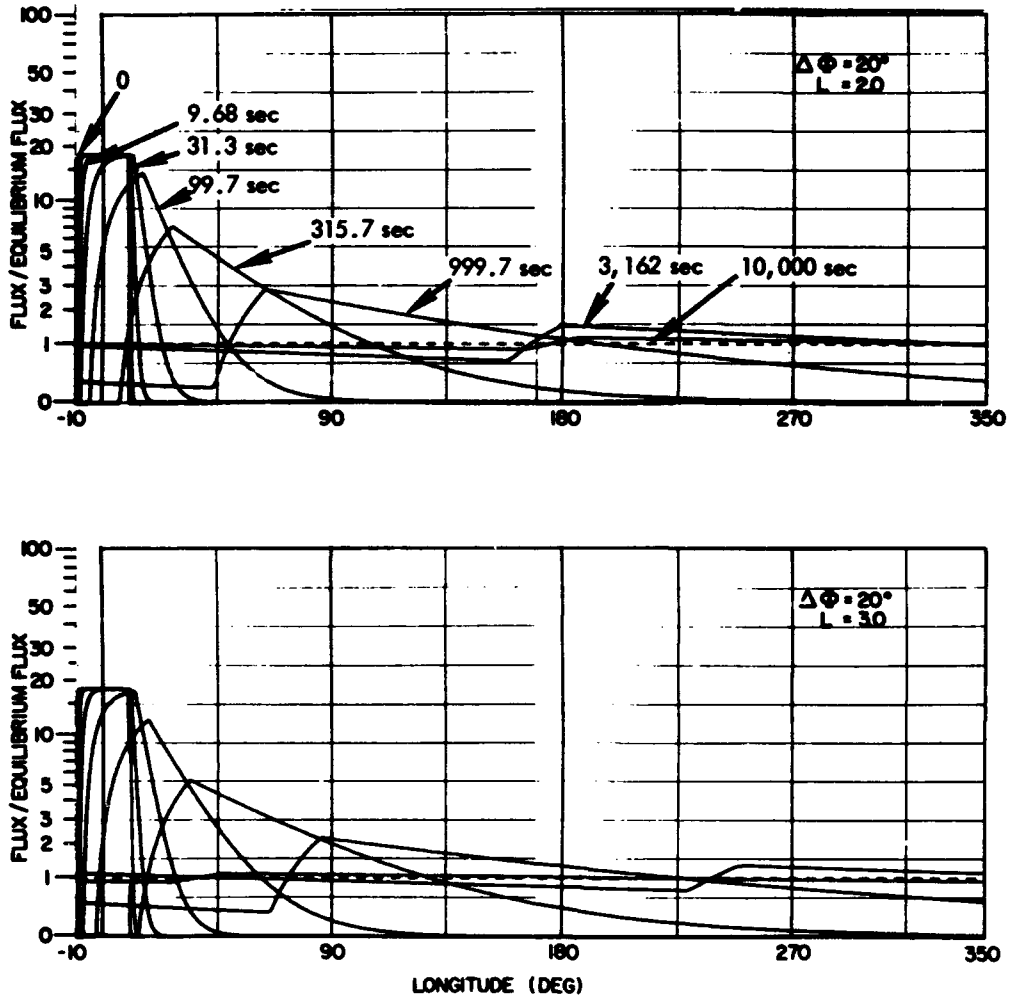

Figure 7-7b. The drift dilution of a group of electrons injected instantaneously in a longitudinal segment of finite width.

energy spectrum with a mean energy of 1.2 MeV was assumed for all these figures. The longitudes are marked off at 45-degree intervals beginning in the center of the injection region. Individual curves are labeled with the time in seconds after the detonation.

7.4.3 The Steady State Flux after Dispersal of Trapped Electrons

As trapped particles drift away from a discrete source, the azimuthal variation in their flux (after passing the South American anomaly) is just proportional to the variation in U. After a long time, the fractional variation ϵ over 360 degrees of longitude is merely

$$\epsilon < 1 - e^{-t_d/t} \approx \frac{t_d}{t} \qquad (7\text{-}26)$$

where t_d is the angular drift period at:

$$T + mc^2 = E = E_o \ . \qquad (7\text{-}27)$$

A variation of less than 10 percent over 360 degrees of longitude probably would not be distinguished by most flux-measuring apparatus. Therefore, a proximate steady state is reached at a time of order (Equation 3-50):

$$t(\text{sec}) \approx \frac{3 \times 10^3}{L[-\ln\ (1-\epsilon)]} \approx \frac{3 \times 10^4}{L} \ . \qquad (7\text{-}28)$$

In practice, the time given by Equation 7-28 is only an order of magnitude. Regarding the flux as uniform after $10^4/L$ seconds often is sufficient. When only the high-energy trapped particles are considered, the steady state is attained somewhat earlier.

If the bounce period, t_b, is assumed relatively independent of pitch angle, the steady state omnidirectional flux of injected electrons after redistribution is

$$J = 2\int_{h_c}^{\infty} dh\ \frac{N}{(\sin I)\, t_b} \sqrt{\frac{B}{B'}} \ln \frac{\sqrt{B'}\sqrt{B_c - B} + \sqrt{B}\sqrt{B_c - B'}}{\sqrt{B_c}\sqrt{|B' - B|}} \ . \qquad (7\text{-}29)$$

The factor containing the magnetic intensities within the integrand has been plotted in Figure 7-8 for several values of B/B_c. The proportional function is

$$Y \equiv \sqrt{\frac{B}{B'}} \ln \frac{\sqrt{B'}\sqrt{B_c - B} + \sqrt{B}\sqrt{B_c - B'}}{\sqrt{B_c}\sqrt{|B' - B|}} .$$

The independent parameters are $X = B/B_c$ and $Z = B/B_c$. The logarithm term in Equation 7-29 can be replaced (for low-altitude injection) approximately by:

$$\ln \frac{\sqrt{B_c - \delta B}\sqrt{B_c - B} + \sqrt{B}\sqrt{\delta B}}{\sqrt{B_c}\sqrt{|B_c - B - \delta B|}} \cong \sqrt{\frac{3\delta h'}{R_E + h'}} \sqrt{\frac{B}{B_c - B}\left(1 + \frac{1}{8L - 6}\right)} . \tag{7-30}$$

Upon replacement of the various factors by their approximate equivalents for injection at low or moderate altitudes (Equation 3-48 gives bounce period), the omnidirectional flux is

$$J(B) = \frac{32}{L\left[1 - 0.22/\sqrt{L^3(1 - 3/4L}\right]} \frac{\sqrt{1 - 5/8L}}{\sqrt{1 - 1/L}} \frac{B}{\sqrt{B_c(B_c - B)}}$$

$$\cdot \int_{h_c}^{\infty} dh\, N \sqrt{\frac{|h' - h_c|}{R_E}} . \tag{7-31}$$

The allowed flux may be further limited by the possibility of hydromagnetic instabilities. However, many nuclear detonations are probably necessary to saturate the trapping region. Figure 5-10 implies that the most elementary hydromagnetic stability criteria are not relevant to a single nuclear detonation of low to moderate yield. When any doubt exists about the ability of the ambient magnetic field to contain the injected particles, the trapping limits of Section 5, especially Section 5.4, should be considered. The first test to make is whether the particle pressure and magnetic pressure balance. The pressure-balance criterion was used to make up the data of Figure 7-1. The interchange stability criterion is difficult to interpret but may be very useful for high L-shell detonations. The other manifestations of instabilities are perhaps best treated as rapid diffusion processes with diffusion coefficients that might be estimated from the formulas given in Section 5.

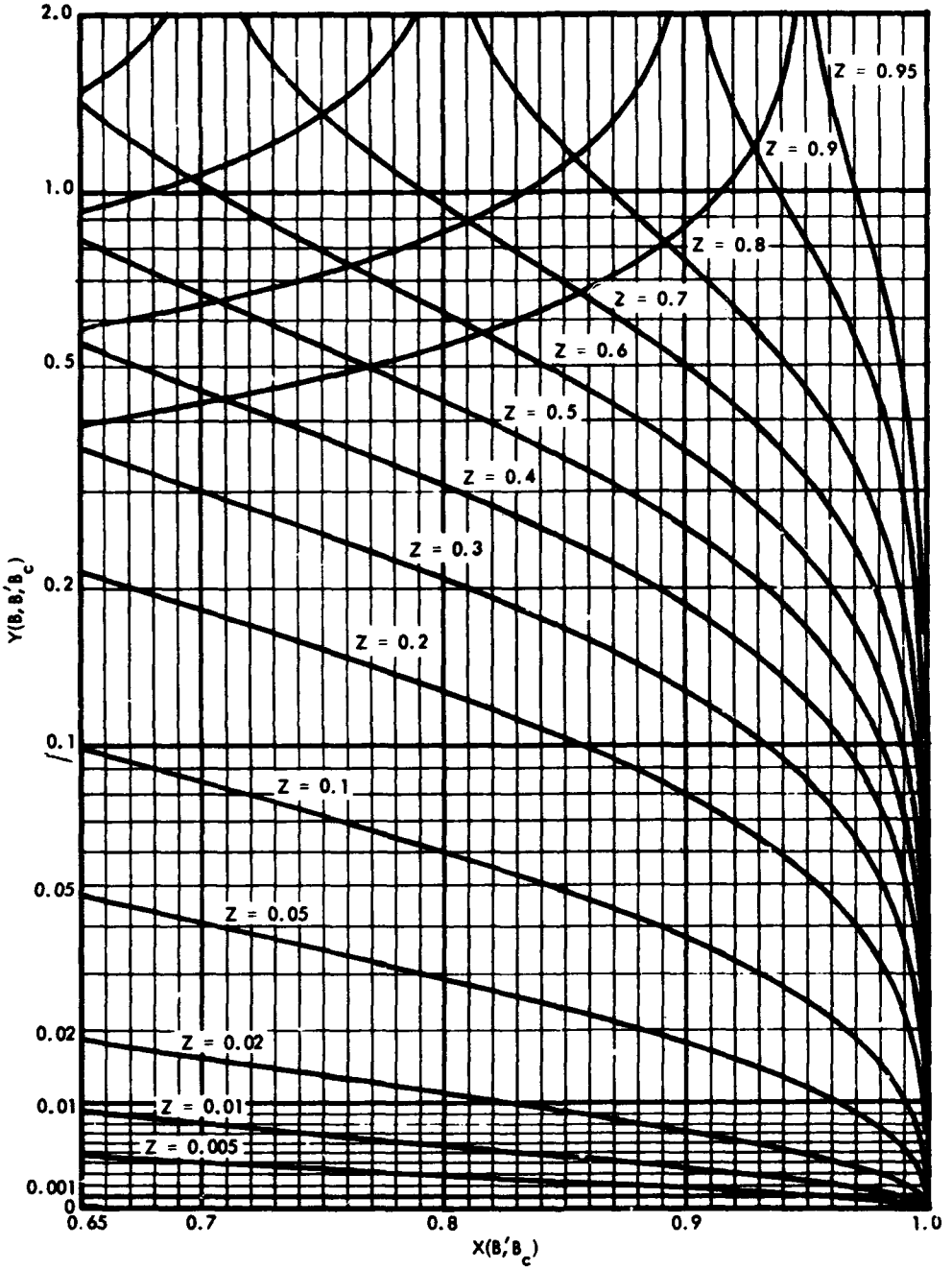

Figure 7-8. The function that is proportional to the contribution of electrons injected at a point B to the total omnidirectional flux. The proportional function is

$$Y \equiv \sqrt{\frac{B}{B'}}\ \ln \frac{\sqrt{B'}\ \sqrt{B_c - B} + \sqrt{B}\ \sqrt{B_c - B'}}{\sqrt{B_c}\ \sqrt{|B' - B|}} \quad . \qquad 7\text{-}29$$

The independent parameters are $X = B/B_c$ and $Z = B/B_c$.

REFERENCES

1. C. M. Crain and P. Tamarkin. "A Note on the Cause of Sudden Ionization Anomalies in Regions Remote from High-AltitudeNuclear Bursts," J. Geophys. Res., 66, 35-39, 1961.

2. J. F. Kenney and H. R. Willard. "Trapped Radiation and Ionospheric Perturbations Due to an Impulsive Neutron Source," J. Geophys. Res., 68, 4645-4657, 1963.

3. H. L. Brode. Fireball Phenomenology, Rand Corporation Report P-3026, Santa Monica, Calif., 1964.

4. J. Zinn, Jr., H. Hoerlin, and A. G. Petschek. "The Motion of Bomb Debris Following the Starfish Test," Radiation Trapped in the Earth's Magnetic Field, ed. by B. M. McCormac, Reidel, New York, 671-692, 1966.

5. J. K. Layton and W. L. Fite. Experimental Studies on Heavy Ion Exchange in Air, General Atomics, Report AFWL-TR-67-2, General Atomic Division, General Dynamics Corp., San Diego, Calif., 1967.

6. R. A. Berg, J. B. Cladis, G. T. Davidson, W. E. Francis, E. F. Gaines, L. L. Newkirk, and M. Walt. Trapping at High L Values of Beta Particles from Nuclear Explosions. Vol. I, Lockheed Missiles and Space Co., Report LMSC-B039917, Sunnyvale, Calif., 1967.

SECTION 8

EFFECTS OF TRAPPED RADIATION ON SPACECRAFT SYSTEMS

D.L. Crowther, Lockheed Palo Alto Research Laboratory
W.H. Harless, Jr., Lockheed Palo Alto Research Laboratory
J.W. Schallau, Lockheed Palo Alto Research Laboratory

8.1 SUMMARY AND INTRODUCTION

8.1.1 Summary

Section 8 presents information pertinent to estimating radiation effects experienced by selected materials and devices in spacecraft systems. The characteristics of the natural radiation environments are specified in detail in Section 4 and the corresponding information on the nature of the trapped electron injection model environments are presented in Section 7.

The effects of the natural trapped radiation environment on representative classes of materials and devices (semiconductor devices, thermal control surfaces, and optical materials) are considered in Sections 8.2, 8.3, and 8.4. Mechanisms of damage production by trapped electrons and protons and consequent effects on sensitive material properties and device characteristics are discussed. For certain semiconductor devices, a correlation between sensitive device characteristics and sensitive material properties is used as the basis of damage device prediction models.

If the reader is already familiar with damage mechanisms, he may go directly to Section 8.5 to obtain the results. Trapped particle doses and fluxes encountered in various orbits and behind various shield thicknesses are presented, and references are made to data that can be used to assess the degradation of certain devices. In Section 8.5, the effects of shield thickness and geometry are discussed. Data are presented to facilitate evaluation of the dose due to monoenergetic electrons incident on slab materials. Estimates are made of the "thick-target" bremsstrahlung intensity as a function of the electron energy and the material, and a representative thick-target differential bremsstrahlung energy spectrum is given for a fission beta spectrum incident on aluminum.

8.1.2 Introduction

Permanent degradation in material properties and system performance in complex satellite systems due to the interaction of both the natural and artifically injected radiation environments has been amply demonstrated over the past decade (Reference 1). Degradation in system performance has been experienced especially in those electronic systems that employ semiconductor devices. The observed effects have been generally traceable to changes in one or more sensitive material properties (Reference 2). The cumulative data from many satellite systems form the basis of techniques enabling the prediction of degradation in system, component, or device characteristics as a function of orbital parameters (Reference 3). The first step in any such procedure is to identify the particular sensitive material properties for each category or class of material or devices and to ascertain changes induced in them as a function of the radiation and material parameters.

A second and crucial requirement is a correlation or model relating the particular device characteristic to the sensitive material properties, e.g., common emitter current gain of a bipolar transistor to base region lifetime. The third step consists of evaluating complex trapped proton or electron energy spectra and fluences as a function of orbital parameters, shielding thickness, and geometry. The final step is the evaluation of degraded material properties and, thus, the degradation of the particular device characteristic as a function of orbital parameters and shielding. Such a procedure is limited primarily by deficiencies in data in Steps 1 and 2. In most cases, only descriptive device information and selected laboratory irradiation studies can be presented.

Energetic particles and gamma rays affect material properties by means of the direct or indirect introduction of lattice or structural imperfections that result from two physical mechanisms of interaction. The first interaction mechanism is that of ionization. Such interaction usually results in a transient change in material properties. For certain inorganic insulating solids, however, the ejected ionized electrons may associate with lattice atoms or imperfections to form relatively long-lived defects (Reference 4). The second and generally most important damage mechanism for most materials is that of displacement of lattice atoms from their equilibrium locations. The result of such interaction is a number of interstitial atoms, vacancies, and more complex entities that may interact with existing lattice imperfections or impurity atoms.

The very great range of device sensitivity to radiation is due primarily to the comparable sensitivity of specific material properties to the introduction of radiation-generated lattice imperfections.

For example, in most structural metals, the strength properties (e. g., tensile strength) are slightly more sensitive than electrical properties to lattice imperfections. However, radiation-induced imperfection densities on the order of 10^{18} to 10^{20} per cubic centimeter are required before densities comparable to the natural imperfection densities present are reached (Reference 5). Electrical conductivity in metals is less affected than tensile strength because of the additional presence of high-equilibrium conduction electron densities (10^{21} per cubic centimeter) (Reference 6).

At the other extreme are the class of semiconductor materials with electrical conduction properties that are quite sensitive to the introduction of lattice imperfections (Reference 7). This sensitivity depends significantly on the small concentration of dopant atoms (typically 10^{16} per cubic centimeter) introduced into the semiconductor material. This small concentration determines the conduction type (n or p) as well as the type of majority carrier (electrons or holes) and minority carrier (holes or electrons).

Inherent lattice defects as well as those introduced by radiation act as recombination centers for electrons and holes (Reference 8). The small density of minority carriers in extrinsic (doped) semiconductors means that they are affected at a much lower level of induced defect density. The property that reflects this is the minority carrier lifetime, τ, which is the mean decay time for the density of minority carriers in a bulk semiconductor (Reference 7). Semiconductor devices that depend on the flow of minority carriers (minority carrier devices) such as solar cells and bipolar transistors are generally the most sensitive to bulk lattice defects. In certain cases, however, the thresholds for minority and majority carrier removal effects might be comparable (Reference 9). Other semiconductor devices that primarily depend on the flow of majority carriers (majority carrier devices) such as the field effect transistor (FET) usually have considerably higher damage thresholds due to lattice defects introduced into the bulk. MOSFET's (metal oxide semiconductor FET's) form an exception and are quite sensitive to defects introduced in oxide passivation layers on the device surface (Reference 10). As a final example, consider certain optical materials and thermal control surfaces. The production of absorption centers or "color centers" by means of ionization and displacement interactions will decrease the optical transmission for the former while increasing the ratio of solar absorptance to thermal emissivity, α_s/ϵ_{th}, for the latter. The sensitivity of particular materials to

radiation is very dependent on the presence of residual impurities or structural imperfections. This may be important in the "color center" type of defect formation process (Reference 11).

The ultimate defects from radiation-induced interactions in materials are complex and of usually unknown structure (Reference 12). The usual procedure used to determine the effect of electron or proton energy, E, and time-integrated particle flux or fluence, Φ, on specific material properties is to lump the effect of all defects into observable damage parameters. For example, for τ in silicon semiconductors, this relation is

$$\Delta\left(\frac{1}{\tau}\right) \equiv \frac{1}{\tau} - \frac{1}{\tau_o} = K_\tau \cdot \Phi \qquad (8\text{-}1)$$

where

$$\Phi \equiv \int J\, dt \ (\text{particles/cm}^2)$$

and J is the omnidirectional flux. The lifetime damage coefficient, K_τ, depends on particle type, energy, and semiconductor characteristics (Reference 3). In many materials, insufficient data of this type exist. When such data do exist (e.g., as in the case of silicon minority carrier devices) and uniform degradation of τ exists, then the effect of an incident complex differential particle number spectrum, $\Psi(E)$, on τ can be described by a damage equivalent, normally incident (DENI), monoenergetic particle (electron) fluence, Φ_{eq}, of a reference energy, E_R, as defined by the relation:

$$\Phi_{eq}(E_R) = \int dE \cdot \Psi_i(E) \cdot \frac{W_i(E)}{W_e(E_R)} \quad . \qquad (8\text{-}2)$$

The subscript i indicates that the expression may be used either for electrons (e) or protons (p) and $W = K_\tau$ for this example (Reference 13).

The prediction procedure now may be invoked to effect orbital device characteristic degradation (e.g., common emitter current gain of a bipolar transistor) as a function of orbital parameters provided that a device model exists. In addition, the device characteristic must depend only on τ degradation, and data from sufficient laboratory irradiations must be available for a wide range of material

characteristics and operating conditions. When these conditions are met, data on $\Phi_{eq}(E_R)$ for 1-MeV electrons can be determined as a function of orbit altitude, shield thickness, and geometry by using the data on natural trapped radiation environments (Section 4) and shielding techniques to be described in Section 8.5.

Section 8.2, 8.3, and 8.4 present separate discussions of trapped radiation effects in semiconductor devices, thermal control surfaces and optical materials. For each of these categories, brief discussions are given on the physics of radiation defect generation processes and subsequent effects on important material properties. Emphasis is placed on the dependence of both defect generation and resultant effects on particle type, energy, fluence, and material properties. For semiconductor devices, data are presented on the evaluation of (1) DENI 1-MeV electron fluence for silicon minority carrier devices and (2) absorbed dose. These data are useful for evaluation of surface effects caused by both the Vette proton and electron model environments. Discussions also are presented on specific discrete minority and majority carrier devices.

Section 8.5 discusses the characteristics of natural and certain injected trapped radiation environments and methods of evaluating the effects of shield thickness and geometry on orbital averaged energy spectra and flux. Curves of the orbital average electron fluxes for four orbit inclinations are presented as a function of circular orbit altitude for each of six injection model environments. The conditions for injection and other pertinent descriptive data are given in Section 7. All irradiation models assume a fission beta electron spectrum constant in time. Additional data are presented on electron energy absorption in materials, bremsstrahlung production, and energy absorption for thick targets as a function of electron energy and material. A thick target bremsstrahlung spectrum for a fission beta electron spectrum incident on aluminum also is presented

8.2 TRAPPED RADIATION EFFECTS ON SEMICONDUCTOR DEVICES *

8.2.1 Introduction

Complex satellite systems or devices that employ semiconductor devices will be most sensitive to permanent radiation effects, with the possible exception of biological or photographic systems (Reference 14). Semiconductors are sensitive to radiation since their material and electrical characteristics are controlled by a small

*The state of knowledge concerning radiation effects in semiconductors is increasing constantly; consequently, this section cannot be considered complete. However, it is believed to be adequate for most applications up to the date indicated at the top of this page. Additional recent information may be found in References 73 and 74.

(1 part in 10^6) density of intentionally introduced impurity atoms. Particle radiation will create additional defects if sufficiently energetic to displace lattice atoms from their equilibrium sites. Ionization processes also may introduce a localized charge buildup that will affect the properties of the bulk material near the semiconductor surface (Reference 10). The current widespread use of semiconductor systems has emphasized the need for methods of estimating degradation in electrical functions.

In the following sections, consideration is given to two specific semiconductor models. The first model is applicable to minority carrier devices, for which minority carrier lifetimes are the basic semiconductor property degraded. The second model applies to certain majority carrier devices and is based on ionization-induced surface effects. These two models relate to a selected set of discrete silicon semiconductor devices for which correlations have been established between the observed degradations and environmental parameters (Reference 14). Although consideration is given only to two specific models, other modes of degradation are important for certain kinds of devices, e.g., emitter injection efficiency in high-frequency transistors. In other types of devices, an increase in resistance of the bulk silicon may be a dominant factor (Reference 15). Only for representative devices and for a particular range of particle exposure will such models be applicable.

One-dimensional device models will be used to illustrate these relationships in a simple manner where such an approximation is valid (Reference 16). Minority carrier devices depend on some form of bulk minority carrier transport and are generally sensitive to radiation-induced changes in minority carrier lifetime. This class of devices includes diodes, solar cells, and bipolar transistors. Consideration also is given to other characteristics that may be sensitive to bulk conductivity changes or ionization-induced surface effects (Reference 9). Selected device electrical degradation data are given, when appropriate, as a function of DENI 1-MeV electron fluence for bulk effects changes or surface dose.

The majority carrier devices depend on carrier transport usually in a thin surface layer; thus, they are most sensitive to either ionization-induced surface effects for the MOSFET type and/or bulk conductivity changes in the channel or lifetime changes in the depletion region for junction FET's (Reference 10). The relationship between electrical characteristics and these property changes will be discussed and illustrative device degradation data given.

The devices that are considered as complex semiconductor devices are integrated circuits (IC) or microcircuits (Reference 17). Unique to these devices are the intimate physical association of many discrete semiconductor devices within a single semiconductor chip. Isolation is ensured by either reversed bias p-n junctions or dielectric materials. This isolation is important in the case of transient radiation effects. However, for permanent radiation-induced effects, the bulk property changes generally are comparable to circuits using corresponding discrete semiconductor devices (Reference 9).

The specific circuit function degradation ("black box parameters") is dependent on design philosophy and operating conditions. Complex semiconductor devices will be classified as minority carrier IC's or majority carrier IC's, depending on the choice of either minority carrier active elements for the former or majority carrier active elements for the latter, with no allowance for combination of the two. Selected types of each IC will be discussed in terms of the specific type of active device degradation as well as the influence of the circuit design and operating conditions on the circuit performance.

8.2.2 Physics of Radiation Effects

Energetic electrons or protons interact with atoms of crystalline solids to produce defect sites that will influence certain important transport properties. Particular emphasis is placed on the dependence on radiation particle-type energy and time-integrated flux or fluence.

PRIMARY INTERACTION MECHANISMS. Radiation-induced defect sites are produced by two basic interaction mechanisms. The first is ionization by charged incident and secondary particles. The second is the displacement of atoms from their equilibrium sites in the crystal lattice to semipermanent interstitial positions.

Ionization. Charged incident particles may directly ionize atoms of the solid. This process takes a certain characteristic amount of energy absorption, δ, to create one ion pair or electron-hole pair. This value has been shown to be essentially independent of the type and energy of the incident particle. For silicon, $\delta = 3.7$ eV (Reference 9). The volume rate of production of electron-hole pairs in a semiconductor or other solid is dependent only on the rate of energy deposition in the solid by the primary or secondary particles.

For charged particles, this is given by the stopping power, $\epsilon(E) = -(dE/dx)$, for which extensive tabulations for various materials and particle type as a function of particle energy, E, are available (Section 5.2). The number of electron-hole pairs per cubic centimeter per unit particle fluence is given by $f = \epsilon(E)/\delta$.

Displacement. The displacement mechanism involves the momentum transfer in close Rutherford coulomb-type collisions of the incident charged particles with the atoms of the solid (Reference 8). Further interactions of the displaced atoms with other atoms of the solid may occur by means of Rutherford collisions or hard sphere elastic scattering. Displacement in crystalline solids requires that the struck atom receive a minimum energy, E_d, which in general will depend on the direction of recoil but usually is taken to be a characteristic value for the solid (Reference 19). E_d = 10 to 30 eV for most solids. This implies that the incident particle must have an energy greater than a minimum value, E_c. For protons incident on a monatomic solid of atomic weight, A:

$$E_c = \frac{(A+1)^2}{4A} E_d \qquad (8\text{-}3)$$

where E_c = 190 eV for Si using E_d = 25 eV. The corresponding relationship for electrons is

$$E_c = 511 \left(\sqrt{1 + 1.80 \times 10^{-3} A E_d} - 1 \right) \text{ (KeV)} \qquad (8\text{-}4)$$

where E_d is in eV and E_c = 260 KeV for Si with E_d = 25 eV (Reference 18).

Calculations have been made by this simple displacement theory to determine the total (i.e., primary plus secondary) number of displaced atoms per centimeter incident particle:

$$\eta_d(E) = N_s \sigma_d(E) \nu(E) \quad . \qquad (8\text{-}5)$$

The variable N_s is the target atom density, $\sigma_d(E)$ is the displacement cross section, and $\nu(E)$ is the mean number of secondary displacements per primary recoil (Reference 18). For protons:

$$\eta_d(E) = \frac{1.95 \times 10^4}{E} \left(\frac{Z}{A}\right)^2 \frac{\rho}{E_d} \left(15.2 - \ell n \left[\frac{(A+1)^2}{A}\right] - \ell n\, E_d + \ell n\, E\right) \quad (8\text{-}6)$$

where Z is atomic number, ρ the density in grams per cubic centimeter, E_d is in eV, and E is in MeV. This relationship is valid for a range of proton energies for which the coulomb interaction is dominant for primary displacements and for which elastic scattering is dominant for secondary displacements. In addition, the energy must be low enough so that the contribution of proton nuclear elastic scattering and inelastic reactions to the displacement cross section is small compared to the coulomb contribution. For electrons, the evaluations are more complex but have been performed and illustrate the rapid rise above threshold to a slowly increasing function of energy above 0.5 MeV (Reference 12).

These evaluations are crude and correspond only to initial displacements rather than actual defects, but they are of qualitative and intuitive importance in comparing displacement production by particles of differing type and energy. For example, Table 8-1 gives values of η_d and ν for 1-MeV electrons, 10-MeV protons, and 100-MeV protons incident on Si. The measured carrier removal rate per unit particle fluence, $-dn/d\Phi$, also is given for comparative purposes (Reference 9).

Table 8-1. Comparison of theoretical displacement parameters with measured carrier removal in silicon.

Particle	η_d (cm^{-1})	ν	n-Si $-dn/d\Phi$ (carriers/cm)	p-Si $-dn/d\Phi$ (carriers/cm)
1-MeV Electrons	4.6	1.3	0.2	0.005
10-MeV Protons	1100.0	6.0	100.0	100.0
100-MeV Protons	130.0	7.0	—	—

RADIATION DEFECT FORMATION PROCESSES. After the primary displacement or ionization processes, several intermediate entities often occur before the final radiation defect sites are established. These will be discussed for displacement processes in the bulk material and ionization near the surface.

For displacement due to electrons irradiating the bulk crystal, secondary displacements are few so that the distribution of defects is approximated closely, at the first stage, by isolated, closely spaced interstitial vacancy (I-V) pairs (Reference 7). Often the vacancy is mobile and migrates to defect or impurity atom sites [oxygen (O) or phosphrous (P)] or, conversely, the impurities may migrate to form stable sites. Another possibility is that the vacancy may recombine. As a consequence of these possibilities, the defect sites will depend on type (n or p) of Si and on impurities. They are more easily annealable than are heavy particle sites.

Much information has been accumulated on the physical structure of these sites (Reference 12). The relative number of such sites is a strong function of temperature. Protons have more secondaries per primary displacement and increased primary displacements per centimeter than do electrons. This suggests that the primary stage consists of closely spaced, small defect clusters. The increased cluster size for protons compared to electrons means that annealing will be less probable but migration of vacancies (or interstitials) should not be impeded. This indicates a strong dependence of the resulting stable defect sites on the type silicon, impurity atoms, resistivity, and residual impurities (O, P).

In terms of ionization-induced defect sites in surface layers [e.g., silicon dioxide (SiO_2) passivation layers], the final defect site may be (1) the initial ionized atom, (2) the result of the migration of the site, or (3) the result of impurity migration to the site. Very little is understood about the details of these processes, but the observed effects have been found to be dependent on the magnitude and distribution of the surface charge (Reference 10).

SEMICONDUCTOR TRANSPORT PROPERTIES DEPENDENCE ON RADIATION-INDUCED DEFECTS. The effects on both the bulk and surface semiconductor transport properties of radiation-induced defect sites are best understood in terms of the concept of a recombination center (Reference 8). Any defect site, whether natural or radiation-induced, may introduce defect energy levels into the forbidden energy band gap of a semiconductor. These levels may be described in terms of their cross section for capture or emission of free electrons and holes. In particular, those states may exist called recombination centers, which, after capturing a conduction electron (hole), will have a large capture cross section for a free hole (electron leading, in effect, to a net loss of an electron-hole

pair. These states strongly affect the resulting lifetimes of free carriers, whereas those states due to trapping centers merely capture and reemit free carriers of one type leading to no net loss (Reference 7). This concept has been used in successful prediction of the order of magnitude of observed carrier lifetimes in both silicon and germanium.

The problem of determining defect energy level characteristics from single-level Shockley-Read (S-R) analysis is complicated for radiation-induced levels. This is a consequence of (1) the usually unknown number or unknown structural or physical characteristics of the ultimate defect sites, (2) the importance of defect motion and association with residual impurities and its dependence on temperature, and (3) the quite complicated S-R analysis for multiple-defect levels.

Dependence of minority carrier lifetime on particle energy, type, and fluence from the measured characteristics of the defect levels introduced is difficult to deduce, even for electron irradiated silicon. Therefore, measurement of bulk lifetime dependence on radiation particle energy, type, and fluence as well as on semiconductor properties has been relied on. The result is described by Equation 8-1. K_f depends on radiation particle type, energy, and semiconductor characteristics. This form is in approximate agreement with the results of a simplified, single-level S-R analysis and has been used widely (Reference 7). Representative variations of K_f for p-type silicon as a function of particle energy are given in Figure 8-1 where $K_f(E)/K_f(1)$ is plotted for electrons and $K_f(E)/K$ (4.6) for protons. These forms are approximately independent of resistivity, impurity atom, or minority carrier injection level (Reference 3)

Recombination centers (RC) remove majority and minority carriers equally effectively, but the considerably greater majority carrier densities mean that higher radiation exposures are required to alter significantly the majority carrier densities. For example: Carrier removal rates, $-dn/d\Phi$, are given in Table 8-1 for 1 ohm-centimeter n-type and p-type silicon caused by 1-MeV electrons and 10-MeV protons. Since the majority carrier density is $\sim 10^{16}$ per cubic centimeter, proton fluences in excess of 10^{14} protons per square centimeter and electron fluences in excess of 10^{17} electrons per square centimeter are required to alter appreciably the majority carrier density. These values will be reduced for higher bulk resistivity, but typically 1 to 2 orders of magnitude higher than those re-

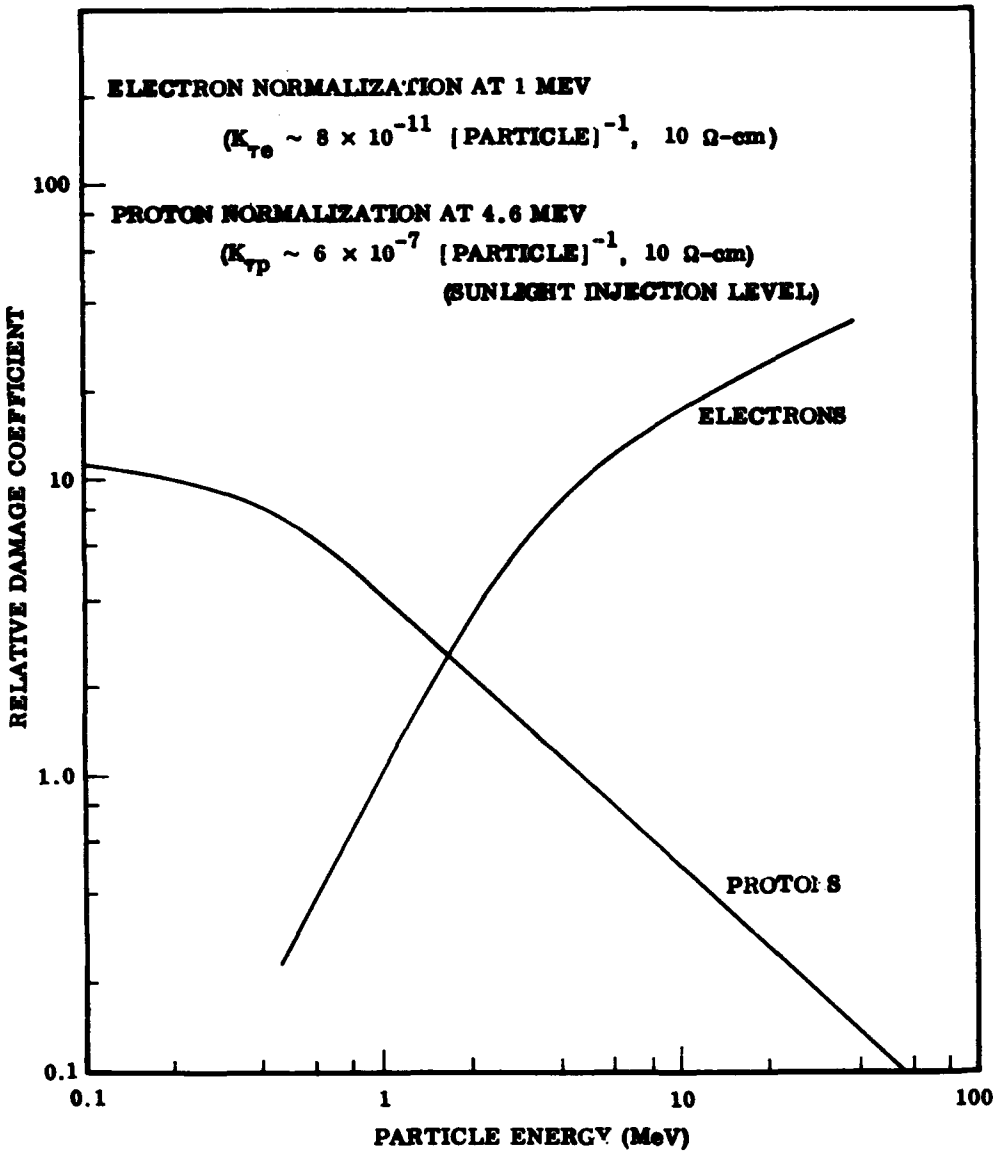

Figure 8-1. Normalized damage coefficients for p-type silicon.

quired for comparable effects on minority carrier lifetime. Mobility also is affected by scattering centers composed of both recombination centers and radiation-induced trapping centers, but again the exposure levels required are comparable to that for bulk carrier removal (Reference 7).

Recombination centers have been proposed to account for the high recombination present in most surface regions (Reference 10). Their magnitude is measured by the recombination velocity, s, which determines the surface recombination rate $R = s\Delta n$ where Δn is the excess minority carrier density. An analogous S-R analysis has shown that natural defect states (RC) are required to explain the observed s values. Very little evidence has been presented to show that direct introduction of radiation-induced defect states has been significant in the observations of the changes in s or the silicon surface potential (U). This presumably is due to the high natural defect density at the surface. Almost all these effects have been attributable to the existence of an electrical charge near the surface that induces changes in U and s (Reference 10).

8.2.3 Radiation Effects in Selected Semiconductor Devices

This section provides data on the changes in selected device characteristics with radiation exposure. Representative device degradation data are only to be considered as indicative of actual devices. Geometrical complexity and variability, the dependence of effects on device manufacturer and processing techniques, as well as the dependence of effects on operating conditions preclude complete characterization or a systematic statistical presentation of device behavior.

For this discussion, semiconductor devices have been categorized according to mode of current conduction. Representative of the minority carrier devices are solar cells, diodes, and bipolar transistors while the Metal-Insulator-Semiconductor (MIS) and junction field effect transistors are the principal members of the majority carrier group.

For each class of device, the particular device's electrical characteristics will be characterized in terms of those bulk or surface properties that will be most affected by radiation. Where it is possible to relate the most sensitive electrical characteristics to minority carrier lifetime changes, representative degradation curves of

the relative changes versus 1-MeV electron fluence will be given. Also, where the change in a specific electrical characteristic can be related uniquely to surface effects, curves of the relative change in the characteristic versus surface dose (rads) in silicon will be given.

MINORITY CARRIER DEVICES

Silicon Solar Cells. Consider a planar solar cell with an n-type diffused layer of thickness d over a p-type base layer of thickness d_c over which is a cover slide of thickness t (Figure 8-2). A theoretical expression can be derived for the short circuit current density, J_{sc}, due to minority carrier generation in the base layer and diffusion to the junction. If a thick base layer, $d_c \gg L$, is assumed, the expression (Reference 20) is

$$J_{sc} = N_p q(1 - R)\left(\frac{\alpha L}{1 + \alpha L}\right)e^{-\alpha d} \qquad (8\text{-}7)$$

where R is the reflectivity of front surface, α is the absorption coefficient (per centimeter), L is the base layer diffusion length (centimeter) $= \sqrt{D\tau}$, D is the diffusion coefficient (square centimeters per second), and N_p is the incident-photon flux per unit wave-length (per square centimeter per second). Note that since $L = \sqrt{D\tau}$, the parameter affected by radiation is L since it depends on τ. L often is measured as a function of damaging fluence Φ by noting that, for small α, J_{sc} is proportional to L. Using a suitable source (1-MeV

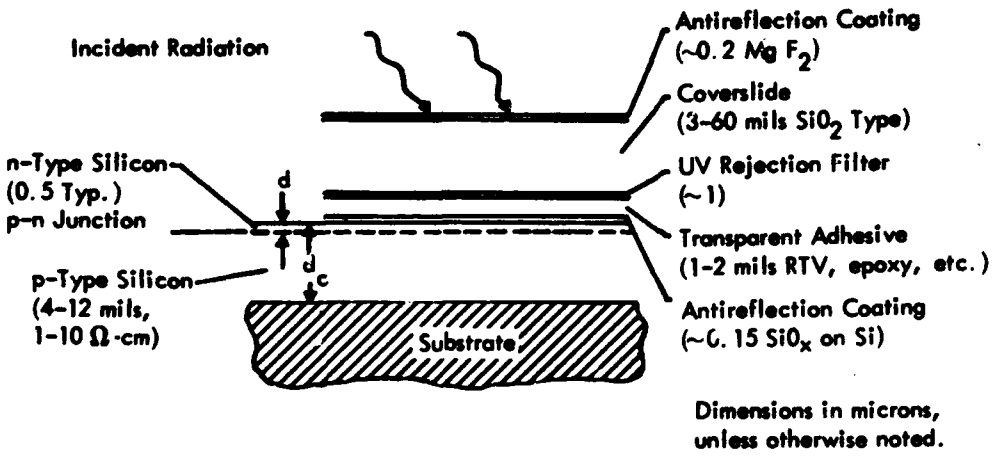

Figure 8-2. Typical solar cell assembly.

electron), L may be evaluated after specific irradiation levels (Reference 13). Using this procedure, L has been observed to degrade in this manner (Reference 3):

$$\frac{1}{L^2} = \frac{1}{L_o^2} + K_L(E)\,\Phi \tag{8-8}$$

where K_L obviously is related to the previously discussed K_τ by $K_L = K_\tau/D$. Much of the recent data on K_L or K_τ as a function of particle type, energy, and temperature has been evaluated in this manner from solar cell studies. The actual short circuit current, I_{sc}, for space sunlight is obtained by integrating $J_{sc}(\lambda)$ over λ, usin $\alpha = \alpha(\lambda)$, the optical absorption coefficient for silicon. In general, a corresponding contribution to I_{sc} from the diffused layer can be estimated, but it is not normally radiation sensitive because of short lifetimes.

The I_{sc} from the base layer also can be computed for base layer thicknesses that are comparable to the diffusion length (100 to 200 microns) (Reference 20). The computed results seem to be at variance with experimental data, so the latter is relied on. The I-V characteristic can be computed from the modified p-n junction diode relation:

$$I = I_\ell - I_s \left\{\exp\left[\frac{q}{AkT}(V - Ir_s)\right] - 1\right\} \tag{8-9}$$

where r_s is the series resistance, A is in the range 1 to 2, I_s is the reverse saturation current, and $I_\ell \simeq I_{sc}$ (Reference 3).

The behavior of $K_L(E)$ and thus $K_\tau(E)$ for low proton energies (<3 MeV) has been inferred from comparisons of the theoretically evaluated I_{sc} and experimental results (Reference 25).

A recent study (Reference 64) has shown K_L to be a function of cell temperature as well as base resistivity, as shown in Figure 8-3. This temperature dependence is particularly significant within the operating range of solar panels in earth orbit.

To assist in the assessment of the change in I-V characteristics as a function of orbital parameters and shield (cover slide) thickness, experimental data are given for relative degradation in I_{sc}, the

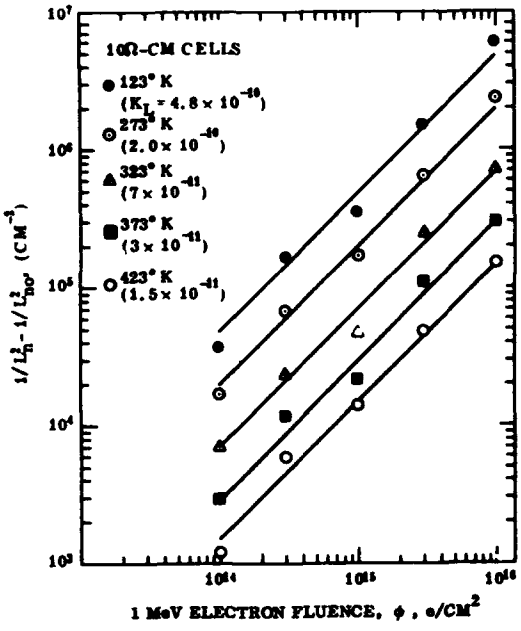

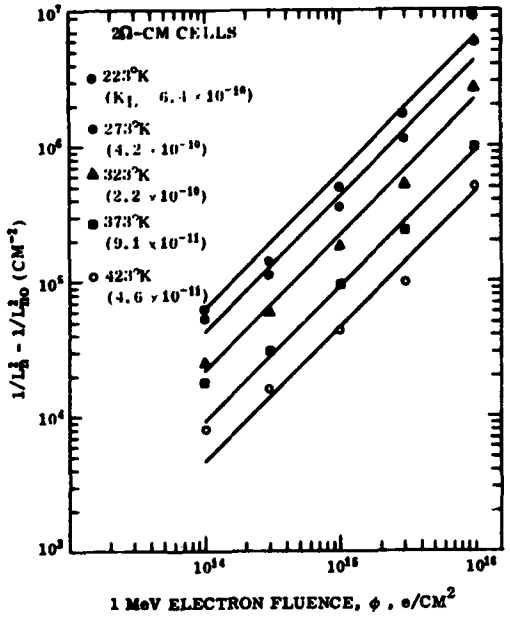

Figure 8-3. Diffusion-length damage coefficient K_L at five cell temperatures (Reference 64).

voltage at maximum power V_{mp}, and maximum power P_m for space sunlight (Reference 26). These are shown as a function of the 1-MeV electron fluence where data for cell thicknesses of 8 and 12 mils of fused silica (SiO_2) are given for 10 ohm-centimeter n/p cells (Figure 8-4) and for 2 ohm-centimeter n/p cells (Figure 8-5). This is to be used in conjunction with the appropriate DENI 1-MeV electron fluence as a function of orbital parameters and cover slide thickness (Figures 8-34 to 8-41). These data should not be used for shield thicknesses <6 mils (0.02 grams per square centimeter) for protons due to the probable nonuniform damage. Since the solar cell will have considerable material on the back side and a planar shield on the front, a correction factor of 3 should be applied to reduce the equivalent fluences given for uniform shield thicknesses for incident protons (Figures 8-34 to 8-37), while a factor of 2 should be used to correct the electron data (Figures 8-38 to 8-41).

The present trend toward more radiation resistance as well as higher power output per unit weight has led to the use of higher base layer resistivities (1 to 10 ohm-centimeter range) and to thinner cells (Reference 3). The so-called drift field solar cell, which has an intentional majority carrier gradient introduced into the base layer to reduce the effects of lifetime degradation, has not proved as radiation resistant as the best n/p solar cells (in terms of end-of-life efficiency) until quite high-exposure levels are reached. As a result, little commercial development has been undertaken and few data are available on radiation degradation characteristics (Reference 20).

The cadmium sulfide (CdS) solar cell has been developed to the point of some use in satellites. Although at least a factor of 2 less efficient per cell, it has a comparable watts per pound factor in arrays (Reference 21). Some instability problems on thermal cycling still exist (Reference 22) and, since few data comparable to that for silicon cells on radiation degradation exists, it will not be considered any further here (Reference 23). Still in the developmental stage is the lithium (Li) drifted p/n solar cell that possesses room temperature self-annealing properties but no definitive radiation response data are available at present (Reference 24).

Diodes. Junction diodes are subject to the same bulk and surface effects problems as are other semiconductor devices that employ p-n junctions. However, for most applications where reverse bias operation is required or for switching, they are about 1 order of magnitude less sensitive (in damaging fluence or dose units) than equivalent solar

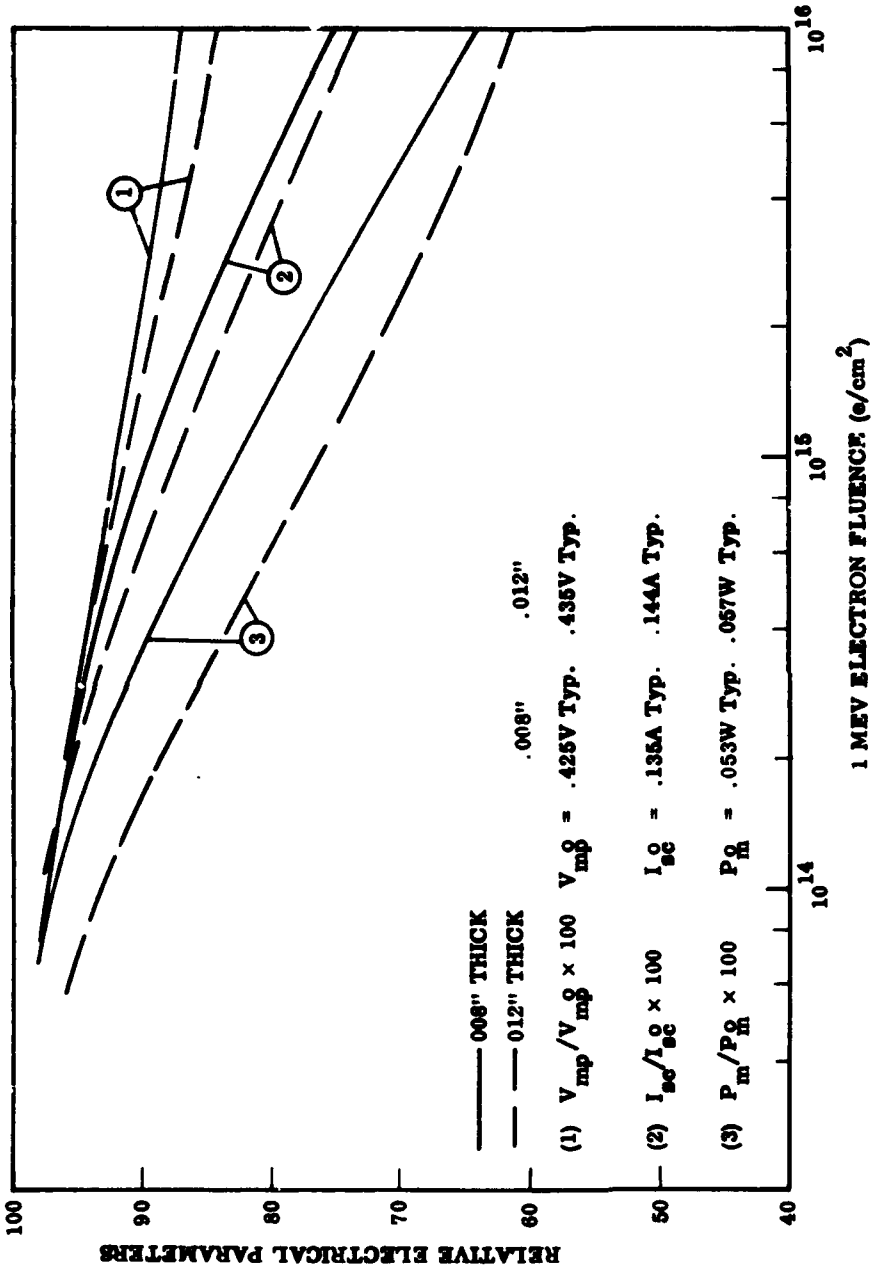

Figure 8-4. Normalized 10 ohm - centimeter n/p cell degradation of 27°C for normal incidence 1-MeV electrons.

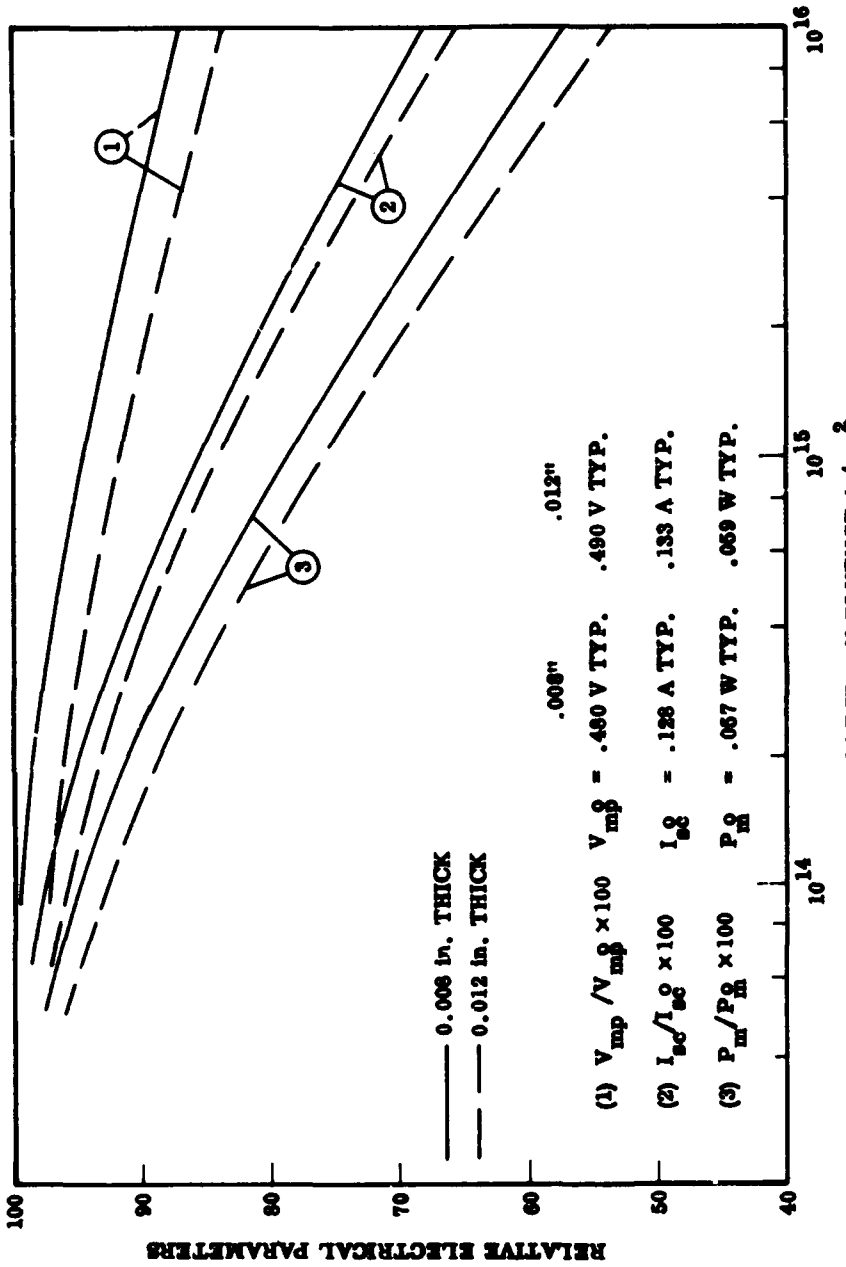

Figure 8-5. Normalized 2 ohm - centimeter n/p cell degradation at 27°C for normal incidence 1-MeV electrons.

cells or bipolar transistors (Reference 9). Some types (e.g., switching diodes) frequently are doped heavily to reduce the dependence on lifetime degradation and to decrease the switching time. Brief consideration now will be given to p-n junction, rectifier power, zener, and tunnel diodes.

In an ideal p-n junction, the current voltage characteristic may be represented by this relation:

$$I = \left(\frac{qD_p p_o}{L_p} + \frac{qD_n n_o}{L_n}\right)\left(e^{\frac{qV}{kT}} - 1\right) \equiv I_s\left(e^{\frac{qV}{kT}} - 1\right), \qquad (8\text{-}10)$$

which is for uniform p and n regions with an abrupt junction, where V is the voltage across the p-n junction (applied voltage-IR drop). D_n, L_n, and n_o are the diffusion coefficient, diffusion length, and minority carrier density, respectively, in the p-region and, correspondingly, in the n-region.

I_s is the reverse saturation current contributed by the bulk regions and is usually many orders of magnitude larger than the "ideal" value. Additional contributions exist to I_s from the finite transition region of the form:

$$I_{st} = \frac{q\Sigma_t d_t n_i}{2\tau} \qquad (8\text{-}11)$$

where d_t is the width of the space charge region, Σ_t its area, and τ and n_i are the lifetime and intrinsic carrier density (Reference 9). The general current-voltage characteristics will be of the form $I = I_{si}[\exp(qV/A_i kT) - 1]$ for each contributor where A_i is in the range 1 to 2 for bulk and transition region contributions (Reference 10). As indicated by the simple relationships I_s will tend to increase initially due to radiation degradation of both bulk and space charge region lifetimes.

Bulk-carrier removal will decrease the bulk conductivity with a resulting increase in forward voltage. For switching diodes that utilize gold doping to reduce bulk lifetimes, radiation damage still may affect transition region lifetime, but the overall threshold for lifetime degradation is increased greatly and may not be perceptible before the onset of carrier removal effects. Due to design and

application variations, radiation sensitivity will cover a broad range of particle fluence.

Diodes clearly will be subject to surface effects resulting from ionization-induced charge in SiO_2 passivation layers or charge accumulation in weakly bound surface states near reverse biased p-n junctions (Reference 10). This often leads to the formation of an induced "channel" in the underlying silicon whose effect will be to contribute a current of the form $I = I_s \exp(qV/AkT)$, where A may be quite large (>3) and the surface contribution often will dominate when present. These surface effects often will saturate at some low fluence (5×10^{14}) electrons per square centimeter.

Other parameters that are less affected by radiation are (1) breakdown voltage that increases from increased resistivity, (2) diode capacitance, and (3) switching times, with the latter decreasing due to decreases in τ.

Zener diodes, because of the highly doped n and p regions and normal mode of operation (near avalanche breakdown), are fairly radiation-resistant structures (Reference 9).

Rectifier diodes, due to the requirements of high breakdown voltage and low-voltage drop at high current and power handling capability, require large volume and long carrier lifetimes. Increased reverse leakage currents due to lifetime reduction are the predominant effects observed. The P-I-N rectifier diodes that use highly doped p and n regions and a relatively thick intrinsic I-region are subject to increases in the voltage across the I-region. This voltage increase is proportional to the regional thickness divided by the diffusion length (Reference 9). These diodes also will be subject to increases in forward voltage due to conductivity changes, but neither type of voltage increase is severe.

Tunnel diodes operate by means of a majority carrier tunneling process between highly doped p and n regions with an abrupt as well as thin transition region. These characteristics result in relatively high radiation resistance (Reference 27). The changes that have been observed at high radiation levels have been correlated with defect production in the transition region, which causes changes in tunneling current by providing alternate states through which to tunnel.

Bipolar Transistors. Bipolar transistors, dependent on minority carrier transport, have been found generally to be one of the more

sensitive devices used in conventiona electronic circuits. Most of the permanent damage in these devices results from minority carrier lifetime degradation in the base region and, to a lesser extent, in the collector. For higher exposure levels, bulk carrier removal may alter the collector bulk resistivity (Reference 14). Certain bipolar transistors, which employ an SiO_2 passivation layer on the exposed semiconductor surface (Figure 8-6), have had problems associated with the effect of charge buildup in the SiO_2 layer (Reference 10).

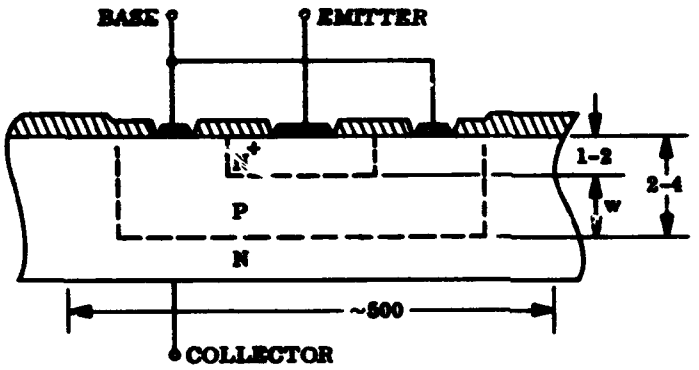

Figure 8-6. Planar transistor construction (schematic).

The general effects of radiation on bipolar transistor electrical characteristics (Reference 9) can be summarized thus:

1. The current gain is usually the most seriously affected device characteristic primarily because of lifetime degradation in the base. Surface effects (ionization), due to charge buildup near or on the emitter base junction, may cause gain degradation through reduction in emitter injection efficiency. This is generally of secondary importance.
2. The reverse leakage current may tend to increase due to surface effects through ionization-induced charge buildup either in passivation layers (SiO_2) or in weakly bound or absorbed surface layers. It also may increase because of lifetime degradation in the junction space charge region.

3. Base-to-emitter and collector-to-base breakdown voltages as well as base emitter punch-through voltages are affected by changes in bulk resistivity and also may be affected by surface effects caused by "channels" induced by positive charge buildup.

4. Base and collector body resistances and saturation voltages are changed because of bulk resistivity changes.

5. The switching characteristics also are changed slightly, i.e., storage time is decreased and turn-on time is increased because of lifetime and resistivity changes.

Although device structure will play an important role in any device's response to radiation, a few general rules concerning attributes that are important to radiation resistance can be given (Reference 9). Those with thinner base, higher frequency, and smaller junction area (size) usually are more resistant. Even though they still are affected by surface ionization, planar, SiO_2-passivated devices are less susceptible than nonpassivated devices as far as surface effects are concerned.

A wide variation in observed gain degradation (4 orders of magnitude of fluence) presumably arises from the equally wide variation in transistor structure and processing techniques. Some understanding of the source of this variation can be gained by use of simplified transistor theory for a planar geometry (Figure 8-6) (Reference 9).

In general, the low-frequency common base current gain, α_1, can be written as the product of 3 factors, $\alpha_1 = \gamma_1 \, b \, \delta_1$, where γ_1 is emitter injection efficiency (fraction of emitter current injected in the base), b is base transport factor (fraction of injected emitter current that reaches collector), and δ_1 is surface and/or transition region recombination factor.

The first order theory states that b is the primary factor affected by radiation since it depends on the base region diffusion length or lifetime (Reference 9) and can be approximated by:

$$b \cong \frac{1}{1 + \frac{w^2}{2L^2}} \qquad (8\text{-}12)$$

where w is the base region (narrow) width. Using the fact that L^2 =

D_τ and τ degrades as a function of Φ (Equation 8-1), it is possible to get a variation (Reference 9) for the common emitter current gain, $\beta = \alpha_1 / 1 - \alpha_1$. This variation is

$$\Delta\left(\frac{1}{\beta}\right) = \frac{1}{\beta} - \frac{1}{\beta_o} = \frac{0.2\, K_\tau \Phi}{f_\alpha} \qquad (8\text{-}13)$$

where f_α is α cutoff frequency $\cong 0.4\ D/w^2 = 1.22\ f_\tau$. f_τ is the gain bandwidth product.

A nomograph (Figure 8-7) has been constructed for NPN silicon transistors on the basis of the previous relations for determining the relative degradation, β/β_o, as a function of 1-MeV electron fluence. K_τ will depend on injection level (emitter current) and will be taken to be of the form $K_\tau = K_{\tau o}(I_E/I_{Eo})^{-0.25}$ with I_E the emitter current density (Reference 10). The nomograph is constructed for one injection level, $I_{Eo} \simeq 1$ ampere per square centimeter. Appropriate scaling of the indicated fluence scale is required to generate the equivalent fluence for different injection conditions.

To use the nomograph, a line is first drawn through the β_o and f_α values. Next a line is drawn through the appropriate intersection of the first line with the pivot line and the equivalent electron fluence for the NPN scale. The intersection with the β/β_o scale gives the gain value. The damage coefficient is more nearly an empirically adjustable coefficient for a given class of device, category of transistor construction, and even manufacturer (Reference 14).

The operating and fluence range is limited to where the simple theory holds. Charged particle irradiation introduces a component of base current that originates in the space charge layer of the base emitter junction and is most important at low injection levels (low emitter current). Also changes in emitter efficiency arising from changes in surface recombination velocity are again more important for low injection levels (Reference 10). This simple theory for homogeneous base regions has been modified for nonuniform doping (drift field transistors) with the f_α value being a function of the doping level variation (Reference 9).

Deviations from this behavior have been observed at low exposures. This is attributed mainly to ionization-induced surface effects that enhance leakage currents and increase surface recombination velocity. A specific example of the effect of surface ionization on $\Delta(1/\beta)$

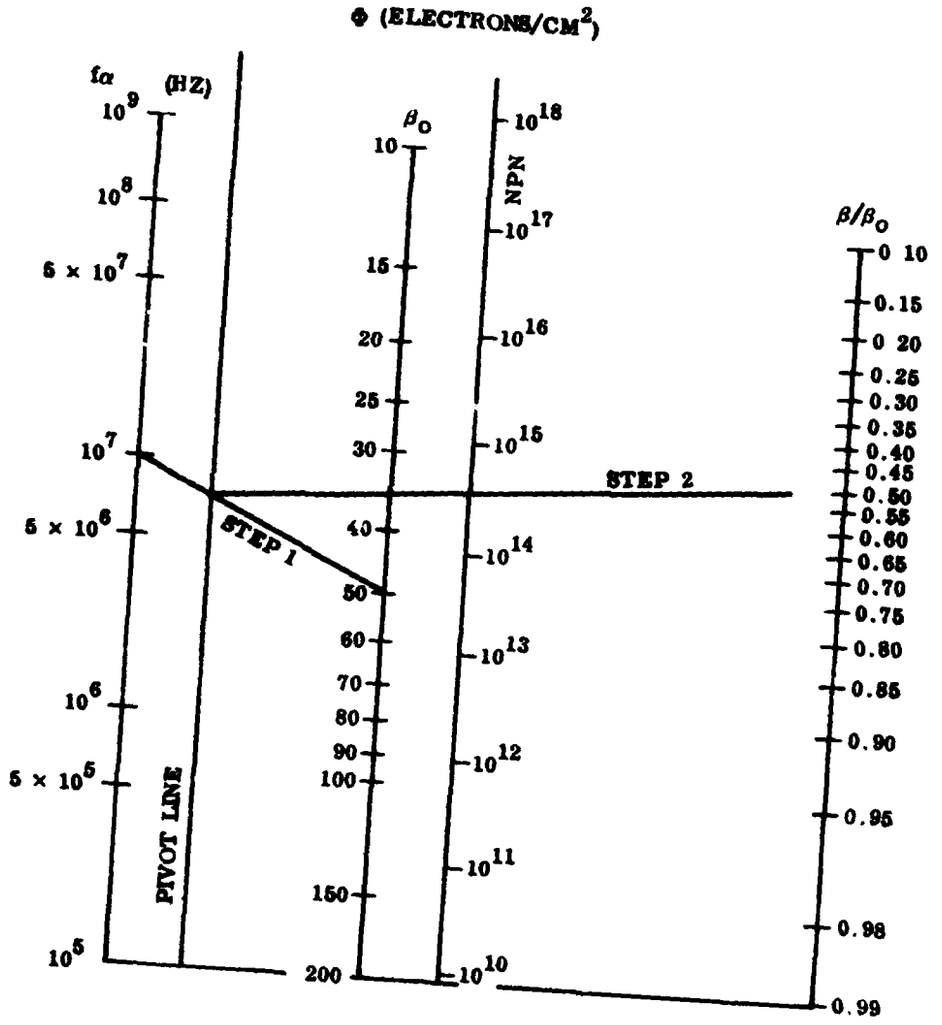

Figure 8-7. Nomograph for obtaining variation in grounded emitter current gain of silicon NPN transistors with equivalent 1-MeV electron fluence.

for particular NPN planar transistors has been given by Brucker for 1-MeV incident electrons (Reference 10). He showed that the experimental data fit the relationship:

$$\Delta\left(\frac{1}{\beta}\right) = K_s\left(\frac{\Phi}{I_E}\right)^a + K_b\frac{\Phi}{I_E{}^m} = \Delta_s\left(\frac{1}{\beta}\right) + \Delta_b\left(\frac{1}{\beta}\right) \qquad (8\text{-}14)$$

where K_s and K_b are surface and bulk damage coefficients, Φ the 1-MeV electron fluence, I_E the emitter current, and with typical values of the exponents $a \simeq 0.5$ and $m \simeq 0.25$. The equation holds for $\Phi \leq 5 \times 10^{14}$ electrons per square centimeter since the surface contribution saturates above this fluence. This relation emphasizes the relative importance of the surface effects contribution at low emitter currents. Brucker has attributed the surface effects contribution to charge accumulation in the SiO_2 passivation layer that results in an increase in the surface recombination velocity in the emitter base depletion layer. He also showed that surface effects contributions are only dependent on ionization. PNP devices did not show any surface effects.

A study of the same problem in NPN planar transistors has been made by Poch and Holmes-Seildle. A Co-60 radiation source was used and results obtained show the same general form for the surface and base contribution with values of the exponent, a , in the range 0.5 to 1 and m values in the range 0.25 to 0.35 (Reference 28). Representative results for a large number of transistors of a single type are given in Figures 8-8 and 8-9 where $\Delta_s(1/\beta)$ and the final β value for $\beta_o = 100$ are plotted first as a function of collector current (Figure 8-8) and then as a function of dose, rads (Si), for 0 to 10 volts applied bias (Figure 8-9).

The next most important group of transistor device characteristics affected by radiation are the reverse-biased leakage currents. These currents usually flow across the collector base junction and are denoted by I_{CBO}. They have been shown to be more sensitive to surface effects due to ionization-induced charge buildup in weakly bound surface states or in passivation layers (SiO_2) and are less dependent on permanent bulk lifetime or resistivity changes (Reference 10). The general class of radiation effects on transistor characteristics would be similar to that already discussed for reverse biased diodes, except for the thinner base and collector regions. Leakage current will be considerably increased because of lifetime reduction in the fairly wide collector base depletion regions due to the low doping for collector and base regions (Reference 9). As indicated in the

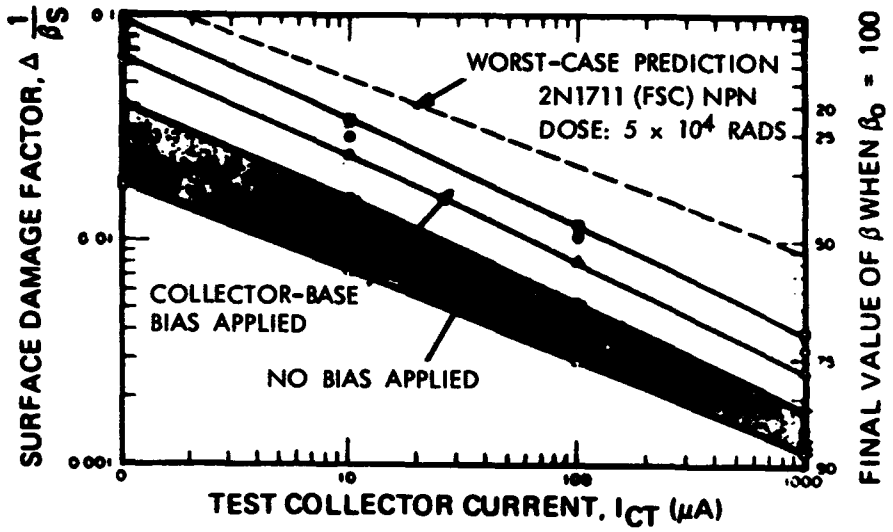

Figure 8-8. Degradation of Fairchild-type 2N1711 transistors versus test collector current at gamma ray dose of 5 x 10^4 rads.

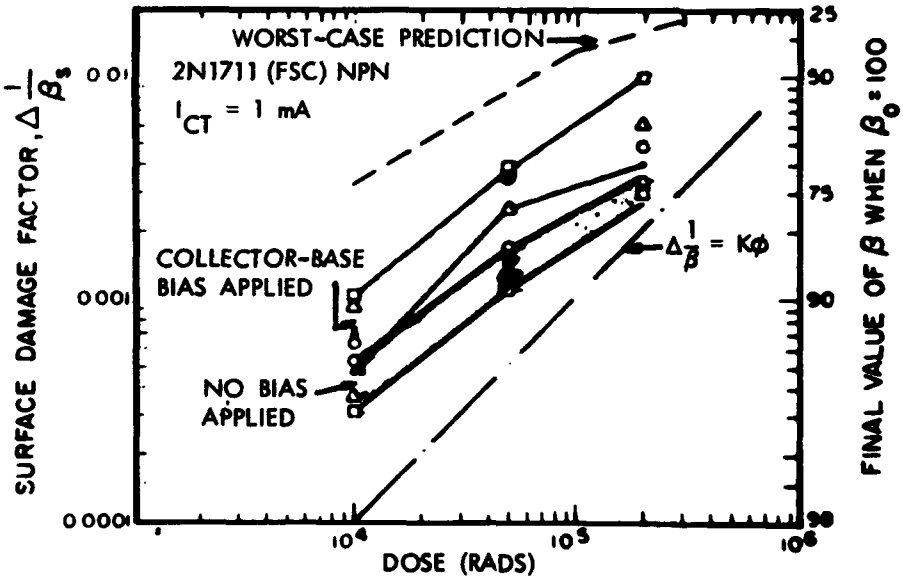

Figure 8-9. Degradation of Fairchild-type 2N1711 transistors versus dose of Cobalt-60 gamma rays, showing effect of irradiation bias and deviation from linearity.

discussion on p-n junction diodes, a fluence considerably greater (1 to 2 orders of magnitude) than for comparable gain degradation is generally necessary to cause appreciable changes in I_{CBO} due to bulk permanent damage.

However, as also discussed in the section on p-n junction diodes, the leakage currents due to surface effects (ionization), when present, usually are dominant over other contributions. They result from the same sources as discussed previously (Reference 10). These effects thus are expected to be most serious for PNP types and not serious for NPN types.

Other transistor parameters (e.g., $V_{CE(SAT)}$ and breakdown voltages) generally will not be as much affected by the space radiation environment as those parameters discussed previously. Figure 8-10 gives representative relative variations of $V_{CE(SAT)}$ and I_{CBO} for an NPN planar transistor as a function of 1-MeV electron fluence. Comparison of the two curves shows that $V_{CE(SAT)}$ is less sensitive than I_{CBO} for the same device (Reference 29).

MAJORITY CARRIER DEVICES. The principal representatives of this class are the insulated gate (or Metal-Insulator-Semiconductor) and the junction field-effect transistors. These devices are much less sensitive to bulk damage than to surface effects; therefore, changes in parameters are reported in terms of radiation dose in rads rather than electron fluence. Radiation effects will be discussed separately for the two basic types.

MIS Field Effect Transistors. The MISFET is made by sandwiching three materials—a metal (usually aluminum) deposited over an insulator (such as SiO_2) which previously had been grown or deposited over a semiconductor material (normally silicon). The geometry of this device is indicated in Figure 8-11.

Radiation-induced changes in the electrical characteristics of MIS transistors are principally demonstrated as a shift in the threshold voltage V_T (i.e., the voltage across the gate insulator necessary to just produce inversion in the channel). The model for threshold voltage is as follows:

$$V_T = \varphi_{ms} + 2\varphi_F - \frac{1}{C_{ox}} \left(Q_{ss} + Q_D\right)$$

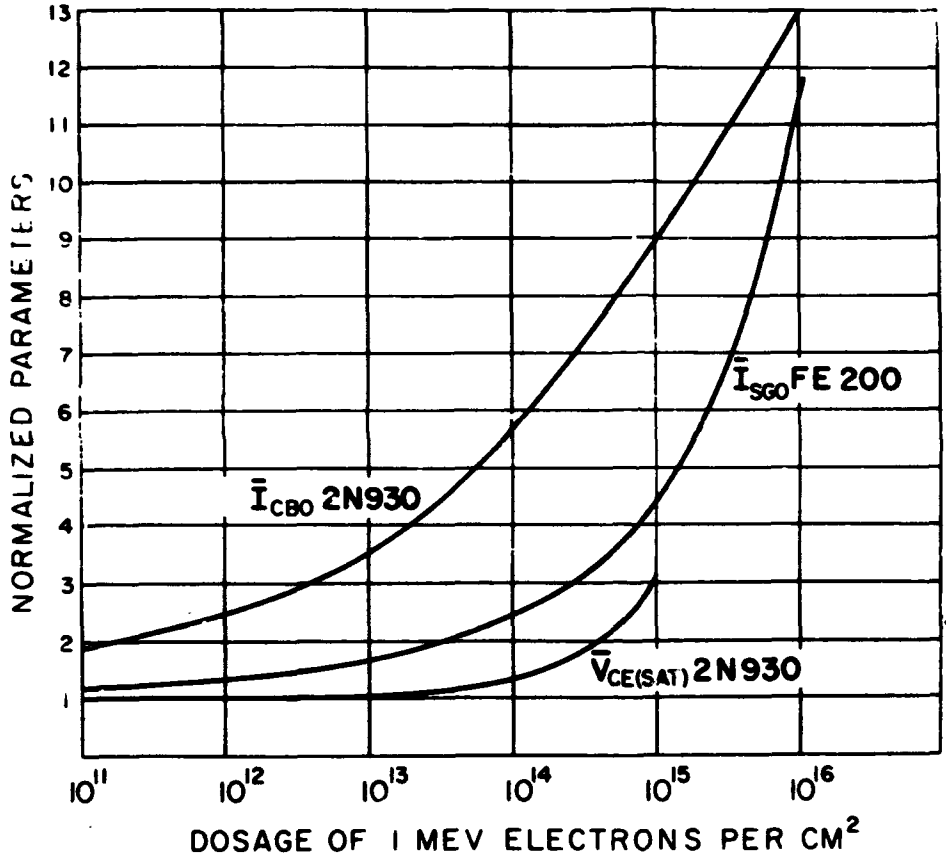

Figure 8-10. Normalized leakage and saturation parameters versus electron irradiation for bipolar type 2N930 and junction FET type FE200 transistors.

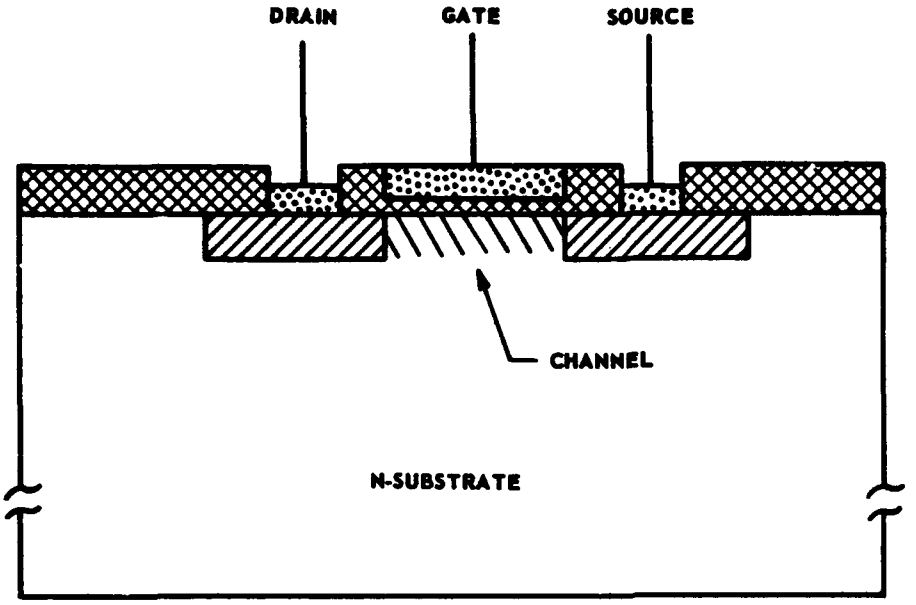

METALIZATION, TYPICALLY 7,000 - 10,000Å

P-TYPE DIFFUSED REGIONS

INSULATOR (USUALLY S_1O_2), TYPICALLY 1000Å BENEATH GATE, 10,000 - 14,000Å ELSEWHERE.

a. Physical Configuration (not to scale)

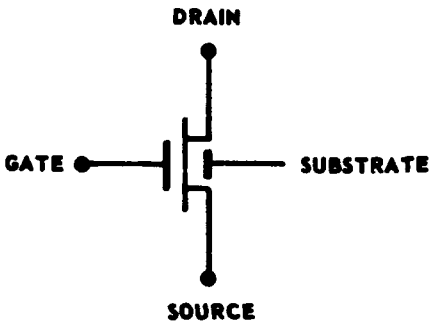

b. Electrical Symbol

Figure 8-11. MIS transistor.

where

φ_{ms} = work function difference between the gate conductor and the bulk silicon

φ_F = Fermi potential

C_{ox} = gate oxide capacitance

Q_{ss} = surface charge in the oxide

Q_D = charge in the bulk depletion region, a positive quantity for p-channel, negative for n-channel.

The V_T shift caused by ionizing radiation is accounted for in the Q_{ss} term, a positive quantity for both p- and n-channel devices. Shifts in V_T then are in the negative direction such that p-channel transistors normally require increasing values of negative gate voltage to maintain constant drain current and n-channel transistors require decreasing values of positive gate voltage to maintain constant drain current.

The basic cause for the V_T shift is a positive charge build-up in the gate oxide due to capture of holes in traps near the oxide-silicon interface. Experiments have shown that this trapped charge is influenced by the oxide field during irradiation. The largest V_T shifts are observed for both p- and n-channel devices when a positive bias is applied to the gate during irradiation since the positive charge appears near the oxide-silicon interface. With the same reasoning, less shift is observed when a negative gate voltage is applied because the positive charge then appears near the gate electrode.

Some of these effects are illustrated by an example from work of Holmes-Siedle (Reference 65) shown in Figure 8-12. First the effect of bias amplitude and polarity is evident, and secondly, a saturation of the threshold voltage occurs at a level dependent on the applied bias.

MIS devices are rarely used in discrete component form since the main advantage of this construction is small size. Additional discussion of parameter changes in complex MIS structures and methods for hardening these devices are included in the next section.

Junction Field Effect Transistors. The junction FET differs from the MISFET in that a reverse biased p-n junction is used to

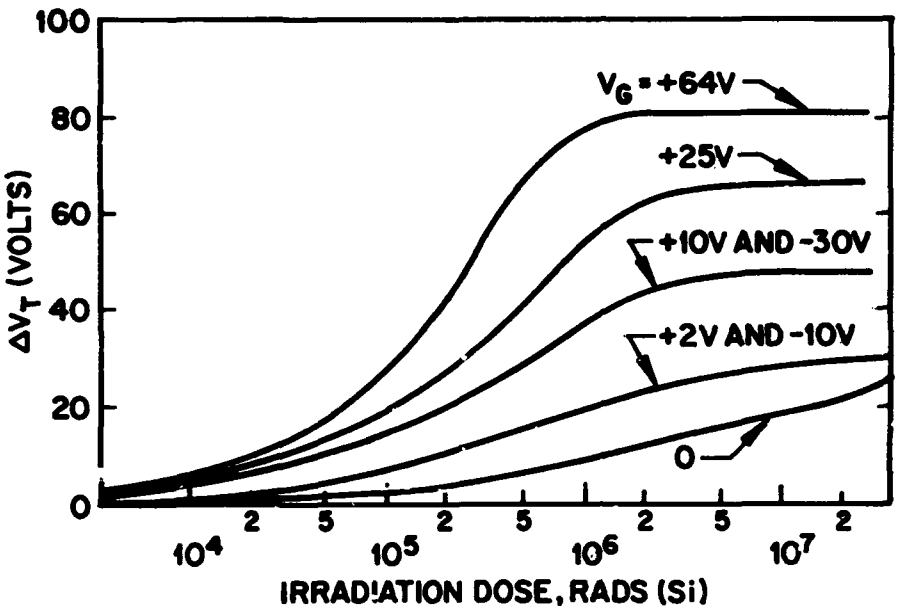

Figure 8-12. General form of shift in MIS transistor characteristics as a function of irradiation (Reference 65).

restrict majority carrier flow in a channel (Reference 34). It therefore does not suffer directly from the positive charge accumulation in an insulator. Experimental studies by Stanley using 1.5-MeV electrons have shown that these devices are generally more resistant to surface ionization effects as well as more resistant to bulk effects than almost any other active transistor (Reference 10). However, surface ionization does produce large leakage currents accross the gate to drain junction when the devices are operated under bias.

Ionization and displacement damage may cause increases in recombination in the space charge region, which results in slightly increased junction leakage currents. Results of a study of these devices are given in Figures 8-10 and 8-13, which compare the relative change in characteristics of a planar NPN bipolar transistor with those of a junction FET as a function of 1-MeV electron fluence (Reference 29). Parameters compared are $h_{FE}(\beta)$ for two injection levels with transconductance, g_m (evaluated at O-gate voltage) for

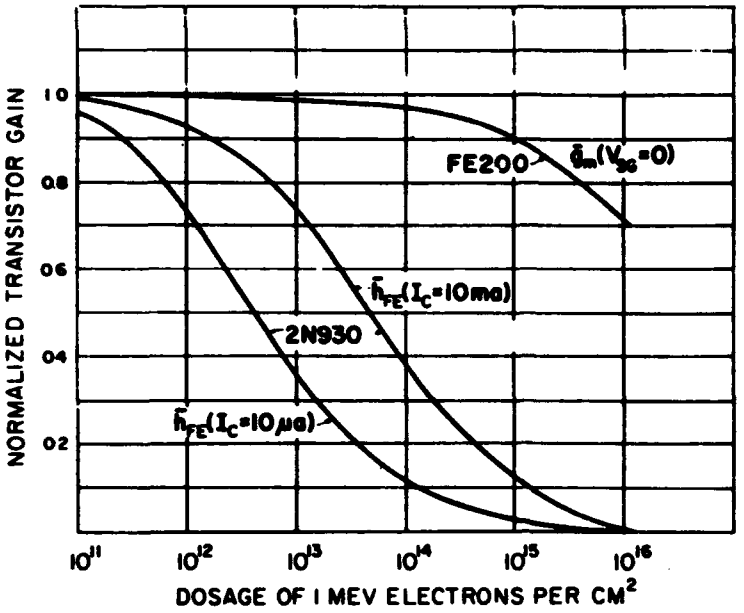

Figure 8-13. Radiation resistance of field-effect transistors (FE200 type) and bipolar transistors (2N930 type) under 1-MeV electron irradiation.

the FET in Figure 8-13, as well as I_{CBO} and $V_{CE(SAT)}$ for the bipolar with I_{SGO} for the FET in Figure 8-9.

INTEGRATED CIRCUITS. Many different types of complex integrated circuit devices exist. Monolithic IC's are those that have all active circuit elements diffused in a single silicon chip with interelement isolation by either a p-n junction or a dielectric layer. Thin film IC's, which utilize thin film epitaxial vacuum deposition techniques to achieve a similar configuration, are the other major construction type. Hybrid IC's combine both techniques.

In general, first order estimates of the radiation-induced changes in IC electrical parameters can be made from a knowledge of individual active element parameter changes; i. e., IC's may be treated as conventional circuits of small dimensions (Reference 9). One specific exception to this approximation, the dielectrically isolated junction FET, will be described in this section.

Bipolar IC's. These devices may utilize either dielectric or p-n junction isolation techniques and are sensitive to minority carrier

lifetime changes in the active element bipolar transistors. Circuit failure, however, is dependent on the sensitivity of the particular design to individual active element gain degradation.

Linear integrated circuits are considerably more sensitive to radiation effects than digital devices, as the result of the lower current levels at which these devices operate and the requirement of active components with high gain and long minority carrier lifetimes (Reference 66). The main effects observed in linear circuits are a reduction in open-loop gain, an increase in input bias current, and frequently a reduction in the maximum output swing.

The radiation failure criterion for digital circuits is usually taken as the point where the low level output voltage is higher than the noise immunity level of the following gates. This output voltage can increase in two ways, by a reduction in the output sink current caused by transistor gain degradation (for devices operated at high fanout) or by an increase in transistor saturation voltage (for devices operated at low fanout).

J-FET IC's. Although integrated circuits which utilize J-FETs for all active elements are rare, J-FETs are sometimes used as input transistors and pinchoff resistors on linear integrated circuits.

One of the methods of increasing speed in J-FET circuits is the use of dielectric isolation between the different active elements. This physical configuration is illustrated in Figure 8-14. Although it is desirable to analyze complex IC's as individual circuits of small size, this configuration is an example of possible interelement effects. A recent investigation was reported by Neamen, et al., of the effect of charge trapping in the dielectric on the electrical characteristics of the J-FET (Reference 67). They reported an increase in the short circuit drain current, I_{DSS}, and the gate turnoff voltage, $V_{GS(Off)}$, to a dose level of $\sim 10^6$ rads (Si) and a decrease in both parameters for further dose accumulation. The shape of this response curve is attributed to a net positive charge in the dielectric.

MIS IC's. The use of MIS IC's in spacecraft systems is very desirable from the standpoint of small size and low standby power. As a majority carrier device, they are expected to be insensitive to bulk damage up to high fluence levels. However, the effect of charge trapping in the gate insulator, characterized by a shift in the gate threshold voltage, can limit the performance of these devices.

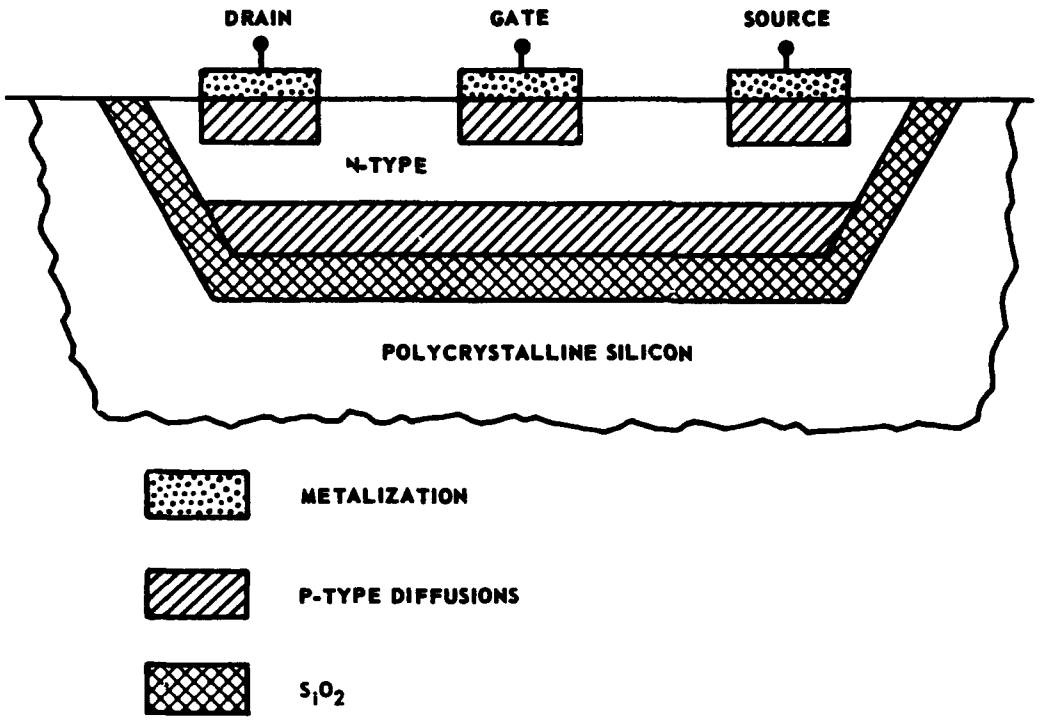

Figure 8-14. Dielectrically isolated junction field effect transistor.

A popular representative of this technology is the complementary MOS (CMOS) structure, an example of which is shown in Figure 8-14A. Since this structure employs both an n-channel transistor (which has a positive gate bias for input high conditions) and a p-channel transistor (which has a negative gate bias for input low conditions), the response of the circuit to ionizing radiation is somewhat dependent on the input voltage level, as shown in Figures 8-14B and 8-14C.

Some of the hardening methods employed for these structures are summarized in the next section.

8.2.4 Radiation Hardening of Semiconductor Devices

Selection of components least affected by radiation is perhaps one of the most logical hardening techniques. As an example, a transistor is first specified to meet particular circuit requirements, e.g., voltage or current gain, power handling capacility, breakdown voltage, etc. From a group of transistors having the desired electrical characteristics, the particular device having the most desirable

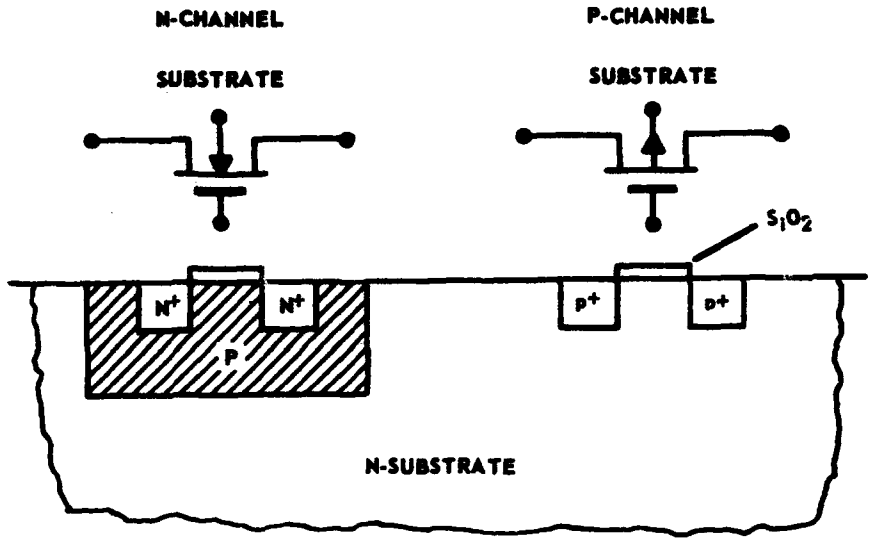

a. Physical Structure

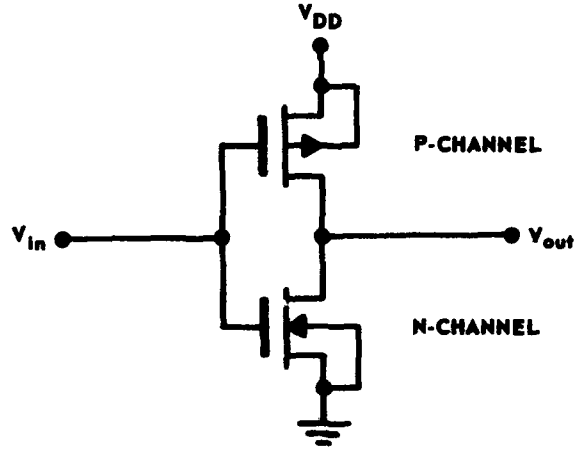

b. Electrical Symbol

Figure 8-14A. Complementary MOS (CMOS) inverter.

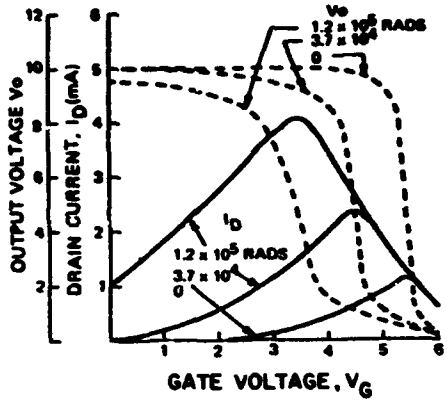

Figure 8-14B. Change in CMOS inverter transfer characteristic for input high condition. (Gate bias on p-channel is 0 volts, +10 volts on n-channel. V_{DD} = +10 volts.) (Reference 68).

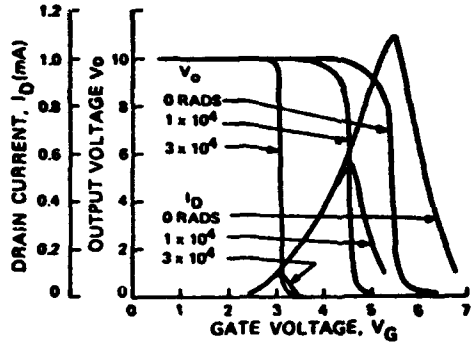

Figure 8-14C. Change in CMOS inverter transfer characteristic for input low condition. (Gate bias on p-channel is +10 volts, 0 volt on n-channel. V_{DD} = +10 volts.) (Reference 68).

radiation characteristics is then chosen. The procedure is much more complicated in the case of integrated circuits for which radiation hardening rules must be applied at the component design level.

Some of the guidelines that can be used in minority carrier device design are as follows:

1. Use high frequency, low voltage transistors
2. Use high gain transistors
3. Operate at low fanout
4. Operate at high emitter injection level and strong base drive, and
5. Incorporate gold doping.

Development of radiation hardened MIS devices has received much attention recently. The methods found to be most effective are (1) modifying the gate dielectric, (2) replacing the typical SiO_2 with a different dielectric, or (3) optimizing the manufacturing process. Some improvement is found with each of these methods.

The dielectric modification techniques include chromium doping reported by Kjar, et al. (Reference 69) and metallic ion implantation reported by Hughes, et al. (Reference 70). Hence, Al ion implant is used only on the end channel regions of complementary MOS structures. In the former, chromium is used for the gate metallization in place of the typical aluminum; in the latter, 10^{14} to 10^{15} aluminum ions per cm^2 are implanted into the oxide. The implant method reduces the sensitivity of those devices operated with positive bias during irradiation, e.g., the n-channel device of a CMOS inverter, but increases the sensitivity of devices with negative bias (Reference 70).

Various dielectric materials have been studied as SiO_2 substitutes. These include aluminum oxide (Reference 71), silicon oxynitride (Reference 72), nitride-oxide sandwich layers (Reference 30), and gallium arsenide phosphide (Reference 31).

Aubuchon (Reference 32) has shown that p-channel MOS devices can be hardened to at least 10^6 rads by optimization of the SiO_2 gate insulator.

A comparison of some of these hardening methods is included as Figure 8-14D. Variations in processing can still result in significant differences in radiation responses. Therefore, data in Figure 8-14D should be regarded only as representative of the several part types tested.

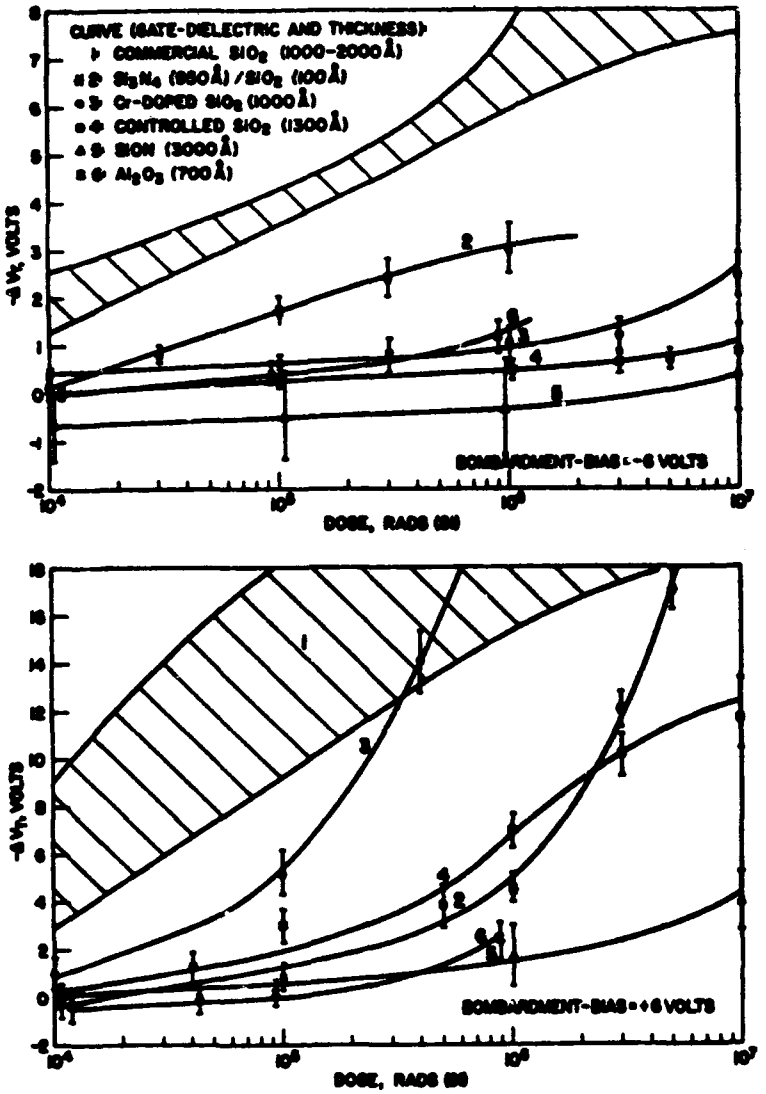

Figure 8-14D. Threshold-voltage shift as a function of radiation-dose at 2 different bombardment biases for MIS transistors possessing various gate-insulator materials (Reference 33).

8.3 TRAPPED RADIATION EFFECTS ON THERMAL CONTROL AND SOLAR REFLECTOR SURFACES

8.3.1 Introduction

Those materials that must necessarily be located on or near the external satellite surface may be exposed to a considerably more damaging trapped proton and trapped electron environment than that experienced by more well-shielded locations as is illustrated in Figures 8-17 to 8-24. Thus, even though these materials may be orders of magnitude less radiation sensitive than, for example, semiconductor devices, their physical location, minimal shielding, and widespread occurrence of intense low-energy radiation environments require consideration of the nature of such radiation effects.

A particularly important example of this situation is provided by materials used for thermal control surfaces and solar reflector surfaces. Considerable experience both in the laboratory and on orbiting satellites has demonstrated the radiation-induced degradation in (1) solar absorptance α_s and (2) the ratio of α_s to total hemispherical emittance, ϵ_{th} or α_s/ϵ_{th}. These are the two basic properties for thermal control application (Reference 35).

Thermal control materials are composed of a pigment, which is most important in determining α_s, and a binder material, which is usually the most important factor for determining ϵ_{th}. Trapped radiation primarily affects these materials by introducing additional defect sites primarily in the pigment, but also in the binder materials, through ionization and displacement processes (Reference 11). The defect sites act as color centers selectively increasing the optical absorption and, thus, the value of α_s. Some unusual circumstances exist in which certain organic binder materials may undergo changes in physical structure and even loss of material due to chain scission of polymerization processes that change the value of ϵ_{th}.

No clear-cut approach to analyzing radiation damage to materials used for passive thermal control surfaces has been very successful. This situation exists primarily because of the fairly complicated materials used for this purpose as well as because of the range of properties required to achieve the necessary ratio of α_s/ϵ_{th} (Reference 36). No one material or class of materials can provide the necessary variation in each of these parameters. Utilizing a pattern of several thermal control materials is not uncommon to achieve (1) a somewhat localized temperature control or (2) a thermodynamic "average" equivalent to that which could be achieved if a

continuous range of α_s/ϵ_{th} were available. Passive thermal control materials can be grouped into four broad categories:

1. Solar reflectors—low α_s, high ϵ_{th}
2. Solar absorbers—high α_s, low ϵ_{th}
3. Flat reflectors—low α_s, low ϵ_{th}
4. Flat absorbers—high α_s, high ϵ_{th}.

The majority of thermal control surfaces are in the solar reflector category and are typified by a pigment such as ZnO, TiO_2, or ZrO_2-SiO_2 in a silicon or silicate binder. Other binders such as acrylics and epoxies also have been used with varying degrees of success.

8.3.2 Physics of Radiation Effects

The diffused light scattering by the pigment material is the source of the low α_s. This characteristic will be affected by the natural presence or the introduction of defect centers that act as optical absorption sites (Reference 36). The emittance is dependent primarily on the lattice vibrational characteristics of the binder material. Thus, it is not as sensitive to the presence of a small concentration of defect centers unless they initiate gross changes in physical structure such as happens in organic binders after prolonger exposure to ionizing radiation. The primary radiation defects produced through ionization are dependent on the total ionization and not on the particle type, whereas the primary displacement cross section will have a range of thresholds.

The defect centers formed affect the optical absorption process through the introduction of defect energy levels in the forbidden gap of the insulator. They act as optical absorption centers for incident photons having the energy equal to the transition energy difference between the level and the valence band. This type of complex defect, often denoted as a color center, may have a rather broadband optical absorption due to the usually complex defect energy levels (Reference 37).

Additional factors that might make the pigment or, possibly, binder less sensitive to radiation-produced defects are the unknown impurity concentrations present as well as the imperfect or multicrystalline character. These factors both lead to "high" natural

defect center densities. Color center formation is not always confined to the pigment and, in certain cases, significant formation occurs in binder materials (Reference 38). Very few studies of the nature of the defect sites have been made other than to measure the reflectance as a function of wavelength for representative thermal control materials and as a function of irradiation conditions.

Color centers formed nearer the external surface are more important in their effect on diffused light scattering or α_s. Thus, low-energy protons (E < 1 MeV) deposit all or most of their energy through ionization in a thin material thickness (1 to 10 mils) and with a nonuniform depth distribution (Reference 35). They also produce correspondingly high atomic displacement densities in the same regions and are the most effective damaging environmental component for thermal control surfaces. Low-energy electrons, although of comparable fluxes, will produce much lower and more uniform displacement densities due to the higher displacement damage thresholds (typically 10 to 200 KeV) as well as the lower displacement cross sections.

8.3.3 Selected Radiation Effects on Thermal Control Surfaces

A few selected experimental studies of thermal control surfaces will be cited for illustrative purposes but are not necessarily representative. Because of the wide range of materials, compositions, methods of preparation, and dependence of observed radiation effects on these properties, reliance must be placed on prior irradiation studies for specific materials (Reference 35).

For certain specific materials and thicknesses, if the observed change in α_s could be verified to be dependent on total energy deposited in the material or on the surface ionization, then the change in α_s could be estimated as a function of orbital parameters using the ionization data of Figures 8-17 to 8-24. At present, insufficient data exist on the change in α_s as a function of proton or electron energy for any of the usual materials to enable the determination of an equivalent damaging particle fluence as a function of orbit.

Another problem in the presentation of experimental data is the recent discovery that considerable annealing occurs in α_s for oxide pigments when optical measurements are not made in a vacuum (Reference 38). Only a limited amount of data is available using

in situ optical measurements. Another complicating factor is the inevitable presence of solar UV degradation and the associated effects (Reference 39).

Irradiation of a large class of oxide pigment thermal control surfaces with protons in the 50- to 400-KeV energy range showed that the percentage increase in solar absorptance was nearly proportional to the energy absorbed or the exposure energy fluence, since all protons of these energies are stopped in the 1- to 10-mil-thick samples (Reference 36). Unfortunately, the optical measurements were not made in situ so that the absolute changes in solar absorptance were not directly applicable to space conditions.

Another set of proton irradiation data using 8-KeV and 2.5-MeV protons incident on two types of oxide pigmented thermal control surfaces is given in Figure 8-15. The percentage increase in α_s or $\alpha_s - \alpha_s^o$, where α_s^o is the initial solar absorptance, is plotted against proton fluence for each of the two materials and proton energies. Again, the optical measurements were not made in situ so that these data would represent only a lower limit on the actual degradations expected in a vacuum. Finally, to enable some assessment of the difference in observed degradation for optical measurements in air and in situ, data given in Figure 8-16 are presented to show the absolute $(\alpha_s - \alpha_s^o)$ for three oxide pigment materials as a function of 2-KeV proton fluence (Reference 38). The curves labeled Z and S are for the same generic materials (S-13 and Z-93) that are presented in Figure 8-15.

Second surface mirrors also are used as solar reflectors. In contrast to pigmented binders (paints), these mirrors take the form of silver or aluminum deposited on fused quartz and are known to be extremely resistant to environmental deterioration (Reference 41). No change in α_s or ϵ_{th} has been observed after 20,000 effective sun hours of UV, 10^{16} 2 KeV protons per square centimeter, 10^{16} 0.8 MeV electrons per square centimeter, or many combined environments. These mirrors must be attached to the external surface with space stable adhesives.

Solar absorbers are generally in the form of electroplated or polished metals, although multilayer coatings have been employed successfully. Protons with energies below 10 KeV and fluences of about 10^{16} per square centimeter are known to give a blistered appearance to vapor deposited aluminum, which consequently affects

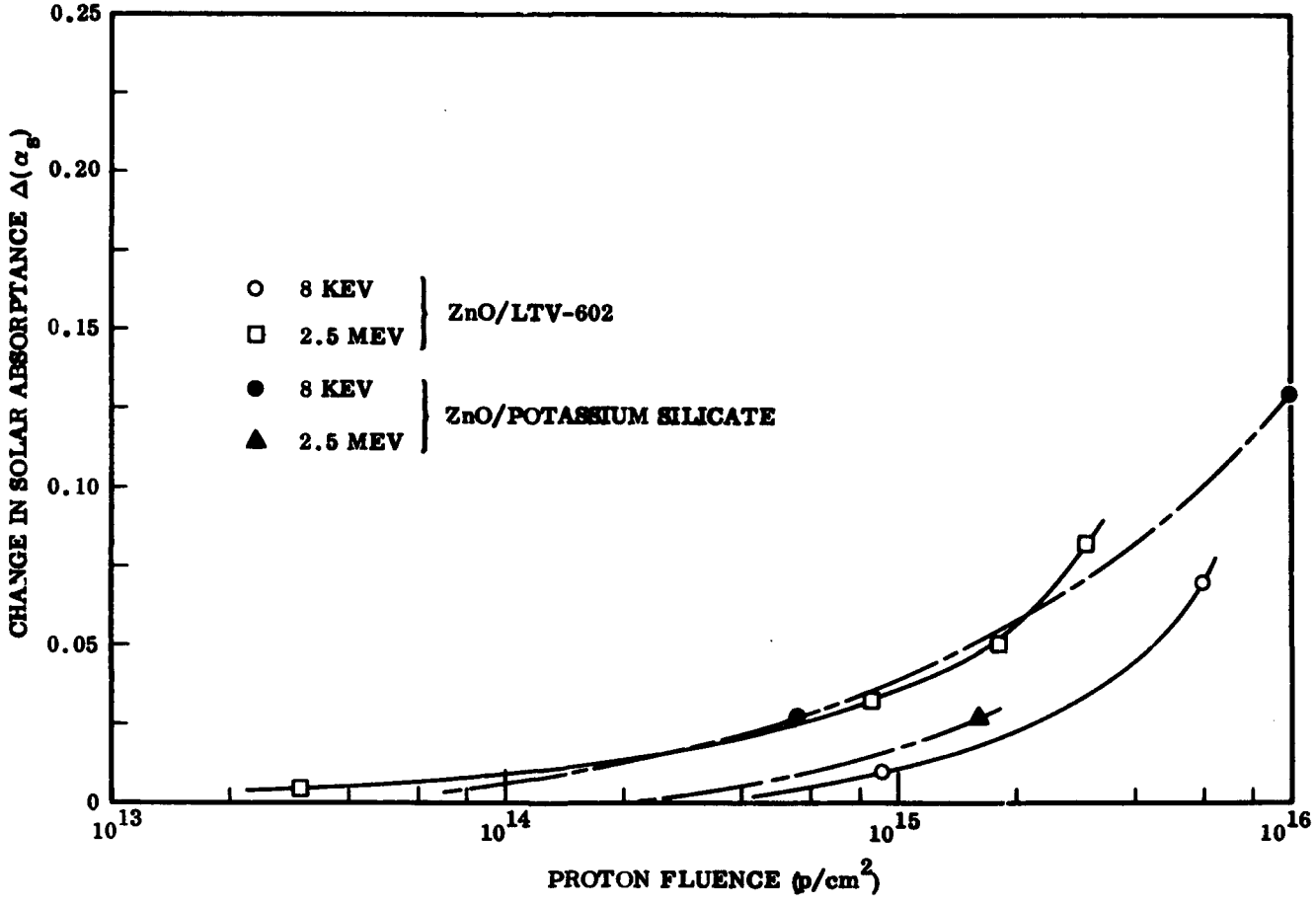

Figure 8-15. Change in solar absorptance due to protons for two oxide pigmented thermal control materials.

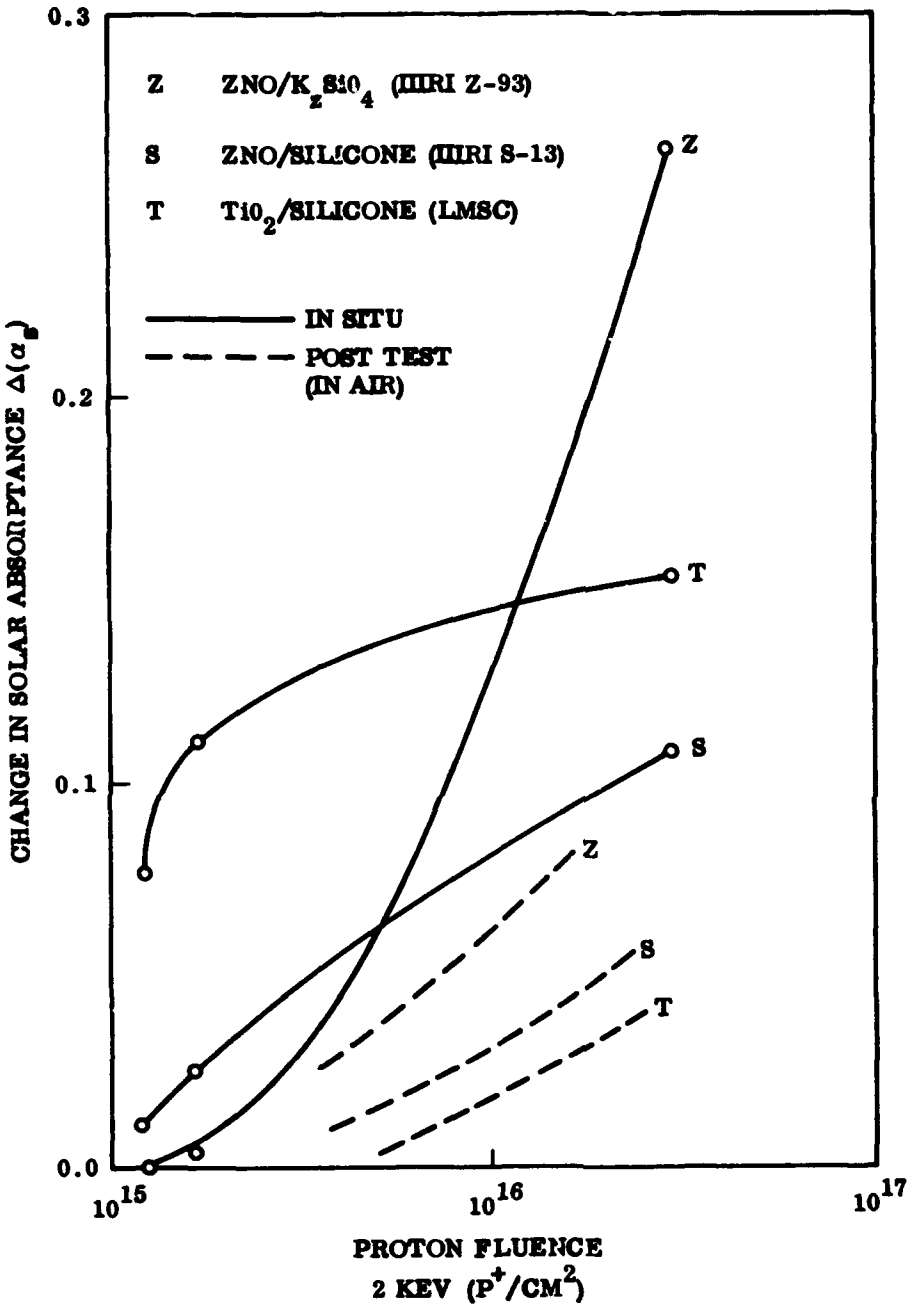

Figure 8-16. Absolute change in solar absorbtance as a function of 2-KeV proton fluence.

the absorptance. Chemically brightened aluminum reacts similarly and the mechanism(s) for this is not understood (Reference 40).

8.4 TRAPPED RADIATION EFFECTS ON SELECTED OPTICAL MATERIALS AND DEVICES

8.4.1 Introduction

Another class of materials or devices that may have a minimum amount of shielding and, therefore, may be exposed directly to the enhanced low-energy components of the trapped radiation environments is optical materials or devices. Optical materials are not classed as exceptionally radiation sensitive when compared to other materials (e.g., semiconductors), but exposure to severe environment means that any radiation effect should be examined.

Most optical materials are inorganic, nonmetallic insulators. The predominant effect of trapped radiation on such materials is the production of defect sites or centers that act as selective optical absorption centers and, thus, decrease the optical transmission (Reference 42). Certain organic optical materials could be subject to physical structural changes due to scission and cross linking induced by ionization interactions. However, these will not be discussed here.

Optical materials, coatings, and adhesives that are used in conjunction with solar cells are considered first. Representative degradation data are presented for selected laboratory proton and electron exposures.

8.4.2 Solar Cell Cover Slides and Associated Optical Coatings

On most spacecraft, the largest area exposed directly to the radiation environment is composed of glass cover slides on silicon solar cells (Figure 8-2) composing the vehicle power source. The cover slides must meet three primary requirements (Reference 3): (1) provide a suitable high-emittance surface that will minimize the operating temperature of the solar cells and thus maximize the power conversion efficiency, (2) provide a shield for the relatively sensitive solar cells from the space radiation environment, which reduces the cell efficiency, and (3) serve as an optical match with an index of refraction that maximizes the optical transmission to the solar cell in the wavelength range 0.4 to 1.1 microns. All these features increase the end-of-life power available from the solar arrays.

The most commonly used materials for solar cell cover slides are Corning 7940 industrial grade fused silica and Corning 0211 microsheet glass in thicknesses ranging from about 3 to 60 mils. The cover slides normally are bonded directly to the cells with a silicon adhesive with or without primer. Clear epoxies occasionally are used also. Because most of these adhesives are darkened by solar ultraviolet (UV) radiation, the cover slides are provided with a multilayer-deposited UV-rejection filter at the adhesive interface to reflect energy at wavelengths below about 0.42 microns. Front surface reflection losses are minimized by the use of a nominal quarter wavelength coating, usually MgF_2.

Very thin integral cover slides are also in development (Reference 43). The most common of these are forms of SiO_n, which is deposited directly onto the solar cell generally by high vacuum sputtering or electron beam evaporation techniques. Ultraviolet rejection filters are not required and antireflection coatings are not employed. The optical darkening from solar ultraviolet can be significant, depending upon the exact stochiometry of this material, but resistance to electron and proton damage is generally comparable to that of 7940 cover slides. Solar ultraviolet can produce transmittance changes due to oxygen desorption in some forms of SiO_x that are reversible upon exposure to air (Reference 35).

Thermal emittance is a decreasing function of the cover slide thickness below about 2 to 3 mils. The minimum acceptable thickness depends upon the expected radiation environment and the thermal emittance requirements.

8.4.3 Physics of Radiation Effects

Radiation damage to cover slides has the ultimate effect of reducing the solar transmittance to the solar cell due either to the low-energy proton damage in the antireflective coating, or damage by electrons or protons within the cover slide materials by formation of color centers.

Little is understood about the details of the coloration in the microsheet, but rather extensive studies on silica materials indicate that the coloration there is due to covalent bond rupture between the Si and O, oxygen vacancies, oxygen interstitials, or an internetwork oxygen molecule of O_2^+ ion (Reference 44). The relative importance of these and other possible color centers is dependent upon impurities present.

8.4.4 Selected Radiation Effects on Solar Cell Cover Slide Materials and Coatings

Table 8-2 summarizes some of the degradation data for selected materials, proton and electron energies, and exposure fluences that may be useful in assessing the magnitude of the expected degradations (Reference 45).

8.5 ORBITAL AND SHIELDING EFFECTS ON DAMAGE PARAMETERS

8.5.1 Introduction

The need for rapid, approximate estimates of the expected degradation in the characteristics of complex materials and devices due to trapped radiation has resulted in the development of radiation damage models for some sensitive classes of materials or devices. These models are based on the correlation between degradation in device characteristics and the degradation in a single bulk or surface material property for a certain range of environmental exposure. In particular, the discussions in Sections 8.2.2, 8.2.3, and 8.2.4 have grouped the materials and devices treated there into three major categories.

The first category comprises those devices for which the radiation-induced changes depend primarily on the total energy deposited near the surface. Typical members of this group are Fairchild Type 2N1711 transistors and MOSFET's. Figures 8-7 through 8-12 show degradation as a function of dose.

The second category comprises devices whose degradation is related most easily to a parameter called the equivalent 1-MeV electron flux. This group includes solar cells, bipolar transistors, and junction FET's. Figures 8-3, 8-4, 8-6, 8-9, and 8-13 show degradation as a function of equivalent 1-MeV electron flux.

The last category consists of materials or surfaces whose performance degradation is neither of the above types but for which representative degradation data have been given for selected electron or proton energies. This group includes thermal control surfaces, solar reflection surfaces, solar cell cover slides, and optical coatings.

The primary purpose of this subsection is to discuss and present figures giving dose and equivalent 1-MeV electron flux values for

Table 8-2. Cover slide transmission losses due to radiation.

		Electrons						Protons							
Fluence (e, P/cm^2)[g]		2.7+15	1.0+16	2.7+15	1.0+17	1.0+16	2.5+16	1.0+17	5.0+17	1.2+12	2.1+13	3.4+14	1.7+15	3.2+15	4.0+11
Energy (MeV)		0.3	1.0	1.2	1.2	2.4	Spectrum[b]	0.002	0.002	3.0	3.0	3.0	3.0	3.0	4.6
Material[a]	Measurement														
7940 Fused Silica	at 0.5μ		1.7(66)												0(30)
	at 0.6μ		2.2(66)												0(30)
	at 0.7μ		1.1(66)												0(30)
	Wideband				1.5	3.9	< 1(12)[d]								
	Solar Transmittance							0(12)[e] 32.5(12)[c] 17.5(3)[d]	0(12)[e] 52.0(12)[c] 4.5(3)[e] 40.0(3)[d]	0(12) 0(3)	0(12) 0(3) 3.4(3)[c]	0(3)	0(12) 0(3)	0(3) 4.3(3)[c] 12.3(40)[f]	
0211 Microsheet	at 0.5μ		5.6(6)												3.4(6)
	at 0.6μ		3.3(6)												1.1(6)
	at 0.7μ		2.2(6)												1.1(6)
	Wideband	3.2		7.6(26)											
	Solar Transmittance									4.3(6)	6.5(6) 3.3(3)	6.5(6) 3.3(3)		6.5(6) 3.3(3)	

Notes:

[a] Transmission losses (percent) given with shield thickness (mils) in parenthesis.

[b] Electron energies in range 0.6 to 2.2 MeV.

[c] With antireflective coating exposed.

[d] UV rejection (blue) filter, but antireflective coating exposed.

[e] UV rejection (blue) filter exposed.

[f] Blue-red filter exposed.

[g] Fluence given as A + 14 means A x 10^{14} per square centimeter.

trapped natural and injected radiation environments experienced by satellites under a variety of earth orbit and shield conditions. This information when combined with that given in the degradation curves of previous sections will yield predictions of performance degradation of various spacecraft system components due to radiation exposure during earth orbit.

To most easily relate this subsection's information to the degradation information in Sections 8.2, 8.3, and 8.4, the analysis of radiation dose as a function of orbital and shielding parameters will be treated first for both natural and injected trapped radiation. Following this, the analogous information giving equivalent 1-MeV electron flux as a function of orbital and shielding parameters is presented.

8.5.2 Method of Calculating the Trapped Radiation Environment

The natural trapped proton and electron environments exhibit wide variations in energy spectra as a function of orbital parameters. Because of this and because displaying dose values for a large number of typical orbital conditions was considered desirable, a rather extensive series of radiation transport calculations was necessary.

A set of computer programs developed by M. O. Burrell was modified for this purpose (References 46 and 47). These programs use tabular input for the daily averaged differential particle fluence and evaluate the absorbed dose as a function of shield thickness for a choice of 3 simple shield geometries. Three modifications were made for the present computations: (1) the range of validity was extended to lower shield thickness, (2) the evaluation of other quantities in addition to absorbed dose was incorporated into the programs, and (3) a plotting routine was added.

For each evaluated quantity in the third category, the results were plotted as a function of circular orbit altitude for specified shield thickness values and for four orbit inclinations. The calculations were based on a one-dimensional, single material shield configuration that provides a useful first approximation to real shielding conditions. The relationship of the simple geometries selected to more complex shielding environments is discussed for electrons and protons.

ELECTRON SHIELDING. The electron dose/equivalent flux computer calculations are based primarily on the results of Berger's

energy and number transmission and reflection factor data for electrons (References 47 and 48). The Burrell computer program is based on analytical fits to these data for normal, isotropic, or cos θ incidence on a slab as a function of the scaled depth z/r_o, where r_o is the extrapolated electron range (Reference 48). These analytical fits hold for electron energies less than 2 MeV and are independent of electron energy other than through r_o.

To obtain probability density functions for electron number and energy absorption, the analytical fits are differentiated by actual depth, z. The total energy or number deposited at a particular depth is evaluated by multiplying the appropriate probability density function by the incident differential electron flux and integrating over incident electron energy. This procedure has been followed for the assumption of anisotropic (or cos θ) electron fluence incident on a slab of aluminum to evaluate dose in aluminum as a function of slab thickness. The results are given in Figures 8-17 to 8-20.

The choice of an isotropically angular distribution incident on a semi-infinite slab rather than normal incidence on an infinite slab or normal incidence on a spherical shield is suggested by two factors. The first is that, in contrast to proton scattering, the effects of electron scattering are important. As the shield thickness increases, the electron direction of travel loses any clear dependence on the original incident direction. Second, the actual time-averaged distribution experienced by a satellite is probably nearly isotropic on a planar surface.

To compare electron and proton dose values, apply two multiplicative correction factors to the electron dose. The first correction factor is 2, which is needed to correct for the infinite back shielding, and the second factor is from 1 to 2 (depending on shield thickness, the electron energy spectrum, and the energy dependence of the dose) to correct from isotropic incidence to normal incidence on a slab. This second factor is identically equal to one for zero shield thickness (surface dose).

PROTON SHIELDING. To compute proton dose, a computational scheme developed by Burrell (Reference 46) was used directly except for aluminum shield thicknesses less than about 0.10 gram per square centimeter. For this thin shield region, modifications were necessary since the original scheme utilized a single analytical fit to the stopping power function $\epsilon(E)$ for proton energies between 5 and 2,000 MeV. To treat adequately situations where proton

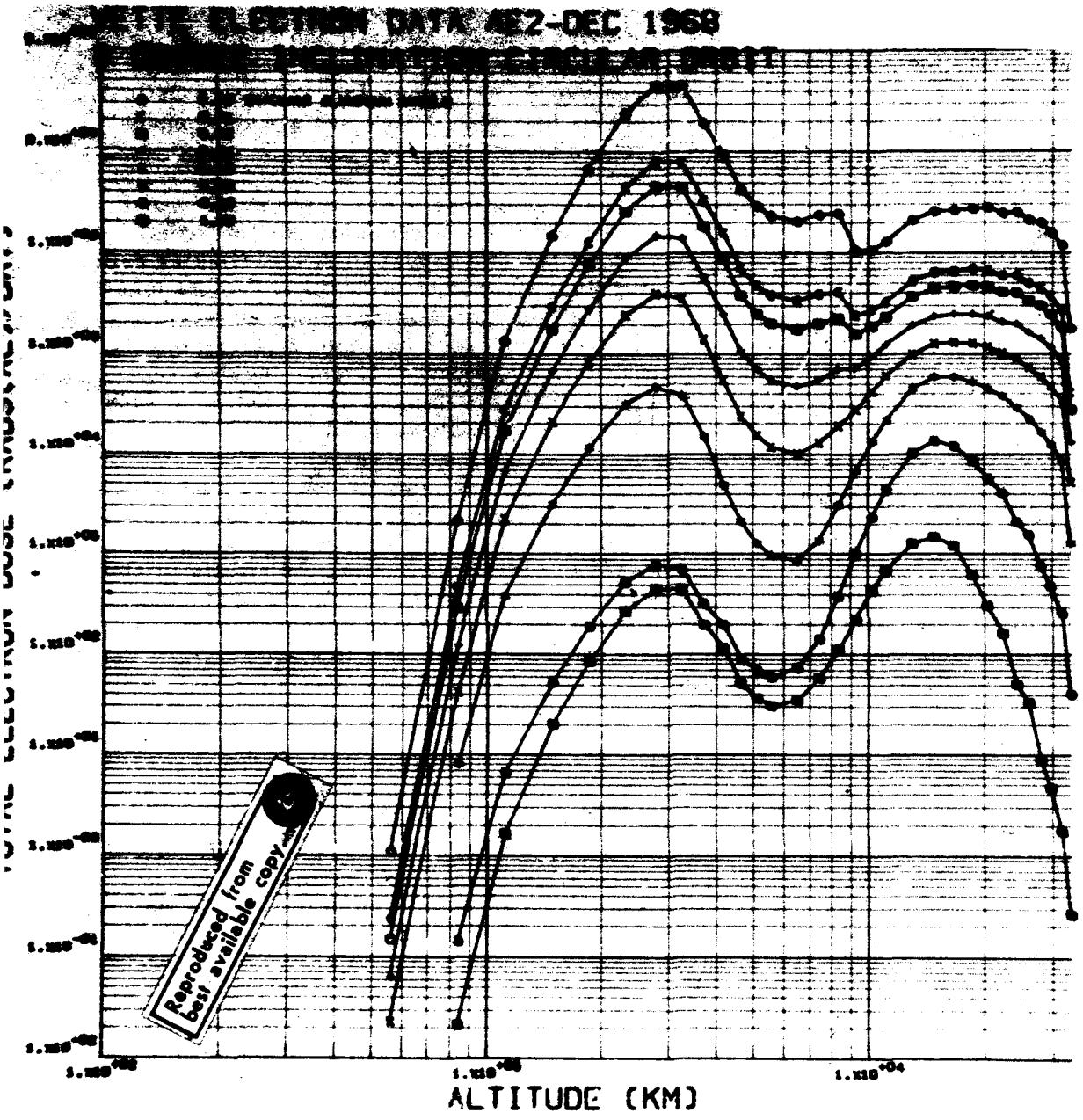

Figure 8-17. Daily dose (natural electrons) in circular orbit satellites as a function of satellite altitude for specified orbital inclination and shielding thickness (inclination = 0 degree).

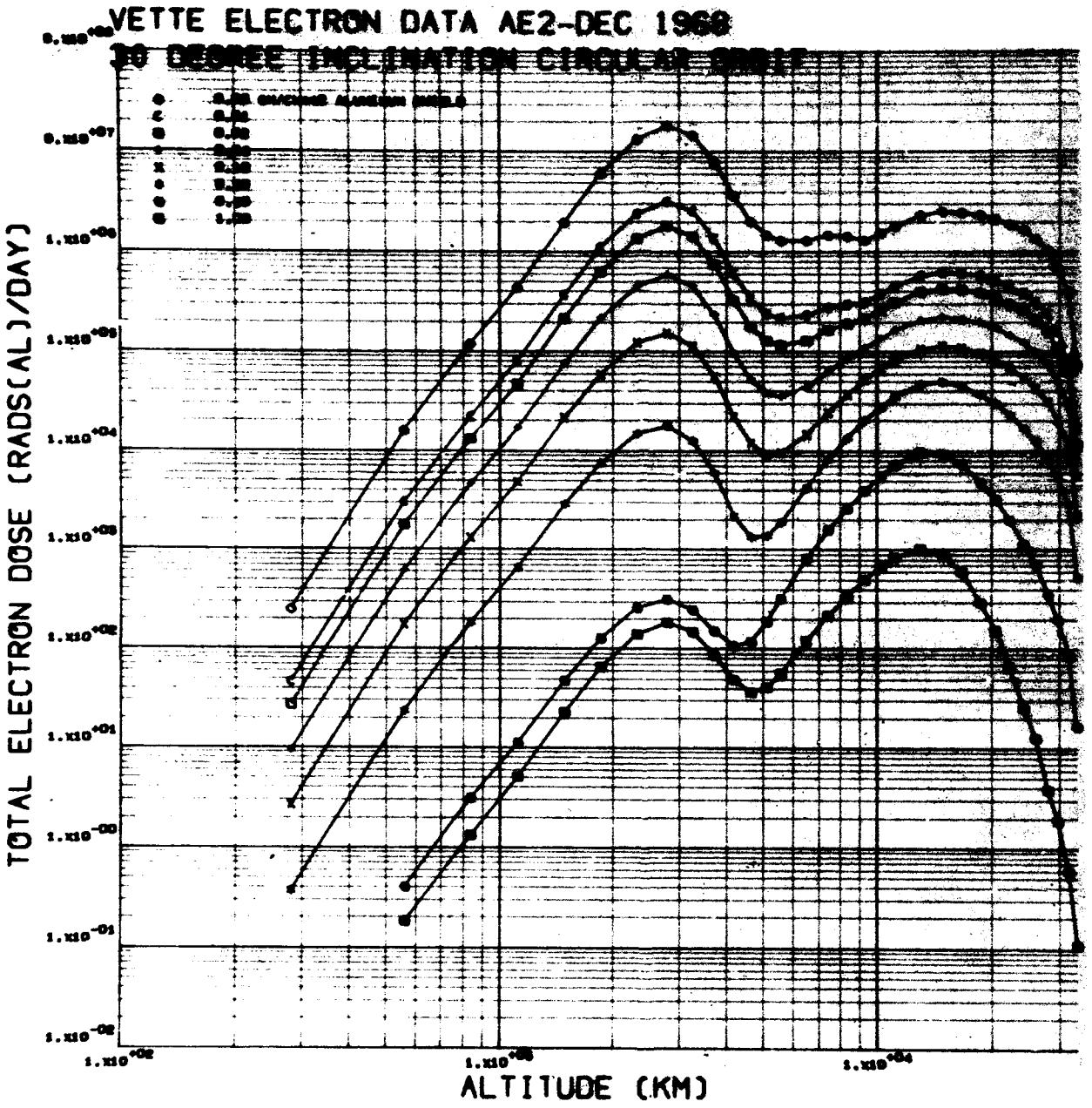

Figure 8-18. Daily dose (natural electrons) in circular orbit satellites as a function of satellite altitude for specified orbital inclination and shielding thickness (inclination = 30 degrees).

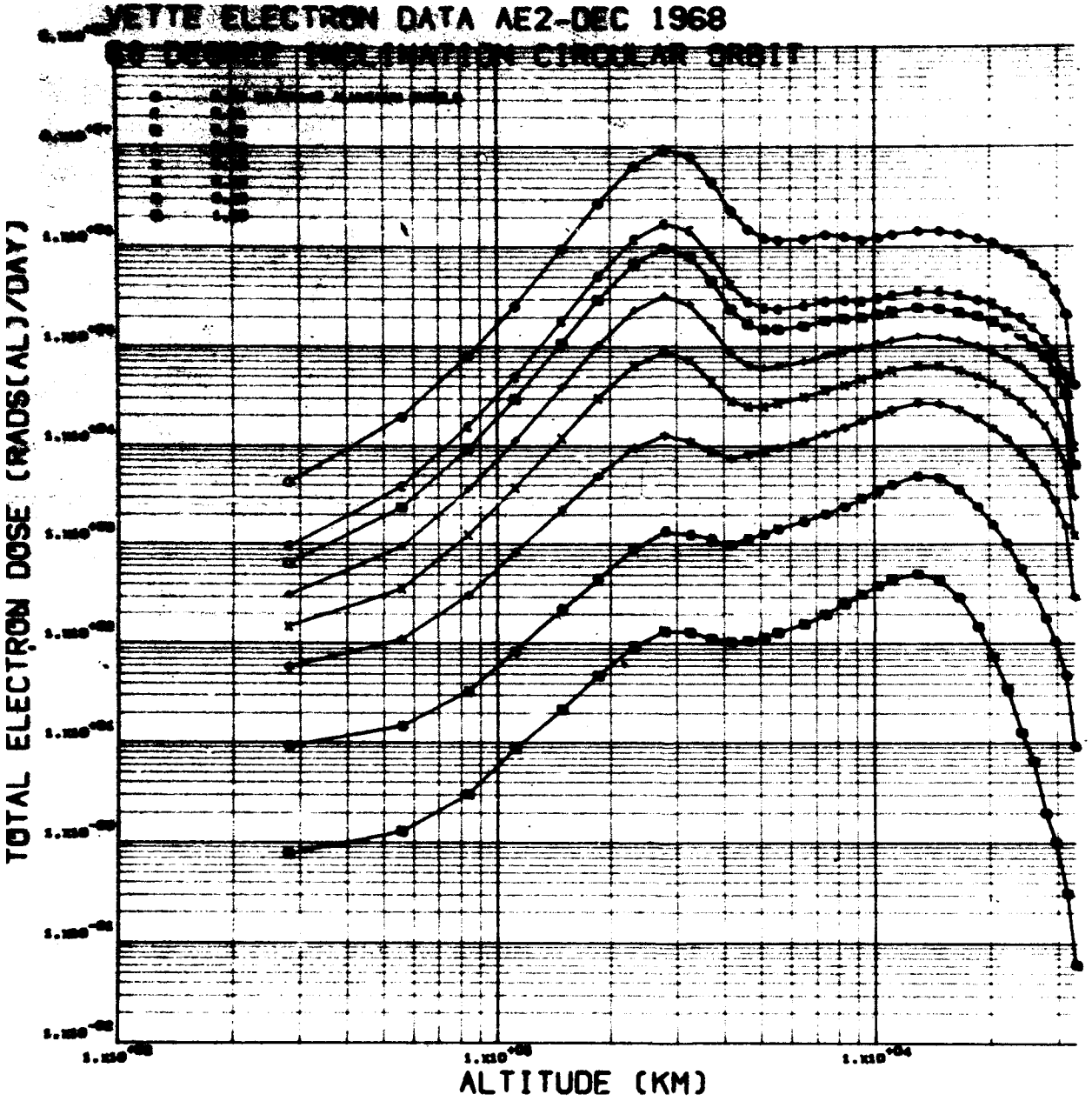

Figure 8-19. Daily dose (natural electrons) in circular orbit satellites as a function of satellite altitude for specified orbital inclination and shielding thickness (inclination = 60 degrees).

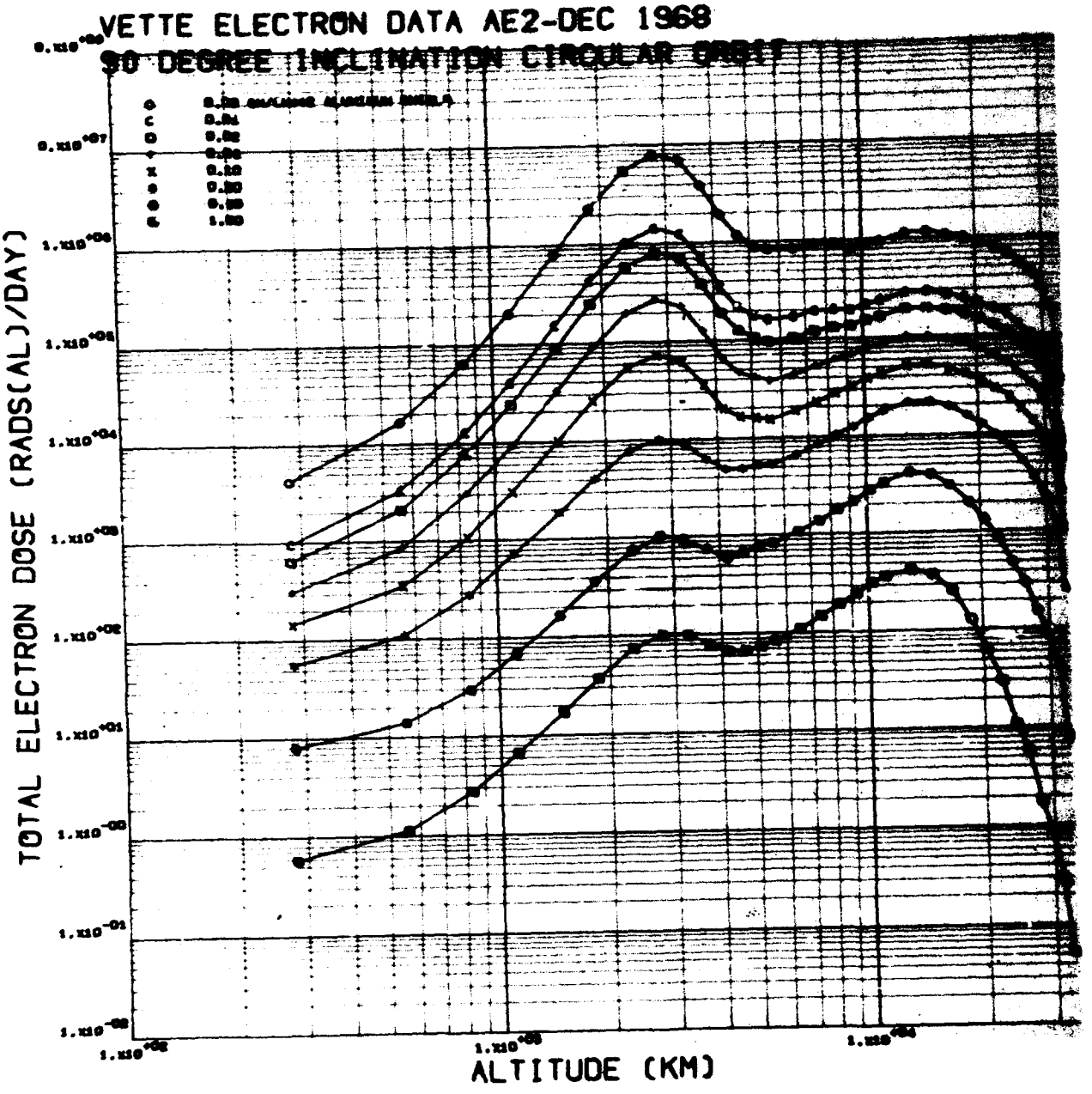

Figure 8-20. Daily dose (natural electrons) in circular orbit satellites as a function of satellite altitude for specified orbital inclination and shielding thickness (inclination = 90 degrees).

energies <5 MeV contribute significantly, the $\epsilon(E)$ data of Whaling (Reference 49) was fitted to a power law in energy for the energy range 0.01 to 10 MeV. An analytical expression was derived for the external energy E_e, given the internal energy E_i and the shield thickness x by using the range energy relation:

$$R(E_e) = R(E_i) + x \quad . \tag{8-17}$$

Equation 8-17 was programmed as a subroutine and used only for internal proton energies $E_i < 10$ MeV. The modified program was used to evaluate the proton dose to aluminum for selected aluminum shield thicknesses from 0 to 1 gram per square centimeter using the Vette AP5 and AP6 model proton environments (References 50 and 51). The results are given in Figures 8-21 through 8-24. The treatment of higher shield thicknesses (up to 10 grams per square centimeter) has been given elsewhere (Reference 52) and involves consideration of the higher energy AP3 and AP1 model proton environments.

The doses that have been calculated apply to protons that are normally incident on a spherical shield. Due to the small effect of scattering of energetic protons, estimating the absorbed dose for isotropic incidence on a complex shield configuration is possible utilizing only the dose dependence for spherical shields as a function of shield thickness, such as:

$$\overline{D} = \frac{\int D[x(\overline{\Omega})]\, d\overline{\Omega}}{4\pi} \tag{8-18}$$

where D(x) is the spherical shield depth dose function for the spectrum under consideration, x is the shield thickness in equivalent grams per square centimeter of aluminum in direction $\overline{\Omega}$ away from the dose point, and $d\overline{\Omega}$ is the solid angle. In practice, this is difficult to evaluate and conversion to one of the simple geometries that were considered for electrons is necessary to combine effects for protons and electrons.

If one wants to convert the proton dose for a spherical shield to that for an isotropic source incident on a semi-infinite slab (such as is specified for the electron dose curves), the proton spherical shield values as presented in Figures 8-21 to 8-24 should be reduced by a factor of 3. This is true except when the zero thickness or surface dose is desired. In that case, a factor of 2 should be used.

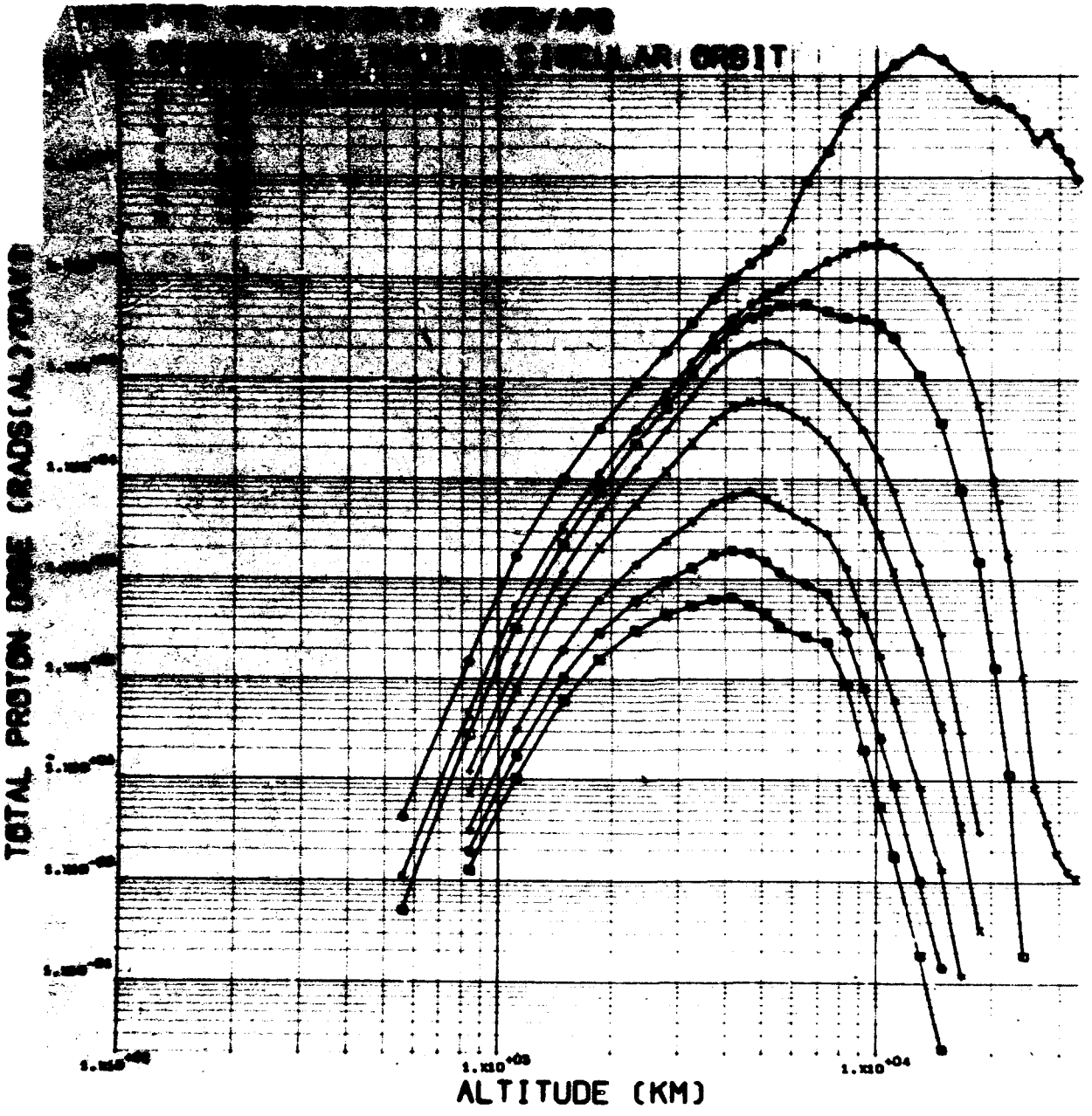

Figure 8-21. Daily dose (natural protons) in circular orbit satellites as a function of satellite altitude for specified orbital inclination and shielding thickness (inclination = 0 degree).

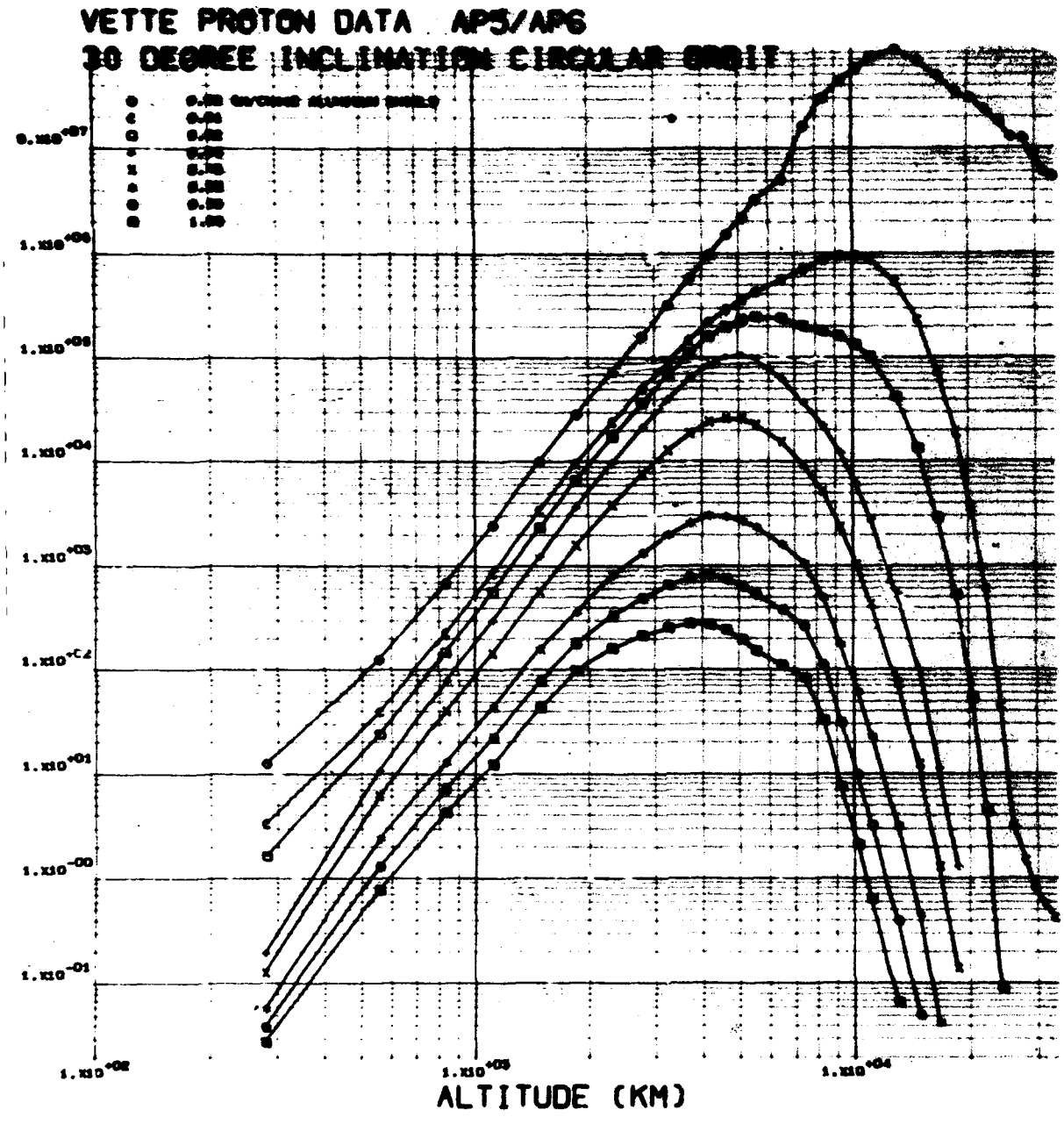

Figure 8-22. Daily dose (natural protons) in circular orbit satellites as a function of satellite altitude for specified orbital inclination and shielding thickness (inclination = 30 degrees).

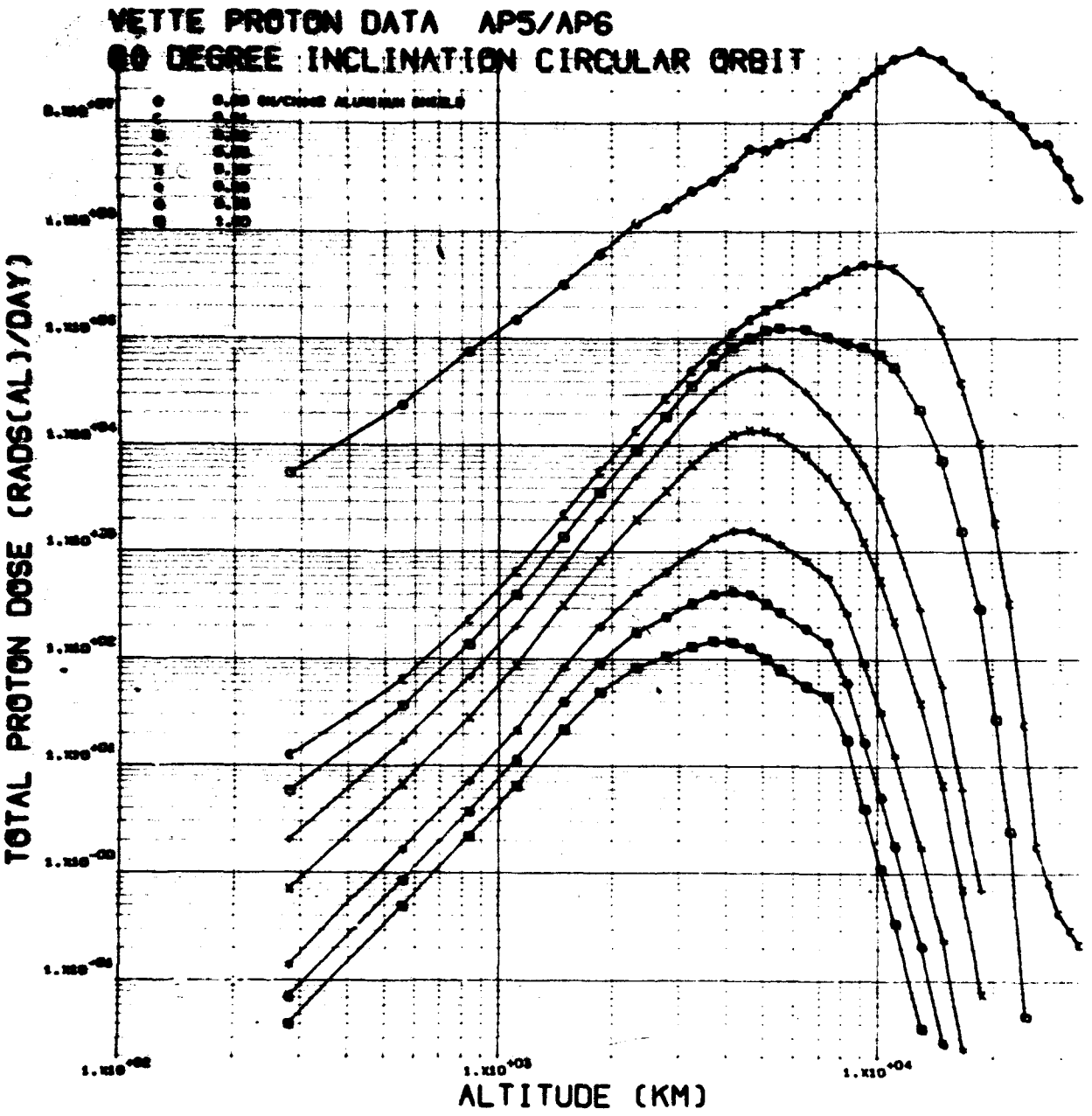

Figure 8-23. Daily dose (natural protons) in circular orbit satellites as a function of satellite altitude for specified orbital inclination and shielding thickness (inclination = 60 degrees).

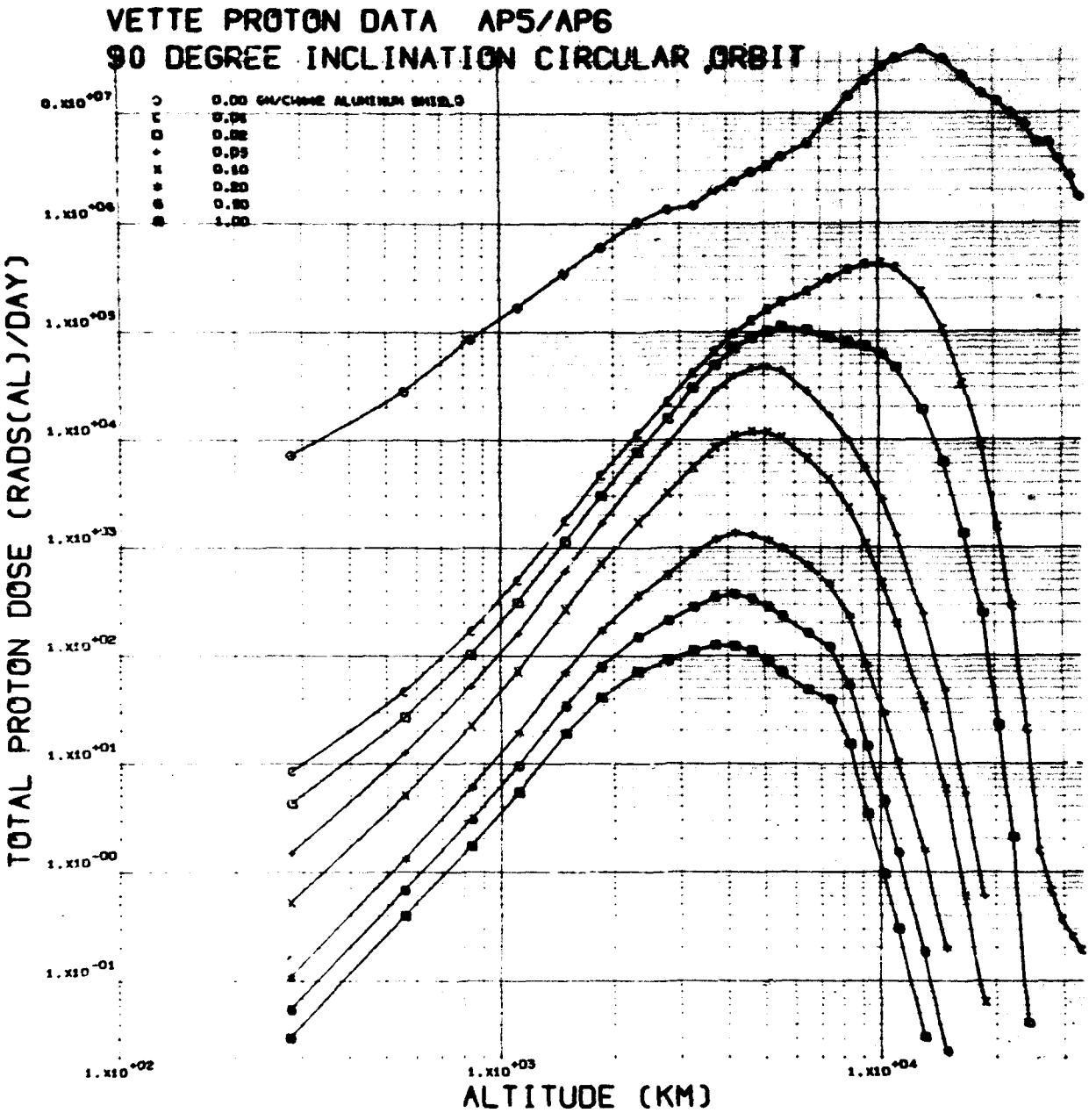

Figure 8-24. Daily dose (natural protons) in circular orbit satellites as a function of satellite altitude for specified orbital inclination and shielding thickness (inclination = 90 degrees).

8.5.3 Effect of Orbital and Shielding Parameters on Radiation Dose

DOSE DUE TO NATURAL TRAPPED RADIATION. The near-surface (low-shielding) dose has been evaluated as a function of orbital and shielding parameters utilizing (1) the Vette AP5 and AP6 trapped proton models, (2) the AE2 (1968 projection) trapped electron (Section 4; Reference 52), and (3) some radiation shielding computer programs that were modified for the purposes of these computations (References 46 and 47). Figures 8-17 through 8-24 give the results in rad (Al) per day for circular orbits from 275- to 33,000-kilometer altitude at 0-, 30-, 60-, and 90-degree inclinations for selected shielding thicknesses of 0, 0.01, 0.02, 0.05, 0.1, 0.2, 0.5, and 1.0 grams per square centimeter aluminum. The computed absorbed dose due to trapped electrons is given in Figures 8-17 through 8-20 for 0-, 30-, 60-, and 90-degree inclinations, respectively, as a function of orbital altitude. The corresponding contribution of trapped protons is given in Figure 8-21 through 8-24.

The doses for protons correspond to uniform shield thickness in all directions about the dose point. The dose for more complex shielding environments can be estimated as discussed in Section 8.5.2. The doses given for zero thickness shielding involve an extrapolation of the AP5 model proton environment below the 0.4-MeV lower energy limit cited. Those for shield thickness of 1.0 gram per square centimeter may be slightly in error because higher energy proton model environments were not included. The doses for electrons correspond to an isotropic flux incident on a dose point at the center of a slab shield of the stated half-thickness value.

DOSE DUE TO ARTIFICIALLY INJECTED TRAPPED RADIATION. The theory for injected trapped electron model environments has been presented in Section 7. To provide an insight into the effects of these environments on satellite systems, six different injection environments are considered here. Flux maps were computed in B, L, ϕ_e coordinates for conditions a short time after injection. Time decay of these environments has been neglected in the approximations made (Section 7).

The first five environments treated resulted from a 1-megaton fission yield injection at an altitude of 200 kilometers. Each of the five cases corresponded to injection at a different L-value, i.e., L = 5.0, 4.0, 3.0, 2.0, and 1.15. The sixth case corresponds to

the hypothetical "worse case" situation resulting from multiple injections sufficient to cause saturation electron trapping. Orbital electron fluences were computed for the same circular orbit conditions that were treated for natural trapped radiation. An existing computer program (Reference 54) was modified to perform these calculations. The results are displayed in Figures 8-25 through 8-30. The case in Figure 8-30 corresponds to the worst situation that would result from multiple injections sufficient to cause saturation electron trapping.

In the treatment here, the shape of the energy spectrum of the injected trapped electrons is assumed to be constant in space and time and is represented by the fission electron energy spectrum of Carter and Reines (Reference 55). As a result of these simplifying assumptions, evaluating the primary electron dose as a function of shield thickness and orbital parameters is possible by supplying a single shielding depth dose curve for a normalized fission beta spectrum. This curve then is used in conjunction with orbital electron fluences ($E > 0$) as a function of orbital parameters and injection conditions (Figures 8-25 through 8-30)

The electron depth-dose relationship for a fission electron energy spectrum normally incident on aluminum was evaluated using the electron dose shielding program described in Section 8.5.2. This program is less accurate for a fission electron spectrum than for most natural trapped electron spectra because of the significantly greater numbers of high-energy electrons. The analytical formulation in the program assumes that the Berger transmission factors depend only on the scaled depth (depth/incident range). This approximation is most valid for electron energies <2 MeV. However, the results in Figure 8-31 seem to agree reasonably with another calculation that is based on considerably different premises (Reference 56).

Besides the fission spectrum electron shielding curve discussed previously, additional data on electron dose as a function of electron energy and shield material have been prepared so that similar normalized shielding curves for arbitrary energy spectra and materials may be constructed. To summarize this information in a useful way, a nomograph has been prepared (Figure 8-32).

Figure 8-32 gives the depth dose relationship for selected normally incident electron energies and absorbing materials. Sets of curves are given for each of three incident energies (1, 4, and 10 MeV) on the nomograph.

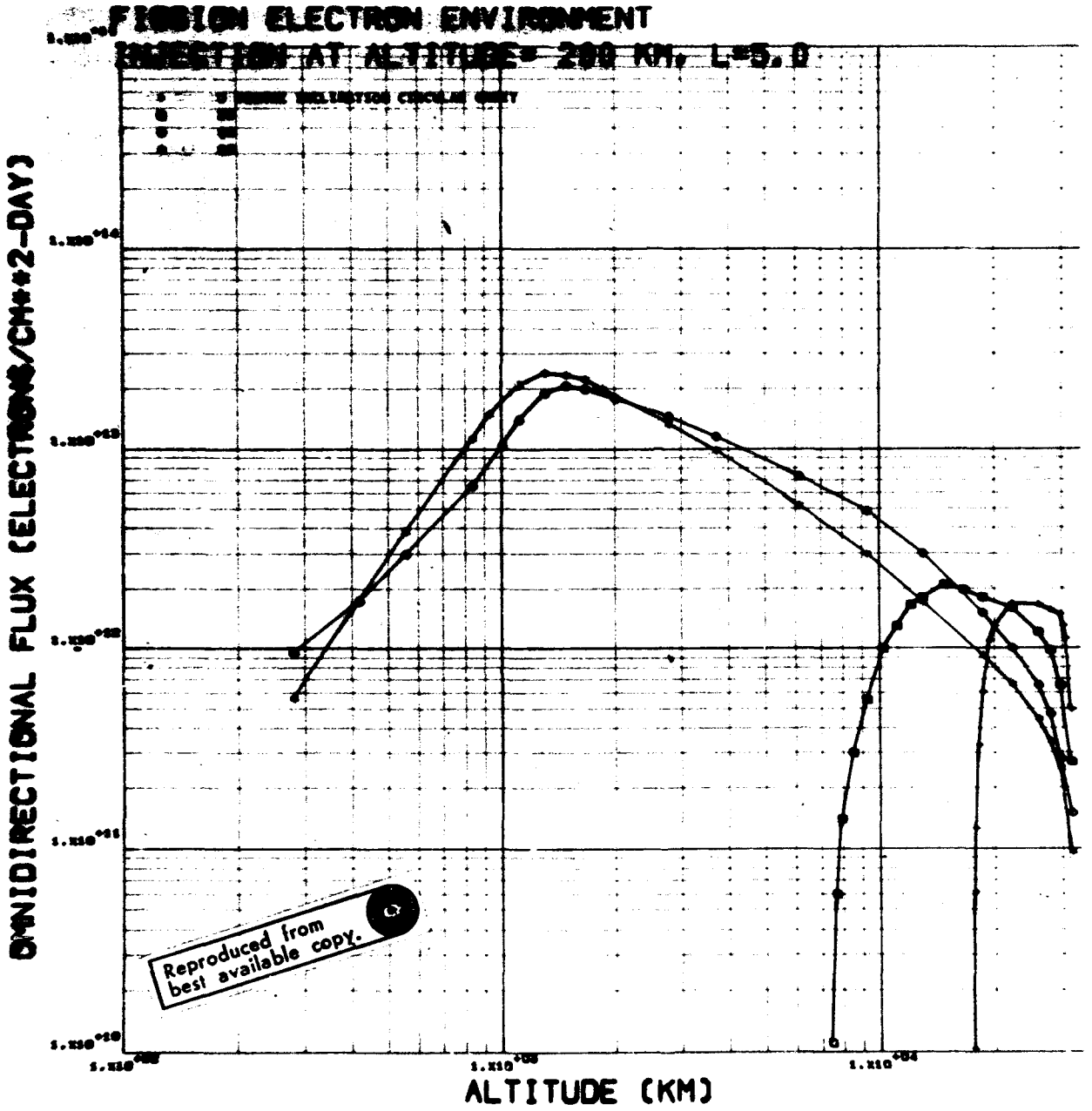

Figure 8-25. Daily omnidirectional flux of fission electrons on circular orbit satellites as a function of satellite altitude for specified orbital inclinations (1-megaton fission yield injection at 200 kilometers, $L = 5.0$).

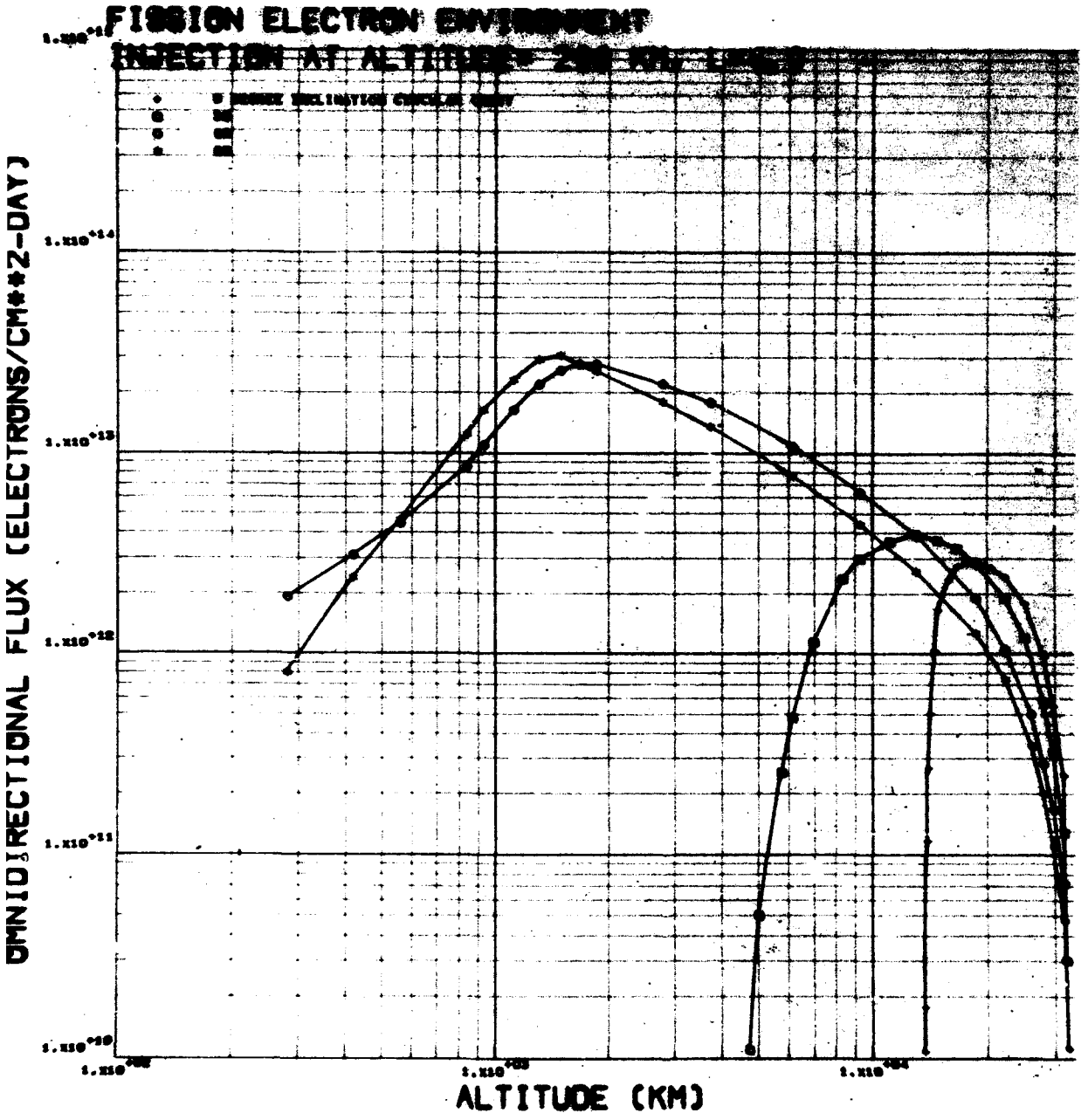

Figure 8-26. Daily omnidirectional flux of fission electrons on circular orbit satellites as a function of satellite altitude for specified orbital inclinations (1-megaton fission yield injection at 200 kilometers, L = 4.0).

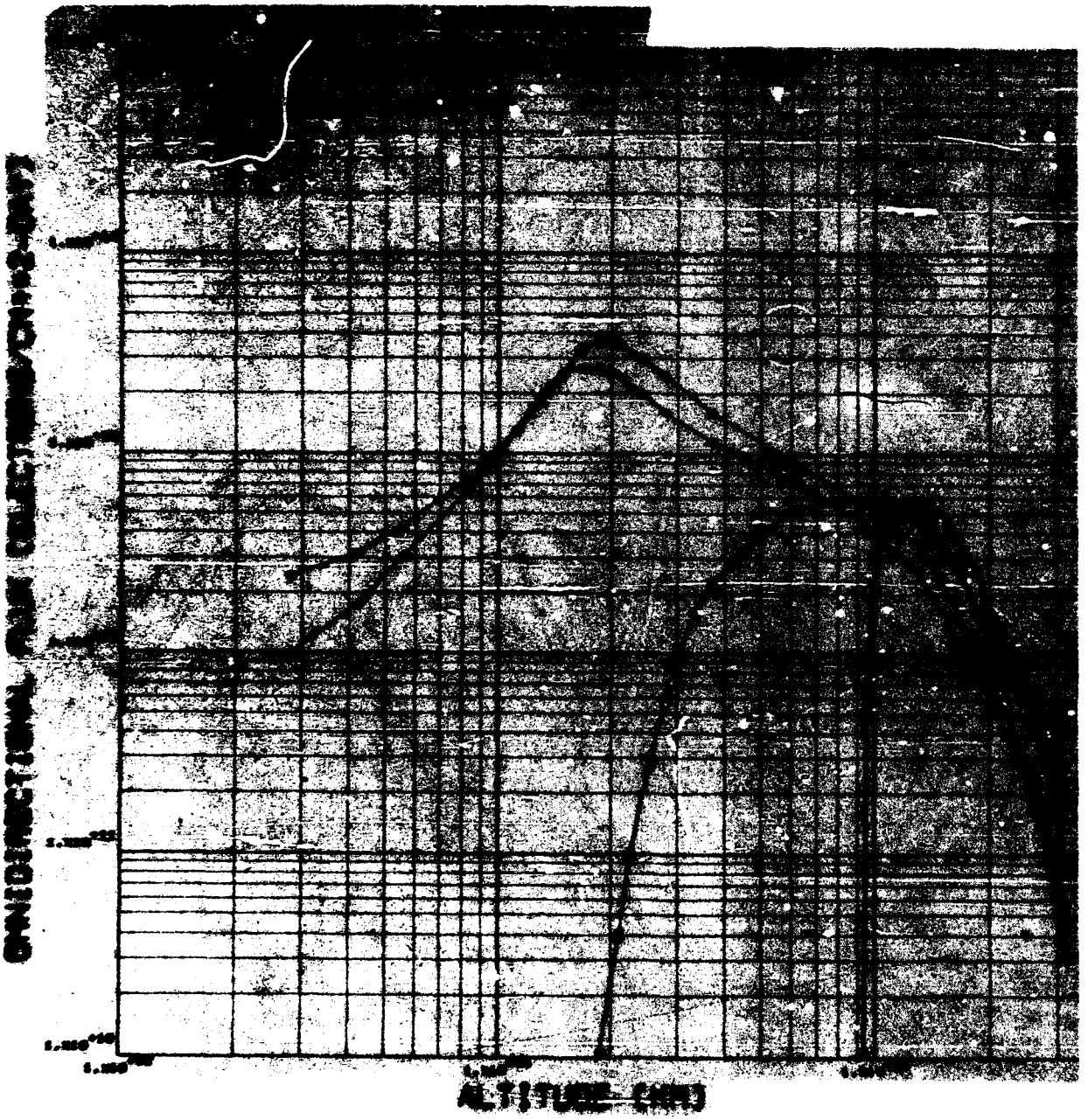

Figure 8-27. Daily omnidirectional flux of fission electrons on circular orbit satellites as a function of satellite altitude for specified orbital inclinations (1-megaton fission yield injection at 200 kilometers, L = 3.0).

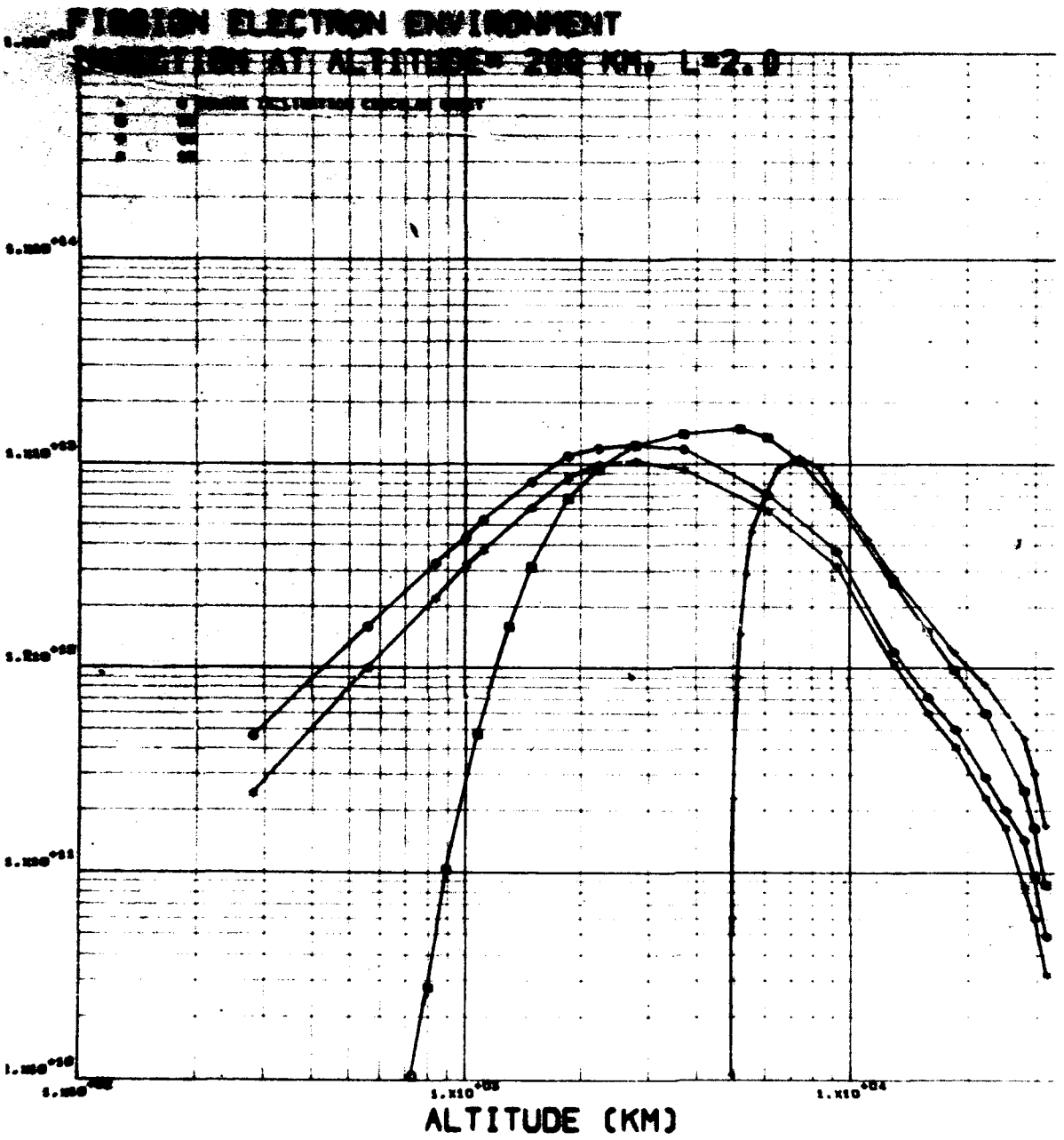

Figure 8-28. Daily omnidirectional flux of fission electrons on circular orbit satellites as a function of satellite altitude for specified orbital inclinations (1-megaton fission yield injection at 200 kilometers, L = 2.0).

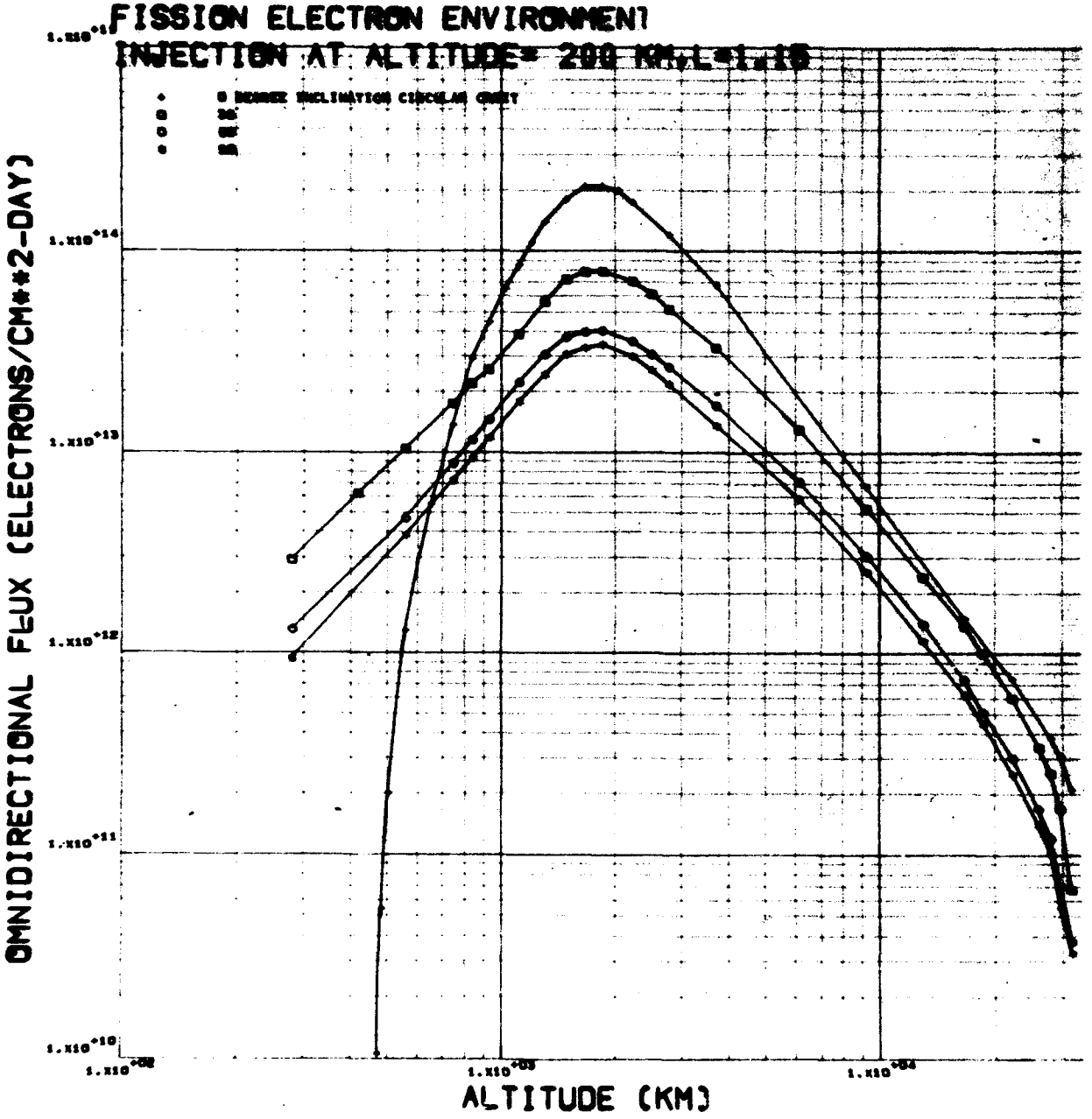

Figure 8-29. Daily omnidirectional flux of fission electrons on circular orbit satellites as a function of satellite altitude for specified orbital inclinations (1-megaton fission yield injection at 200 kilometers, L = 1.15).

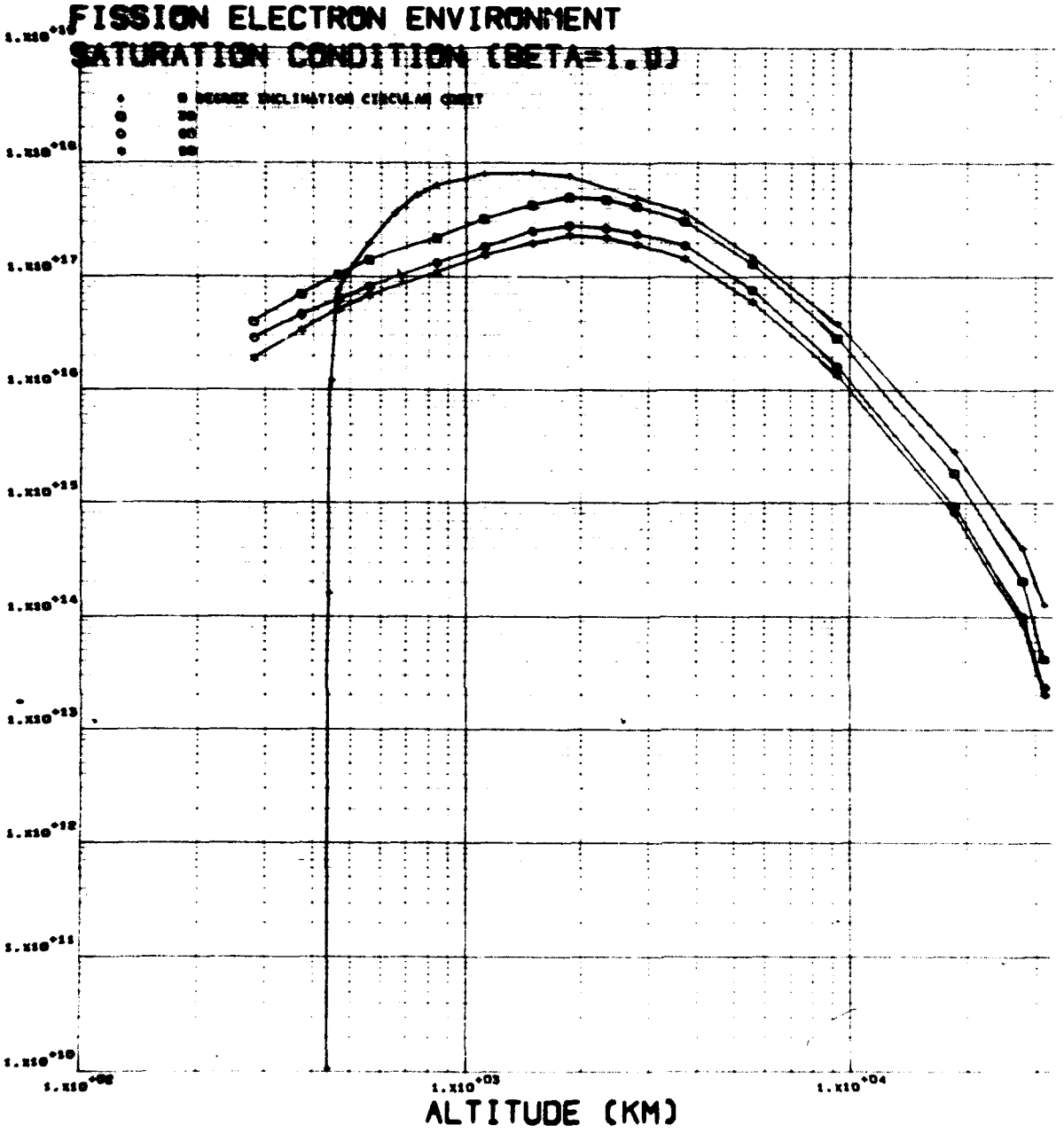

Figure 8-30. Daily omnidirectional flux of fission electrons on circular orbit satellites as a function of satellite altitude for specified orbital inclinations (saturation condition, beta = 1.0).

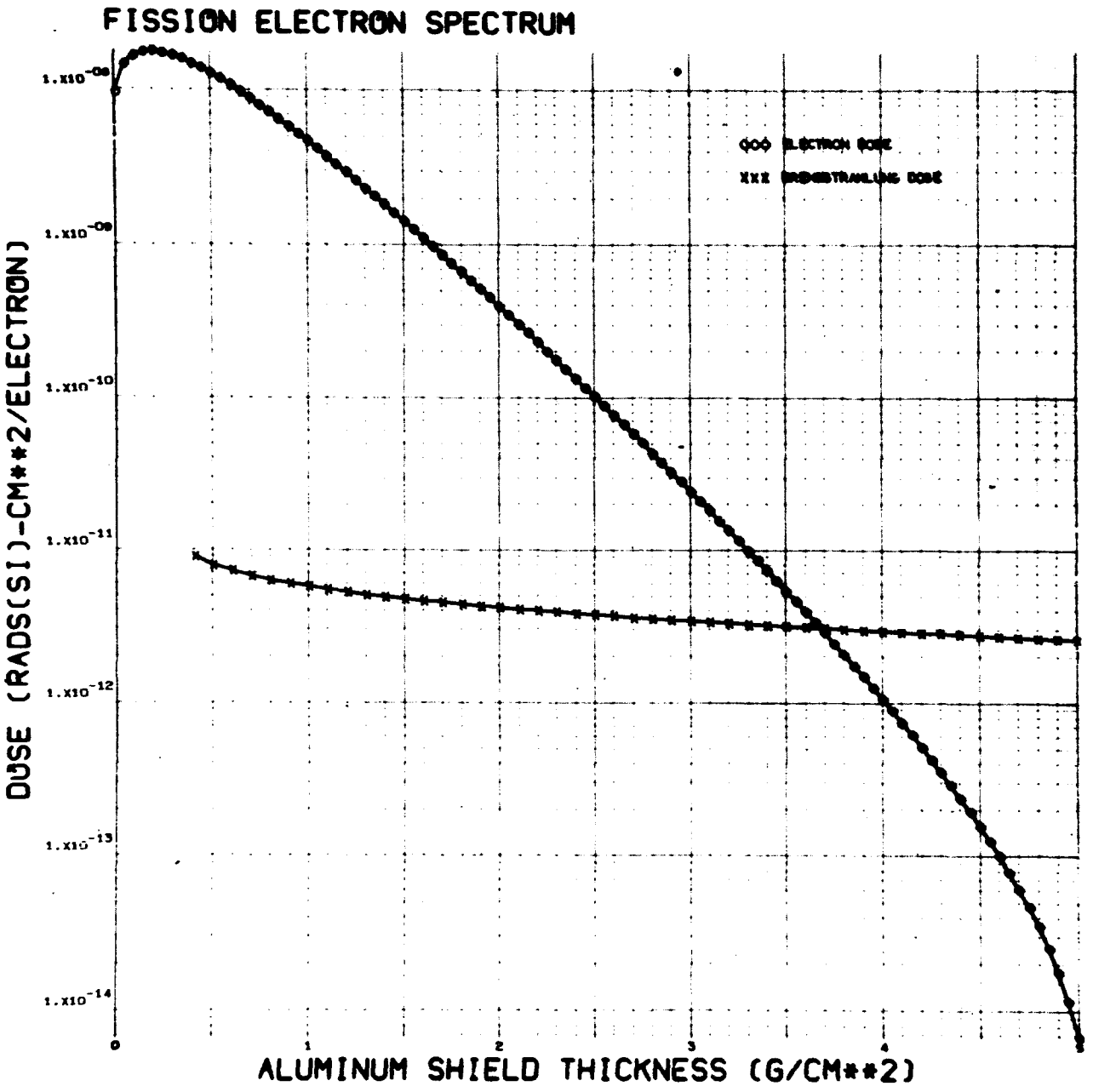

Figure 8-31. Electron and bremsstrahlung depth dose for fission electrons as a function of thickness of aluminum.

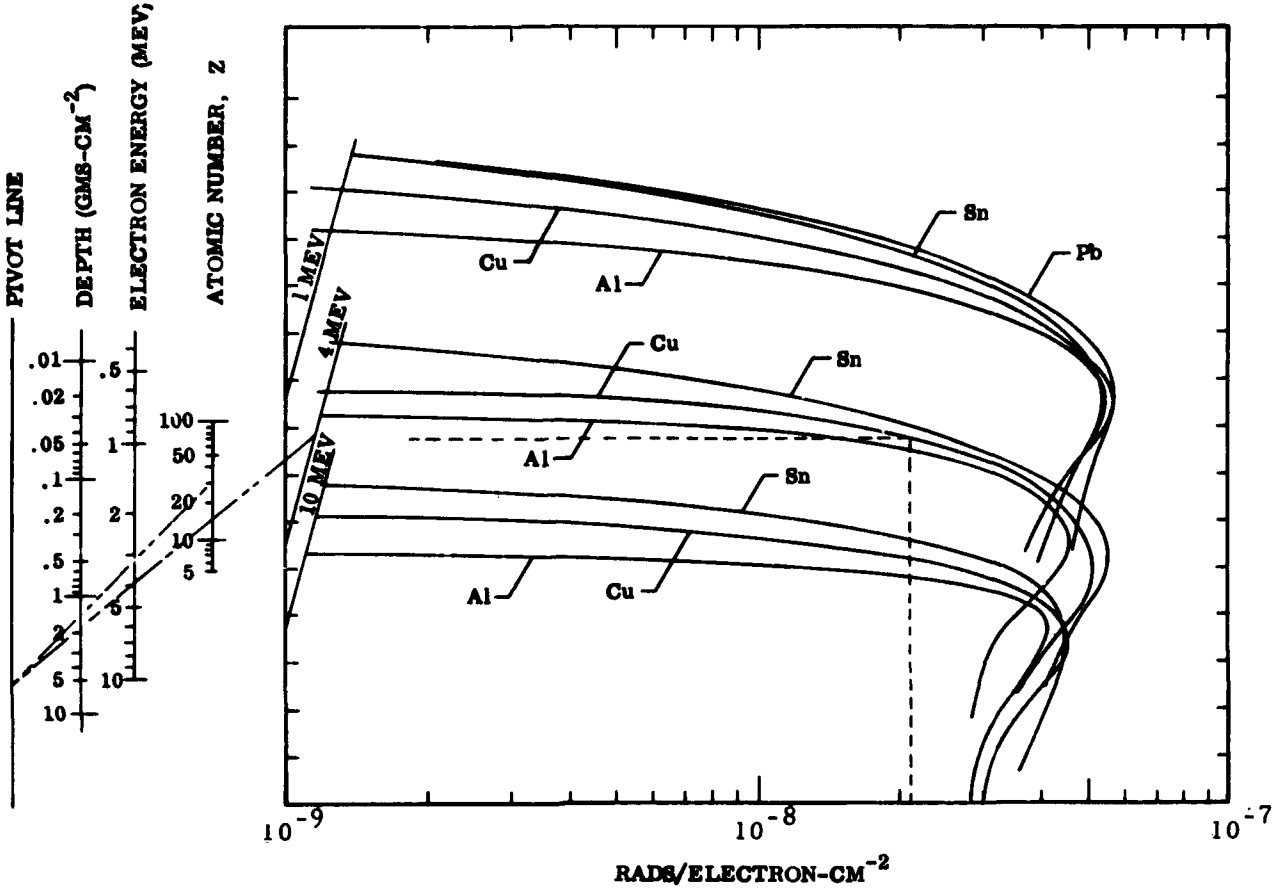

Figure 8-32. Electron dose nomograph.

To use the nomograph, a line is drawn through given atomic number value and the shield thickness value. Its intersection is determined with the pivot line. Another line is drawn through this intersection point and the appropriate energy value (1, 4, or 10 MeV) and its intersection with the appropriately labeled short inclined scale is determined. Finally, a horizontal line is drawn between this intersection point and the appropriate curve for the energy and material under consideration. A vertical line dropped from the intersection on the material curve to the abscissa will give the absorbed dose value in rads per electron per square centimeter.

The data used in the nomograph for 1-MeV electrons are based both on experimental measurements and theoretical calculations (Reference 57), whereas the data for both 4- and 10-MeV electrons is based primarily on the theoretical calculations of Spencer (Reference 58). A sufficient range of z-values is given for each energy to enable approximate interpolation for materials with intermediate z-values.

DOSE DUE TO ELECTRON BREMSSTRAHLUNG. Although subordinate to the spacecraft system components discussed, an evaluation of the possible dose due to electron bremsstrahlung will be included for the sake of completeness.

High energy electrons generate X rays and gamma rays in shield materials by means of the bremsstrahlung interaction. This interaction results in photon emission when the electron is decelerated by the nuclear coulomb field. Although the basic cross section has been evaluated by using the Born approximation and neglecting screening effects of the atomic electrons, adequate agreement by experiment has required rather complex formulas to correct for these deficiencies. These corrections are discussed thoroughly in Reference 59.

Besides this theoretical information, fairly accurate experimental measurements of thick target differential bremsstrahlung cross sections have been made recently (References 60 and 61) that cover a range of thicknesses and electron energies of interest here. The production of bremsstrahlung in an aluminum slab shield by a fission electron spectrum is first considered and the resultant absorbed dose is calculated as a function of thickness (Figure 8-31). Thick target bremsstrahlung production for monoenergetic electrons normally incident on a slab shield then is discussed, and the effect of the atomic

number of the shield material and incident electron energy is described. A typical thick target bremsstrahlung energy spectrum for an incident fission electron spectrum also is presented (Figure 8-33)

The accurate determination of the bremsstrahlung depth dose relationship for the bremsstrahlung produced by electrons incident on a slab shield involves the evaluation of the differential electron energy spectrum as a function of depth, the use of accurate thin target differential bremsstrahlung angular distributions, and the use of appropriate attenuation coefficient data. For the purposes of the study, a computer program that depends on appropriate techniques (Reference 47) was used. This program was employed to calculate the bremsstrahlung depth dose curve in aluminum for a normally incident normalized fission beta spectrum (Figure 8-31). The incident differential energy spectrum was approximated by the Carter/ Reines relation (Reference 55):

$$\Psi(E) = N_1 \exp(-V_1 E^2 - V_2 E) \qquad (8\text{-}19)$$

which is valid for E in the range $0 < E < 10$ MeV. The constants have the values $N_1 = 0.7104$, $V_1 = 0.055/\text{MeV}^2$, and $V_2 = 0.575/\text{MeV}$. Figure 8-31 gives both the electron and the bremsstrahlung depth dose curves for a normalized fission electron spectrum and shows that the bremsstrahlung dose does not exceed the electron dose until a depth of about 3.5 grams per square centimeter of aluminum is reached.

BREMSSTRAHLUNG ENERGY SPECTRA. To provide an insight into the material and electron energy dependence of bremsstrahlung production, a useful approximate formula is given for thick targets. The yield Y(E) of bremsstrahlung energy per normally incident electron per square centimeter is given by:

$$Y(E) = C\,Z\,E^2 \ \text{(MeV)} \qquad (8\text{-}20)$$

where C varies slightly with E and Z but typically is $\sim 4 \times 10^{-4}$, Z is the atomic number, and E is the electron energy in MeV.

To provide some idea of the differential photon number and energy spectra for thick targets, experimental data (Reference 60) and results of some Monte Carlo calculations (Reference 62) have been used to generate the spectra resulting from a normalized fission electron spectrum The results are given in Figure 8-32, which displays both

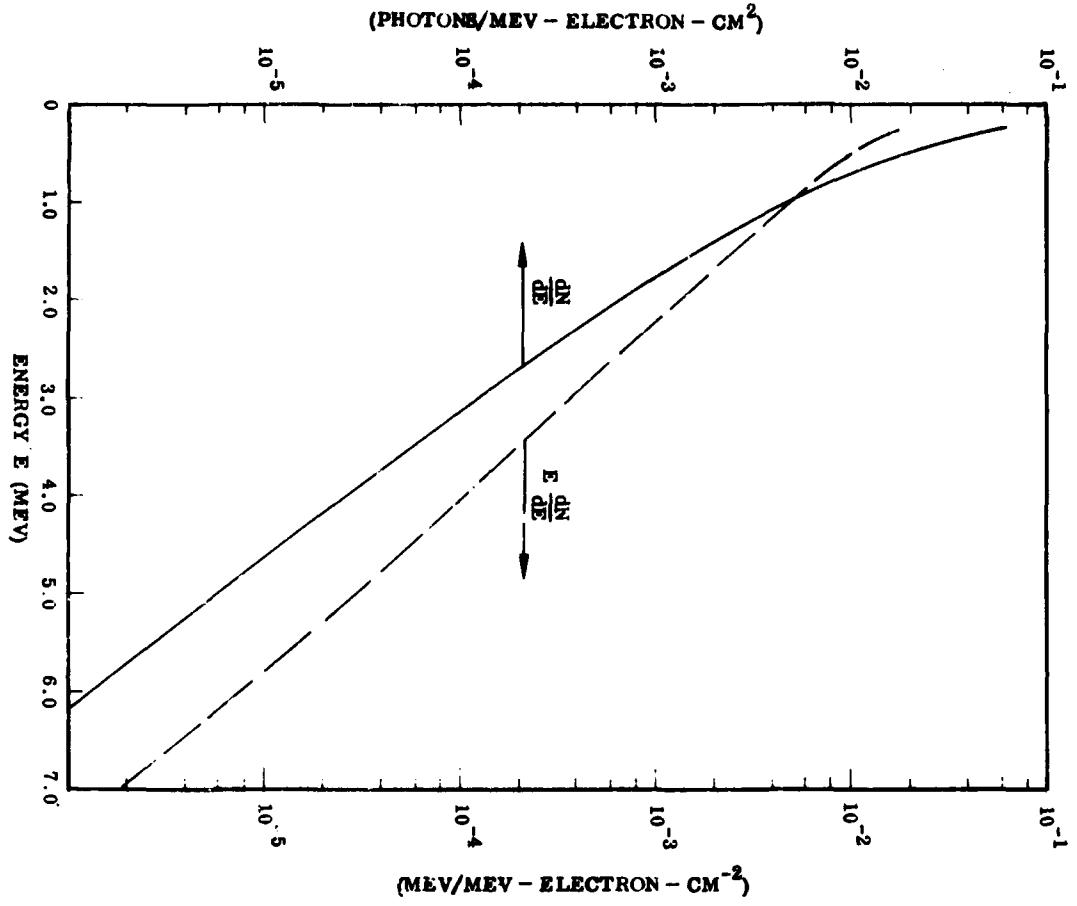

Figure 8-33. Bremsstrahlung number and energy spectra resulting from a fission electron spectrum normally incident on a thick aluminum target.

the number and energy spectra of photons emitted in the forward 2π solid angle at depths of 3.5 to 4.0 grams per square centimeter of aluminum where the bulk of the primary electrons have been stopped.

8.5.4 Effect of Orbital and Shielding Parameters on Equivalent 1-MeV Electron Fluence

METHOD FOR CALCULATING EQUIVALENT 1-MeV ELECTRON FLUENCE. For minority carrier semiconductor devices (e.g., solar cells) minority carrier lifetime τ is the primary property degraded (onset at 1 to 2 orders of magnitude less exposure than for bulk conductivity). For these devices, performances degradation is evaluated in terms of an equivalent fluence concept rather than a dose. The data presented in Figures 8-3, 8-4, 8-6, 8-9, and 8-13 are in terms of a damage equivalent normally incident (DENI) 1-MeV electron fluence for minority carrier lifetime damage prediction in silicon devices. This 1-MeV equivalent fluence is evaluated by means of an integral similar to the one giving dose, for instance:

$$\Phi_{eq}(1\ \text{MeV}) = \int dE \cdot \Psi(E) \cdot W_R(E) \quad . \tag{8-21}$$

where $W_R(E) = [W(E)/W(E_R)]_{E_R = 1\ \text{Mev}}$ is the relative energy and material dependent weighting function and $W(E)$ is the electron or proton lifetime damage coefficient for p-type silicon $K_\tau(E)$ as given in Figure 8-1.

Formally, this is analogous to an evaluation of the absorbed dose [in this case $W_R(E) = C \cdot \epsilon(E)$], and $\epsilon(E)$ is the stopping power of the shield material. To compute the equivalent 1-MeV electron fluence for incident protons, the proton dose was modified by replacing the $\epsilon(E)$ subroutine with a subroutine that evaluated $W_R(E)$ where W is the lifetime damage coefficient for protons incident on p-type silicon.

This procedure is valid for evaluations in which $\Psi(E)$ is the shielded differential energy spectrum. It is not valid if the integration is taken over external particle energy, as is the case with the electron dose program that was used here to evaluate $\Phi_{eq}(1)$ for incident orbitally averaged electron spectra. For an isotropic spectrum of electrons incident on a semi-infinite slab shield, Equation 8-21 may be used with $W_R \rightarrow W_R(E, X)$ provided that data on $W_R(E, X)$ for p-type silicon are available for a range of shield thicknesses x. This function was approximated by an analytical fit in electron energy

that was divided into several energy intervals and used coefficients appropriate for each of the desired thickness values.

The recommendations given previously for correcting electron or proton dose values to a common shield environment depend slightly on the nature of the energy dependence of $\epsilon(E)$. Similarly, recommendations for correcting equivalent fluence values to a common environment depend slightly on the nature of the energy dependence of $W = K_f(E)$. However, the energy dependence of W is not considered to be a large effect so that the suggestions made in Sections 8.5.2 apply also for correcting electron or proton equivalent fluence values to a common shield environment.

EQUIVALENT 1-MeV ELECTRON FLUENCE DUE TO NATURAL TRAPPED RADIATION. As discussed, the effect of an incident differential energy spectrum $\Psi(E)$ on τ can be approximated by an equivalent monoenergetic damaging particle fluence $\Phi_{eq}(E_R)$ of a selected reference energy E_R using data for $K_f(E)$ (Figure 8-1) and $W = K_f(E)$ in Equation 8-2. The choice of E_R usually is dictated by the availability of laboratory device irradiation data (1.0 MeV for electrons, 4.6 MeV for protons) (Reference 63). The choice of the reference energy should be such that it does not differ greatly from the effective damaging energy E_f, defined by:

$$K_f(E_f) = \overline{K}_f \equiv \frac{\int K_f(E)\,\Psi(E)dE}{\int \Psi(E)dE} \quad . \tag{8-22}$$

The energy E_f should not be chosen to be <3 MeV for protons to validate the approximation that uniform damage is generated throughout the sensitive region.

Thus, a completely analogous evaluation can be made of Φ_{eq} (E_R = 1 MeV) for trapped electrons as a function of the same orbital parameters and shielding thicknesses as described for the dose evaluation. This is done by replacing the stopping power in the expression for evaluating dose by a relative energy- and material-dependent weighting function and repeating all the required computations as described in Section 8.5.3. This has been done and the results are given in Figures 8-34 through 8-37 in the same form and order as for the dose evaluations.

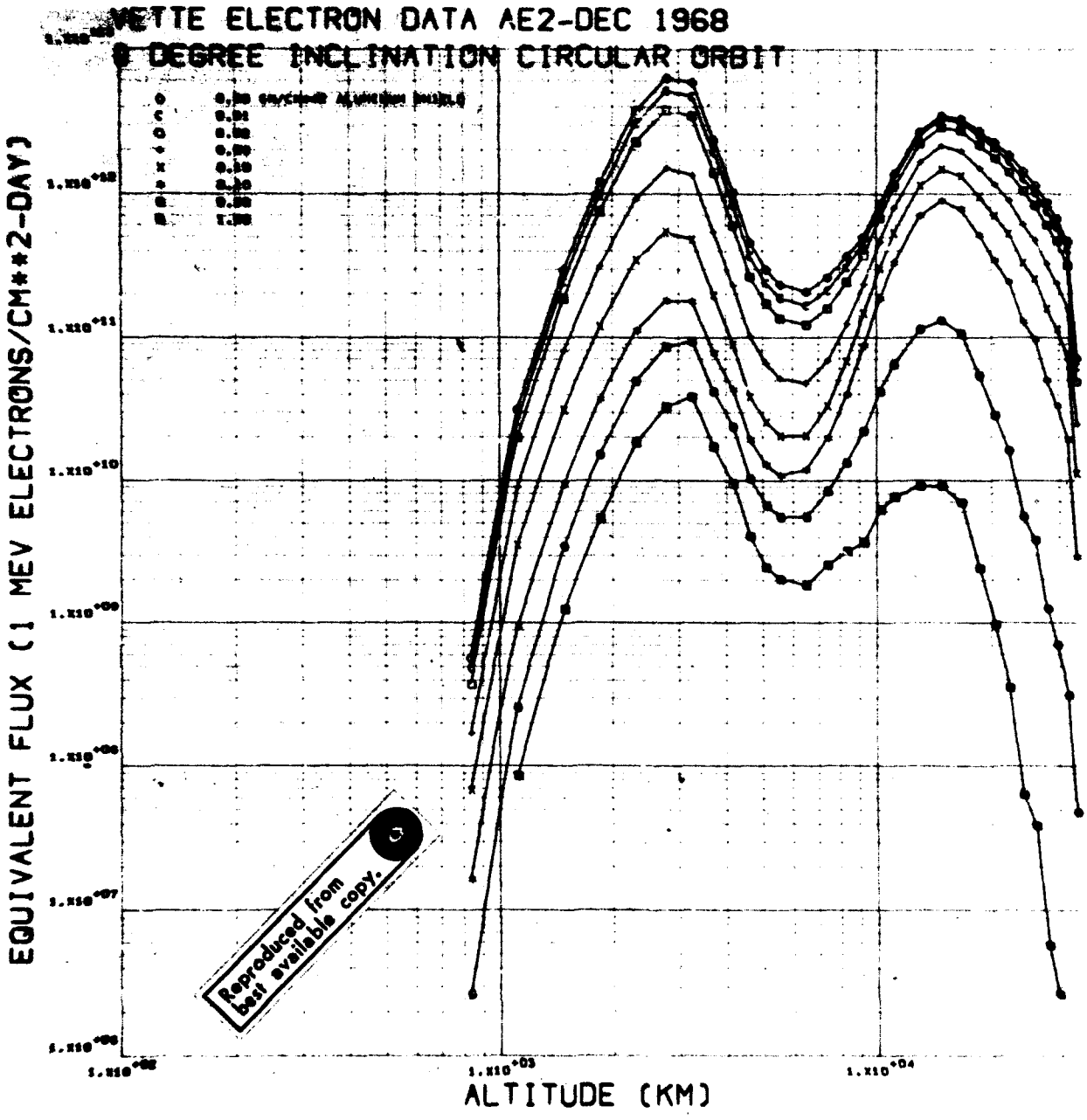

Figure 8-34. Daily fluence of equivalent 1-MeV electrons (for natural trapped electron environment) in circular orbit satellites as a function of satellite altitude for specified orbital inclinations and shielding thicknesses (inclination = 0 degree).

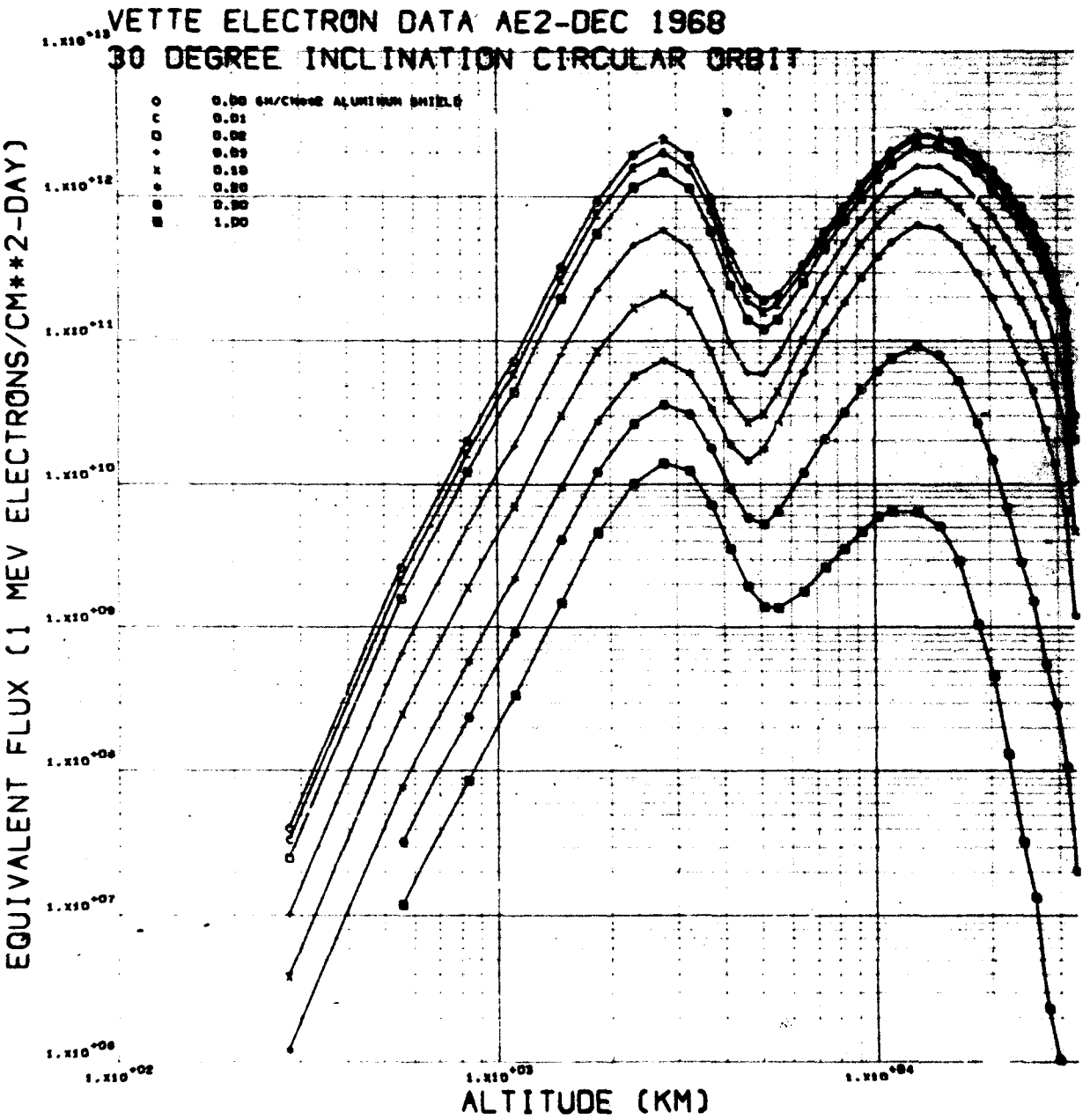

Figure 8-35. Daily fluence of equivalent 1-MeV electrons (for natural trapped electron environment) in circular orbit satellites as a function of satellite altitude for specified orbital inclinations and shielding thicknesses (inclination = 30 degrees).

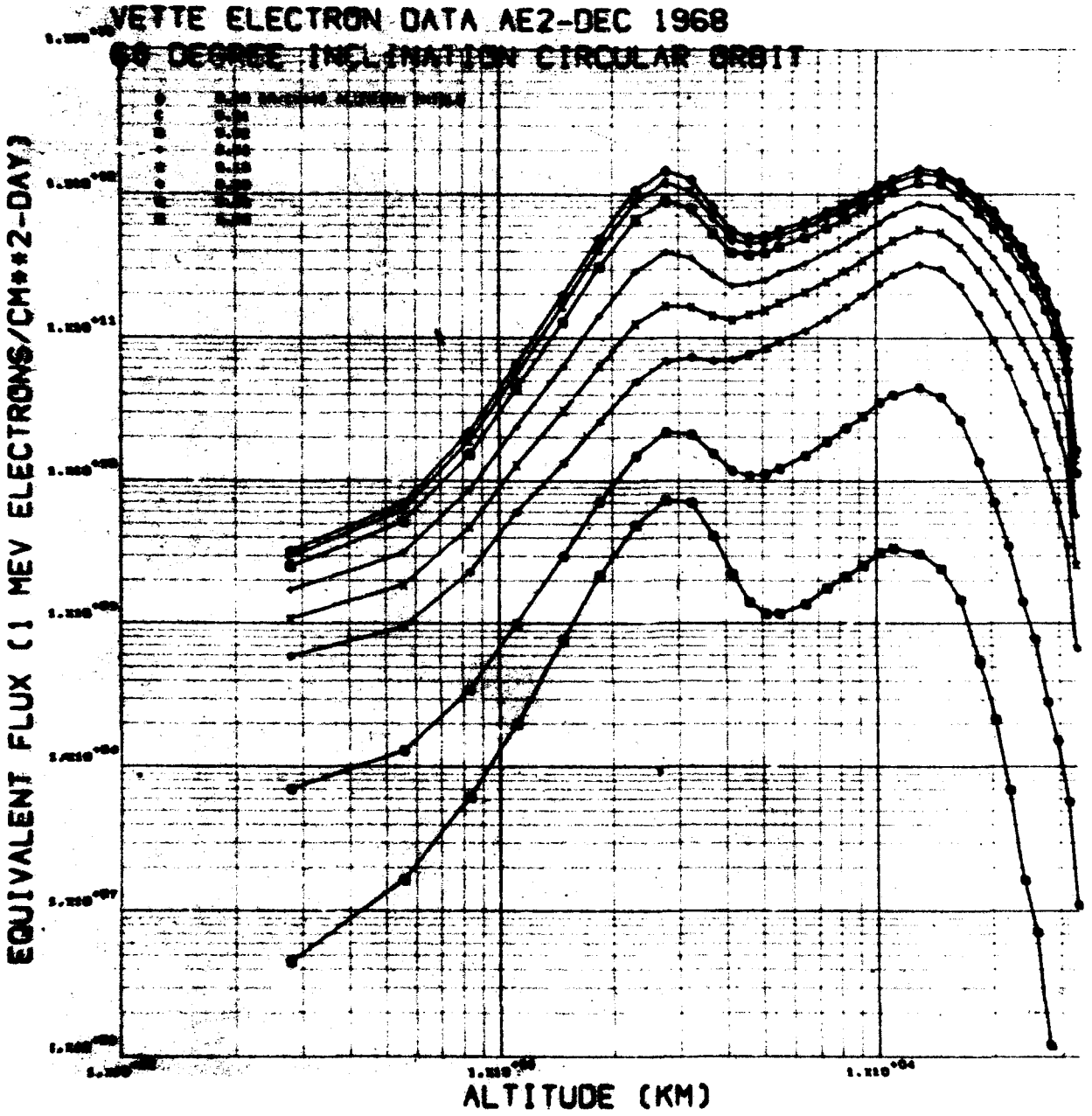

Figure 8-36. Daily fluence of equivalent 1-MeV electrons (for natural trapped electron environment) in circular orbit satellites as a function of satellite altitude for specified orbital inclinations and shielding thicknesses (inclination = 60 degrees).

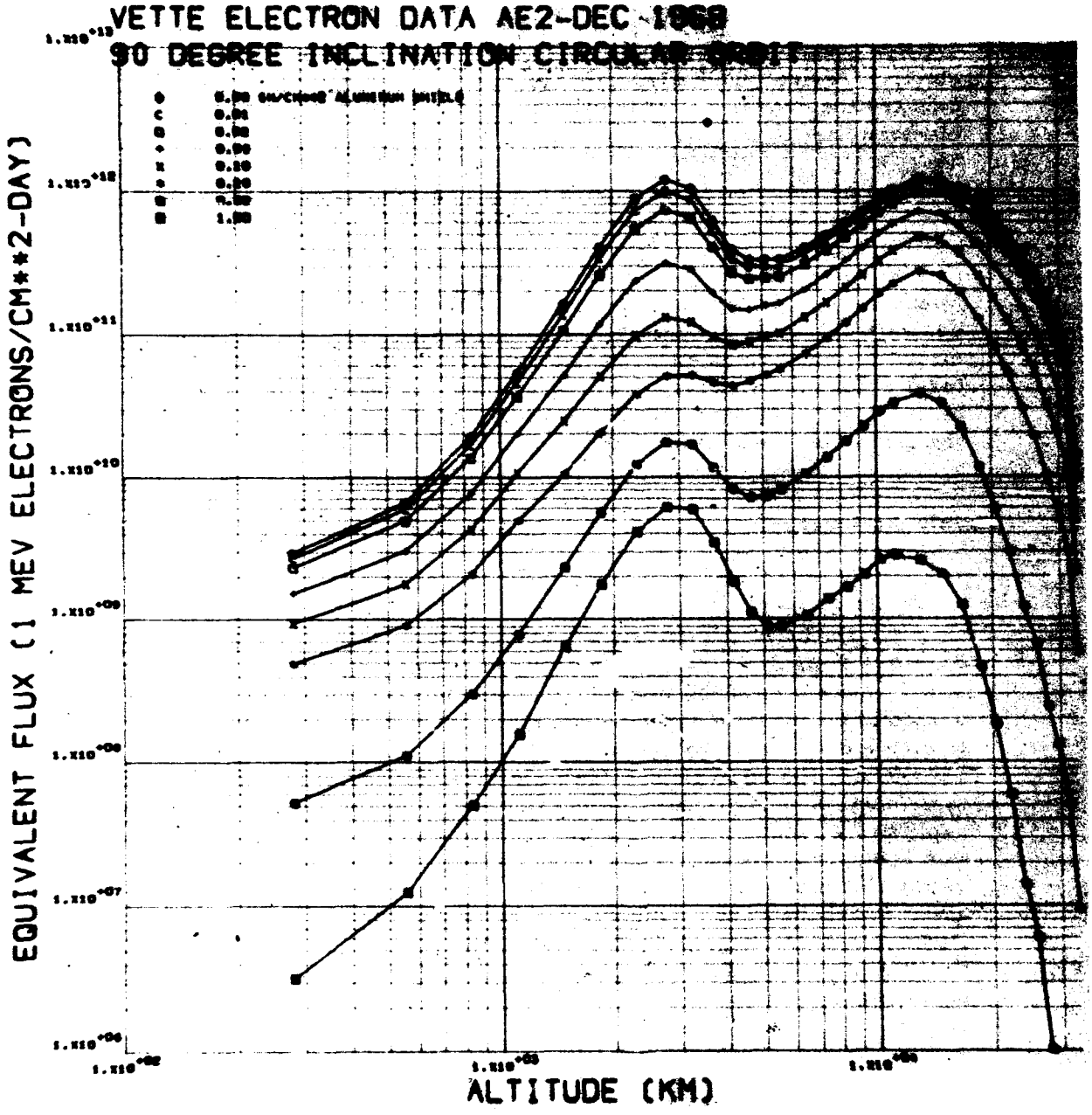

Figure 8-37. Daily fluence of equivalent 1-MeV electrons (for natural trapped electron environment) in circular orbit satellites as a function of satellite altitude for specified orbital inclinations and shielding thicknesses (inclination = 90 degrees).

An analogous procedure could be followed for the trapped proton contribution by replacing the proton ϵ (E) with the relative proton damage factor $[K_\tau(E)]/[K_\tau(4.6)]$ to enable conversion to equivalent 4.6-MeV proton fluence. However, the availability of 1.0-MeV electron device irradiation data vis-a-vis 4.6-MeV proton data has dictated the conversion of the proton data to equivalent 1.0-MeV electron data. Conversion is accomplished by multiplying Φ_{eq} (4.6 MeV) by $[K_{\tau p}(4.6)]/[K_{\tau e}(1.0)]$. This is an energy-dependent ratio that can be obtained from Figure 8-1. The results of these computations are shown in Figures 8-38 through 8-41.

The conversion of the proton data equivalent 1-MeV electron fluence values is less satisfying physically than would be the case if equivalent 4.6-MeV proton fluences were used. This is because electron- and proton-induced damage sites have considerable structural differences. Also, very little study has been made for combined particle damage. For this equivalence procedure to be valid, the particular device-sensitive property must be uniformly degraded in the sensitive region of interest. This will impose a lower limit on the shield thickness for protons. For this reason only, data for shield thicknesses in excess of 0.01 grams per square centimeter of aluminum are given.

EQUIVALENT 1-MeV ELECTRON FLUENCE DUE TO ARTIFICIALLY INJECTED TRAPPED RADIATION. As in the treatment of dose due to artificially injected trapped radiation given in Section 8.5.3, the shape of the injected trapped electron spectrum was assumed to be constant in space and time and was represented by the fission electron energy spectrum of Carter and Reines (Reference 55). Thus, the equivalent 1-MeV electron fluence could be evaluated as a function of aluminum shield thickness and orbital parameters by supplying a single curve for a normalized fission beta spectrum. For this spectrum, the equivalent 1-MeV electron fluence as a function of aluminum shield thickness per unit fluence of incident betas is given in Figure 8-42. This curve may be used in conjunction with Figures 8-25 through 8-30 to evaluate the equivalent 1-MeV electron fluence as a function of aluminum shield thickness and orbital parameters.

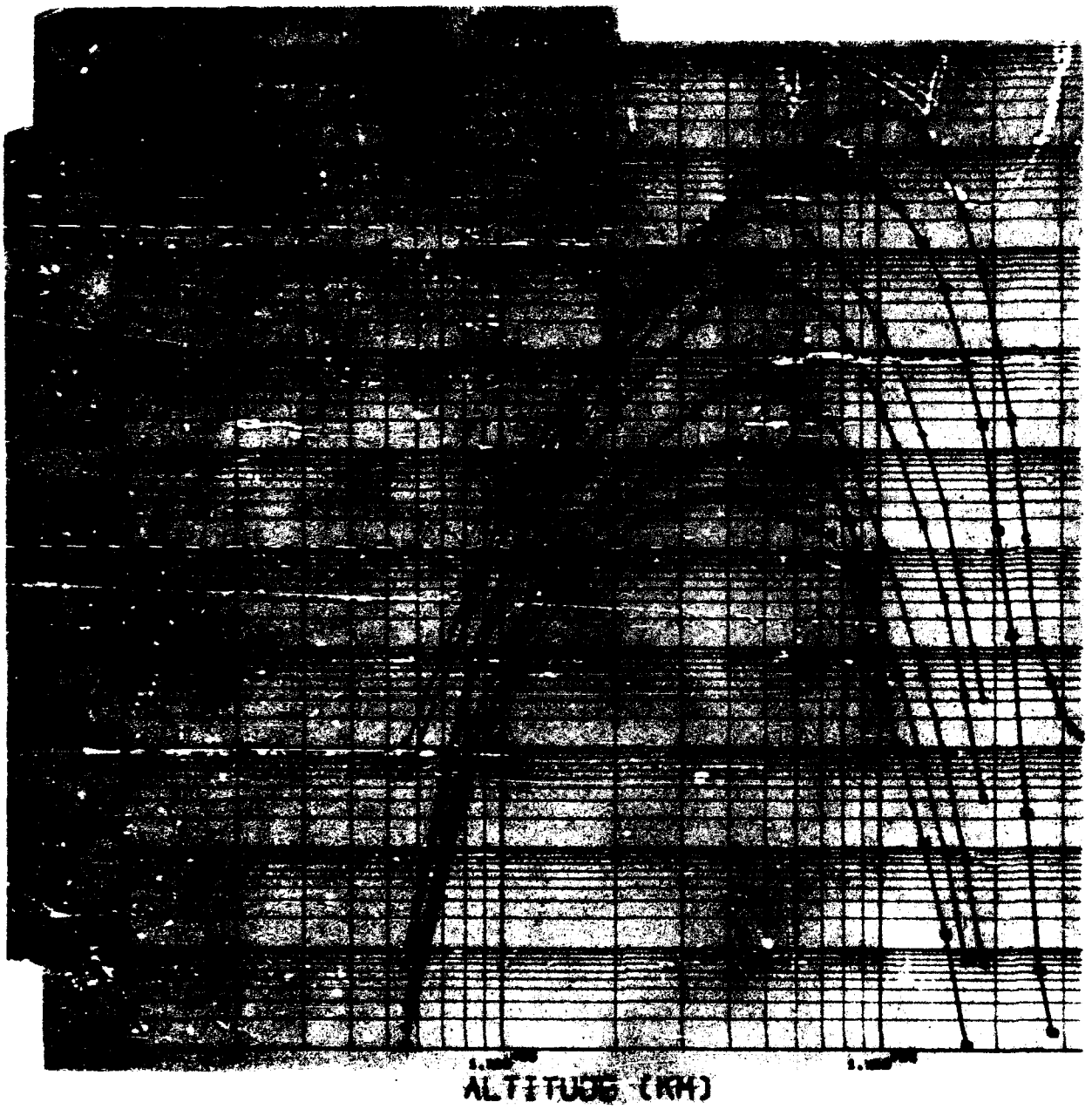

Figure 8-38. Daily fluence of equivalent 1-MeV electrons (for natural trapped proton environment) in circular orbit satellites as a function of satellite altitude for specified orbital inclinations and shielding thicknesses (inclination = 0 degree).

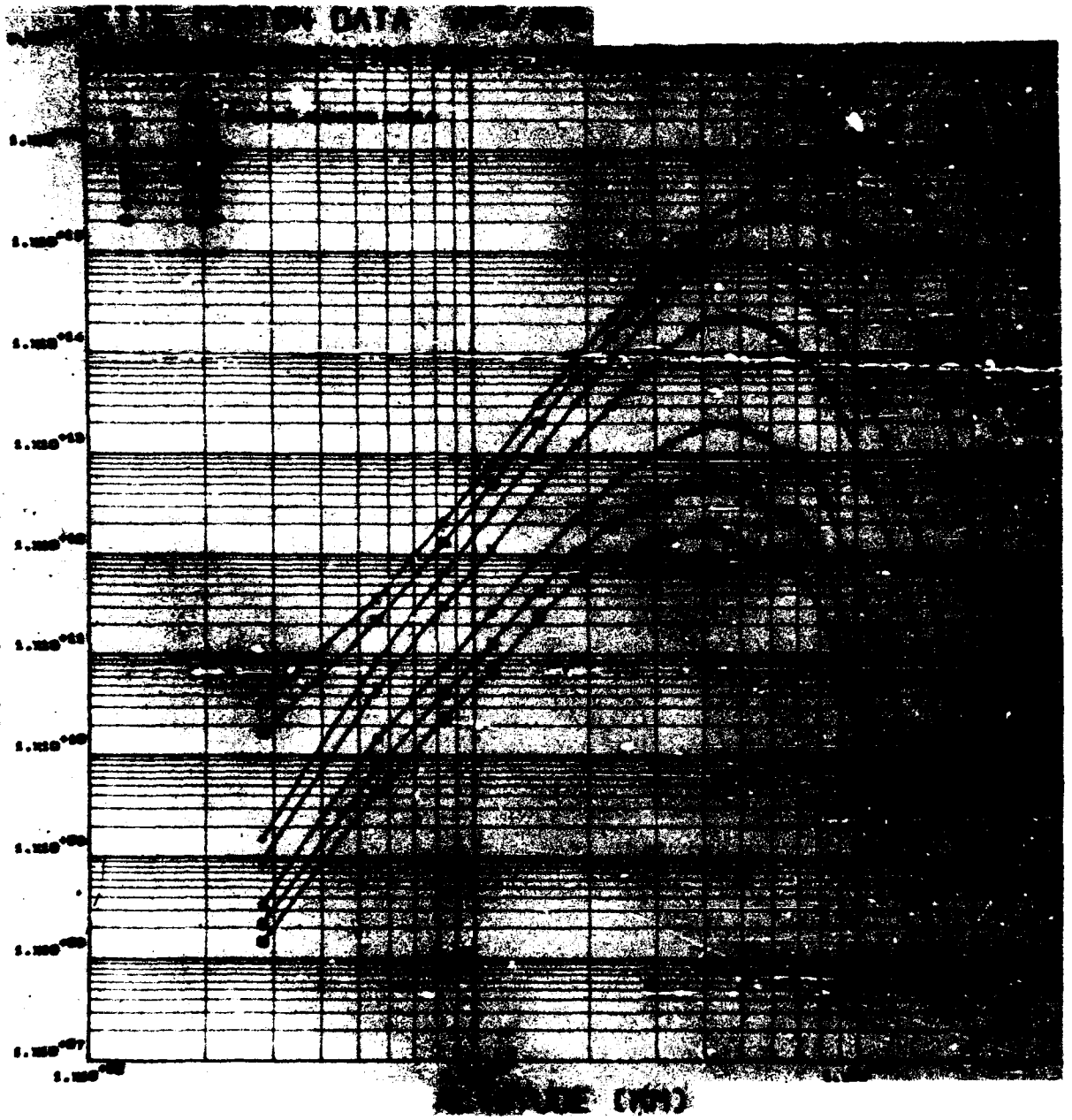

Figure 8-39. Daily fluence of equivalent 1-MeV electrons (for natural trapped proton environment) in circular orbit satellites as a function of satellite altitude for specified orbital inclinations and shielding thicknesses (inclination = 30 degrees).

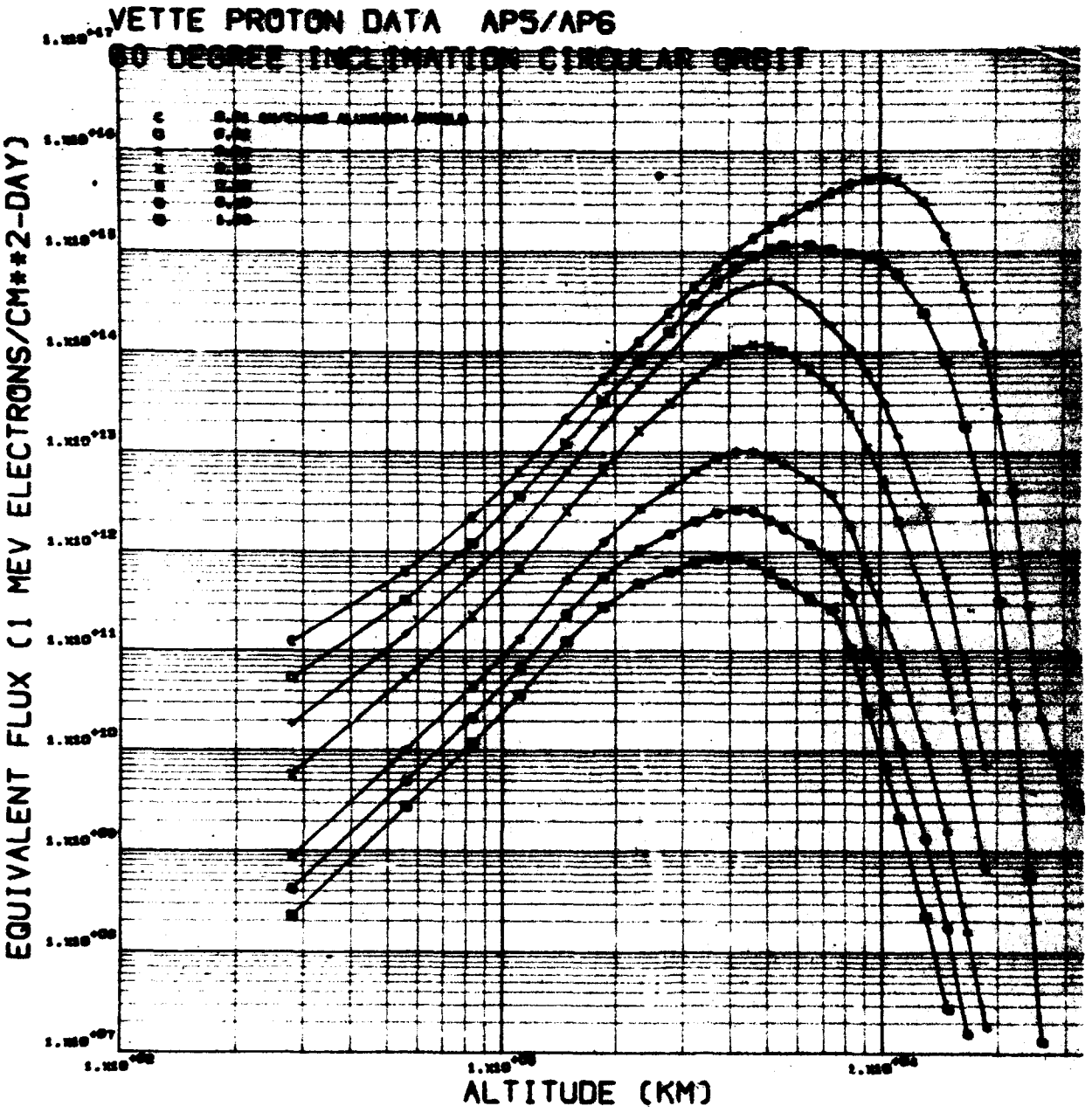

Figure 8-40. Daily fluence of equivalent 1-MeV electrons (for natural trapped proton environment) in circular-orbit satellites as a function of satellite altitude for specified orbital inclinations and shielding thicknesses (inclination = 60 degrees).

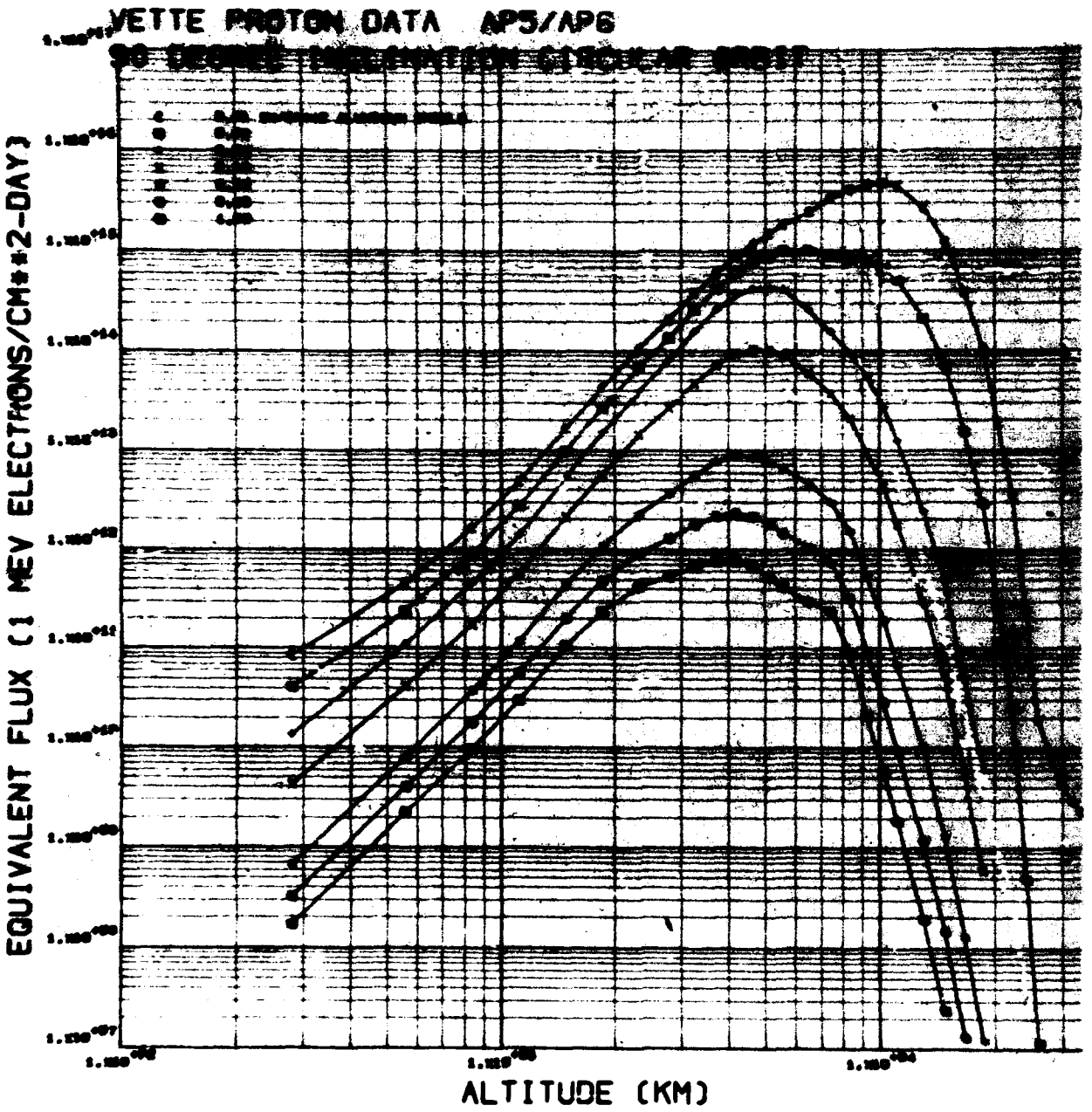

Figure 8-41. Daily fluence of equivalent 1-MeV electrons (for natural trapped proton environment) in circular orbit satellites as a function of satellite altitude for specified orbital inclinations and shielding thicknesses (inclination = 90 degrees).

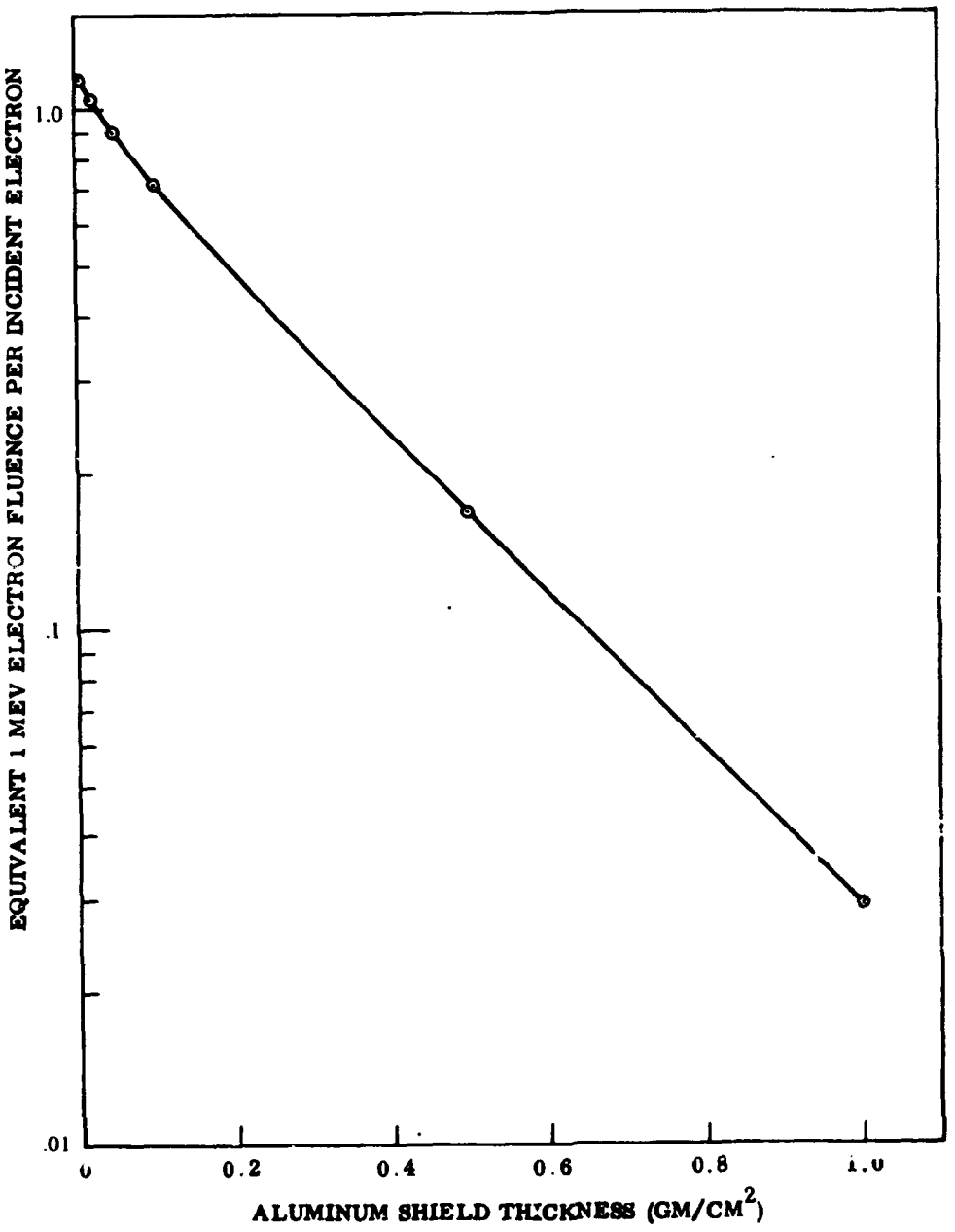

Figure 8-42. Equivalent 1-MeV electron fluence as a function of aluminum shield thickness produced by unit fluence of fission beta electrons incident on shield.

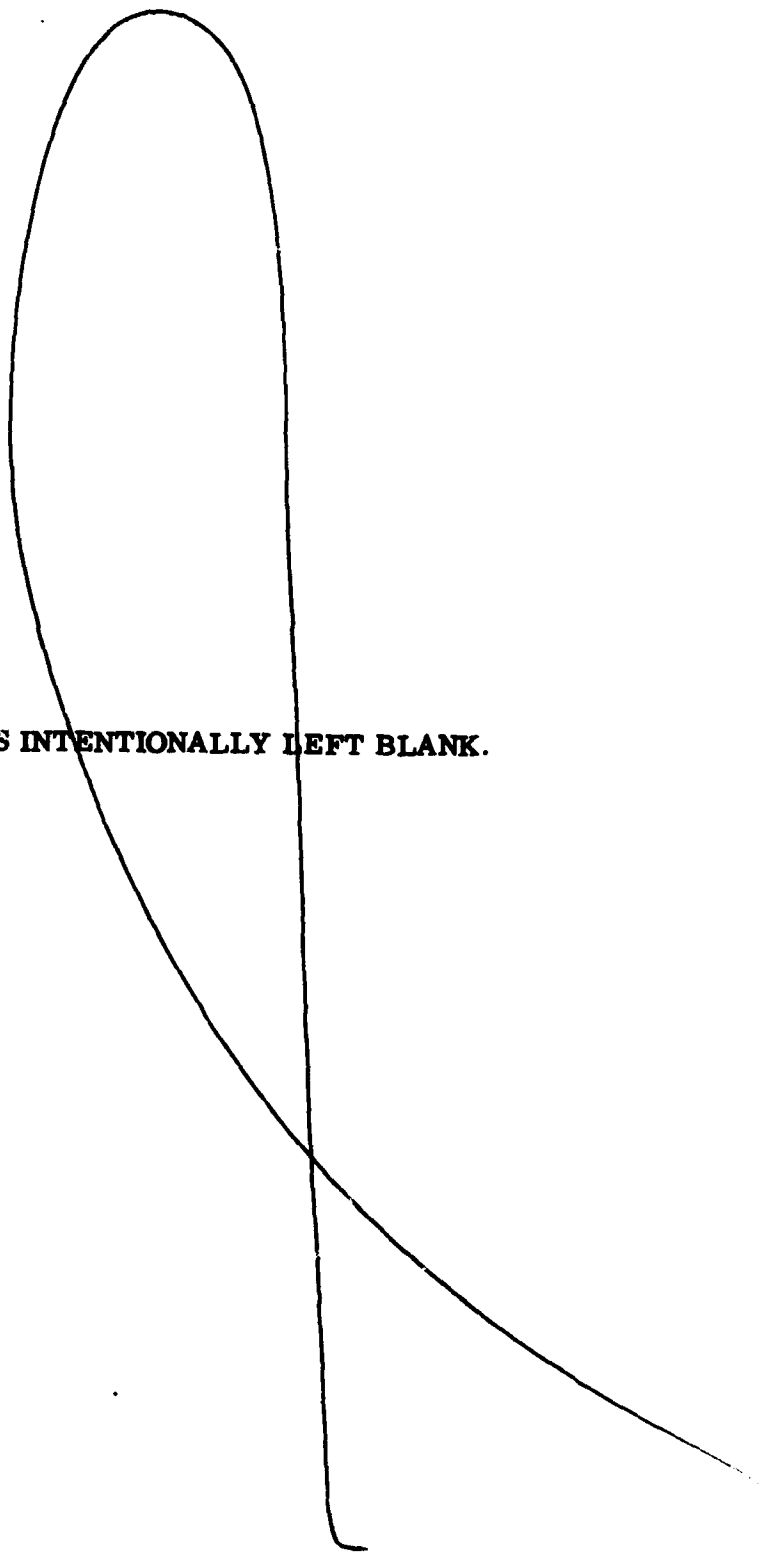

THIS PAGE IS INTENTIONALLY LEFT BLANK.

REFERENCES

1. J.B. Rittenhouse, ed., and J.B. Singletary, ed. Space Materials Handbook: Supplement 1 to the Second Edition: Space Materials Experience, Lockheed Palo Alto Research Laboratory, NASA-SP-3025 (ML-TDR-64-40: Supp. 1), Palo Alto, Calif., S-1 to S-84, 1966.

2. D.L. Dye. "Current Status of Space Radiation Effects in Materials and Components," Proceedings of Symposium on Protection Against Space Radiation, NASA-SP-169 (ANS-SO-5), NASA, Washington, D.C., 19-32, 1968.

3. W.C. Cooley and M.J. Barrett. "Handbook of Space Environmental Effects on Solar Cell Power Systems," Exotech, TR-014, Washington, D.C., 1968.

4. W.D. Compton. "Radiation Effects in Ionic Crystals," The Interaction of Radiation with Solids, ed. by R. Strumane, J. Nihoul, R. Givens, and S. Amelinckex, North Holland, Amsterdam, 386-420, 1964.

5. F. Seitz. "The Effect of Irradiation on Metals," Rev. Mod. Phys., 34, 656-666, 1962.

6. D.S. Billington. "Radiation Effects in Metals and Alloys," Effects of Radiation on Materials, ed. by J.J. Harwood, H.H. Hausner, J.G. Morse, and W.G. Rauch, Reinhold, New York, 99-125, 1958.

7. J.H. Crawford, Jr. "Radiation Effects and Defect Structures in Diamond Structure Semiconductors," The Interaction of Radiation with Solids, ed. by R. Strumane, J. Nihoul, R. Givens, and S. Amelinckex, North Holland, Amsterdam, 421-470, 1964.

Preceding page blank

8. G. Bemski. "Recombination in Semiconductors," Proc. IRE, 46, 990-1004, 1958.

9. R.K. Thatcher, ed. "Transient Radiation Effects on Electronics (TREE) Handbook," Battelle Mem. Inst., DASA 1420, Edition No. 2, Revision No. 1, Columbus, Ohio, 1967.

10. J.P. Mitchell and D.K. Wilson. "Surface Effects of Radiation on Semiconductor Devices," Bell. Syst. Tech. J., XLVI, 1-80, 1967.

11. W.E. Spicer. "Radiation Effects in Optical Materials," Second Symposium on Protection Against Radiations in Space, Stanford Electronics Labs., NASA-SP-71, Palo Alto, Calif., 123-129, 1964.

12. J.W. Corbett. "Electron Radiation Damage in Semiconductors and Metals Supp. No. 7," Adv. in Solid State Physics, ed. by F. Seitz and D. Turnbull, Academic Press, New York, 1966.

13. W.L. Brown, J.D. Gabbe, and W. Rosenzweig. "Results of the Telstar Radiation Experiments," Bell. Syst. Tech. J., XLII, 1505-1559, 1963.

14. H.L. Olesen. Radiation Effects on Electronic Systems, Plenum Press, New York, 1966.

15. R.K. Thatcher, D.J. Hamman, W.E. Chapin, C.L. Hanks, and E.N. Wyler. "The Effect of Nuclear Radiation on Electronic Components, Including Semiconductors," Battelle Mem. Inst., REIC Report No. 6, Columbus, Ohio, 1964.

16. J.G. Linvill. Models of Transistors and Diodes, McGraw-Hill, New York, 1963.

17. G.E. Moore. "Semiconductor Integrated Circuits," Microelectronic Theory, Design, and Fabrication, ed. by E. Keonjian, McGraw-Hill, New York, 262-359, 1963.

18. F. Seitz and J.S. Koehler. "Displacement of Atoms During Irradiation," Adv. in Solid State Physics: Vol. 2, ed. by F. Seitz and D. Turnbull, Academic Press, New York, 305-448, 1956.

19. C. Erginsoy. "Dynamics of Atomic Displacement Processes," The Interaction of Radiation with Solids, ed. by R. Strumane, J. Nihoul, R. Givens, and S. Amelinckex, North-Holland, Amsterdam, 51-83, 1964.

20. P.A. Crossley, G.T. Noel, and M. Wolf. Review and Evaluation Past Solar Cell Development Efforts - Final Report, RCA Astro-Electronics Div., AED-R-3346, Princeton, N.J., 1968.

21. J.H. Martin and F.A. Shirland. "Integrated CdS Solar Cell Array," Conference Record of Seventh Photovoltaic Specialists Conference, IEEE, New York, 131-145, 1968.

22. A.E. Spakowski and A.F. Forestieri. "Observations on CdS Solar Cell Stability," Conference Record of Seventh Photovoltaic Specialists Conference, IEEE, New York, 155-160, 1968.

23. D.J. Curtin. "Irradiation Studies on State-of-the-Art Cadmium Sulfide Cells," Conference Record of Seventh Photovoltaic Specialists Conference, IEEE, New York, 206-213, 1968.

24. T.J. Faith, G.J. Brucker, A.G. Holmes-Seidle, and J. Wysocki. "Long Term Stability of Lithium Doped Solar Cells Irradiated with Electrons, Protons and Neutrons," Conference Record of Seventh Photovoltaic Specialists Conference, IEEE, New York, 131-145, 1968.

25. D.L. Crowther, E.A. Lodi, J. DePangher, and A. Andrew. "An Analysis of Non-Uniform Proton Irradiation Damage in Silicon Solar Cells," IEEE Trans. Nucl. Sci., NS-13, 37-46, 1966.

26. J.H. Martin, R.L. Statler, and E.L. Ralph. "Radiation Damage to Thin Silicon Solar Cells," Photovoltaic Workshop, 1967 Intersociety Energy Conversion Engineering Conference, Heliotek, Sylmar, Calif., 1967.

27. F.J. Reid. "Semiconductor Devices," Effects of Radiation on Materials and Components, ed. by J.F. Kircher and R.E. Bowman, Reinhold, New York, 473-556, 1964.

28. W. Poch and A.G. Holmes-Seidle. "A Prediction and Selection System for Radiation Effects in Silicon Planar Transistors," IEEE Trans. Nucl. Sci., NS-15, 213-223, 1968.

29. C.S. Roberts and J.A. Hoerni. "Comparative Effects of 1 MeV Electron Irradiation of Field Effect and Injection Transistors," Amelco Semiconductor, Technical Bulletin No. 1, Mt. View, Calif., 1963.

30. H.A.R. Wegener, M.B. Doig, P. Marraffino, and B. Robinson. "Radiation Resistant MNOS Memories," IEEE Transactions on Nuclear Science, NS-19, December 1972.

31. G.J. Kuhlmann and W.W. Grannemann. "Ionizing Radiation Effects on GaAsP MIS Capacitor Structures," paper presented at IEEE Conference on Nuclear Space Radiation Effects, Logan, Utah, July 1973.

32. K.G. Aubuchon. "Radiation Hardening of P-MOS Devices by Optimization of the Thermal SiO_2 Gate Insulator," IEEE Transactions on Nuclear Science, NS-18, December 1971.

33. H.L. Hughes. "A Survey of Radiation-Induced Perturbations in Metal-Insulator Semiconductor Structures," IEEE Reliability Physics Symposium, Las Vegas, Nevada, March 1971.

34. W. Gosling. Field Effect Transistors Applications, John Wiley, New York, 1965.

35. M.E. Sibert. "Thermal Control Materials," Space Materials Handbook, Third Edition.

36. R.A. Miller and F.J. Campbell. "Effects of Low Energy Protons on Thermal Control Coatings," Progress in Astronautics and Aeronautics: Vol. 18, ed. by G.B. Heller, Academic Press, New York, 399-412, 1966.

37. R. Smoluchowski. "Radiation Effects in Dielectric Solids," The Effects of Radiation in Materials, ed. by J.J. Harwood, H.H. Hausner, J.G. Morse, and W.G. Rauch, Reinhold, New York, 144-158, 1958.

38. R.A. Breuch and S.A. Greenberg. "Recent Coating Developments and Exposure Parameters," Proceedings of the Joint Air Force - NASA Thermal Control Working Group, ed. by W.P. Johnson and C.P. Boebel, Air Force Materials Laboratory, Report AFML-TR-68-198, Wright-Patterson AFB, Ohio, 485-528, 1968.

39. R.A. Breuch. "Exploratory Trapped Particle and Trapped Particle Plus Ultraviolet Effects on the Optical Properties of Spacecraft Thermal Control Coatings," Progress in Astronautics and Aeronautics: Vol. 18, ed. by G.B. Heller, Academic Press, New York, 365-388, 1966.

40. R.B. Gillette, R.R. Brown, R.F. Seiler, and W.R. Sheldon. "Effects of Protons and Alpha Particles on Thermal Properties of Spacecraft and Solar Concentrater Coatings," Progress in Astronautics and Aeronautics: Vol. 18, ed. by G.B. Heller, Academic Press, New York, 413-440, 1966.

41. K.N. Marshall and R.A. Breuch. "Optical Solar Reflector: A Highly Stable, Low α_s/ϵ Spacecraft Thermal Control Surface," J. of Spacecraft and Rockets, 5, no. 9, 1051-1056, September 1968.

42. J. Schulman and W. Compton. Color Centers in Solids, MacMillan, New York, 1962.

43. P.A. Iles. "Integral Glass Coatings for Solar Cells," Proceedings of the Fifth Photovoltaic Specialists Conference, Interagency Advanced Power Group, Philadelphia, Pa., B-4-1-B-4-20, 1965.

44. T.H. Davies. "A Survey of Recent Irradiation Studies with Glass," Fourth International Conference on Glass, Paris, 1956.

45. A.C. Wilbur and D.L. Anderson. "An Exploratory Study of the Interplanetary Environmental Effects on Solar Cell Cover Glasses," Conference Record of the Seventh Photovoltaic Specialists Conference, IEEE, New York, 184-188, 1968.

46. M.O. Burrell. "The Calculation of Proton Penetration and Dose Rates," NASA TM X-53063, Marshall Space Flight Center, Huntsville, Ala., August 1964.

47. M.O. Burrell, J.J. Wright, and J.W. Watts, Jr. "The Calculation of Electron and Bremsstrahlung Dose Rates," Code Package ELBA, Radiation Shielding Information Center, Oak Ridge National Laboratory, Oak Ridge, Tenn., 1969.

48. C.E. Wuller, Jr. Electron Transport from a Cosine Law Source, IN-SSL-N-68-13, Marshall Space Flight Center, Huntsville, Ala, September 1968.

49. W. Whaling. "The Energy Loss of Charged Particles in Matter," Handbuch der Physik, XXXIV, p. 202, Springer-Verlag, 1958.

50. J. H. King. Models of the Trapped Radiation Environment, Vol. IV: Low Energy Protons, NASA SP-3024, National Aeronautics and Space Adminstration, Washington, D.C., 1967.

51. J.P. Lavine and J.I. Vette. Models of the Trapped Radiation Environment, Vol. V: Inner Belt Protons, NASA-SP-3024, National Aeronautics and Space Administration, Washington, D.C., 1969.

52. J.I. Vette, A.B. Lucero, and J.A. Wright. Models of the Trapped Radiation Environment, Vol. II, NASA SP-3024, National Aeronautics and Space Administration, Washington, D.C., 1966.

53. M.O. Burrell, J.J. Wright, and J.W. Watts. An Analysis of Energetic Space Radiation and Dose Rates, NASA TN D-4404, Marshall Space Flight Center, Huntsville, Ala., February 1968.

54. M.O. Burrell and J.J. Wright. Orbital Calculation and Trapped Radiation Mapping, NASA TM X-53406, Marshall Space Flight Center, Huntsville, Ala., March 1966.

55. R.E. Carter, F. Reines, J.J. Wagner, and M.E. Nyman. "Free Anti-Neutrino Absorption Cross Section - II. Expected Cross Section from Measurements of Fission Fragment Electron Spectrum," Phys. Rev., 113, 280-286, 1959.

56. B.W. Mar. Radiation Trapped in the Earth's Magnetic Field, ed. by B. M. McCormac, Gordon and Breach, New York, 1966.

57. J.E. Rauch. Experimental and Theoretical Energy Dissipation Distributions by Monoenergetic Electrons in Matter: An Analysis of Nakai's Experimental Data for Be, Al, Cu, Ag, and Pb, LMSC, Report 6-77-67-30, Palo Alto, Calif., 20 June 1967.

58. L.V. Spencer. Energy Dissipation by Fast Electrons, National Bureau of Standards Monograph #1, Supt. of Documents, Washington, D.C., September 1959.

59. H. W. Koch and J. W. Motz. "Bremsstrahlung Cross-Section Formulas and Related Data," Reviews of Mod. Phys., 31, 920-955, 1959.

60. W. E. Dance et al. Investigation of Bremsstrahlung Produced by the Interaction of Electrons with Matter, LTV Research Center, Report 0-71000/4R-14, Dallas, Texas, June 1964.

61. D. H. Rester and W. E. Dance. Electron Bremsstrahlung Cross-Section Measurements, NASA SP-169, National Aeronautics and Space Administration, Washington, D. C., p. 215, 1968.

62. M. J. Berger and S. M. Seltzer. Penetration of Electrons and Associated Bremsstrahlung Through Aluminum Targets, NASA SP-169, NASA, Washington D. C., 285-322, 1968.

63. W. R. Cherry and L. W. Slifer. Solar Cell Radiation Damage Studies with 1 MeV and 4.6 MeV Protons, Goddard Space Flight Center, NASA-GSFC Report X-636-63-110, Greenbelt, Md., 1963.

64. T. J. Faith. "Temperature Dependence of Damage Coefficient in Electron Irradiated Solar Cells," paper presented at IEEE Conference Nuclear and Space Radiation Effects, Logan, Utah, July 23-26, 1973.

65. A. G. Holmes-Sieldle and Karl H. Zaininger. "The Physics of Failure of MIS Devices Under Radiation," IEEE Transactions on Reliability, R-17, 34-44, March 1968.

66. A. G. Stanley and P. F. McKenzie. "Effects of Electron Irradiation on Operational Amplifiers," IEEE Trans. Nucl. Sci., NS-20, 100-107, April 1973.

67. D. Neamen, W. Shedd, and B. Buchanan. "Permanent Ionizing Radiation Effects in Dielectrically Bounded Field Effect Transistors," paper presented at IEEE Conference Nuclear and Space Radiation Effects, Logan, Utah, July 23-26, 1973.

68. W. J. Poch and A. G. Holmes-Sieldle. "The Long-Term Effects of Radiation on Complementary MOS Logic Networks," IEEE Transactions on Nuclear Science, NS-17 (December 1970).

69. R.A. Kjar, J.L. Peel, and C.Y. Wrigley. "Effects of Metallic Doping on Ionization Damage in MOSFETS," IEEE Transactions on Nuclear Science, NS-16, December 1969.

70. H.L. Hughes, R.D. Baxter, and B. Phillips. "Dependence of MOS Device Radiation – Sensitivity on Oxide Impurities," IEEE Transactions on Nuclear Science, NS-19, December 1972.

71. F.B. Michelelli and K.H. Zaininger. "Permanent Radiation Effects in Hardened Al_2O_3 MOS Integrated Circuits," IEEE Transactions on Nuclear Science, NS-17, December 1970.

72. P.F. Schmidt and J.D. Ashner. "Radiation-Insensitive Silicon Oxynitride Films for Use in Silicon Devices – Part II," IEEE Transactions on Nuclear Science, NS-17, December 1970.

73. "Annual Conference on Nuclear and Space Radiation Effects," IEEE Transactions on Nuclear Science, NS-19, No. 6, December 1972.

74. "Annual Conference on Nuclear and Space Radiation Effects," IEEE Transactions on Nuclear Science, NS-18, No. 6, December 1971.

SECTION 9

SYNCHROTRON RADIATION FROM ELECTRONS TRAPPED IN THE EARTH'S MAGNETIC FIELD

A.M. Peterson, Stanford Research Institute
J.F. Vesecky, Stanford Research Institute

9.1 INTRODUCTION

The process of synchrotron emission from high-energy electrons spiraling in a magnetic field has received considerable attention in recent years not only because of its relevance to particle accelerators and thermonuclear reactors but also because of its wide application to geophysical and astrophysical problems. The case of interest here is the synchrotron emission from fission-beta electrons injected into the earth's magnetic field by a high-altitude nuclear explosion such as the Starfish explosion of July 1962. In the case of Starfish, 30- and 50-megahertz radio noise was observed at ground stations for more than 1 year after the event. The relevant portions of synchrotron theory will be summarized and general techniques for computing numerical results will be illustrated. Two examples will be considered in some detail—one example being the Starfish event.

9.2 SUMMARY OF SYNCHROTRON THEORY

9.2.1 General Physical Description of the Process and Parameters Involved

A charge moving uniformly in free space does not radiate since the Poynting vector corresponding to the fields of the moving charge falls off too rapidly to contribute to energy flow over a distant surface. In the case of an accelerated charge, however, the fields may fall off as $1/r$ instead of $1/r^2$, and the charge thus gives rise to radiation fields in the usual sense. If the acceleration is perpendicular to the velocity—as for a charge moving at any angle to a uniform magnetic field—the motion is helical and the resulting emission is referred to by the terms synchrotron radiation, cyclotron radiation, gyro-radiation, or magnetic bremsstrahlung.

At low-electron energies, the emission from the revolving charge equals emission from two dipoles at right angles to each other and to the field. It thus occurs at the angular frequency of the circular

motion (the gyro-frequency) and is maximum at right angles to the plane of the circular motion, i.e., along the magnetic field. This is the case referred to by the terms cyclotron or gyro-radiation.

The terms synchrotron radiation and magnetic bremsstrahlung apply when the electron velocities are relativistic. For such particles, the emission is concentrated strongly in the direction of the instantaneous velocity. Thus, emission in the direction of an observer located in the orbital plane of a revolving particle occurs only while the electron is moving very nearly toward that observer and is received in the form of short pulses that recur at the gyro-frequency. Consideration of the Fourier components of such a waveform indicates that a characteristic of the radiation will be its high harmonic content as shown in Section 9.2.3. In the case of relativistic electrons, the fundamental frequency is low, i.e., at the gyro-frequency. At L = 4 over the geomagnetic equator, the gyro-frequency is about 5 kilohertz for a 1-MeV electron. Hence, at VHF frequencies, the separation is so small that the spectrum essentially is continuous.

In general, the factors influencing the power emitted by a single electron in free space are summarized thus:

1. Frequency of observation (ν)
2. Kinetic energy of the electron (T)
3. Instantaneous radius of curvature of the electron's trajectory (R)—R itself is a function of the local magnetic field flux density (B), the electron energy (T), and the pitch angle (α)
4. Angle (Ψ) between the direction of emission and the instantaneous orbital plane of the electron (Figure 9-1).

The power spectral density (P) radiated by an electron into a unit solid angle is the $P(\nu, T, B, \alpha)$. $P(\nu)$ will be used to indicate that the remaining variables T, B, Ψ, and α are held constant at specified values.

9.2.2 Radiation Fields from an Electron in Circular Motion

The vector expressions for the radiation fields from a charge in circular motion may be obtained from classical electrodynamic theory using the retarded Liénard-Weichert potentials [References 1 (p. 363) or 2 (p. 481)]. Examination of the expressions for these fields shows that, for circular motion, the emission has a strong

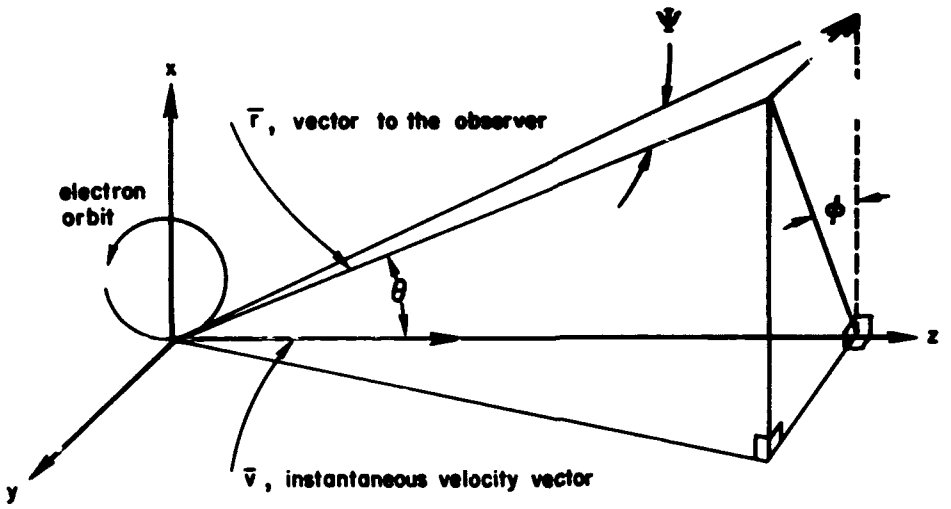

Figure 9-1. Coordinate system for an electron in circular motion.

linear polarization perpendicular to the local magnetic field line when $\Psi << 1$. This is a very important characteristic and provides a possible means for experimentally identifying the process. From the Poynting vector corresponding to the aforementioned radiation fields, the angular distribution of the radiated power per ster in the frame of the electron may be derived with this result (Reference 3) in gaussian cgs units:

$$\frac{dP(\theta,\phi)}{d\Omega} = \frac{e^2 R\omega_c^2}{4\pi c^3} \quad \frac{(1 - \beta \cos\theta)^2 - (1 - \beta^2) \sin^2\theta \cos^2\phi}{(1 - \beta \cos\theta)^5} \qquad (9\text{-}1)$$

where e is the electron's charge, ω_c is the angular gyro-frequency (for circular motion $\omega_c = eB/m_o\gamma c$; m_o is the electron's rest mass, γ is the Lorentz factor), $\beta = v/c$, and $R = v/\omega_c$. The angles θ and ϕ are defined in Figure 9-1 and some rough sketches of sample radiation patterns are given in Figure 9-2 where the instantaneous electron velocity is directed along the z-axis. The dipole pattern corresponding to low electron energies changes into extremely directional patterns for the higher energies. The maximum values of $P(\theta,\phi)$ relative to the low-energy ($\beta = 0.01$) case are given in the figures, as are the approximate half-power beamwidths. The patterns are not symmetrical about the z-axis, as can be noted by examining the cross sections in the planes $\phi = 0$ degrees and $\phi = 90$ degrees.

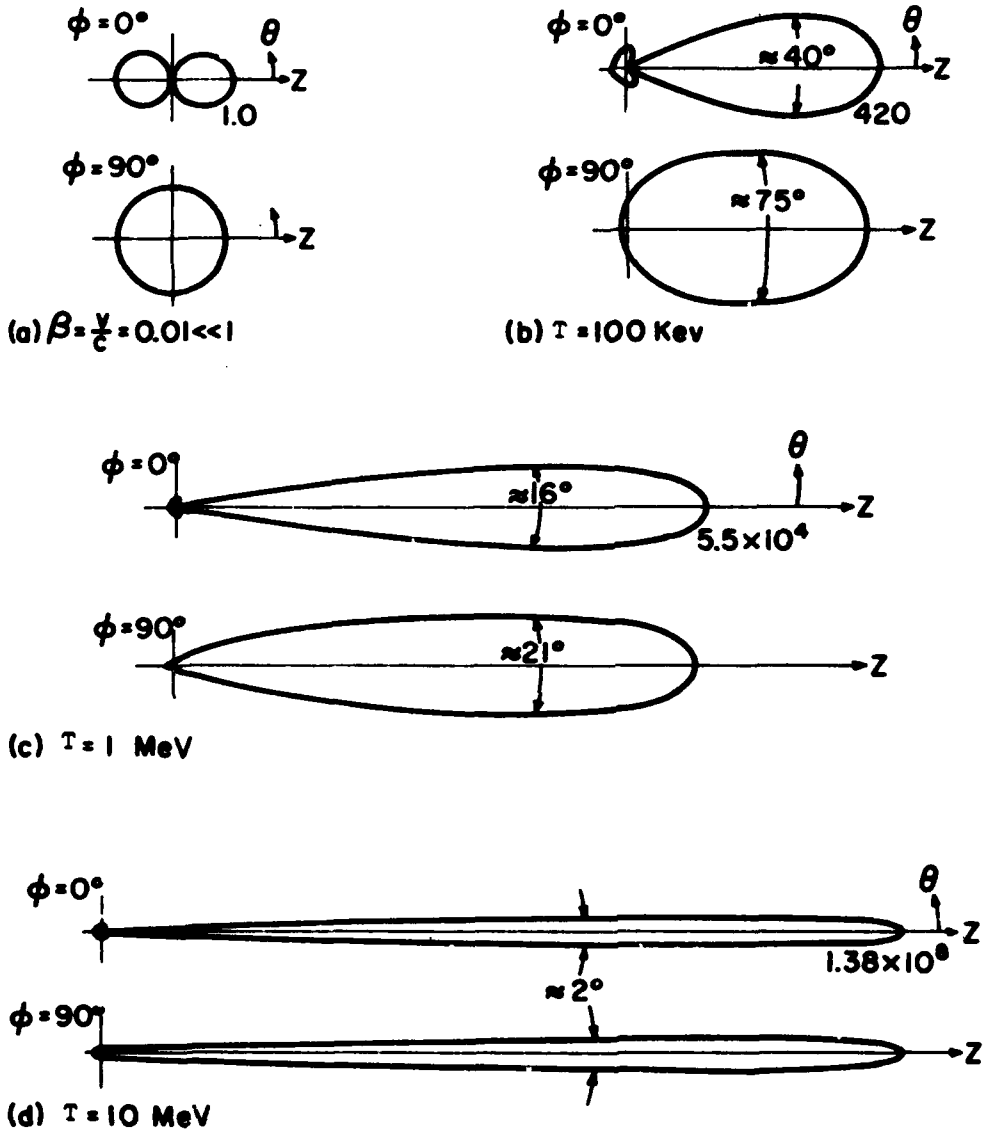

Figure 9-2. Examples of radiation patterns (total power) at various electron energies. Coordinates are defined in Figure 9-1.

In the plane ϕ = 0 degrees, zeros occur at $\theta = \pm\cos^{-1}(v/c)$, whereas no zeros occur in the plane ϕ = 90 degrees. Although the difference is great at low energies, the distinction disappears in the patterns for higher energies.

At high energies, the important region of the diagrams occurs for $\theta << 1$. By approximating the sine and cosine terms in Equation 9-1, the beamwidth of the pattern may be shown to be on the order of $m_o c^2/E$, where E is the total energy of the electron.

9.2.3 Frequency Spectrum

Consider an electron in circular motion ($\alpha = \pi/2$) and a distant observer in the plane of the electron's orbit ($\Psi = 0$). From the radiation patterns of Figure 9-2, the observer can be seen to receive appreciable radiation from a high-energy electron only when the electron is traveling approximately toward him. Hence, the observer will receive a pulse of radiation for every revolution of the electron, and the distribution of the radiated power with respect to frequency should consist of harmonics of the angular gyro-frequency ω_c. Thus, the power received by the observer is

$$P(\omega) = \sum_{n=1}^{\infty} \delta(\omega - n\omega_c) P_n \quad .$$

Remember that ω_c is dependent on both B and the electron energy. Schwinger (Reference 4) presents the following expression for the power radiated at the frequency of the n^{th} harmonic into a unit solid angle at an angle Ψ from the orbital plane:

$$P_n(\Psi) = \frac{e^2 \omega_c \beta^3 n^2}{2\pi R} \left[J_n'^2(n\beta \cos\Psi) + \frac{\tan^2\Psi}{\beta^2} J_n^2(n\beta \cos\Psi) \right] . \quad (9\text{-}2)$$

In Equation 9-2, n is the harmonic number ($2\pi\nu/\omega_c$) and J denotes a Bessel function of order n.

Following Schwinger's work, some limiting cases of Equation 9-2 may be examined. If $\beta \cos\Psi << 1$, as would be the case for either low electron energies or for directions nearly at right angles to the orbital plane, Equation 9-2 may be approximated as:

$$P_n(\Psi, B, T) = \frac{e^2 \omega_c \beta}{2\pi R} \frac{(n\beta/2)^{2n}}{[(n-1)!]^2} (\cos\Psi)^{2n-2} (1 + \sin^2\Psi) \quad . \qquad (9\text{-}3)$$

The radiated power thus decreases rapidly with increasing harmonic number in the case of low-energy ($\beta << 1$) electrons. For example, in this energy range the fundamental frequency (gyro-frequency) at auroral altitudes will have its maximum value on the order of 1 megahertz. Emission at 12 megahertz ($n \approx 12$) for $\beta \approx 0.1$ is then less than emission at the fundamental frequency by a factor on the order of 10^{-18}. Emission by electrons whose energies lie in the range of this approximation clearly will not contribute to synchrotron emission at frequencies above 10 megahertz.

The total power radiated at a frequency $\omega = n\omega_c$ may be obtained by integrating Equation 9-2 over all angles. In the relativistic limit ($\gamma >> 1$), the integral of Equation 9-2 may be evaluated to a close approximation for two ranges of n (Reference 5):

$$\int P_n d\Omega = 0.52 \frac{e^2}{c} \omega_c^2 n^{1/3} \quad \text{for} \quad 1 << n << \gamma^3 \qquad (9\text{-}4)$$

$$\int P_n d\Omega = \frac{1}{2\sqrt{\pi}} \frac{e^2}{c} \omega_c^2 \frac{n^{1/2}}{\gamma^{1/2}} \exp\left(\frac{2n}{3\gamma^3}\right) \quad \text{for} \quad n >> \gamma^3 \, . \qquad (9\text{-}5)$$

From the sketch of Figure 9-3, which is based on Equations 9-4 and 9-5, the emission is seen to be appreciable up to at least a frequency of the order of $\nu_c \gamma^3$, where $\omega_c = 2\pi\nu_c$.

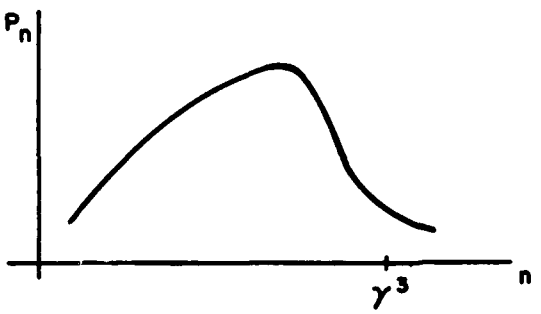

Figure 9-3. Total power radiated by a high-energy electron ($\gamma^2 >> 1$) at the n^{th} harmonic of the gyro-frequency.

In Reference 4, Schwinger gives a high-energy approximation that is similar to Equation 9-4, but only for the ergs sec^{-1} $ster^{-1}$ radiated in the orbital plane. From Equation 9-2, with $\Psi = 0$ and $\beta \approx 1$,

$$P_n(B,T) = \frac{e^2 \omega_c n^2}{2\pi R} [J_n'(n)]^2 \approx 1.93 \times 10^{-20} \frac{\omega_c n^{2/3}}{R} \qquad (9\text{-}6)$$

for $\gamma^2 >> 1$ and $1 << n << (3/2)\gamma^3$. Again, as with Equation 9-4, the emission increases with frequency over this range of n. Retaining the angular dependence, the general expression of Equation 9-2 in the region of interest ($\Psi^2 << 1$) becomes

$$P_n(T, B, \Psi) = \frac{e^2 \omega_c n^2}{6\pi^3 R} (1 - \beta^2 + \Psi^2)^2 \left[K_{2/3}^2(\zeta) + \frac{\Psi^2}{1 - \beta^2 + \Psi^2} K_{1/3}^2(\zeta) \right] \qquad (9\text{-}7)$$

where

$$\zeta = \frac{n}{3\gamma^3} \left(\frac{1 - \beta^2 + \Psi^2}{1 - \beta^2} \right)^{3/2} = \frac{n}{3} (1 - \beta^2 + \Psi^2)^{3/2} .$$

Equation 9-7 is valid for $\gamma^2 >> 1$, $\Psi^2 << 1$, and $n >> 1$. In Equation 9-7, the original Bessel functions have been replaced by their asymtotic forms for larger order and argument, i.e., modified Bessel functions of the second kind, $K_{1/3}$ and $K_{2/3}$.

Since the spectrum is essentially continuous, n may be replaced by ω/ω_c and $P_{\omega/\omega_c}(\Psi)$ may be considered as a continuous function of ω. Also, the number of harmonics in an interval $\Delta\omega$ is the integer value of $\Delta\omega/\omega_c$, so that the number of harmonics in a unit interval $\Delta\omega = 1$ is $1/\omega_c$. Therefore, $(1/\omega_c)P_{\omega/\omega_c}(\Psi)$ is the power radiated at frequency ω into a solid angle at an angle Ψ from the orbital plane per unit angular frequency interval [i.e., ergs sec^{-1} $ster^{-1}$(radian/second)$^{-1}$]. Then, $(2\pi/\omega_c)P_{\omega/\omega_c}(\Psi)$ is the emission in ergs sec^{-1} $ster^{-1}$ Hz^{-1}.

After inserting the numerical values, this expression for the instantaneous power per unit solid angle per hertz at an angle Ψ from the orbital plane is obtained. Equation 9-8 expresses the synchrotron power for the conditions $\alpha = \pi/2$, $\Psi^2 << 1$, $n >> 1$, $\gamma^2 >> 1$.

$$P(\nu, T, B, \Psi) = 3.4 \times 10^{-40} \frac{R\nu^2}{\beta^2} (1 - \beta^2 + \Psi^2)^2 \left[K^2_{2/3}(\zeta) + \frac{\Psi^2}{1 - \beta^2 + \Psi^2} K^2_{1/3}(\zeta) \right] \quad (9\text{-}8)$$

where

$$\zeta = 7.0 \times 10^{-11} \frac{\nu R}{\beta} (1 - \beta^2 + \Psi^2)^{3/2} \quad .$$

The functions $K_{1/3}(\zeta)$ and $K_{2/3}(\zeta)$ in Equations 9-7 and 9-8 are modified Bessel functions of the second kind. Because tabulations of these functions are not available widely, the reader is referred to Reference 6 (p. 721) where plots of both functions for $10 > \zeta > 0.01$ are given. Reference 12 (p. 197) gives relevant formulas as well as asymptotic series for large ζ, which for the present work are adequate for $\zeta > 3$, using only three terms of the series. Reference 18 (Chapter 10) also gives some useful tables.

Spectra for cases of special interest now will be calculated and plotted. Consider first the case for high-energy ($\gamma^3 >> 1$) electrons in the frequency range where $n >> 1$ with $\Psi = 0$. Equation 9-7 becomes, after multiplication by $2\pi/\omega_c$, the emission in ergs sec^{-1} $ster^{-1}$ Hz^{-1} in terms of harmonic number n:

$$P(n, T, B) = 4.1 \times 10^{-23} \frac{B\gamma}{\beta} \left(\frac{n}{3\gamma^3} \right)^2 K^2_{2/3}\left(\frac{n}{3\gamma^3} \right) \quad (9\text{-}9)$$

or, using Equation 9-8, the emission is in terms of frequency:

$$P(\nu, T, B) = 4.1 \times 10^{-23} \frac{B\gamma}{\beta} \left(1.2 \times 10^{-7} \frac{\nu}{B\gamma^2} \right)^2 \cdot K^2_{2/3}\left(1.2 \times 10^{-7} \frac{\nu}{B\gamma^2} \right) \quad . \quad (9\text{-}10)$$

Figure 9-4 is a plot of either $P(n, T, B)$ versus $n/3\gamma^3$ or $P(\nu, T, B)$ versus $1.2 \times 10^{-7} (\nu/B\gamma^2)$. The curve may be regarded as a

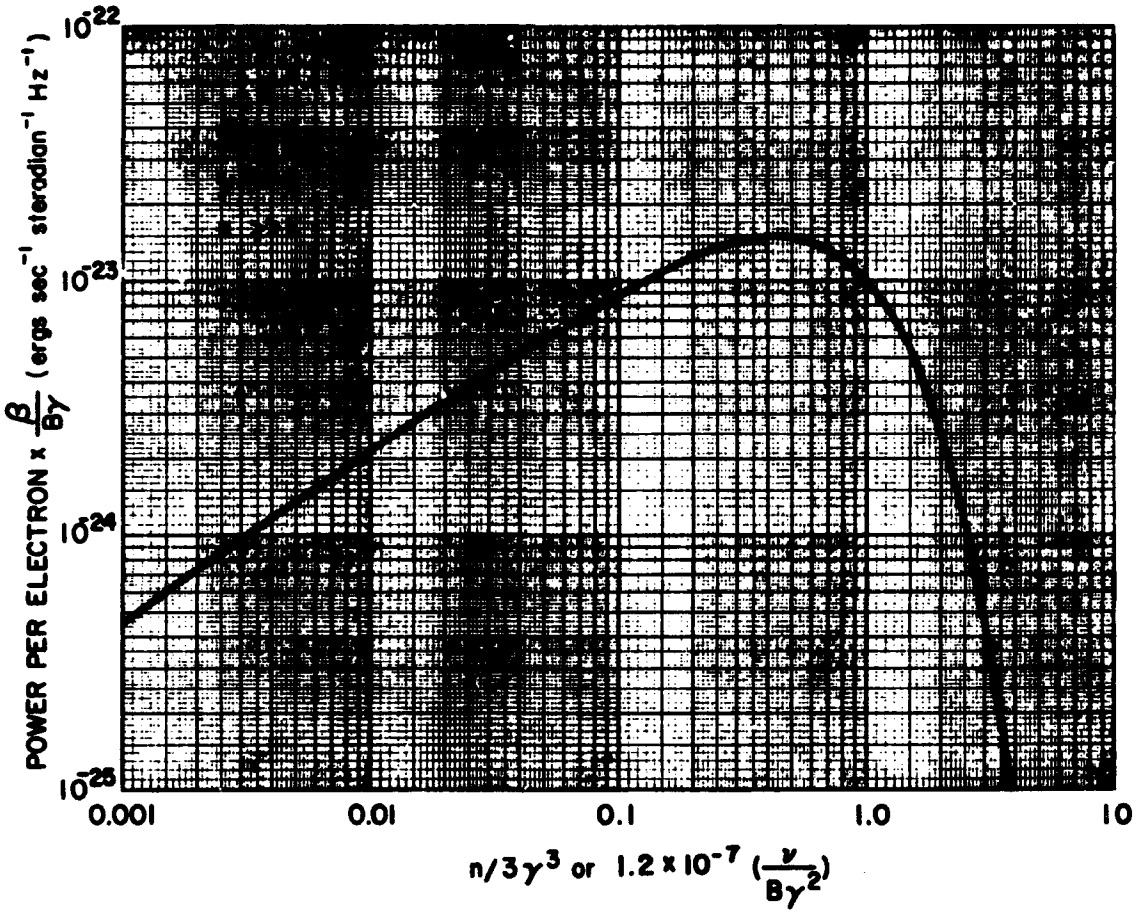

Figure 9-4. Normalized spectrum of a high-energy electron ($\gamma^2 \gg 1$) when $\nu \gg \nu_c$, α = 90 degrees, and $\Psi = 0$.

normalized curve from which the spectrum in the range $n \gg 1$ may be obtained for any high-energy ($\gamma^2 \gg 1$) electron at any desired value of B (remember that $\Psi = 0$ and that the electron is assumed to be in circular motion $\alpha = \pi/2$). For conditions ($\Psi = 0$, $n \gg 1$, and $\gamma^2 \gg 1$), Figure 9-4 shows that peak emission occurs when $(n/3\gamma^3) \approx (1/2)$. Thus, the frequency of peak emission $\nu_{pk} \approx 1.5\nu_c\gamma^3$. Knowing the energy of the electron (and thus β and γ) and the ambient magnetic field (B), one can find the power radiated by the electron (per hertz per ster) in the electron's instantaneous orbital plane ($\Psi = 0$) at a frequency ν from Figure 9-4.

To obtain frequency spectra where the conditions $\gamma^2 \gg 1$ and $n \gg 1$ do not hold (i.e., for energies less than about 1.5 MeV), calculations must be based on the more general expression given in Equation 9-3. Equation 9-10 of course may be used when $\gamma^2 \gg 1$ and $n \gg 1$. Figure 9-5 is a plot of frequency spectra for several particle energies when $B \approx 0.4$ gauss. It should be noted that the previous calculations assume the emitting electron to be in free space. This assumption is good when $\nu \gg (2/3)(f_p^2/\nu_c)$ at the emitting electron, f_p being the plasma frequency. If not, synchrotron emission may be reduced greatly (References 14 and 15).

9.2.4 Effects of a Change in the Magnetic Field

The curves of Figure 9-5 are shown for fixed values of Ψ, α, and B ($\Psi = 0$, $\alpha = 90$ degrees, and B = 0.4 gauss). From Equation 9-10, B is seen to enter into both the coefficient and the argument so that a change in B affects both the ordinate and abscissa of Figure 9-4. Hence, the curves of Figure 9-5 may be used for values of B other than 0.4 gauss by shifting the curves horizontally and then vertically. For example, a 25 percent reduction in B would shift a curve to the left and downward so that a new peak emission is 25 percent of the original peak and occurs at a frequency that is 25 percent of the previous frequency of peak emission. In the case of the 10-MeV curve, the new value of B would be 10^{-1} gauss, the new value of peak emission about 3.2×10^{-23} ergs sec^{-1} $ster^{-1}$ Hz^{-1}, and the new frequency of peak emission about 150 megahertz. A transparent overlay made by the reader would help accomplish the curve-sliding process.

9.2.5 Effect of the Angle Ψ

The determination of the effect of viewing the emission away from the orbital plane ($\Psi \neq 0$) is somewhat more difficult, as can be seen

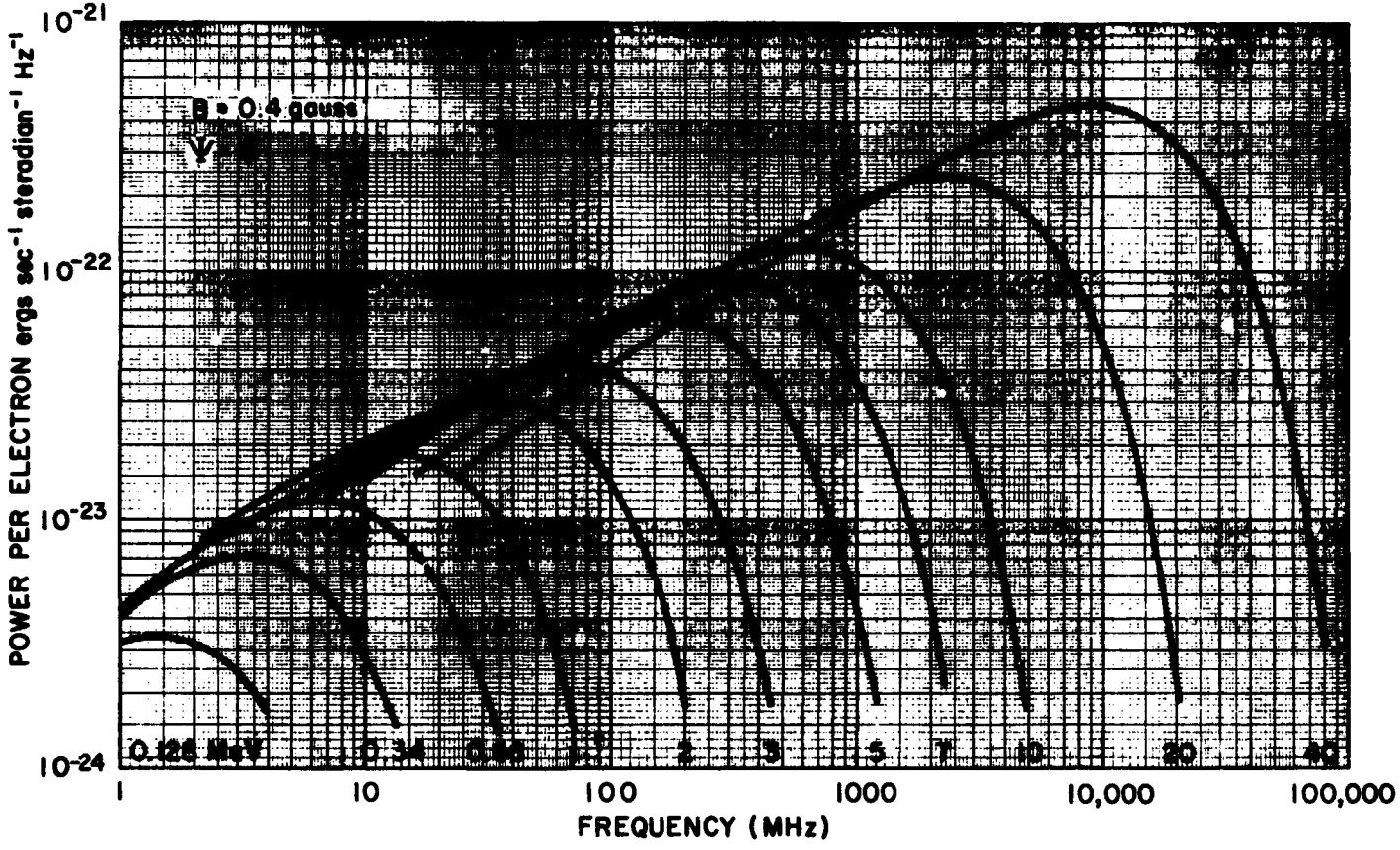

Figure 9-5. Power (per hertz per ster) radiated in the orbital plane ($\Psi = 0$) by electrons in circular motion ($\alpha = 90$ degrees) with energies of 128 KeV to 40 MeV.

by examining Equation 9-8. In this case, the total emission must be computed as the sum of two terms whose relative magnitudes are dependent on Ψ. For computational purposes, defining the quantity:

$$Z \equiv \frac{1}{1 - \beta^2 + \Psi^2} = \frac{\gamma^2}{1 + \gamma^2 \Psi^2}$$

and rewriting Equation 9-7 or Equation 9-8 in this form:

$$P(\nu, T, B, \Psi) = 4.1 \times 10^{-23} \frac{BZ^2}{\beta\gamma} \left(\frac{n}{3Z^3}\right)^2 K^2_{2/3}\left(\frac{n}{3Z^3}\right)$$

$$+ 4.1 \times 10^{-23} \frac{BZ^4\Psi^2}{\beta\gamma} \left(\frac{n}{3Z^3}\right)^2 K^2_{1/3}\left(\frac{n}{3Z^3}\right) \qquad (9\text{-}11)$$

is helpful. To study the variation of $P(\Psi)$, let

$$W_\Psi = \frac{\text{Emission at frequency } \nu \text{ in direction } \Psi}{\text{Emission at frequency } \nu \text{ in direction } \Psi = 0} .$$

A plot of this quantity as a function of Ψ then represents the desired pattern. From Equation 9-7, obtain

$$W_\Psi = (1 + \Psi^2\gamma^2)^2 \left[\frac{K^2_{2/3}\left(\frac{n}{3Z^3}\right)}{K^2_{2/3}\left(\frac{n}{3\gamma^3}\right)} + (\Psi Z)^2 \frac{K^2_{1/3}\left(\frac{n}{3Z^3}\right)}{K^2_{2/3}\left(\frac{n}{3\gamma^3}\right)} \right] . \qquad (9\text{-}12)$$

Some examples of the patterns obtained from Equation 9-12 are given in Figure 9-6. Figure 9-6a shows the patterns at three different frequencies for a 10-MeV electron. Figure 9-6b shows the 30-megahertz emission patterns for three different electron energies. These sketches indicate that the emission at a particular frequency actually may increase away from the orbital plane. However, it quickly reaches a maximum and thereafter falls rapidly with further increases of Ψ. For the lower energies, this effect disappears and the beam patterns are approximately gaussian in shape, i.e., proportional to $\exp(-\Psi^2/\text{constant})$.

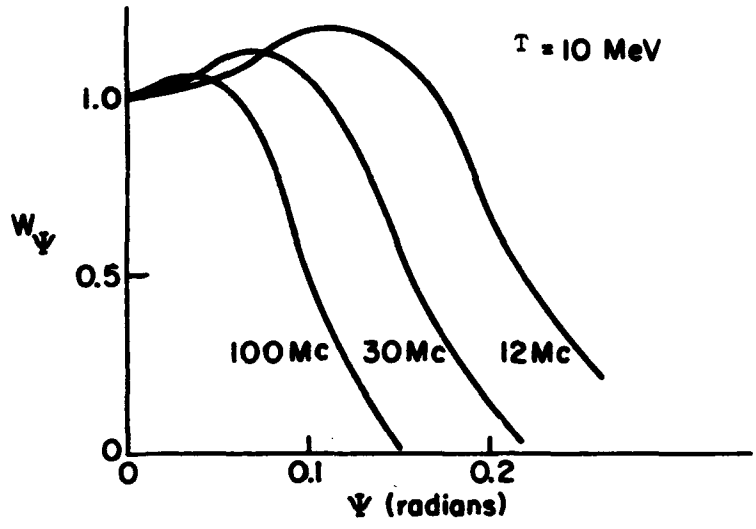

(a) Emission Pattern at Several different Frequencies

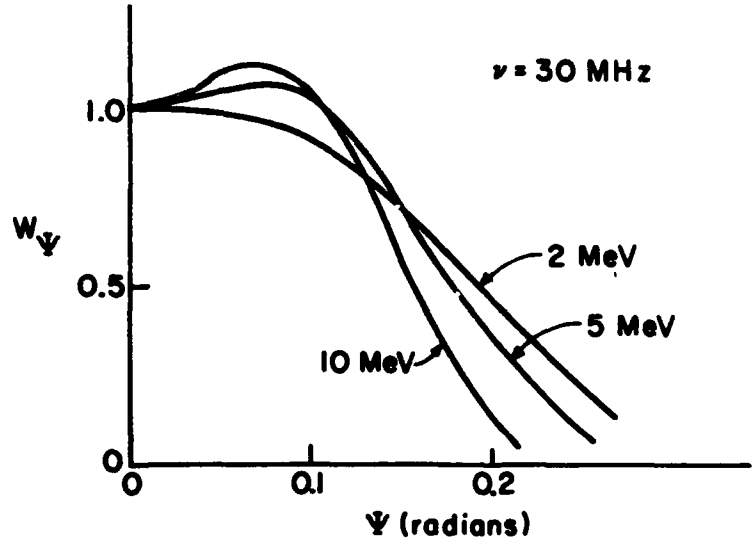

(b) Emission Pattern at Several Different Energies

Figure 9-6. Examples of the variation of $W_\Psi(\Psi)$ with electron energy and the observed frequency.

Additional information of a more general nature may be obtained by plotting W_Ψ as a function of $n/3Z^3$ for various values of $n/3\gamma^3$. Some examples of these curves are shown in Figure 9-7a. For $n/3\gamma^3 < 0.1$ and $n/3Z^3 > 0.5$, the curves are essentially the same. The value of W_Ψ is reduced to 0.5, in this case at approximately $n/3Z^3 = 0.82$. When $n/3\gamma^3 < 0.1$, this condition leads to the following expression for the angle (radians) at which the power falls by 0.5:

$$\Psi_{1/2}^2 \approx 3.6 \times 10^4 \left(\frac{B}{\nu\gamma}\right)^{2/3} - \frac{1}{\gamma^2} \quad . \tag{9-13}$$

The emission beamwidths thus decrease with increasing energy in this range.

In Figure 9-7b, the value of the quantity $\gamma^2\Psi^2$ at which W_Ψ becomes equal to 0.5 is plotted as a function of $n/3\gamma^3$ (solid line). The dotted line is a plot of the expression $\gamma^2\Psi^2 = 0.3(n/3\gamma^3)$, which is a good representation of the desired curve in the range $n/3\gamma^3 > 0.1$. Therefore,

$$\gamma^2\Psi_{1/2}^2 \approx \frac{0.3}{n/3\gamma^3} = \frac{0.3\gamma^2 B}{1.2 \times 10^{-7}\nu}$$

and the synchrotron beamwidth (radians) for $n/3\gamma^3 > 0.1$ is

$$\Psi_{1/2} \approx 1.6 \times 10^3 \sqrt{B/\nu} \quad . \tag{9-14}$$

Equation 9-14 shows that the beamwidth of emission is essentially independent of energy in this range of $n/3\gamma^3$. For the case of VHF emission from electrons in the earth's magnetic field, this would be the generally applicable equation. This situation occurs because the density of particles falls off rapidly with increasing energy in this range, so that the dominant contribution to the received signal comes from the energy range characterized by values of $n/3\gamma^3$ between 0.1 and 3.

9.2.6 Effect of the Pitch Angle α

The emission from an electron in uniform circular motion that would occur in the case where the electron's velocity is at right

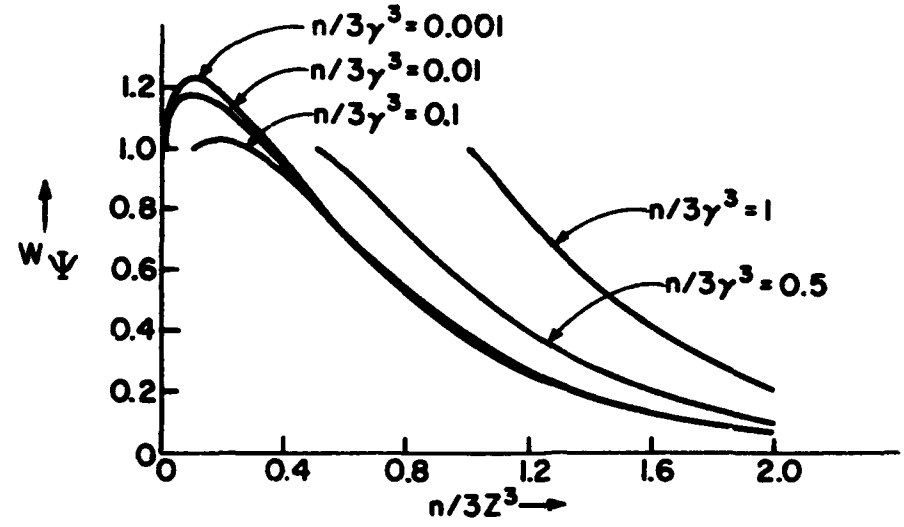

(a) W_Ψ vs $n/3Z^3$ for Various Values of $n/3\gamma^3$

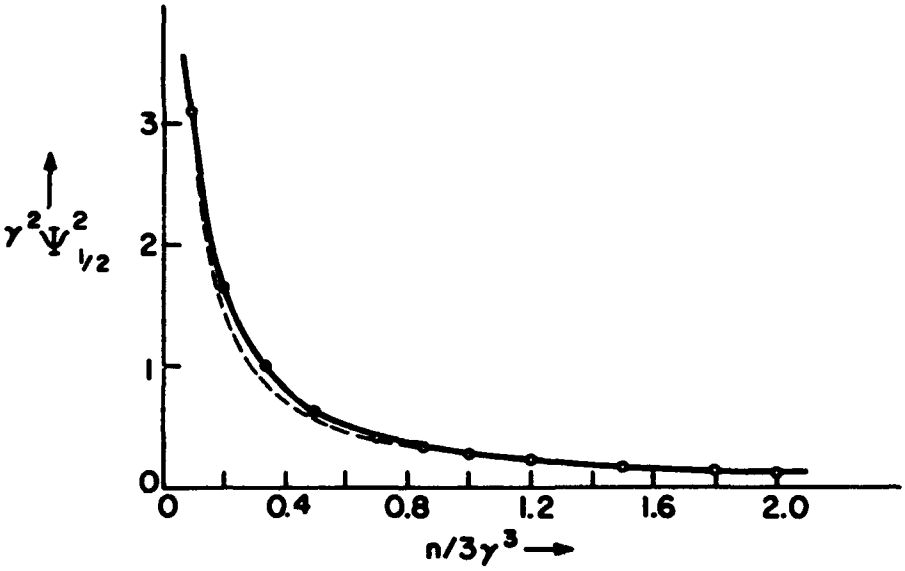

(b) $\gamma^2\Psi^2_{1/2}$ vs $n/3\gamma^3$ for $W_\Psi = 0.5$

Figure 9-7. Examples of the variation of the beamwidth (with respect to Ψ) of the radiation from a high-energy electron.

angles to a uniform magnetic field has been considered. In the case of an electron trapped in the earth's magnetic field, the particle spirals around a magnetic field line, oscillating back and forth along a field line between the mirror points in opposite hemispheres.

Radiation from these high-energy electrons moving in helical paths again is confined essentially within a cone-of-apex angle m_0c^2/E whose axis lies along the instantaneous direction of motion. The emission from such an electron is thus no longer a maximum at right angles to the field but in a direction making an angle α with the field. Reference 3 considers radiation from a high-energy ($\gamma^2 >> 1$) electron moving in an arbitrary path. The result obtained is identical with Equation 9-8, if R is interpreted as the instantaneous radius of curvature of the path, and Ψ as the angle between the direction of emission and the instantaneous orbital plane. The frequency spectra for an electron moving at an angle α with the field thus may be obtained by replacing the R in Equation 9-8 by $R/\sin\alpha$ [Reference 7: note that in Equation 2, the term $(1 + k^2)$ should read $(1 + k^2)^2$]. For this situation, Equation 9-10 becomes the synchrotron power for an electron in helical motion:

$$P(\nu, T, B, \alpha) = 4.1 \times 10^{-23} \frac{B\gamma \sin\alpha}{\beta} \left(\frac{1.2 \times 10^{-7}}{\sin\alpha} \frac{\nu}{B\gamma^2} \right)^2 \cdot K_{2/3}^2 \left(\frac{1.2 \times 10^{-7}}{\sin\alpha} \frac{\nu}{B\gamma^2} \right) . \quad (9\text{-}15)$$

Therefore, the normalized curve of Figure 9-3 applies if the abscissa scale is considered to represent the quantity $(1.2 \times 10^{-7}/\sin\alpha) \times (\nu/B\gamma^2)$ and the ordinate scale is considered to represent the power per electron multiplied by $\beta/(B\gamma \sin\alpha)$. After sketching the spectrum of a given particle for a particular α, the spectrum for other values of α may be obtained by the technique of sliding the curve. For example, if the spectrum for $\alpha = 90$ degrees is given and the spectrum for $\alpha = 45$ degrees is desired, the given curve must be shifted downward and to the left so that the peak emission is reduced to $\sin\alpha = 0.707$ of its former value and the peak occurs at a frequency that is 0.707 times the former frequency of peak emission.

The effect of the angle α on the spectrum of a 10-MeV electron is shown in Figure 9-8. Each curve is for emission in the direction $\Psi = 0$, which now corresponds to the direction making an angle α

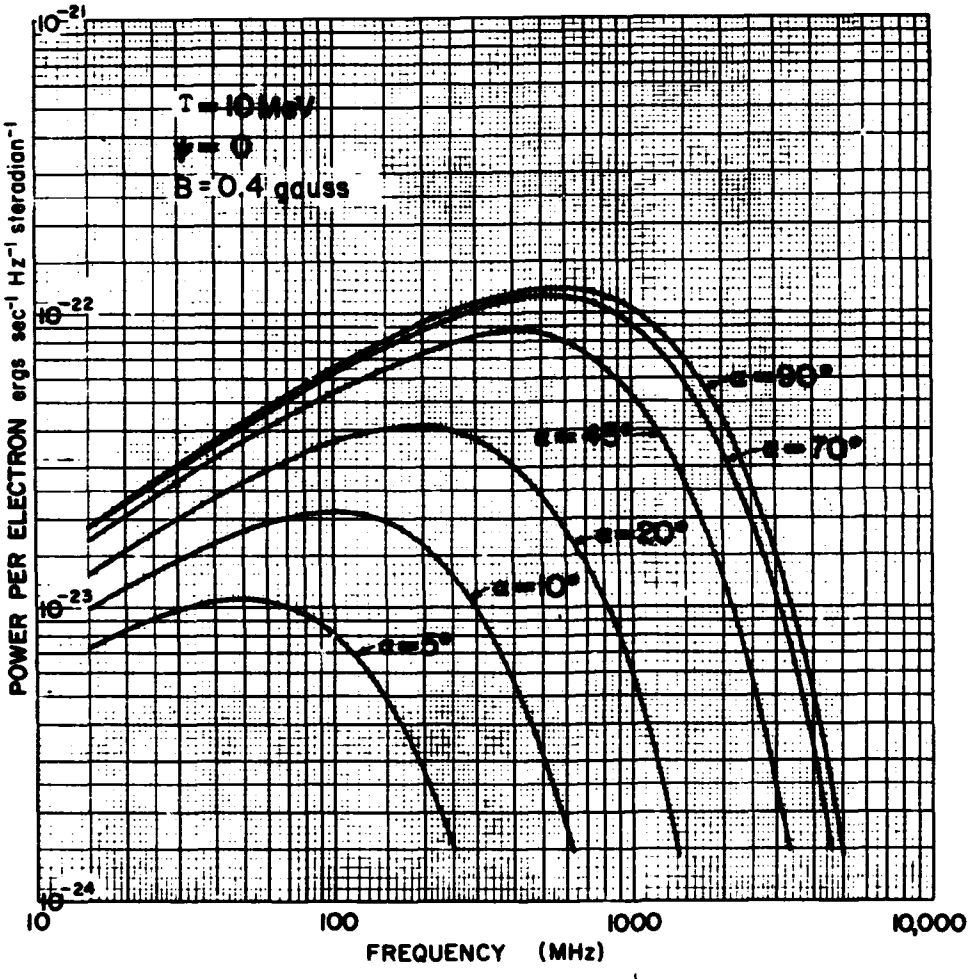

Figure 9-8. Effect of changes in the pitch angle α on the spectrum of a 10-MeV electron.

with the magnetic field. The variations with Ψ in each case would be just those considered in Section 9.2.5. Two important points are that as α departs from 90 degrees the high-frequency portion of the spectrum for a particular particle drops off much faster than the low-frequency portion and the emission spectra are essentially unchanged for α within 20 degrees of α = 90 degrees.

Some confusion has existed recently on the subject of synchrotron radiation from electrons in helical motion. It centers on the question of frames of reference, i.e., whether the observer's or electron's point of view is taken. The question is discussed in considerable detail by Ginzburg and Syrovatskii (Reference 16) and a particularly lucid discussion is given by Scheuer (Reference 17). In any case, the result is that the formulas given previously are correct and applicable to the situation considered without modification.

9.2.7 Emission from an Ensemble of Electrons Having a Variety of Pitch Angles and Energies

The objective of this calculation is to find the power available at the antenna due to the synchrotron source. If the source can be assumed to be relatively constant over the beam solid angle Ω of the antenna, the power available at the antenna terminals in a bandwidth $\Delta\nu$ can be written as $(1/2)\, SA_{[eff]}\Delta\nu$, where S is the radiation flux (ergs sec^{-1} cm^{-2}) and $A_{[eff]}$ is the effective antenna area. The 1/2 implies an unpolarized source, whereas a synchrotron source is actually partially polarized. Now the flux $S = b\Omega$ where the quantity b, known as the brightness, is a characteristic of the source alone; b will be calculated in the following examples. The quantity b is obtained by integrating the emission coefficient along the ray path from the source to the antenna. Of course, only portions of the ray path within the emitting region will be of importance. In general, b measured in ergs sec^{-1} cm^{-2} $ster^{-1}$ Hz^{-1} is given by:

$$b(\nu) = \oint_{path} q(x,\nu)dx \qquad (9\text{-}16)$$

where the emission coefficient q is the power radiated from a unit volume of the emitting region measured in ergs sec^{-1} cm^{-3} Hz^{-1} $ster^{-1}$ and x is the distance along the ray path. The quantity q is given by:

$$\epsilon(x,\nu) = \iint P[T, B(x), \nu, \Psi(\alpha, x), \alpha] n(\alpha, T, x)(2\pi \sin\alpha \, d\alpha)dT \qquad (9\text{-}17)$$

where $n(\alpha, T, x)$ is the number density per unit energy per unit solid angle of electrons at a point x along the ray path. The total density n_T of particles of all energies at a point x is then

$$n_T(x) = \int_0^\infty \int_0^\pi n(\alpha, T, x)dT(2\pi \sin\alpha \, d\alpha) \quad . \qquad (9\text{-}18)$$

Thus, knowing $n(\alpha, T, x)$ and the observational geometry, $b(\nu)$ can be calculated and then used to calculate P, once the parameters of the receiving system are known. Equations 9-17 and 9-18 are general and a number of simplifying assumptions can often be made, as can be seen in later examples.

It is useful to convert the brightness b into a "brightness temperature" T_b that is the temperature a black body would have if it was characterized by a brightness b at wavelength λ:

$$T_b = \frac{\lambda^2 b}{2k} \qquad (9\text{-}19)$$

where k is the Boltzmann constant.

9.3 SYNCHROTRON RADIATION FROM STARFISH ELECTRONS

An artificial component of the earth's trapped radiation belt was created by the large numbers of high-energy electrons coming from the Starfish high-altitude nuclear explosion of 9 July 1962. Omnidirectional electron flux maps were prepared by Nakada from the estimates of Brown and Gabbe (Reference 8) and Van Allen, Frank, and O'Brien (Reference 9). Figure 9-9 shows the variation of electron number density with height over the magnetic equator corresponding to the estimates of References 8 and 9, together with a curve based on an estimate by Hess (Reference 10). The estimate by Hess, curve c in Figure 9-9 was used in the computations below. However, a calculation by Peterson and Hower (Reference 6) based on the data of Reference 9, curve a in Figure 9-9, yielded results quite close to those based on Reference 10 and shown in Figure 9-11. The electrons are assumed to have a fission β-decay energy spectrum as given by Carter (References 9, 10, and 11):

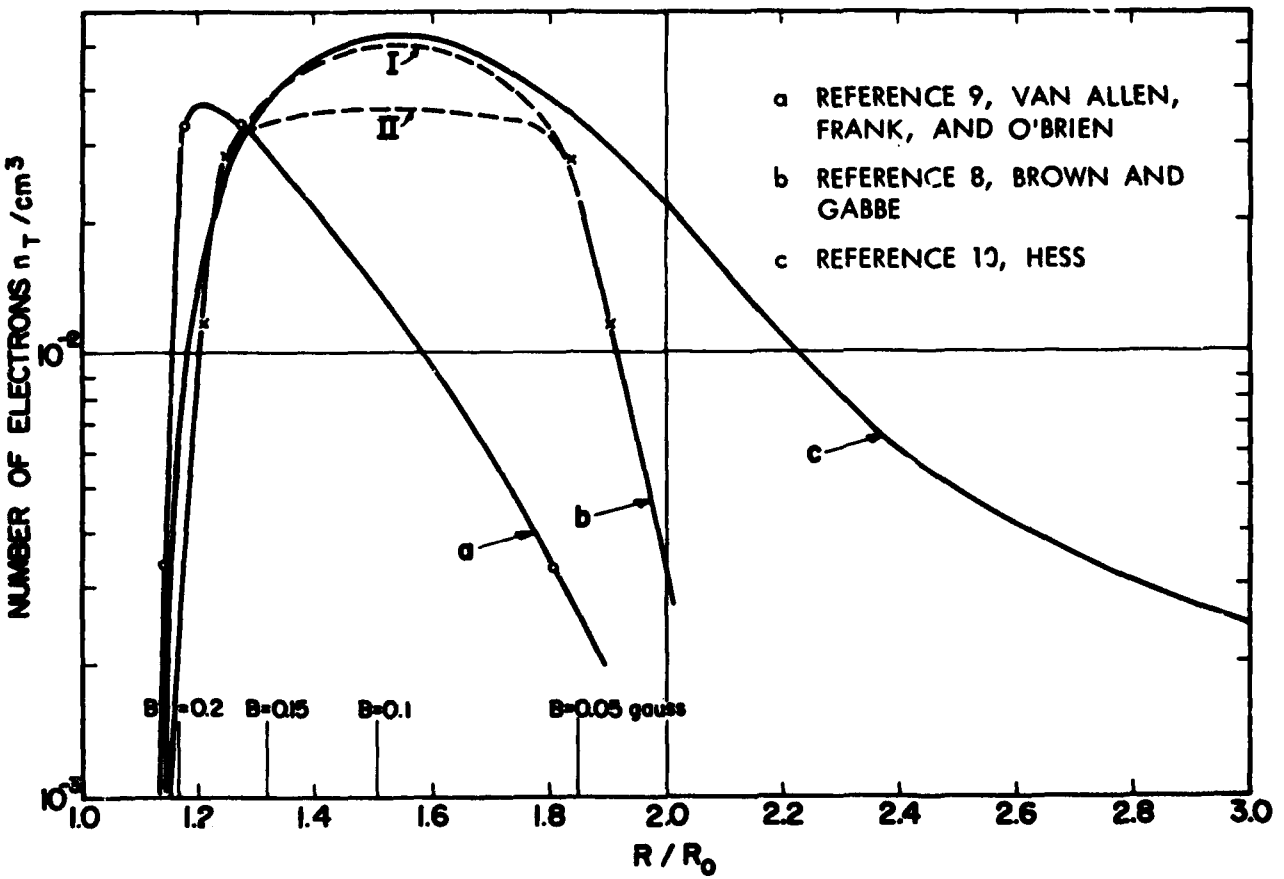

Figure 9-9. Density of electrons versus height over the magnetic equator in earth radii.

$$n(T) \approx n_T \, e^{-(0.575T + 0.55T^2)} \qquad (9\text{-}20a)$$

where T is electron energy in MeV, n_T is total number density, and n(T) is number density per unit energy (Section 11.2). All the electrons are assumed to be in circular motion, i.e., $\alpha_o = 90$ degrees. Although this assumption is not strictly correct, the electrons will tend to have α_o close to 90 degrees since electrons with pitch angles close to 0 or 180 degrees will tend to become lost by scattering in the denser portions of the atmosphere near the mirror points. Also, the emission varies little for α within 20 degrees of 90 degrees (Section 9.2.6). The quantity Ψ is set equal to zero for the case of observation from the geomagnetic equator.

Using Equation 9-17, one obtains

$$q(\nu, x) = \int P[T, B(x), \nu, \Psi=0, \alpha_o=90°] n_T(x) e^{-(0.575T + 0.55T^2)} dT \quad . \qquad (9\text{-}20b)$$

The integrations were performed numerically, with the value of $n_T(x)$ taken from the model of Hess (Reference 10). The results are shown in Figure 9-10. These curves were in turn integrated according to Equation 9-16 and the result used to obtain a brightness temperature according to Equation 9-19. Figure 9-11 compares the brightness temperature thus calculated with cosmic and lightning storm noise as well as experimental observations of radio noise made by looking overhead near the geomagnetic equator about three weeks after the Starfish explosion. A more detailed exposition of these calculations is given in Reference 6.

9.4 SYNCHROTRON RADIATION FROM A MODEL ELECTRON FLUX DISTRIBUTION

9.4.1 Model of the Emitting Region

The quantities that specify the emitting region are the geometrical configuration, the energy spectrum, and the pitch angle distribution. Consider a case in which saturation electron flux is in a magnetic shell bounded by $L = 4 \pm 0.53$. The thickness of the shell at 200-kilometer altitude is 500 kilometers and the thickness of the shell in the geomagnetic equatorial plane is 6,850 kilometers; for further details see Section 2. Figure 9-12 gives a rough idea of the shape

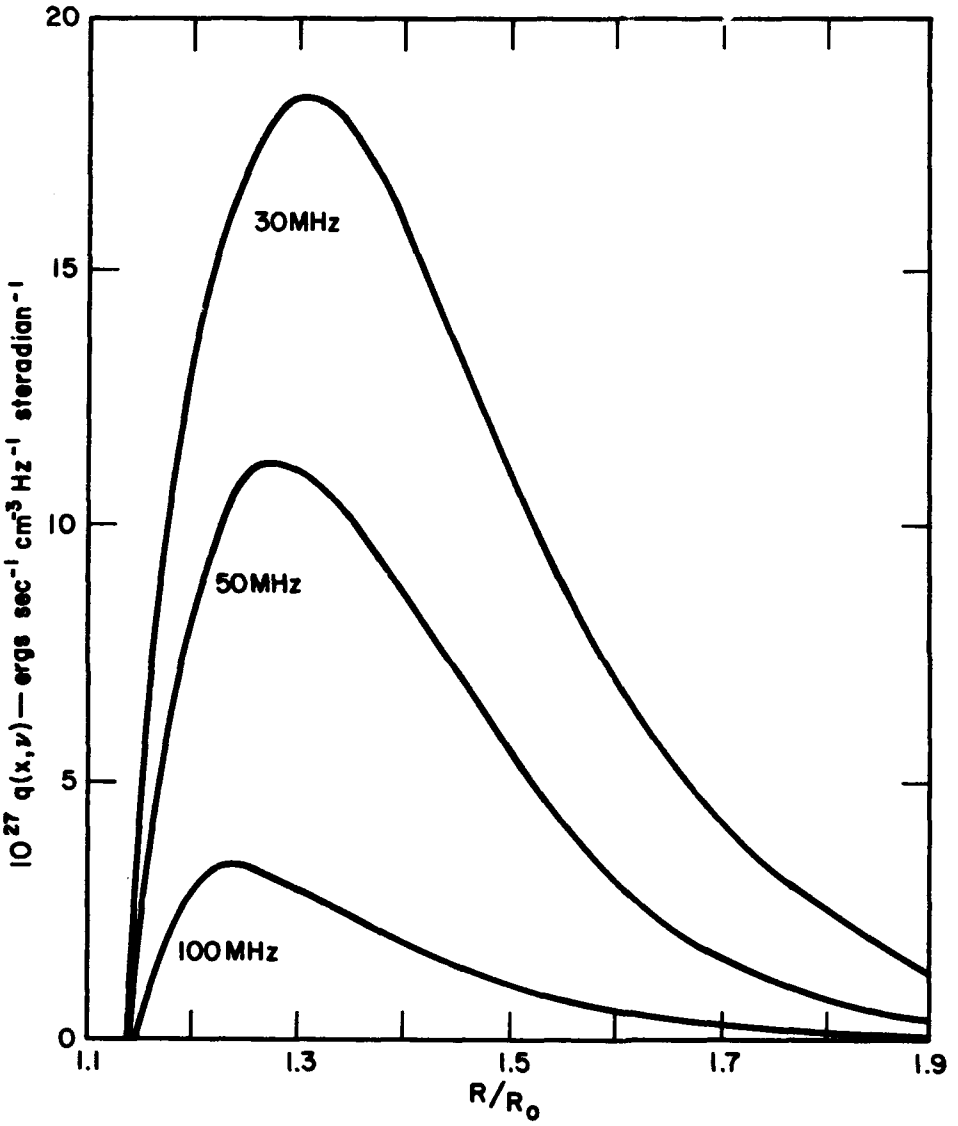

Figure 9-10. Emission coefficient $q(x,\nu)$ versus height (in earth radii) over the magnetic equator for frequencies of 30, 50, and 100 MHz.

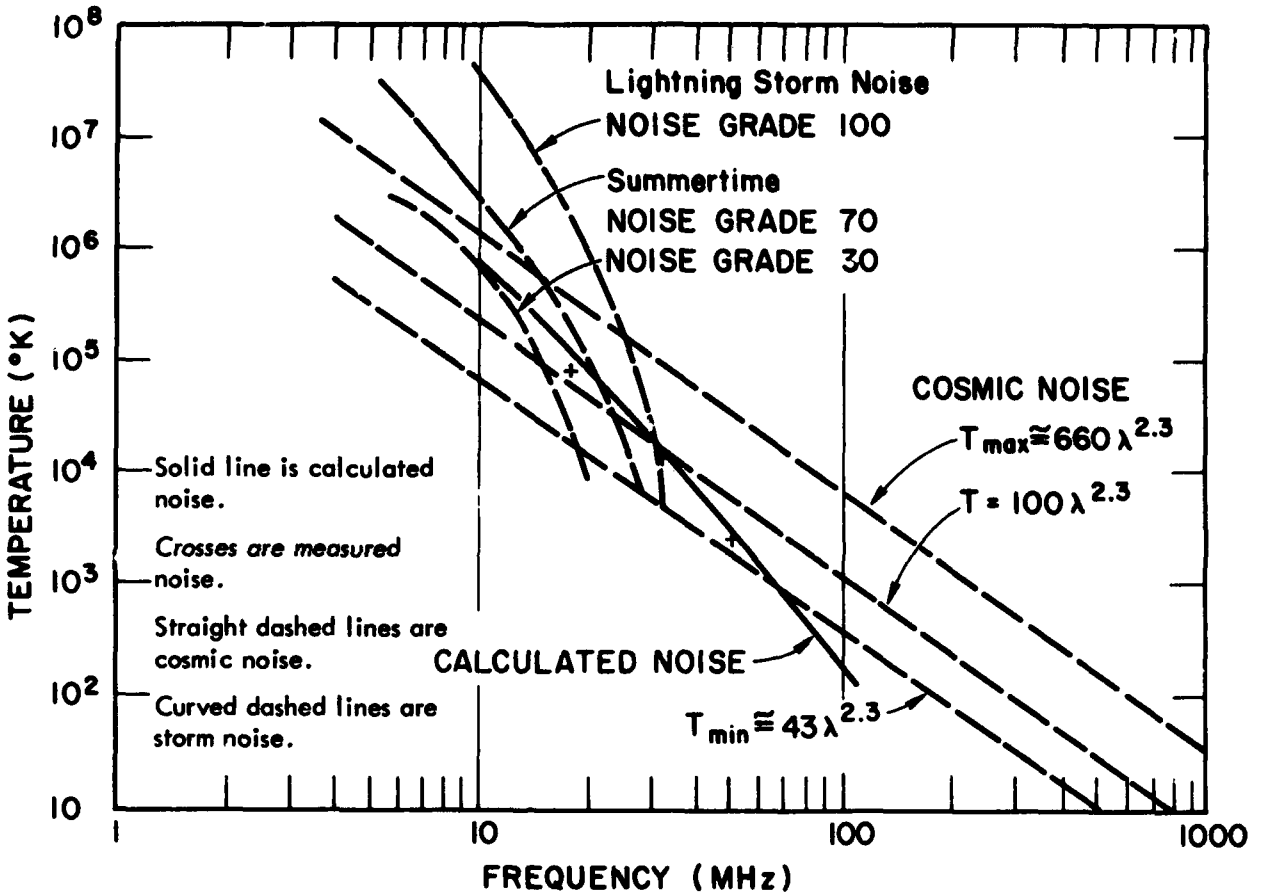

Figure 9-11. Comparison of synchrotron noise from Starfish electrons with cosmic noise and lightning storm noise. λ is in meters.

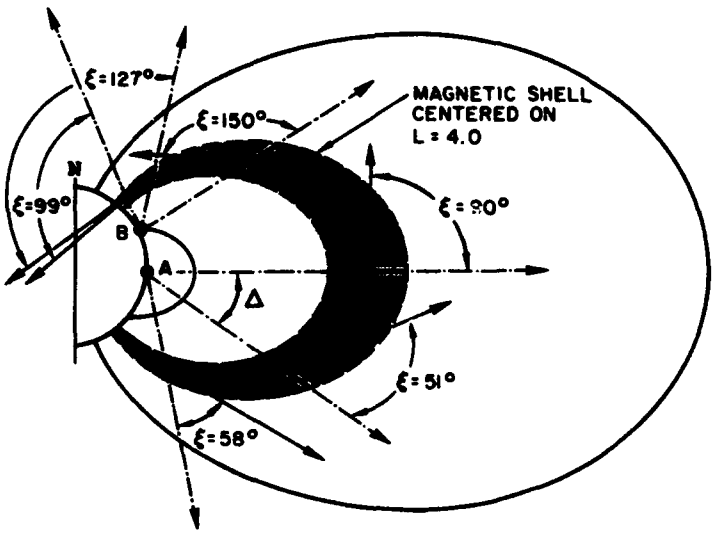

Figure 9-12. Observational geometry for an observer on the geomagnetic equator (A) and at 45-degree geomagnetic latitude (B).

of the emitting region. Straight-line ray paths from each observer are shown at angles (Δ) from the observer's zenith of 0, 45, and 80 degrees. The darker shading on the inner half of the magnetic shell indicates that the major contribution to synchrotron emission comes from this region.

A fission-β energy spectrum is assumed as in Equation 9-20. The equatorial pitch angle distribution is assumed to be proportional to $\mu_o^{-1} \sin(\pi \mu_o/\mu_c)$ in electrons cm^{-2} sec^{-1} $ster^{-1}$ where $\mu_o = \cos \alpha_o$ and $\mu_c = [1 - (0.60/L^3)]^{1/2}$. The saturation omnidirectional flux in the geomagnetic equatorial plane at L = 4 is assumed to be about 6×10^8 electrons cm^{-2} sec^{-1}, which, if $\beta \approx 1$ is assumed, implies a density of $6 \times 10^8/c \approx 2 \times 10^{-2}$ cm^{-3}. Then, on the geomagnetic equator, assuming $\beta \approx 1$

$$n(T,\alpha_o) = A \sec \alpha_o \sin(\pi \cos \alpha_o/\mu_c) \exp(-0.575T - 0.55T^2) \quad (9\text{-}21)$$

where A = saturation density divided by $4\pi(1.85) = 9 \times 10^{-4}$ and n is measured in electrons cm^{-3} MeV^{-1} $ster^{-1}$. A is obtained from Equation 9-18.

9.4.2 Calculation of the Emission Coefficient and Brightness

A straightforward calculation of the emission coefficient $q(x,\nu)$ using Equation 9-17 and $n(\alpha,T)$ given previously would be a rather lengthy process. Fortunately, some simplifying assumptions can be made. First, the range of Ψ, over which W_Ψ (Equation 9-12) is close to unity, is known to be small. Now, if $n(\alpha,T)$ is reasonably constant over a range of α comparable with $\Psi_{1/2}$, we would be justified in assuming that all the power radiated within $\Psi = 0 \pm \Psi_{1/2}$ is concentrated at $\Psi = 0$. In such a case, the product $P(\nu,T,B,\Psi,\alpha)$ $n(\alpha,T)$ would be nonzero only when the observer's line of sight makes an angle ξ with the magnetic field direction (at the emitting electron) that equals the pitch angle α of that electron, i.e., when the observer is in the instantaneous orbital plane of the electron. Then,

$$q(\nu,x) = \int P[\nu,T,B(x),\Psi=0,\alpha=\xi]\,2\Psi_{1/2}[\nu,B(x)]\,n(T,\alpha=\xi)\,dT \quad . \tag{9-22}$$

In the situation at hand, the high-energy approximations to P and $\Psi_{1/2}$ given in Equations 9-14 and 9-15 can be used. In general, the integral of Equation 9-16 must be approximated, e.g.,

$$b(\nu) \approx \sum_{i=0}^{i=m} q(\nu,x_i)\,\Delta x_i \quad . \tag{9-23}$$

9.4.3 Case of a Ground-Based Observer on the Geomagnetic Equator

Consider the case of an observer located on the geomagnetic equator (Point A in Figure 9-12). For simplicity, a centered dipole model will be used for the geomagnetic field. When the observer looks toward his zenith, the situation is relatively uncomplicated. Since $\xi = 90$ degrees, the expression for $n(T,\alpha)$ given in Equation 9-21 may be used as it stands. When the observer looks away from his zenith, $\xi \neq 90$ degrees and $n(T,\alpha)$ must be modified. It is fairly easy to find ξ using the centered dipole model for the geomagnetic field—some useful charts are given in Chapter 2 in Reference 13.

The pitch angle distribution given in Equation 9-21 applies only to the geomagnetic equator. The pitch angle-distribution at other points along an L-shell, however, is related to the equatorial distribution since the equatorial values of pitch angle (α_o) and

magnetic flux density B_0 are known for any particular electron to be related to α and B elsewhere along the field line by $\sin^2\alpha/B = \sin^2\alpha_0/B_0$. Hence, to generalize Equation 9-21 for use away from the geomagnetic equator, α_0 must be replaced by arc $\sin(\sqrt{B_0/B}\sin\alpha_0)$, B_0 and B being known from the geometry of the problem. Also, while moving away from the equator along an L-shell, the flux density increases as does the particle density. Hence, a factor (B/B_0) should be inserted into Equation 9-21, giving this expression for $n(T,\alpha,x)$:

$$n(T,\alpha,x) = 9 \times 10^{-4} (B/B_o) \sec[\arcsin(\sqrt{B_o/B}\sin\alpha)] \cdot \sin\left\{\frac{\pi}{\mu_c}\cos[\arcsin(\sqrt{B_o/B}\sin\alpha)]\right\} \cdot \exp(-0.575T - 0.55T^2) \quad . \qquad (9\text{-}24)$$

This is, of course, a very simple approximation to the true variation of n along an L-shell, but it will suffice for the case at hand.

Using Equation 9-24 and following the procedure suggested in Section 9.4.2, the emission coefficient was calculated where the ray path from the observer crosses L = 3.46, 4.00, and 4.54, i.e., where it crosses the boundaries and midpoint of the magnetic shell containing the particles. The ray paths were assumed to be straight lines lying in the plane of the observer's magnetic dipole meridian and making angles (Δ) of 0 , 45 , and 80 degrees with the observer's zenith (Figure 9-12). The values of $q(\nu,x)$ vary considerably along the line of sight as well as with zenith distance Δ , as shown in Figure 9-13. It is evident that the magnetic shell boundary nearest the observer is critical since the emission coefficient is in most cases much higher there. Hence, inward radial diffusion of particles would tend to increase synchrotron emission.

Figure 9-14 shows the brightness temperature T_b as a function of frequency for zenith distances of 0 , 45 , and 80 degrees. The calculations were made according to Equations 9-19 and 9-23. The principal feature is that the synchrotron emission is always well below the cosmic noise level and, hence, unobservable in general. However, a possibility does exist that appropriate measurements might detect the polarized component of the synchrotron emission against the randomly polarized cosmic background. An average value

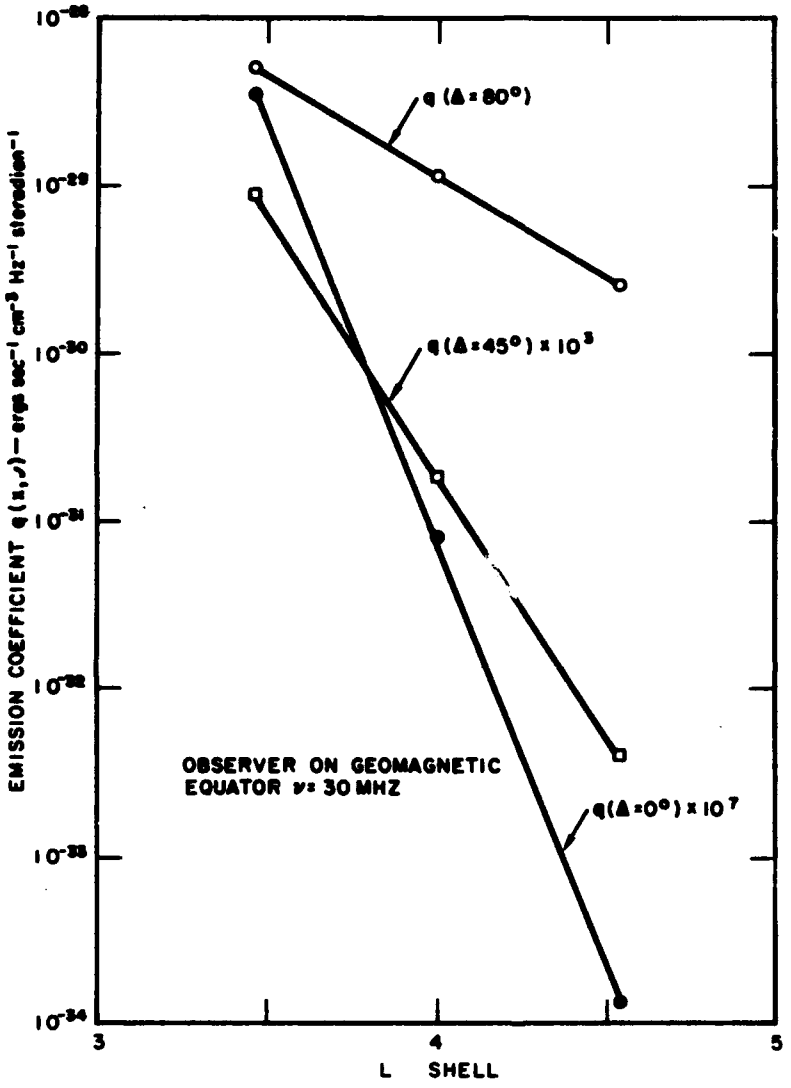

Figure 9-13. 30-MHz emission coefficient $q(x, \nu)$ as a function of the intersection of the ray path with a sequence of L-shells.

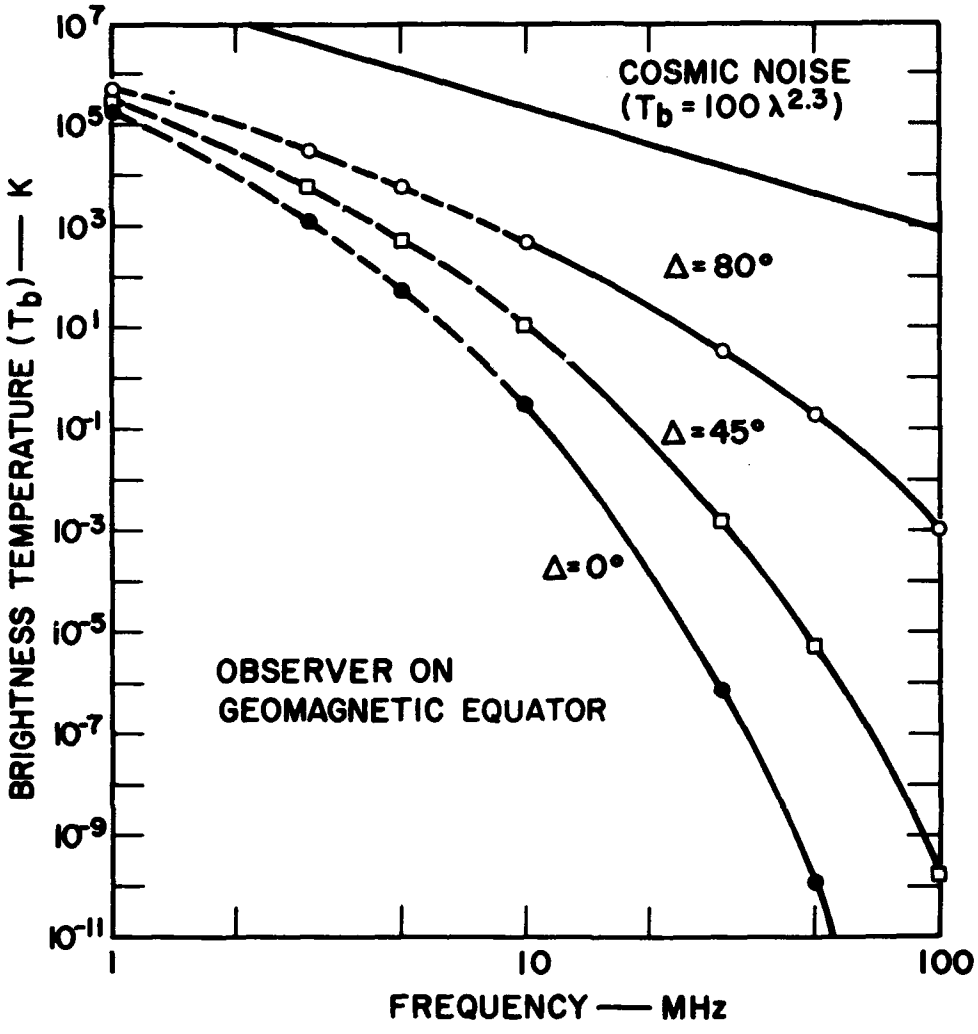

Figure 9-14. Brightness temperature T_b versus frequency for three zenith distances (Δ).

for the cosmic background noise T_b also is shown (λ in meters). At frequencies below about 30 megahertz, the values of T_b become unreliable because of refraction effects in the ionosphere. In this case, a ray tracing is necessary. In fact, for frequencies of less than about 10 megahertz, the synchrotron emission

would be unable to penetrate the ionosphere at all. However, for frequencies of about 30 megahertz and above, ionospheric effects are reduced, and these calculations should be a fairly good approximation.

9.4.4 Case of a Ground-Based Observer Located at 45-Degree Geomagnetic Latitude

Now consider an observer at 45-degree geomagnetic latitude (Point B in Figure 9-12) looking along ray paths that lie in the plane of his magnetic meridian, i.e., ray paths that lie in the plane containing the observer and the dipole axis. The procedure described in Section 9.4.3 was again used to calculate $q(x,\nu)$ at the points where the ray path crosses $L = 3.46$, 4.00, and 4.54. The results are displayed in Figure 9-15. The emission coefficient does not vary as much across the magnetic shell as in the case of an equatorial observer. This is due in large measure to the fact that the magnetic field varies less from one side of the magnetic shell to the other in the present case than in the case of the equatorial observer. Also interesting is that the emission coefficient is higher for the ray path at $\Delta = 80$ degrees than at $\Delta = 90$ degrees.

Figure 9-16 displays the brightness temperature as a function of frequency for several values of the angle Δ, which is measured northward from the observer's zenith. The values of T_b below 30 megahertz should be considered as only a rough approximation due to refraction effects in the ionosphere, and below 10 megahertz the synchrotron emission usually will fail to penetrate the ionosphere. The most striking difference between the present case and that of Section 9.4.3 is that the brightness temperature for a given value of Δ is similar at low frequencies; the value of T_b falls off much less rapidly at high frequencies in the present case. This situation occurs because the magnetic field is higher for a given value of Δ in the present case. The higher value of B causes lower energy electrons to make the main contribution to the emission coefficient (Figure 9-4) and, since the electron energy spectrum varies less rapidly at lower energies [i.e., from Equation 9-20, $dn/dT = -n_T\,(0.575 + 1.10\,T)\exp(-0.575T - 0.55T^2)$], the value of T_b varies less rapidly with frequency.

9.5 SUMMARY

By way of a suggestion, a sequence of steps summarizing a procedure by means of which the synchrotron brightness b may be calculated is listed thus:

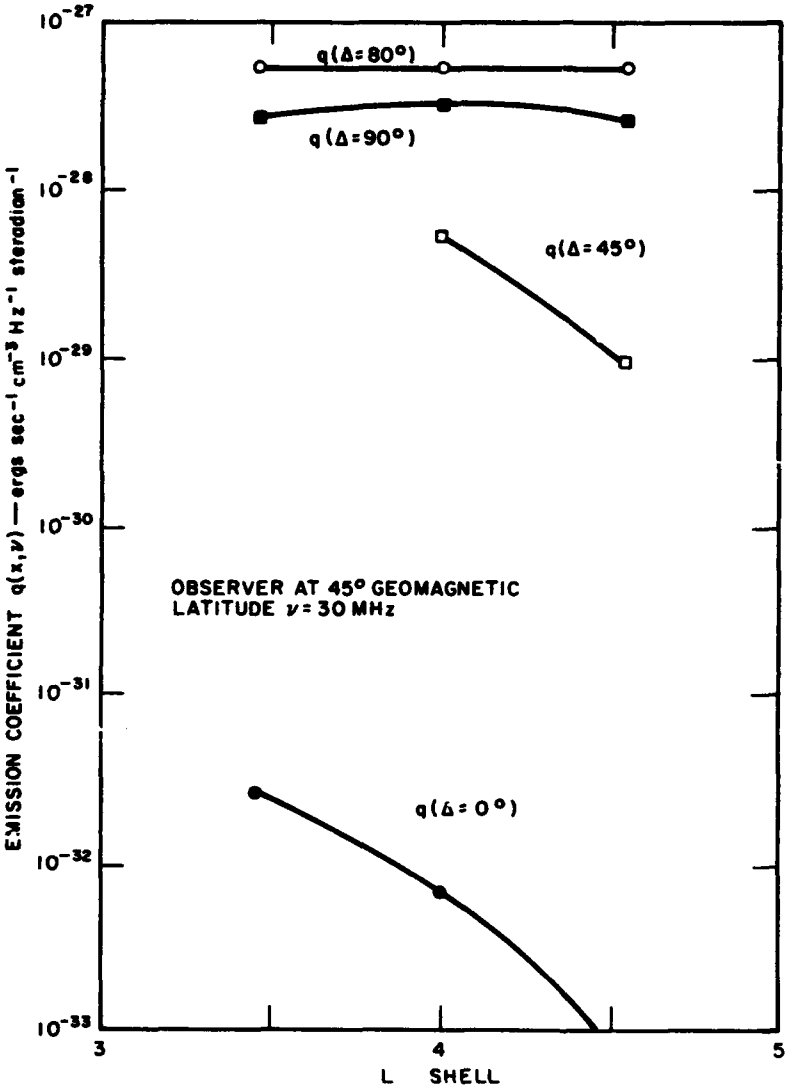

Figure 9-15. 30-MHz emission coefficient $q(x,\nu)$ as a function of the intersection of the ray path with a sequence of L-shells.

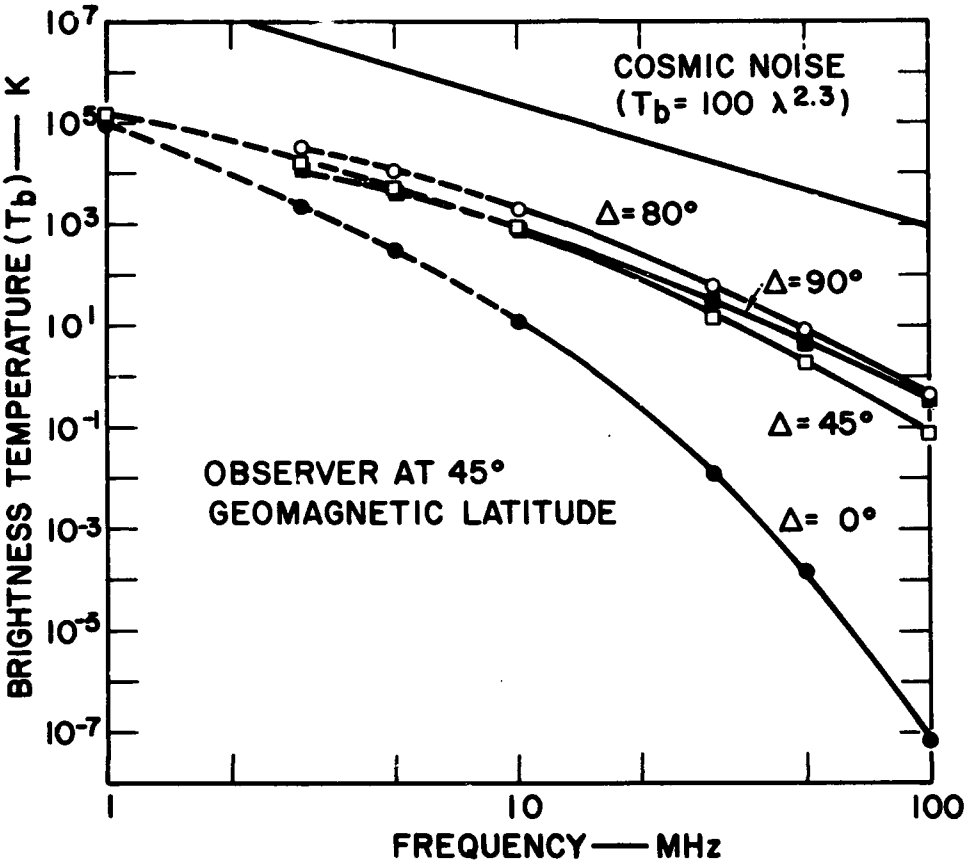

Figure 9-16. Brightness temperature T_b versus frequency for four zenith distances (Δ). λ is in meters.

1. Since the integral of Equation 9-16 is taken along the ray path, the geometry of the ray path must be known. For sufficiently high frequencies, a straight-line approximation may be used, but, for frequencies less than about 30 megahertz, a ray tracing will probably be necessary.

2. With the ray path geometry known, the electron density $n(T, \alpha)$ can be found as a function of x , the distance along the ray path, and likewise the synchrotron power per electron, $P[T, B(x), \nu, \Psi(x, \alpha), \alpha]$. Integrating the product nP over all α and T according to Equation 9-17 is a complex and time-consuming task. It is useful to consult the graphs and approximations of P given in Sections 9. 2. 3 through 9. 2. 6. A few pilot

calculations often make it evident that, to make a good estimate of the emission coefficient q, the nP product only need be calculated over a small range of T and α. In fact, eliminating the integration over α entirely may be possible, as in Section 9.4.2.

3. The final integration to obtain b from Equation 9-16 usually can be approximated by a summation over a relatively small range of x, as in Sections 9.4.2 and 9.4.3. Here again pilot calculations with the aid of the approximations and graphs of Section 9.2 often can reduce to reasonable proportions the computations needed to make a good estimate of b.

4. Once it is calculated, b must be compared with the many possible competing sources of noise, e.g., lightning, cosmic noise, and man-made signals. In making the comparison, remember that the synchrotron emission is often highly polarized and thereby may be identified.

REFERENCES

1. W. K. H. Panofsky and M. Philips. Classical Electricity and Magnetism, 2nd Edition, Addison-Wesley Publishing Company, Reading, Mass., 1962.

2. J. D. Jackson. Classical Electrodynamics, John Wiley and Sons, New York, 1962.

3. W. Priester and J. Rosenberg. Extragalactic Radio Sources, NASA TN D-2888, National Aeronautics and Space Administration, Washington, D. C., 1965.

4. J. Schwinger. "On the Classical Radiation from Accelerated Electrons," Phys. Rev., 75, 1912-1949, 1949.

5. L. Landau and E. Lifshitz. The Classical Theory of Fields, Addison-Wesley Publishing Company, Reading, Mass., 1951.

6. A. M. Peterson and G. L. Hower. "Theoretical Model of Synchrotron Radiation and Comparison with Observations," Radiation Trapped in the Earth's Magnetic Field, ed. by B. M. McCormac, D. Riedel Publishing Company, Dordrecht, Holland, 718-738, 1966.

7. R. B. Dyce and M. P. Nakada. "On the Possibility of Detecting Synchrotron Radiation from Electrons in the Van Allen Belt," J. Geophys. Res., 68, 4079, 1963.

8. W. L. Brown and J. Gabbe. "The Electron Distribution in the Earth's Radiation Belts During July 1962 as Measured by Telstar," J. Geophys. Res., 68, 607, 1963.

9. J. A. Van Allen, L. A. Frank, and B. J. O'Brien. "Satellite Observations of the Artificial Radiation Belt of July 1962," J. Geophys. Res., 68, 619, 1963.

10. W.N. Hess. "The Artificial Radiation Belt Made on July 9, 1962," J. Geophys. Res., 68, 667, 1963.

11. R.E. Carter, F. Reines, J.J. Wagner, and M.E. Wyman. "Free Antineutrino Absorption Cross Section, 2, Expected Cross Section from Measurements of Fission Fragment Electron Spectrum," Phys. Rev., 113, 280, 1959.

12. H.B. Dwight. Tables of Integrals and Other Mathematical Data, 4th Edition, MacMillan, New York, 1961.

13. R.F. Mlodnosky and R.A. Helliwell. "Graphic Data on the Earth's Main Magnetic Field in Space," J. Geophys. Res., 67, p. 2207, 1962.

14. J.F. Vesecky. "Radio Frequency Synchrotron Radiation from Electrons Trapped in the Earth's Magnetic Field," TR-3606-2, Stanford Electronics Labs., Stanford University, Stanford, Calif., 1967.

15. R. Ramaty. "Influence of Ionized Medium on Synchrotron Emission of Intermediate Energy Electron," J. Geophys. Res., 73, 3573, 1968.

16. V.L. Ginzburg and S.I. Syrovatskii. "Synchrotron Radiation and its Reabsorption," Annual Review of Astronomy and Astrophysics, 7, 1969, ed. by L. Goldberg et al, Annual Reviews, Palo Alto, Calif., 1969.

17. P.A.G. Scheuer. "Synchrotron Radiation Formulae," Ap. J. (Letters), 151, L139, March 1968.

18. M. Abramowitz, ed., and I. Stegun, ed. Handbook of Mathematical Functions, U.S. Government Printing Office, Washington, D.C., 1964.

SELECTED ADDITIONAL REFERENCES

1. G. Bekefi. Radiation Processes in Plasmas, John Wiley and Sons, New York, 1966.

2. V. L. Ginzburg and S. I. Syrovatskii. The Origin of Cosmic Rays, MacMillan, New York, 1964.

3. V. L. Ginzburg and S. I. Syrovatskii. "Cosmic Magnetobremsstrahlung (Synchrotron Radiation)," ed. by L. Goldberg et al, Annual Review of Astronomy and Astrophysics, 3, Annual Reviews, Palo Alto, Calif., 1965.

4. A. M. Peterson and G. L. Hower. "Synchrotron Radiation from High Energy Electron," J. Geophys. Res., 68, p. 723, 1963.

SECTION 10

VULNERABILITY OF OPERATIONAL SYSTEMS TO TRAPPED RADIATION

J.B. Cladis, Lockheed Palo Alto Research Laboratory
B.M. McCormac, Lockheed Palo Alto Research Laboratory

10.1 INTRODUCTION

Section 10 contains a discussion of the use of material presented in previous sections to assess the vulnerability of operational systems to energetic particles. Section 10 considers manned and unmanned satellites in the natural trapped radiation environment, unmanned satellites in beta particle environments (trapped and untrapped betas) produced by high-altitude nuclear detonations at L-values of 1.15, 2, 3, 4, and 5, and satellites in a wartime trapped electron environment. The particle environments are given in Sections 4, 6, and 7, and the synchrotron radiation, which may be of importance to some systems, is described in Section 9. Specific damaging effect in materials and devices, orbital flux integrations, bremsstrahlung, and the effectiveness of shields are described in Section 8.

10.2 SATELLITE SYSTEMS IN NATURAL ENVIRONMENT

10.2.1 Manned Systems in Natural Environment

The biological effects of radiation on man generally are related to dose in roentgen equivalent per man (rem). A rem is equal to the radiation dose in rads (100 ergs absorbed radiation per gram) times the relative biological effectiveness (RBE) of the radiation. For the particles in the radiation belts under a shield thickness of 1 gram per centimeter, which is probably the minimum thickness of a vehicle containing a man, the RBE is 1 for electrons and bremsstrahlung and about 1.4 for protons (Reference 1). The dose limits recommended by NASA for the design of earth-orbital and lunar Apollo missions are discussed in Reference 2. These limits are given in Table 10-1.

Table 10-1. Dose limits of radiation exposure.

Critical Organ	Maximum Permissible Integrated Dose (rem)	RBE (rem/rad)	Average Yearly Dose (rad)	Maximum Permissible Single Acute Emergency Exposure (rad)	Dose Point Location
Skin of Whole Body	1,600	~1.4	250	500[a]	0.07-mm depth from surface of cylinder 2 at highest dose-rate point
Blood-Forming	270	1.0	55	200	5-cm depth from surface of cylinder 2
Feet, Ankles, and Hands	4,000	1.4	550	700[b]	0.07-mm depth from surface of cylinder 3 at highest dose-rate point
Eyes	270	2[c]	27	100	3-mm depth from surface on cylinder 1 along eyeline

Notes:

[a] Based on skin erythema level.

[b] Based on skin erythema level, but these appendages are believed to be less radiosensitive.

[c] Slighly higher RBE assumed since eyes are believed more radiosensitive.

For missions in the radiation belts, the average yearly doses are used as limits. The eyes constitute the most sensitive part of the human body. If special shielding would be provided for the eyes, then the blood-forming organs would be the most critical.

The dose of natural trapped particles, which an astronaut would receive in circular orbits of various inclinations and under various shielding thicknesses, can be estimated from Figures 8-17 through 8-24. These figures give the daily doses in rads (Al) due to ionization by electrons and protons that penetrate the specified shields. In this report, a distinction will not be made between rads (Al) and rads (tissue). Note that the daily dose is small in low-altitude, low-inclination orbits and that, in these orbits, shielding is much more effective against the electrons than the protons because of the high-energy distribution of the inner-belt protons. Note also that as the orbit inclination increases, the dose rate at low altitudes increases. This increase occurs because the satellite traverses the region of the South American geomagnetic anomaly. Both the proton- and electron-dose rates increase sharply

and steadily as the altitude of the orbit increases from the "top" of the atmosphere to several thousand kilometers. At higher altitudes, the electron-dose rate under most of the specified shield thicknesses exhibits two peaks, one at about 3,000 kilometers, and the other around 15,000 kilometers, whereas the proton-dose rate has a single maximum in the range 4,000 to 5,000 kilometers. The dose rates then decrease sharply as the orbit expands toward the outer limit of the trapping region.

If the dose he receives is to be limited to 27 rads during an earth-orbit mission, the astronaut can remain in a low-inclination orbit, below 600 kilometers and under ≥ 1 gram per square centimeter Al shield, for a period approaching 1 year. In a polar-orbiting satellite at an altitude of 600 kilometers, his exposure behind the 1 gram per square centimeter shield should be limited to about 20 days. In the heart of the belt, at 4,000 kilometers under the same shield and in an equatorial orbit, the astronaut would receive the limiting dose in about 1 hour.

A realistic estimate of the deleterious effects of the radiation for a specified mission must take into consideration the transport of the radiation through the structures of the vehicle and through the astronaut himself. The bremsstrahlung dose is generally negligible in comparison with the dose due to the charged particles, as discussed in Section 8 (Figure 8-31). However, bremsstrahlung would constitute the limiting environment in regions outside the inner proton belt when the shielding is sufficient to stop essentially all the electrons. Since, in a thick target, the bremsstrahlung production is proportional to the atomic number Z of the material, the bremsstrahlung dose can be reduced by using low-Z materials at the surface of the spacecraft. Moreover, if the spacecraft goes near or beyond the outer trapping boundary, the danger due to solar flare radiation must be assessed (References 3 and 4).

10.2.2 Unmanned Systems In Natural Environment

As discussed in Section 8, solid state devices (solar cells, MOSFETs, integrated circuits) are the most sensitive elements in unmanned systems to the trapped radiation. The deleterious effects of the radiation on these devices generally are expressed as a function of the equivalent 1-MeV electron fluence. The daily fluence of the natural trapped electrons, in terms of 1-MeV equivalent electrons, is given in Figures 8-34 through 8-37 as a function of the altitude of a circular-orbit satellite for various orbit inclinations and under various shielding thicknesses. The effectiveness of the natural trapped proton flux in solid state devices is

also reduced to an equivalent 1-Mev electron flux. The daily fluence of the equivalent electrons is given in Figures 8-38 through 8-41. Note that the distributions of these daily fluences are similar to those of the daily doses discussed in Section 10.2.1.

The information given in Section 8 on the degradation of devices as a function of the fluence can be used to assess the vulnerability of a particular system in the environment given in Figures 8-34 through 8-41. It appears that most operational systems may suffer significant degradation at a fluence of about 5×10^{12} 1-MeV equivalent electrons per square centimeter. An examination of Figures 8-34 through 8-41 reveals that the proton flux constitutes the most hazardous component of the environment. If the element that limits the operation of the system is shielded by 1 gram per square centimeter of Al, the damaging fluence would be received in about 6 months by a satellite in an orbit at an altitude of 1,000 kilometers. At this altitude, the irradiation does not vary appreciably with the inclination of the orbit. Note that the most restrictive orbit would be one at the equator at an altitude of 4,000 kilometers. There a fluence of 4×10^{12} per square centimeter would be reached in about 1 day. At the synchronous altitude, the energies of the trapped particles are low (tens of KeV), and the particle fluxes are generally small but highly variable depending on solar activity and conditions in interplanetary space. In this orbit, the solar flare protons, which occasionally reach energies of hundreds of MeV, constitute an important radiation hazard.

10.3 SPACECRAFT SYSTEMS IN WEAPONS TEST ENVIRONMENT

This subsection contains a discussion of the vulnerability of a satellite system to the beta environment produced by a 1-megaton fission yield device that is detonated above the sensible atmosphere. The vulnerability will be considered for these parts of the beta environment: (1) the trapped betas at times after the flux becomes uniform in longitude, (2) the trapped betas at early times, before uniformity is achieved, and (3) the untrapped betas, which appear on field lines containing the fission fragments.

10.3.1 Effect of Long-Term Trapped Betas

Several hours after a nuclear device is detonated, the flux of the high-energy trapped betas becomes approximately uniform along the azimuthal drift direction of the electrons. At that time, the average omnidirectional flux incident on a satellite in a circular orbit is given

in Figures 8-25 through 8-29 as a function of the altitude of the orbit for various orbit inclinations and for various detonation locations. The distributions of the trapped betas, which were averaged over the orbits to obtain these results, were computed by using the jetting model of the fission-debris motion (Section 7.2.2). The distributions computed for detonations at L = 1.15 and 1.76 are in agreement, respectively, with the environments produced by Starfish and the USSR test of 28 October 1962.

Note from the curves drawn in Figures 8-25 through 8-29 for the equatorial orbits that the flux increases rapidly as the L-shell of the detonation is approached from lower L-values. It peaks at an L-value somewhat higher than that of the detonation. Then, toward higher L-values, it decreases steadily but remains finite to the outer limit of the trapping region. For detonations of devices having total yields greater than 1 megaton, the daily fluences incident on satellites can be estimated by adjusting the daily fluences given in Figures 8-25 through 8-29 by amounts proportional to the fission yields of the devices. For total yields much less than 1 megaton, this procedure would lead to large errors. The model used to determine the environment is not valid for low-yield devices.

At later times, the flux decays at a rate dependent on B, L, and T, as discussed in Section 5. After the normal decay mode is reached, the decay of the flux can be estimated from the data given in Figure 5-14. For fluxes at L-values greater than about 2.0 (this includes all the electrons injected by detonations at L > 2.0) an e-folding decay time of about 2 weeks may be used.

The radiation dose and the 1-MeV equivalent electron fluence that are received under an Al shield when a fission beta-spectrum fluence is incident on the shield can be determined from Figures 8-31 and 8-42. Figure 8-31 gives the dose in rads (Si) as a function of the thickness of the shield due to bremsstrahlung as well as penetrating electrons for an incident fluence of 1 fission beta per square centimeter. Similarly, Figure 8-42 gives the 1-MeV equivalent electron fluence as a function of the shield thickness for a unit fluence of incident betas.

As an example of the use of the figures discussed previously, assume that a component shielded by 1 gram per square centimeter of

Al may be damaged by a 1-MeV equivalent electron fluence of 5×10^{12} per square centimeter. From Figure 8-42, under this shield, the 1-MeV equivalent fluence is 2.9×10^{-2} for an incident fluence of 1 beta-spectrum electron per square centimeter. Hence, the estimated damage would occur at an incident beta fluence of $5 \times 10^{12} / 2.9 \times 10^{-2}$ or about 2×10^{14} per square centimeter. If the betas are injected by the detonation of a 1-megaton fission yield device at L = 2.0 and at an altitude of 200 kilometers or more, Figure 8-28 gives the beta fluence that would be incident on a circular-orbit satellite at the end of 1 day. This fluence would be about 10^{13} per square centimeter if the circular-orbit satellite is at an altitude of 3,000 kilometers, regardless of the inclination of the orbit. Hence, if the flux is assumed to decay exponentially with an e^{-1} time of 14 days, the limiting fluence would be reached in about 20 days.

10.3.2 Irradiation by Early Time Trapped Betas

Shortly after the detonation of a nuclear device, the trapped beta flux incident on a satellite depends sensitively on the trajectory of the satellite with respect to the magnetic meridian of the detonation and on the time after the burst. The flux of the trapped betas as a function of magnetic longitude at various times after the burst and in various L-shells is shown in Figures 7-8, 7-9, and 7-10. These fluxes are relative to a steady state flux of 1 per square centimeter as shown by the dotted line. The source width $\Delta\phi$ is the azimuthal angle between the magnetic meridional planes that contain the fully expanded magnetic bubble. For a 1-megaton fission yield explosion at L = 1.2, $\Delta\phi \approx$ 5 degrees. The distributions given in Figure 7-8 are applicable for this case. Note that a spacecraft located in the beta tube or just east of the tube at early times would be irradiated by a trapped beta flux that exceeds the steady state flux by as much as a factor of 70. Moreover, at low L-values the maximum value of the flux moves toward the east at a rate that is about the same as that of a low-altitude satellite. Hence, a satellite in a direct, equatorial orbit may remain in the enhanced-flux environment for the entire time (2 hours or so) required for the flux to become uniform in longitude. Figures 7-8, 7-9, and 7-10 may be used to estimate the beta fluence incident on the vehicle during this early time period.

10.3.3 Irradiation by Untrapped Betas

If the satellite is located on magnetic field lines containing fission fragments, the irradiation rate of the vehicle by the untrapped betas

at early times may be high. The flux of the untrapped betas can be estimated from Figure 7-6, which gives $J/n\delta h$ as a function of B/B_c for various L-values. The value of $n\delta h$, the number of betas emitted per second per square centimeter, is given by Equation 7-16 in terms of the fission yield and the area of the debris deposition. Figure 7-6 shows that the flux is high at low altitudes near the fission fragments where $B \approx B_c$ and it decreases rapidly toward higher altitudes.

As an example, assume that a 1-megaton fission yield device is detonated above the atmosphere at $L = 2.2$ at the center of the South American anomaly. From Figure 2D-4, the magnetic field intensity at the highly absorptive level of the atmosphere (100 kilometers) B_c is about 0.47 gauss. At the equator, B has the value 0.030 gauss (Figure 2-13). Hence, $B/B_c = 0.064$ and, from Figure 7-6, $J/n\delta h \approx 0.08$. If the fission fragments are deposited uniformly over a circular area with a diameter of 600 kilometers, Equation 7-16 gives $n\delta h \approx 5 \times 10^9$ electrons per square centimeter per second at $t = 10$ seconds. Thus, at the magnetic equator, the untrapped flux intensity would be about 4×10^8 per square centimeter per second. Nearer the fission fragments, at $B/B_c = 0.8$, the flux would be about 7×10^9 per square centimeter per second at that time. An integration of this flux over the time required for the satellite to traverse the tube, using the time dependence of the flux given in Equation 7-16, yields the fluence due to these untrapped betas. Of course, if it is near the beta tube at the time of the burst, the satellite also may become strongly irradiated by other emissions (X rays, neutrons, gamma rays) that are not considered in this handbook.

10.4 SPACECRAFT SYSTEMS IN WARTIME ENVIRONMENT

In the event of a nuclear war, many nuclear devices presumably would be detonated over a wide range of L within a short interval of time. Initially, the distribution of the trapped betas injected by multiple detonations would consist approximately of a linear combination of the distribution produced by a single detonation. Of course, this situation is not expected to exist indefinitely. As demonstrated in laboratory experiments, plasma instabilities develop as the energy density of trapped particles normal to the field lines approaches the energy density of the magnetic field. These instabilities redistribute the particles and limit the flux that is contained by the field.

The maximum flux that would result from multiple detonations has been estimated by using the model discussed in Section 7.2.2. The distribution of the flux is shown in Figure 7-1. The daily fluence incident on satellites in circular orbits, obtained by integrating this

beta flux along the orbits, is shown in Figure 8-30. Note that the daily irradiation in this environment is more than 3 orders of magnitude greater than it is in the beta environment produced by a single 1-megaton fission yield burst at L = 1.15. The effects of the betas on system components can be estimated by using Figures 8-31 and 8-42 as discussed in Section 10.3.1.

REFERENCES

1. S. Russak and K. Richardson. "Proton Flux, Dosage, and Damage Estimates in the Van Allen Belt," Second Symposium on Protection Against Radiations in Space, NASA SP-71, ed. by A. Reetz, Jr., Scientific and Technical Information Division, National Aeronautics and Space Administration, Washington, D.C., 1965.

2. J. Billingham. "Status Report on the Space Radiation Effects on the Apollo Mission," Second Symposium on Protection Against Radiations in Space, NASA SP-71, ed. by A. Reetz, Jr., Scientific and Technical Information Division, National Aeronautics and Space Administration, Washington, D.C., 1965.

3. A. Reetz, Jr., and K. O'Brien. Protection Against Space Radiations, NASA-SP-169, Scientific and Technical Information Division, National Aeronautics and Space Administration, Washington, D.C., 1968.

4. A. Reetz, Jr. Second Symposium on Protection Against Radiations in Space, NASA-SP-71, Scientific and Technical Information Division, National Aeronautics and Space Administration, Washington, D.C., 1968.

SECTION 11

SUPPLEMENTARY TOPICS

G.H. Nakano, Lockheed Palo Alto Research Laboratory
G.H. Humphrey, Lockheed Palo Alto Research Laboratory
A.D. Anderson, Lockheed Palo Alto Research Laboratory
L.L. Newkirk, Lockheed Palo Alto Research Laboratory
F.H. Sage, III, General Electric Company—TEMPO

11.1 TECHNIQUES OF RADIATION MEASUREMENT

11.1.1 Introduction

Radiation belt detectors might be classified into the broad categories of omnidirectional and unidirectional types. Omnidirectional measurements are independent of vehicle attitude to the degree that the geometry approaches 4π ster and provides a particularly simple and immediately useful answer concerning overall intensities of trapped particles. Omnidirectional response is achieved by 2π detectors where the radiation can be assumed to be symmetric as in the electron flux and low-energy proton flux.

If complete coverage in B as well as L is to be achieved to make an adequate flux map, omnidirectional measurements would require sampling of the corresponding positions in space. On the other hand, with directional counters, a complete flux mapping can be obtained from measurements only at the magnetic equator of the L-shells of interest. The distributions along the field lines can be inferred from the equatorial pitch angle distributions. Directional response in detectors usually is accomplished by one or a combination of these methods: (1) passive collimation, (2) active anticoincidence shield, (3) telescopic coincidence array of two or more detectors, or (4) visual observation of the particle track.

11.1.2 Detection Devices

GEIGER COUNTERS. Although rather simple in design and concept, Geiger counter experiments provided the bulk of the early mappings of particles trapped in the earth's magnetic field (References 1 and 2). Even at the time of the Starfish detonation, more than 4 years later, the most useful early time measurements were obtained with a heavily shielded Geiger counter (Reference 3). Although they have provided a wealth of information, such detectors suffer from very serious limitations in regard to identification of particle type

or measurements of energy spectra. The voltage pulse is developed by a self-quenching avalanche discharge initiated by ionizing radiation of any type passing within the confine of the Geiger tube.

SCINTILLATION COUNTERS. Besides Geiger counters, the types of detection elements that have been used most commonly are scintillator-photomultiplier combinations and solid state detectors. Since they had been used widely at the time of discovery of the radiation belts, scintillators found almost immediate application in space measurements. In the general operation of a scintillation counter, the scintillator is viewed by one or more photomultiplier tubes. Whenever a charged particle passes through the scintillator, light is emitted in proportion to the energy loss by the particle in the phosphor, and this light is converted into an electrical signal at the photocathode of the photomultiplier. The photomultiplier in turn amplifies the signal, generally providing a relatively large output signal that in turn may be amplified and/or further processed by on-board electronics. Although photomultipliers are relatively complex instruments, techniques are available to mount them in such a fashion as to avoid difficulties associated with the mechanical shocks occurring at vehicle takeoff. Furthermore, rugged, high-voltage supplies have been built with fairly low power requirements (Reference 4).

In perhaps their simplest application, scintillators have been used in shielded threshold counters in either a unidirectional or an omnidirectional fashion in a manner equivalent to that used with Geiger counters. In such applications, the major advantage involves the identification of particle type (Reference 5) and/or good discrimination against backgrounds on the basis of pulse height. However, if instead of merely requiring that all accepted pulses be above a given threshold, the amplitudes are measured with a digital pulse-height analyzer, then detailed spectral information can be obtained (References 6 and 7).

By using more than one scintillator, more accurate directional information can be obtained as well as better background rejection and particle identification. To reduce the bulkiness of such systems, viewing two scintillators in an independent manner with only one photomultiplier has been possible in some instances. In such a scheme, known as a phoswich, signals from the two scintillators are analyzed separately on the basis of their time decay constant (Reference 8).

SOLID STATE DETECTORS. Solid state detectors, which have been somewhat slower to come into general use, have several advantages over scintillators. The units are generally much smaller

and lighter than scintillator-photomultiplier combinations and are thereby very useful in many space applications. For example, a compact electron magnetic spectrometer using solid state sensing elements has been used in several satellites (References 9 and 10). Solid state detectors also have been used as the sensing element of small omnidirectional counters (Reference 11) as well as unidirectional counters, both in collimated and telescopic arrangements (Reference 12).

Solid state detectors operate as solid ionization chambers in which the average energy required to form an electron hole pair is 3.6 eV as compared to about 32 to 34 eV for gaseous ionization chambers. For energy analysis, the inherent pulse-height resolution is much better than that provided by scintillation counters. On the other hand, the signals from solid state detectors are generally much smaller than the outputs of photomultipliers, thereby placing a greater burden upon the electronics, with an associated greater hazard from noise or pickup. In addition, solid state detectors are more subject to radiation damage that, in some satellite experiments, has proved to be a serious difficulty.

NUCLEAR EMULSIONS. Nuclear emulsions are a type of highly sensitive photographic film that upon development renders visible under microscopic examination tracks of charged particles passing through the film. The track of this particle is a signature for its identity, energy, and angular distribution. The particle energy is deduced from its range and/or its specific ionization. The existence of high-energy trapped protons in the inner radiation belt was discovered (Reference 13) with the use of nuclear emulsions flown on a recoverable Atlas pod.

In regard to identification of particle type and the measurement of energy spectra, emulsions constitute an excellent detector. On an oriented vehicle, detailed directional information can be obtained, as demonstrated in a series of more than 30 satellite flights (References 14 and 15). On the other hand, because they are time-integrating devices and must be recovered, their general usefulness in regard to radiation belt studies has been quite limited. However, with the aid of on-board mechanical motion, energy spectrum measurements as a function of spatial position (Reference 16) have been obtained.

MISCELLANEOUS DETECTORS. Considering their importance in selected energy regions, the Faraday cup, the channel multiplier,

and the Cerenkov detector are listed in a miscellaneous group. The Faraday cup is simply a current collector that can be made energy selective by the application of retarding potentials (Reference 17). The channel multiplier is a relatively new device, a continuous film-electron multiplier, that presently is being used to detect low-energy auroral particles (References 18 and 19). The Cerenkov detector is a high-energy, charged-particle detector that registers light quanta emitted whenever the velocity of the particle exceeds the velocity of light in a given medium. A few Cerenkov detectors have been flown in space experiments (Reference 20).

11.1.3 Table of Detector Types

Many different versions of these types of detectors have been employed in the study of energetic particles trapped in the earth's magnetosphere. These detectors are summarized in Table 11-1 on the basis of detector type and in terms of the physical parameters measured. The listed references are not intended to be exhaustive nor complete, but rather a representation of the types of detectors used by various experimenters in the field. Emphasis has been placed on instruments designed to study energetic-particle constituents of the radiation belts from both natural and artificial sources.

11.2 FISSION PHYSICS

Section 11.2 summarizes certain aspects of nuclear fission that pertain to the sources of trapped radiation. The fission process normally produces two fragments of roughly equal mass that have acquired large amounts of kinetic energy. Several neutrons and photons also are ejected in each fission event.

The mass distribution of the fission fragments resulting from fission induced in U-235, U-238, and Pu-239 by thermal neutrons is shown in Figure 11-1. The peaks of the distribution are nearly unchanged with energy whereas the valley between the peaks is sensitive to neutron energy. The average total kinetic energy of the two fission fragments is 166 ± 2 MeV for U-235, 166 ± 3 MeV for U-238, and 172 ± 2 MeV for Pu-239 (Reference 1). Obukhov and Perfilov (Reference 2) recently have reviewed this subject and found that the average kinetic energy is given by $T = 17.5 + 0.1092Z^2/A^{1/3}$ MeV, where Z and A are the atomic number and atomic weight, respectively. They also discuss the variation of average kinetic energy

Table 11-1. Summary of radiation belt detectors.

DETECTOR	DIRECTIONALITY	SELECTION	PARTICLE TYPE	REF.	COMMENTS
Geiger - Muller	Omnidirectional	shield-threshold	e^-,γ,p	1-3 21-24	G. M. tubes were used extensively in the early exploration of the radiation belts. This detector is highly reliable but cannot distinguish particle types without additional discrimination, such as in a magnetic spectrometer.
	Unidirectional: Collimated	"	e^-,p	25,26	
	Telescopic	"	e^-,p	27	
	Magnetic	rigidity selection	e^-	28	
Scintillation	Omnidirectional	threshold and/or ΔE	e^-,p	5,23, 29,30,36	Scintillation counters and spectrometers have been widely used to measure the energy spectra of electrons and protons and to determine the spatial extent of the radiation belts.
	Unidirectional: Collimated	PHA[1]	e^-,p	7,8	
	Telescopic	PHA(dE,dx,E)	e^-,p	31	
	Phoswitch	PHA		8	
	Magnetic	PHA	e^-	8	
Solid State	Omnidirectional	threshold and/or ΔE	e^-,p	11,32	Parameters measured by solid state detectors are similar to those obtained by scintillation counters. Its inherent smallness and good energy resolution are mixed advantages in space experiments; however, its sensitivity to radiation damage can be a serious limitation.
	Unidirectional: Collimated	threshold and/or PHA	e^-,p	12,33 38,39	
	Telescopic	PHA(dE/dx,E)	e^-,p,α	33,34	
	Magnetic	rigidity selection	e^-	9,10	Detailed information on artifical radiation belts, created by nuclear detonations, has been obtained with a magnetic spectrometer using solid state detectors.

Table 11-1—continued.

Nuclear Emulsions	Directional	range, dE/dx	- 13-16 p, 37 heavier	Nuclear emulsions afford high resolution in energy and angular measurements as well as particle identification but are integrating devices and hence limited in time and spatial resolution.
Miscellaneous:				These miscellaneous detectors have been seldom used for the measurements of concern here, but are listed because of their importance in restricted energy regions, either low or very high energies.
Faraday Cups	Unidirectional wide angle	ret. pot. " "	- e,p 35 e,p 17	
Channeltrons	Unidirectional:		- 19	
	Magnetic	rigidity selection	e,p 18	
	Electrostatic	cross elect. field	- 18 e,p	
Cerenkov	Omnidirectional	velocity thres.	chgd. part	
	Unidirectional	velocity selection	chgd. 20 part	

1) Pulse Height Analyzer

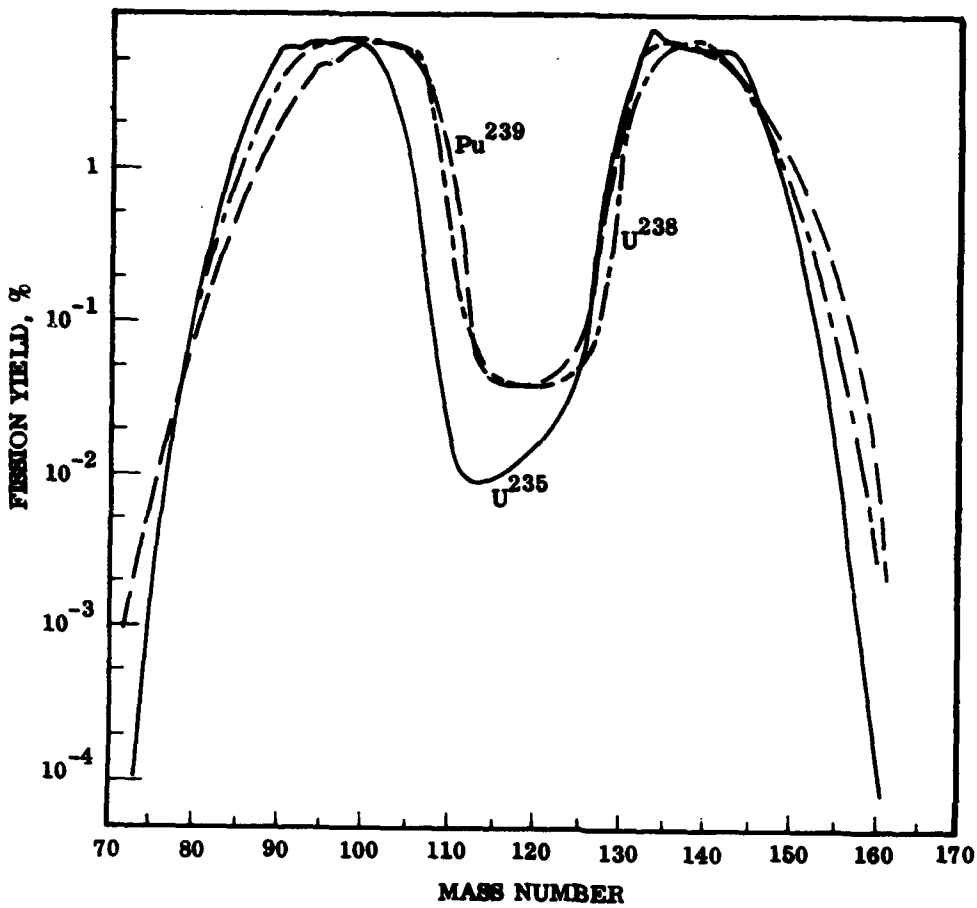

Figure 11-1. Mass distribution for fission of U^{235}, U^{238}, and Pu^{239}.

with fragment mass ratio (about 20 percent) and with excitation energy. The kinetic energy of the two separate fragments is determined by conservation of total mass and momentum.

The fission fragments separate with velocities in the neighborhood of 10^9 centimeters per second and net charges of roughly 15e for the heavier fragments and 20e for the lighter fragments. Fission recoil and its effects have been reviewed by Walton (Reference 3). He discusses the measurements of Katcoff, Miskel, and Stanley (Reference 4) who found that the mean range of the lighter component of the fragments from the fission of plutonium is approximately 2.5 centimeters in air at standard temperature and pressure and that the mean range

of the heavier component is approximately 2.0 centimeters. These results recently were verified by Menzel, Hollstein, and Ishimori (Reference 5).

The number $\bar{\nu}$ of prompt neutrons accompanying the fission process is 2.4 for thermal fission of U-235 , approximately the same for fission of U-238 , and 2.8 for thermal fission of Pu-239 (Reference 6). The prompt neutrons have an energy distribution that is quite close to a Maxwellian distribution. The average kinetic energy is given by a formula by Terrell (Reference 7):

$$T = 0.75 + 0.65(\bar{\nu} + 1)^{1/2} \quad \text{MeV} \qquad (11\text{-}1)$$

which gives 1.95 MeV for U-235 and 2.02 for Pu-239 . The number of neutrons released per fission event increases with the energy of the neutron inducing the fission process. At 14 MeV , about 4 neutrons are released. The number also varies with mass of the fission fragments (Reference 2).

When fission of U-235 occurs after capture of a slow neutron, a long-range alpha particle is emitted in approximately 1 out of 500 events. The energy distribution of these alpha particles has a maximum near 15 to 17 MeV and the maximum alpha particle energy is as great as 29 MeV .

The energy in prompt gammas accompanying the fission process is approximately 8 MeV . Thus, roughly 20 of the 200 MeV produced in the fission process are retained as excitation energy of the fission fragments. This energy subsequently is released in beta decay, delayed-neutron emission, and gamma emission.

The yield of delayed neutrons is quite small. Typical values of the number of delayed neutrons per fission (Reference 8) are 0.016 for U-235 , 0.04 for U-238 , and 0.006 for Pu-239 . The average energy of these delayed neutrons is approximately 400 KeV . Thus, very little energy is emitted in delayed neutrons. These values are relatively insensitive to the energy of the neutron that induces fission when the neutron energy is less than about 4 MeV . However, when the neutron energy increases to 14 MeV , the delayed neutron yields increase by about a factor of two.

Relatively large amounts of energy are emitted in the form of gamma rays and neutrinos accompanying the beta decay of the fission

fragments. The electrons from the beta decay have an average energy as shown in Figure 11-2. Kutcher (Reference 9) and West (Reference 10) have measured time-dependent energy spectra of betas from U-235 and Heller (Reference 11) has made theoretical calculations for betas from a number of fissioning nuclei. Figure 11-3 shows the fission-beta spectra measured by West as well as the equilibrium fission-beta spectrum determined by Carter and others (Reference 12). The curve in Figure 11-2 represents a compromise of the quoted values. The average value is affected by the low-energy portion of the distribution, which only recently has been measured.

Figure 11-4 shows the rate of beta emission. The values for U-235 and Pu-239 were taken from the recent experiments of Seyfarth (Reference 14). The values for U-238 were obtained by scaling the results of Griffin (Reference 15) by the same factor as necessary to bring his results for U-235 into agreement with the results of Seyfarth. Seyfarth's results show that one half of the betas from U-235 are emitted within 60 seconds and one half of the betas from Pu-239 are emitted within 200 seconds.

11.3 PROPERTIES OF THE EARTH'S ATMOSPHERE AND IONOSPHERE

11.3.1 Neutral Atmosphere

The main regions of the earth's atmosphere are listed in Table 11-2. The homosphere is the region from 0 to 90 kilometers where the composition of the air and the mean molecular weight remain constant. The three main constituents in the homosphere and their percentages by volume are molecular nitrogen (78.084 percent), molecular oxygen (20.9476 percent), and argon (0.934 percent). The atmosphere is well mixed up to the turbopause at about 110 kilometers.

In the heterosphere, the molecular weight decreases markedly as the composition changes with altitude because of molecular dissociation and diffusion. The 1962 U.S. Standard Atmosphere (Reference 1) is a useful reference for average atmospheric properties in the homosphere. The 1962 U.S. Standard Atmosphere is a midlatitude (approximately 45 degrees), year-round mean over the range of solar activity between sunspot minimums and maximums.

Seasonal and latitudinal variations of properties in the homosphere can be taken into account by using the 1966 U.S. Standard Atmosphere

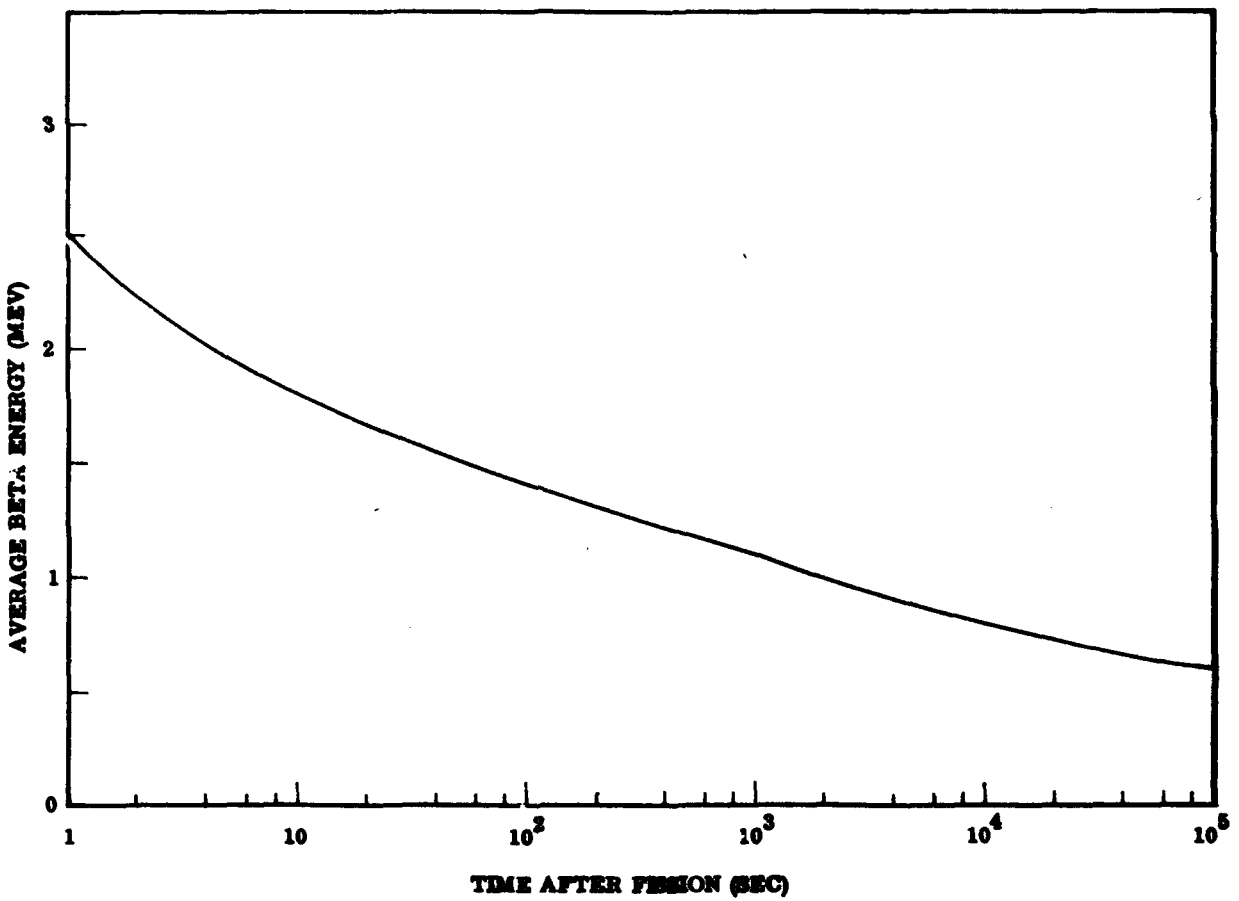

Figure 11-2. Average beta energy for U^{235} as a function of time.

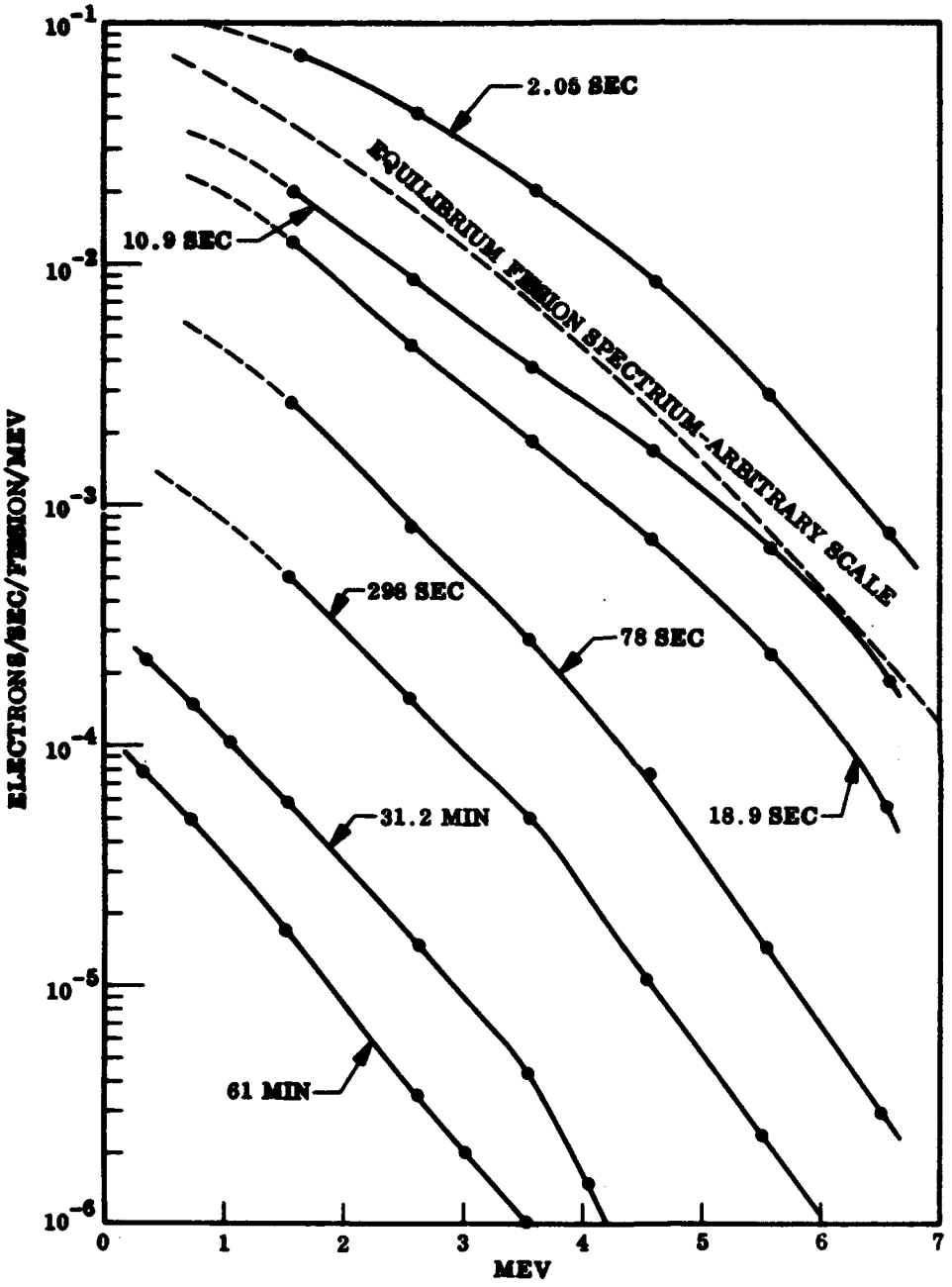

Figure 11-3. Fission spectra at different times after instantaneous fission and the equilibrium fission spectrum.

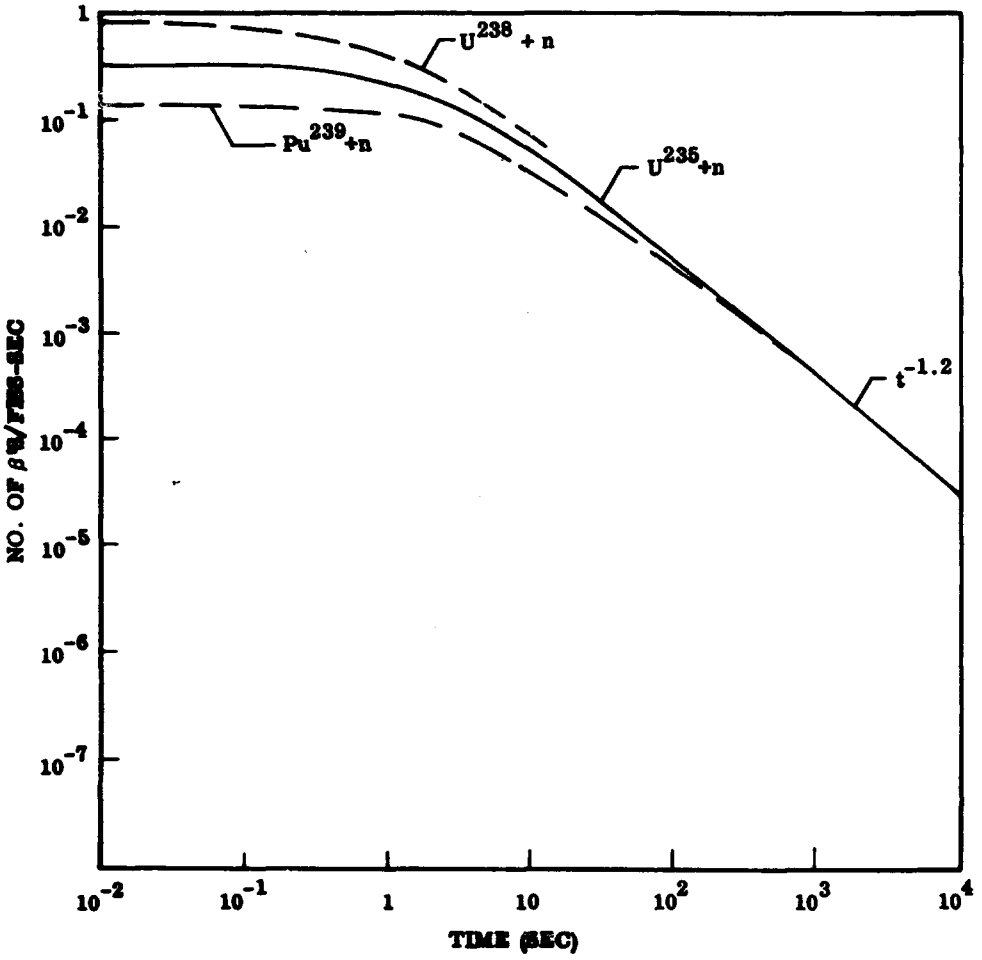

Figure 11-4. Rate of beta decay following fission for U^{235}, U^{238}, and Pu^{239}.

Supplements (Reference 2). The values in the homosphere below 90 kilometers given in Table 11-3 conform closely to those in Reference 2. The average atmospheric properties for latitude 45 degrees, spring or fall, do not vary significantly with the solar cycle (solar activity) or local time.

The heterosphere is divided into two regions: the thermosphere (from about 90 to 550 kilometers) and the exosphere (above about 550 kilometers). The neutral atmosphere in the thermosphere is

Table 11-2. Main regions of the earth's atmosphere.

Atmospheric Region	Subregion	Approximate Altitude Range (km)	Characteristic Features
Homosphere	Troposphere	0 to 12	Mean molecular weight constant; heat transfer by convection
	Stratosphere	12 to 50	Constant molecular weight; increasing temperature; region strongly heated by both earth-infrared and solar-ultraviolet radiation
	Mesosphere	50 to 90	Constant molecular weight; decreasing temperature; mixing processes dominant throughout homosphere
Heterosphere	Thermosphere	90 to 550	Frequent particle collisions; diffusion process dominant
	Exosphere	550 to 60,000	Collisions rare; temperature constant with altitude to about 8,500 km; diffusion process dominant; heat transfer by conduction

Table 11-3. Lower atmosphere average neutral properties versus altitude (spring or fall; latitude 45 degrees).

Altitude h(km)	Temp. T(°K)	Scale ht.(km)	Mean mol.wt.	Concent. $n(cm^{-3})$	Pressure ($dyne\ cm^{-2}$)	Density ($gm\ cm^{-3}$)	Constituent Concentrations					
							$n(H)(cm^{-3})$	$n(He)(cm^{-3})$	$n(O)(cm^{-3})$	$n(N_2)(cm^{-3})$	$n(O_2)(cm^{-3})$	$n(A)(cm^{-3})$
0	282	8	28.96	2.61(19)*	1.02(6)	1.26(-3)	---	1.37(14)	---	2.04(19)	5.47(18)	2.44(17)
5	257	8	28.96	1.52(19)	5.41(5)	7.33(-4)	---	7.99(13)	---	1.19(19)	3.19(18)	1.42(17)
10	226	7	28.96	8.54(18)	2.67(5)	4.11(-4)	---	4.48(13)	---	6.67(18)	1.79(18)	7.98(16)
20	217	6	28.96	1.87(18)	5.61(4)	9.01(-5)	---	9.62(12)	---	1.46(18)	3.92(17)	1.75(16)
30	224	7	28.96	3.87(17)	1.20(4)	1.86(-5)	---	2.03(12)	---	3.02(17)	8.11(16)	3.62(15)
40	249	7	28.96	8.30(16)	2.86(3)	3.99(-6)	---	4.35(11)	5.38(1)	6.48(16)	1.74(16)	7.76(14)
50	270	8	28.96	2.13(16)	7.92(2)	1.02(-6)	---	1.12(11)	9.05(4)	1.66(16)	4.46(15)	1.99(14)
60	253	8	28.95	6.36(15)	2.22(2)	3.06(-7)	9.54(8)	3.33(10)	3.65(7)	4.97(15)	1.33(15)	5.94(13)
70	225	7	28.96	1.78(15)	5.54(1)	8.58(-8)	2.68(8)	9.35(9)	3.53(9)	1.39(15)	3.74(14)	1.67(13)
80	194	6	28.95	4.17(14)	1.12(1)	2.00(-8)	6.25(7)	2.18(9)	8.18(10)	3.25(14)	8.73(13)	3.89(12)
90	180	6	28.78	7.23(13)	1.79	3.46(-9)	1.08(7)	3.77(8)	4.54(11)	5.61(13)	1.51(13)	6.71(11)

*Denotes $n = 2.61 \times 10^{19}$ particles cm^{-3}.

composed almost wholly of molecular nitrogen and oxygen and atomic nitrogen and oxygen. Helium and hydrogen become important in the exosphere. The relative concentrations of these constituents depend strongly on altitude and temperature.

Several models of the neutral upper atmosphere are currently in use (References 3 through 6). Nicolet's model is a steady state theoretical model. Boundary values for the properties and the major constituents are introduced at 120 kilometers, and the altitude profiles of the atmospheric properties are computed taking diffusion and heat conduction into account using a priori temperature profiles. Exospheric temperatures are derived in Jacchia's model using densities deduced from satellite drag and the latest version of Nicolet's theoretical model.

Harris and Priester's model (Reference 3) starts with the boundary conditions taken from Nicolet at 120 kilometers, and diffusion is assumed to prevail above this height. The altitude profile of the atmospheric constituents are derived by a simultaneous integration of the heat conduction equation and the hydrostatic equation, using an ad hoc variable heat source. Harris and Priester's model does not take into account the escape of hydrogen. Consequently, in the exosphere their model shows an increase rather than the expected decrease of atomic hydrogen with solar activity. Moe (Reference 7) presents a review of atmospheric models in the 100- to 1,000-kilometer altitude range. CIRA's model (Reference 6) is based on the other three models.

Note that the previous four models depend on the same boundary values at 120 kilometers (presented by Nicolet as average conditions)—latitudinal, seasonal, diurnal, and solar cycle variations in the boundary conditions are ignored. The U.S. Standard Atmosphere Supplements (Reference 2) were derived partly to take into account latitudinal and seasonal variations in the lower heterosphere (Reference 8).

Anderson and Francis' model (Reference 9) was used to calculate the tables presented in this handbook. This model gives an improved description of the upper atmosphere by including diurnal and solar activity effects on the atmospheric properties in the lower heterosphere. The lower boundary (90-kilometer) values of this model are those given by the U.S. Standard Atmosphere Supplements (Reference 2). Hence, the latitudinal and seasonal variations are maintained. This

model has been selected for inclusion because it extends the altitude range beyond the 1,000 to 3,000 kilometers covered by most models and because computations of atmospheric scattering of radiation belt particles based on the model are in good agreement with experimental data (Section 5; References 10 through 17).

The model has been developed to include the neutral properties and composition to 10,000 kilometers. To accomplish this, the effect of the escape of hydrogen from the exosphere must be considered. Also, the model takes into account the diurnal variation of hydrogen in the exosphere, a factor neglected in previous models. The primary properties are calculated by starting with a density profile as the input; diffusive equilibrium above the turbopause at 110 kilometers and isothermal conditions above 400 kilometers are assumed.

The density profile is represented by an empirical model (Reference 18) as a function of local time and solar activity from 200 to 800 kilometers. This density model accounts for the variations in density that occur from day to day by employing corrected values of the 10.7-centimeter solar flux S' as an indicator of the sun's extreme ultraviolet radiation, which is responsible for heating the upper atmosphere. Thus, S' is derived from the 10.7-centimeter data and drag data from satellite 1958 Alpha by correcting the 10.7-centimeter flux for the amount by which the density model (Reference 18) fails to predict the observed satellite drag. A good correlation between the 10.7-centimeter flux and the extreme ultraviolet radiation (EUV) from the sun responsible for heating and causing density changes in the earth's upper atmosphere generally has been assumed.

Anderson (Reference 19) has shown that the 10.7-centimeter flux cannot represent satisfactorily the changes in the EUV over any part of the solar cycle. Comparisons made between observed drag data for several satellites and drag values calculated from the density model (Reference 18) with both the 10.7-centimeter data and S' indicate that marked reductions in the relative error result from using S' instead of the 10.7-centimeter data (Reference 20).

The remaining properties are derived by using the hydrostatic equation (Equation 5-32) and the equation of state to relate the density, pressure, temperature, mean molecular mass, and individual particle concentrations to the altitude, together with boundary values based on measurements and the U.S. Standard Atmosphere Supplements (Reference 2). The density in the exosphere also is corrected for the departure from a Maxwellian velocity distribution caused by escape of atomic hydrogen from the earth's atmosphere.

Tables 11-4 through 11-12 show the results of the numerical computations of the atmospheric properties versus altitude from 100 to 10,000 kilometers. Minimum, average, and maximum solar activity correspond to $S' = 50$, 125, and 200 RU, respectively, where 1 RU (radioastronomy unit) equals 10^{-22} watts per square meter per hertz. The scale height given in the tables refers to the pressure scale height kT/mg, where k is the Boltzmann constant, T is the temperature of the neutral atmosphere, m is the mean molecular mass, and g is the gravitational acceleration.

Tables 11-4, 11-7, and 11-10 are for local time $t = 21$ hours (or 8 hours) because the density for this time has been found to approximate closely the diurnally averaged density. The time $t = 5$ hours (Tables 11-5, 11-8, and 11-11) corresponds to immediately before "sunrise" when the thermosphere has reached its minimum temperature (density, pressure, and concentration) due to cooling. The time $t = 14$ hours (Tables 11-6, 11-9, and 11-12) corresponds to the maximum daily values of the previous properties.

Figure 11-5 is a graph of the concentrations of various constituents versus altitude up to 1,000 kilometers for average solar activity conditions, at $t = 21$ hours. Figure 11-6 shows the diurnal variations of the concentrations up to 1,000 kilometers for average solar activity. Figure 11-7 shows the variation of the diurnal average ($t = 21$ hours) concentrations over the solar cycle.

Calculations of density from the model are based on neutral particles only. Ions do not contribute significantly to the total (ambient) density below 2,000 kilometers. Above this altitude, the contribution of H^+ (Table 11-13) should be taken into account in any calculation of the ambient density.

Francis (Reference 21) has shown that the computations of the basic atmospheric properties (pressure, temperature, and mean molecular weight) from Anderson and Francis' model (Reference 9) are in good agreement with values from other models that employ the same density profile; the error is less than about 5 percent throughout the region specified by the input data. Also, the basic atmospheric concentrations of N_2, O_2, O, and He agree with values given by other models within errors of 6, 20, 12, and 6 percent, respectively, at 120 kilometers.

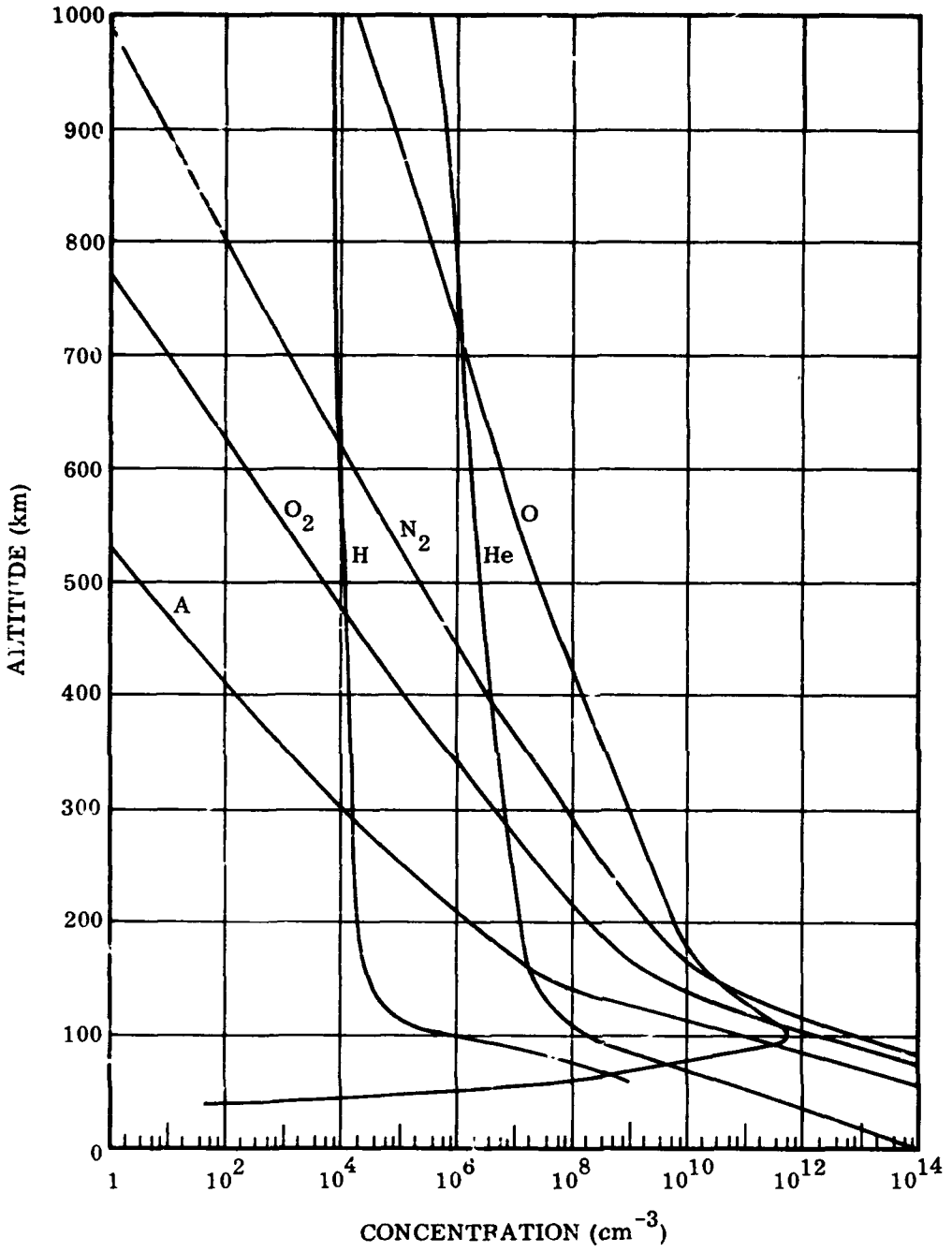

Figure 11-5. Distribution of major constituents of neutral atmosphere at local times t = 21 or 8 hours (diurnal average) for average solar activity (S' = 125 RU).

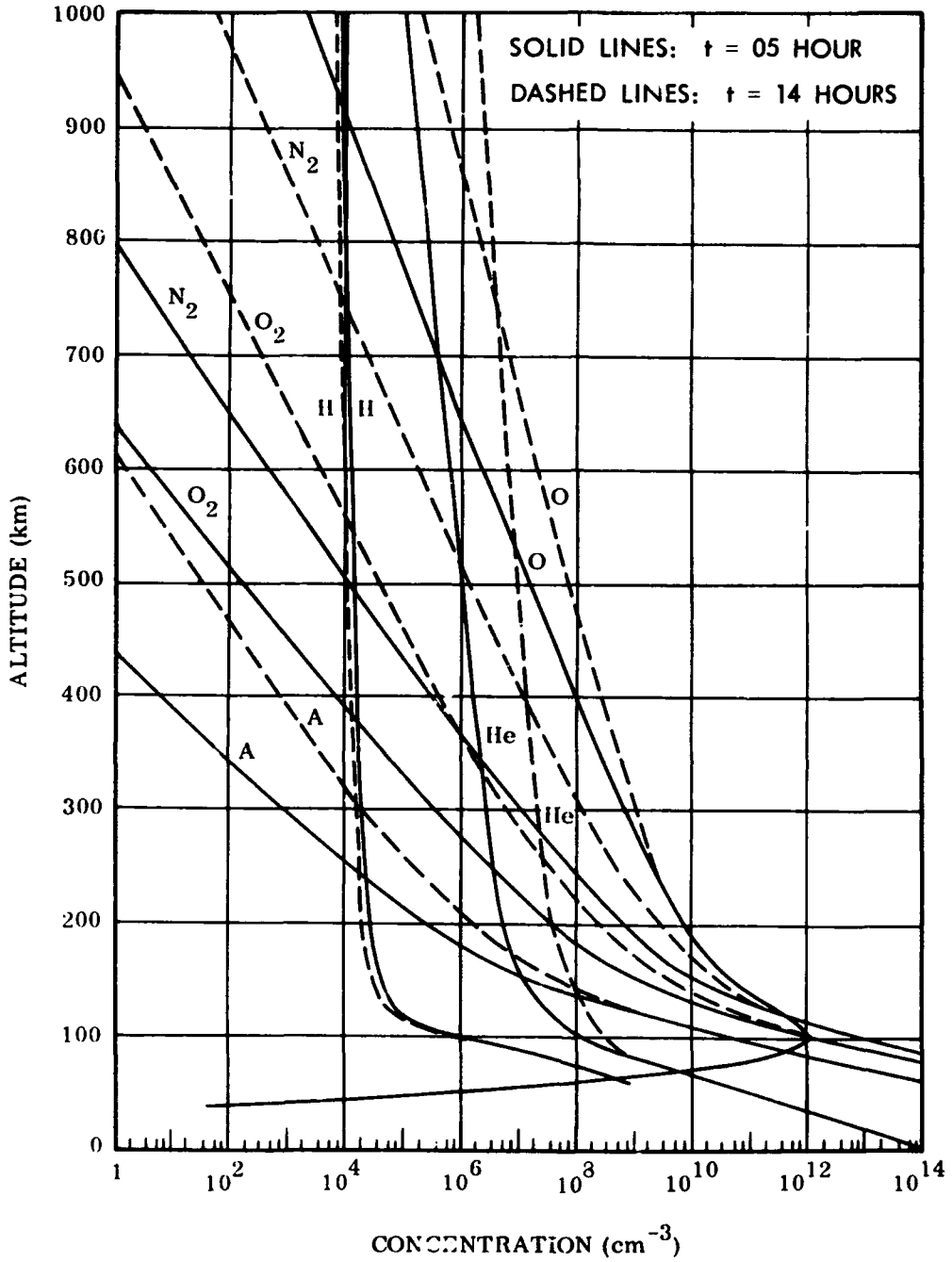

Figure 11-6. Distributions of major constituents of neutral atmosphere at extremes of diurnal variation for average solar activity (S' = 125 RU).

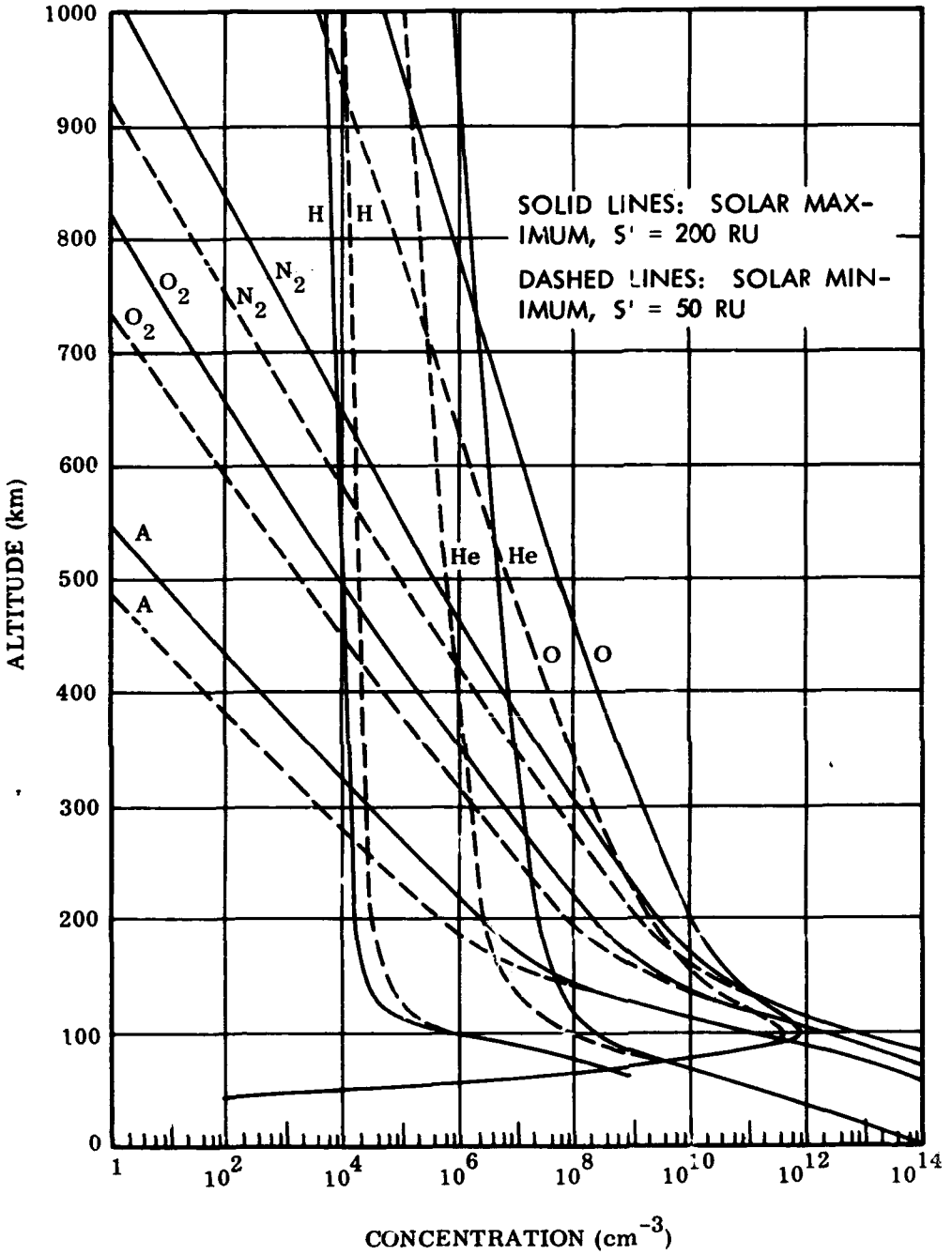

Figure 11-7. Distributions of major constituents of neutral atmosphere at extremes of solar activity.

Table 11-4. Upper atmosphere neutral properties versus altitude near sunspot minimum (spring or fall; latitude 45 degrees; t = 21 hours; diurnal average).

Altitude h(km)	Temp. T(°K)	Scale ht.(km)	Mean mol.wt.	Concent. $n(cm^{-3})$	Pressure ($dyne\ cm^{-2}$)	Density ($gm\ cm^{-3}$)	Constituent concentrations					
							$n(H)(cm^{-3})$	$n(He)(cm^{-3})$	$n(O)(cm^{-3})$	$n(N_2)(cm^{-3})$	$n(O_2)(cm^{-3})$	$n(A)(cm^{-3})$
100	204	6	28.22	1.12(13)*	3.16(-1)	5.26(-10)	8.59(5)	6.94(7)	4.98(11)	6.76(12)	1.89(12)	7.79(10)
120	283	9	26.75	5.81(11)	2.27(-2)	2.56(-11)	1.07(5)	1.66(7)	8.29(10)	4.34(11)	6.24(10)	1.51(9)
140	410	15	24.97	7.08(10)	4.00(-3)	2.93(-12)	6.94(4)	8.75(6)	1.96(10)	4.50(10)	5.06(9)	7.18(7)
160	575	22	23.34	1.65(10)	1.31(-3)	6.39(-13)	4.73(4)	5.19(6)	6.68(9)	8.98(9)	8.22(8)	8.05(6)
180	718	29	22.02	6.04(9)	5.98(-4)	2.21(-13)	3.65(4)	3.62(6)	3.08(9)	2.74(9)	2.18(8)	1.62(6)
200	810	35	20.92	2.87(9)	3.21(-4)	9.96(-14)	3.14(4)	2.85(6)	1.71(9)	1.08(9)	7.63(7)	4.49(5)
240	935	44	19.22	9.09(8)	1.17(-4)	2.90(-14)	2.59(4)	2.02(6)	6.65(8)	2.28(8)	1.32(7)	5.23(4)
300	992	52	17.61	2.51(8)	3.44(-5)	7.34(-15)	2.29(4)	1.46(6)	2.15(8)	3.31(7)	1.47(6)	3.40(3)
340	993	55	16.92	1.19(8)	1.64(-5)	3.35(-15)	2.19(4)	1.23(6)	1.08(8)	9.90(6)	3.70(5)	6.06(2)
400	993	59	16.22	4.17(7)	5.71(-6)	1.12(-15)	2.05(4)	9.51(5)	3.90(7)	1.67(6)	4.84(4)	4.76(1)
500	993	64	15.18	8.17(6)	1.12(-6)	2.06(-16)	1.85(4)	6.29(5)	7.43(6)	9.18(4)	1.76(3)	
600	993	76	13.29	1.93(6)	2.64(-7)	4.26(-17)	1.67(4)	4.20(5)	1.49(6)	5.49(3)	7.04(1)	
700	993	103	10.05	6.11(5)	8.38(-8)	1.02(-17)	1.51(4)	2.34(5)	3.11(5)	3.56(2)	3.08	
800	993	157	6.81	2.76(5)	3.79)-8)	5.12(-18)	1.37(4)	1.94(5)	6.80(4)	2.49(1)		
900	993	223	4.92	1.62(5)	2.23(-8)	1.32(-18)	1.25(4)	1.34(5)	1.55(4)	1.87		
1,000	993	276	4.09	1.09(5)	1.49(8)	7.40(-19)	1.14(4)	9.38(4)	3.68(3)			
1,400	993	385	3.25	3.26(4)	4.47(-9)	1.76(-19)	8.16(3)	2.44(4)	1.69(1)			
2,000	993	625	2.32	9.34(3)	1.28(-9)	3.60(-20)	5.22(3)	4.12(3)				
4,000	993	2,059	1.08	1.74(3)	2.38(-10)	3.13(-21)	1.69(3)	4.86(1)				
6,000	993	3,145	1.01	7.79(2)	1.07(-10)	1.31(-21)	7.77(2)	2.40				
10,000	993	5,554	1.00	2.79(2)	3.82(-11)	4.63(-22)	2.79(2)					

*Denotes $n = 1.12 \times 10^{13}$ particles cm^{-3}.

Table 11-5. Upper atmosphere neutral properties versus altitude near sunspot minimum (spring or fall; latitude 45 degrees; t = 5 hours; diurnal minimum).

Altitude h(km)	Temp. T(°K)	Scale ht. (km)	Mean mol. wt.	Concent. n(cm^{-3})	Pressure (dyne cm^{-2})	Density (gm cm^{-3})	Constituent Concentrations					
							n(H)(cm^{-3})	n(He)(cm^{-3})	n(O)(cm^{-3})	n(H_2)(cm^{-3})	n(O_2)(cm^{-3})	n(A)(cm^{-3})
100	203	6	28.15	1.12(13)*	3.14(-1)	5.24(-10)	1.02(6)	4.66(7)	5.58(11)	8.73(12)	1.86(12)	7.55(10)
120	277	9	26.46	5.76(11)	2.20(-2)	2.53(-11)	1.33(5)	6.56(6)	9.56(10)	4.19(11)	6.00(10)	1.46(9)
140	395	14	24.44	6.94(10)	3.79(-3)	2.82(-12)	8.70(4)	3.49(6)	2.22(10)	4.26(10)	4.62(9)	6.48(7)
160	551	22	22.66	1.60(10)	1.22(-3)	6.03(-13)	5.95(4)	2.06(6)	7.37(9)	7.94(9)	7.12(8)	6.75(6)
180	680	29	21.27	5.87(9)	5.51(-4)	2.07(-13)	4.65(4)	1.45(6)	3.35(9)	2.34(9)	1.81(8)	1.29(6)
200	733	33	20.15	2.85(9)	2.89(-4)	9.54(-14)	4.18(4)	1.18(6)	1.88(9)	9.04(8)	6.19(7)	3.44(5)
240	792	39	18.45	8.71(8)	9.52(-5)	2.67(-14)	3.65(4)	8.71(5)	6.94(8)	1.67(8)	9.06(6)	3.18(4)
300	837	46	17.03	2.02(8)	2.34(-5)	5.72(-15)	3.19(4)	6.00(5)	1.84(8)	1.70(7)	6.72(5)	1.25(3)
340	840	48	16.52	8.60(7)	9.96(-6)	2.36(-15)	3.02(4)	4.88(5)	8.12(7)	4.08(6)	1.32(5)	1.62(2)
400	840	50	16.06	2.53(7)	2.93(-6)	6.74(-16)	2.80(4)	3.61(5)	2.44(7)	4.96(5)	1.18(4)	8.02
500	840	54	15.24	3.70(6)	4.29(-7)	9.35(-17)	2.48(4)	2.21(5)	3.44(6)	1.61(4)	2.36(2)	
600	840	65	13.07	6.72(5)	7.79(-8)	1.46(-17)	2.20(4)	1.37(5)	5.12(5)	5.76(2)	5.24	
700	840	99	8.87	1.87(5)	2.16(-8)	2.75(-18)	1.96(4)	8.65(4)	8.06(4)	2.26(1)		
800	840	172	5.25	8.61(4)	9.98(-9)	7.50(-19)	1.75(4)	5.52(4)	1.34(4)			
900	840	255	3.64	5.37(4)	6.22(-9)	3.25(-19)	1.57(4)	3.57(4)	2.32(3)			
1,000	840	316	3.02	3.78(4)	4.39(-9)	1.90(-19)	1.41(4)	2.33(4)	4.24(2)			
1,400	840	530	2.00	1.42(4)	1.65(-9)	4.73(-20)	9.48(3)	4.74(3)				
2,000	840	959	1.26	6.18(3)	7.16(-10)	1.31(-20)	5.60(3)	5.80(2)				
4,000	840	1,875	1.01	1.50(3)	1.73(-10)	2.50(-21)	1.49(3)	3.04				
6,000	840	2,683	1.00	6.05(2)	7.01(-11)	1.00(-21)	6.05(2)					
10,000	840	4,700	1.00	1.87(2)	2.16(-11)	3.10(-22)	1.87(2)					

*Denotes n = 1.12 x 10^{13} particles cm^{-3}.

Table 11-6. Upper atmosphere neutral properties versus altitude near sunspot minimum (spring or fall; latitude 45 degrees; t = 14 hours; diurnal maximum).

Altitude h(km)	Temp. T(°K)	Scale ht. (km)	Mean mol. wt.	Concent. $n(cm^{-3})$	Pressure (dyne cm^{-2})	Density (gm cm^{-3})	Constituent Concentrations					
							$n(H)(cm^{-3})$	$n(He)(cm^{-3})$	$n(O)(cm^{-3})$	$n(N_2)(cm^{-3})$	$n(O_2)(cm^{-3})$	$n(A)(cm^{-3})$
100	204	6	28.10	1.13(13)*	3.17(-1)	5.26(-10)	9.06(5)	1.45(8)	5.99(11)	8.74(12)	1.86(12)	7.60(10)
120	280	9	26.21	5.97(11)	2.31(-2)	2.60(-11)	1.04(5)	6.30(7)	1.10(11)	4.24(11)	6.05(10)	1.50(9)
140	408	15	24.12	7.48(10)	4.20(-3)	3.00(-12)	6.68(4)	3.31(7)	2.58(10)	4.41(10)	4.80(9)	6.92(7)
160	580	23	22.36	1.79(10)	1.44(-3)	6.65(-13)	4.48(4)	1.93(7)	8.64(9)	8.48(9)	7.69(8)	7.64(6)
180	739	32	21.05	6.74(9)	6.88(-4)	2.36(-13)	3.40(4)	1.32(7)	3.95(9)	2.58(9)	2.04(8)	1.55(6)
200	851	38	20.04	3.30(9)	3.87(-4)	1.10(-13)	2.87(4)	1.03(7)	2.19(9)	1.02(9)	7.24(7)	4.39(5)
240	1,043	51	18.60	1.10(9)	1.58(-4)	3.39(-14)	2.24(4)	6.97(6)	8.50(8)	2.27(8)	1.33(7)	5.58(4)
300	1,189	64	17.31	3.43(8)	5.63(-5)	9.85(-15)	1.85(4)	4.86(6)	2.96(8)	3.97(7)	1.85(6)	4.88(3)
340	1,204	68	16.72	1.85(8)	3.07(-5)	5.13(-15)	1.76(4)	4.16(5)	1.66(8)	1.45(7)	5.85(5)	1.16(3)
400	1,204	72	16.01	7.83(7)	1.30(-5)	2.08(-15)	1.67(4)	3.37(6)	7.15(7)	3.33(6)	1.09(5)	1.42(2)
500	1,204	80	14.80	2.10(7)	3.48(-6)	5.14(-16)	1.54(4)	2.40(6)	1.82(7)	3.04(5)	7.08(3)	4.66
600	1,204	95	12.89	6.59(6)	1.10(-6)	1.41(-16)	1.40(4)	1.72(6)	4.83(6)	2.98(4)	4.97(2)	
700	1,204	124	10.17	2.59(6)	4.30(-7)	4.37(-17)	1.29(4)	1.24(6)	1.33(6)	3.11(3)	3.77(1)	
800	1,204	173	7.47	1.30(6)	2.16(-7)	1.62(-17)	1.19(4)	9.10(5)	3.79(5)	3.46(2)	3.06	
900	1,204	235	5.65	7.94(5)	1.32(-7)	7.45(-18)	1.10(4)	6.71(5)	1.12(5)	4.10(1)		
1,000	1,204	291	4.70	5.43(5)	9.02(-8)	4.24(-18)	1.02(4)	4.99(5)	3.42(4)	5.14		
1,400	1,204	390	3.89	1.72(5)	2.86(-8)	1.11(-18)	7.73(3)	1.64(5)	4.02(2)			
2,000	1,204	485	3.63	4.32(4)	7.18(-9)	2.60(-19)	5.32(3)	3.79(4)	1.14			
4,000	1,204	1,380	1.96	3.03(3)	5.04(-10)	9.87(-21)	2.06(3)	9.70(2)				
6,000	1,204	3,172	1.21	1.15(3)	1.90(-10)	2.31(-21)	1.06(3)	8.12(1)				
10,000	1,204	6,579	1.02	4.41(2)	7.32(-11)	7.49(-22)	4.37(2)	3.50				

*Denotes $n = 1.13 \times 10^{13}$ particles cm^{-3}.

Table 11-7. Upper atmosphere neutral properties versus altitude for average sunspot conditions (spring or fall; latitude 45 degrees; t = 21 hours; diurnal average).

Altitude h(km)	Temp. T(°K)	Scale ht. (km)	Mean mol. wt.	Concent. n(cm^{-3})	Pressure (dyne cm^{-2})	Density ($gm\ cm^{-3}$)	Constituent concentrations					
							n(H)(cm^{-3})	n(He)(cm^{-3})	n(O)(cm^{-3})	$n(N_2)$(cm^{-3})	$n(O_2)$(cm^{-3})	n(A)(cm^{-3})
100	213	7	27.94	1.16(13)*	3.40(-2)	5.36(-10)	7.04(5)	1.38(8)	7.65(11)	8.83(12)	1.89(12)	7.83(10)
120	310	11	25.32	7.19(11)	3.08(-2)	3.02(-11)	6.00(4)	5.58(7)	1.85(11)	4.64(11)	6.81(10)	1.78(9)
140	474	18	23.20	1.11(11)	7.27(-3)	4.28(-12)	3.70(4)	2.88(7)	4.67(10)	5.76(10)	6.66(9)	1.08(8)
160	649	27	21.63	3.30(10)	2.96(-3)	1.18(-12)	2.59(4)	1.79(7)	1.79(10)	1.37(10)	1.35(9)	1.59(7)
180	750	33	20.44	1.46(10)	1.52(-3)	4.97(-13)	2.18(4)	1.37(7)	9.34(9)	4.86(9)	4.22(8)	3.86(6)
200	821	38	19.49	7.60(9)	8.61(-4)	2.46(-13)	1.93(4)	1.11(7)	5.42(9)	2.01(9)	1.56(8)	1.14(6)
240	938	47	18.13	2.60(9)	3.37(-4)	7.83(-14)	1.61(4)	7.98(6)	2.13(9)	4.34(8)	2.75(7)	1.34(5)
300	1030	56	16.98	7.51(8)	1.07(-4)	2.12(-14)	1.37(4)	5.59(6)	6.79(8)	6.28(7)	3.06(6)	8.86(3)
340	1048	60	16.52	3.71(8)	5.37(-5)	1.02(-14)	1.29(4)	4.66(6)	3.46(8)	1.96(7)	8.10(5)	1.68(3)
400	1050	63	16.01	1.39(8)	2.02(-5)	3.70(-15)	1.21(4)	3.65(6)	1.32(8)	3.62(6)	1.18(5)	1.51(2)
500	1050	69	15.11	3.02(7)	4.38(-6)	7.58(-16)	1.10(4)	2.47(6)	2.75(7)	2.33(5)	2.13(3)	3.01
600	1050	80	13.38	7.72(6)	1.12(-6)	1.72(-16)	9.98(3)	1.69(6)	6.01(6)	1.63(4)	2.44(2)	
700	1050	105	10.45	2.55(6)	3.69(-7)	4.42(-17)	9.09(3)	1.17(6)	1.37(6)	1.22(3)	1.27(1)	
800	1050	153	7.38	1.15(6)	1.66(-7)	1.41(-17)	8.31(3)	8.14(5)	3.25(5)	9.88(1)		
900	1050	214	5.42	6.62(5)	9.60(-8)	5.96(-18)	7.61(3)	5.74(5)	8.04(4)	8.56		
1,000	1050	264	4.52	4.36(5)	6.33(-8)	3.27(-18)	6.98(3)	4.09(5)	2.06(4)			
1,400	1050	341	3.89	1.20(5)	1.74(-8)	7.72(-19)	5.07(3)	1.14(5)	1.27(2)			
2,000	1050	428	3.60	2.46(4)	3.57(-9)	1.47(-19)	3.32(3)	2.13(4)				
4,000	1050	1423	1.66	1.46(3)	2.11(-10)	4.01(-21)	1.14(3)	3.20(2)				
6,000	1050	3053	1.10	5.61(2)	8.13(-11)	1.02(-21)	5.42(2)	1.85(1)				
10,000	1050	5834	1.01	2.03(2)	2.95(-11)	3.41(-22)	2.03(2)					

*Denotes n = 1.16×10^{13} particles cm^{-3}

Table 11-8. Upper atmosphere neutral properties versus altitude for average sunspot conditions (spring or fall; latitude 45 degrees; t = 5 hours; diurnal minimum).

Altitude h(km)	Temp. T(°K)	Scale ht. (km)	Mean mol. wt.	Concent. n(cm^{-3})	Pressure (dyne cm^{-2})	Density (gm cm^{-3})	Constituent concentrations					
							n(N)(cm^{-3})	n(He)(cm^{-3})	n(O)(cm^{-3})	n(N_2)(cm^{-3})	n(O_2)(cm^{-3})	n(A)(cm^{-3})
100	207	7	27.42	1.18(13)*	3.36(-1)	5.35(-10)	8.70(5)	1.09(8)	1.25(12)	8.61(12)	1.80(12)	8.31(10)
120	266	11	22.07	8.05(11)	2.95(-2)	2.95(-11)	8.57(4)	3.20(7)	4.15(11)	3.42(11)	4.67(10)	1.45(9)
140	392	18	19.48	1.26(11)	6.81(-3)	4.07(-12)	5.41(4)	1.63(7)	9.05(10)	3.20(10)	3.28(9)	5.79(7)
160	545	27	18.18	3.65(10)	2.75(-3)	1.10(-12)	3.71(4)	9.67(6)	3.01(10)	5.95(9)	5.03(8)	6.03(6)
180	639	33	17.46	1.60(10)	1.41(-3)	4.63(-13)	3.04(4)	7.10(6)	1.41(10)	1.78(9)	1.29(8)	1.15(6)
200	692	37	17.00	8.32(9)	7.94(-4)	2.35(-13)	2.72(4)	5.74(6)	7.62(9)	6.45(8)	4.11(7)	2.80(5)
240	780	43	16.49	2.72(9)	2.92(-4)	7.44(-14)	2.28(4)	4.01(6)	2.60(9)	1.07(8)	5.38(6)	2.27(4)
300	853	49	16.15	6.83(8)	8.04(-5)	1.83(-14)	1.92(4)	2.67(6)	6.69(8)	1.07(7)	3.90(5)	8.73(2)
340	869	51	16.02	3.02(8)	3.62(-5)	8.04(-15)	1.80(4)	2.15(6)	2.97(8)	2.62(6)	7.85(4)	1.18(2)
400	871	53	15.84	9.49(7)	1.14(-5)	2.49(-15)	1.66(4)	1.60(6)	9.29(7)	3.42(5)	7.68(3)	6.47
500	871	57	15.20	1.51(7)	1.81(-6)	3.80(-16)	1.48(4)	1.00(6)	1.40(7)	1.26(4)	1.76(2)	
600	871	66	13.31	2.89(6)	3.47(-7)	6.38(-17)	1.32(4)	6.32(5)	2.24(6)	5.07(2)	4.48	
700	871	94	9.66	7.94(5)	9.55(-8)	1.27(-17)	1.18(4)	4.05(5)	3.77(5)	2.24(1)		
800	871	150	6.26	3.40(5)	4.09(-8)	3.53(-18)	1.06(4)	2.63(5)	6.67(4)	1.08		
900	871	208	4.62	1.94(5)	2.34(-8)	1.49(-18)	9.51(3)	1.72(5)	1.24(4)			
1000	871	246	4.02	1.25(5)	1.51(-8)	8.37(-19)	8.59(3)	1.14(5)	2.40(3)			
1400	871	321	3.43	3.05(4)	3.67(-9)	1.74(-19)	5.84(3)	2.46(4)	5.18			
2000	871	523	2.44	6.76(3)	8.13(-10)	2.74(-20)	3.51(3)	3.25(3)				
4000	871	1844	1.06	1.00(3)	1.20(-10)	1.77(-21)	9.82(2)	2.05(1)				
6000	871	2771	1.00	4.10(2)	4.94(-11)	6.85(-22)	4.10(2)					
10,000	871	4874	1.00	1.31(2)	1.58(-11)	2.18(-22)	1.31(2)					

*Denotes n = 1.18 x 10^{13} particles cm^{-3}

Table 11-9. Upper atmosphere neutral properties versus altitude for average sunspot conditions (spring or fall; latitude 45 degrees; t = 14 hours; diurnal maximum).

Altitude h(km)	Temp. T(°K)	Scale ht. (km)	Mean mol. wt.	Concent. n(cm^{-3})	Pressure (dyne cm^{-2})	Density (gm cm^{-3})	Constituent concentrations					
							n(H)(cm^{-3})	n(He)(cm^{-3})	n(O)(cm^{-3})	n(N_2)(cm^{-3})	n(O_2)(cm^{-3})	n(A)(cm^{-3})
100	214	7	27.95	1.16(13)*	3.42(-1)	5.37(-10)	6.93(5)	2.44(8)	7.64(11)	8.84(12)	1.90(12)	7.84(10)
120	316	11	25.36	7.27(11)	3.17(-2)	3.06(-11)	5.77(4)	1.73(8)	1.85(11)	4.71(11)	6.39(10)	1.82(9)
140	492	19	23.30	1.14(11)	7.77(-3)	4.42(-12)	3.50(4)	8.82(7)	4.71(10)	6.00(10)	7.07(9)	1.16(8)
160	684	28	21.79	3.46(10)	3.27(-3)	1.25(-12)	2.42(4)	5.45(7)	1.83(10)	1.47(10)	1.49(9)	1.80(7)
180	797	35	20.64	1.57(10)	1.73(-3)	5.38(-13)	2.02(4)	4.14(7)	9.73(9)	5.45(9)	4.89(8)	4.64(6)
200	888	41	19.70	8.27(9)	1.01(-3)	2.71(-13)	1.76(4)	3.34(7)	5.72(9)	2.33(9)	1.88(8)	1.44(6)
240	1060	54	18 37	2.90(9)	4.32(-4)	8.84(-14)	1.39(4)	2.30(7)	2.29(9)	5.46(8)	3.68(7)	1.97(5)
300	1296	70	17.19	9.20(8)	1.65(-4)	2.62(-14)	1.09(4)	1.54(7)	8.00(8)	9.93(7)	5.38(6)	1.87(4)
340	1321	75	16.65	5.21(8)	9.51(-5)	1.44(-14)	1.04(4)	1.33(7)	4.67(8)	3.92(7)	1.87(6)	5.00(3)
400	1321	79	15.99	2.39(8)	4.36(-5)	6.34(-15)	9.90(3)	1.10(7)	2.17(8)	1.03(7)	4.04(5)	7.38(2)
500	1321	88	14.86	7.18(7)	1.31(-5)	1.77(-15)	9.16(3)	8.03(6)	6.25(7)	1.16(6)	3.35(4)	3.28(1)
600	1321	102	13.18	2.47(7)	4.51(-6)	5.41(-16)	8.36(3)	5.94(6)	1.86(7)	1.40(5)	2.98(3)	1.59
700	1321	128	10.81	1.02(7)	1.86(-6)	1.83(-16)	7.76(3)	4.24(6)	5.76(6)	1.79(4)	2.84(2)	
800	1321	172	8.27	5.17(6)	9.43(-7)	7.09(-17)	7.22(3)	3.32(6)	1.84(6)	2.42(3)	2.89(1)	
900	1321	231	6.31	3.13(6)	5.71(-7)	3.28(-17)	6.72(3)	2.52(6)	6.04(5)	3.46(2)	3.13	
1000	1321	292	5.14	2.13(6)	3.90(-7)	1.82(-17)	6.28(3)	1.92(6)	2.05(5)	5.22(1)		
1400	1321	413	4.04	7.07(5)	1.29(-7)	4.74(-18)	4.85(3)	6.99(5)	3.58(3)			
2000	1321	490	3.95	1.87(5)	3.41(-8)	1.22(-18)	3.44(3)	1.84(5)	1.71(1)			
4000	1321	858	3.46	7.95(3)	1.45(-9)	4.56(-20)	1.44(3)	6.51(3)				
6000	1321	1758	2.40	1.45(3)	2.65(-10)	5.80(-21)	7.74(2)	6.80(2)				
10,000	1321	5640	1.31	3.74(2)	6.85(-11)	8.14(-22)	3.36(2)	3.88(1)				

*Denotes n = 1.16 x 10^{13} particles cm^{-3}

Table 11-10. Upper atmosphere neutral properties versus altitude near sunspot maximum (spring or fall; latitude 45 degrees; t = 21 hours; diurnal average.)

Altitude h(km)	Temp. T(°K)	Scale ht.(km)	Mean mol.wt.	Concent. n(cm^{-3})	Pressure (dyne cm^{-2})	Density ($gm\ cm^{-3}$)	Constituent Concentrations					
							n(H)(cm^{-3})	n(He)(cm^{-3})	n(O)(cm^{-3})	n(N_2)(cm^{-3})	n(O_2)(cm^{-3})	n(A)(cm^{-3})
100	218	7	27.77	1.18(13)*	3.54(-1)	5.42(-10)	5.79(5)	1.82(8)	9.43(11)	8.81(12)	1.92(12)	8.32(10)
120	322	12	24.09	8.19(11)	3.64(-2)	3.28(-11)	4.38(4)	1.04(8)	2.91(11)	4.58(11)	6.82(10)	1.90(9)
140	508	21	21.9	1.43(11)	1.00(-2)	5.39(-12)	2.63(4)	5.29(7)	7.52(10)	6.03(10)	7.18(9)	4.27(8)
160	684	30.	20.45	4.78(10)	4.52(-3)	1.62(-12)	1.88(4)	3.38(7)	3.06(10)	1.56(10)	1.60(9)	2.10(7)
180	762	35	19.42	2.33(10)	2.45(-3)	7.50(-13)	1.64(4)	2.68(7)	1.68(10)	5.92(9)	5.36(8)	5.51(6)
200	828	40	18.61	1.26(10)	1.44(-3)	3.89(-13)	1.46(4)	2.21(7)	9.88(9)	2.49(9)	2.02(8)	1.66(6)
240	942	49	17.53	4.51(9)	5.87(-4)	1.31(-13)	1.22(4)	1.59(7)	3.92(9)	5.44(8)	3.61(7)	1.99(5)
300	1,049	58	16.66	1.34(9)	1.94(-4)	3.70(-14)	1.03(4)	1.10(7)	1.24(9)	7.92(7)	4.06(6)	1.33(4)
340	1,076	62	16.31	5.73(8)	9.99(-5)	1.82(-14)	9.65(3)	9.14(6)	6.38(8)	2.51(7)	1.09(6)	2.60(3)
400	1,083	65	15.90	2.61(8)	3.90(-5)	6.89(-15)	9.05(3)	7.19(6)	2.49(8)	4.85(6)	1.68(5)	2.50(2)
500	1,083	71	15.08	5.97(7)	8.92(-6)	1.49(-15)	8.23(3)	4.92(6)	5.44(7)	3.40(5)	8.02(3)	5.58
600	1,083	82	13.44	1.59(7)	2.37(-6)	3.54(-16)	7.46(3)	3.40(6)	1.24(7)	2.56(4)	4.18(2)	
700	1,083	106	10.65	5.35(6)	7.99(-7)	9.46(-17)	6.82(3)	2.38(6)	2.96(6)	2.08(3)	2.38(1)	
800	1,083	152	7.64	2.42(6)	3.61(-7)	3.06(-17)	6.25(3)	1.68(6)	7.34(5)	1.82(2)	1.46	
900	1,083	213	5.62	1.39(6)	2.08(-7)	1.30(-17)	5.74(3)	1.19(6)	1.89(5)	1.69(1)		
1,000	1,083	265	4.65	9.14(5)	1.37(-7)	7.05(-18)	5.28(3)	8.58(5)	5.06(4)	1.68		
1,400	1,083	344	3.97	2.54(5)	3.80(-8)	1.68(-18)	3.87(3)	2.50(5)	3.62(2)			
2,000	1,083	412	3.85	5.15(4)	7.69(-9)	3.29(-19)	2.56(3)	4.89(4)				
4,000	1,083	998	2.44	1.74(3)	2.59(-10)	7.02(-21)	9.04(2)	8.32(2)				
6,000	1,083	2,618	1.32	4.92(2)	7.35(-11)	1.08(-21)	4.39(2)	5.28(1)				
10,000	1,083	5,892	1.03	1.70(2)	2.54(-11)	2.90(-22)	1.68(2)	1.60				

*Denotes n = 1.18×10^{13} particles cm^{-3}.

Table 11-11. Upper atmosphere neutral properties versus altitude near sunspot maximum (spring or fall; latitude 45 degrees; t = 5 hours; diurnal minimum).

Altitude h(km)	Temp. T(°K)	Scale ht. (km)	Mean mol. wt.	Concent. $n(cm^{-3})$	Pressure (dyne cm^{-2})	Density (gm cm^{-3})	Constituent Concentrations					
							$n(H)(cm^{-3})$	$n(He)(cm^{-3})$	$n(O)(cm^{-3})$	$n(N_2)(cm^{-3})$	$n(O_2)(cm^{-3})$	$n(A)(cm^{-3})$
100	207	7	26.64	1.22(13)*	3.49(-1)	5.40(-10)	9.10(5)	1.86(8)	2.05(12)	8.36(12)	1.71(12)	9.70(10)
120	249	12	19.01	1.01(12)	3.48(-2)	3.20(-11)	6.92(4)	6.76(7)	7.69(11)	2.15(11)	2.76(10)	1.26(9)
140	399	20	17.41	1.70(11)	9.36(-3)	4.91(-12)	4.02(4)	3.16(7)	1.51(11)	1.76(10)	1.69(9)	4.33(7)
160	567	30	16.82	5.38(10)	4.21(-3)	1.50(-12)	2.70(4)	1.84(7)	5.02(10)	3.43(9)	2.66(8)	4.69(6)
180	651	35	16.53	2.55(10)	2.30(-3)	7.01(-13)	2.27(4)	1.39(7)	2.44(10)	1.05(9)	7.24(7)	9.54(5)
200	707	39	16.36	1.37(10)	1.34(-3)	3.73(-13)	2.02(4)	1.12(7)	1.33(10)	3.87(8)	2.34(7)	2.37(5)
240	802	45	16.16	4.69(9)	5.20(-4)	1.26(-13)	1.68(4)	7.83(6)	4.62(9)	6.68(7)	3.19(6)	2.03(4)
300	880	51	16.02	1.24(9)	1.51(-4)	3.31(-14)	1.42(4)	5.25(6)	1.23(9)	7.08(6)	2.49(5)	8.57(2)
340	894	53	15.95	5.68(8)	7.00(-5)	1.50(-14)	1.33(4)	4.27(6)	5.62(8)	1.82(6)	5.27(4)	1.23(2)
400	894	54	15.81	1.85(8)	2.28(-5)	4.85(-15)	1.24(4)	3.21(6)	1.81(8)	2.51(5)	5.49(3)	7.31
500	894	58	15.21	3.09(7)	3.81(-6)	7.79(-16)	1.10(4)	2.03(6)	2.88(7)	1.00(4)	1.39(2)	
600	894	68	13.44	6.13(6)	7.57(-7)	1.37(-16)	9.86(3)	1.39(6)	4.83(6)	4.40(2)	3.89	
700	894	94	9.99	1.70(6)	2.10(-7)	2.82(-17)	8.85(3)	8.41(5)	8.50(5)	2.11(1)		
800	894	146	6.60	7.17(5)	8.85(-8)	7.85(-18)	7.96(3)	5.51(5)	1.57(5)	1.10		
900	894	204	4.85	4.03(5)	4.98(-8)	3.25(-18)	7.18(3)	3.66(5)	3.05(4)			
1,000	894	241	4.21	2.58(5)	3.19(-8)	1.80(-18)	6.50(3)	2.45(5)	6.17(3)			
1,400	894	299	3.78	5.96(4)	7.35(-9)	3.74(-19)	4.47(3)	5.51(4)	1.56(1)			
2,000	894	408	3.21	1.04(4)	1.28(-9)	5.53(-20)	2.72(3)	7.65(3)				
4,000	894	1,679	1.20	8.40(2)	1.04(-10)	1.67(-21)	7.85(2)	5.52(1)				
6,000	894	2,810	1.02	3.36(2)	4.16(-11)	5.68(-22)	3.35(2)	1.96				
10,000	894	5,002	1.00	1.10(2)	1.36(-11)	1.82(-22)	1.10(2)					

*Denotes $n = 1.22 \times 10^{13}$ particles cm^{-3}.

Table 11-12. Upper atmosphere neutral properties versus altitude near sunspot maximum (spring or fall; latitude 45 degrees; t = 14 hours; diurnal maximum).

Altitude h(km)	Temp. T(°K)	Scale ht. (km)	Mean mol. wt.	Concent. $n(cm^{-3})$	Pressure (dyne cm^{-2})	Density (gm cm^{-3})	Constituent Concentrations					
							$n(H)(cm^{-3})$	$n(He)(cm^{-3})$	$n(O)(cm^{-3})$	$n(N_2)(cm^{-3})$	$n(O_2)(cm^{-3})$	$n(A)(cm^{-3})$
100	220	7	27.85	1.18(13)*	3.57(-1)	5.43(-10)	5.99(5)	3.14(8)	8.69(11)	8.88(12)	1.92(12)	8.00(10)
120	339	12	24.82	8.09(11)	3.79(-2)	3.33(-11)	4.13(4)	2.80(8)	2.40(11)	4.92(11)	7.43(10)	2.01(9)
140	549	21	22.84	1.42(11)	1.08(-2)	5.40(-12)	2.62(4)	1.40(8)	6.40(10)	6.96(10)	8.52(9)	1.51(8)
160	746	31	21.46	4.86(10)	5.01(-3)	1.73(-12)	1.72(4)	8.97(7)	2.70(10)	1.94(10)	2.07(9)	2.78(7)
180	846	37	20.40	2.38(10)	2.78(-3)	8.06(-13)	1.48(4)	7.06(7)	1.52(10)	7.78(9)	7.41(8)	8.00(6)
200	948	44	19.54	1.30(10)	1.70(-3)	4.20(-13)	1.29(4)	5.71(7)	9.13(9)	3.47(9)	2.99(8)	2.64(6)
240	1,133	57	18.30	4.87(9)	7.61(-4)	1.48(-13)	1.03(4)	4.03(7)	3.88(9)	8.87(8)	6.46(7)	4.05(5)
300	1,317	71	17.16	1.65(9)	2.99(-4)	4.69(-14)	8.42(3)	2.81(7)	1.43(9)	1.74(8)	1.03(7)	4.23(4)
340	1,370	78	16.65	9.25(8)	1.75(-4)	2.56(-14)	7.84(3)	2.38(7)	8.29(8)	6.88(7)	3.57(6)	1.14(4)
400	1,390	83	16.01	4.33(8)	8.30(-5)	1.15(-14)	7.38(3)	1.95(7)	3.94(8)	1.89(7)	8.17(5)	1.81(3)
500	1,391	92	14.95	1.38(8)	2.64(-5)	3.41(-15)	6.85(3)	1.45(7)	1.20(8)	2.38(6)	7.66(4)	9.40(1)
600	1,391	105	13.43	4.94(7)	9.49(-6)	1.10(-15)	6.25(3)	1.09(7)	3.82(7)	3.19(5)	7.70(3)	5.32
700	1,391	129	11.27	2.08(7)	3.99(-6)	3.89(-16)	5.82(3)	8.24(6)	1.25(7)	4.52(4)	8.26(2)	
800	1,391	169	8.83	1.05(7)	2.02(-6)	1.54(-16)	5.43(3)	6.28(6)	4.22(6)	6.77(3)	9.42(1)	
900	1,391	226	6.80	6.30(6)	1.21(-6)	7.12(-17)	5.08(3)	4.83(6)	1.47(6)	1.07(3)	1.14(1)	
1,000	1,391	288	5.48	4.26(6)	8.19(-7)	3.88(-17)	4.75(3)	3.73(6)	5.27(5)	1.77(2)	1.46	
1,400	1,391	430	4.09	1.44(6)	2.77(-7)	9.79(-18)	3.71(3)	1.43(6)	1.13(4)			
2,000	1,391	512	3.98	4.04(5)	7.76(-8)	2.67(-18)	2.68(3)	4.02(5)	7.04(1)			
4,000	1,391	821	3.81	1.80(4)	3.46(-9)	1.14(-19)	1.16(3)	1.68(4)				
6,000	1,391	1,362	3.27	2.61(3)	5.01(-10)	1.42(-20)	6.40(2)	1.97(3)				
10,000	1,391	4,012	1.94	4.14(2)	7.96(-11)	1.34(-21)	2.85(2)	1.30(2)				

*Denotes $n = 1.18 \times 10^{13}$ particles cm^{-3}.

11.3.2 Ionosphere

The principal ions formed in the E-region (85 to 140 kilometers) of the ionosphere are N_2^+, O_2^+, and O^+. The N_2^+ ions rapidly recombine with free electrons and also may react with oxygen, so that the concentration of N_2^+ is small. Ion-atom exchange reactions of the type:

$$X^+ + YZ = XY^+ + Z \qquad (11\text{-}2)$$

proceed very rapidly so that reactions of O^+ with O_2 and N_2 quickly remove O^+ ions and produce either NO^+ or O_2^+.

The dominant ions in the F_1 region (140 to 200 kilometers) are NO^+ and O_2^+ near the lower altitude boundary, with a gradual transition to O^+ as the principal ion at the upper boundary. O^+ becomes the dominant ion because of the rapid decrease with altitude of the neutral molecular constituents that otherwise would tend to eliminate O^+ by the reaction shown in Equation 11-2. In the F_2 region (200 to 800 kilometers), O^+ ions predominate, with significant numbers of N^+ ions also present.

Figure 11-8 shows day and night average electron concentrations from 50 to 1,000 kilometers for minimum and maximum solar activity at geomagnetic latitudes from 30 to 40 degrees (Reference 22). During the day, several distinct ionospheric "layers" (D, E, F_1, F_2) are recognized. From a comparison of the day and night curves in Figure 11-8, one can infer that large diurnal effects occur in the lower ionosphere. The F_1 and F_2 layers merge at night, and a depression in electron concentration appears between the E- and F-regions. The depth of this "valley" is quite variable with time and local conditions. The D-layer electron concentrations also decrease drastically at night except in a narrow region near 100-kilometer altitude. The electron concentration essentially is equal to the total ion concentration everywhere throughout the ionosphere.

The helium ion begins to become dominant between 800 and 1,400 kilometers, depending on atmospheric temperature. Likewise, protons become the dominant ion above some altitude that varies between 1,400 and 4,000 kilometers. Thus, two transition regions occur from oxygen to helium ions and from helium to hydrogen ions in the upper ionosphere. The transition regions can be expected to be quite variable, depending upon the latitude, local time, sunspot cycle, and magnetic disturbances.

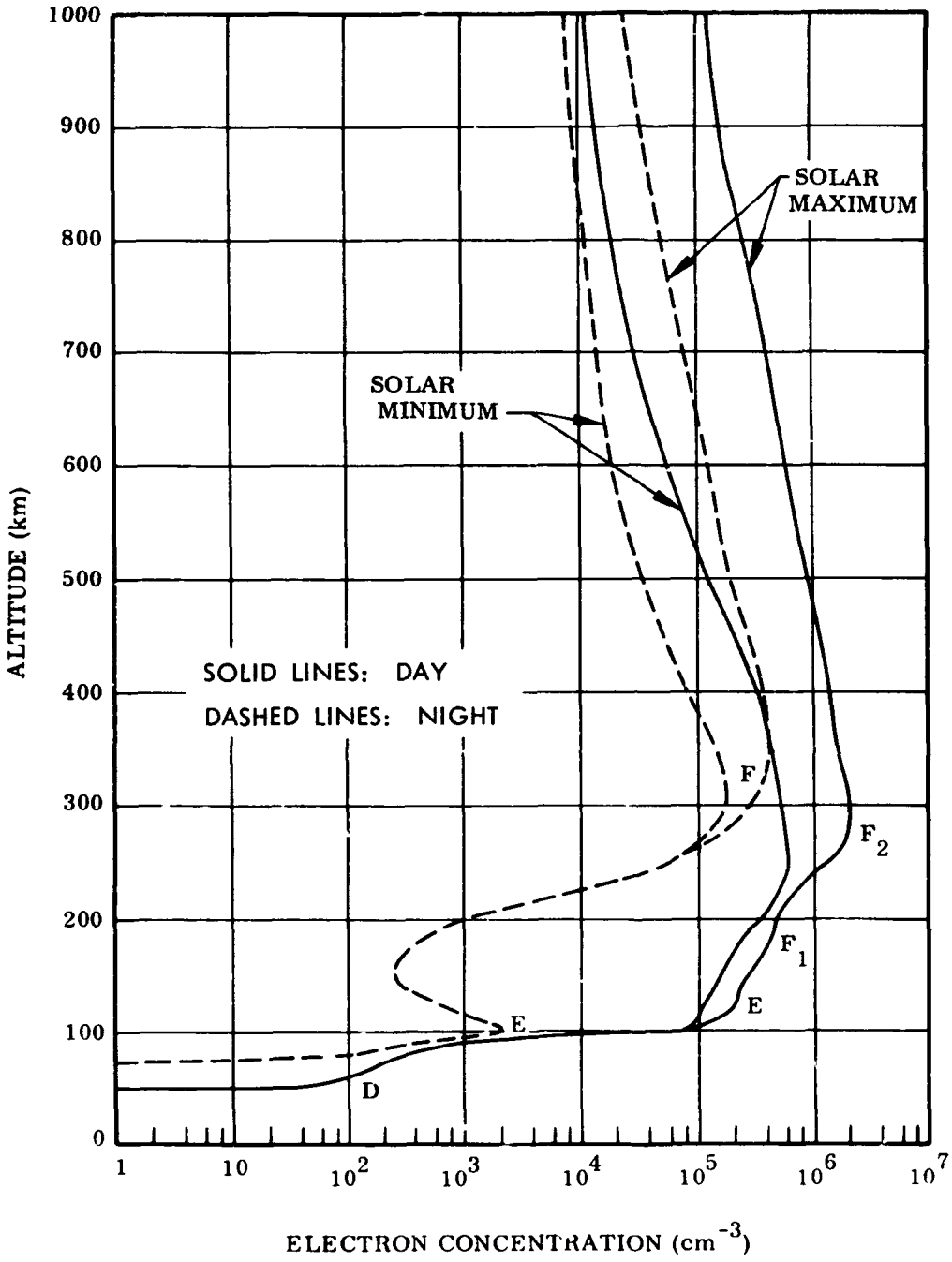

Figure 11-8. Distributions of free electrons in atmosphere at extremes of diurnal and solar cycle variations.

During solar minimum, He^+ is never dominant; in the polar regions, N^+ concentrations generally may exceed He^+ concentration (Reference 23). The outer portion of the earth's atmosphere (extending 20,000 to 50,000 kilometers above the earth's surface) consists mainly of protons. The protons predominate over the H atoms in the earth's outer atmosphere because the confining effect of the earth's magnetic field makes their rate of escape much less than for the neutral hydrogen atoms.

The distribution of the thermal positive ions H^+ and He^+ in the magnetosphere has been determined from OGO-1 measurements made in 1964 and 1965 (Reference 24). The distribution was found to be controlled strongly by the geomagnetic field. The main feature of the field is a region of toroidal form, the plasmasphere, bounded roughly by the $L = 4.5$ shell within which the ion concentration decreases slowly with increasing altitude from an initial value of about 2×10^3 ions per cubic centimeter at 2,000 kilometers.

At the boundary of the plasmasphere, which is compressed during periods of high magnetic activity (Reference 25), a sharp decrease in the ion concentration by a factor of 10 or more corresponding to an altitude increase of less than 1 R_E at the equator is observed. The concentration beyond the boundary, the plasmapause, is therefore less than about 10 ions per cubic centimeter. The plasmapause appears to conform to local magnetic field lines. Within the plasmasphere, the concentrations of H^+ and He^+ have a constant ratio of 300 to 1, indicating departure from simple diffusive equilibrium. Measurements made by OGO-3 generally confirm these properties of the plasmasphere (Reference 25). Also, significant correlation of the OGO-3 results with whistler observations of the magnetospheric thermal electron distribution exists.

Three typical H^+ distributions are shown in Figure 11-9 (Table 11-13) for geomagnetic latitudes 0°N, 35°N, and 40°N, respectively. The H^+ concentration in the altitude range from 2,000 to 5,000 kilometers is about 2×10^3 to 5×10^3 ions per cubic centimeter. The concentration decreases gradually until the plasmapause is reached. Beyond the edge of the plasmapause, the concentration exhibits a sharp decrease.

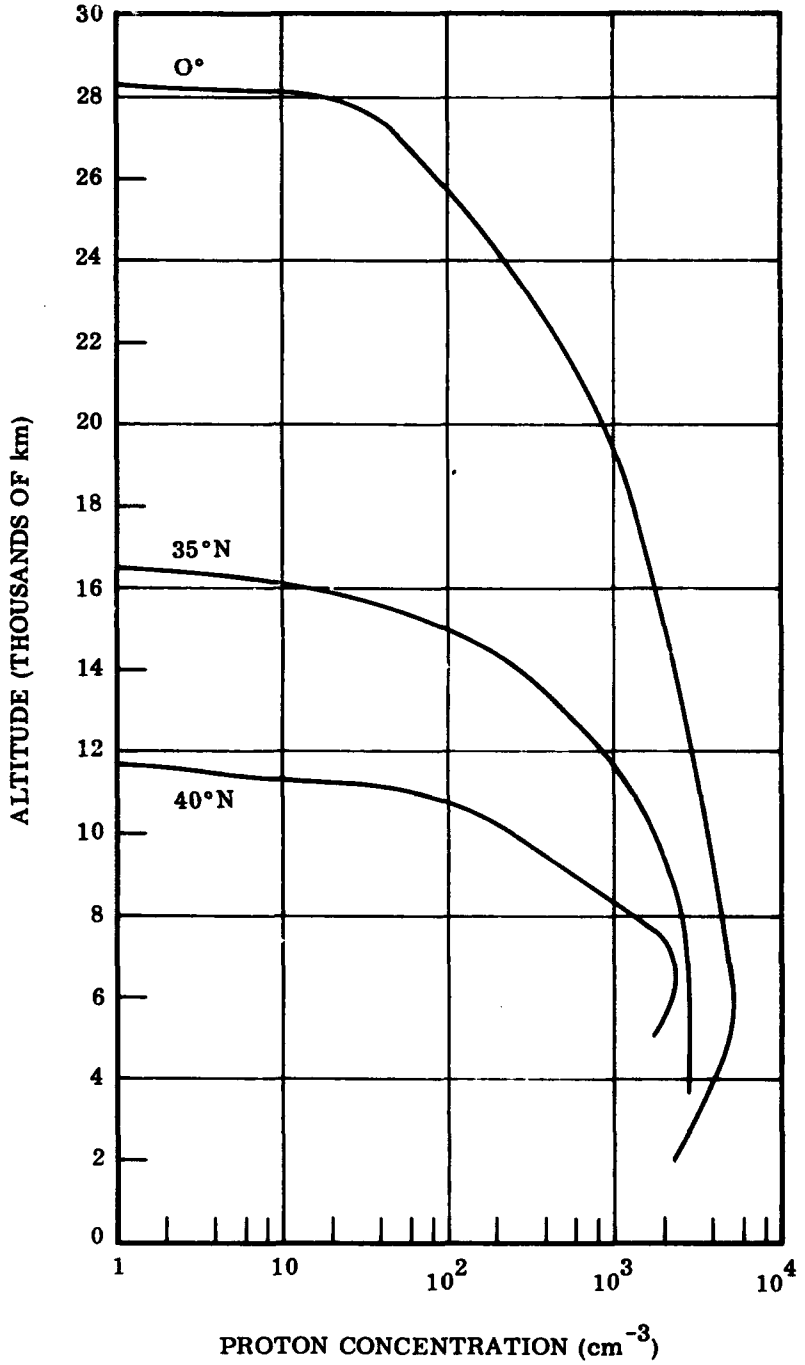

Figure 11-9. Typical measurements of proton distributions at geomagnetic latitudes of 0°N, 35°N, and 40°N from 2,000 to 30,000 kilometers.

Table 11-13. Proton concentration versus altitude and geomagnetic latitude.

Altitude (km)	0° (cm^{-3})	35°N (cm^{-3})	40°N (cm^{-3})
2,000	2.3(3)[a]	—	—
3,000	3.1(3)	—	—
4,000	3.8(3)	2.8(3)	—
5,000	5.2(3)	2.8(3)	1.7(3)
6,000	5.1(3)	2.7(3)	2.3(3)
7,000	4.6(3)	2.6(3)	2.3(3)
8,000	4.0(3)	2.5(3)	1.3(3)
9,000	3.8(3)	2.1(3)	5.2(2)
10,000	3.5(3)	1.5(3)	2.2(2)
11,000	3.1(3)	1.3(3)	6.1(1)
12,000	2.9(3)	8.0(2)	—
14,000	2.3(3)	2.8(2)	—
16,000	1.7(3)	1.5(1)	—
18,000	1.3(3)	—	—
20,000	9.0(2)	—	—
22,000	4.9(2)	—	—
24,000	2.1(2)	—	—
26,000	5.6(1)	—	—
28,000	1.8(1)	—	—

Note:

[a]The parenthesized numbers indicate powers of 10; e.g., 2.3(3) = 2.3×10^3 cm^{-3} and 1.8(1) = 1.8×10 cm^{-3}.

11.4 COMPILATION OF AVAILABLE COMPUTER PROGRAMS

Section 11.4 contains selected bibliographies of useful computer programs relevant to the subject of trapped radiation. Despite the care taken in the compilation, the list is probably not exhaustive. Moreover, many very useful special purpose codes that are not included have been developed.

"Computer Programs for the Computation of B and L (May 1966)"

A. Hassitt and C.E. McIlwain
DATA USERS' NOTE
National Space Science Data Center, NASA, Greenbelt, Maryland

NSSDC 67-27
May 1967

This NOTE describes a series of computer codes, their source listings, and some sample outputs that can be used to calculate values of B and L. As of June 1968, these codes* were used and distributed by the National Space Science Data Center.

1. INVAR is a routine that controls the use of other subroutines in computing the values of B and L at a point P, given the latitude, longitude, and altitude of the point P. The last revision to this routine is dated December 1965.
2. START is a routine required by INVAR to initiate the solution of the differential equations for a line of force. It requires the use of the routine NEWMAG. The latest revision to this routine is dated December 1965.
3. LINES is a routine required by INVAR to continue the solution initiated by START. This routine requires the use of the routine NEWMAG. The latest revision to this routine is dated May 1965.
4. INTEG is a routine required by INVAR to carry out the action integral I along a line of force between mirror points. This routine has not been changed since June 1963.

*With a few exceptions, the first five routines mentioned are identical to those described in "Useful High-Altitude Nuclear-Effects Computer Programs," Vol 2, January 1964, DASA 1311-2, RM 63TMP-28.

5. CARMEL is a routine required by INVAR to compute the value of L given the values of B and I. This routine has not been changed since June 1963.

6. NEWMAG is a newer, faster, more versatile version of the routine MAGNET and FIELD (p. 11-36, p. 11-38), both of which compute the magnetic field. NEWMAG contains one particular model of the earth's field. Since it may be necessary to use other models, several additional routines are given whose sole purpose is to take the coefficients of any model of the field and produce data cards that are necessary for and directly insertable into NEWMAG. These routines are NUFLDG, GETMX, and FIELD.

"A Computational Model of the Geomagnetic Field"

James V. Herod, Captain, U.S. Air Force
Kirtland Air Force Base, New Mexico

AFWL-TR-66-89
September 1966

The computer programs and subroutines described in this report provide a computational model that will trace the magnetic field line passing through a point in space by following the direction of the gradient of the geomagnetic field potential. The point may be specified by giving the altitude, latitude, and longitude or the field intensity, shell, and longitude of the point. The capability for tracing a single field line, a single shell, or a sequence of shells is provided. Most of the currently published spherical harmonic expansions for the geomagnetic field may be used. FORTRAN listings are given for these routines: SEARCH, INVAR*, START*, LINES*, INTEG*, CARMEL*, NEWMAG†, EQUAT, INSECT, BLRING, FIELDC, FIELD†, FINAL, SPLINE, and YSPLN.

"Computation of the Main Geomagnetic Field
from Spherical Harmonic Expansions"

Shirley Hendricks Cain
DATE USER'S NOTE
National Space Science Data Center, NASA, Greenbelt, Maryland

NSSDC 68-11
May 1968

In this NOTE, the latest versions of five constantly used computer subroutines are discussed and presented by way of FORTRAN IV listings. These subroutines are:

1. FIELDG initializes constants, reads coefficients, and performs coordinate transformations.

2 and 3. FIELD has two versions (one executes more rapidly; the other occupies less storage). Each of the versions computes the field components.

4. FIELD has a routine that generates the coding for the fast version.

5. A conversion routine changes Schmidt normalized coefficients to gauss normalization and vice versa.

These subroutines are very similar to others reported under the same NAME. The only differences are subtitle changes and additions in order to accomplish more versatility.

"Atmospheric Density Calculations for Charged Particles Trapped in the Earth's Magnetic Field"

A.R. Sims and H.S. Porjes
Aerospace Corporation
El Segundo, California

Report No. TOR-469 (5260-20)-1
January 1965

This report discusses a computer program that computes the atmospheric density experienced by charged particles that mirror on surfaces of constant-L. Inputs to the program consist of specifying a point on an L-shell and a list of minimum mirror point altitudes and a list of longitudes. The program computes the average density experienced by a charged particle during the course of one revolution about the earth. These calculations are used for particles mirroring at each of the given mirror altitudes, based upon density samples taken along the lines of force having approximate equatorial longitudes coinciding with those of the list. As of 1965, this program had the

*These subroutines are modified slightly and implemented versions of McIlwain's program INVAR mentioned elsewhere in this section.
†These subroutines are slightly modified versions of those listed in "Computation of the Main Geomagnetic Field from Spherical Harmonic Expansions" by J.C. Cain et al, mentioned elsewhere.

capability of carrying out density calculations for 66 particles simultaneously for each given value of L and for 40 sample lines of force. A FORTRAN listing of the code may be found in the report.

"A Computational Model for Geomagnetically Trapped Particle Shells and Kinematic Parameters"

Juan G. Roederer
Goddard Space Flight Center, Greenbelt, Maryland
James V. Herod, Captain, U.S. Air Force
Kirtland Air Force Base, New Mexico

AFWL-TR-66-78
September 1966

This report describes a computer code that calculates a model for geomagnetically trapped particle shells and the associated kinematic parameters. Also included is the calculation of longitude-dependent drift velocities and bounce paths. Flow charts, FORTRAN listings, and input data instructions are given.

"A Proposal for Trapped Particle Flux Mapping in the Outer Magnetosphere"

Juan G. Roederer
Goddard Space Flight Center, Greenbelt, Maryland

NASA TM X-55615
X-640-66-313
June 1966

This report describes a computer code named ORGAN that can be used for a two-dimensional mapping of directional fluxes of energetic particles trapped in the outer magnetosphere. G. Mead's model of the magnetospheric field is used. The main function of the code is to find, on a fixed reference meridian, the field line, equatorial pitch angle, and other parameters of the shell generated by the particles in their longitudinal drift, provided they are stably trapped. A series of curves that can be used for a first rough, graphical attempt of flux mapping is given. FORTRAN listings of the code are presented in the document.

"A Code to Predict Trapped Radiation Resulting from a High-Altitude Nuclear Detonation"

R. E. Herman, Captain, U.S. Air Force
G. D. Guthrie, Captain, U.S. Air Force
Kirtland Air Force Base, New Mexico

AFWL-TR-65-81
June 1965

This report describes a computer code that calculates the resultant electron flux from a high-altitude nuclear detonation. Included in the code are calculations for early (seconds) to late (days) times after the detonation. In the early time calculations, an electron flux map is constructed as a function of time and the coordinates B, L, and longitude. The late-time electron flux map uses time and B, L. Phenomena that also are treated in some detail are debris motion, electron injection, electron drift, loss-rate formulation, and energy spectra. Flow charts and FORTRAN listings are provided in the report.

"Geomagnetic Trapping of Fission Debris Beta Rays: A Computer Code"

R. W. Hendrick, Jr.
General Electric—TEMPO, Santa Barbara, California

RM 65TMP-20
DASA 1660
April 1965

This report describes a computer program that provides a means for predicting the number and location of electrons injected into the earth's radiation belts as a result of fission debris beta decay.

The program is a Monte Carlo code that follows a discrete number of decaying nuclei. A series of beta decay chains are entered into the program via input cards and the history of atoms is followed as they progress down the chain. All the beta emissions are recorded. The first phase of the particle motion is assumed to be controlled by the initial fireball dynamics. Because of recoil following beta emission, the atom may escape the fireball and move independently under the influence of the magnetic field and gravity. The atom's motion is followed until the last beta emission in the particular decay chain or until it falls below a specified altitude where collisions with the atmosphere become dominant and it becomes "deposited."

All beta decays are recorded (time of decay, location in B, L space, and energy) as are depositions (time, location in L, and nuclei number in input decay chain list).

After all the atoms specified have been followed through their chains, the injection events are sorted to give various summaries. The data are put on plot tapes for a Benson-Lehner plotter as well as printed. The depositions are sorted and the activity of the local and conjugate sources computed as functions of time. The data are placed on plotting tapes and printed. Flow charts, FORTRAN listings, and input data instructions are included in the report.

"Theoretical Investigation of Geomagnetically Trapped Electrons from High-Altitude Nuclear Explosives"

A. D. Anderson, G. E. Crane, W. E. Francis, L. L. Newkirk, and M. Walt
Lockheed Missiles and Space Company, Palo Alto, California

LMSC 895355
DASA 1480
June 1964

Among the several topics presented in this report, two computer programs are discussed. These programs are

1. The VBAR program computes the angular drift velocity of a geomagnetically trapped particle at a given point in space specified by the altitude, latitude, and longitude. The velocity is expressed in terms of the ratio p/T, where p is the momentum of the particle and T is the total bounce period of the particle. Neither p nor T is evaluated by the program. The magnetic field is represented in the program by the 48-term spherical-harmonic expansion proposed by Jensen and Cain. No FORTRAN listing of this program is given.
2. The DAV program determines drift-weighted averages of the atmospheric particle concentrations encountered by a geomagnetically trapped particle along a given contour of constants B and L. Results for the given contour in both hemispheres are averaged. Up to 10 (B, L) values may be considered. Input to the program consists of (1) altitudes specified along the given contour at uniform intervals as small as 1 degree in longitude, (2) relative values of the angular drift velocities at the specified altitudes, and (3) a table of particle concentrations as a function of altitude for up to 12 atmospheric constituents. No FORTRAN listing of this program is given.

"Geomagnetically Trapped Radiation"

M. B. Baker
Space Sciences Department
Douglas MSSD, Huntington Beach, California

SM-47635
October 1964

This report describes the basis upon which the computer program OGRE was developed. OGRE, which is an acronym for Orbiting Geophysical Radiation Environment, is designed to compute the exposure of a satellite or probe to trapped protons and electrons and to a solar cosmic ray event. The code, which is being updated continually, has four possible modes of operation. These are

1. A table of geographic positions can be an input, and the fluxes at those positions the resulting output.
2. A previously calculated ephemeris for a vehicle can be an input. The fluxes at each position and the total time-integrated fluxes versus energy produced is the output.
3. The orbital elements of an elliptically orbiting satellite can be an input and the total fluxes and energy spectra produced is the output.
4. An approximate method for determining the total integrated flux encountered by a satellite that is in orbit long enough that its path has covered fairly well all the regions of space available to it.

Other features of the program are

1. It can calculate variations of proton and electron intensity as a function of solar cycle.
2. It can calculate the intensity of input solar cosmic ray events, including cutoff effects.
3. It can calculate trapped proton dose as a function of shield thickness.
4. Different model environments can be used as inputs.
5. Any orbital elements for any trajectory can be used as inputs.

"TRECO, An Orbital Integration Computer Program for Trapped Radiation"

A. B. Lucero
DATA USER'S NOTE
National Space Science Data Center, NASA, Greenbelt, Maryland

NSSDC 68-02
January 1968

This NOTE describes an operational computer program that computes the flux and energy spectra encountered in sateilite orbits passing through the earth's geomagnetically trapped radiation environment. FORTRAN IV listings are given for all required subroutines.

Program TRECO was designed so that, for a given model environment (an input quantity), either a new orbit could be generated or previously generated orbit coordinates stored on magnetic tape or punched cards could be input. In either case, as each orbit coordinate is fully determined, the flux at the energy of the flux map is found, and the flux is computed for each energy requested. Then each of these fluxes is multiplied by the time interval in seconds, and the results are summed for each energy. At this point, detailed output is performed. The radiation environment can be described by up to 50 B-values per L , for as many as 60 L-values. The orbital radiation is approximated by interpolations of the model environment in B, L space. The geomagnetic field is computed through use of Hassitt and McIlwain's INVAR PACKAGE.

"Computer Codes for the Evaluation of Space Radiation Hazards—Vol 2, Van Allen Radiation"

Wing U. Wong
The Boeing Co., Seattle, Washington

D2-90418-2
N64-29364 (NASA accession number)
1964

The computer program discussed in this report computes the flux and the total time-integrated fluxes of protons and electrons for vehicle trajectories along the Van Allen Radiation Belt. For study purposes, this belt is differentiated into four separate belts:

1. High-energy proton belt for protons with energy greater than 20 MeV
2. Low-energy proton belt for protons with energy less than 20 MeV
3. AFSWC threat electron belt, which is a theoretical belt
4. Electron belt as it existed on 20 October 1962.

These belts are represented by spatial flux maps that are read in as inputs to the program and, hence, can be modified or changed to incorporate the latest data available. Flux values are given as functions of B and L. At each point of calculation, the program prints out the input quantities (or generated trajectory points), the corresponding B, L coordinates, the individual values of flux, the product of flux and time increment, and the total integrated fluxes for each of the flux belts. FORTRAN listings of the program, as well as instructions for input data preparation, are given in the report.

"A Computer Program Incorporating the Whitaker Threat Model into the Space Radiation Environment and Shielding Computer Program"

J.A. Barton, W.R. Doherty, and P.G. Hahn
The Boeing Company, Seattle, Washington

AFWL-TR-65-10
May 1965

As indicated by the title, the computer code described in this document is a modified version of the Trajectory and Environment Code* also mentioned in this section. This modified version incorporates the transient radiation environment that is artificially produced by high-altitude nuclear detonations. To accomplish this, the injection model was modified to treat the effect of extended sources at early times, the emission-rate spectrum was extrapolated to 0.5 MeV, and the spectrum of the electrons impinging on the vehicle was decomposed into energy bins suitable for dose rate and dose calculations. A description of the methods used and the resulting computer code is given.

*"Computer Codes For Space Radiation Environment and Shielding," The Boeing Co., Seattle, Washington, August 1964, WL-TDR-64-71, Vol I and II.

"On the Adiabatic Motion of Energetic Particles in a Model Magnetosphere"

Juan G. Roederer
Goddard Space Flight Center, Greenbelt, Maryland

NASA TM X-55614
X-640-66-304
July 1964

This report discusses the basis upon which the computer code SPLIT was developed. This code, which also is described, was set up to determine particle shells in the meadosphere (Mead's model of the magnetosphere), to study shell splitting and longitude dependence of drift velocities and equatorial pitch angles, and to analyze the evolution of a system of particle shells in a time-dependent case. The code consists of these main parts:

1. Field line geometry
2. Shell geometry
3. Third invariant (flux)
4. Nonadiabatic compression
5. Shell deformation during adiabatic time variations.

FORTRAN listings are given also.

"Orbital Calculations and Trapped Radiation Mapping"

M. O. Burrell and J. J. Wright
George C. Marshall Space Flight Center, Huntsville, Alabama

NASA TM X-53406
8 March 1966

This technical memorandum discusses the Burrell Orbital Flux and Energy Spectra (BOFES) code, which gives an accurate calculation of the orbital position of earth satellites and simultaneously computes the geomagnetic B, L coordinates of the satellite. The code utilizes the B, L coordinates to determine the radiation fluxes and energy spectra at any point of the orbit. The code allows the complete mapping of the trapped radiation field traversed by the spacecraft on any feasible elliptical or circular orbit around the earth and out as far as the lunar radius.

Two versions of the code exist. These are the BOFES Electron Code and the BOFES Proton Code. Input data instructions are given in the report. FORTRAN listings and source decks are available from the authors. Their present address is Space Sciences Laboratory, R-SSL-NR, Redstone Arsenal, Huntsville, Alabama.

"Computer Codes for Space Radiation Environment and Shielding"

The Boeing Company
Seattle, Washington

WL-TDR-64-71, Vol I and II
August 1964

Volume I contains the theoretical development and numerical methods used in the generation of the computer codes. Volume II contains flow charts, FORTRAN listings, and input/output instructions. Although the programs described in these reports are devoted primarily to the shielding problem, the description of the trapped radiation environment encountered by a spacecraft in orbit is of use by itself. Sections 2 and 3 of Volume I pertain to the spacecraft trajectory and radiation environment and Section 1 of Volume II describes and lists the Trajectory and Environment Code, which is used to calculate proton and electron flux encountered by the spacecraft. The general procedure is to calculate trajectory points and to compute radiation flux at these points.

Trajectory points may be given as input data or, if initial conditions are given, they may be generated for circular, elliptic, or Hohmann transfer orbits (Volume I). Given a description of the orbit and the point of injection, subsequent trajectory points are calculated as a function of time, using orbital flight equations. The trajectory points are converted to McIlwain's geomagnetic coordinates (B, L and R, λ). The B, L representation is necessary for consistency with flux map data; the R, λ representation is used only for plotting.

Proton or electron flux at each point is determined by consulting a table and making an interpolation. Numerical integration (in conjunction with an interpolation scheme on B and L) gives a time-integrated flux for each point. The integral is tested to determine the optimum increment for computing trajectory points in the particular region of the flux map with which the current computation is concerned. This test is giverned by accuracy and minimum increment criteria that are input to the program. A table consultation and interpolation on an array of spectral coefficients determines the

spectral coefficients for the point. The flux at the point, dose conversion factors, and the spectral coefficients are used to determine dose rate and total dose at the point.

Angular distribution is determined for each trajectory point by solution of a pitch angle distribution function. In the study of solar protons, the time and L-value associated with each point are used to determine the flux. Dose information also may be determined.

"A Computer Program to Calculate Artificial Radiation Belt Decay Factors"

E. G. Stassinopoulos
Goddard Space Flight Center, Greenbelt, Maryland

NASA TN D-2874
July 1965

In this technical NOTE, the computer subroutine DECAY is described and a FORTRAN listing presented. This subroutine was written as part of an orbital flux code for calculating omnidirectional, vehicle-encountered fluxes. By means of this code, anticipated fluxes at any epoch may be predicted from known radiation levels at a given time.

11.5 STATISTICAL DATA ON SATELLITES

11.5.1 Data and Information

Some statistical data and information of a general nature concerning the numerous satellites launched over the years are given in Section 11.5. Both U.S. and foreign satellites are considered. Unless otherwise noted, the results apply to the time period from 1957, when the first satellites were launched, through 1969. Detailed information concerning individual spacecraft characteristics may be obtained by consulting the references listed in the Bibliography at the end of this subsection. Most of the results presented here were condensed from Reference 1.

Table 11-14 gives the number of U.S. spacecraft launched per year, listed according to various mission purposes or applications. The table includes all spacecraft (earth-orbit or earth-escape) launched successfully except a few satellites that could not be identified with any of the various classifications shown, such as tests of

Table 11-14. Number of U.S. spacecraft launched per year on various missions.

Mission	1957	1958	1959	1960	1961	1962	1963	1964	1965	1966	1967	1968	1969	Total
Applications:														
Communications		1		2	1	3	3	3	3	8	15	10	4	53
Geodesy						1		1	5	4	1	1	1	14
Navigation				2	3	1	3	3	3	4	3	1		23
Weather Observations				2	1	3	2	1	2	5	4	2	2	24
Defense Support (classified payloads)					1	32	28	37	33	42	29	26	19	247
Scientific		6	5	3	11	10	8	19	19	20	21	15	13	150
Experimental and Test			6	7	12	1	7		14	5	8		3	63
Missile and Nuclear Explosion Detection					2		2	2	2		2		2	12
Manned and Unmanned Space Flight					2	3	1		5	5	1	4	4	25
TOTAL		7	11	16	33	54	54	66	86	93	84	59	48	611

the Atlas-Centaur vehicles and targets for docking maneuvers in space. The classification assigned to certain satellites was somewhat arbitrary in a few cases where the data given did not show clearly whether the satellite had an experimental or scientific mission.

Some of the typical payloads carried on board experimental and test satellites involved instrument calibration, tests of materials and auxiliary power systems, radiation damage experiments, and engineering tests of the vehicle subsystems or components. The Discoverer satellites (26 orbited) were considered to be primarily engineering test vehicles and were assigned to this category. Defense support satellites carried classified payloads, and, hence, their respective missions could not be identified.

Table 11-15 shows the number of spacecraft launched per year by various foreign countries. The information for the Russian spacecraft was taken from Reference 2 (1970) and includes successfully launched earth-orbit and earth-escape spacecraft. Of the Russian spacecraft, 25 were launched on earth-escape missions, 12 were intended for escape missions but attained only earth orbit, and 23 were used as launching platforms in low-altitude parking orbits for higher orbit missions or earth escape. Most of the Russian spacecraft carried unannounced payloads and could not be classified according to mission purpose, as were the U.S. spacecraft. The remaining spacecraft listed in Table 11-15 for the other foreign countries were launched into earth orbit and are, primarily, scientific vehicles.

A total of 406 spacecraft were in orbit on 30 September 1969 (Reference 1). All except 27 were in earth orbit. Of the total, 311 were U.S. spacecraft and 81 were Russian spacecraft. The remainder belonged to Canada (3), ESRO (European Satellite Research Organization)(3), the United Kingdom (3), and France (5). At the end of 1969, a total of 1,848 manmade objects were in space, the majority being fragments or debris that have been identified with satellites that disintegrated in space (Reference 6, 1970). On 1 January 1969, of a total of 357 satellites in orbit, 257 earth satellites (United States and foreign) were identified as active satellites (private communication, H.J. Boissevain, Rand Corporation). In this determination, all Russian and classified U.S. satellites were considered to be active satellites since information on whether they were functioning was not available.

Table 11-15. Number of foreign spacecraft launched per year by various countries.

Country	1957	1958	1959	1960	1961	1962	1963	1964	1965	1966	1967	1968	1969	Total
Australia											1			1
Canada						1			1				1	3
ESRO												3	1	4
France									2	1	2			5
Germany													1	1
Italy								1			1			2
Russia	2	1	3	3	7	21	18	38	73	51	67	74	70	428
United Kingdom						1		1			1		1	4
TOTAL	2	1	3	3	7	23	18	40	76	52	72	77	74	448

The percentage of initial satellite orbits at launch contained in the various altitude intervals is

- 0 to 500 kilometers; 46 percent
- 500 to 1,000 kilometers; 23 percent
- 1,000 to 2,000 kilometers; 14 percent.

The results are based on all satellites, both U.S. and foreign, that were launched successfully into earth orbit from 1957 through 30 September 1969. The list shows that most of these satellites were launched into orbits close to earth, with roughly one half having orbits completely contained within the 500-kilometer altitude.

Satellites whose orbital periods are about 1,440 minutes (the rotational period of the earth) will hover above a particular longitude in so-called synchronous orbits at about 6.6 R_E. A total of 46 satellites (all U.S.), about 5 percent of the total, were launched through 30 September 1969 with initial orbits in the vicinity of 6.6 R_E. This leaves about 10 percent of the satellites with initial orbits falling in the range from 2,000 kilometers to 6.6 R_E.

Figure 11-10 is a histogram of the initial orbital inclination to the equator of all U.S. and Russian satellites that were launched into earth orbit through 30 September 1969. Not included in the figure are 16 U.S. satellites with orbital inclinations in the range 110 to 140 degrees. In Figure 11-10, the U.S. satellites were launched into orbit at inclination angles covering the range from 0 (equatorial orbits) to 90 degrees (polar orbits). A large number of U.S. satellites also were launched at greater than 90-degree inclination into retrograde orbits. The majority of U.S. satellites were launched with inclinations in the interval 70 to 110 degrees. The Russian satellites, however, were launched with inclination angles of a more limited range and clustered about 50 and 65 degrees, with no launches into retrograde orbits.

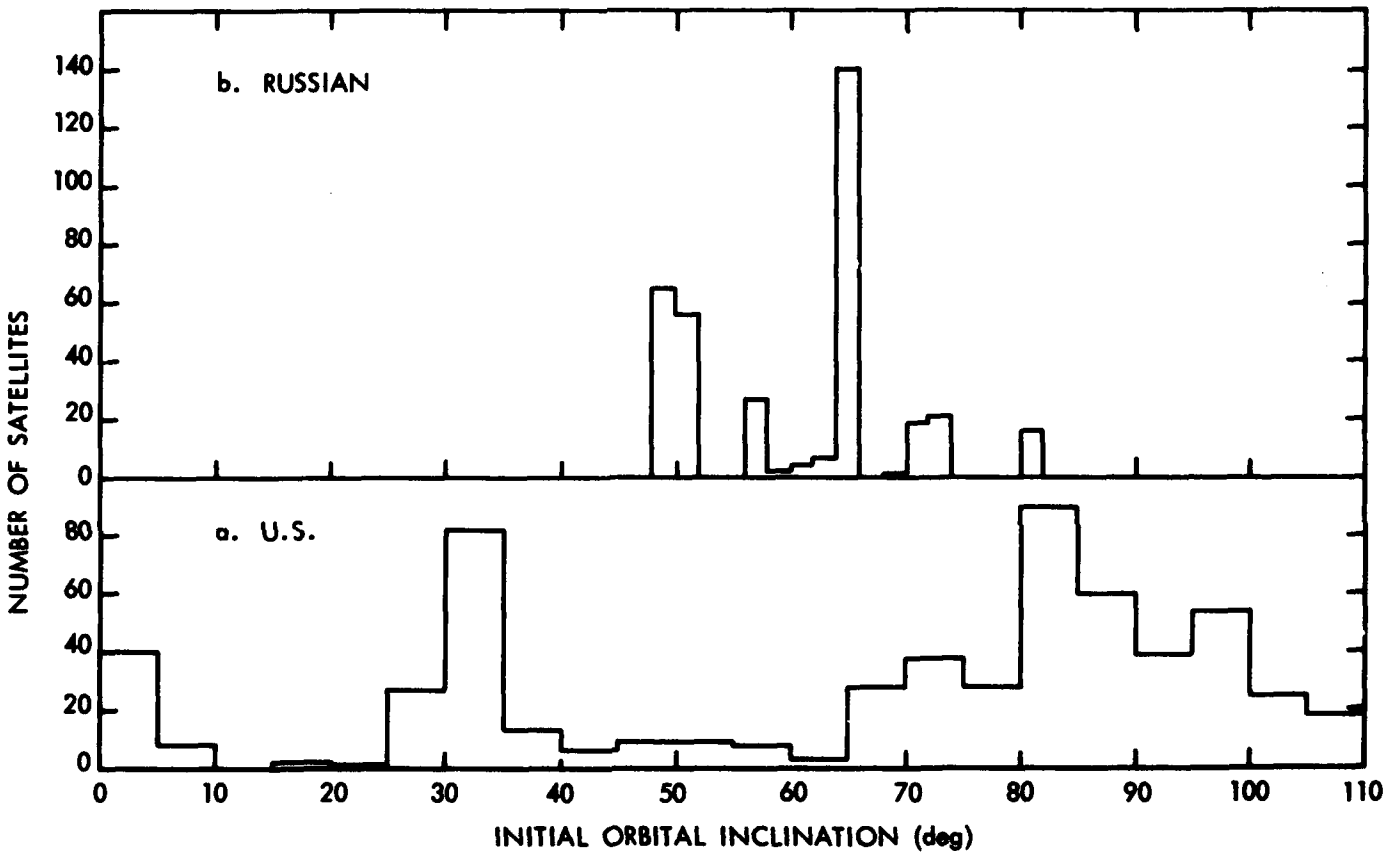

Figure 11-10. Initial orbital inclinations of U.S. and Russian satellites.

11.5.2 Bibliography

1. TRW Space Log, a log of space projects updated and published quarterly by TRW Systems Group, One Space Park, Redondo Beach, Calif. Orbital parameters at launch are given.

2. Aeronautics and Space Report of the President, National Aeronautics and Space Council, Washington, D.C., a yearly Presidential report to the U.S. Congress that includes statistical data on U.S. and foreign spacecraft and details of U.S. launches. Available from the U.S. Government Printing Office, Washington, D.C.

3. The Radiation Belt and Magnetosphere, by Wilmot N. Hess, Blaisdell Publishing Company, Waltham, Mass., 522-541, 1968. The appendix of this book provides a table of data on satellites launched through June 1966 that were used to make scientific measurements in the magnetosphere.

4. Space Physics, ed. by Donald P. LeGalley and Alan Rosen, John Wiley and Sons, Inc., New York, 522-535, 1964. This book includes a table giving details of satellites used in scientific studies of the radiation belts through 1961 only.

5. Satellite Situation Report, a log of all space objects (spacecraft and fragments) in space, updated monthly by the GSFC Operations Control Center, Greenbelt, Md. Current orbital parameters are given. The report is distributed on a monthly basis by the Office of Public Affairs, Goddard Space Flight Center, Greenbelt, Md.

6. Sky and Telescope, published monthly by Sky Publishing Corp., Cambridge, Mass. A roster of space activity for each previous year appears in the January issue, except for 1970 when the roster appeared in the February issue. The first 5-year summary appeared in the March 1963 issue.

7. "Astronautics: an outline of utility," by Harry O. Ruppe in Advances in Space Science and Technology, 10, Academic Press, N.Y., 139-271, 1970. This reference is a review article on astronautics that includes some general information and statistical data on U.S. and foreign satellites and spacecraft.

REFERENCES

11.1 TECHNIQUES OF RADIATION MEASUREMENT

1. J.A. Van Allen. First public lecture on the discovery of geomagnetically trapped radiation, National Academy of Sciences, Washington, D.C., 1 May 1958.

2. J.A. Van Allen, G.H. Ludwig, E.C. Ray, and C.E. McIlwain. "Observation of High Intensity Radiation by Satellites 1958 Alpha and Gamma," Jet Propulsion, 28, 588, 1958.

3. B.J. O'Brien, C.O. Laughlin, and J.A. Van Allen. "Preliminary Study of the Geomagnetically Trapped Radiation Produced by a High-Altitude Nuclear Explosion on July 9, 1962," Nature, 195, 939, 1962.

4. R.V. Smith, J.B. Reagan, and R.A. Alber. "Use of Scintillation Counters for Space Radiation Measurements," IRE Trans. on Nuc. Sci., NS-9, 386, 1962.

5. C.E. McIlwain. "The Radiation Belts, Natural and Artificial," Sci., 142, 355, 1963.

6. W.L. Imhof and R.V. Smith. "Energy Spectrum of Electrons at Low Altitudes," J. Geophys. Res., 70, 2129, 1965.

7. W.L. Imhof and R.V. Smith. "The Behavior of Trapped Electrons and Protons at the Lower Edge of the Inner Radiation Belt," J. Geophys. Res., 71, 4157, 1966.

8. F.S. Mozer, D.D. Elliott, J.D. Mihalov, G.A. Paulikas, A.L. Vampola, and S.C. Freden. "Preliminary Analysis of the Fluxes and Spectrums of Trapped Particles after the Nuclear Test of July 9, 1962," J. Geophys. Res., 68, 641, 1963.

9. Harry West. "The Trapped Electron Spectra from the Starfish Detonation and from the Outer Belt in the Fall of 1962," Radiation Trapped in the Earth's Magnetic Field, ed. by B.M. McCormac, D. Reidel, 1966.

10. Harry West. "Some Observations of the Trapped Electrons Produced by the Russian High Altitude Nuclear Detonation of October 28, 1962," D. Reidel, 1966.

11. S.C. Freden and G.A. Paulikas. "Trapped Protons at Low Altitudes in the South Atlantic Magnetic Anomaly," J. Geophys. Res., 69, 1259, 1964.

12. W.L. Brown, J.D. Gabbe, and W. Rozenzweig. "Results of the Telstar Radiation Experiments," Bell System Tech. J., 42, 1505, 1963.

13. S.C. Freden and R.S. White. "Protons in the Earth's Magnetic Field," Phys. Rev. Letters, 3, 9,1959; errata 3, 145, 1959.

14. G.H. Nakano and H.H. Heckman. "Evidence for Solar Cycle Changes in the Inner Belt Protons," Phys. Rev. Letters, 20, 806, 1968.

15. H.H. Heckman and G.H. Nakano. "Direct Observation of Mirroring Protons in the South Atlantic Anomaly," Space Research V, ed. by D.G. King-Hele et al, North-Holland Pub. Co., Amsterdam, 329, 1965.

16. J.E. Naugle and D.A. Kniffen. "Flux and Energy Spectra on the Protons in the Inner Van Allen Belt," Phys. Rev. Letters, 7, 3, 1961.

17. W.C. Knudsen and G.W. Sharp. "Evidence for Temperature Stratification in the E Region," J. Geophys. Res., 70, 143, 1965.

18. M.F. Shea, G.B. Shook, J.B. Reagan, L.F. Smith, and T.C. Sanders. "Channel Multiplier Instrumentation for the Measurement of Low Energy Auroral Particles," IEEE, NS-14, 96, 1967.

19. D.S. Evans. "Low Energy Charged Particle Detection Using Continuous Channel Electron Multipliers," RSI, 36, 375, 1965.

20. G. Garmire. "Geomagnetically Trapped Protons with Energies Greater Than 350 Mev," J. Geophys. Res., 68, 2627, 1963.

21. C.E. McIlwain, "Coordinates for Mapping the Distribution of Magnetically Trapped Particles," J. Geophys. Res. 66, 3681, (1961).

22. A.C. Durney, H. Elliott, R.J. Hynds, and J. J. Quenby, "Satellite Observations of the Energetic Particle Flux Produced by the High Altitude Nuclear Explosions of July 9, 1962", Nature 195, 1245, (1962).

23. S.N. Vernov, I.A. Savenko, P.I. Shavrin, "Investigation of the Earth's Radiation Belts in the Region of the Brazilian Magnetic Anomaly at Altitudes of 200-400 Km.", Space Research V, 343, (1965).

24. Yu. I. Galperin, and A.D. Bolyunova, "The Study of the Drastic Changes of the Radiation in the Upper Atmosphere in July, 1962", Space Research V, 446, (1965).

25. L.A. Frank, "A Survey of Electrons E > 40 Kev Beyond 5 Earth Radii with Explorer 14," J. Geophys. Res. 70,1593, (1965).

26. I.B. McDiarmid, J.R. Burrows, E.E. Budzinski and D.C. Rose, "Satellite Measurements in the Starfish Articifial Radiation Zone," Can. J. Phys. 41, 1332, (1963).

27. C.Y. Fan, P. Meyer, and J.A. Simpson, "Dynamics and Structure of the Outer Radiation Belt," J. Geophys. Res. 66, 2607, (1961).

28. J.B. Cladis, L.F. Chase, Jr., W.L. Imhof, and D.J. Knecht, "Energy Spectrum and Angular Distribution of Electrons Trapped in the Geomagnetic Field," J. Geophys. Res. 66, 2297, (1961).

29. C.E. McIlwain, "The Redistribution of Trapped Protons During a Magnetic Storm," Space Research V, 374, (1965).

30. W.L. Imhof and R.V. Smith, "Proton Intensities and Energy Spectrums in the Inner Van Allen Belt," J. Geophys. Res. 69, 91, (1964).

31. J.H. Rowland, J.C. Bakke, W.L. Imhof, and R.V. Smith. "Instrumentation for Space Radiation Measurements II," IEEE, NS-10, 178, 1963.

32. S.C. Freden, J.B. Blake, and G.A. Paulikas. "Spatial Variation of the Trapped Proton Spectrum," J. Geophys. Res., 70, 3113, 1965.

33. R.W. Fillius and C.E. McIlwain. "The Anomalous Energy Spectrum of Protons in the Earth's Radiation Belt," Phys. Rev. Letters, 12, 609, 1964.

34. S.M. Krimigis and J.A. Van Allen. "Geomagnetically Trapped Alpha Particles," J. Geophys. Res., 72, 5779, 1967.

35. G.W. Sharp. "Midlatitude Trough in the Night Ionosphere," J. Geophys. Res., 71, 1345, 1966.

36. J. Valerio. "Protons from 40-110 Mev Observed on Injun 3," J. Geophys. Res., 69, 4949, 1964.

37. R.C. Filz and E. Holeman. "Time and Altitude Dependence of 55 Mev Trapped Protons, August 1961 to June 1964," J. Geophys. Res., 70, 5807, 1965.

38. D.J. William and A.M. Smith. "Daytime Trapped Electron Intensities at High Latitudes at 1100 Kilometers," J. Geophys. Res., 70, 541, 1965.

39. C.O. Bostrom, A.J. Zmuda, and G.F. Pieper. "Trapped Protons in the South Atlantic Magnetic Anomaly, July through December 1961, 2; Comparisons with Nerv and Relay 1 and Discussion of the Energy Spectrum," J. Geophys. Res., 70, 2035, 1965.

11.2 FISSION PHYSICS

1. J. Terrell. "Fission Neutron Spectra and Nuclear Temperatures," Phys. Rev., 113, 527, 1959.

2. A.I. Obukhov and N.A. Perfilov. "Nuclear Fission," Sov. Phys. Usp., 10, 559, 1968.

3. G.N. Walton. "Fission Recoil and its Effects," Progress in Nuclear Physics, 6, 1957.

4. S. Katcoff, J.A. Miskel, and C.W. Stanley. "Ranges in Air and Mass Identification of Plutonium Fission Fragments," Phys. Rev., 74, 631, 1948.

5. H. Munzel, M. Hollstein, and T. Ishimori. "Range and Range Dispersion of Some Fission Products Formed by the Pu^{239} (n_{th}, f) Reaction," Proc. of the Symposium on Physics and Chemistry of Fission Held by the Intern. Atomic Energy Agency in Salzburg, 22 to 26 March 1965, Intern. Atomic Energy Agency, Vienna, Austria.

6. H. Conde and G. During. "Fission-Neutron Spectra of U^{235}, Pu^{239}, and Cf^{252}," Proc. of the Symposium on Physics and Chemistry of Fission Held by the Intern. Atomic Energy Agency in Salzburg, 22 to 26 March 1965, Intern. Atomic Energy Agency, Vienna, Austria.

7. J. Terrell. "Prompt Neutrons from Fission," Proc. of the Symposium on Physics and Chemistry of Fission Held by the Intern. Atomic Energy Agency in Salzburg, 22 to 26 March 1965, Intern. Atomic Energy Agency, Vienna, Austria.

8. G.R. Keepin. "Neutron Data for Reactor Kinetics, 1. Delayed Neutrons from Fission," Nucleonics, 20, 150, 1962.

9. J.W. Kutcher. "An Experimental Study of the Time Dependence of the Beta Spectrum from U^{235} Fission Fragments," Nucl. Sc. and Engr., 26, 435, 1966.

10. H.I. West, Jr. "The Beta Spectra of the Fission Products of U-235, 1 to 300 Seconds after Fission," Trans. American Nuclear Soc., 3, 537, 1960.

11. R.B. Heller, S. Chakravarty, J. Frawley, and M. Silver. "Energy and Time Beta Spectra of Fission Products," Nucleonics, 23, 92, 1965.

12. R.E. Carter, F. Reines, J.J. Wagner, and M.E. Wyman. "Free Antineutrino Absorption Cross Section II. Expected Cross Section from Measurements of Fission Fragments Electron Spectrum," Phys. Rev., 113, 280, 1959.

13. N. Tsoulfanidis. Thesis, Univ. of Illinois, 1968.

14. H. Seyfarth. "Die Mittlere β-Aktivitat der Spaltproduktgesamtheit als Funktion der Zeit nach der Thermischen Spaltung von U^{233}, U^{235}, and Pu^{239}," Nukleonik, 10, 193, 1967.

15. J. Griffin. "Re-evaluation of Optimal Parameters for Post-Fission Beta Decay," LA-2811, Add. II, Los Alamos Scientific Laboratory, Los Alamos, N.M., 1964.

11.3 PROPERTIES OF THE EARTH'S ATMOSPHERE AND IONOSPHERE

1. U.S. Standard Atmosphere, 1962. U.S. Govt. Print. Off., Washington, D.C.

2. U.S. Standard Atmosphere Supplements, 1966. U.S. Govt. Print. Off., Washington, D.C.

3. I. Harris and W. Priester. "Theoretical Models for the Solar-Cycle Variation of the Upper Atmosphere," J. Geophys. Res., 67, 4585-4591, 1962.

4. M. Nicolet. Geophysics. the Earth's Environment, Gordon and Breach, Science Publishers, New York, 201-207, 1963.

5. L.G. Jacchia. "Static Diffusion Models of the Upper Atmosphere with Empirical Temperature Profiles," Smith, Inst. Astrophys. Obs. Spec. Rep., 170, 1-53, 1964.

6. CIRA. COSPAR International Reference Atmosphere 1965, North-Holland Publishing Co., Amsterdam, 1965.

7. K. Moe. A Review of Atmospheric Models in the Altitude Range 100 to 1000 km, paper presented at AIAA 7th Aerospace Sciences Meeting, New York, 20 January 1969.

8. K.S.W. Champion, F.A. Marcos, and J. Slowey. New Model Atmospheres Giving Latitudinal and Seasonal Variations in the Thermosphere, Air Force Cambridge Research Lab., Report AFCRL-67-0330, 1967.

9. A.D. Anderson and W.E. Francis. "The Variation of the Neutral Atmospheric Properties with Local Time and Solar Activity from 100 to 10,000 km," J. Atmosp. Sci., 23, 110-124, 1966.

10. Martin Walt. "The Effects of Atmospheric Collisions on Geomagnetically Trapped Electrons," J. Geophys. Res., 69, 3947-3958, 1964.

11. W.L. Imhof and R.V. Smith. "Longitudinal Variations of High Energy Electrons at Low Altitudes," J. Geophys. Res., 70, 575, 1965.

12. J. Cladis et al. "Search for Possible Loss Processes for Geomagnetically Trapped Particles," Defense Atomic Support Agency, Report 1713, 31 December 1965, 27-32.

13. G.T. Davidson. "Expected Spatial Distribution of Low-Energy Protons Precipitated in the Auroral Zones," J. Geophys. Res., 70, 1062, 1965.

14. A. Hassitt. "An Average Atmosphere for Particles Trapped in the Earth's Magnetic Field," Research Report, Dept. of Physics, Univ. of California at San Diego, La Jolla, Calif., 1965.

15. R.W. Filius. "Trapped Protons of the Inner Radiation Belt," J. Geophys. Res., 71, 97, 1966.

16. R.H. Eather. "Red Shift of Auroral Hydrogen Profiles," J. Geophys. Res., 71, 5027, 1966.

17. W.L. Imhof, J.B. Reagan, and R.V. Smith. "Long-Term Study of Electrons Trapped on Low L Shells," J. Geophys. Res., 72, 2371, 1967.

18. A.D. Anderson. "On the Inexactness of the 10.7-cm Flux from the Sun as an Index of the Total Extreme Ultraviolet Radiation," J. Atmos. Sci., 21, 1-14, 1964.

19. A.D. Anderson. "Long-Term (Solar Cycle) Variation of the Extreme Ultraviolet Radiation and 10.7 Centimeter Flux from the Sun," J. Geophys. Res., 70, 3231-3234, 1965.

20. A.D. Anderson and W.E. Francis. Tables of Neutral Atmospheric Properties as a Function of Solar Activity and Local Time from 90 to 10,000 km, Lockheed Missiles & Space Company, Report 6-75-65-19, 1965.

21. W.E. Francis. "A Least Squares Method of Computing Density-Based Model Atmospheres," J. Atmos. Sci., 23, 431-442, 1966.

22. W.B. Hanson. "Structure of the Ionosphere," Satellite Environment Handbook, Second Edition, Stanford University Press, Stanford, Chapter 21, 1965.

23. H.A. Taylor, H.C. Brinton, M.W. Pharo, and N.K. Rahman. "Thermal Ions in the Exosphere: Evidence of Solar and Geomagnetic Control," J. Geophys. Res., 73, 5521-5533, 1968.

24. H.C. Brinton, R.A. Pickett, and H.A. Taylor. "Thermal Ion Structure of the Plasmasphere," Planet. Space Sci., 16, 899-909, 1968.

25. H.A. Taylor, H.C. Brinton, and M.W. Pharo. "Contraction of the Plasmasphere During Geomagnetically Disturbed Periods," J. Geophys. Res., 73, 961-968, 1968.

SECTION 12

PROGRESS AND PROBLEMS OF THE TRAPPED RADIATION ENVIRONMENT

J.B. Cladis, Lockheed Palo Alto Research Laboratory

A short review will be given of the present understanding of the natural radiation belt and of unknown processes that restrict the ability to predict the distributions of artificially injected electrons.

A considerable improvement in the knowledge of the terrestrial environment has been made since man first wondered about phenomena such as the "northern lights," the "gegenschein," and the "systems of geomagnetic variations." The scientific effort devoted to the study of the upper atmosphere and the magnetosphere has mushroomed since the radiation belt was discovered by Van Allen. The principal constituents of the upper atmosphere have been identified, and data have been obtained on the temporal and spatial distributions of the ionized components. Rocket measurements through the lower ionospere have confirmed the predicted Sq current system. Moreover, nearly simultaneous determinations of ionospheric conductivities (based on measurements of electron density profiles) and electric field distributions (based on Ba cloud measurements) have verified the dynamo theory as the source of this current system. The sources of other ionospheric current systems are still uncertain to various degrees as discussed in Section 5.

The mapping of the earth's field has been extended to radial distances of many earth radii. Relatively near the ecliptic plane, field measurements have been obtained from the magnetopause on the sunward side of the magnetosphere to nearly 1,000 R_E in the antisolar direction. Observations near the magnetopause have been made of dynamical interactions between the field and the solar wind, and of the inflation of the magnetosphere by the entry of charged particles. As discussed in Section 2, models of the geomagnetic field that include the effects of the currents in the magnetopause and in the tail are now available.

Fairly good measurements have been made of the temporal, spatial, and energy distributions of the energetic trapped particles as discussed in Section 4. Mathematical expressions have been derived

to describe the synchrotron radiation emitted by the trapped electrons, and the results have been verified by measurements of the synchrotron radiation emitted by the Starfish electrons (Section 9). Moreover, the daily doses and equivalent 1-MeV electron fluxes produced by the natural trapped particles and by bomb-injected electrons for various satellite orbits and under various shielding thicknesses have been computed. The results are presented in graphical form in Section 8 (also see Section 10).

Extensive measurements of charged particles have been made in interplanetary space (the solar wind), the plasmasheath, and the magnetotail. Observations of particle injections into the outer belt from the magnetotail have been correlated with occurrences of magnetic bays, and rapid transport of protons from the region of the magnetotail to the plasmapause (in about 1 hour) has been found to occur during some magnetic storms. Whether the particles in the outer zone are due principally to these impulsive injections or to the slower diffusion processes discussed in Section 5 is not known.

The "equatorial ring current," which was inferred before the advent of instrumented spacecraft from ground measurements of the magnetic field, has been found to be caused by the rapid inward transport of protons, which was mentioned previously. As discussed in Section 5.5.5, the transport is believed to occur by Bohm diffusion, and the apparent termination of the "flow" at the plasmapause is believed to result from the high loss rate of the protons in that region due to the interaction of the protons with unstable waves.

The serious discrepancies previously associated with the cosmic ray, albedo neutron theory as the source of the high-energy protons in the inner belt have been resolved. Now the distribution of these protons is in general agreement with the equilibrium distribution resulting from this source and the diffusion of the protons along and across field lines.

The neutron-decay theory is not adequate, however, to account for the intensity or the spectrum of the inner-belt electrons. These electrons are believed to result principally from stochastic acceleration events and attendant inward diffusion from the outer boundary of the trapping region.

The artificial radiation belts which have been produced by nuclear detonations at high altitudes have yielded much significant geophysical information. The low-yield devices detonated near $L \approx 2$

formed thin, stable shells which verified the concepts of the particle motion and demonstrated the usefulness of MacIlwain's L-parameter. Moreover, measurements of these injected electrons revealed that the distributions relaxed much more rapidly along the field lines by pitch angle diffusion than across field lines by radial diffusion.

The high-yield Starfish device, which was detonated at $L \approx 1.15$, produced an artificial belt that extended over a wide range of L-values. Observations of the subsequent changes in the energy and angular distributions of the injected electrons yielded valuable information on diffusion and loss rates. A significant finding was that the loss rates and the energy variations of the electrons were in good agreement at $L \leq 1.25$ with the theoretical predictions based on atmospheric scattering. At the higher L-values, appreciably higher loss rates were observed than those predicted by atmospheric scattering alone. The enhanced rates presumably are caused by interactions of the electrons with time-varying magnetic or electric fields as discussed in Section 5. Fairly good evidence now indicates that the inner edge of the "slot" in the electron distribution arises from an anomalously high loss rate in that region due to the interaction of the electrons with unstable waves (Section 5.5.5).

The theory of magnetospheric convection appears to account for many correlated observations in the magnetosphere, such as the energization of plasma in the tail and injection into the auroral zones and the outer trapping region, the inward motion of the plasma sheet, certain ionospheric current systems, and the features of the plasmapause.

Even though the progress made during the past decade has been impressive, many perplexing difficulties remain that are not only of geophysical interest but that have an important bearing on the practical problem of predicting the environment produced by tests of nuclear devices or by a nuclear war. From the material presented in Sections 8 and 10, even the natural environment is found to restrict severely the design of spacecraft systems, especially manned systems. Clearly, the environment produced by a high-yield weapon test at a high altitude would result in damage to tens of the hundreds of satellites that are now in near-earth orbits (Section 11.5). As discussed previously, several satellites were damaged by the trapped radiation produced by Starfish. In the event of a nuclear war, the environment would be much more severe, as discussed in Section 10. However, the uncertainty in the estimate of the maximum flux that the field can contain is large.

By improving the predicted environment, the radiation hardening measures that are taken to assure the survival of a system could be reduced. Such a refinement would improve the system performance and reduce the cost. Significant savings would ensue since hardening against a fission-beta environment and the attendant bremsstrahlung is not a simple matter. A shielding thickness of about 4 grams per square centimeter is required to stop essentially all the electrons. The bremsstrahlung dose [rads (Si)] received through the shield that stops the electrons is reduced only by a factor of 2 by an additional thickness of 6.6 grams per square centimeter of Al. Hence, if the bremsstrahlung intensity is too high over an appreciable volume of sensitive components, the betas may have to be attenuated at the surface of the vehicle using low Z-materials. If this measure still does not reduce sufficiently the bremsstrahlung, magnets may have to be used to prevent the betas from impinging upon the vehicle.

Probably the most pertinent problems are those associated with the motion of the debris and processes that limit the trapping of the beta flux. Some of the former problems are discussed in Section 7 and the latter in Section 5. Generally, an improvement in the estimate of the maximum beta flux requires investigations of (1) plasma instabilities that are produced by the betas, using various distributions of the injected betas and realistic three-dimensional models with appropriate boundary conditions, (2) the effects of the instabilities of the distributions of the betas, (3) the interactions of the betas with magnetic field disturbances, electric fields, and waves (hydromagnetic, electrostatic, and electromagnetic) produced by single and multiple explosions in the upper atmosphere, and (4) the effects on the beta distribution of magnetospheric convection and other disturbances produced by external sources.

Most of these investigations are difficult, and, since appropriate experiments cannot be performed now, the investigations should be supplemented by observations of natural phenomena. Such observations should include the collision-free bow shock; the distribution, intensity, and relaxation mechanisms of naturally injected or redistributed particles in the radiation belts; the plasma instabilities initiated by these fluxes, especially the anomalous resistivity that may be produced by field-aligned currents; and the natural externally driven disturbances (convection, etc.) that cause the redistribution of particles in the radiation belts.

Of course, the remaining problems that are specifically of geophysical interest appear to have grown even more rapidly than problems that have been resolved. Note that although some of the framework of the phenomena which initially attracted man's attention to the upper atmosphere has been delineated, the phenomena themselves are not yet understood satisfactorily.

SECTION 13
SYMBOLS

The symbols that are most helpful in using this handbook are listed and defined in Section 13. The respective sections in which the symbols appear are noted in the right-hand column.

A	area of a surface, or the area of a surface transverse to the magnetic field	1, 3, 7
$\overline{A}$	vector potential	3
A	asymmetric part of a magnetic field fluctuation	5
a	radius of a spherical volume	7
A_i	empirical exponential coefficient in p-n junction current-voltage relation	8
A	atomic weight	8, 11
$A_{[eff]}$	effective antenna area of a receiver	9
A	parameter related to the saturation density of trapped electrons	9
$\overline{B}$ or B	magnetic field intensity	1, 2, 3, 4, 5, 7, 9, 11
B_m	magnetic field intensity at the mirror point of a trapped particle	1, 3, 5
B_o	magnetic field intensity at the equator in a dipole field	2, 3, 5, 9
B_E	mean equatorial field intensity at the surface of the earth = 0.312 gauss	2, 3, 5
$\overline{B}_1$	oscillating magnetic field associated with an electromagnetic wave	5

$B_{\parallel}$, $B_{\perp}$	amplitudes, measured parallel and transverse to the steady magnetic field, of the magnetic part of an electromagnetic wave	5
b	base transport factor of a transistor	8
b	brightness of synchrotron emission	9
B_r	radial magnetic field component in spherical coordinates	2, 11
B_θ	polar magnetic field component in spherical coordinates	2, 11
B_ϕ	azimuthal magnetic field component in spherical coordinates	2, 11
B_R	radial magnetic field component in cylindrical coordinates	2
B_z	"vertical" magnetic field component in cylindrical coordinates	2
c	speed of light = 2.9979×10^{10} centimeters per second	3, 5, 9
C_s	Störmer unit of distance	3
C	arbitrary constant	5
C	gate-to-substrate capacitance per unit area for FET transistor	8
D	magnetic declination	2
$\mathcal{D}$	function of pitch angle that appears in the drift velocity formulas of Section 3	3
D	diffusion coefficient (= $\mu(kT)/q$: Section 8)	5, 8
D	angular azimuthal drift velocity divided by total particle energy	7
d_t	thickness of transition region of p-n junction	8
d	solar cell diffused layer depth	8
d_c	total depth of a solar cell	8

$\overline{E}$ or E	electric field strength	1, 3, 5
E	total energy of a particle	3, 5, 7, 9
e	electrical charge of an electron	3, 5, 9
E_i	induced electric field	3
exp	exponential function [usually written $e^x = \exp(x)$]	5
erf	error function	5
$\overline{E}_1$	oscillating electric field associated with an electromagnetic wave	5
$E_\parallel$, $E_\perp$	amplitudes, measured parallel and transverse to the steady magnetic field, of the electrical part of an electromagnetic wave	5
E	kinetic energy of a particle (also T or T)	4, 8
E_R	reference particle energy	8
E_d	effective energy for atomic displacement	8
E_c	minimum energy required for an incident particle to displace an atom	8
E_f	effective particle-damaging energy	8
$\overline{F}$ or F	mechanical force on a particle	3
$\overline{F}_c$	force experienced by a particle in a collision with another particle	3
$\overline{F}_\parallel$, $\overline{F}_\perp$	components of a force parallel and transverse to the magnetic field	3
$\int$	arbitrary function	3
f	particle distribution function, density of particles in phase space	3
F	net flux of particles crossing a surface	3
f_k	distribution function of the k'th component of a gas	3

F_d	diamagnetic force on a volume of gas	7
F_G	gravitational force on a volume of gas	7
f_α	transistor α cutoff frequence	8
f_τ	transistor gain frequency bandwidth product	8
f	electron hole volume generation rate	8
$\bar{G}$	gravitational field	3
G	function used in evaluating Fokker-Planck coefficients for slowing of a fast particle	5
g	factor of the particle distribution function	5
g	gravitational acceleration	7, 11
g_m	FET channel transconductance	8
g_n^m	gaussian coefficients (g_n^m, h_n^m)	2
H	horizontal intensity	2
H	magnetic field intensity	3
H	Hamiltonian of a particle or system of particles	3
h	altitude	3, 5, 7, 11
$\hbar$	Planck's constant divided by 2π	5
H	atmospheric scale height	5, 7
h	factor of the particle distribution function	5
h^*	altitude of a nuclear detonation or electron injection event	7
h_{FE}	common emitter current gain of a transistor (also β)	8
h_n^m	gaussian coefficients (g_n^m, h_n^m)	2

I	inclination of a magnetic field line measured from the horizontal	2, 3, 5, 7
I	degenerate integral invariant	3
i	index, e, g, , x_i	3
i	$= \sqrt{-1}$	3, 5
J	degenerate integral invariant in units of R_o	3
I^*	mean excitation-ionization potential	5
I_{sc}	short circuit current of a solar cell	8
I_{CBO}	collector-base reverse leakage current of a transistor	8
I	light-generated current density in the equivalent circuit model for a solar cell	8
I_s	p-n junction reverse-bias leakage current	8
I_{si}	i'th component of the p-n junction reverse-bias leakage current	8
I_E	emitter current density of a transistor	8
I_{ct}	collector current of a transistor being tested	8
I_D	drain current of an FET	8
I_{SGO}	gate-to-substrate leakage current	8
$\bar{J}$ or J	electrical current density	2, 3, 5
j_i	Hamilton-Jacobi action integral	3
J	second adiabatic invariant	1, 3, 5
J	omnidirectional flux of streaming particles	3, 4, 5, 7, 3
j	intensity (or flux) of particles streaming in some arbitrary direction	3, 5

j	index, e.g., x_j	3, 5
J	Jacobian of a coordinate transformation	5
j_o	streaming particle intensity at the equator	5
J_o	omnidirectional flux at the equator	5
$\overline{J}_1$	oscillating electrical current associated with an electromagnetic wave	5
$J_{\parallel}, J_{\perp}$	amplitudes, measured parallel and transverse to the steady magnetic field, of the current fluctuations associated with an electromagnetic wave	5
J_{sc}	short circuit current density of a solar cell	8
J_n	Bessel function of order n	9
k	index denoting particle species, e.g., x_k	3
k	Boltzmann's constant	3, 5, 8, 9, 11
K_τ	electron or proton lifetime damage coefficient	8
$K_{\tau e}$	electron lifetime damage coefficient	8
$K_{\tau p}$	proton lifetime damage coefficient	8
K_L	diffusion length damage coefficient	8
K_s	surface damage coefficient	8
K_b	bulk damage coefficient	8
$K_{n/3}$	Bessel function of the second kind	9
L	McIlwain L-parameter, or R_o/R_E	1, 2, 3, 4, 5, 7, 11
L	minority carrier diffusion length for electrons or holes	8

L_n	minority carrier diffusion length for electrons	8
L_p	minority carrier diffusion length for holes	8
l	length of the source to drain channel in a MOSFET	8
m	mass of a particle, or the total mass of a body or collection of particles	1, 2, 3, 4
M_E	magnetic dipole moment of the earth	3
M	magnetic moment of a charged particle in a magnetic field, the first adiabatic invariant	1, 2, 3, 5
m_k	mass of a particle of species k	3
m_r	reduced mass	5
m_e	mass of an electron	3, 5
m_p	mass of a proton	3, 5
m_1, m_2	integer numbers that appear in the treatment of the dilution of trapped electrons drifting away from a finite source region	7
m_o	rest mass of an electron (= m_e)	9
m	mean molecular mass of the atmosphere	11
n_+, n_-	number densities of positively and negatively charged particles, respectively	3
n	exponent of some parameter, (e.g., x^n	3
N	total number of particles in some volume element	3, 7
n_e	number density of electrons	3, 5
n_k	number density of the k'th component of a gas	3

n_i	number density of positive ions or protons	3, 5
n	number density of particles of arbitrary species	1, 2, 3, 4, 11
n_b	number density of bound electrons (all species)	5
N_o	number of trapped particles in a magnetic flux tube per unit cross-sectional area at the equator	5
$n(\delta n)$	mirror point density of trapped particles	7
n	rate of production of electrons (per unit volume)	7
n	conduction electron density	8
n_i	intrinsic (undoped) semiconductor carrier density	8
n_o	thermal equilibrium conduction electron density	8
N_p	incident photon flux per unit wavelength	8
N	fan-out of an IC device	8
$dn/d\Phi$	majority carrier removal rate per unit incident particle fluence	8
N_s	atomic density	8
Δn	excess carrier density = $n - n_o$	8
n	integer	9
n_T	total number density of electrons	9
n	number density of electrons per unit energy	9
$\overline{p}$ or p	momentum of a particle	1, 3, 5, 11
$\overline{p}_{\parallel}$, $\overline{p}_{\perp}$	momentum components parallel and transverse to a magnetic field	3
p_i	generalized canonical momentum coordinate	3

$\bar{\bar{P}}_k$	pressure tensor of the k'th component of a gas	3
P_A	power spectral density of symmetric magnetic field fluctuations	5
P_k	power spectral density of the k'th component of the harmonic decomposition of electric field fluctuations	5
P	power spectral density	5, 9
p_w	momentum of a charged particle relative to the phase velocity of a transverse plasma wave	5
p_R	momentum at which trapped particles are in resonance with a plasma wave	5
p	density of conduction holes	8
p_o	density of conduction holes in thermal equilibrium	8
P_m	maximum power of a solar cell	8
P_n	power radiated as syncrotron radiation at the n'th harmonic of an electron's gyro-frequency	9
$\bar{\bar{P}}$	pressure tensor	5
P_n^m	Schmidt functions	2
$P_{n,m}$	associated Legendre functions	2
q	charge on an individual particle	3, 5
q_i	generalized canonical position coordinate	3
Q	total electrical charge of a body or assembly of particles	3
q	strength of a source of particles per unit solid angle (per volume element per unit time)	5

Q	strength of a source of particles (per volume element per unit time)	5
q	electrical charge of an electron (= e)	8
q	syncrotron radiation power emitted per unit volume	9
R	radial distance in cylindrical coodrinates (R, ϕ, z)	3
R_o	equatorial intersection of a dipole field line	3, 5
R	range of a fast particle	5
R_w	reflection coefficient for plasma waves entering the inosphere	5
R	beta decay rate of fission debris	7
R	reflection coefficient for photons of arbitrary wavelength incident on silicon	8
R	recombination rate at a surface	8
R_i	resistance connected to V_{cc} in a base circuit	8
R_B	resistance connected to the largest negative supply voltage in a base circuit	8
R_c	resistance in a collector circuit	8
r	radial distance in spherical coordinates (r, θ, ϕ)	2, 3, 5, 9
R	instantaneous radius of curvature of an electron's trajectory	9
R_E	radial distance in units of earth radii	1, 2, 4, 11
R or r	radial distance in R, λ coordinate system	2, 4, 11
R_b	geocentric distance to the magnetosphere boundary along the earth-sun line	2
s	distance measured along the trajectory of a particle	1, 3, 5

S	distance measured along a field line	2, 3, 5, 7
$\mathcal{S}$	total length of the trajectory of a trapped particle (between successive reflections) in units of R_o	3
S_m	distance along a field line from the equator to the mirror point of a trapped particle	3
S	probability of an arbitrary deflection	5
S	symmetric part of a magnetic field fluctuation	5
s	recombination velocity at a surface	8
S	radiation flux of syncrotron emission	9
T or T	kinetic energy of a particle = $E - mc^2$	3, 5, 7, 9, 11
T	temperature	3, 5, 8, 11
t_b or T	bounce period of a trapped particle	3, 5, 7, 11
t_d	azimuthal drift period of a particle trapped in a magnetic field with azimuthal symmetry (a dipole field)	3, 5, 7
t	time	3, 5, 7, 9, 11
T_e	temperature of the electron component of a gas	3
$\bar{\bar{T}}$	Maxwell stress tensor	5
t_w	lifetime of a plasma wave in the trapped particle belts	5
t	cover slide thickness of a solar cell	8
T_b	brightness temperature of a radiation emitter	9
$\bar{u}_k$	streaming velocity of the k'th component of a gas	3
u_i	generalized position coordinate	5
U	parameter that appears in the treatment of interactions of trapped protons with plasma waves	5

U	drift dilution factor of injected electrons	7
U	surface potential of a semiconductor	8
u	streaming velocity of the solar wind	2
$\bar{v}$ or v	velocity of a particle	3, 5, 7, 9
V_D	the drift velocity perpendicular to the magnetic field lines or the $\bar{E} \times \bar{B}$ drift velocity	3
V_G	gravitational drift velocity of trapped particles	3
V_c	field line curvature drift velocity	3
V_g	gradient-B drift velocity or the total drift velocity due to field line curvature and the field gradient	1, 3
$\bar{v}_{\parallel}, \bar{v}_{\perp}$	components of velocity parallel and transverse to the magnetic field	3
V_R	radial velocity of dipole field lines during a change in the field intensity	3
v_i	i'th component of a velocity vector	3
$\bar{V}$	total mass velocity or fluid velocity of a gas	1, 3, 4
V_m	velocity along the direction of the magnetic field of a moving mirror point	5
V_A	Alfvén velocity	5
V_p	phase velocity of an electromagnetic wave	5
$V_{CE(SAT)}$	collector-emitter saturation voltage of a transistor	8
V_{mp}	voltage at maximum power point of a solar cell	8
V_G	gate voltage of a FET	8
V_T	turn-on voltage of a FET	8

V_{ds}	source-to-drain voltage of a FET	8
V_{cc}	supply voltage	8
V_{BE}	base-to-emitter voltage of a transistor	8
V	volume between earth and a given shell of field lines	2
w_i	generalized coordinate canonically conjugate to an action integral	3
W_k	normalized probability that a reaction with a particle of species k will result in an arbitrary change in the trajectory of a specified particle	5
W	function used in evaluating the growth rate of plasma waves	5
w	base region width of a transistor	8
W_i	energy-dependent damage weighting function for the i'th particle species	8
W_l	depth of the source to drain channel in a MOSFET	8
W_Ψ	ratio of syncrotron emission in two directions	9
$\bar{x}$	spatial position of a particle	3
x	coordinate in a rectangular coordinate system (x, y, z)	2, 3
x	distance along a ray path of synchrotron emission	9
X	north component of the geomagnetic field	2
y	coordinate in a rectangular coordinate system (x, y, z)	2, 3
Y	function used in evaluating the losses of trapped electrons due to pitch angle deflections	5

Y	east component of the geomagnetic fields	2
Y_F	fission yield of a nuclear detonation	7
z	"vertical" coordinate in rectangular (x, y, z) or cylindrical (R, ϕ, z) coordinates	2, 3
Z_k	atomic number or number of orbital electrons in an atom of species k	5
Z	parameter related to the geometry of synchrotron emission	9
Z	atomic number	11
Z	vertical component of the geomagnetic field	2
α_p	pitch angle of a charged particle in a magnetic field	3, 5, 7
α_c	equatorial pitch angle of a trapped particle that mirrors at the top of the atmosphere, the cutoff pitch angle	3, 5, 7
α_b	pitch angle at the equatorial crossing of a trapped particle	1, 2, 3, 5, 7, 9
α	Euler potential (α, β, χ)	3, 5
α_s	absorptance integrated over the solar spectrum	8
α	absorption coefficient for photons of arbitrary wavelength in silicon	8
α_l	low-frequency common base current gain of a transistor	8
α	pitch angle of a charged particle in a magnetic field	1, 9
β	Euler potential (α, β, χ)	3, 5
β_P	ratio of the transverse components of the pressure tensor and the Maxwell stress tensor, the ratio of particle pressure to magnetic pressure	5, 7

β	common emitter current gain of a transistor	8
β	ratio of particle velocity to the speed of light	9
γ	relativistic dilation factor	3, 5, 9
Γ	Störmer "angular momentum" parameter	3
Γ	function used in evaluating the radial diffusion coefficient of trapped particles	5
γ_w	effective relativistic dilation factor for a traveling wave	5
γ_1	emitted injection efficiency for a bipolar transistor	8
γ_s	series resistance in the equivalent circuit of a solar cell	8
δ	small increment in an arbitrary quantity, e.g., δx	7
$\langle \Delta x \rangle$	first-order Fokker-Planck coefficient for expected changes in the quantity x	5
$\langle \Delta x \Delta y \rangle$	second-order Fokker-Planck coefficient for expected changes in the quantities x and y	5
δ	characteristic mean energy absorbed in the creation of one electron hole pair	8
δ_1	emitter surface recombination factor for a bipolar transistor	8
δ	Dirac delta function	9
Δ	angle between an observer's line of sight and the zenith	9
ϵ, ϵ_i	dimensionless parameter much less than 1	3
ϵ	growth or damping rate for plasma waves	5

ϵ	trapping fraction of particles injected into radiation belts	7
ϵ_{th}	thermal emissivity	8
$\epsilon(E)$	stopping power	8
ζ	angle	5
ζ	parameter that appears in the formula for power radiated as syncrotron emission	9
η	fraction of a trapped protron trajectory that is accessible to decaying neutrons	5
η_d, η	displacement density per unit of incident particle fluence	8
θ	polar angle in spherical coordinates (r, θ, ϕ) = 90 degrees latitude	2, 3, 5, 9
Θ	scattering angle measured in the center of mass reference frame of two particles	5
Θ	invariant colatitude = 90-Λ	4
k	wave number of an electromagnetic wave = 2π divided by wavelength	5
λ	latitude	2, 3, 4, 5, 7, 11
λ_D	Debye length	3, 5
λ_m	latitude of the mirror point of a trapped particle	3, 5, 7
Λ	parameter used in evaluating Fokker-Planck coefficients for the slowing of a fast particle	5
λ_c	critical or cutoff latitude of trapped particles that mirror at the top of the atmosphere	7
λ^*	latitude of a nuclear detonation	7
Λ	invariant latitude	2, 4

μ	cosine of the pitch angle of a trapped particle	3, 5, 7
μ_o	cosine of the equatorial pitch angle of a trapped particle	3, 5
μ_c	cosine of the critical or cutoff pitch angle; trapped particles with larger μ are lost in the atmosphere	5, 7, 8
μ	carrier mobility, channel (majority carrier) mobility of FET's	8
ν_e	"linear" gyro-frequency of an electron	3
ν_i	"linear" gyro-frequency of a positive ion or proton	3
ν_c	frequency of collisions between particles	3, 5
ν_e	frequency of collisions between electrons and all heavy particles (ions and neutral particles)	3
ν_i	frequency of collisions between positive ions and neutral particles	3
ν	arbitrary frequency	5, 9
ν_m	frequency of encounters of a trapped particle with a moving mirror region	5
ν	mean number of secondary displacements per unit incident primary displacement	8
Ξ	constant of integration in Störmer orbit theory	3
ξ	angle between an observer's line of sight and the magnetic field lines, or $\xi = \sin \lambda$	2, 9
ρ_c	gyro-radius of a charged particle in a magnetic field	3, 9
ρ	mass density of a gas or material	5, 8
ρ^*	mass density of the atmosphere at the location of a nuclear detonation	7

σ	electrical conductivity	3
$\bar{\bar{\sigma}}$	electrical conductivity tensor	3
σ_o	specific electrical conductivity	3
σ_1	Pederson conductivity	3
σ_2	Hall conductivity	3
σ_k	cross section for reactions of a specified particle with particles of species k	5
σ_{10}	charge-exchange cross section of a stream of atoms or molecules	7
σ_{01}	ionization cross section of a stream of atoms or molecules	7
σ_d	cross section for atomic displacement	8
τ_E	energy-loss lifetime of a fast particle	5
τ_D	deflection lifetime of a fast particle	5
τ	lifetime of a trapped particle	4, 5
τ_a	lifetime of a trapped particle according to atmospheric losses alone	5
τ	minority carrier lifetime	8
ϕ	azimuthal angle in spherical (r, θ, ϕ) or cylindrical (R, ϕ, z) coordinates	3, 9, 11
Φ	magnetic flux across a surface or the third adiabatic invariant	1, 3
Φ_1, Φ_2	longitudes of the edges of a region where electrons are injected into the trapping region	7
Φ	particle fluence: the omnidirectional flux integrated over time	8
Φ_{eq}	DENI equivalent fluence at some arbitrary energy	8

Φ_{th}	threshold voltage for failure of a DTL gate	8
χ	third Euler potential (α, β, χ)	3
Ψ	electrical potential	3
ψ	azimuthal angle referred to a field line	5
ψ	phase correction in the harmonic decomposition of a fluctuating field into cosine terms	5
ψ	phase angle of a wave expressed in since and cosine terms	5
Ψ	$= d\Phi/dE$	8
Ψ	angle between the direction of radiation emission and the instantaneous orbital plane of an electron	9
$\Psi_{1/2}$	beam half-width of syncrotron emission	9
Ψ_m	magnetic potential	2
ω_c	gyro-frequency or cyclotron frequency of a charged particle in a magnetic field (angular frequency)	3, 5, 9
ω_e	gryo-frequency of an electron	3
ω_i	gyro-frequency of a positive ion or proton	3
ω_d	azimuthal drift angular velocity of a trapped particle	3
Ω	solid angle	3, 5, 9
ω	arbitrary angular frequency	3, 9
ω_{pe}	plasma frequency for the electron component of a plasma	5
ω_{pi}	plasma frequency for the positive ion component of a plasma	5

ω_p	plasma frequency	5
Ω_p	total plasma frequency, electrons and ions	5
ω_{LH}	lower hybrid resonant frequency	5

SECTION 14
USEFUL CONSTANTS AND CONVERSION FACTORS

c	speed of light	2.9979×10^{10} cm/sec
e	electrical charge of an electron	4.803×10^{-10} esu
m_e	mass of an electron	9.108×10^{-28} g
m_p	mass of a proton	1.6724×10^{-24} g
m_p/m_e	ratio of proton and electron masses	1,836.1
e/m_e		5.273×10^{17} esu/g
$m_e c^2$	rest-mass energy of an electron	0.5110 MeV
$m_p c^2$	rest-mass energy of a proton	0.9382 GeV
G	universal gravitation constant	6.668×10^{-8} cm^4/sec
h	Planck's constant	6.625×10^{-27} erg sec
$\hbar$	$= h/2\pi$	1.0544×10^{-27} erg sec
		5.817×10^{-16} eV sec

k	Boltzmann's constant	1.3805×10^{-16} erg/K
		8.617×10^{-5} eV/K
1/k		1.1605×10^{4}/KeV
A	Avogrado's number	6.02×10^{23} molecules/g
	ergs per million eV	1.6021×10^{-12} erg/MeV
	rest-mass energy per unit atomic mass	1.4918×10^{-3} erg/AMU
		931.1 MeV
	speed of a 1-eV electron	5.931×10^{7} cm/sec
	cgs momentum units per MeV/c	5.344×10^{-17} gm cm/sec/MeV/c
	radius of gyration (B = 0.1 gauss)	
	electron: 1 KeV	0.01067 km
	1 MeV	0.4743 km
	proton: 1 KeV	0.4569 km
	1 MeV	14.45 km
	rest mass energy per gram	5.610×10^{26} MeV/g
	energy per kiloton of TNT	4.2×10^{19} erg/KT
		2.6×10^{25} MeV/KT

R_E	the radius of the earth (mean)	6.371×10^8 cm
M_E	the magnetic dipole moment of the earth	8.07×10^{25} gauss cm^3
B_E	The mean surface equatorial field	0.312 gauss
	1 day (solar)	86,400.0 sec
	1 day (sidereal)	86,164.1 sec
	1 year (sidereal)	3.155815×10^7 sec
	mean sunspot cycle period	11.04 yr
S	solar constant, the total radiation flux received at the earth	1.388×10^6 erg/cm^2/sec
	escape velocity from earth's gravitational field	11.19 km/sec
	velocity of particles streaming from sun	
	great storms (S.C.)	1,600 km/sec
	minor sunspot streams	600 km/sec
	recurrent storms	500 km/sec
	density of cloud of solar particles causing storm of magnetic intensity Ap	$2 \times Ap/cm^3$

cosmic ray flux
outside earth's
magnetic field

sunspot maximum	$0.6/cm^2/sec$ ($\sim$ 5 GeV/cm^2/sec)
sunspot minimum	$0.3/cm^2/sec$ ($\sim$ 5 GeV/cm^2/sec)

Most of these numbers were extracted from Astrophysical Quantities, C.W. Allen, Athlone Press, U. of London, 1963, which is highly recommended as a source of interesting data of a generally useful nature.

SECTION 15

INDEX

-A-

-B-

-C-

-D-

-G-

-M-

-N-

-T-